UNIVERSIDAD AUTÓNOMA DE MADRID
DEPARTAMENTO DE FÍSICA DE LA MATERIA CONDENSADA

PHONONS AND ELECTRONS IN 2D MATERIALS AND LAYERED STRUCTURES

Tesis doctoral presentada por
BRUNO ANTÓNIO CAMPOS AMORIM

Directores:

PROF. FRANCISCO GUINEA LÓPEZ

PROF. NUNO MIGUEL MACHADO REIS PERES

Tutor:

PROF. GUILLERMO GÓMEZ SANTOS

Madrid, Octubre 2016

Bruno Amorim acknowledges financial support
from Fundação para a Ciência e a Tecnologia, Portugal,
through grant SFRH/BD/78987/2011

Aos meus pais.

A ti, Mariana.

ABSTRACT

This thesis is focused on the theoretical study of the mechanical and electronic properties of two-dimensional (2D) crystals, such as graphene, and of layered materials based on them, with emphasizes on both fundamental physics and on potential applications. We start on the study of mechanical properties of free 2D crystals, moving then to mechanical and electronic transport properties of 2D crystals, in particular graphene, supported by a substrate. Then we move to layered structures formed by 2D crystals, studying the phenomena of Coulomb drag and electronic vertical tunneling transport.

This thesis is split into two main parts. In the first one we study the mechanical properties of 2D crystals, or crystalline membranes. We start by studying the effect of anharmonicities and quantum fluctuations to the dispersion relation of the lattice vibrations, in particular of out-of-plane vibrations, and how these affect the thermodynamics properties of thermal expansion and specific heat. The we consider 2D crystals supported by a substrate. We study the spectral properties of the out-of-plane vibrations of the 2D crystal, when these are coupled to the lattice degrees of freedom of the substrate. We also study how the thermal expansion of the 2D crystal cannot be considered as an intrinsic property, but instead, becomes dependent on the substrate that supports it.

In the second part of this thesis, we focus on electronic transport phenomena in 2D crystals and layered structures. We pay special attention to graphene and graphene based structures. We start by studying the limits imposed by electronic scattering by lattice vibrations to the resistivity of graphene. In particular, we study the role of scattering by in-plane and out-of-plane vibrations both in suspend and supported graphene samples, comparing the relative importance of the two in both cases. Next we move to electronic transport phenomena in layered structures. We study the phenomena of Coulomb drag between two parallel arbitrary metallic layers. Then we specialize to the case of drag between two graphene layers and study the effect of polar substrate phonons to drag. We finally study the phenomena of vertical tunneling transport in van der Waals structures, specializing graphene–hexagonal boron nitride–graphene vertical structures. We study how lattice misalignment between the graphene layers and simultaneous energy and momentum conservation in the tunneling process leads to the occurrence of negative differential conductance in these devices. We then show that, by controlling the relative alignment between the graphene layers and the boron nitride slab, processes involving the transference of momentum by the boron nitride crystal can lead to the occurrence of multiple negative differential conductance regions in the I-V characteristics of the device. The effect of scattering by optical phonons of the structure is also analyzed and we show that it opens up new inelastic tunneling channels, which manifest themselves as sharp features in the low temperature I-V characteristics of the device.

RESUMEN

Esta tesis se centra en el estudio teórico de las propiedades mecánicas y electrónicas de cristales bidimensionales (2D), como el grafeno, y de estructuras en capas basadas en ellos, con énfasis tanto en la física fundamental como en las aplicaciones potenciales. Comenzamos con en el estudio de las propiedades mecánicas de los cristales 2D libres, siguiendo luego con las propiedades mecánicas y electrónicas de transporte de cristales 2D, en particular el grafeno, apoyados sobre un sustrato. A continuación, pasamos a estructuras en capas formadas por cristales 2D, estudiando los fenómenos de fricción de Coulomb y transporte electrónico vertical por efecto de túnel.

Esta tesis se divide en dos partes principales. En la primera estudiamos las propiedades mecánicas de los cristales 2D, o membranas cristalinas. Empezamos por estudiar el efecto de las no linealidades y las fluctuaciones cuánticas en la relación de dispersión de las vibraciones de la red, en particular, de las vibraciones fuera del plano, y cómo éstas afectan las propiedades termodinámicas de la expansión térmica y el calor específico. A continuación, consideramos cristales 2D apoyados sobre un sustrato. Estudiamos las propiedades espectrales de las vibraciones fuera del plano del cristal 2D cuando éstos están acoplados a los grados de libertad del sustrato. También estudiamos cómo la expansión térmica del cristal 2D no se puede considerar como una propiedad intrínseca, sino que depende del sustrato que la soporta.

En la segunda parte de la tesis nos centramos en los fenómenos de transporte electrónico en cristales 2D y estructuras en capas. Prestamos especial atención al grafeno y a las estructuras basadas en él. Empezamos por el estudio de los límites impuestos a la resistividad del grafeno por la dispersión electrónica causada por vibraciones de la red. En particular, estudiamos el papel de la dispersión por vibraciones en y fuera del plano, tanto en muestras suspendidas como en muestras apoyadas sobre un sustrato, compararando la importancia relativa de los dos en ambos casos. A continuación pasamos a fenómenos de transporte electrónico en estructuras formadas por múltiples capas. Estudiamos los fenómenos de fricción de Coulomb entre dos capas metálicas paralelas arbitrarias. Después, nos especializamos en el caso de la fricción entre dos capas de grafeno y estudiamos el efecto de fonones de sustratos polares en la fricción. Finalmente estudiamos los fenómenos de transporte vertical por efecto de túnel en estructuras de van der Waals, en particular estructuras verticales de grafeno–nitruro de boro hexagonal–grafeno. Estudiamos la forma como la desalineación entre las capas de grafeno y la conservación simultánea de la energía y del momento en el proceso de túnel lleva a la aparición de conductancia diferencial negativa en estos dispositivos. A continuación, mostramos que, mediante el control de la alineación relativa entre las capas de grafeno y la losa de nitruro de boro, los procesos que llevan a la transferencia de momento por el cristal de nitruro de boro pueden dar lugar a la aparición de múltiples regiones de conductancia diferencial negativa en las características I-V del dispositivo. El efecto de la dispersión por fonones ópticos de la estructura también se analiza y se muestra que abre nuevos canales de túneles inelásticos, que se manifiestan marcadamente en las características I-V del dispositivo a bajas temperaturas.

PUBLICATIONS

The research performed during the development of this thesis lead to the following publications:

1. *On Coulomb drag in double layer systems*
   Bruno Amorim and N. M. R. Peres
   Journal of Physics: Condensed Matter **24**, 335602 (2012)

2. *Coulomb drag in graphene–boron nitride heterostructures: Effect of virtual phonon exchange*
   Bruno Amorim, Jürgen Schiefele, Fernando Sols and Francisco Guinea
   Physical Review B **86**, 125448 (2012)

3. *Flexural mode of graphene on a substrate*
   Bruno Amorim and Francisco Guinea
   Physical Review B **88**, 115418 (2013)

4. *Thermodynamics of quantum crystalline membranes*
   B. Amorim, R. Roldán, E. Cappelluti, A. Fasolino, F. Guinea and M. I. Katsnelson
   Physical Review B **89**, 224307 (2014)

5. *Reply to "Comment on 'Thermodynamics of quantum crystalline membranes"'*
   B. Amorim, R. Roldán, E. Cappelluti, A. Fasolino, F. Guinea and M. I. Katsnelson
   Physical Review B **90**, 176302 (2014)

6. *Thermodynamical Properties and Stability of Crystalline Membranes in the Quantum Regime*
   B. Amorim, R. Roldán, E. Cappelluti, A. Fasolino, F. Guinea and M. I. Katsnelson
   MRS Proceedings **1727**, mrsf14-1727-k03-03 (2015)

7. *Multiple negative differential conductance regions and inelastic phonon assisted tunneling in graphene/h-BN/graphene structures*
   B. Amorim, R. M. Ribeiro and N. M. R. Peres
   Physical Review B **93**, 235403 (2016)

Other publications during this period

1. *Active magneto-optical control of spontaneous emission in graphene*
   W. J. Kort-Kamp, B. Amorim, G. Bastos, F. A. Pinheiro, F. S. S. Rosa, N. M. R. Peres and C. Farina
   Physical Review B **92**, 205415 (2015)

2. *Novel effects of strains in graphene and other two dimensional materials*
   B. Amorim, A. Cortijo, F. de Juan, A. G. Grushin, F. Guinea, A. Gutiérrez-Rubio, H. Ochoa, V. Parente, R. Roldán, P. San-Jose, J. Schiefele, M. Sturla and M. A. H. Vozmediano
   Physics Reports **617**, 1–54 (2016)

ACKNOWLEDGEMENTS

This was tough, but this thesis has finally reached its end. And it is now time to thank all the people that helped me in this endeavour.

During my PhD I was fortunate enough to work not in one, but in two excellent research groups: Paco's group (at the time) at ICMM in Madrid and Nuno's group at Minho University in Braga. So first of all, I must thank my two supervisors, Paco and Nuno, two excellent scientists and human beings. When you work with the best you are always at risk of learning, and indeed they have taught me much. It was a honour working with you.

The list of people at ICMM whom I have to thank is a long one. I will start with Jürgen Schiefele, with whom I worked in the early stages of my PhD.

I would also like to express my deepest gratitude towards Rafael Róldan and Emmanuelle Capelluti, which combine being great researchers with being great people and with whom it was, and I hope will continue to be in the future, a pleasure working with.

A special thanks to my PhD brothers, Hector Ochoa and Ángel Gutierrez, for the long coffee breaks which I will always remember fondly. I must also add to these two Jose Silva, as the times when we was visiting Madrid were always fun times. I must also no forget my younger PhD siblings: Francesca, Ignacio and Luis.

I am very grateful to Geli and Alberto for always being available to talk, about physics or otherwise.

I must also thank all the other people who contributed to the good memories I have from ICMM: Maurício, Yago, Luca, Laura, Vicenzo, Pablo, Elsa, Ramón, Bélen, Leni, Maria José and Pilar.

The list of people from Minho University whom I must thank is also not small. I will start by thanking my two PhD brothers from Nuno's side, Paulo André Gonçalves and André Chaves, for making an empty university during summer months such an enjoyable place.

I would also like to thank João Viana, Ricardo Ribeiro, Jaime Santos, Yuliy Bludov and Mikhail Vasilevskiy which helped make my period in Braga such a great time.

I must also thank all the other collaborators with whom I had the pleasure to work during these years: Fernando Sols, Mikhail Katsnelson, Annalisa Fasolino, Wilton Kort-Kamp, Carlos Farina, Felipe Rosa, Felipe Pinheiro and Guilherme Bastos.

I would also like to thank Tobias Stauber and Guillermo Gómez for the time they spent as my tutors and all the support they provided me throughout these years.

I will also take this opportunity to express my gratitude towards Joaquín Rossier for hiring me to INL in Braga, during a period when I mostly focused on writing this thesis. I also want to thank José Lado and Noel García for receiving me during my period at INL and making me appreciate numerical tight-binding models.

I must also not forget my two room mates in Madrid, Rui and Sebástian, which helped Madrid fell a bit like home to me. Rui, não me esquecerei das longas partidas de Dead of Alive. Sebastián, thanks for the long conversations (and helping me translate the abstract and the conclusions of this thesis into Spanish). I would also like to thank Edwin, who together with Sebastián, let me stay at their place in my time of direst need.

Acima de tudo devo agradecer à minha família. Aos meus pais, por tudo o que fizeram por mim até agora. Obrigado por me apoiarem em todos os aspectos da minha vida. Tudo o que consegui até agora teria sido impossível sem a vossa ajuda. Ao meu irmão, pelas longas conversas, por ser um amigo e ao mesmo tempo uma inspiração. E a ti Mariana. Por estes longos anos em que me aturas e pelos que se seguirão. Por todo o apoio que me dás e por seres uma companheira de todos os momentos. Obrigado. Amo-te.

CONTENTS

LIST OF TABLES

LIST OF ACRONYMS

1BZ first Brillouin zone

2D two-dimensional

3D three-dimensional

2DEG two-dimensional electron gases

DFT density functional theory

NDC negative differential conductance

NEGF non-equilibrium Green's function

hBN hexagonal Boron Nitride

HREELS High Resolution Electron Energy Loss Spectroscopy

I-V current-voltage

QHA quasi-harmonic approximation

RPA random phase approximation

SCBA self-consistent Born approximation

SCSA self-consistent screening approximation

STMDC semiconducting transition metal dichalcogenides

vdW van der Waals

VTFET Vertical Tunnelling Field Effect Transistor

LIST OF SYMBOLS

$\hbar$	Reduced Plank constant
k_B	Boltzmann constant
β	Inverse temperature: $\beta = (k_B T)^{-1}$
$f(\omega)$	Fermi-Dirac function: $f(\omega) = \left(e^{\beta\omega} + 1\right)^{-1}$
$b(\omega)$	Bose-Einsten function: $b(\omega) = \left(e^{\beta\omega} - 1\right)^{-1}$
Id	Identity operator

1 INTRODUCTION

The goals of Condensed Matter Physics are to unravel and tame new materials, new phases and the phenomena that these display. By understanding the properties of different materials, we can hope to harness their potential for practical applications. In this respect, the isolation of graphene in 2004 [1] proved to be a pivotal moment in Condensed Matter.

Graphene is an allotrope of carbon. It is formed by a single layer of carbon atoms with an sp^2 hybridization that are arranged in a honeycomb lattice. It is essentially a single layer of graphite and can be described as a two-dimensional (2D) material. While graphene and its oxide have been observed before [2], the 2004 experiments where special in that for the first time electrical properties of graphene where studied, revelling graphene as a material with extraordinary electrical properties. Graphene displays the curious feature that its low energy charge carriers behave as massless particles, with their behaviour governed by a effective relativistic massless Dirac equation [3, 4]. But that was not all. Besides its electrical properties, graphene was also shown to be a material with extraordinary optical, mechanical and thermal properties. Graphene was shown to a have a nearly constant optical absorption in the visible range [5] and to supported highly localized electromagnetic modes, surface plasmons, in the terahertz regime [6]. Graphene is the stiffest material measured to date [7]. Graphene has an extremely high thermal conductivity [8], which in conjunction with its high thermal conductivity makes it extremely promising for electronic applications. All these extraordinary properties more than justify the continued attention that graphene has received for more than a decade now. But what truly makes graphene a paradigm changer in Condensed Matter, is the fact that graphene was the first in a family of many other 2D materials.

Soon after the isolation of graphene, several other 2D materials where isolated, including monolayers of hexagonal Boron Nitride (hBN), several transition metal dichalcogenides [9] and black phosphorus [10]. These 2D materials come in a variety of flavours: while graphene is a semimetal (zero bandgap material with a vanishing density of states), hBN is a highly insulating material, transitional metal dichalcogenides can be either semiconducting or metallic and black phosphorus is an highly anisotropic semiconductor. Recently it was also verified that the metallic transitional metal dichalcogenide $NbSe_2$, a material which in its bulk form displays transitions in charge density wave and superconducting phases, also displays the same phases in its monolayer form [11]. Graphene was, therefore, the herald of a new field of research in Condensed Matter: the study of *2D materials*.

Besides the great variety of properties that 2D materials present, arguably one of the their most interesting features, when compared to usual bulk three-dimensional (3D) materials, is the possibility to easily tune those same properties. Due to the low dimensionality of these materials, their properties can be easily tuned by external parameters. This was made made clear in the early stages of research of graphene [1], where the conductivity of graphene was shown to be easily tuned by electrostatically controlling its density of states with a metallic gate. The all surface nature of these materials also means that they can be easily modified by chemical methods [12–14]. Another strategy to modified the properties of 2D materials is based on the strong

interplay between the electronic and the lattice degrees of freedom in 2D materials. By applying, in a controlled way, strain in a 2D material, it is possible to tune its electronic properties in a continuous way. This led to the development of the field of strain engineering [15, 16]. By controlling strain it was shown that effective pseudo-magnetic fields can be generated in graphene, which can give origin to Landau levels [17]. The field of strain engineering also extended to other 2D materials, particularly to semiconducting transition metal dichalcogenides (STMDC) and black phosphorus [18], where strain can be used to control the band gap of these materials allowing a tuning their electronic and optical properties.

This ease in externally controlling the properties of 2D materials comes, however, with a price. The reasons that make 2D materials easily tunable also make them extremely susceptible to the surrounding environment. Therefore, properties which in bulk materials are generally though of as being intrinsic, in 2D materials will be sample dependent. We will see several examples of this fact in this thesis.

A prime example of this sample dependence are the elastic properties of 2D materials. Strictly speaking, a 2D free crystal does not have well defined elastic constants. As a matter of fact even the mere existence of flat 2D crystals was doubted for a long time [19–21], as violent thermally activated fluctuations were expect to destroy the 2D crystalline order. It was, however, understood that a weaker form of order can still be defined, which still gives origin to Bragg peaks in a scattering experiment [22]. Nevertheless, thermally activated thermal fluctuations still have drastic consequences in 2D crystals. This is specially true in free flat crystals. In a 2D crystal, the long wavelength, low energy lattice vibrational modes can be split into in-plane and out-of-plane modes. While the dynamics of in-plane modes can be understood in terms of central forces, which lead to the usual linear relation between frequency and wavenumber; for out-of-plane modes the restoring force can only be described at microscopic level in terms of bond-bending forces. This microscopic bond-bending forces are translated to the macroscopic level to a restoring force that is proportional to the local curvature of the 2D crystal. This modifies the linear dispersion of the out-of-plane modes from linear to quadratic in wavevector. Since the restoring force that governs the dynamics of the out-of-plane modes being due to a bending energy, they are generally refereed to as flexural modes. The low energy of flexural modes means that that can be easily excited with temperature leading to even stronger fluctuations than the ones due to in-plane vibrations. These strong fluctuations lead to a break down of the superposition principle for lattice vibrations and anharmonic coupling between in-plane and out-of-plane motion must be taken into account [23, 24]. It was shown that this anharmonic coupling between lattice vibrations makes the elastic constants of a 2D crystalline membrane strongly scale dependent and should actually vanish in the limit of an infinite crystal! [25, 26] This mechanism is universal, being valid for any 2D crystal. In particular it should also apply to graphene which is a prototypical crystalline membrane. This fact is clearly at odds with the statement that graphene is the strongest material ever measured. However, graphene samples are never infinite. Furthermore, graphene samples are not free, but are typically supported by a substrate or suspended over a trench. In all of these cases, long wavelength flexural fluctuations should be suppressed and a finite value for the elastic constant of graphene will be possible. This value should be, however, sample dependent. So far no dependence of the elastic constants of graphene on sample size has been observed. However an anomalous increase of graphene Young modulus with defect concentration [27] and strain application [28] has been observed, which has been interpreted in terms of suppression of anharmonic fluctuations. Another

related problem is the role played by quantum fluctuations to the elastic properties of 2D crystals. This should be particular important in light and strong materials, such as graphene, which have high Debye temperatures, meaning that at room temperatures quantum fluctuations cannot be neglected. We will see in this thesis that anharmonic fluctuations driven by zero temperature quantum effects can contribute to a reconstruction of the dispersion relations of flexural modes, having direct consequences in thermodynamic properties of a free 2D crystal.

2D crystals have the peculiarity that they tend to contract, rather than expand, with increasing temperature. This phenomena of negative thermal expansion is not exclusive to 2D materials (notably water also displays it), but in 2D crystal it is a direct consequence of the quadratic dispersion relation of flexural vibrations and of their coupling to in-plane modes. This effect is generally refereed as the membrane effect having been predicted for a long time [29]. Layered materials, such as graphite, which can be seen as stacked 2D crystals, also inherit the property of negative thermal expansion in the directions parallel to the material basal plane [30]. In graphene, negative thermal expansion has been observed both in suspended samples and supported samples. In suspended samples, the thermal expansion was found to the negative up to temperatures of 350 K, with a room temperature value of -7×10^{-6} K^{-1} [31]; while in supported samples, thermal expansion was found to the negative in the temperature range of 200-400 K, with a room temperature value of -8×10^{-6} K^{-1} [32]. Once again, this suggests that the thermal expansion of graphene, and more generically of any 2D crystal, is not an intrinsic quantity but is instead sample dependent. Further evidence for this was presented in Ref. [33], where it was shown that the thermal expansion of supported graphene samples depends on the interaction between graphene and the substrate. In this thesis, we will see how the coupling between a substrate and a 2D crystal leads to a reconstruction of the spectral weight of the 2D crystal flexural mode, which in turn will affect the low temperature negative thermal expansion.

Another example of the dependence of properties of 2D materials to the external environment is the electrical conductivity of graphene. There are drastic changes to be mobility of charge carriers between supported [34] and suspended samples [35]. This as been attributed to the different scattering mechanics that dominate scattering in the different samples. In suspended samples, scattering by flexural modes has been identified as a dominant scattering mechanism at room temperature [35]. Scattering by flexural phonons in materials with mirror symmetry along the basal plane is always a two phonon process leading to a dependence of the resistivity quadratic with temperature. The scattering rate is dominated by long wavelength flexural modes being divergent for phonons with a quadratic dispersion relation. Therefore, scattering by flexural phonons in graphene samples will be extremely sensitive to any perturbation, such as in-plane stresses [35–37]. We will see how the spectral reconstruction of the flexural mode of graphene supported by a substrate affects electronic scattering by these modes. Coupling to a substrate will severely quench the flexural modes leading to a suppression of the flexural phonon limited resistivity in graphene samples.

It is also possible to use 2D materials to form layered structures [38, 39]. A particularly important example of these kind of structure is the graphene double layer separated by an insulator. These structures display the phenomena of Coulomb drag [39–41], which consists in the build up of a voltage across a metallic system due to a current driven in a second nearby metal. This phenomenon is not new in itself, having been observed in semiconducting double quantum wells [42–46]. We will also see that for highly doped graphene layers separated by a large distance, Coulomb drag

between graphene layers is actually very similar to Coulomb drag between semiconducting double quantum wells. However, structures based on 2D crystal allow for the study of Coulomb drag for layer separations previous unattainable [41]. More importantly, Coulomb drag in graphene double layers shows that different 2D crystal can be combined to build devices displaying new properties and effects.

One of the most exciting developments in the field of 2D materials, is the possibility of creating hybrid structures by stacking - or growing - different 2D crystals on top of each other [38]. The different layers are held together by weak van der Waals (vdW) forces and for these reason, this structures are generally referred to as *vdW structures*. By combining different 2D crystals, with different properties, and controlling their stacking order one can tailor the properties of the vdW structure at will and, by doing so, can create materials on demand [47]. One can for instance imagine that by combining a 2D (semi-)metallic material with another one which is insulating/semiconducting one can create a structure which can operate as a switch. This has been realized by sandwiching a few layers of hBN between two graphene layers. This graphene–hBN–graphene vertical structure was shown to operate as a Vertical Tunnelling Field Effect Transistor (VTFET) [48, 49]. The same kind of device has also been realized by replacing the hBN layers by the STMDC WSe_2 leading to an increase in the ON/OFF ratio by a factor of 10^2 [50]. A particularly important aspect of vdW structures is the fact the interfaces between different layers displays an extremely high quality, being atomically sharp [51]. This will lead to the conservation of the in-plane momentum of charge carriers during the tunnelling process, which will be sensitive to the relative alignment between different layers. This dependence of the tunnelling on the layer alignment has been exploited to create graphene–hBN–graphene devices displaying negative differential conductance (NDC) [52, 53]. Besides all the possible ways to tune the properties of 2D materials, in vdW materials crystal alignment between different layers provides yet another route to give origin to and tune material properties.

1.1 STRUCTURE OF THIS THESIS

This thesis is divided into two parts. Part i deals with the mechanical and thermodynamic properties of generic 2D crystals, or crystalline membranes. Part ii deals with electronic transport phenomena in 2D crystals and in layered materials formed out of these.

Part i is split into two chapters. Chapter 2 discusses the role played by anharmonic effects on the physics of free crystalline membranes in the low temperature limit. We start by discussing what is meant by crystalline order in two dimensions. Then we make a brief review of the classical theory of free crystalline membranes, discussing the effect of anharmonicities on the elastic constants of the membrane. We proceed by quantizing the theory in order to study the effect of anharmonicities in the low temperature, quantum regime. We give special attention to the anharmonic corrections to the dispersion relation of the flexural phonon and to the thermodynamic properties of thermal expansion and specific heat. In Chapter 3, we shift the focus from free membranes to membranes supported by a substrate. We consider the effect of the coupling between the membrane and the bulk substrate on the membrane lattice vibrations, specially on the membrane flexural mode. We focus on the dispersion relation and spectral properties of the flexural mode, taking into account the dynamics of the substrate and comparing theory with High Resolution Electron Energy Loss Spectroscopy (HREELS)

measurements. We also see how coupling to the substrate makes the thermal expansion of the membrane substrate dependent.

Part ii is split into three chapters, each devoted to a different electronic transport phenomenon. In Chapter 4, we study the effect of acoustic phonon scattering to the resistivity of graphene. We focus on both scattering by in-plane acoustic phonons and also by flexural phonons. In particular, by using the results of Chapter. 3, we study the effect of scattering by flexural phonons when graphene is supported by a substrate. In this chapter we also make a brief introduction to the description of graphene low energy electrons in terms of a massless Dirac equation. This overview also provides the basis for the subsequent two chapters. In Chapter 5, we study the phenomena of Coulomb drag between two metallic layers. We discuss Coulomb drag between layers with arbitrary electronic dispersion relations and arbitrary intralayer scattering mechanisms, establishing the dependence of the drag resistance as a function of temperature, layer separation and electronic densities. Next we specialize to the case of Coulomb drag between two graphene layers. We also study the role played by substrate longitudinal optical phonons on drag. Finally, in Chapter 6, we study the vertical tunnelling current between two graphene layers separated by few layers of hBN. We study the tunnelling current for small lattice misalignments between the graphene layers and the graphene layers and the hBN slab. We analyse how transference of momentum by the hBN crystalline structure to the tunnelling electrons can lead to the occurrence of multiple NDC regions. We also study the effect of inelastic scattering by optical phonons to the tunnelling current.

At the end of this thesis several appendices can be found. These appendices play three roles: (i) setting definitions for quantities used throughout the main text, (ii) contain technical details for proofs or lengthier calculations whose results are simply stated in the main text, and finally, (iii) acting as a short exposition for some of the techniques and formalisms employed in this thesis. Regarding this last point, this thesis makes heavy use of Green's functions techniques to many-body problem in Condensed Matter, a topic for which many excellent text books have been written. In my work during this thesis I have found Refs. [54] and [55] to be excellent books on the use of equilibrium Green's functions techniques in Condensed Matter and Refs. [56] and [57] to be excellent books for the non-equilibrium case. Therefore, Appendices A, C, B and H are to be seen just as quick references. All of the definitions used in this thesis regarding Green's functions, both in real and imaginary time, are provided in Appendix. A. Throughout this thesis, during intermediate steps we will usually work in units where $\hbar$, the reduced Planck constant, is set to 1, only restoring $\hbar$ when presenting final results.

Part I

CRYSTALLINE MEMBRANES

2

FREE QUANTUM CRYSTALLINE MEMBRANES

2.1 INTRODUCTION

The existence of 2D crystals has been a topic of debate. It was argued by Peierls [19] and Landau [20] that infinite strictly 2D crystals (with no atomic motion along the out-of-plane direction) where thermodynamically unstable at any finite temperature. Crystalline order in 2D would be destroyed by long wavelength thermally activated acoustic phonons, which would give origin to large amplitude fluctuations of the atoms around their equilibrium positions. This argument was formalized by Mermin [21], who proved, in a rigorous way, that there can be no *conventional* long-range crystalline order in two dimensions. As such, there seems to be a contradiction between theory and experimental observation, which tells us that 2D crystals exist. In fact no such contradiction exists. First of all, as pointed out by Gunther [58] and by Mermin himself [21], the average square amplitude of the fluctuations for a large, but finite, 2D crystal only grows logarithmically with the linear size of the sample. Namely, using a harmonic elasticity theory and employing the equipartition theorem, it is easy to show that

$$\frac{\left\langle \mathbf{u}^2 \right\rangle}{a^2} \sim \frac{k_B T}{2\pi M} \left(\frac{1}{v_L^2} + \frac{1}{v_T^2} \right) \log \left(\frac{L}{a} \right), \tag{2.1}$$

where $\mathbf{u}$ is the atomic displacement variable, T is the temperature, k_B is Boltzmann constant, M is the mass of the atoms, $v_{L/T}$ is the longitudinal/transverse sound velocity of the 2D crystal, a is the lattice parameter, L is the linear size of the sample and $\langle ... \rangle$ represents a thermodynamic average. Therefore, even if we have a very large 2D crystal, $\log(L/a)$ can still be relatively small. As an example, using typical graphene values, see Table 2.1, for a flake with linear size of 10 μm at 300 K we would obtain $\left\langle \mathbf{u}^2 \right\rangle / a^2 \simeq 0.2\%$. Secondly, and most importantly, one must be careful in what is meant by 2D crystalline order. Peierls' argument consists in studying the displacement correlation function $\left\langle (\mathbf{u}(\mathbf{x}) - \mathbf{u}(\mathbf{0}))^2 \right\rangle$. Once again employing the equipartition theorem one obtain

$$\left\langle (\mathbf{u}(\mathbf{x}) - \mathbf{u}(\mathbf{0}))^2 \right\rangle \sim \begin{cases} |\mathbf{x}|^{-1} & \text{, in 3D} \\ \log\left(|\mathbf{x}| / a \right) & \text{, in 2D} \end{cases}, \tag{2.2}$$

and therefore, while in a three-dimensional (3D) crystal the displacement correlation function goes to zero for large separations, in 2D it grows logarithmically. Mermin's paper defined crystalline order in terms of the Fourier transform of the atomic density,

$$\langle \rho_{\mathbf{q}} \rangle = \frac{1}{N} \sum_n \left\langle e^{-i\mathbf{q}\cdot\mathbf{R}_n} \right\rangle, \tag{2.3}$$

with N the number of atoms which are at positions $\mathbf{R}_n$, as a phase in which $\langle \rho_{\mathbf{q}} \rangle$ is non-zero when $\mathbf{q}$ is a reciprocal lattice vector, $\mathbf{G}$, and zero otherwise. Mermin's analysis showed that for large but finite systems $\langle \rho_{\mathbf{G}} \rangle \lesssim (\log N)^{-1/2}$, which vanishes in the thermodynamic limit. However, crystalline order is not experimentally characterized by either $\left\langle (\mathbf{u}(\mathbf{x}) - \mathbf{u}(\mathbf{0}))^2 \right\rangle$ or $\langle \rho_{\mathbf{q}} \rangle$, but instead by the observation of Bragg peaks

in a scattering experiment. The signal observed in a x-ray scattering experiment is proportional to the structure factor

$$S(\mathbf{q}) = \frac{1}{N}\sum_{n,m}\left\langle e^{-i\mathbf{q}\cdot(\mathbf{R}_n-\mathbf{R}_m)}\right\rangle, \tag{2.4}$$

where $\mathbf{q}$ is the transferred wavevector. If the atomic positions are frozen at the lattice sites, $S(\boldsymbol{q})$ presents a δ-function like divergence in the thermodynamic limit when $\boldsymbol{q}$ is a reciprocal lattice vector ($S(\mathbf{G}) = N$) , and averages to zero for any other generic wavevector. Writing the atomic positions as $\mathbf{R}_n = \mathbf{R}_n^0 + \mathbf{u}_n$, where $\mathbf{R}_n^0$ are the equilibrium positions of the frozen crystal and $\mathbf{u}_n$ are the displacements around that configuration, for an harmonic crystal using the general property of Gaussian integration

$$\begin{aligned} z(\boldsymbol{b}) &= \int d[\boldsymbol{x}] e^{-\frac{1}{2}\boldsymbol{x}\cdot\boldsymbol{M}\cdot\boldsymbol{x}+\boldsymbol{b}\cdot\boldsymbol{x}} \\ &= z(\mathbf{0}) e^{\frac{1}{2}\boldsymbol{b}\cdot\langle\boldsymbol{x}\boldsymbol{x}\rangle_0\cdot\boldsymbol{x}}, \end{aligned} \tag{2.5}$$

where $\langle\boldsymbol{x}\boldsymbol{x}\rangle_0 = \boldsymbol{M}^{-1}$, the structure factor reads

$$S(\mathbf{q}) = \frac{1}{N}\sum_{n,m} e^{-i\mathbf{q}\cdot(\mathbf{R}_n^0-\mathbf{R}_m^0)} e^{-\frac{1}{2}q^i q^j\left\langle(u_n^i-u_m^i)(u_n^j-u_m^j)\right\rangle_0}. \tag{2.6}$$

From the above equation and Eq. (2.2), one can see that in 3D the decay of the displacement-displacement correlation function with the distance as $|\mathbf{x}|^{-1}$ ensures that, in the thermodynamic limit, $S(\mathbf{q})$ diverges for $\mathbf{q} = \mathbf{G}$ and is zero for any other wavevector. For the 2D case, it was showed by Jancovici [22] that $S(\mathbf{G})$ will still diverge in the thermodynamic limit for temperatures $T < T_{\mathbf{G}}$ with $T_{\mathbf{G}}$ given by

$$T_{\mathbf{G}}^{-1} \simeq \frac{k_B A_{\text{cell}}}{8\pi M}|\mathbf{G}|^2\left(\frac{1}{v_L^2}+\frac{1}{v_T^2}\right), \tag{2.7}$$

where A_{cell} the area of the unit cell. For wave vectors close to a reciprocal lattice vector $\mathbf{G}$, instead of a δ-function-like divergence, $S(\mathbf{q})$ presents a power law divergence [59]

$$S(\mathbf{q}) \sim |\mathbf{q}-\mathbf{G}|^{-2(1-T/T_{\mathbf{G}})}. \tag{2.8}$$

Therefore, a purely 2D crystal still displays Bragg peaks in a scattering experiment and it is in this sense that it is possible to talk about 2D crystals. The observation of sharp Bragg peaks characteristic of a 2D crystal was observed in Xe atoms absorbed on a graphite surface [60]. In this system the Xe atoms form a triangular lattice weakly coupled to the graphite substrate. At low temperature, power law peaks characteristic of a 2D crystalline phase were observed and above a certain temperature, these peaks become less intense and broader, indicating that the system has transitioned into a liquid like phase.

Having settled that such a thing as a purely 2D crystal can be defined, we now turn our attention to crystalline membranes. A membrane is a two dimensional object that is embedded in three dimensions. Therefore, differently from a purely 2D crystal, a membrane can also fluctuate in the out-of-plane direction. For a free membrane not subject to any external stress, these fluctuations can lead to the destruction not only of the in-plane order but also make the flat configuration unstable, in which case the membrane becomes crumpled. The issue of the stability of a flat phase in membranes and the physics of the crumpling transition were extensively studied in the late 80's

[23, 25, 26, 61–68]. It was found that in *crystalline membranes*, membranes with an internal structure which gives rise to a finite shear modulus (also referred to as solid, tethered or polymerized membranes), anharmonic effects can make such a flat phase stable at low enough temperatures.

It was found that in the flat phase, the coupling between in-plane and out-of-plane displacements and their corresponding large fluctuations make the flat phase strongly anharmonic and anomalous [23]. In-plane elastic constants become scale dependent, vanishing for large length scales, while in the same limit the scale dependent bending rigidity grows. While the growth of the bending rigidity at large scales protects the flat phase against fluctuations, the reduction of the in-plane elastic constants makes in-plane order less well defined. This softening of the in-plane elastic constants in free crystalline membranes leads to a further suppression of Bragg peaks, which become just oscillations in the structure factor with the periodicity of the reciprocal lattice space, showing that while in-plane translational order has been destroyed, long range orientational order is still preserved [69–71].

Graphene and other 2D crystals are atomically thin, while displaying an in-plane structure due to the covalent bonding between atoms. While samples supported by a substrate or encapsulated between bulk materials are closer to a purely 2D crystal than a free membrane[1], suspended samples [72–75] appear as prototypical crystalline membranes. Suspended 2D crystal give origin to broadened but well defined Bragg peaks in scattering experiments [72–74]. The fact that the Bragg peaks are well defined is most likely due to stabilizing effect of the clamped edges of the sample, while the fact that these are broadened is due to static corrugations that the sample displays. The exact origin of these corrugations is still not clear. Corrugations might either be intrinsic, having its origin in an instability due to electron-phonon or anharmonic effects, or extrinsic, being caused by residual stresses induced by the edges, fabrication process or adsorbed impurities [76]. Most importantly, while graphene has been reported as the stiffest material ever measured [7], suspended graphene was later found to display very anomalous mechanical properties. Suspended graphene samples were shown to become stiffer when vacancies are induced [27] or when an external stress is applied [28]. This behaviour has been interpreted as due to a suppression of anharmonic effects, which as previously said, lead to a softening of the in-plane elastic constants.

Therefore in order to properly understand the mechanical properties of 2D crystals, one must take into account anharmonic effects. However, the standard descriptions of anharmonic effects in flat crystalline membranes [24] is a classical theory, mostly aimed at describing biological and lipidic membranes. A simple estimation of graphene's Debye temperature gives us $T_D \sim 1000$ K and as such it is doubtful that a classical theory is suitable to describe the lattice dynamics of graphene and other 2D crystal even at room temperature. It is therefore necessary to perform a study of anharmonic effects within a quantum mechanical approach.

In this chapter, we study the properties of flat crystalline membranes in the low temperature, quantum regime, analysing how anharmonic effects lead to a reconstruction of the dispersion relations of acoustic phonons and how this impacts thermodynamic properties in the low temperature limit. The chapter is organized as follows. In Section 2.2 we make a brief review of the standard classical theory for flat crystalline membranes, which will pave the way for the discussion of quantum effects (for a more general an in-depth discussion on the physics of classical membranes the reader is re-

1 We will see in the next chapter that coupling to the substrate quenches the out-of-plane displacements and strongly hybridizes them with substrate modes

ferred to Refs. [24, 77, 78]). The classical theory of crystalline membranes is quantized in Section 2.3. The effect of anharmonicity in the dispersion relation of long wavelength acoustic phonons is studied. In Section 2.4, the effect of anharmonicity in the the low temperature thermodynamic properties of thermal expansion and specific heat is studied. Finally, in Section 2.5 the results of this chapter are analysed and discussed.

2.2 REVIEW OF THE CLASSICAL THEORY OF FREE CRYSTALLINE MEMBRANES

Within the description of lattice dynamics, the degrees of freedom are the positions of the atoms that form the crystal. We label the atoms by an index n and each atom has a position given by $\vec{R}_n$, a 3D vector. The theory describing the crystal must be invariant under rigid translations and rotations of the atomic positions. Therefore, the classical Hamiltonian can only the a function of inner products of quantities like $\vec{R}_n - \vec{R}_m$. Focusing on low energy, long wavelength properties and assuming that the forces between atoms are short ranged we can use a continuous description of the crystal. To do this we consider a virtual reference crystal with atomic positions given by $\mathbf{x}_n$ and label the atomic positions $\vec{R}_n$ by this reference position, which is promoted to a continuous variable, $\mathbf{x}_n \to \mathbf{x}$. Assuming $\vec{R}_n$ varies smoothly, which will be true for acoustic lattice vibrations, we can write $\vec{R}_n - \vec{R}_m \simeq \tau^i_{n,m}\partial_i\vec{R}(\mathbf{x})$, where $\boldsymbol{\tau}_{n,m} = \mathbf{x}_n - \mathbf{x}_m$ and the latin indice runs over the spacial dimensions of the membrane. We are using Einstein's convention, with summation over repeated indices implied. To lowest order in $\partial_i\vec{R}(\mathbf{x})$ and its derivatives, Paczuski, Kardar and Nelson [64] proposed the classical Hamiltonian to describe 2D crystalline membranes[2]

$$\begin{aligned}\mathcal{H}_{PKN} = &\frac{1}{2}\int d^2\mathbf{x}\kappa^{ijkl}\partial_i\partial_j\vec{R}\cdot\partial_k\partial_l\vec{R} \\ &+\frac{1}{8}\int d^2\mathbf{x}c^{ijkl}\left(\partial_i\vec{R}\cdot\partial_j\vec{R}-\delta_{ij}\right)\left(\partial_k\vec{R}\cdot\partial_l\vec{R}-\delta_{kl}\right),\end{aligned} \tag{2.9}$$

where the first term is a bending energy term, describing resistance of the membrane to being curved, with κ^{ijkl} the bending rigidity tensor; and the second is a stretching energy term, describing resistance of the membrane against in-plane compression/extension and shearing, with c^{ijkl} the stiffness, or elastic moduli, tensor. These tensors obey the symmetries

$$c^{ijkl} = c^{klij} = c^{jikl}, \tag{2.10}$$

and similarly for κ^{ijkl}. Equation (2.9) is clearly invariant under rigid translations and rotations of the $\vec{R}(\mathbf{x})$ variables. The structure of the tensors κ^{ijkl} and c^{ijkl} depends on the underlying symmetries of the membrane's crystalline structure. We will focus on crystalline membranes with hexagonal symmetry, such as graphene, in which case c^{ijkl} must have the form [79]

$$c^{ijkl} = \lambda\delta^{ij}\delta^{kl} + \mu\left(\delta^{ik}\delta^{jl}+\delta^{il}\delta^{jk}\right), \tag{2.11}$$

where λ and μ are 2D Lamé coefficients. We point out that this form of the elastic moduli tensor is the same as for an isotropic system. For a system with hexagonal

2 Originally this Hamiltonian was proposed to study the crumpling transition of a generic membrane with D dimensions embedded in a d dimensional space. We will restrict ourselves to the physical case, $D = 2$ and $d = 3$.

symmetry κ^{ijkl} must have the same form as Eq. (2.11), but by using integration by parts and ignoring surface terms we can write

$$\kappa^{ijkl} = \kappa\delta^{ij}\delta^{kl}. \tag{2.12}$$

For a flat membrane, it is possible to write the position of the atoms in a Monge representation as

$$\vec{R}(\mathbf{x}) = (\mathbf{x} + \mathbf{u}(\mathbf{x}), h(\mathbf{x})) \tag{2.13}$$

where $\mathbf{x}$ is the equilibrium position of the atom, $\mathbf{u}(\mathbf{x})$ is the in-plane displacement vector and $h(\mathbf{x})$ is an out-of-plane displacement. Therefore, Eq. (2.9) becomes

$$\mathcal{H}_{PKN} = \frac{1}{2}\int d^2\mathbf{x}\left(\kappa\left[\left(\partial^2\mathbf{u}\right)^2 + \left(\partial^2 h\right)^2\right] + c^{ijkl}\varepsilon_{ij}\varepsilon_{kl}\right). \tag{2.14}$$

where ε_{ij} is the *full strain tensor*

$$\varepsilon_{ij} = \frac{1}{2}\left(\partial_i u_j + \partial_j u_i + \partial_i h\partial_j h + \partial_i\mathbf{u}\cdot\partial_j\mathbf{u}\right). \tag{2.15}$$

When studying the flat phase of the membrane it is a common approximation to neglect the bending contribution from the in-plane phonons, $\left(\partial^2\mathbf{u}\right)^2$, and the quadratic term in $\mathbf{u}$ in the strain tensor Eq. (2.15) [23, 66]. Doing this one obtains the *thin plate* classical Hamiltonian

$$\mathcal{H}\left[\mathbf{u}, h\right] = \frac{1}{2}\int d^2\mathbf{x}\left(\kappa\left(\partial^2 h\right)^2 + c^{ijkl}\gamma_{ij}\gamma_{kl}\right), \tag{2.16}$$

with

$$\gamma_{ij} = \frac{1}{2}\left(\partial_i u_j + \partial_j u_i + \partial_i h\partial_j h\right), \tag{2.17}$$

the *relevant strain tensor*. Notice that in Eq. (2.16), and (2.14), the out-of-plane displacement field only occurs in even powers. This is due to the fact that a flat membrane is invariant under the mirror symmetries $z \to -z$. We also point out that the classical Hamiltonian Eq. (2.16) has the same form as Landau's free energy for thin plates [79]. However, one should notice that while for a thin plate the bending rigidity is related to the Young's modulus, Y_{3D}, and Poisson's ratio, ν_{3D}, of the bulk material and to its thickness, Δh, by

$$\kappa \underset{\text{for plates}}{=} \frac{Y_{3D}\left(\Delta h\right)^3}{12\left(1-\nu_{3D}^2\right)}, \tag{2.18}$$

no such relation should exist for a crystalline membrane, as it is not possible to properly define the thickness of a 2D crystal. Therefore, in a crystalline membrane, the bending rigidity and the in-plane elastic constants are to be understood as independent parameters. Equation (2.16) is the minimal model that includes the coupling of in-plane and out-of-plane displacements and is the starting point for the study of anharmonic effects in a membrane. But first, we will analyse the harmonic theory.

2.2.1 *Harmonic theory*

A crystalline membrane supports three acoustic lattice vibration modes: two in-plane modes, which in an isotropic membrane can be classified as longitudinal and transverse, and one out-of-plane mode. In order to study these modes at harmonic level, we neglect

	κ [eV]	λ [eV Å^{-2}]	μ [eV Å^{-2}]	v_L [m/s]	v_T [m/s]
$T = 0$ K	0.82	3.25	9.44	2.15×10^4	1.41×10^4
$T = 300$ K	1.1	2.57	9.95	2.17×10^4	1.44×10^4

Table 2.1: Typical elastics constant for graphene at $T = 0$ and at $T = 300$ K. Taken from Ref. [80]. The in-plane phonon velocities were calculated using a graphene mass density of $\rho/\hbar^2 = 1104$ eVÅ^{-2}.

the term $\partial_i h \partial_j h$ in Eq. (2.17), such that the classical Hamiltonian Eq. (2.16) becomes quadratic in the displacement variables reading

$$\mathcal{H}_0[\mathbf{u}, h] = \frac{1}{2}\int d^2\mathbf{x}\left(\kappa\left(\partial^2 h\right)^2 + \lambda\left(\partial_i u_i\right)^2 + \mu\left(\partial_i u_j \partial_i u_j + \partial_i u_j \partial_j u_i\right)\right), \tag{2.19}$$

and the in-plane and out-of-plane displacement variables are completely decoupled. Writing the displacement fields in Fourier components

$$h(\mathbf{x}) = \frac{1}{\sqrt{A}}\sum_{\mathbf{q}} e^{i\mathbf{q}\cdot\mathbf{x}} h_{\mathbf{q}}, \tag{2.20}$$

$$u^i(\mathbf{x}) = \frac{1}{\sqrt{A}}\sum_{\mathbf{q}} e^{i\mathbf{q}\cdot\mathbf{x}} u^i_{\mathbf{q}}, \tag{2.21}$$

where A is the area of the membrane, the quadratic Hamiltonian is given by

$$\mathcal{H}_0[\mathbf{u}, h] = \frac{1}{2}\sum_{\mathbf{q}}\left(\kappa|\mathbf{q}|^4 h_{\mathbf{q}} h_{-\mathbf{q}} + \left[(\lambda+\mu)\delta_{ij}|\mathbf{q}|^2 + \mu q_i q_j\right] u^i_{\mathbf{q}} u^j_{-\mathbf{q}}\right). \tag{2.22}$$

We define the equal-time classical phonon correlation functions as

$$D^0_{F,\mathbf{q}} = \langle h_{\mathbf{q}} h_{-\mathbf{q}}\rangle_0, \tag{2.23}$$

$$D^{0,ij}_{uu,\mathbf{q}} = \left\langle u^i_{\mathbf{q}} u^j_{-\mathbf{q}}\right\rangle_0, \tag{2.24}$$

where where $\langle ...\rangle_0$ represents a classical thermodynamic average with respect to the Hamiltonian Eq. (2.19), which is defined as

$$\langle ...\rangle_0 = \frac{\int D[\mathbf{u}, h]\, ... e^{-\beta\mathcal{H}_0[\mathbf{u},h]}}{\int D[\mathbf{u}, h]\, e^{-\beta\mathcal{H}_0[\mathbf{u},h]}}, \tag{2.25}$$

with $\beta^{-1} = k_B T$, and $D[\mathbf{u}, h]$ is the functional integration measure. Since Eq. (2.19) is quadratic, using Gaussian integration we obtain, in accordance with the equipartition theorem,

$$D^0_{F,\mathbf{q}} = \frac{k_B T}{\kappa|\mathbf{q}|^4}, \tag{2.26}$$

$$D^{0,ij}_{uu,\mathbf{q}} = D^0_{L,\mathbf{q}} P^{ij}_{L,\mathbf{q}} + D^0_{T,\mathbf{q}} P^{ij}_{T,\mathbf{q}}, \tag{2.27}$$

where, using isotropy, we have decomposed $D^{0,ij}_{uu,\mathbf{q}}$ into longitudinal and transverse components, with respect to the direction defined by the wavevector $\mathbf{q}$, and introduced the longitudinal/transverse projectors $P^{ij}_{L/T,\mathbf{q}}$

$$P^{ij}_{L,\mathbf{q}} = \frac{q^i q^j}{|\mathbf{q}|^2}, \qquad P^{ij}_{T,\mathbf{q}} = \delta^{ij} - \frac{q^i q^j}{|\mathbf{q}|^2}, \tag{2.28}$$

and $D^0_{L/T,\mathbf{q}}$ are the correlation functions for the longitudinal/transverse in-plane displacements

$$D^0_{L,\mathbf{q}} = \frac{k_B T}{(\lambda + 2\mu)\,|\mathbf{q}|^2}, \qquad D^0_{T,\mathbf{q}} = \frac{k_B T}{\mu\,|\mathbf{q}|^2}. \tag{2.29}$$

From Eq. (2.22) one can also obtain the dynamics of the displacement field. According to the Euler-Lagrange equations we have

$$\rho \ddot{h}_{\mathbf{q}} = -\frac{\delta \mathcal{H}_0}{\delta h_{-\mathbf{q}}}, \tag{2.30}$$

$$\rho \ddot{u}^i_{\mathbf{q}} = -\frac{\delta \mathcal{H}_0}{\delta u^i_{-\mathbf{q}}}, \tag{2.31}$$

where ρ is the mass density of the membrane. Therefore, we obtain the dispersion relations for the out-of-plane, *flexural* or some times capillary, phonons

$$\omega_{F,\mathbf{q}} = \sqrt{\frac{\kappa}{\rho}}\,|\mathbf{q}|^2\,, \tag{2.32}$$

while for the in-plane longitudinal and transverse phonons we obtain

$$\omega_{L,\mathbf{q}} = v_L\,|\mathbf{q}|\,, \tag{2.33}$$

$$\omega_{T,\mathbf{q}} = v_T\,|\mathbf{q}|\,, \tag{2.34}$$

where $v_L = \sqrt{(\lambda+2\mu)/\rho}$ and $v_T = \sqrt{\mu/\rho}$ are the in-plane longitudinal and transverse sound velocities. Typical graphene values for the bending rigidity, in-plane Lamé coefficients and sound velocities are provided in Table (2.1).

Using these results we obtain that for the harmonic theory, in-plane correlation functions behave just like in the case for a purely 2D crystal. For the out-of-plane fluctuations we obtain

$$\begin{aligned}\left\langle (h(\mathbf{x}) - h(\mathbf{0}))^2 \right\rangle_0 &= 2\int \frac{d^2\mathbf{q}}{(2\pi)^2}\,\langle h_{\mathbf{q}} h_{-\mathbf{q}}\rangle_0\,(1-\cos(\mathbf{q}\cdot\mathbf{x})) \\ &\simeq 2\int_{2\pi/|\mathbf{x}|} \frac{d^2\mathbf{q}}{(2\pi)^2}\,\langle h_{\mathbf{q}} h_{-\mathbf{q}}\rangle \\ &\sim |\mathbf{x}|^2\,,\end{aligned} \tag{2.35}$$

The fact that the the out-of-plane displacement between two points of the membrane scales linearly with their separation, shows that a flat phase within the harmonic theory is impossible and the membrane is always in a crumpled phase. If one also looks at the local normal of the membrane which is approximately given by $\mathbf{n}(\mathbf{x}) \simeq \mathbf{e}_z - \nabla h(\mathbf{x})$, the normal-normal correlation function reads

$$\begin{aligned}\left\langle (\delta\mathbf{n}(\mathbf{x}) - \delta\mathbf{n}(\mathbf{0}))^2 \right\rangle_0 &\simeq 2\int \frac{d^2\mathbf{q}}{(2\pi)^2}\,|\mathbf{q}|^2\,\langle h_{\mathbf{q}} h_{-\mathbf{q}}\rangle_0\,(1-\cos(\mathbf{q}\cdot\mathbf{x})) \\ &\sim \log\left(\frac{|\mathbf{x}|}{a}\right).\end{aligned} \tag{2.36}$$

and therefore there is also no long range out-of-plane orientational order. We will see that inclusion of anharmonic effects fixes this pathology.

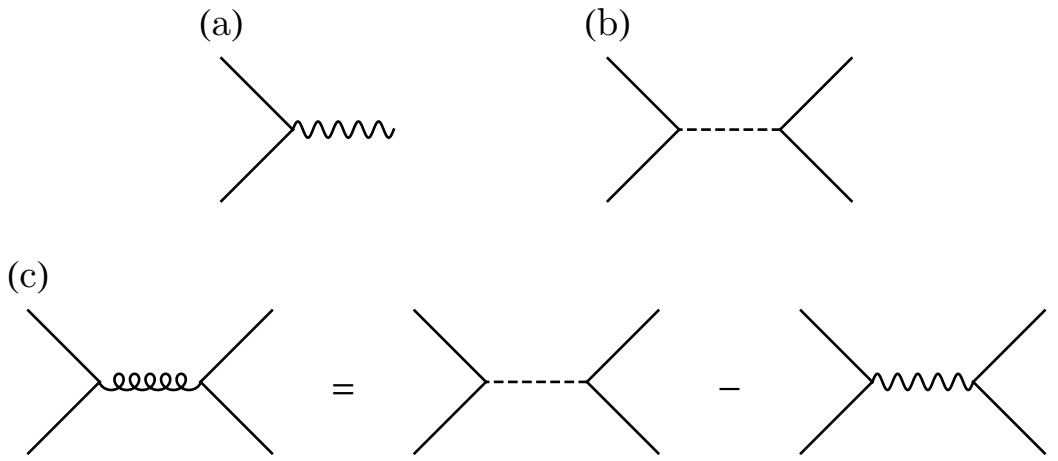

Figure 2.1: Diagrammatic Feynman rules for the anharmonic theory of crystalline membranes: (a) interaction vertex for the cubic interaction of Eq. (2.38); (b) interaction vertex for the quartic interaction of Eq. (2.39); (c) effective quartic interaction between out-of-plane displacements, Eq. (2.44). The solid straight and wavy lines represents, respectively, in-plane and out-of-plane displacement propagators. The dashed straight line represents the quartic interaction of Eq. (2.39) and the coil shaped line represents the effective quartic interaction of Eq. (2.44).

2.2.2 *Anharmonic effects*

Notice that the inclusion of the term $\partial_i h \partial_j h$ in the relevant strain tensor γ_{ij}, Eq (2.17), makes the classical Hamiltonian Eq. (2.16) an interacting one. We can split the interacting Hamiltonian as

$$\mathcal{H}\left[\mathbf{u}, h\right] = \mathcal{H}^{(0)}\left[\mathbf{u}, h\right] + \mathcal{H}^{(3)}_{\text{int}}\left[\mathbf{u}, h\right] + \mathcal{H}^{(4)}_{\text{int}}\left[h\right], \tag{2.37}$$

where $\mathcal{H}_0\left[\mathbf{u}, h\right]$ is the quadratic part of the Hamiltonian, given by Eq. (2.19) or (2.22), and $\mathcal{H}^{(3)}_{\text{int}}\left[\mathbf{u}, h\right]$ together with $\mathcal{H}^{(4)}_{\text{int}}\left[h\right]$ are interaction terms which read

$$\mathcal{H}^{(3)}_{\text{int}}\left[\mathbf{u}, h\right] = \frac{1}{2}\int d^2\mathbf{x} c^{ijkl}\partial_i u_j \left(\partial_k h \partial_l h\right), \tag{2.38}$$

$$\mathcal{H}^{(4)}_{\text{int}}\left[h\right] = \frac{1}{8}\int d^2\mathbf{x} c^{ijkl}\left(\partial_i h \partial_j h\right)\left(\partial_k h \partial_l h\right). \tag{2.39}$$

The term $\mathcal{H}^{(3)}_{\text{int}}\left[\mathbf{u}, h\right]$ is a cubic interaction term that couples the in-plane displacement field with the out-of-plane displacement field and $\mathcal{H}^{(4)}_{\text{int}}\left[h\right]$ is a quartic interaction involving only the out-of-plane displacements. These interaction terms are represented diagrammatically in Fig. 2.1(a) and (b). The partition function of the membrane is given by

$$Z = \int D\left[\mathbf{u}, h\right] e^{-\beta\mathcal{H}[\mathbf{u},h]}. \tag{2.40}$$

Notice, that although $\mathcal{H}\left[\mathbf{u}, h\right]$ describes an interacting system, it is still quadratic in the in-plane displacement field. In this situation it is possible, and useful, to integrate out the in-plane displacements exactly, in order to obtain a theory that only involves the out-of-plane displacements [23]. Using the general property of Gaussian integration Eq. (2.5), it is possible to write the partition function of the membrane as

$$Z = Z_{\mathbf{u},0}\int D\left[h\right] e^{-\beta\mathcal{H}_{\text{eff}}[h]}, \tag{2.41}$$

where $Z_{\mathbf{u},0}$ is the partition function for the non-interacting in-plane displacement, which is just an unimportant multiplicative factor, and $\mathcal{H}_{\text{eff}}[h]$ is the effective classical Hamiltonian for the out-of-plane displacements, which reads

$$\mathcal{H}_{\text{eff}}[h] = \mathcal{H}^{(0)}[h] + \mathcal{H}^{(4)}_{\text{eff}}[h], \tag{2.42}$$

where $\mathcal{H}^{(0)}[h]$ is the part of $\mathcal{H}^{(0)}[\mathbf{u}, h]$ only involving the out-of-plane displacement and $\mathcal{H}^{(4)}_{\text{eff}}[h]$ is the effective interaction Hamiltonian which reads

$$\mathcal{H}^{(4)}_{\text{eff}}[h] = \frac{1}{8}\int d^2\mathbf{x}\int d^2\mathbf{x}' \left(\partial_i h \partial_j h\right)(\mathbf{x}) \mathcal{R}^{ijkl}(\mathbf{x},\mathbf{x}') \left(\partial_k h \partial_l h\right)(\mathbf{x}'), \tag{2.43}$$

where the effective quartic interaction between the out-of-plane displacements is given by

$$\begin{aligned}\mathcal{R}^{ijkl}(\mathbf{x},\mathbf{x}') = {} & c^{ijkl}\delta^{(2)}\left(\mathbf{x}-\mathbf{x}'\right) \\ & - c^{iji'j'}\left\langle u_{i'j'}(\mathbf{x}) u_{k'l'}(\mathbf{x}')\right\rangle_0 c^{k'l'kl},\end{aligned} \tag{2.44}$$

with $u_{ij}(\mathbf{x}) = \left(\partial_i u_j(\mathbf{x}) + \partial_j u_i(\mathbf{x})\right)/2$ the linear strain tensor and $\langle u_{ij}(\mathbf{x}) u_{kl}(\mathbf{x}')\rangle_0$ its corresponding correlation function. The effective quartic interaction is represented diagrammatically in Fig. 2.1(c). The first term of $\mathcal{R}^{ijkl}(\mathbf{x},\mathbf{x}')$ corresponds to the local quartic interaction from Eq. (2.39), while the second term corresponds to a non-local interaction that is mediated by the in-plane displacements. In terms of Fourier components Eq. (2.43) is given by

$$\mathcal{H}^{(4)}_{\text{eff}}[h] = \frac{1}{8A}\sum_{\mathbf{q},\mathbf{q}',\mathbf{p}} \mathcal{R}^{ijkl}_{\mathbf{p}} \left(q+p\right)_i q_j \left(q'-p\right)_k q'_l h_{\mathbf{q}+\mathbf{p}} h_{-\mathbf{q}} h_{\mathbf{q}'-\mathbf{p}} h_{-\mathbf{q}'}, \tag{2.45}$$

with the effective interaction written in Fourier components as

$$\mathcal{R}^{ijkl}_{\mathbf{p}} = c^{ijkl} - c^{iji'j'}\left\langle u_{i'j',\mathbf{p}} u_{k'l',-\mathbf{p}}\right\rangle_0 c^{k'l'kl}. \tag{2.46}$$

It is important to treat the cases with $\mathbf{p}=\mathbf{0}$ and $\mathbf{p}\neq\mathbf{0}$ differently [24], which involve, respectively, homogeneous deformations and fluctuating (phonon) displacements. First we notice that according to general linear response theory, see Appendix B, the quantity $\langle u_{ij,\mathbf{p}} u_{kl,-\mathbf{p}}\rangle_0$ is the response function due to an applied in-plane stress, $\sigma^{ij}_{\mathbf{p}}$. Therefore, in the presence of an applied in-plane stress, the in-plane displacement is given by

$$\langle u_{ij,\mathbf{p}}\rangle_0 = \langle u_{ij,\mathbf{p}} u_{kl,-\mathbf{p}}\rangle_0 \sigma^{kl}_{\mathbf{p}}. \tag{2.47}$$

The $\mathbf{p}=\mathbf{0}$ case describes the homogeneous distortion due to an homogeneous strain tensor. The homogeneous stress-strain constitutive relation in linear elasticity is described by the stiffness tensor, c^{ijkl}, as

$$\sigma^{ij} = c^{ijkl} u_{kl}. \tag{2.48}$$

The inverse relation is expressed in terms of the compliance tensor, c^{-1}_{ijkl}, as

$$u_{ij} = c^{-1}_{ijkl}\sigma^{kl}, \tag{2.49}$$

with the compliance tensor defined as the inverse of the stiffness tensor,

$$c^{-1}_{ijkl} c^{klmn} = \frac{1}{2}\left(\delta_{im}\delta_{jn} + \delta_{in}\delta_{jm}\right). \tag{2.50}$$

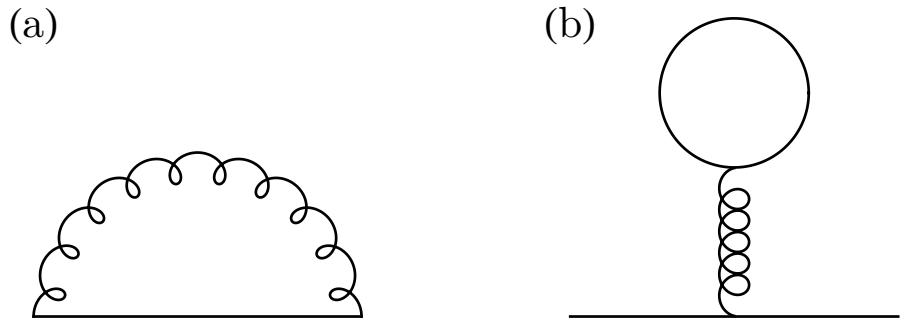

Figure 2.2: Feynman diagrams contributing to the out-of-plane displacement self-energy to lowest order in perturbation theory. (a) Fock diagram that leads to the self-energy in Eq. (2.57). (b) Hartree diagram. This kind of diagram does not occur due to the exclusion of the $\mathbf{p} = \mathbf{0}$ case in Eq. (2.55).

For an isotropic 2D crystal the compliance tensor is expressed in terms of the Lamé coefficients as

$$c^{-1}_{ijkl} = -\frac{\lambda}{4\mu\left(\lambda+\mu\right)}\delta_{ij}\delta_{kl} + \frac{1}{4\mu}\left(\delta_{ik}\delta_{jl} + \delta_{il}\delta_{jk}\right). \tag{2.51}$$

Therefore, comparing Eqs. (2.47) and (2.49) we identify

$$\left\langle u_{ij,\mathbf{0}} u_{kl,\mathbf{0}} \right\rangle_0 = c^{-1}_{ijkl}. \tag{2.52}$$

Therefore, we obtain

$$\mathcal{R}^{ijkl}_{\mathbf{0}} = c^{ijkl} - c^{iji'j'} c^{-1}_{i'j'k'l'} c^{k'l'kl} = 0. \tag{2.53}$$

For $\mathbf{p} \neq \mathbf{0}$, the in-plane strain-strain correlation function can be expressed in terms of the phonon correlation functions Eqs. (2.29). Performing all the contractions, the following result is obtained

$$\begin{aligned}\mathcal{R}_{\mathbf{q},\mathbf{q}',\mathbf{p}} &= \mathcal{R}^{ijkl}_{\boldsymbol{p}} \left(q+p\right)_i q_j \left(q'-p\right)_k q'_l \\ &= Y_{2D} \frac{\left(\mathbf{q}\times\mathbf{p}\right)^2_z}{\left|\mathbf{p}\right|^2} \frac{\left(\mathbf{q}'\times\mathbf{p}\right)^2_z}{\left|\mathbf{p}\right|^2},\end{aligned} \tag{2.54}$$

where $Y_{2D} = 4\mu\left(\lambda+\mu\right)/\left(\lambda+2\mu\right)$ is the 2D Young modulus. Therefore, the effective quartic interaction Hamiltonian, $\mathcal{H}^{(4)}_{\text{eff}}\left[h\right]$, can be written as

$$\mathcal{H}^{(4)}_{\text{eff}}\left[h\right] = \frac{1}{8A} \sum_{\substack{\mathbf{q},\mathbf{q}' \\ \mathbf{p}\neq\mathbf{0}}} Y_{2D} \frac{\left(\mathbf{q}\times\mathbf{p}\right)^2_z}{\left|\mathbf{p}\right|^2} \frac{\left(\mathbf{q}'\times\mathbf{p}\right)^2_z}{\left|\mathbf{p}\right|^2} h_{\mathbf{q}+\mathbf{p}} h_{-\mathbf{q}} h_{\mathbf{q}'-\mathbf{p}} h_{-\mathbf{q}'}. \tag{2.55}$$

Due to presence of interactions in the classical Hamiltonian (2.37), the out-of-plane correlation function is no longer given by Eq. (2.26), but is instead given by the Dyson equation

$$D_{F,\mathbf{q}} = D^0_{F,\mathbf{q}} - D^0_{F,\mathbf{q}} \beta \Sigma_{F,\mathbf{q}} D_{F,\mathbf{q}}, \tag{2.56}$$

where $D_{F,\mathbf{q}}$ is the exact correlation function and $\Sigma_{F,\mathbf{q}}$ is the out-of-plane displacement self-energy, which encodes the effect of interactions. The inverse temperature factor was introduced for latter convenience, when comparing with the quantum case. Since $D_{F,\mathbf{q}}$ only involves out-of-plane variables, we can use the effective interaction Hamiltonian

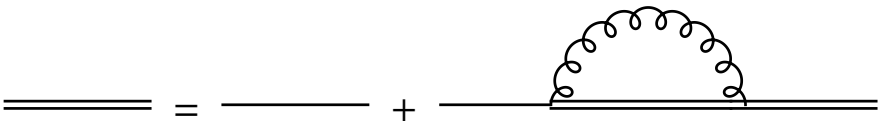

Figure 2.3: Diagrammatic representation of the Nelson and Peliti SCBA for crystalline membranes [23]. The double straight line represents the full out-of-plane correlation function, $D_{F,\mathbf{q}}$. The self-energy is computed using the full out-of-plane correlation function.

(2.55) to compute $\Sigma_{F,\mathbf{q}}$. The lowest order contribution to the self-energy is given by the Fock diagram represented in Fig. 2.2(a), which translates into

$$\beta\Sigma^{(0)}_{F,\boldsymbol{q}} = \frac{Y_{2D}}{A}\sum_{\mathbf{p}} \frac{(\mathbf{q}\times\mathbf{p})_z^2}{|\mathbf{p}|^2}\frac{(\mathbf{q}\times\mathbf{p})_z^2}{|\mathbf{p}|^2}\beta D^0_{F,\mathbf{q}+\mathbf{p}}, \tag{2.57}$$

The fact that the $\mathbf{p}=\mathbf{0}$ case is excluded from Eq. (2.55) means that in a diagrammatic perturbative expansion of the self-energy, $\Sigma_{F,\mathbf{q}}$, Hartree diagrams, like the one in Fig. 2.2(b), do not occur. Using Eq. (2.26) and transforming the sum in momentum into an integration, the self-energy is computed yielding

$$\begin{aligned}\Sigma^{(0)}_{F,\mathbf{q}} &= Y_{2D}k_BT\,|\mathbf{q}|^4\int\frac{d^2\mathbf{p}}{(2\pi)^2}\frac{\sin^4\theta_{\mathbf{q},\mathbf{p}}}{\kappa\,|\mathbf{q}+\mathbf{p}|^4}\\ &= \frac{3Y_{2D}k_BT}{16\pi\kappa}\,|\mathbf{q}|^2\,.\end{aligned} \tag{2.58}$$

The obtained self-energy behaves as $|\mathbf{q}|^2$, while the inverse bare propagator behaves as $\left(D^0_{F,\mathbf{q}}\right)^{-1}\propto|\mathbf{q}|^4$. In order for perturbation theory to be valid, the self-energy correction to the correlation function should be smaller than the inverse bare correlation function. Therefore, Eq. (2.58) shows that at low enough momenta perturbation theory breaks down and the crystalline membrane theory becomes strongly coupled. Using a Ginzburg argument we can estimate the momentum scale, k_c, bellow which perturbation theory breaks down by comparing [24, 81–83]

$$\left(D^0_{F,\mathbf{k}_c}\right)^{-1}\simeq\beta\Sigma^{(0)}_{F,\mathbf{k}_c}, \tag{2.59}$$

from which we obtain

$$k_c\simeq\sqrt{\frac{3Y_{2D}k_BT}{16\pi\kappa^2}}. \tag{2.60}$$

Using typical graphene values we obtain $k_c\simeq 0.17\,\text{Å}^{-1}$. This cross-over momentum also corresponds to a critical size of the membrane, $L_c=2\pi/k_c$, above which it will display strong anharmonic effects. For graphene we obtain $L_c\simeq 6\,\text{Å}$.

In order to obtain a non-perturbative result, Nelson and Peliti [23] proposed a self-consistent Born approximation (SCBA) theory for the out-of-plane propagator. Neglecting dressing of the effective interaction Eq. (2.55), a self-consistent theory is obtained by replacing the bare out-of-plane correlation function, $D^0_{F,\mathbf{q}+\mathbf{p}}$, by the full one, $D_{F,\mathbf{q}+\mathbf{p}}$, in Eq. (2.57), obtaining

$$\beta\Sigma^{\text{SCBA}}_{F,\mathbf{q}} = \frac{Y_{2D}}{A}\sum_{\mathbf{p}} \frac{(\mathbf{q}\times\mathbf{p})_z^2}{|\mathbf{p}|^2}\frac{(\mathbf{q}\times\mathbf{p})_z^2}{|\mathbf{p}|^2}\beta D_{F,\mathbf{q}+\mathbf{p}}, \tag{2.61}$$

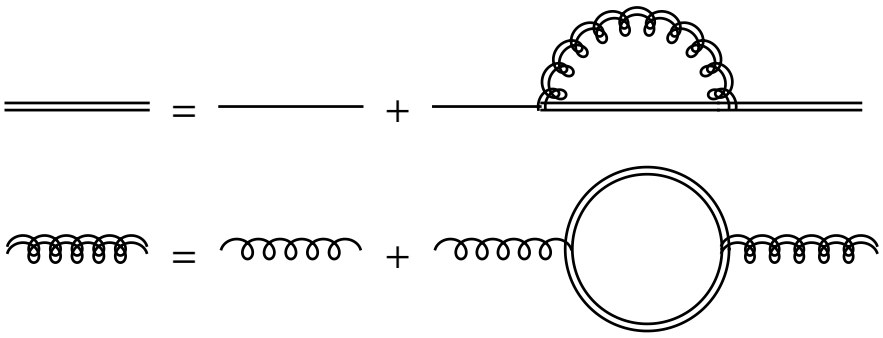

Figure 2.4: Diagrammatic representation of the SCSA for crystalline membranes. The double straight line represents the full out-of-plane propagator, $D_{F,\mathbf{q}}$, while the double coil line, represents the screened effective quartic interaction, which is described by the effective Young's modulus. These diagrammatic equations lead to Eqs. (2.68) and (2.69).

and using the Dyson equation (2.56) the full correlation function is given by

$$D_{F,\mathbf{q}} = \frac{k_B T}{\kappa \left|\mathbf{q}\right|^4 + \Sigma_{F,\mathbf{q}}^{\mathrm{SCBA}}}. \tag{2.62}$$

The SCBA is represented in terms of Feynman diagrams in Fig. 2.3. In the light of the perturbative result, Eq. (2.58), it is assumed that $\Sigma_{F,\mathbf{q}} \gg \kappa \left|\boldsymbol{q}\right|^4$ and it is furthermore assumed a power law dependence of $\Sigma_{F,\mathbf{q}}$ on momentum, $\Sigma_{F,\mathbf{q}} \sim \kappa q_0^{\eta_h} |\mathbf{q}|^{4-\eta_h}$, with η_h and anomalous exponent and q_0 some intrinsic momentum scale. Therefore, the full correlation function is approximated by the self-energy contribution

$$D_{F,\mathbf{q}} \sim \frac{k_B T}{\kappa q_0^{\eta_h} \left|\mathbf{q}\right|^{4-\eta_h}}. \tag{2.63}$$

Inserting the previous expression into Eq. (2.61), it is obtained

$$\beta \kappa q_0^{\eta_h} \left|\mathbf{q}\right|^{4-\eta_h} \sim \frac{Y_{2D}}{2\pi \kappa q_0^{\eta_h}} \left|\mathbf{q}\right|^{2+\eta_h}, \tag{2.64}$$

which can only be satisfied provided $4 - \eta_h = 2 + \eta_h$, which gives us the Nelson and Peliti result: $\eta_h = 1$. The previous equation also implies that the momentum scale q_0 must be of the order of [83]

$$q_0 \sim \sqrt{\frac{Y_{2D} k_B T}{2\pi \kappa^2}} \tag{2.65}$$

This correction to the out-of-plane correlation function can be interpreted as a dressing of the bending rigidity by anharmonic effects which make it momentum dependent. We can therefore write

$$D_{F,\mathbf{q}} = \frac{k_B T}{\kappa_{\mathrm{eff}}(\mathbf{q}) \left|\mathbf{q}\right|^4}, \tag{2.66}$$

with the effective, momentum dependent, bending rigidity being given by

$$\kappa_{\mathrm{eff}}(\mathbf{q}) \sim \kappa \left(\frac{q_0}{|\mathbf{q}|}\right)^{\eta_h}. \tag{2.67}$$

The SCBA neglects the effects of interactions to the in-plane elastic constants. These can be seen as a screening of the effective interaction Eq. (2.55). Taking these effects into account results in the self-consistent screening approximation (SCSA) [70, 84]

$$\beta\Sigma^{\mathrm{SCSA}}_{F,\mathbf{q}} = \frac{1}{A}\sum_{\mathbf{p}} Y^{\mathrm{SCSA}}_{2D,\mathrm{eff}}(\mathbf{p})\frac{(\mathbf{q}\times\mathbf{p})_z^2}{|\mathbf{p}|^2}\frac{(\mathbf{q}\times\mathbf{p})_z^2}{|\mathbf{p}|^2}\beta D_{F,\mathbf{q}+\mathbf{p}}, \tag{2.68}$$

where the effective Young's modulus is given by the screening equation

$$Y^{\mathrm{SCSA}}_{2D,\mathrm{eff}}(\mathbf{p}) = Y_{2D} - Y^{\mathrm{SCBA}}_{2D,\mathrm{eff}}(\mathbf{p})\frac{Y_{2D}}{2A}\sum_{\mathbf{q}}\frac{(\mathbf{q}\times\mathbf{p})_z^2}{|\mathbf{p}|^2}\frac{(\mathbf{q}\times\mathbf{p})_z^2}{|\mathbf{p}|^2}\beta D_{F,\mathbf{q}+\mathbf{p}}\beta D_{F,\mathbf{q}}. \tag{2.69}$$

These equations are represented diagrammatically in Fig. 2.4. The SCSA equations, Eqs. (2.68) and (2.69) , must be solved self-consistently. But even without solving them, some important information can be extracted from these equations. Assuming that for long wavelengths we have a scaling behaviour

$$D^{-1}_{F,\mathbf{q}} \simeq \beta\Sigma^{\mathrm{SCSA}}_{F,\mathbf{q}} \sim |\mathbf{q}|^{4-\eta_h}, \tag{2.70}$$

$$Y^{\mathrm{SCSA}}_{2D,\mathrm{eff}}(\mathbf{q}) \sim |\mathbf{q}|^{\eta_u}, \tag{2.71}$$

where η_u is another anomalous exponent, and that the integral in Eq. (2.68) is dominated by values with small $\mathbf{p}$, from dimensional analysis it can be seen that Eq. (2.68) is only compatible with Eqs. (2.70) and (2.71) provided [70]

$$\eta_u = 2 - 2\eta_h. \tag{2.72}$$

The same relation can be obtained from Eq. (2.69). We see that the Nelson and Peliti result, $\eta_h = 1$, implies $\eta_u = 0$, as it should since that result was obtained ignoring possible screening effects. The relation between exponents Eq. (2.72) is the particular case of a more general result for a D–dimensional membrane embedded in a d–dimensional space ($d > D$): $\eta_u = 4 - D - 2\eta_h$ [25, 66]. The SCSA equations were solved analytically in the scaling limit [84] yielding a value of $\eta_h \simeq 0.821$, which through Eq. (2.72) implies $\eta_u \simeq 0.358$. These exponents have also been computed using perturbative renormalization group calculations [66], functional renormalization group calculations [85–88], molecular dynamics [89] and Monte Carlo simulations [90–94] with obtained values for η_h ranging from 0.72 to 0.85. The anomalous momentum dependence of the effective Young modulus is also shared by the in-plane elastic constants [66]. Therefore, as said in the introduction of this chapter, in a free crystalline membrane anharmonic effects make both the bending rigidity and the in-plane elastic constant momentum (or scale) dependent as

$$\kappa_{\mathrm{eff}}(\mathbf{q}) \sim |\mathbf{q}|^{-\eta_h}, \tag{2.73}$$

$$\lambda_{\mathrm{eff}}(\mathbf{q}),\ \mu_{\mathrm{eff}}(\mathbf{q}) \sim |\mathbf{q}|^{\eta_u}, \tag{2.74}$$

with both $\eta_h > 0$ and $\eta_u > 0$. This implies that the out-of-plane and normal-normal correlation functions in real space scale with distance as

$$\left\langle (h(\mathbf{x}) - h(\mathbf{0}))^2 \right\rangle \sim |\mathbf{x}|^{2-\eta_h}, \tag{2.75}$$

$$\left\langle (\delta\mathbf{n}(\mathbf{x}) - \delta\mathbf{n}(\mathbf{0}))^2 \right\rangle \sim |\mathbf{x}|^{-\eta_h}, \tag{2.76}$$

showing that anharmonic effects lead to a suppression of the out-of-plane fluctuations and restore the long range ordering of the local normals. At the same time, in-plane ordering is further destroyed and instead of the logarithmic behaviour of the in-plane correlation functions, Eq. (2.2), we obtain

$$\left\langle (\mathbf{u}(\mathbf{x}) - \mathbf{u}(\mathbf{0}))^2 \right\rangle \sim |\mathbf{x}|^{\eta_u} . \tag{2.77}$$

Nevertheless, if we focus on the quantity

$$\left\langle (\partial_i u_j(\mathbf{x}) - \partial_i u_j(\mathbf{0}))^2 \right\rangle \sim |\mathbf{x}|^{\eta_u - 2} , \tag{2.78}$$

we can see that in-plane orientational order is still preserved [25] provided $\eta_u < 2$. According to Eq. (2.72), $\eta_u < 2$ also implies that $\eta_h > 0$, and therefore provided $\eta_h > 0$ both in-plane and out-of-plane orientational orders are preserved.

Now that we have discussed the basics of physics of classical free crystalline membranes, we are in a position to discuss the quantum problem.

2.3 QUANTUM THEORY OF FREE CRYSTALLINE MEMBRANES

In order to access the possible importance of quantum effects in the properties of a crystalline membrane we estimate its Debye temperature. Due to the fact that a crystalline membrane has three acoustic phonons, we can also estimate three Debye temperatures by

$$T_{D,\zeta} = \frac{\hbar \omega_{\zeta,\mathbf{q}_D}}{k_B}, \tag{2.79}$$

with $\zeta = F, L, T$ indicating, respectively, the flexural, in-plane longitudinal and in-plane transverse phonon mode with dispersion relations given by Eqs. (2.32), (2.33) and (2.34); and $q_D = \sqrt{4\pi/A_{\text{cell}}}$ being the Debye momentum of the 2D crystal, with A_{cell} its unit cell area. For graphene we have $A_{\text{cell}} = \sqrt{3}a_{\text{g}}^2/2$, with $a_{\text{g}} = 2.46\text{Å}$ its lattice constant, giving us $q_D \simeq 1.5\text{Å}^{-1}$. We therefore estimate the Debye temperatures for graphene as $T_{D,L} \simeq 2500$ K, $T_{D,T} \simeq 1700$ K and $T_{D,F} \simeq 880$ K. This simple estimation indicates that, at least for graphene, quantum effects should play an important role for all the acoustic modes even at room temperature.

In order to take quantum effects into account, and since we will be interested mostly in equilibrium quantities, we proceed to quantize the classical theory defined by the classical Hamiltonian Eq. (2.37) using the Matsubara imaginary time path integral formalism (see Ref. [55] for a good introduction on the formalism). The partition function of the quantum crystalline membrane is expressed as

$$Z = \int D\left[\mathbf{u}, h\right] e^{-\mathcal{S}_E[\mathbf{u},h]}, \tag{2.80}$$

where $S_E\left[\mathbf{u}, h\right]$ is the Euclidean action of the membrane, which is obtained by adding a imaginary time kinetic energy term to the classical Hamiltonian, Eq. (2.16), being given by

$$\begin{aligned} \mathcal{S}_E\left[\mathbf{u}, h\right] = & \frac{1}{2}\int_0^\beta d\tau \int d^2\mathbf{x}\rho \left[(\partial_\tau \mathbf{u})^2 + (\partial_\tau h)^2\right] \\ & + \frac{1}{2}\int_0^\beta d\tau \int d^2\mathbf{x} \left[\kappa \left(\partial^2 h\right)^2 + c^{ijkl}\gamma_{ij}\gamma_{kl}\right] . \end{aligned} \tag{2.81}$$

As before in the classical case, γ_{ij} is the relevant strain tensor given by Eq. (2.17). The displacement fields are now a function of both the spacial coordinate, $\mathbf{x}$, and the imaginary time, $0 < \tau < \beta$: $\mathbf{u} = \mathbf{u}(\tau, \mathbf{x})$ and $h = h(\tau, \mathbf{x})$. The first line in Eq. (2.81) is the imaginary time kinetic energy term which takes into account quantum fluctuations. By neglecting this term the classical partition function, Eq. (2.40), is recovered. Expectation values of variables are computed as

$$\langle ... \rangle = \frac{\int D\left[\mathbf{u}, h\right] ... e^{-\mathcal{S}_E[\mathbf{u},h]}}{\int D\left[\mathbf{u}, h\right] e^{-\mathcal{S}_E[\mathbf{u},h]}}. \tag{2.82}$$

Just like for the classical Hamiltonian, we can split the Euclidean action into quadratic, cubic and quartic parts as

$$\mathcal{S}_E\left[\mathbf{u}, h\right] = \mathcal{S}_E^{(0)}\left[\mathbf{u}\right] + \mathcal{S}_E^{(0)}\left[h\right] + \mathcal{S}_{E,\text{int}}^{(3)}\left[\mathbf{u}, h\right] + \mathcal{S}_{E,\text{int}}^{(4)}\left[h\right], \tag{2.83}$$

where the quadratic part of the action is given by

$$\mathcal{S}_E^{(0)}\left[\mathbf{u}\right] = \frac{1}{2}\int_0^\beta d\tau \int d^2\boldsymbol{x}\left[\rho\left(\partial_\tau \mathbf{u}\right)^2 + c^{ijkl}\partial_i u_j \partial_k u_l\right], \tag{2.84}$$

$$\mathcal{S}_E^{(0)}\left[h\right] = \frac{1}{2}\int_0^\beta d\tau \int d^2\boldsymbol{x}\left[\rho\left(\partial_\tau h\right)^2 + \kappa\left(\partial^2 h\right)^2\right], \tag{2.85}$$

and the cubic and quartic interaction terms are given by

$$\mathcal{S}_{E,\text{int}}^{(3)}\left[\mathbf{u}, h\right] = \frac{1}{2}\int_0^\beta d\tau \int d^2\mathbf{x} c^{ijkl}\partial_i u_j\left(\partial_k h \partial_l h\right), \tag{2.86}$$

$$\mathcal{S}_{E,\text{int}}^{(4)}\left[h\right] = \frac{1}{8}\int_0^\beta d\tau \int d^2\mathbf{x} c^{ijkl}\left(\partial_i h \partial_j h\right)\left(\partial_k h \partial_l h\right). \tag{2.87}$$

Writing the displacement fields in terms of Fourier components

$$h(\tau, \mathbf{x}) = \frac{1}{\sqrt{\beta A}}\sum_{\tilde{\mathbf{q}}} h_{\tilde{\mathbf{q}}} e^{-iq_n\tau} e^{i\mathbf{q}\cdot\mathbf{x}}, \tag{2.88}$$

$$\mathbf{u}(\tau, \mathbf{x}) = \frac{1}{\sqrt{\beta A}}\sum_{\tilde{\mathbf{q}}} \mathbf{u}_{\tilde{\mathbf{q}}} e^{-iq_n\tau} e^{i\mathbf{q}\cdot\mathbf{x}}, \tag{2.89}$$

where we have written $\tilde{\mathbf{q}} = (iq_n, \mathbf{q})$, with $q_n = 2\pi n/\beta$ bosonic Matsubara frequencies defined such that $\mathcal{O}(\tau + \beta) = \mathcal{O}(\tau)$ for $\mathcal{O}$ a bosonic operator. In terms of Fourier components, and for an isotropic crystalline membrane, the quadratic action becomes

$$\mathcal{S}_E^{(0)}\left[h\right] = \frac{1}{2}\sum_{\tilde{\mathbf{q}}} h_{\tilde{\mathbf{q}}}\left[-\rho\left(iq_n\right)^2 + \kappa\left|\mathbf{q}\right|^4\right] h_{-\tilde{\mathbf{q}}}. \tag{2.90}$$

$$\mathcal{S}_E^{(0)}\left[\mathbf{u}\right] = \frac{1}{2}\sum_{\tilde{\mathbf{q}}} u^i_{\tilde{\mathbf{q}}}\left[-\rho\left(iq_n\right)^2 + \left(\lambda + \mu\right)\delta_{ij}\left|\mathbf{q}\right|^2 + \mu q_i q_j\right] u^j_{-\tilde{\mathbf{q}}}. \tag{2.91}$$

The interaction terms of the action can be written as

$$\mathcal{S}_{E,\text{int}}^{(3)}\left[\mathbf{u}, h\right] = \frac{i}{2\sqrt{\beta A}}\sum_{\tilde{\mathbf{q}},\tilde{\mathbf{p}}} u^i_{\tilde{\mathbf{p}}} c^{ijkl} p_j \left(q - p\right)_k q_l h_{\tilde{\mathbf{q}}-\tilde{\mathbf{p}}} h_{-\tilde{\mathbf{q}}}, \tag{2.92}$$

$$\mathcal{S}_{E,\text{int}}^{(4)}\left[h\right] = \frac{1}{8\beta A}\sum_{\tilde{\mathbf{q}},\tilde{\mathbf{q}}',\tilde{\mathbf{p}}} c^{ijkl}\left(q + p\right)_i q_j \left(q' - p\right)_k q'_l h_{\tilde{\mathbf{q}}+\tilde{\mathbf{p}}} h_{-\tilde{\boldsymbol{q}}} h_{\tilde{\mathbf{q}}'-\tilde{\mathbf{p}}} h_{-\tilde{\mathbf{q}}'}. \tag{2.93}$$

We are now in a position to study the anharmonic theory for crystalline membranes taking into account quantum mechanical effects.

2.3.1 *Anharmonic effects: perturbative calculation*

The Matsubara Green's functions for the in-plane and flexural phonons are defined as

$$D_{F,\tilde{\mathbf{q}}} = -\langle h_{\tilde{\mathbf{q}}} h_{-\tilde{\mathbf{q}}} \rangle , \tag{2.94}$$

$$D^{ij}_{uu,\tilde{\mathbf{q}}} = -\left\langle u^i_{\tilde{\mathbf{q}}} u^j_{-\tilde{\mathbf{q}}} \right\rangle . \tag{2.95}$$

Ignoring interaction terms, the bare Green's function can be read from the quadratic action, Eqs. (2.90) and (2.91), giving us

$$D^0_{F,\tilde{\mathbf{q}}} = \frac{1}{\rho\,(iq_n)^2 - \rho\omega^2_{F,\mathbf{q}}}, \tag{2.96}$$

$$D^0_{L/T,\tilde{\mathbf{q}}} = \frac{1}{\rho\,(iq_n)^2 - \rho\omega^2_{L/T,\mathbf{q}}}. \tag{2.97}$$

Just like in the classical case, $D^{ij}_{uu,\tilde{\mathbf{q}}}$ is decomposed into longitudinal and transverse components and the bare dispersion relations are given by Eqs. (2.32)-(2.34). The corresponding retarded Green's functions are obtained via analytic continuation $iq_n \to \omega + i0^+$, where 0^+ is an infinitesimal, positive constant (see Appendix (A.2)), giving us

$$D^{R,0}_{F,\mathbf{q}}(\omega) = \frac{1}{\rho\omega^2 - \rho\omega^2_{F,\mathbf{q}} + i\mathrm{sgn}(\omega)0^+}, \tag{2.98}$$

$$D^{R,0}_{L/T,\mathbf{q}}(\omega) = \frac{1}{\rho\omega^2 - \rho\omega^2_{L/T,\mathbf{q}} + i\mathrm{sgn}(\omega)0^+}. \tag{2.99}$$

The classical correlation functions (2.26) and (2.27) are obtained as the high temperature limit of

$$\begin{aligned} \langle h_{\mathbf{q}}(\tau) h_{-\mathbf{q}}(0)\rangle_0 &= -\frac{1}{\beta}\sum_{iq_n} D^0_{F,\tilde{\mathbf{q}}} e^{-iq_n\tau}, \\ \left\langle u^i_{\mathbf{q}}(\tau) u^j_{-\mathbf{q}}(0)\right\rangle_0 &= -\frac{1}{\beta}\sum_{iq_n} D^{ij,0}_{uu,\tilde{\mathbf{q}}} e^{-iq_n\tau}, \end{aligned} \tag{2.100}$$

for $\tau = 0$. In the limit $T \to \infty$, only the $q_n = 0$ term contributes to the sum over Matsubara frequencies and we recover Eqs. (2.26) and (2.29).

Now we wish to study the effect of the interaction terms Eqs. (2.86) and (2.87). In the interacting theory, the Matsubara Green's functions, Eqs (2.94) and (2.95), obey the Dyson equations

$$D_{F,\tilde{\mathbf{q}}} = D^0_{F,\tilde{\mathbf{q}}} + D^0_{F,\tilde{\mathbf{q}}}\Sigma_{F,\tilde{\mathbf{q}}} D_{F,\tilde{\mathbf{q}}}, \tag{2.101}$$

$$D^{ij}_{uu,\tilde{\mathbf{q}}} = D^{0,ij}_{uu,\tilde{\mathbf{q}}} + D^{0,ik}_{uu,\tilde{\mathbf{q}}}\Sigma^{kl}_{uu,\tilde{\mathbf{q}}} D^{lj}_{uu,\tilde{\mathbf{q}}}, \tag{2.102}$$

where $\Sigma_{F,\tilde{\mathbf{q}}}$ and $\Sigma^{ij}_{F,\tilde{\mathbf{q}}}$ are, respectively, the self-energies of the flexural and in-plane phonon modes. Due to the fact that the interaction terms of the Euclidean action, Eqs. (2.86) and (2.87), have the same structure as their classical counterparts, Eqs. (2.38) and (2.39), the perturbative evaluation of the self-energies in the quantum case has the same diagrammatic structure as in the classical theory, with interactions still being represented diagrammatically as in Fig. 2.1. It is our aim to evaluate the phonon

self-energies in the long wavelength, low energy limit in order to study the possible reconstruction of the phonons dispersion relation, which is given by

$$\Omega^2_{\zeta,\mathbf{q}} = \omega^2_{\zeta,\mathbf{q}} + \mathrm{Re}\Sigma^R_{\zeta,\mathbf{q}}(\omega_{\zeta,\mathbf{q}})/\rho, \tag{2.103}$$

where $\Sigma^R_{\zeta,\mathbf{q}}(\omega)$ is the retarded self-energy, which can be obtained from the Matsubara self-energy, $\Sigma_{\zeta,\tilde{\mathbf{q}}} = \Sigma_{\zeta,\mathbf{q}}(iq_n)$ by the analytic continuation $iq_n \to \omega + i0^+$.

2.3.1.1 *Flexural phonon self-energy*

In order to study the correction to the flexural phonon Green's function, it is useful to first integrate out the in-plane phonons. The advantage of the path integral formalism is that the calculation follows the exact same steps as in the classical case. After integrating out the in-plane modes, the quantum partition function becomes

$$Z = Z_{\mathbf{u},0} \int D[h] e^{-\mathcal{S}_{E,\mathrm{eff}}[h]}, \tag{2.104}$$

where $Z_{\mathbf{u},0}$ is the partition function for the non-interacting in-plane modes and $\mathcal{S}_{\mathrm{eff}}[h]$ is the effective Euclidean action, which is given by

$$\mathcal{S}_{E,\mathrm{eff}}[h] = \mathcal{S}^{(0)}_E[h] + \mathcal{S}^{(4)}_{E,\mathrm{eff}}[h], \tag{2.105}$$

where $S^{(4)}_{E,\mathrm{eff}}[h]$ describes the effective interaction for the flexural phonons, which in terms of Fourier components is given by

$$\mathcal{S}^{(4)}_{E,\mathrm{eff}}[h] = \frac{1}{8\beta A} \sum_{\substack{\tilde{\mathbf{q}},\tilde{\mathbf{q}}' \\ \tilde{\mathbf{p}}\neq\tilde{\mathbf{0}}}} \mathcal{R}^{ijkl}_{\tilde{\mathbf{p}}} (q+p)_i q_j (q'-p)_k q'_l h_{\tilde{\mathbf{q}}+\tilde{\mathbf{p}}} h_{-\tilde{\mathbf{q}}} h_{\tilde{\mathbf{q}}'-\tilde{\mathbf{p}}} h_{-\tilde{\mathbf{q}}'}, \tag{2.106}$$

with $\mathcal{R}^{ijkl}_{\tilde{\mathbf{p}}}$ the effective interaction for the flexural phonons

$$\mathcal{R}^{ijkl}_{\tilde{\mathbf{p}}} = c^{ijkl} - c^{iji'j'} \left\langle u_{i'j',\tilde{\mathbf{p}}} u_{k'l',-\tilde{\mathbf{p}}} \right\rangle_0 c^{k'l'kl}. \tag{2.107}$$

Just as in the classical case the first term of Eq. (2.107) is due to the local direct interaction, Eq. (2.93), while the second term is an in-plane phonon mediated interaction. For the same reasons as in the classical case, for processes where the exchanged momentum and Matsubara frequency are zero, $\tilde{\mathbf{p}} = \tilde{\mathbf{0}}$, the direct quartic interaction is cancelled by the interaction mediated by the in-plane phonons, $\mathcal{R}^{ijkl}_{\tilde{\mathbf{p}}=\tilde{\mathbf{0}}} = 0$, and therefore we have explicitly excluded these processes from Eq. (2.106). Therefore, the effective interaction in the quantum case as the same formal structure as the one in the classical case, Eq. (2.46), with the only difference that now the average $\langle\rangle_0$ represents a quantum thermodynamic average. However, while in the classical case the contraction of the effective interaction tensor with the momenta of the flexural phonons gave origin to a very simple result, Eq. (2.55), the situation will now be more complex. First we notice that the effective interaction tensor $\mathcal{R}^{ijkl}_{\tilde{\mathbf{p}}}$ has the same symmetries as the stiffness tensor, (2.10), namely

$$\mathcal{R}^{ijkl}_{\tilde{\mathbf{p}}} = \mathcal{R}^{klij}_{\tilde{\mathbf{p}}} = \mathcal{R}^{jikl}_{\tilde{\mathbf{p}}}. \tag{2.108}$$

For an isotropic membrane a forth order tensor that is a function of the wavevector $\mathbf{p}$ can be expressed in terms of the longitudinal and transverse projectors, $P^{ij}_{L,\mathbf{p}}$ and $P^{ij}_{T,\mathbf{p}}$. In a space of arbitrary dimensionality there are 5 independent components for such a

tensor with the symmetry Eq. (2.108) that can be expressed just in terms of $P^{ij}_{L,\mathbf{p}}$ and $P^{ij}_{T,\mathbf{p}}$. The five possible combinations of the projection tensors are

$$\begin{aligned}
&P^{ij}_{L,\mathbf{p}}P^{kl}_{L,\mathbf{p}},\\
&P^{ij}_{T,\mathbf{p}}P^{kl}_{T,\mathbf{p}},\\
&P^{ik}_{T,\mathbf{p}}P^{jl}_{T,\mathbf{p}}+P^{il}_{T,\mathbf{p}}P^{jk}_{T,\mathbf{p}},\\
&P^{ij}_{L,\mathbf{p}}P^{kl}_{T,\mathbf{p}}+P^{ij}_{T,\mathbf{p}}P^{kl}_{L,\mathbf{p}},\\
&P^{ik}_{L,\mathbf{p}}P^{jl}_{T,\mathbf{p}}+P^{jk}_{L,\mathbf{p}}P^{il}_{T,\mathbf{p}}+P^{il}_{L,\mathbf{p}}P^{jk}_{T,\mathbf{p}}+P^{jl}_{L,\mathbf{p}}P^{ik}_{T,\mathbf{p}}.
\end{aligned}$$

In terms of these projectors we can write for $\tilde{\mathbf{p}}\neq\mathbf{0}$

$$\begin{aligned}
-\left\langle u_{ij,\tilde{\mathbf{p}}}u_{kl,-\tilde{\mathbf{p}}}\right\rangle_0 &= \frac{1}{2}\left|\mathbf{p}\right|^2 D^0_{L,\tilde{\mathbf{p}}}\left(P^{ik}_{L,\mathbf{p}}P^{jl}_{L,\mathbf{p}}+P^{jk}_{L,\mathbf{p}}P^{il}_{L,\mathbf{p}}\right)\\
&\quad+\frac{1}{2}\left|\mathbf{p}\right|^2 D^0_{T,\tilde{\mathbf{p}}}\left(P^{ik}_{L,\mathbf{p}}P^{jl}_{T,\mathbf{p}}+P^{jk}_{L,\mathbf{p}}P^{il}_{T,\mathbf{p}}\right),
\end{aligned}\tag{2.109}$$

such that

$$\begin{aligned}
-c^{iji'j'}\left\langle u_{i'j',\tilde{\mathbf{p}}}u_{k'l',-\tilde{\mathbf{p}}}\right\rangle_0 c^{k'l'kl} &=\\
&=\lambda^2\left|\mathbf{p}\right|^2 D^0_{L,\tilde{\mathbf{p}}}P^T_{ij,\mathbf{p}}P^T_{kl,\mathbf{p}}+(\lambda+2\mu)^2\left|\mathbf{p}\right|^2 D^0_{L,\tilde{\mathbf{p}}}P^L_{ij,\mathbf{p}}P^L_{kl,\mathbf{p}}\\
&\quad\lambda(\lambda+2\mu)\left|\mathbf{p}\right|^2 D^0_{L,\tilde{\mathbf{p}}}\left(P^L_{ij,\mathbf{p}}P^T_{kl,\mathbf{p}}+(ij\leftrightarrow kl)\right)\\
&\quad+\mu^2\left|\mathbf{p}\right|^2 D^0_{T,\tilde{\mathbf{p}}}\left(P^T_{ik,\mathbf{p}}P^L_{jl,\mathbf{p}}+(i\leftrightarrow j)+(k\leftrightarrow l)+(ik\leftrightarrow jl)\right).
\end{aligned}\tag{2.110}$$

We also notice that the stiffness tensor can be written in terms of $P^{ij}_{L,\mathbf{p}}$ and $P^{ij}_{T,\mathbf{p}}$ as

$$\begin{aligned}
c^{ijkl} &= \lambda P^{ij}_{T,\mathbf{p}}P^{kl}_{T,\mathbf{p}}+\mu\left(P^{ik}_{T,\mathbf{p}}P^{jl}_{T,\mathbf{p}}+(i\leftrightarrow j)\right)\\
&\quad+(\lambda+2\mu)P^{ij}_{L,\mathbf{p}}P^{kl}_{L,\mathbf{p}}+\lambda\left(P^{ij}_{T,\mathbf{p}}P^{kl}_{L,\mathbf{p}}+(ij\leftrightarrow kl)\right)\\
&\quad+\mu\left(P^{ik}_{T,\mathbf{p}}P^{jl}_{L,\mathbf{p}}+(i\leftrightarrow j)+(k\leftrightarrow l)+(ik\leftrightarrow jl)\right).
\end{aligned}\tag{2.111}$$

We now notice that in 2D we can introduce a basis $\left\{\mathbf{e}_{\parallel,\mathbf{p}},\mathbf{e}_{\perp,\mathbf{p}}\right\}$, with $\mathbf{e}_{\parallel,\mathbf{p}}=\mathbf{p}/\left|\mathbf{p}\right|$ and $\mathbf{e}_{\perp,\mathbf{p}}=\mathbf{e}_z\times\mathbf{e}_{\parallel,\mathbf{p}}$, such that the projection operators can be written as

$$P^{ij}_{L,\mathbf{p}} = e^i_{\parallel,\mathbf{p}}e^j_{\parallel,\mathbf{p}},\tag{2.112}$$

$$P^{ij}_{T,\mathbf{p}} = e^i_{\perp,\mathbf{p}}e^j_{\perp,\mathbf{p}}.\tag{2.113}$$

With this, it is easy to see that in 2D $P^{ik}_{T,\mathbf{p}}P^{jl}_{T,\mathbf{p}}+P^{il}_{T,\mathbf{p}}P^{jk}_{T,\mathbf{p}}=2P^{ij}_{T,\mathbf{p}}P^{kl}_{T,\mathbf{p}}$. Therefore, in 2D $\mathcal{R}^{ijkl}_{\tilde{\mathbf{p}}}$ only has four independent components. We can thus write $\mathcal{R}^{ijkl}_{\tilde{\mathbf{p}}}$ in terms of the $\left\{\boldsymbol{e}_{\parallel,\mathbf{p}},\boldsymbol{e}_{\perp,\mathbf{p}}\right\}$ basis as

$$\begin{aligned}
\mathcal{R}^{ijkl}_{\tilde{\mathbf{p}}} &= \mathcal{R}^{\perp\perp\perp\perp}_{\tilde{\mathbf{p}}}e^i_{\perp,\mathbf{p}}e^j_{\perp,\mathbf{p}}e^k_{\perp,\mathbf{p}}e^l_{\perp,\mathbf{p}}+\mathcal{R}^{\parallel\parallel\parallel\parallel}_{\tilde{\mathbf{p}}}e^i_{\parallel,\mathbf{p}}e^j_{\parallel,\mathbf{p}}e^k_{\parallel,\mathbf{p}}e^l_{\parallel,\mathbf{p}}\\
&\quad+\mathcal{R}^{\perp\perp\parallel\parallel}_{\tilde{\mathbf{p}}}\left(e^i_{\perp,\mathbf{p}}e^j_{\perp,\mathbf{p}}e^k_{\parallel,\mathbf{p}}e^l_{\parallel,\mathbf{p}}+(ij\leftrightarrow kl)\right)\\
&\quad+\mathcal{R}^{\perp\parallel\perp\parallel}_{\tilde{\mathbf{p}}}\left(e^i_{\perp,\mathbf{p}}e^j_{\parallel,\mathbf{p}}e^k_{\perp,\mathbf{p}}e^l_{\parallel,\mathbf{p}}+(i\leftrightarrow j)+(k\leftrightarrow l)+(ik\leftrightarrow jl)\right).
\end{aligned}\tag{2.114}$$

Summing up the two contributions to the effective interaction, Eqs. (2.110) and (2.111), the different components of $\mathcal{R}^{ijkl}_{\tilde{\mathbf{p}}}$ are given by

$$\mathcal{R}^{\perp\perp\perp\perp}_{\tilde{\mathbf{p}}} = \lambda\left(1+\lambda\left|\mathbf{p}\right|^2 D^0_{L,\tilde{\mathbf{p}}}\right)+2\mu, \tag{2.115}$$

$$\mathcal{R}^{\parallel\parallel\parallel\parallel}_{\tilde{\mathbf{p}}} = (\lambda+2\mu)\left(1+(\lambda+2\mu)\left|\mathbf{p}\right|^2 D^0_{L,\tilde{\mathbf{p}}}\right), \tag{2.116}$$

$$\mathcal{R}^{\perp\perp\parallel\parallel}_{\tilde{\mathbf{p}}} = \lambda\left(1+(\lambda+2\mu)\left|\mathbf{p}\right|^2 D^0_{L,\tilde{\mathbf{p}}}\right), \tag{2.117}$$

$$\mathcal{R}^{\perp\parallel\perp\parallel}_{\tilde{\mathbf{p}}} = \mu\left(1+\mu\left|\mathbf{p}\right|^2 D^0_{T,\tilde{\mathbf{p}}}\right). \tag{2.118}$$

Using Eq. (2.97) the components of $\mathcal{R}^{ijkl}_{\tilde{\mathbf{p}}}$ are given by

$$\mathcal{R}^{\perp\perp\perp\perp}_{\tilde{\mathbf{p}}} = Y_{2D}+\frac{\lambda^2}{\lambda+2\mu}\tilde{D}^0_{L,\tilde{\mathbf{p}}}, \tag{2.119}$$

$$\mathcal{R}^{\parallel\parallel\parallel\parallel}_{\tilde{\mathbf{p}}} = (\lambda+2\mu)\,\tilde{D}^0_{L,\tilde{\mathbf{p}}}, \tag{2.120}$$

$$\mathcal{R}^{\perp\perp\parallel\parallel}_{\tilde{\mathbf{p}}} = \lambda\tilde{D}^0_{L,\tilde{\mathbf{p}}}, \tag{2.121}$$

$$\mathcal{R}^{\perp\parallel\perp\parallel}_{\tilde{\mathbf{p}}} = \mu\tilde{D}^0_{T,\tilde{\mathbf{p}}}, \tag{2.122}$$

where we have introduced

$$\tilde{D}^0_{L/T,\tilde{\mathbf{p}}} = \frac{\rho\left(ip_n\right)^2}{\rho\left(ip_n\right)^2-\rho\omega^2_{\mathbf{p},L/T}}. \tag{2.123}$$

As we have said previously, the classical theory is recovered if we neglect the imaginary time kinetic energy term in the Euclidean action Eq. (2.81). Doing this amounts to neglecting all the terms involving in-plane phonons Matsubara frequencies, that is setting $ip_n = 0$. In this situation all of the components of the effective interaction are zero but for $\mathcal{R}^{\perp\perp\perp\perp}_{\tilde{\mathbf{p}}}$, which for $ip_n = 0$ is reduced to Y_{2D} and we recover the classical effective interaction Eq. (2.55). Therefore, it is convenient to distinguish between the frequency independent *classical* interaction,

$$\mathcal{R}^{\perp\perp\perp\perp,\mathrm{cl}}_{\tilde{\mathbf{p}}} = Y_{2D}, \tag{2.124}$$

and the frequency dependent, which are zero for $ip_n = 0$, *quantum* interactions,

$$\mathcal{R}^{M,\mathrm{qt}}_{\tilde{\mathbf{p}}} = C^M\tilde{D}^0_{M,\tilde{\mathbf{p}}}. \tag{2.125}$$

We have introduced the index M, which runs over $\left\{^{\perp\perp\perp\perp},\ ^{\parallel\parallel\parallel\parallel},\ ^{\perp\perp\parallel\parallel},\ ^{\perp\parallel\perp\parallel}\right\}$, defined

$$C^{\perp\perp\perp\perp} = \frac{\lambda^2}{\lambda+2\mu}, \tag{2.126}$$

$$C^{\parallel\parallel\parallel\parallel} = \lambda+2\mu, \tag{2.127}$$

$$C^{\perp\perp\parallel\parallel} = \lambda, \tag{2.128}$$

$$C^{\perp\parallel\perp\parallel} = \mu, \tag{2.129}$$

and denote $\tilde{D}^0_{M,\tilde{\mathbf{p}}} = \tilde{D}^0_{L,\tilde{\mathbf{p}}}$ for $M = ^{\perp\perp\perp\perp}, ^{\parallel\parallel\parallel\parallel}, ^{\perp\perp\parallel\parallel}$ and $\tilde{D}^0_{M,\tilde{\mathbf{p}}} = \tilde{D}^0_{L,\tilde{\mathbf{p}}}$ for $M = ^{\perp\parallel\perp\parallel}$.

To lowest order in the effective interaction, the self-energy of the flexural phonon is represented diagrammatically by Fig. 2.2(a) an is explicitly given by

$$\begin{aligned}\Sigma^{(0)}_{F,\tilde{\mathbf{q}}} &= -\frac{1}{\beta A}\sum_{\tilde{\mathbf{p}}}\mathcal{R}^{ijkl}_{\tilde{\mathbf{p}}}\left(q+p\right)_i q_j\left(q+p\right)_k q_l D^0_{F,\tilde{\mathbf{q}}+\tilde{\mathbf{p}}}\\ &= -\frac{1}{\beta A}\sum_{\tilde{\mathbf{p}},M}\mathcal{R}^{M}_{\tilde{\mathbf{p}}}\,g^M_{\mathbf{q},\mathbf{p}}D^0_{F,\tilde{\mathbf{q}}+\tilde{\mathbf{p}}},\end{aligned} \tag{2.130}$$

where we have introduced the geometrical factors

$$g^{\perp\perp\perp\perp}_{\mathbf{q},\mathbf{p}} = |\mathbf{q}|^4 \sin^4\theta_{\mathbf{q},\mathbf{p}}, \tag{2.131}$$

$$g^{\parallel\parallel\parallel\parallel}_{\mathbf{q},\mathbf{p}} = |\mathbf{q}|^2 \cos^2\theta_{\mathbf{q},\mathbf{p}} \left(|\mathbf{q}|\cos\theta_{\mathbf{q},\mathbf{p}} + |\mathbf{p}|\right)^2, \tag{2.132}$$

$$g^{\perp\perp\parallel\parallel}_{\mathbf{q},\mathbf{p}} = 2\,|\mathbf{q}|^3 \sin^2\theta_{\mathbf{q},\mathbf{p}} \cos\theta_{\mathbf{q},\mathbf{p}} \left(|\mathbf{q}|\cos\theta_{\mathbf{q},\mathbf{p}} + |\mathbf{p}|\right), \tag{2.133}$$

$$g^{\perp\parallel\perp\parallel}_{\mathbf{q},\mathbf{p}} = |\mathbf{q}|^2 \sin^2\theta_{\mathbf{q},\mathbf{p}} \left(2\,|\mathbf{q}|\cos\theta_{\mathbf{q},\mathbf{p}} + |\mathbf{p}|\right)^2, \tag{2.134}$$

where $\theta_{\mathbf{q},\mathbf{p}}$ is the angle formed between the wavevectors $\mathbf{p}$ and $\mathbf{q}$. We analyse the contributions due to the *classical* and *quantum* interactions separately. For the *classical* interaction we obtain

$$\Sigma^{(0),\mathrm{cl}}_{F,\tilde{\mathbf{q}}} = -Y_{2D}\frac{1}{\beta A}\sum_{\tilde{\mathbf{p}}} g^{\perp\perp\perp\perp}_{\mathbf{q},\mathbf{p}} D^0_{F,\tilde{\mathbf{q}}+\tilde{\mathbf{p}}}. \tag{2.135}$$

$\Sigma^{(0),\mathrm{cl}}_{F,\tilde{\mathbf{q}}}$ is thus frequency independent. The sum over Matsubara frequencies is performed using standard contour integration techniques. Writing $D^0_{F,\tilde{\mathbf{q}}} = D^0_{F,\mathbf{q}}(iq_n)$ we obtain

$$\begin{aligned}\Sigma^{(0),\mathrm{cl}}_{F,\mathbf{q}} &= -Y_{2D}\frac{1}{A}\sum_{\mathbf{p}} g^{\perp\perp\perp\perp}_{\mathbf{q},\mathbf{p}} \oint \frac{dz}{2\pi i} b(z) D^0_{F,\mathbf{q}+\mathbf{p}}(z) \\ &= -Y_{2D}\frac{1}{A}\sum_{\mathbf{p}} g^{\perp\perp\perp\perp}_{\mathbf{q},\mathbf{p}} \int \frac{d\nu}{\pi} b(\nu)\mathrm{Im}D^{0,R}_{F,\mathbf{q}+\mathbf{p}}(\nu),\end{aligned} \tag{2.136}$$

where $b(\nu) = \left(e^{\beta\nu}-1\right)^{-1}$ is the Bose-Einstein distribution function and $D^{0,R}_{F,\mathbf{q}}(\nu)$ is the retarded Green's function. From Eq. (2.98), we have that $\mathrm{Im}D^{0,R}_{F,\mathbf{q}}(\nu)$ is given by

$$\mathrm{Im}D^{0,R}_{F,\mathbf{q}}(\nu) = -\frac{1}{\rho}\pi\mathrm{sgn}(\nu)\delta\left(\nu^2 - \omega^2_{F,\mathbf{q}}\right). \tag{2.137}$$

Using the δ-function to perform the integration over frequency, the self-energy becomes

$$\Sigma^{(0),\mathrm{cl}}_{F,\mathbf{q}} = Y_{2D}\,|\mathbf{q}|^4 \int \frac{d^2\mathbf{p}}{(2\pi)^2}\sin^4\theta_{\mathbf{q},\mathbf{p}} \frac{\coth\left(\beta\omega_{F,\mathbf{q}+\mathbf{p}}/2\right)}{2\rho\omega_{F,\mathbf{q}+\mathbf{p}}}. \tag{2.138}$$

In the high temperature limit, $T\to\infty$, we approximate $\coth\left(\beta\omega_{F,\mathbf{q}+\mathbf{p}}/2\right) \simeq 2k_BT/\omega_{F,\mathbf{q}+\mathbf{p}}$ and thus obtain

$$\lim_{T\to\infty}\Sigma^{(0),\mathrm{cl}}_{F,\mathbf{q}} = Y_{2D}\,|\mathbf{q}|^4 \int \frac{d^2\mathbf{p}}{(2\pi)^2}\frac{\sin^4\theta_{\mathbf{q},\mathbf{p}}}{\kappa\,|\mathbf{q}+\mathbf{p}|^4} = \frac{3Y_{2D}k_BT}{16\pi\kappa}\,|\mathbf{q}|^2, \tag{2.139}$$

recovering the classical result Eq. (2.58) as expected. In the low temperature limit, $T\to 0$, we have that $\coth\left(\beta\omega_{F,\mathbf{q}+\mathbf{p}}/2\right) \simeq 1$ and, for small momenta $\mathbf{q}$, Eq. (2.138) becomes

$$\begin{aligned}\lim_{T\to 0}\Sigma^{(0),\mathrm{cl}}_{F,\mathbf{q}} &= Y_{2D}\,|\mathbf{q}|^4 \int \frac{d^2\mathbf{p}}{(2\pi)^2}\frac{\sin^4\theta_{\mathbf{q},\mathbf{p}}}{2\rho\omega_{F,\mathbf{q}+\mathbf{p}}} \\ &\simeq Y_{2D}\frac{\hbar}{2\sqrt{\rho\kappa}}\frac{3}{16\pi}\,|\mathbf{q}|^4\log\left(\frac{\Lambda}{|\mathbf{q}|}\right),\end{aligned} \tag{2.140}$$

where we have restored $\hbar$ and Λ is a high momentum cut-off, which we identify as the Debye momentum, $\Lambda = q_D$. Notice that differently from the high temperature case, in

the zero temperature limit $\Sigma^{(0),\mathrm{cl}}_{F,\mathbf{q}} \propto |\mathbf{q}|^4$ with logarithmic accuracy and, therefore, the *classical* interaction does not lead to a reconstruction of the flexural phonon dispersion relation.

Now let us focus on the *quantum* contributions to the self-energy. These can be written as

$$\Sigma^{(0),\mathrm{qt}}_{F,\tilde{\mathbf{q}}} = \sum_M \Sigma^{(0)M,\mathrm{qt}}_{F,\tilde{\mathbf{q}}}, \tag{2.141}$$

with each component $\Sigma^{(0)M,\mathrm{qt}}_{F,\tilde{\mathbf{q}}}$ being given by

$$\Sigma^{(0)M,\mathrm{qt}}_{F,\mathbf{q}}(iq_n) = -\frac{C^M}{\beta A}\sum_{ip_m,\mathbf{q}} g^M_{\mathbf{q},\mathbf{p}} \tilde{D}^0_{M,\mathbf{p}}(ip_m) D^0_{F,\mathbf{q}+\mathbf{p}}\left(iq_n + ip_m\right). \tag{2.142}$$

Performing the sum over Matsubara frequencies we obtain

$$\begin{aligned}\Sigma^{(0)M,\mathrm{qt}}_{F,\mathbf{q}}(iq_n) &= -\frac{C^M}{A}\sum_{\mathbf{p}} g^M_{\mathbf{q},\mathbf{p}} \oint \frac{dz}{2\pi i} b(z)\tilde{D}^0_{M,\mathbf{p}}(z) D^0_{F,\mathbf{q}+\mathbf{p}}\left(iq_n + z\right) \\ &= -\frac{C^M}{A}\sum_{\mathbf{p}} g^M_{\mathbf{q},\mathbf{p}} P\int \frac{d\nu}{\pi} b(\nu)\mathrm{Im}\tilde{D}^{0,R}_{M,\mathbf{p}}(\nu) D^0_{F,\mathbf{q}+\mathbf{p}}\left(iq_n + \nu\right) \\ &\quad - \frac{C^M}{A}\sum_{\mathbf{p}} g^M_{\mathbf{q},\mathbf{p}} P\int \frac{d\nu}{\pi} b(\nu)\tilde{D}^{0,R}_{M,\mathbf{p}}(iq_n - \nu)\mathrm{Im} D^{0,R}_{F,\mathbf{q}+\mathbf{p}}\left(\nu\right), \end{aligned} \tag{2.143}$$

where P indicates Cauchy's principal value. Using the δ-functions in $\mathrm{Im}\tilde{D}^{0,R}_{M,\mathbf{p}}(\nu)$ and $\mathrm{Im}D^{0,R}_{F,\mathbf{q}+\mathbf{p}}\left(\nu\right)$ to perform the integration over real frequencies we obtain

$$\Sigma^{(0)M,\mathrm{qt}}_{F,\mathbf{q}}(iq_n) = C^M \int \frac{d^2\mathbf{p}}{(2\pi)^2} g^M_{\mathbf{q},\mathbf{p}} \mathcal{K}^M_{\mathbf{q},\mathbf{p}}(iq_n). \tag{2.144}$$

where we have defined

$$\begin{aligned}\mathcal{K}^M_{\mathbf{q},\mathbf{p}}(iq_n) = &\frac{1}{2\rho\omega_{F,\mathbf{q}+\mathbf{p}}} \frac{\omega_{F,\mathbf{q}+\mathbf{p}}\left(\omega_{F,\mathbf{q}+\mathbf{p}} + \omega_{M,\mathbf{p}}\right) - \left(iq_n\right)^2}{\left(\omega_{F,\mathbf{q}+\mathbf{p}} + \omega_{M,\mathbf{p}}\right)^2 - \left(iq_n\right)^2} \\ &+ \frac{b(\omega_{M,\mathbf{p}})}{\rho\omega_{M,\mathbf{p}}} \frac{\omega^2_{M,\mathbf{p}}\left((iq_n)^2 + \omega^2_{M,\mathbf{p}} - \omega^2_{F,\mathbf{q}+\mathbf{p}}\right)}{\left((iq_n)^2 + \omega^2_{M,\mathbf{p}} - \omega^2_{F,\mathbf{q}+\mathbf{p}}\right)^2 - 4\left(iq_n\right)^2\omega^2_{M,\mathbf{p}}} \\ &+ \frac{b(\omega_{F,\mathbf{q}+\mathbf{p}})}{\rho\omega_{F,\mathbf{q}+\mathbf{p}}} \frac{\left((iq_n)^2 - \omega^2_{F,\mathbf{q}+\mathbf{p}}\right)^2 - \omega^2_{M,\mathbf{p}}\left((iq_n)^2 + \omega^2_{F,\mathbf{q}+\mathbf{p}}\right)}{\left((iq_n)^2 - \omega^2_{M,\mathbf{p}} + \omega^2_{F,\mathbf{q}+\mathbf{p}}\right)^2 - 4\left(iq_n\right)^2\omega^2_{F,\mathbf{q}+\mathbf{p}}}. \end{aligned} \tag{2.145}$$

The first line of the previous expression takes into account zero point quantum fluctuations, while the last two lines are due to thermally activated phonons. We are interested in the real part of the retarded self-energy, which is obtained by performing the analytic continuation $iq_n \to \omega + i0^+$, such that

$$\mathrm{Re}\Sigma^{(0)M,\mathrm{qt},R}_{F,\mathbf{q}}(\omega) = C^M P\int \frac{d^2\mathbf{p}}{(2\pi)^2} g^M_{\mathbf{q},\mathbf{p}} \mathcal{K}^M_{\mathbf{q},\mathbf{p}}(\omega), \tag{2.146}$$

and $\mathcal{K}^M_{\mathbf{q},\mathbf{p}}(\omega) = \mathrm{Re}\mathcal{K}^M_{\mathbf{q},\mathbf{p}}(iq_n \to \omega + i0^+)$. In the high-temperature limit limit, we can neglect zero point quantum fluctuations and approximate $b(\omega) \simeq k_B T/\omega$. Therefore, we obtain

$$\lim_{T\to\infty} \mathcal{K}^M_{\mathbf{q},\mathbf{p}}(\omega) = \frac{k_B T}{\rho\omega^2_{F,\mathbf{q}+\mathbf{p}}} \times \\ \times \frac{\omega^2\left(\omega^2 - \omega^2_{M,\mathbf{p}} - \omega^2_{F,\mathbf{q}+\mathbf{p}}\right)}{\left[\omega^2 - (\omega_{F,\mathbf{q}+\mathbf{p}} + \omega_{M,\mathbf{p}})^2\right]\left[\omega^2 - (\omega_{F,\mathbf{q}+\mathbf{p}} - \omega_{M,\mathbf{p}})^2\right]}. \quad (2.147)$$

In this form we can see explicitly that for $\omega = 0$ we have $\lim_{T\to\infty} \mathcal{K}^M_{\mathbf{q},\mathbf{p}}(\omega) = 0$ and the *quantum* interactions do not give any contribution to the self-energy in the $T \to \infty$ limit. Notice, however, that even if we take $T \to \infty$ but keep $\omega \neq 0$, we obtain a non zero value of $\mathrm{Re}\Sigma^{M,\mathrm{qt}}_{\mathbf{q}}(\omega)$. The analysis of this situation is subtle. For small ω and $\mathbf{q}$, $\lim_{T\to\infty} \mathcal{K}^M_{\mathbf{q},\mathbf{p}}(\omega)$ displays poles when for $|\mathbf{p}| = q_{L/T}$, with

$$q_L = \sqrt{\frac{\lambda + 2\mu}{\kappa}}, \quad (2.148)$$

$$q_T = \sqrt{\frac{\mu}{\kappa}}, \quad (2.149)$$

when $\omega_{F,\mathbf{p}} = \omega_{M,\mathbf{p}}$. For typical graphene values we have $q_L \simeq 4.2\text{Å}^{-1}$ and $q_T \simeq 2.8\text{Å}^{-1}$, which are larger than the Debye momentum. Keeping ω finite, $\mathcal{K}^M_{\mathbf{q},\mathbf{p}}(\omega)$ changes sign at this divergence which is split into two. Since the integration in Eq. (2.146) is performed in the principal value sense the overall result is finite. For small momenta we approximate $\omega_{F,\mathbf{q}+\mathbf{p}} \pm \omega_{M,\mathbf{p}} \simeq \omega_{M,\mathbf{p}}$ and therefore obtain

$$\lim_{T\to\infty} \mathcal{K}^M_{\mathbf{q},\mathbf{p}}(\omega) \simeq \frac{k_B T}{\rho\omega^2_{F,\mathbf{q}+\mathbf{p}}} \frac{\omega^2}{\omega^2 - \omega^2_{M,\mathbf{p}}}. \quad (2.150)$$

Notice that another possible divergence can occur when $\mathbf{q} = -\mathbf{p}$. In order to see if this divergence is integrable or not we must also consider the effect of the geometrical factors $g^M_{\mathbf{q},\mathbf{p}}$. For the contributions with $M = {}^{\perp\perp\perp\perp}$ and $M = {}^{\perp\perp\parallel\parallel}$ this divergence if suppressed by the respective geometrical factor $g^M_{\mathbf{q},\mathbf{p}}$. The same does not happen for the terms with $M = {}^{\parallel\parallel\parallel\parallel}$ and $M = {}^{\perp\parallel\perp\parallel}$ and the divergence of the integral at $\mathbf{q} = -\mathbf{p}$ makes the integral diverge logarithmically. However, this divergence is a pathology of the first order perturbation theory that should disappear if a more complete self-consistent calculation is performed. It can be checked that if for long wavelengths the dispersion relation of flexural phonons is reconstructed as $\omega^2_{F,\mathbf{q}} \propto |\mathbf{q}|^{4-\eta_h}$ with $\eta_h > 0$, this divergence is regularized. Ignoring this issue, the integrals can be performed approximately yielding

$$\lim_{T\to\infty} \mathrm{Re}\Sigma^{(0)M,\mathrm{qt},R}_{F,\mathbf{q}}(\omega) \sim C^M \frac{k_B T}{\kappa} |\mathbf{q}|^2 \left(\frac{\omega}{\omega_{M,\mathbf{q}}}\right)^2 \log\left(\frac{\omega}{\omega_{M,\mathbf{q}}}\right). \quad (2.151)$$

Therefore, we conclude that in the limit $T \to \infty$, in the low energy and long wavelength limit, the contributions due to the *quantum* interactions will be much smaller than the ones due to the *classical* interaction, Eq. (2.58), as expected. From this discussion, we conclude that to lowest order in perturbation theory the dominant contribution to the flexural phonon self-energy in the high temperature limit is given by (Eq. (2.139))

$$\lim_{T\to\infty} \mathrm{Re}\Sigma^{(0),R}_{F,\mathbf{q}}(\omega) \simeq \frac{3Y_{2D} k_B T}{16\pi\kappa} |\mathbf{q}|^2, \quad (2.152)$$

We now turn our attention to the low temperature limit, $T \to 0$. In this limit, we approximate $b(\omega_{M,\mathbf{p}}) \simeq 0$ and $b(\omega_{F,\mathbf{q}+\mathbf{p}}) \simeq 0$. Therefore, we obtain

$$\lim_{T\to 0} \mathcal{K}^{M}_{\mathbf{q},\mathbf{p}}(\omega) = \frac{1}{2\rho\omega_{F,\mathbf{q}+\mathbf{p}}} \frac{\omega_{F,\mathbf{q}+\mathbf{p}}\left(\omega_{F,\mathbf{q}+\mathbf{p}} + \omega_{M,\mathbf{p}}\right) - \omega^2}{\left(\omega_{F,\mathbf{q}+\mathbf{p}} + \omega_{M,\mathbf{p}}\right)^2 - \omega^2}. \tag{2.153}$$

We are interested in results to lowest order in ω and $\mathbf{q}$. We obtain a finite contribution even in the $\omega = 0$ case, on which we will focus. For $\omega = 0$ we obtain

$$\lim_{T\to 0} \mathcal{K}^{M}_{\mathbf{q},\mathbf{p}}(0) = \frac{1}{2} \frac{1}{\omega_{F,\mathbf{q}+\mathbf{p}} + \omega_{M,\mathbf{p}}}. \tag{2.154}$$

Expanding the the integrand of Eq. (2.146) to lowest order in $\mathbf{q}$ and performing the integration over $\mathbf{p}$ we obtain the contribution due to the *quantum* interactions in the $T \to 0$ limit

$$\lim_{T\to 0} \mathrm{Re}\Sigma^{(0)\perp\perp\perp\perp,\mathrm{qt},R}_{F,\mathbf{q}}(0) \simeq \frac{\hbar}{2\sqrt{\rho\kappa}} \frac{\lambda^2}{\lambda + 2\mu} \frac{3\left|\mathbf{q}\right|^4}{16\pi} \log\left(1 + \frac{\Lambda}{q_L}\right), \tag{2.155}$$

$$\lim_{T\to 0} \mathrm{Re}\Sigma^{(0)\parallel\parallel\parallel\parallel,\mathrm{qt},R}_{F,\mathbf{q}}(0) \simeq \frac{\hbar}{2\sqrt{\rho\kappa}} \frac{(\lambda + 2\mu)^2}{\kappa} \frac{\left|\mathbf{q}\right|^2}{4\pi} \Phi\left(\frac{\Lambda}{q_L}\right), \tag{2.156}$$

$$\lim_{T\to 0} \mathrm{Re}\Sigma^{(0)\perp\perp\parallel\parallel,\mathrm{qt},R}_{F,\mathbf{q}}(0) \simeq \frac{\hbar}{2\sqrt{\rho\kappa}} \frac{\lambda\left|\mathbf{q}\right|^4}{8\pi} \left(\frac{2\Lambda}{q_L + \Lambda} - \log\left(1 + \frac{\Lambda}{q_L}\right)\right), \tag{2.157}$$

$$\lim_{T\to 0} \mathrm{Re}\Sigma^{(0)\perp\parallel\perp\parallel,\mathrm{qt},R}_{F,\mathbf{q}}(0) \simeq \frac{\hbar}{2\sqrt{\rho\kappa}} \frac{\mu^2}{\kappa} \frac{\left|\mathbf{q}\right|^2}{4\pi} \Phi\left(\frac{\Lambda}{q_T}\right). \tag{2.158}$$

where we have restored $\hbar$, introduced the function

$$\Phi(x) = \frac{1}{2} x\left(x - 2\right) + \log\left(1 + x\right), \tag{2.159}$$

and introduced once again Λ as a high momentum cut-off, the Debye momentum. While the contributions due to the $^{\perp\perp\perp\perp}$ and $^{\perp\perp\parallel\parallel}$ terms depend on momentum as $\left|\mathbf{q}\right|^4$, the $^{\parallel\parallel\parallel\parallel}$ and $^{\perp\parallel\perp\parallel}$ terms have a $\left|\mathbf{q}\right|^2$ dependence and will therefore be dominant at long wavelengths. Notice that besides high momentum logarithmic divergences, we have also obtained power law divergences. By splitting the effective interaction $\mathcal{R}^{ijkl}_{\tilde{\mathbf{q}}}$ into the contributions for the quartic on-site interaction and the in-plane phonon mediated contribution and carefully analysing each contribution allows us to see that the main Λ^2 divergence comes from the quartic local interaction while the Λ and $\log(\Lambda)$ divergences come from the interaction between in-plane and out-of-plane modes. It can be checked that, in the long wavelength limit, the result obtained for $\mathrm{Re}\Sigma^{(0),R}_{F,\mathbf{q}}(\omega_{F,\mathbf{q}})$ is the same as the result of Eqs. (2.155)-(2.158). This tells us that, for physical excitations, the frequency dependence of the self-energy can be neglected in the low temperature and long wavelength limit. We can therefore write

$$\lim_{T\to 0} \mathrm{Re}\Sigma^{(0),R}_{F,\mathbf{q}}(\omega) \simeq \frac{\hbar\kappa}{2\sqrt{\rho\kappa}} \frac{\left|\mathbf{q}\right|^2}{4\pi} \left(q_L^4 \Phi\left(\frac{\Lambda}{q_L}\right) + q_T^4 \Phi\left(\frac{\Lambda}{q_T}\right)\right). \tag{2.160}$$

To first order in perturbation theory, the dispersion relation, $\Omega_{F,\mathbf{q}}$, of the physical excitations is given by $\rho\Omega^2_{F,\mathbf{q}} = \kappa\left|\mathbf{q}\right|^4 + \mathrm{Re}\Sigma_{\mathbf{q}}\left(\omega_{F,\mathbf{q}}\right)$. Note that, for $\mathbf{q} \to 0$, $\Omega_{F,\boldsymbol{q}} \sim \left|\mathbf{q}\right|$ instead of $\omega_{F,\mathbf{q}} \sim \left|\mathbf{q}\right|^2$. Therefore, we have found that in the zero temperature limit $\Omega^2_{F,\mathbf{q}} \propto \left|\mathbf{q}\right|^{4-\eta_h}$ with $\eta_h = 2$ in the perturbative calculation.

Just as in the classical case, we can estimate, in both the high temperature and low temperature limits, the momentum scale, k_c, below which anharmonic effects become dominant, as determined by the Ginzburg criterion $\Sigma^{(0)}_{hh,\mathbf{k}_c}(\omega_{F,\mathbf{k}_c}) \simeq \kappa k_c^4$. By using Eqs. (2.139) and (2.160), for the self-energy, respectively, in the high and low temperature limits, we obtain

$$k_c^{(T\to\infty)} \simeq \sqrt{\frac{3k_BTY_{2D}}{16\pi\kappa^2}}, \tag{2.161}$$

$$k_c^{(T\to 0)} \simeq \sqrt{\frac{\hbar}{8\pi\rho^{1/2}\kappa^{1/2}}\left[q_L^4\Phi\left(\frac{\Lambda}{q_L}\right)+q_T^4\Phi\left(\frac{\Lambda}{q_T}\right)\right]^{1/2}}. \tag{2.162}$$

For typical graphene values we obtain $k_c^{(T\to\infty)} \simeq 0.17\text{Å}^{-1}$ at $T = 300$ K, and setting $\Lambda = q_D$, we obtain $k_c^{(T\to 0)} \simeq 0.1\text{Å}^{-1}$ at $T = 0$. It is useful to write approximate expressions for k_c in the limit $T \to 0$ when $\Lambda/q_{T/L} \gg 1$ and $\Lambda/q_{T/L} \ll 1$. Expanding the function $\Phi(x)$, we obtain the following approximate expressions:

$$k_c^{(T\to 0)} \simeq \begin{cases} \left(\dfrac{\hbar}{16\pi\sqrt{\rho\kappa}}\dfrac{\lambda+3\mu}{\kappa}\right)^{1/2}\Lambda, & \Lambda \gg q_{T/L}, \\ \left(\dfrac{\hbar}{24\pi\sqrt{\rho\kappa}}\right)^{1/2}(q_L+q_T)^{1/2}\,\Lambda^{3/2}. & \Lambda \ll q_{T/L}. \end{cases} \tag{2.163}$$

To determine the actual importance of the anharmonic effects in suspended crystalline membranes, one has to compare the anharmonic scale k_c, with the minimum momentum allowed by the finite size of the sample $\sim L^{-1}$ and with the momentum scale due to residual strains $\sim \sqrt{(\lambda+\mu)\,\bar{u}/\kappa}$, where $\bar{u}$ is the strain [35], see Eq. (2.197) ahead. If $L^{-1}, \sim \sqrt{(\lambda+\mu)\,\bar{u}/\kappa} \gg k_c$ then anharmonic effects will be strongly suppressed.

We can also estimate the quantum-to-classical crossover temperature, T^*, above which the classical behaviour sets in by comparing the perturbative results for the self-energy in the low and high temperature limits

$$\lim_{T\to\infty} \mathrm{Re}\Sigma^R_{\mathbf{q}}(\omega_{F,\mathbf{q}}) \simeq \lim_{T\to 0} \mathrm{Re}\Sigma^R_{\mathbf{q}}(\omega_{F,\mathbf{q}}). \tag{2.164}$$

We obtain

$$T^* \simeq \frac{2\hbar}{3k_B\rho^{1/2}\kappa^{1/2}}\frac{\kappa^2}{Y_{2D}}\times \\ \times\left[q_L^4\Phi\left(\frac{\Lambda}{q_L}\right)+q_T^4\Phi\left(\frac{\Lambda}{q_T}\right)\right], \tag{2.165}$$

a quantity that depends on the UV cutoff Λ. Notice that since in both the high and low temperature limits the leading contribution to the self-energy goes like $|\mathbf{q}|^2$, this is equivalent to comparing $k_c^{(T\to\infty)}$ with $k_c^{(T\to 0)}$. Expanding once again the function $\Phi(x)$ we obtain

$$T^* \simeq \begin{cases} \dfrac{\hbar\kappa^{1/2}}{3k_B\rho^{1/2}}\dfrac{(\lambda+2\mu)\,(\lambda+3\mu)}{4\mu\,(\lambda+\mu)}\Lambda^2, & \Lambda \gg q_{T/L}, \\ \dfrac{2\hbar\kappa}{9k_B\rho^{1/2}}\dfrac{\lambda+2\mu}{4\mu\,(\lambda+\mu)}\left(\sqrt{\lambda+2\mu}+\sqrt{\mu}\right)\Lambda^3, & \Lambda \ll q_{T/L}. \end{cases} \tag{2.166}$$

For typical graphene values, setting $\Lambda = q_D$, we obtain a value of $T^* \sim 70 - 90$ K (depending on the values we take for the elastic constants, which depend themselves

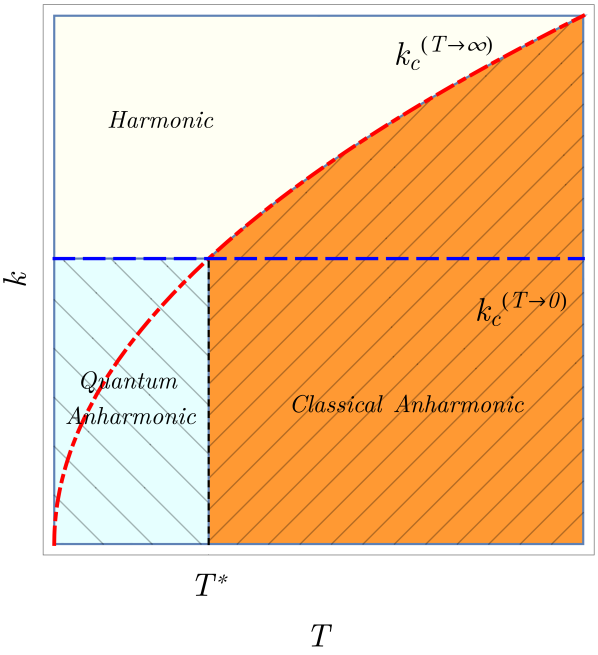

Figure 2.5: Diagram in (T, q) space representing the regions where anharmonic effects are weak and where they dominate for a free quantum crystalline membrane. At high enough momentum q, we are in the *Harmonic* region: anharmonic effects are weak and the dispersion relation for the flexural phonon is given by $\Omega_{F,\mathbf{q}} \propto |\mathbf{q}|^2$. For small momentum, anharmonic effects become dominant and we obtain $\Omega_{F,\mathbf{q}} \propto |\mathbf{q}|^{2-\eta_h/2}$. At temperatures above T^*, anharmonic effects are driven by thermal fluctuations, and we are in the *Classical Anharmonic* regime. Bellow T^*, anharmonic effects are driven by quantum fluctuations, and we are in the *Quantum Anharmonic* regime. The dash-dotted red and the dashed blue lines are respectively given by Eqs. (2.161) and (2.162) , which split the harmonic and anharmonic regions in the high and low temperature limits. Their intersection determines the quantum-to-classical temperature T^*.

on the temperature [80]). Below this temperature, the contribution to the self-energy from the quantum interaction terms $\mathcal{R}^{\parallel\parallel\parallel\parallel}_{\tilde{\mathbf{q}}}$ and $\mathcal{R}^{\perp\parallel\perp\parallel}_{\tilde{\mathbf{q}}}$ will become dominant. Fig. 2.5 shows the different regions in the (T, k) space where anharmonic and quantum effects become dominant.

2.3.1.2 *In-plane Green's functions*

To lowest order in perturbation theory, the cubic interaction term Eq. (2.92) gives origin to the following self-energy for the in-plane phonons

$$\Sigma^{(0)ij}_{uu,\tilde{\mathbf{q}}} = c^{irkl} q_r \chi^{(0)klmn}_{\tilde{\mathbf{q}}} q_s c^{mnsj}, \tag{2.167}$$

where we have introduced the flexural phonon bubble tensor, $\chi^{(0)ijkl}_{\tilde{\mathbf{q}}}$, which is defined as

$$\begin{aligned}\chi^{(0)ijkl}_{\tilde{\mathbf{q}}} = -\frac{1}{8\beta A}\sum_{\tilde{\mathbf{p}}} \Big[(p+q)_i\, p_j + p_i\,(p+q)_j\Big] \times \\ \times \left[(p+q)_k\, p_l + p_k\,(p+q)_l\right] D^0_{F,\tilde{\mathbf{p}}} D^0_{F,\tilde{\mathbf{p}}+\tilde{\mathbf{q}}},\end{aligned} \tag{2.168}$$

where we have symmetrized the tensor with respect to the first and last two indices, since they are contracted with the stiffness tensor. With this definition, $\chi^{(0)ijkl}_{\tilde{\mathbf{q}}}$ has the same symmetries as that of the stiffness tensor, Eq. (2.10). Just as for the effective interaction for the flexural phonons, Eq. (2.114), we write the tensor $\chi^{(0)ijkl}_{\tilde{\mathbf{q}}}$ in the terms of the $\left\{\mathbf{e}_{\parallel,\mathbf{q}}, \mathbf{e}_{\perp,\mathbf{q}}\right\}$ basis as

$$\begin{aligned}\chi^{(0)ijkl}_{\tilde{\mathbf{q}}} &= e^i_{\perp,\mathbf{q}} e^j_{\perp,\mathbf{q}} e^k_{\perp,\mathbf{q}} e^l_{\perp,\mathbf{q}} + \chi^{(0)\parallel\parallel\parallel\parallel}_{\tilde{\mathbf{q}}} e^i_{\parallel,\mathbf{q}} e^j_{\parallel,\mathbf{q}} e^k_{\parallel,\mathbf{q}} e^l_{\parallel,\mathbf{q}} \\ &+ \chi^{(0)\perp\perp\parallel\parallel}_{\tilde{\mathbf{q}}} \left(e^i_{\perp,\mathbf{q}} e^j_{\perp,\mathbf{q}} e^k_{\parallel,\mathbf{q}} e^l_{\parallel,\mathbf{q}} + (ij \leftrightarrow kl) \right) \\ &+ \chi^{(0)\perp\parallel\perp\parallel}_{\tilde{\mathbf{q}}} \left(e^i_{\perp,\mathbf{q}} e^j_{\parallel,\mathbf{q}} e^k_{\perp,\mathbf{q}} e^l_{\parallel,\mathbf{q}} + (i \leftrightarrow j) + (k \leftrightarrow l) + (ik \leftrightarrow jl) \right). \end{aligned} \tag{2.169}$$

The four independent components of $\chi^{(0)ijkl}_{\tilde{\mathbf{q}}}$ are explicitly given by

$$\chi^{(0)\perp\perp\perp\perp}_{\tilde{\mathbf{q}}} = -\frac{1}{2\beta A} \sum_{\tilde{\mathbf{p}}} g^{\perp\perp\perp\perp}_{\mathbf{p},\mathbf{q}} D^0_{F,\tilde{\mathbf{p}}+\tilde{\mathbf{q}}} D^0_{F,\tilde{\mathbf{p}}}, \tag{2.170}$$

$$\chi^{(0)\parallel\parallel\parallel\parallel}_{\tilde{\mathbf{q}}} = -\frac{1}{2\beta A} \sum_{\tilde{\mathbf{p}}} g^{\parallel\parallel\parallel\parallel}_{\mathbf{p},\mathbf{q}} D^0_{F,\tilde{\mathbf{p}}+\tilde{\mathbf{q}}} D^0_{F,\tilde{\mathbf{p}}}, \tag{2.171}$$

$$\chi^{(0)\perp\perp\parallel\parallel}_{\tilde{\mathbf{q}}} = -\frac{1}{4\beta A} \sum_{\tilde{\mathbf{p}}} g^{\perp\perp\parallel\parallel}_{\mathbf{p},\mathbf{q}} D^0_{F,\tilde{\mathbf{p}}+\tilde{\mathbf{q}}} D^0_{F,\tilde{\mathbf{p}}}, \tag{2.172}$$

$$\chi^{(0)\perp\parallel\perp\parallel}_{\tilde{\mathbf{q}}} = -\frac{1}{8\beta A} \sum_{\tilde{\mathbf{p}}} g^{\perp\parallel\perp\parallel}_{\mathbf{p},\mathbf{q}} D^0_{F,\tilde{\mathbf{p}}+\tilde{\mathbf{q}}} D^0_{F,\tilde{\mathbf{p}}}, \tag{2.173}$$

with $g^M_{\mathbf{p},\mathbf{q}}$ given by Eqs. (2.131)-(2.134). Using this decomposition and performing the contractions of indices in Eq. (2.167) we conclude, as expected for an isotropic system, that the self-energy for the in-plane phonons can be decomposed into a longitudinal and a transverse component

$$\Sigma^{(0)ij}_{uu,\tilde{\mathbf{q}}} = \Sigma^{(0)}_{L,\tilde{\mathbf{q}}} P^{ij}_{L,\mathbf{q}} + \Sigma^{(0)}_{T,\tilde{\mathbf{q}}} P^{ij}_{T,\mathbf{q}}, \tag{2.174}$$

with

$$\Sigma^{(0)}_{L,\tilde{\mathbf{q}}} = (\lambda + 2\mu)^2 |\mathbf{q}|^2 \chi^{\parallel\parallel\parallel\parallel}_{\tilde{\mathbf{q}}} + \lambda(\lambda + 2\mu) |\mathbf{q}|^2 \chi^{\perp\perp\parallel\parallel}_{\tilde{\mathbf{q}}} + \lambda^2 |\mathbf{q}|^2 \chi^{\perp\perp\perp\perp}_{\tilde{\mathbf{q}}} \tag{2.175}$$

$$\Sigma^{(0)}_{T,\tilde{\mathbf{q}}} = 4\mu^2 |\mathbf{q}|^2 \chi^{\perp\parallel\perp\parallel}_{\tilde{\mathbf{q}}}. \tag{2.176}$$

Performing the sum over Matsubara frequencies in Eq. (2.168) we obtain

$$\begin{aligned}\chi^{(0)M}_{\mathbf{q}}(iq_n) \propto &- \int \frac{d^2\mathbf{p}}{(2\pi)^2} g^M_{\mathbf{p},\mathbf{q}} P \int \frac{d\nu}{\pi} b(\nu) \mathrm{Im} D^{0,R}_{F,\boldsymbol{p}}(\nu) D^0_{F,\mathbf{p}+\mathbf{q}}(iq_n + \nu) \\ &- \int \frac{d^2\mathbf{p}}{(2\pi)^2} g^M_{\mathbf{p},\mathbf{q}} P \int \frac{d\nu}{\pi} b(\nu) D^{0,R}_{F,\mathbf{p}}(iq_n - \nu) \mathrm{Im} D^{0,R}_{F,\mathbf{p}+\mathbf{q}}(\nu). \end{aligned} \tag{2.177}$$

The proportionality factor is due to the extra factors of 1/2 and 1/4 that appear in $\chi^{(0)\perp\perp\parallel\parallel}_{\tilde{\mathbf{q}}}$ and $\chi^{(0)\perp\parallel\perp\parallel}_{\tilde{\mathbf{q}}}$. Performing the integration over ν, we obtain

$$\chi^{(0)M}_{\mathbf{q}}(iq_n) \propto \frac{1}{2} \int \frac{d^2\mathbf{p}}{(2\pi)^2} g^M_{\mathbf{p},\mathbf{q}} \mathcal{F}_{\mathbf{p},\mathbf{q}}(iq_n), \tag{2.178}$$

where

$$\mathcal{F}_{\mathbf{p},\mathbf{q}}(iq_n) = \frac{1}{2\rho^2\omega_{F,\mathbf{p}}\omega_{F,\mathbf{p}+\mathbf{q}}}\frac{\omega_{F,\mathbf{p}}+\omega_{F,\mathbf{p}+\mathbf{q}}}{(iq_n)^2-(\omega_{F,\mathbf{p}}+\omega_{F,\mathbf{p}+\mathbf{q}})^2} + \frac{b(\omega_{F,\mathbf{p}})}{\rho^2\omega_{F,\mathbf{p}}}\frac{\left((iq_n)^2+\omega_{F,\mathbf{p}}^2-\omega_{F,\mathbf{p}+\mathbf{q}}^2\right)}{\left((iq_n)^2-(\omega_{F,\mathbf{p}}+\omega_{F,\mathbf{p}+\mathbf{q}})^2\right)\left((iq_n)^2-(\omega_{F,\mathbf{p}}-\omega_{F,\mathbf{p}+\mathbf{q}})^2\right)} + \frac{b(\omega_{F,\mathbf{p}+\mathbf{q}})}{\rho^2\omega_{F,\mathbf{p}+\mathbf{q}}}\frac{\left((iq_n)^2-\omega_{F,\mathbf{p}}^2+\omega_{F,\mathbf{p}+\mathbf{q}}^2\right)}{\left((iq_n)^2-(\omega_{F,\mathbf{p}}+\omega_{F,\mathbf{p}+\mathbf{q}})^2\right)\left((iq_n)^2-(\omega_{F,\mathbf{p}}-\omega_{F,\mathbf{p}+\mathbf{q}})^2\right)}. \quad (2.179)$$

As previously, we focus on the real part of the retarded self-energy, which is obtained by performing the analytic continuation $iq_n \to \omega + i0^+$. The retarded flexural phonon bubble is given by

$$\mathrm{Re}\chi_{\mathbf{q}}^{(0)M,R}(\omega) \propto \frac{1}{2}P\int\frac{d^2\mathbf{p}}{(2\pi)^2}g_{\mathbf{p},\mathbf{q}}^{M}\mathcal{F}_{\mathbf{p},\mathbf{q}}(\omega). \quad (2.180)$$

We will focus on the low temperature limit, $T \to 0$, in which case $\mathcal{F}_{\mathbf{p},\mathbf{q}}(\omega)$ reduces to

$$\lim_{T\to 0}\mathcal{F}_{\mathbf{p},\mathbf{q}}(\omega) = \frac{1}{2\rho^2\omega_{F,\mathbf{p}}\omega_{F,\mathbf{p}+\mathbf{q}}}\frac{\omega_{F,\mathbf{p}}+\omega_{F,\mathbf{p}+\mathbf{q}}}{\omega^2-(\omega_{F,\mathbf{p}}+\omega_{F,\mathbf{p}+\mathbf{q}})^2}. \quad (2.181)$$

If we furthermore focus on the $\omega = 0$, $\mathbf{q} = 0$ limit, we have

$$\mathcal{F}_{\mathbf{p},\mathbf{0}}(0) = -\frac{1}{4\rho^2\omega_{F,\mathbf{p}}^3}. \quad (2.182)$$

Since for large values of $\mathbf{p}$ we have that $g_{\mathbf{p},\mathbf{q}}^{M} \propto |\mathbf{p}|^4$, we conclude that Eq. 2.180 diverges logarithmically both for large and small momenta. Inclusion of a finite ω or $\mathbf{q}$ effectively cuts off the integration for small values. With these considerations, we estimate $\chi_{\mathbf{q}}^{(0)M,R}(\omega)$ as

$$\lim_{T\to 0}\mathrm{Re}\chi_{\mathbf{q}}^{(0)M,R}(\omega) \sim -\frac{\hbar}{2\rho^{1/2}\kappa^{3/2}}\log\left(\frac{\Lambda^2}{\max\left(\sqrt{\kappa/\rho}\omega, |\mathbf{q}|^2\right)}\right). \quad (2.183)$$

Therefore, we will just have a weak logarithmic correction to the correlation function of the in-plane modes. Notice that the minus sign in Eqs. (2.183) leads to a reduction of the in-plane elastic constants. To first order in perturbation theory, the in-plane mode dispersion relations would be modified to $\Omega_{L/T,\mathbf{q}}^2 = \omega_{L/T,\mathbf{q}}^2 + \Sigma_{L/T,\mathbf{q}}\left(\omega_{L/T,\mathbf{q}}\right)/\rho$. Taking the limit $\mathbf{q} \to 0$, we would obtain a negative dispersion relation, indicating that the theory is unstable. We attribute this, not to a physical instability of the membrane, but to a breakdown of the perturbation theory, showing that one should go beyond the first order.

2.3.2 *Anharmonic effects: self-consistent Born approximation*

The next step to go beyond first order perturbation theory for $T \to 0$, is to perform a SCBA calculation in the spirit of what was done by Nelson and Peliti in Ref. [23]. First, as we have seen in Section 2.3.1.2, in first order perturbation theory, the in-plane

mode propagator has only logarithmic corrections due to anharmonic effects. This is a much weaker effect than for the out-of-plane phonons and therefore we will ignore it. Next, according to Eq. (2.160) we also neglect the frequency dependence of the flexural phonon self-energy and write the full out-of-plane correlation function as

$$D_{F,\tilde{\mathbf{q}}}^{-1} \simeq \rho \left(iq_n\right)^2 - \rho\omega_{F,\mathbf{q}}^2 - \kappa q_0^{\eta_h} \left|\mathbf{q}\right|^{4-\eta_h}, \tag{2.184}$$

where we have neglected the frequency dependent of the self-energy on the Matsubara frequency and have further made the ansatz $\Sigma_{F,\tilde{\mathbf{q}}}^{\mathrm{SCBA}} \simeq \kappa q_0^{\eta_h} \left|\mathbf{q}\right|^{4-\eta_h}$, with η_h an anomalous exponent and q_0 a momentum scale both of which are to be determined in a self-consistent way. Therefore, the self-energy in the SCBA is written as

$$\Sigma_{F,\tilde{\mathbf{q}}}^{\mathrm{SCBA}} = -\frac{1}{\beta A} \sum_{\tilde{\mathbf{p}},M} \frac{\mathcal{R}_{\tilde{\mathbf{p}}}^{M} g_{\mathbf{q},\mathbf{p}}^{M}}{\rho \left(ip_m\right)^2 - \rho\omega_{F,\mathbf{q}+\mathbf{p}}^2 - \kappa q_0^{\eta_h} \left|\mathbf{q}+\mathbf{p}\right|^{4-\eta_h}}. \tag{2.185}$$

Performing the sum over Matsubara frequencies, making the analytic continuation to real frequencies we obtain in the $T \to 0$ limit, using Eqs. (2.146) and (2.154),

$$\begin{aligned} \lim_{T\to 0} \mathrm{Re}\Sigma_{F,\mathbf{q}}^{\mathrm{SCBA}}(\omega) = \left|\mathbf{q}\right|^4 \int \frac{d^2\mathbf{p}}{\left(2\pi\right)^2} \frac{Y_{2D} \sin^4\theta_{\mathbf{q},\mathbf{p}}}{2\rho\sqrt{\omega_{F,\mathbf{q}+\mathbf{p}}^2 + \kappa q_0^{\eta_h} \left|\mathbf{q}+\mathbf{p}\right|^{4-\eta_h}/\rho}} \\ + \frac{1}{2} \sum_M C^M P \int \frac{d^2\mathbf{p}}{\left(2\pi\right)^2} \frac{g_{\mathbf{q},\mathbf{p}}^{M}}{\sqrt{\omega_{F,\mathbf{q}+\mathbf{p}}^2 + \kappa q_0^{\eta_h} \left|\mathbf{q}+\mathbf{p}\right|^{4-\eta_h}/\rho} + \omega_{M,\mathbf{p}}}. \end{aligned} \tag{2.186}$$

It is easy to see that in the $\mathbf{q} \to 0$, the leading contribution to the self-energy comes from the terms involving $\mathcal{R}_{\tilde{\mathbf{p}}}^{\parallel\parallel\parallel}$ and $\mathcal{R}_{\tilde{\mathbf{p}}}^{\perp\parallel\perp\parallel}$, just as in the perturbative calculation. This is due to the fact that the geometrical factors $g_{\mathbf{q},\mathbf{p}}^{\parallel\parallel\parallel}$ and $g_{\mathbf{q},\mathbf{p}}^{\perp\parallel\perp\parallel}$ behave as $\sim \left|\mathbf{q}\right|^2$ for $\mathbf{q} \to 0$, while $g_{\mathbf{q},\mathbf{p}}^{\perp\perp\perp\perp}$ behaves as $\sim \left|\mathbf{q}\right|^4$ and $g_{\mathbf{q},\mathbf{p}}^{\perp\perp\parallel\parallel}$ as $\sim \left|\mathbf{q}\right|^3$. In the $\mathbf{q} \to 0$ limit, we can thus focus only on the $^{\parallel\parallel\parallel}$ and $^{\perp\parallel\perp\parallel}$ contributions, which give origin to a energy that still behaves as $\lim_{T\to 0} \mathrm{Re}\Sigma_{F,\mathbf{q}}^{\mathrm{SCBA}}(\omega) \propto \left|\mathbf{q}\right|^2$. Therefore, in the SCBA calculation we still obtain a value of $\eta_h = 2$, in agreement with first order perturbation theory. This is an important result which justifies the use of first order perturbation theory. This in in contrast with the classical regime, where the perturbative $\eta_h = 2$ exponent is changed to $\eta_h = 1$ obtain within the SCBA [23]. The present result of $\eta_h = 2$ indicates that quantum anharmonic effects act as an effective positive external strain, which contributes to the stabilization of the 2D phase of the membrane.

Using the value of $\eta_h = 2$ and focusing in the $\mathbf{q} \to 0$ limit, the momentum scale q_0 is determined by

$$\begin{aligned} q_0^2 = \frac{\left(\lambda+2\mu\right)\hbar}{8\pi\rho^{1/2}\kappa^{3/2}} \int \frac{dpp^3}{\sqrt{p^4 + q_0^2p^2} + q_L p} \\ + \frac{\mu\hbar}{8\pi\rho^{1/2}\kappa^{3/2}} \int \frac{dpp^3}{\sqrt{p^4 + q_0^2p^2} + q_T p}. \end{aligned} \tag{2.187}$$

Notice that the integral over p is convergent in the $p \to 0$ limit and the denominator in the integrand of Eq. (2.187) is dominated by the terms $q_{L/T}p$ for small q_0. On the other hand, for large values of p, the term p^2 dominates. Therefore, the integral will only be weakly dependent on the term $q_0^2p^2$, and we anticipate that the solution for q_0^2

will be very well approximated by setting $q_0 = 0$ in the RHS of Eq. (2.187). Performing the integral over momentum we obtain

$$q_0^2 = \frac{\hbar}{8\pi\rho^{1/2}\kappa^{1/2}}\left[q_L^4 F\left(\frac{\Lambda}{q_L}, \frac{q_0}{q_L}\right) + q_T^4 F\left(\frac{\Lambda}{q_T}, \frac{q_0}{q_T}\right)\right], \tag{2.188}$$

where we have defined the function

$$\begin{aligned} F(x,y) = {} & \frac{1}{2}x\left(\sqrt{x^2+y^2}-2\right) + \frac{1}{2}\left(2-y^2\right)\sinh^{-1}\left(\frac{x}{y}\right) \\ & + \sqrt{1-y^2}\tanh^{-1}\left(\frac{x}{\sqrt{1-y^2}}\right) - \sqrt{1-y^2}\tanh^{-1}\left(\frac{x}{\sqrt{(1-y^2)(x^2+y^2)}}\right). \end{aligned} \tag{2.189}$$

The function $F(x,y)$ reduces to $\Phi(x)$, Eq. (2.159), in the limit of $y \to 0$. Solving the self-consistent Eq. (2.188) numerically for q_0 we obtain a value that, for typical graphene parameters, is nearly unchanged with respect to the perturbative result $k_c \simeq 0.1\,\text{Å}^{-1}$, Eq. (2.162). The relative difference between the perturbative result for k_c and self-consistent value for q_0 is of the order of 10^{-4}.

2.4 THERMODYNAMIC PROPERTIES OF FREE CRYSTALLINE MEMBRANES

In the previous section, we have studied the effect of anharmonicities in the phonon dispersion relation of free crystalline membranes, in the low temperature limit. These anharmonic effects will also manifest themselves in the low temperature behaviour of several thermodynamic properties, which probe the low-energy elementary excitations of the system. In the following, we will focus on the study of the areal thermal expansion and of the specific heat of a crystalline membrane.

2.4.1 *Thermal expansion*

The areal thermal expansion coefficient is defined as

$$\alpha_A = \frac{1}{A}\left.\frac{\partial \Delta A}{\partial T}\right|_P, \tag{2.190}$$

where ΔA is the change in the area of the membrane (to be understood as the area of the membrane projected onto the reference $x-y$ plane), A is the reference area of the undistorted membrane, and the index P indicates that the process occurs at constant pressure or in this case at constant stress. The thermal expansion is an intrinsically anharmonic effect and a purely harmonic crystal does not expand or contract under a change of temperature.

The most common approach to compute the thermal expansion coefficient is the quasi-harmonic approximation (QHA) [95]. The QHA is a minimal extension of the harmonic theory, which treats the phonons at an harmonic level, but assumes that the phonon frequencies have a dependence on the overall expansion of the crystal lattice. The Helmholtz free energy density for a harmonic crystal is given by

$$F(\Delta A, T) = E_0(\Delta A) + \frac{k_B T}{A}\sum_n \log\left[2\sinh\left(\frac{\omega_n(A)}{2k_B T}\right)\right], \tag{2.191}$$

where ω_n are phonon frequencies, which in the quasi-harmonic approximation are assumed to depend in the change of area, ΔA, and $E(\Delta A)$ is the zero temperature elastic energy density due to the expansion, which for a 2D isotropic material is given by

$$E_0(\Delta A) = \frac{1}{2} B \left(\frac{\Delta A}{A} \right)^2 , \tag{2.192}$$

where $B = \lambda + \mu$ is the bulk modulus. Using the triple product rule the thermal expansion can be written as

$$\alpha_A = -\frac{1}{A} \frac{\frac{\partial P}{\partial T}\big|_A}{\frac{\partial P}{\partial A}\big|_T} = -\frac{1}{B} \frac{\partial^2 F}{\partial T \partial A}, \tag{2.193}$$

with the 2D bulk modulus written as $B = -A \left(\partial P/\partial A\right)|_T$ and F the Helmholtz free energy . Using this previous result and assuming that in Eq. (2.191) the term $E_0(\Delta A)$ does not depend on temperature we obtain the QHA result for thermal expansion

$$\alpha_A^{\text{QHA}} = \frac{k_B}{BA} \sum_n \left(\frac{\hbar \omega_n}{k_B T} \right)^2 \frac{\gamma_n}{4 \sinh^2 \left(\frac{\hbar \omega_n}{2 k_B T} \right)}, \tag{2.194}$$

where we have restored $\hbar$ and

$$\gamma_n = -\frac{A}{\omega_n} \frac{\partial \omega_n}{\partial A}, \tag{2.195}$$

is the Grüneisen coefficient of mode n, which describes the change of frequency with the expansion.

We will now see how the quasi-harmonic approximation breaks down for a crystalline membrane. It is possible to compute the Grüneisen coefficient for the flexural mode from Eq. (2.81). In order to do this we notice that a homogeneous, isotropic expansion can be modelled by the replacement $\partial_i u_j \to \bar{u} \delta_{ij}/2 + \partial_i u_j$, where $\bar{u} = \Delta A/A$ is the relative change of area. Under this transformation the cubic interaction term, Eq. (2.86), generates a new quadratic coupling to the flexural phonon [96]

$$\delta \mathcal{S}_E^{(0)} [h] = \frac{1}{2} \int_0^\beta d\tau \int d^2 \mathbf{x} \, (\lambda + \mu) \, \bar{u} \, (\partial h)^2 , \tag{2.196}$$

which modifies the bare dispersion relation of the flexural phonons to

$$\omega_{F,\mathbf{q}} (\bar{u}) = \sqrt{\frac{\kappa}{\rho} |\mathbf{q}|^4 + \frac{(\lambda + \mu) \, \bar{u}}{\rho} |\mathbf{q}|^2}, \tag{2.197}$$

where $\lambda + \mu$ is the bulk modulus of the membrane. From this expression, the Grüneisen coefficient is found to be negative and is given by

$$\begin{aligned} \gamma_{F,\mathbf{q}} &= -\frac{1}{\omega_{F,\mathbf{q}}} \frac{\partial \omega_{F,\mathbf{q}} (\bar{u})}{\partial \bar{u}} \bigg|_{\bar{u}=0} \\ &= -\frac{1}{2} \frac{(\lambda + \mu)}{\kappa |\mathbf{q}|^2}. \end{aligned} \tag{2.198}$$

Using Eqs. (2.194) and (2.198), we obtain the QHA result for the thermal expansion of a crystalline membrane

$$\alpha_A^{\text{QHA}} = -\frac{\hbar^2}{8 \rho k_B T^2} \int_{q_{\min}}^{\Lambda} \frac{d^2 \mathbf{q}}{(2\pi)^2} \frac{|\mathbf{q}|^2}{\sinh^2 \left(\hbar \omega_{F,\mathbf{q}} / \left(2 k_B T \right) \right)}, \tag{2.199}$$

where we have introduce a low, $q_{\min} \sim 2\pi/L$, and a large, $\Lambda \sim 2\pi/a$, momentum cut-off, where L is the linear size of the membrane. Notice that the previous result predicts a negative thermal expansion, or thermal contraction, for the crystalline membrane. This is the so called *membrane effect* [29]. Using the bare dispersion relation for the flexural phonon $\omega_{F,\mathbf{q}} \propto |\mathbf{q}|^2$, it is easy to see that the previous integral is divergent for $q_{\min} \to 0$. The integration in Eq. (2.199) can be performed analytically for $\Lambda \to \infty$ yielding

$$\alpha_A^{\text{QHA}} = -\frac{k_B}{8\pi\kappa}\mathcal{I}\left(\frac{k_B T \rho^{1/2}}{\hbar\kappa^{1/2} q_{\min}^2}\right), \tag{2.200}$$

where we have introduced the function

$$\mathcal{I}(t) = \frac{1}{2t}\coth\left(\frac{1}{2t}\right) - \log\left(2\sinh\left(\frac{1}{2t}\right)\right). \tag{2.201}$$

Now we notice that in the QHA the zero temperature, thermodynamic limit is not well defined, since the order of the limits $T \to 0$ and $L \to \infty$ does not commute. As a matter of fact for $t \gg 1$ (taking $L \to \infty$ first) we have $\mathcal{I}(t) \simeq 1 + \log(t)$, which leads to $\alpha_A = -\infty$ for any finite temperature and the QHA predicts that an infinite flat membrane is unstable. In the opposite $t \ll 1$ limit (taking $T \to 0$ first) we obtain $\mathcal{I}(t) \simeq e^{-1/t}/t$ and therefore for any finite size membrane, the thermal expansion coefficient vanishes as $T = 0$ is approached, in accordance with the third law of thermodynamics. We will now see that taking anharmonic effects into account beyond the QHA will lead to a vanishing thermal expansion in the zero temperature limit, even for an infinite membrane. The simplest approach is to notice that the bare, harmonic dispersion relation $\omega_{F,\mathbf{q}} = \sqrt{\kappa/\rho}\,|\mathbf{q}|^2$ is only valid, at high temperatures, for $|\mathbf{q}| > k_c$ with k_c given by Eq. (2.161). Therefore, the integration in Eq. (2.199) should not be cut-off at small momenta by $2\pi/L$ but by k_c [96]. Therefore, the high temperature thermal expansion of a membrane becomes finite and is given by

$$\alpha_A \simeq -\frac{k_B}{8\pi\kappa}\mathcal{I}\left(\frac{16\pi\kappa^{3/2}\rho^{1/2}}{3\hbar Y_{2D}}\right) \simeq -\frac{k_B}{8\pi\kappa}\log\left(\frac{16\pi\kappa^{3/2}\rho^{1/2}}{3\hbar Y_{2D}}\right), \tag{2.202}$$

which leads to a temperature independent value of $\alpha_A \simeq -10^{-5}\ \text{K}^{-1}$. This indicates that inclusion of anharmonic effects makes the thermal expansion finite, but the obtained constant thermal expansion can not be extrapolated to the $T \to 0$ limit, where the thermal expansion should vanish.

In order to study the thermal expansion in the low temperature limit and taking into account anharmonic effects in a rigorous way, we first notice that according to general elasticity theory the relative change of area is given by

$$\frac{\Delta A}{A} = \langle \partial_i u_i \rangle . \tag{2.203}$$

In order to compute $\langle \partial_i u_i \rangle$ we add an external stress, σ, to the Euclidean action, Eq. (2.81), obtaining the stress dependent partition function

$$Z[\sigma] = \int D[\mathbf{u}, h]\, e^{-\mathcal{S}_E[\mathbf{u},h] - \mathcal{S}_E^{\sigma}[\mathbf{u}]}, \tag{2.204}$$

with $\mathcal{S}_E^{\sigma}[\mathbf{u}]$ the stress dependent part of the action

$$\mathcal{S}_E^{\sigma}[\mathbf{u}] = -\sigma \int_0^{\beta} d\tau \int d^2\mathbf{x}\, \partial_i u_i. \tag{2.205}$$

With this, the relative change of area can be computed from the partition function as

$$\frac{\Delta A}{A} = \frac{1}{\beta A}\frac{\partial}{\partial \sigma}\log Z\left[\sigma\right]\Big|_{\sigma=0}. \tag{2.206}$$

Notice that σ couples to the $\mathbf{q}=0$ component of $\partial_i u_i$. Therefore, we can perform a shift of $\partial_i u_j$ in the functional path integral $\partial_i u_j \to \partial_i u_j + c^{-1}_{ijkl}\delta^{kl}\sigma$, in order to cancel the linear term in $\partial_i u_i$ included by $\mathcal{S}^{\sigma}_{E}\left[\mathbf{u}\right]$. By doing this the partition function becomes

$$Z\left[\sigma\right] = e^{-\frac{\beta V}{2}c^{-1}_{iijj}\sigma^2}\int D\left[\mathbf{u},h\right]e^{-\mathcal{S}_E[\mathbf{u},h]-\mathcal{S}^{\sigma}_{E}[h]}, \tag{2.207}$$

where we have generated an additional term for the action involving the out-of-plane displacement $\mathcal{S}^{\sigma}_{E}\left[h\right]$, which is given by

$$\mathcal{S}^{\sigma}_{E}\left[h\right] = \frac{1}{2}\sigma\int_0^{\beta}d\tau\int d^2\mathbf{x}\partial_i h\partial_i h. \tag{2.208}$$

Therefore, the thermal expansion can be expressed as

$$\alpha_A = -\frac{1}{2}\frac{\partial}{\partial T}\left\langle\partial_i h\partial_i h\right\rangle. \tag{2.209}$$

This is an exact result for the theory defined by the action Eq. (2.81). The previous expression also provides a very interesting geometrical interpretation for the negative thermal expansion of a crystalline membrane, as it expresses the thermal expansion as a normal normal correlation function: $\langle\partial_i h\partial_i h\rangle \simeq \langle\delta\mathbf{n}\cdot\delta\mathbf{n}\rangle$. Furthermore, Eq. (2.209) shows that the crystalline membrane theory defined by Eq. (2.81) always has a negative thermal expansion. Of course that at high enough temperature cubic and quartic anharmonic effects involving the in-plane displacements, that are not captured by Eq. (2.81), will also become relevant and will compete with the negative contribution due to the flexural phonons, Eq. (2.209) [80]. The membrane thermal expansion can be expressed in terms of the flexural phonon Green's function as

$$\begin{aligned}\alpha_A &= \frac{1}{2}\frac{\partial}{\partial T}\left(\frac{1}{\beta A}\sum_{\tilde{\mathbf{q}}}\left|\mathbf{q}\right|^2 D_{F,\tilde{\mathbf{q}}}\right)\\ &= \frac{1}{2}\frac{\partial}{\partial T}\left(\int\frac{d^2\mathbf{q}}{\left(2\pi\right)^2}\int\frac{d\omega}{\pi}b(\omega)\left|\mathbf{q}\right|^2\mathrm{Im}D^{R}_{F,\mathbf{q}}(\omega)\right).\end{aligned} \tag{2.210}$$

where in the last line we performed the sum over Matsubara frequencies. Notice that the expression for the thermal expansion in terms of the retarded Green's function can be directly obtained from Eq. (2.209) by using the fluctuation-dissipation theorem (see Appendix C). Taking into account the results from Section 2.3.1, we neglect the frequency dependence of the flexural phonon self-energy, and write the full flexural phonon retarded Green's function as

$$D^{R}_{F,\mathbf{q}}(\omega) = \left(\rho\omega^2 - \rho\Omega^2_{F,\mathbf{q}} + i\mathrm{sgn}(\omega)i0^{+}\right)^{-1}, \tag{2.211}$$

where $\Omega_{F,\mathbf{q}} = \sqrt{\left(\kappa |\mathbf{q}|^4 + \kappa q_0^{\eta_h} |\mathbf{q}|^{4-\eta_h}\right)/\rho}$ is the dispersion relation of the flexural phonon taking into account anharmonic effects. The thermal expansion is thus given by

$$\alpha_A = -\frac{k_B}{2\kappa}\int \frac{d^2\mathbf{q}}{(2\pi)^2}\frac{\hbar^2\kappa|\mathbf{q}|^2}{\rho\left(k_BT\right)^2}\frac{1}{4\sinh^2\left(\frac{\hbar\Omega_{F,\mathbf{q}}}{2k_BT}\right)}\left(1-\frac{\partial\log\Omega_{F,\mathbf{q}}}{\partial\log T}\right)$$
$$+\frac{k_B}{2\kappa}\int\frac{d^2\mathbf{q}}{(2\pi)^2}\frac{\hbar\kappa|\mathbf{q}|^2}{2k_BT\rho\Omega_{F,\mathbf{q}}}\coth\left(\frac{\hbar\Omega_{F,\mathbf{q}}}{2k_BT}\right)\frac{\partial\log\Omega_{F,\mathbf{q}}}{\partial\log T}, \tag{2.212}$$

where we have allowed for $\Omega_{F,\mathbf{q}}$ to be temperature dependent. If one ignores this temperature dependence and replaces $\Omega_{F,\mathbf{q}}$ by the bare dispersion relation, $\omega_{F,\mathbf{q}}$, we recover the QHA result from Eq. (2.199). We now focus on the low temperature limit, which will be dominated by quantum fluctuations and long wavelength phonons and therefore we approximate $\Omega_{F,\mathbf{q}} \simeq \sqrt{\kappa q_0^{\eta_h}/\rho}\,|\mathbf{q}|^{2-\eta_h/2}$. Furthermore, for $T \ll T^*$ the flexural phonon self-energy saturates to a constant and therefore we also ignore the temperature dependence of $\Omega_{F,\mathbf{q}}$. Contrary to the divergent result obtained in the QHA, the integral in Eq. (2.212) is now finite for small momenta for any $\eta_h > 0$ (it is also finite for large momenta) and a straightforward calculation gives us

$$\alpha_A \simeq -\frac{k_B}{2\pi\left(4-\eta_h\right)\kappa}\left(\frac{2\rho^{1/2}k_BT}{\hbar\kappa^{1/2}q_0^2}\right)^{2\eta_h/(4-\eta_h)} I_{\eta_h},\ T \ll T^* \tag{2.213}$$

with I_{η_h} the function defined by

$$I_{\eta_h} = \int_0^\infty dx \frac{x^{(4+\eta_h)/(4-\eta_h)}}{\sinh^2 x}. \tag{2.214}$$

For the low temperature result, obtained both in perturbation theory and with the SCBA, of $\eta_h = 2$ we obtain $I_2 = 3\zeta(3)/2$ and a temperature dependence of the thermal expansion of $\alpha_A \propto -T^2$. Most importantly, this result correctly predicts a vanishing thermal expansion coefficient for $T \to 0$, satisfying the third law of thermodynamics even in the limit of an infinite membrane, $L \to \infty$.

For low temperature compared with the Debye temperature, but higher than the quantum-to-classical temperature T^*, $T^* \ll T \ll T_{D,F}$, classical anharmonic effects start dominating the physics and we can no longer neglect the temperature dependence of $\Omega_{F,\boldsymbol{q}}$ which is encoded in the momentum scale $q_0 = q_0(T)$. Doing the same long wavelength approximations and cutting off the integral at $|\mathbf{q}| < q_0(T)$ for the terms proportional to $\partial\log\Omega_{F,\mathbf{q}}/\partial\log T$ in Eq. (2.212) (since above $q_0(T)$ anharmonic effects are weak and therefore the temperature dependence of $\Omega_{F,\mathbf{q}} \simeq \omega_{F,\mathbf{q}}$ is weak), we obtain

$$\alpha_A \simeq -\frac{k_B}{2\pi\left(4-\eta_h\right)\kappa}\left(\frac{2\rho^{1/2}k_BT}{\hbar\kappa^{1/2}q_0^2(T)}\right)^{2\eta_h/(4-\eta_h)} \times$$
$$\times\left[I_{\eta_h} - \eta_h^T\left(\tilde{I}_{\eta_h}\left(\frac{\hbar\kappa^{1/2}q_0^2(T)}{\rho^{1/2}k_BT}\right) + \tilde{J}_{\eta_h}\left(\frac{\hbar\kappa^{1/2}q_0^2(T)}{\rho^{1/2}k_BT}\right)\right)\right],\ T^* \ll T \ll T_{D,F}, \tag{2.215}$$

where we introduced

$$\tilde{I}_{\eta_h}(y) = \int_0^y dx \frac{x^{(4+\eta_h)/(4-\eta_h)}}{\sinh^2 x}, \tag{2.216}$$
$$\tilde{J}_{\eta_h}(y) = \int_0^y dx x^{2\eta_h/(4-\eta_h)}\coth x, \tag{2.217}$$

and defined the exponent $\eta_h^T = \partial \log \Omega_{F,\boldsymbol{q}} / \partial \log T$. Using the classical result from Eq. (2.65), $q_0(T) \propto T^{1/2}$, we have that $\Omega_{F,\boldsymbol{q}} \propto T^{\eta_h/4}$ and therefore $\eta_h^T = \eta_h/4$. The fact that $q_0(T) \propto T^{1/2}$ also implies that the thermal expansion for $T^* \ll T \ll T_{D,F}$ becomes temperature independent. As such for graphene we obtain that for $T^* \ll T \ll T_{D,F}$ the thermal expansion is of the order of

$$\alpha_A \simeq -\frac{k_B}{\kappa}, \tag{2.218}$$

confirming the result from Eq. (2.202).

2.4.2 *Specific heat*

The specific heat at constant pressure/stress is defined as the change of enthalpy with temperature

$$c_p = \left.\frac{\partial \mathrm{H}}{\partial T}\right|_P, \tag{2.219}$$

where for a crystal the enthalpy per unit area is given by

$$\mathrm{H} = U - \langle u_{ij} \rangle \, \sigma_{ij},$$

with σ_{ij} the externally applied stress, $\langle u_{ij} \rangle$ the in-plane linear strain tensor and U is the total energy of the system per unit area. Since we are working at zero external stress, the enthalpy coincides with the total internal energy. We prove in Appendix D that the total energy of an interacting system with cubic and quartic interaction, such as the one defined by Eq. (2.81), can be expressed in terms of two-point Green's functions, using a modified Migdal–Galitskii–Koltun energy sum rule [97, 98]. The total energy of the membrane per unit area can be written as

$$U = U^{(\mathrm{out})} + U^{(L)} + U^{(T)}, \tag{2.220}$$

where $U^{(\mathrm{out})}$ involves the *exact* flexural phonon Green's function and $U^{(L/T)}$ involves the *exact* in-plane Green's function for the longitudinal/transverse phonon. The different contributions are given by

$$U^{(\mathrm{out})} = -\frac{1}{4}\frac{1}{\beta A}\sum_{\tilde{\mathbf{q}}} \left(3\rho\,(iq_n)^2 + \kappa\,|\boldsymbol{q}|^4\right) D_{F,\tilde{\mathbf{q}}}, \tag{2.221}$$

$$U^{(L/T)} = -\frac{1}{\beta A}\sum_{\tilde{\mathbf{q}}} \rho\,(iq_n)^2\, D_{L/T,\tilde{\mathbf{q}}}. \tag{2.222}$$

Although anharmonic effects couple in-plane and out-of-plane phonons, we can still interpret the contribution $U^{(\mathrm{out})}$ as being mostly due to the flexural phonon and the the contributions $U^{(L/T)}$ as being mostly due to the in-plane longitudinal/transverse phonon modes.

Just as for the thermal expansion, we ignore the frequency dependence of the phonon self-energies and therefore obtain

$$U^{(\mathrm{out})} = \frac{\hbar}{8}\int \frac{d^2\mathbf{q}}{(2\pi)^2} \coth\left(\frac{\hbar\Omega_{F,\mathbf{q}}}{2k_BT}\right)\left(3\Omega_{F,\mathbf{q}} + \frac{\omega_{F,\mathbf{q}}^2}{\Omega_{F,\mathbf{q}}}\right), \tag{2.223}$$

$$U^{(L/T)} = \frac{\hbar}{2}\int \frac{d^2\mathbf{q}}{(2\pi)^2}\Omega_{L/T,\mathbf{q}} \coth\left(\frac{\hbar\Omega_{L/T,\mathbf{q}}}{2k_BT}\right). \tag{2.224}$$

The specific heat can therefore be written as

$$c_p = c_p^{(\mathrm{out})} + c_p^{(L)} + c_p^{(T)} \tag{2.225}$$

$$c_p^{(\mathrm{out})} = \frac{\partial U^{(\mathrm{out})}}{\partial T} \tag{2.226}$$

$$c_p^{(L/T)} = \frac{\partial U^{(L/T)}}{\partial T}, \tag{2.227}$$

with

$$c_p^{(\mathrm{out})} = \frac{k_B}{4}\int \frac{d^2\mathbf{q}}{(2\pi)^2}\left(\frac{\hbar\Omega_{F,\mathbf{q}}}{2k_BT}\right)^2 \frac{3+(\omega_{F,\mathbf{q}}/\Omega_{F,\mathbf{q}})^2}{\sinh^2\left(\frac{\hbar\Omega_{F,\mathbf{q}}}{2k_BT}\right)}\left(1-\frac{\partial\log\Omega_{F,\mathbf{q}}}{\partial\log T}\right) + \frac{k_B}{4}\int \frac{d^2\mathbf{q}}{(2\pi)^2}\frac{\hbar\Omega_{F,\mathbf{q}}}{2k_BT}\coth\left(\frac{\hbar\Omega_{F,\mathbf{q}}}{2k_BT}\right)\left[3-\left(\frac{\omega_{F,\mathbf{q}}}{\Omega_{F,\mathbf{q}}}\right)^2\right]\frac{\partial\log\Omega_{F,\mathbf{q}}}{\partial\log T}, \tag{2.228}$$

and

$$c_p^{(L/T)} = k_B\int \frac{d^2\mathbf{q}}{(2\pi)^2}\left(\frac{\hbar\Omega_{L/T,\mathbf{q}}}{2k_BT}\right)^2 \frac{1}{\sinh^2\left(\frac{\hbar\Omega_{L/T,\mathbf{q}}}{2k_BT}\right)}\left(1-\frac{\partial\log\Omega_{L/T,\mathbf{q}}}{\partial\log T}\right) + k_B\int \frac{d^2\mathbf{q}}{(2\pi)^2}\frac{\hbar\Omega_{L,\mathbf{q}}}{2k_BT}\coth\left(\frac{\hbar\Omega_{L,\mathbf{q}}}{2k_BT}\right)\frac{\partial\log\Omega_{L/T,\mathbf{q}}}{\partial\log T}. \tag{2.229}$$

We now focus on the low temperature behaviour of the specific heat. Just as for the thermal expansion, the low temperature properties will be dominated by long wavelength phonons such that we can approximate $\Omega_{F,\mathbf{q}} \simeq \sqrt{\kappa q_0^{\eta_h}/\rho}\,|\mathbf{q}|^{2-\eta_h/2}$. If we are in the low temperature quantum regime $T \ll T^*$, we also neglect the temperature dependence of $\Omega_{F,\mathbf{q}}$ and obtain the contribution to the specific heat

$$c_p^{(\mathrm{out})} = \frac{3}{8\pi}k_Bq_0^2\left(\frac{2\rho^{1/2}k_BT}{\hbar\kappa^{1/2}q_0^2}\right)^{4/(4-\eta_h)} L_{\eta_h},\ T \ll T^*, \tag{2.230}$$

where

$$L_{\eta_h} = \int_0^\infty dx \frac{x^{(8-\eta_h)/(4-\eta_h)}}{\sinh^2(x)}. \tag{2.231}$$

For the obtained value of $\eta_h = 2$ at $T \to 0$, we have $L_2 = 3\zeta(3)/2$ and $c_p^{(\mathrm{out})} \propto T^2$. This result is to be contrasted with the one obtained at the harmonic level, which would predict $c_p^{(\mathrm{out})} \propto T$, and is a consequence of the change of long wavelength dispersion of flexural modes from $\propto |\mathbf{q}|^2$ to $\propto |\mathbf{q}|$. Regarding the contribution mostly due to in-plane modes, $c_p^{(L/T)}$, as discussed in Section 2.3.1.2, anharmonic effects only lead to a logarithmic correction of the in-plane phonon Green's function, which we will neglect. Therefore, the contribution mostly due to the in-plane modes reduces to the non-interacting one, which for $T \to 0$ yields the expected T^2 dependence

$$c_p^{(\mathrm{in})} = k_B\left(\frac{2k_BT}{\hbar}\right)^2\left(\frac{\rho}{\lambda+2\mu}+\frac{\rho}{\mu}\right)L_2. \tag{2.232}$$

Therefore, taking into account at the same time anharmonic and quantum effects, we predict an intermediate behaviour $T < T^{4/(4-\eta_h)} \leqslant T^2$ for the specific heat, which

results from the non-linear coupling between in-plane and out-of-plane modes. For the obtained value of $\eta_h = 2$ both $c_p^{(\mathrm{out})}$ and $c_p^{(\mathrm{in})}$ are proportional to T^2. Notice, that the harmonic theory calculated for graphene [99, 100], predicts $c_p \propto T$ up to temperatures as high as 100 K which is about close to the value we found for T^*. That is why we believe that the linear T dependence should not be observable in graphene for which we predict instead a T^2 dependence.

2.5 CONCLUSIONS

In this chapter, we have studied the properties of free crystalline membranes. In a free membrane, the absence of an applied tension or of coupling to a substrate allows for strong out-of-plane fluctuations, which naively make a flat phase of the membrane impossible. These out-of-plane fluctuations are inevitably accompanied by in-plane stretching of the membrane and this fact is at the origin of an anharmonic coupling between out-of-plane and in-plane phonons. In the high temperature limit, classical statistical mechanics predicts that these anharmonic affects lead to a strong correction to the in-plane elastic constants and bending rigidity of the membrane, which become scale dependent. Motived by the high Debye temperature of graphene ($\simeq 1000$ K), a prototypical crystalline membrane, we studied the importance of these anharmonic effects in the low temperature, quantum regime. In particular, we focused on the effect of anharmonicities in the dispersion relation of the flexural phonon and in low temperature behaviour of the thermal expansion and specific heat of a crystalline membrane.

In order to describe quantum effects in a crystalline membrane, we quantized the thin plate model of a crystalline membrane, which includes anharmonic coupling between in-plane and out-of-plane phonons, employing a functional path integral approach. Using the obtained model, we computed, to lowest order in perturbation theory and using a self-consistent Born approximation (neglecting corrections to the in-plane phonons), the correction to the dispersion relation of the flexural phonons. By keeping retardation effects in the effective interaction between flexural modes, due to the exchange of in-plane phonons, we have found out that the long wavelength dispersion relation for flexural phonons is changed from the bare result $\omega_{F,\mathbf{q}} \propto |\mathbf{q}|^2$ into $\Omega_{F,\mathbf{q}} \propto |\mathbf{q}|^{2-\eta_h/2}$, having obtained $\eta_h = 2$ in the $T \to 0$ limit, both in the perturbative and in the self-consistent calculation. This is to be contrasted with the classical result, where a lowest order perturbation calculation leads to $\eta_h = 2$, but a self-consistent Born approximation changes this result to $\eta_h = 1$. We also estimated the momentum scale, k_c, bellow which anharmonic effects become dominant, having found for graphene $k_c \simeq 0.1\,\text{Å}^{-1}$ in the $T \to 0$ limit, which is about 0.6 of the corresponding momentum scale estimated within classical statistical mechanics at room temperature. We also estimated the crossover temperature, T^*, bellow which quantum mechanical fluctuations dominate the dispersion relation of the flexural phonon. For typical graphene parameters, this crossover temperature is $T^* \sim 70 - 90$ K.

By using the calculated flexural phonon Green's functions in the quantum anharmonic regime, we established the low temperature dependence of the thermal expansion and of the specific heat. In the $T \to 0$ limit, we find a power-law behaviour for both the (areal) thermal expansion coefficient α_A and the specific heat c_p. We found that for the thin plate model considered, thermal expansion is always negative and that anharmonic effects render it finite in the thermodynamic limit, vanishing for $T \to 0$ in agreement with the third law of thermodynamics. The low temperature behaviour of the thermal expansion is found to the $\alpha_A \propto -T^{2\eta_h/(4-\eta_h)}$, which for the obtained value

of $\eta_h = 2$, yields $\alpha_A \propto -T^2$. Notice, that this result is to be contrasted with the one obtained within a quasi-harmonic approximation, which predicts an infinite thermal expansion at any finite temperature in the thermodynamic limit. The low temperature behaviour of the specific heat is also affected by the characteristic exponent η_h of the elementary phonon excitations and we have obtained a specific heat due to the flexural phonons behaving as $c_p^{(\mathrm{out})} \propto T^{4/(4-\eta_h)}$. For $\eta_h = 2$, we obtain $c_p^{(\mathrm{out})} \propto T^2$, while the harmonic theory predicts $c_p^{(\mathrm{out})} \propto T$. The contribution to the specific heat due to in-plane phonons is found to not be significantly changed by anharmonic effects in the $T \to 0$ limit, retaining the behaviour of $c_p^{(\mathrm{in})} \propto T$, predicted by the harmonic theory.

This work is a first step towards the full understanding of the physics of quantum crystalline membranes, such as graphene. Many question remain unanswered. First, since we focused our study on the $T \to 0$ limit, it is not clear how the transition occurs between the low temperature quantum behaviour and the high temperature classical one. In particular since we have obtain $\eta_h = 2$ for $T \to 0$ and studies based on classical statistical mechanics yield $\eta_h \simeq 0.72$ - 0.85, one expects that there will be an intermediate region where η_h will be temperature dependent. Secondly, although the lowest order perturbation theory calculation and the self-consistent Born approximation results agree in the value $\eta_h = 2$, it is still necessary to perform a calculation that properly takes into account corrections to the in-plane phonons. Finally, it is also necessary to explore the robustness of the obtained results to deformations of the model used to describe a crystalline membrane. In particular, it is necessary to access the possible effect of higher order anharmonic couplings, which appear naturally in a geometrical description of a membrane, namely, of quartic coupling between in-plane and out-of-plane displacements and of cubic and quartic couplings between in-plane displacements. Nevertheless, the perturbative calculation presented in the chapter is already sufficient to show that a simultaneous treatment of quantum and anharmonic effects is necessary to have a vanishing thermal expansion at zero temperature in the thermodynamic limit, in accordance with the third law of thermodynamics. The present calculation also allows to estimate the crossover temperature between the classical and the quantum regime and of the crossover momentum scale between harmonic and anharmonic behaviour in the low temperature regime.

3 CRYSTALLINE MEMBRANE SUPPORT BY A SUBSTRATE

3.1 INTRODUCTION

In the previous chapter, we have seen how anharmonic effects play a fundamental role in the elastic and thermodynamic properties of free (under zero stress and decoupled from other systems) crystalline membranes, such as graphene and other 2D crystals. While the physics of suspended samples of 2D crystals will be controlled by anharmonic effects, the picture will be drastically different for samples supported by a substrate. In this scenario, it will be the coupling of the 2D crystal to the substrate, and not intrinsic anharmonic effects, that will dominate the low energy long wavelength physics of the 2D crystal. As a matter of fact it has been know since the early 90's [101–104] that the phonon dispersion relation of supported graphene samples is greatly affected by the substrate, depending on the coupling between the substrate and the graphene overlayer. The presence of the substrate breaks the out-of-plane mirror symmetry of an isolated monolayer, which will have a particularly strong effect in the dispersion relation of the out-of-plane acoustic phonon (also commonly referred to as flexural) of the graphene overlayer.

We have also seen in the previous chapter that the thermal expansion of a crystalline membrane is greatly dependent on the dispersion relation of the out-of-plane phonons of the membrane. Therefore, provided the dispersion of the out-of-plane phonon is significantly altered, coupling of the membrane to a substrate should play an important role in the thermal expansion of a membrane.

In more recent times, numerical solutions of the Boltzmann equation for phonons, indicate that the thermal conduction in graphene is dominated by out-of-plane acoustic phonons [105]. It was found experimentally [106] and theoretically [107], based on molecular dynamics calculations, that the thermal conductivity of supported samples is significantly reduced when compared to the one of suspended samples. The lifetime of the out-of-plane phonons is also significantly reduced due to the coupling of the graphene layer to the substrate [108]. Thus, it is necessary to have a good understanding of the properties of the flexural phonon of graphene samples supported by a substrate.

In this chapter, we study the effect of coupling to a substrate in the dynamics of the flexural phonon of a crystalline membrane. The chapter is organized as follows. In Section 3.2, we introduce a minimal model Hamiltonian, based on elasticity theory, that describes the coupled system of crystalline membrane and substrate. We focus on the effect of the substrate on the membrane flexural phonon. In order to study the spectral properties of the membrane flexural mode, taking into account its coupling to the substrate degrees of freedom, we introduce a dissipation function in Section 3.3 and compare the results of our model with phonon dispersion data for graphene on top of different substrate obtained via HREELS in Ref. [103]. In Section 3.4, we also study the effect of coupling to the substrate for the membrane out-of-plane fluctuations and thermal expansion, finding that both quantities become substrate dependent. Finally, in Section 3.5 we summarize the results from this chapter.

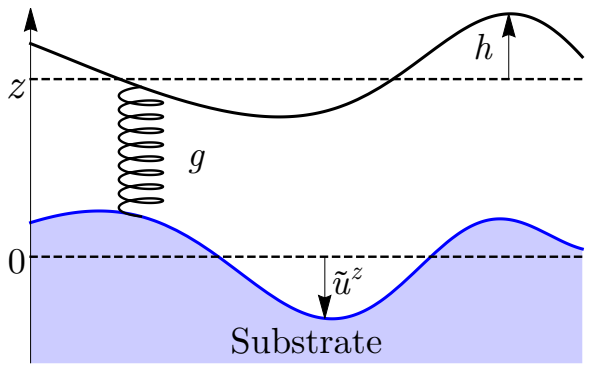

Figure 3.1: Schematic representation of coupling between a membrane and the substrate that supports it, Eq. 3.8.

3.2 MODEL OF CRYSTALLINE MEMBRANE COUPLED TO A SUBSTRATE

In order to describe a crystalline membrane coupled to a substrate we will use a continuous description based on elasticity theory. This approach is suitable to describe the long wavelength and low energy lattice dynamics of the coupled system. We consider a crystalline membrane supported by a semi-infinite flat substrate that occupies the half-space $z < 0$. Employing a canonical quantization formalism, the Hamiltonian of the coupled membrane-substrate system can be written as

$$H = H_{\text{out}} + H_{\text{in}} + H_{\text{subs}} + H_{\text{coup}}, \tag{3.1}$$

Where $H_{\text{out}} + H_{\text{in}}$ is the Hamiltonian describing the isolated crystalline membrane, H_{subs} is the Hamiltonian describing the substrate and H_{coup} is the coupling Hamiltonian between the membrane and the substrate. $H_{\text{out}}+H_{\text{in}}$ has the same form as Eq. (2.81) of the previous chapter but in real time. However, the anticipate that the coupling to the substrate will play a much more important role than intrinsic membrane anharmonic effects. We therefore neglect anharmonic terms in Eq. (2.81) and obtain

$$H_{\text{out}} = \int d^2\mathbf{x} \left(\frac{\pi_h^2}{2\rho} + \frac{1}{2}\kappa \left(\partial^2 h\right)^2 \right), \tag{3.2}$$

$$H_{\text{in}} = \int d^2\mathbf{x} \left(\frac{\boldsymbol{\pi}^2}{2\rho} + \frac{1}{2} c^{ijkl} u_{ij} u_{kl} \right), \tag{3.3}$$

where once again ρ is the mass density (per unit area) of the membrane, κ is the bending rigidity and c^{ijkl} is the elastic moduli tensor. h is the out-of-plane displacement field and $u_{ij} = \left(\partial_i u_j + \partial_j u_i\right)/2$ is the linear strain tensor, with $\mathbf{u}$ the in-plane displacement field. The canonical conjugate momenta for h and $\mathbf{u}$ are, respectively, π_h and $\boldsymbol{\pi}$, obeying the equal time commutation relations

$$\left[h(\mathbf{x}), \pi_h(\mathbf{x}')\right] = i\delta^{(2)}(\mathbf{x} - \mathbf{x}'), \tag{3.4}$$

$$\left[u_i(\mathbf{x}), \pi_j(\mathbf{x}')\right] = i\delta_{ij}\delta^{(2)}(\mathbf{x} - \mathbf{x}'),\ i, j = x, y. \tag{3.5}$$

The Hamiltonian for the long wavelength acoustic modes of the substrate half-space is described within linear elasticity theory as

$$H_{\text{subs}} = \int_{z<0} d^3\vec{x} \left(\frac{\vec{\pi}_s^2}{2\rho_{3D}} + \frac{1}{2}\tilde{c}^{\alpha\beta\gamma\delta} \partial_\alpha u_{s,\beta} \partial_\gamma u_{s,\delta} \right), \tag{3.6}$$

	g [10^{20}N m^{-3}]	ω_0 [meV]	γ_0 [meV]
SiO_2	1.82 [113]	10	9
hBN	1.2-2.7 [114]	10	15
TaC	20.23 [103]	34	14
HfC	21.72 [103]	35	18
TiC	23.82 [103]	37	32

Table 3.1: Membrane-substrate coupling parameter g for different materials and computed gap, ω_0 Eq. (3.68), and dissipation, γ_0 Eq. (3.70), parameters.

where $\vec{x} = (\mathbf{x}, z)$, $u_{s,\alpha}$ is the displacement field for the substrate, with $\pi_{s,\alpha}$ the conjugate momenta. ρ_{3D} is the mass density per unit volume of the substrate and $\tilde{c}^{\alpha\beta\gamma\delta}$ is its elastic moduli tensor, with Greek indices running over the x, y, z coordinates. $u_{s,\alpha}$ and $\pi_{s,\alpha}$ obey the canonical commutation relations

$$\left[u_{s,\alpha}(\vec{x}), \pi_{s,\alpha}(\vec{x}')\right] = i\delta_{\alpha\beta}\delta(\vec{x} - \vec{x}'),\ \alpha, \beta = x, y, z, \tag{3.7}$$

Since the out-of-plane phonons of graphene are the most affected by the substrate [101–103, 109–111] and assuming that the fluctuations around the equilibrium distance between the substrate and the membrane are small, we consider a quadratic coupling between the out-of-plane displacements of the membrane and the substrate [112], which reads

$$H_{\text{coup}} = \frac{g}{2}\int d^2\mathbf{x}\left(h(\mathbf{x}) - u_{s,z}(\mathbf{x}, 0)\right)^2, \tag{3.8}$$

with g a spring constant per unit area coupling the membrane and the substrate. The model is schematically shown in Fig. 3.1. The value of the constant g greatly varies from substrate to substrate (see Table 3.1). It was estimated in Ref. [113] to have a value of $1.82 \times 10^{20}\text{J/m}^4$ for graphene on SiO_2. For graphene on hBN its value can be estimated from density functional theory (DFT) calculations [114], to be around $1.2 - 2.7 \times 10^{20}\text{J/m}^4$, depending on the orientation of graphene on hBN. For the (111) surface of transition metal carbides it is of the order of $2 \times 10^{21}\text{J/m}^4$, while for the (001) face is approximately zero [103], as it is for graphene on platinum (111) [104, 111].

3.2.1 *Green's function for membrane-substrate coupled system*

Having neglected anharmonic effects in Eq. 3.3, the in-plane and out-of-plane modes of the crystalline membrane become completely decoupled. Using the commutation relations Eqs. (3.4) and (3.7) we obtain the coupled Heisenberg equations for motion for the membrane out-of-plane and the substrate displacement fields

$$\left(-\rho\partial_t^2 - \kappa\partial^4 - g\right) h(t, \mathbf{x}) = -g\tilde{u}_z(t, \mathbf{x}, 0), \tag{3.9}$$

$$\left(-\rho_{3D}\delta^{\alpha\beta}\partial_t^2 - L^{\alpha\beta}(\partial) - g\delta^{z\beta}\delta(z)\right) u_{s,\beta}(t, \mathbf{x}, z) = -gh(t, \mathbf{x}), \tag{3.10}$$

where we have introduce the acoustic differential operator

$$L^{\alpha\beta}(\partial) = -\tilde{c}^{\alpha\mu\nu\beta}\partial_\mu\partial_\nu. \tag{3.11}$$

We now introduce the retarded membrane-membrane and substrate-substrate Green's functions

$$D^R_{hh}(t,\mathbf{x};t',\mathbf{x}') = -i\Theta(t-t')\left\langle\left[h(t,\mathbf{x}),h(t',\mathbf{x}')\right]\right\rangle, \tag{3.12}$$

$$D^R_{u_s^\alpha u_s^\beta}(t,\mathbf{x},z;t',\mathbf{x}',z') = -i\Theta(t-t')\left\langle\left[u_{s,\alpha}(t,\mathbf{x},z),u_{s,\beta}(t',\mathbf{x}',z')\right]\right\rangle, \tag{3.13}$$

and the membrane-substrate mixed Green's function

$$D^R_{hu_s^\alpha}(t,\mathbf{x};t',\mathbf{x}',z') = -i\Theta(t-t')\left\langle\left[h(t,\mathbf{x}),u_{s,\alpha}(t',\mathbf{x}')\right]\right\rangle, \tag{3.14}$$

$$D^R_{u_s^\alpha h}(t,\mathbf{x},z;t',\mathbf{x}') = -i\Theta(t-t')\left\langle\left[u_{s,\alpha}(t,\mathbf{x},z),h(t',\mathbf{x}')\right]\right\rangle. \tag{3.15}$$

For the components of the Green's function only involving the membrane out-of-plane displacement we will use the notation $D^R_F(t,\mathbf{x};t',\mathbf{x}') = D^R_{hh}(t,\mathbf{x};t',\mathbf{x}')$. The Heisenberg equations of motion, Eqs. (3.9) and (3.10), imply that the Green's functions obey the coupled equations

$$\begin{bmatrix} -\rho\partial_t^2-\kappa\partial^4-g & g\delta^{z\alpha}\delta^{\alpha\gamma}\delta(z) \\ g & -\rho_{3D}\delta^{\alpha\gamma}\partial_t^2 - L^{\alpha\gamma}(\partial) - g\delta^{z\alpha}\delta^{\alpha\gamma}\delta(z) \end{bmatrix} \cdot \begin{bmatrix} D^R_F(t,\mathbf{x};t',\mathbf{x}') & D^{R,}_{hu_s^\beta}(t,\mathbf{x};t',\mathbf{x}',z') \\ D^R_{u_s^\gamma h}(t,\mathbf{x},z;t',\mathbf{x}') & D^R_{u_s^\gamma u_s^\beta}(t,\mathbf{x},z;t',\mathbf{x}',z') \end{bmatrix} = \\ = \delta(t-t')\delta(\mathbf{x}-\mathbf{x}')\begin{bmatrix} 1 & \mathbf{0} \\ \mathbf{0} & \delta^{\alpha\beta}\delta(z-z') \end{bmatrix}. \tag{3.16}$$

The problem is greatly simplified by introducing the Green's function in the absence of coupling, $g=0$,

$$D^{0,R}_F = \left(-\rho\partial_t^2-\kappa\partial^4\right)^{-1}, \tag{3.17}$$

$$D^{0,R}_{u_s^\alpha u_s^\beta} = \left(-\rho_{3D}\delta^{\alpha\beta}\partial_t^2 - L^{\alpha\beta}(\partial)\right)^{-1}. \tag{3.18}$$

The problem is further simplified by taking advantage of translation invariance in the $x-y$ plane and in time, by introducing the Fourier transforms

$$D^R_{F,\mathbf{q}}(\omega) = \int dt \int d^2\mathbf{x} e^{i\omega t}e^{-i\mathbf{q}\cdot\mathbf{x}}D^R_F(t,\mathbf{x};0,\mathbf{0}), \tag{3.19}$$

$$D^R_{u_s^\alpha u_s^\beta,\mathbf{q}}(\omega,z,z') = \int dt \int d^2\mathbf{x} e^{i\omega t}e^{-i\mathbf{q}\cdot\mathbf{x}}D^R_{u_s^\beta u_S^\gamma}(t,\mathbf{x},z;0,\mathbf{0},z'), \tag{3.20}$$

and similarly for the mixed Green's functions. With these definitions and noticing that Eq. (3.16) only couples the membrane to the z components of $D^R_{u_s^\alpha u_s^\beta}$ at $z=z'=0$, the equations of motion for the Green's function become

$$\begin{bmatrix} \left(D^{0,R}_{F,\mathbf{q}}(\omega)\right)^{-1}-g & g \\ g & \left(D^{0,R}_{u_s^z u_s^z,\mathbf{q}}(\omega)\right)^{-1}-g \end{bmatrix} \cdot \begin{bmatrix} D^R_{F,\mathbf{q}}(\omega) & D^{R,}_{hu_s^z,\mathbf{q}}(\omega,0) \\ D^R_{u_s^z h,\mathbf{q}}(\omega,0) & D^R_{u_s^z u_s^z,\mathbf{q}}(\omega) \end{bmatrix} = \begin{bmatrix} 1 & 0 \\ 0 & 1 \end{bmatrix}, \tag{3.21}$$

	ρ_{3D} [g/cm^3]	c_{11} [GPa]	c_{12}	c_{13}	c_{33}	c_{44}	K_z [GPa]	v_R [m/s]
SiO_2	2.20	78	-	-	-	31	37	3392
hBN	2.28	811 [115]	169[115]	0 [115]	27 [115]	7.7 [115]	14	1835
TaC	14.65	634 [116]	-	-	-	216 [116]	285	3525
HfC	12.27	500 [116]	-	-	-	195 [116]	234	3681
TiC	4.94	500 [117]	113 [117]	-	-	175 [117]	228	5453

Table 3.2: Mass densities and elastic constants for different possible substrates: SiO_2, hBN and the transition metal carbides TaC, HfC and TiC. The transition metal carbides where approximated by isotropic materials using constants c_{11} and c_{44}: the data for TaC and HfC was taken from polycrystalline samples (Ref. [116]) while for TiC only the constants $c_{11}$and c_{44} are used. The Rayleigh velocities, v_R, are computed from the zeros of Eq. (3.55). K_z is obtained from Eq. (3.64).

where we have written $D^{0,R}_{u_s^z u_s^z,\mathbf{q}}(\omega) \equiv D^{0,R}_{u_s^z u_s^z,\mathbf{q}}(\omega, z = 0, z' = 0)$. The bare flexural phonon propagator is given in Fourier components as, see also Eq. (2.98),

$$D^{0,R}_{F,\mathbf{q}}(\omega) = \frac{1}{\rho\omega^2 - \kappa\,|\mathbf{q}|^4 + \mathrm{sgn}(\omega) i0^+}. \tag{3.22}$$

The Green's function for the flexural mode tacking into account the coupling to the substrate can be obtained from Eq. (3.21) and we write it as

$$D^{R}_{F,\mathbf{q}}(\omega) = \frac{1}{\rho\omega^2 - \kappa\,|\mathbf{q}|^4 - \Pi^{R}_{F,\mathbf{q}}(\omega)}, \tag{3.23}$$

where $\Pi^R_{F,\mathbf{q}}(\omega)$ is the self-energy induced by the substrate

$$\Pi^{R}_{F,\mathbf{q}}(\omega) = \frac{g}{1 - g D^{0,R}_{u_s^z u_s^z,\mathbf{q}}(\omega)}. \tag{3.24}$$

Therefore, provided we know the substrate Green's function, $D^{0,R}_{u_s^z u_s^z,\mathbf{q}}(\omega)$, Eq. (3.23) provides a simple expression for the membrane flexural Green's function in the presence of the substrate. We point out that obtaining the membrane flexural Green's function from Eq. (3.21) is equivalent to the procedure of integrating out the substrate degrees of freedom. Therefore, in order to describe the properties of the out-of-plane membrane vibrations we just need to know the Green's function of the isolated substrate.

In order to have a complete description of the membrane flexural mode coupled to a dynamic substrate, we are still lacking the knowledge of $D^{0,R}_{u_s^z u_s^z,\mathbf{q}}(\omega)$. We will compute it in the next section in the case of a uniaxial elastic material, such as hexagonal boron nitride.

3.2.2 *Green's function for isolated uniaxial substrate*

We wish to determine the form of $D^{0,R}_{u_s^z u_s^z,\mathbf{q}}(\omega, z = 0, z' = 0)$ for a semi-infinite substrate. In order to do this we use the fact that in a quadratic theory, such as the one defined by Eq. (3.6), the quantum mechanical retarded Green's function coincides with the classical Green's function[1], since they both obey the same equation of motion. In our

1 By classical Green's function we mean the mathematical definition of Green's function as the inverse of a linear differential operator

case, both the quantum mechanical Green's function and the classical one, obey the bulk equation of motion

$$\left(-\rho_{3D}\delta^{\alpha\gamma}\partial_t^2 - L^{\alpha\gamma}(\partial)\right) D^{0,R}_{u_s^\gamma u_s^\beta,\mathbf{q}}(t,\mathbf{x},z;t',\mathbf{x}',z') = \delta_{\alpha\beta}\delta(\mathbf{x}-\mathbf{x}')\delta(z-z'). \tag{3.25}$$

In order to determine the Green's function of a semi-infinite elastic substrate we must introduce boundary conditions at $z = 0$. Instead of doing that, we will instead use the fact that the Green's function relates an induced displacement field to a time and position dependent applied pressure, $\vec{f}(t,\mathbf{x})$, at $z = 0$ by

$$\delta u_{s,\alpha}(t,\mathbf{x},z) = -\int dt' \int d^2\mathbf{x}' D^{0,R}_{u_s^\alpha u_s^\beta}(t,\mathbf{x},z;t',\mathbf{x}',0) f^\beta(t',\mathbf{x}'), \tag{3.26}$$

which can be understood as the integral from of the boundary condition in the presence of $\vec{f}(t,\mathbf{x})$ at $z = 0$. We also point out that Eq. (3.26) is just the Kubo formula for linear response (see Appendix B) applied in the context of linear elasticity theory, due to a term added to the Hamiltonian Eq. (3.6) of the form

$$V_f(t) = -\int d^2\mathbf{x}\vec{f}(t,\mathbf{x})\cdot\vec{u}_s(\mathbf{x},0). \tag{3.27}$$

We also point out that for a quadratic theory and if the external source couples linearly to the dynamical degrees of freedom, the response to the source is always linear, that is, Kubo formula is exact. Therefore in order to determine teh quantum mechanical Green's function, $D^{0,R}_{u_s^z u_s^z,\mathbf{q}}$, we just need to study the response of the substrate to an external pressure at $z = 0$.

The displacement induced by the external pressure $\vec{f}(t,\mathbf{x})$ at $z = 0$, $\delta u_{s,\alpha}(t,\boldsymbol{x},z)$, obeys the bulk equation of motion for $z < 0$,

$$\left(-\rho_{3D}\delta^{\alpha\beta}\partial_t^2 - L^{\alpha\beta}(\partial)\right)\delta u_{s,\beta}(t,\boldsymbol{x},z) = 0. \tag{3.28}$$

In the presence of the external pressure $\vec{f}(t,\mathbf{x})$ at $z = 0$, we have the boundary equation

$$B^{\alpha\beta}(\partial)u_{s,\beta}(t,\mathbf{x},0) = f^\alpha(t,\mathbf{x}). \tag{3.29}$$

with the boundary condition differential operator defined as

$$B^{\alpha\beta}(\partial) = \tilde{c}^{\alpha z\mu\beta}\partial_\mu. \tag{3.30}$$

In order to proceed, we must specify the form of the substrate elastic tensor, $\tilde{c}^{\alpha\beta\gamma\delta}$. We will focus on uniaxial materials (also refereed to as transverse isotropic or polar anisotropic), which are isotropic with relation to rotations along a single axis, the c-axis. Crystals with hexagonal symmetry fall into this category [79]. A uniaxial material has 5 independent elastic constants. These are conveniently expressed in matrix form using Voigt notation

$$\tilde{c}_{IJ} = \begin{bmatrix} c_{11} & c_{12} & c_{13} & 0 & 0 & 0 \\ c_{12} & c_{11} & c_{13} & 0 & 0 & 0 \\ c_{13} & c_{13} & c_{33} & 0 & 0 & 0 \\ 0 & 0 & 0 & c_{44} & 0 & 0 \\ 0 & 0 & 0 & 0 & c_{44} & 0 \\ 0 & 0 & 0 & 0 & 0 & (c_{11}-c_{12})/2 \end{bmatrix}, \tag{3.31}$$

where the Voigt indices I, J which run over $\{1,2,3,4,5,6\}$ and correspond to the pairs of spacial indices $\{xx, yy, zz, yz, xz, xy\}$. Therefore, in Voigt notation, c_{13} corresponds to $\tilde{c}^{xxzz}$, for example. In the case of an isotropic substrate, the 5 constants are reduced to two: $c_{11} = c_{33} = \lambda_{3D}^{\text{iso}} + 2\mu_{3D}^{\text{iso}}$, $c_{12} = c_{13} = \lambda_{3D}^{\text{iso}}$, $c_{44} = \mu_{3D}^{\text{iso}}$, with $\lambda_{3D}^{\text{iso}}$ and μ_{3D}^{iso} Lamé coefficients for a isotropic 3D material. Therefore, for an uniaxial material, the acoustic differential operator $L^{\alpha\beta}(\partial)$ is explicitly given by

$$-L^{\alpha\beta}(\partial) = \begin{bmatrix} c_{11}\partial_x^2 + \frac{1}{2}(c_{11}-c_{12})\partial_y^2 + c_{44}\partial_z^2 & \frac{1}{2}(c_{11}+c_{12})\partial_x\partial_y & (c_{13}+c_{44})\partial_x\partial_z \\ \frac{1}{2}(c_{11}+c_{12})\partial_x\partial_y & \frac{1}{2}(c_{11}-c_{12})\partial_x^2 + c_{11}\partial_y^2 + c_{44}\partial_z^2 & (c_{13}+c_{44})\partial_y\partial_z \\ (c_{13}+c_{44})\partial_x\partial_z & (c_{13}+c_{44})\partial_y\partial_z & c_{44}\left(\partial_x^2+\partial_y^2\right) + c_{33}\partial_z^2 \end{bmatrix} \tag{3.32}$$

and the boundary condition operator becomes

$$B^{\alpha\beta}(\partial) = \begin{bmatrix} c_{44}\partial_z & 0 & c_{44}\partial_x \\ 0 & c_{44}\partial_z & c_{44}\partial_y \\ c_{13}\partial_x & c_{13}\partial_y & c_{33}\partial_z \end{bmatrix}. \tag{3.33}$$

It is useful to take into account the translational invariance of the problem along the $x-y$ plane and write the induced displacement field in terms of Fourier components in $(t, \mathbf{x})$ variables as

$$\delta\vec{u}_s(t,\mathbf{x},z) = \int \frac{d\omega}{2\pi} \int \frac{d^2\mathbf{q}}{(2\pi)^2} \delta\vec{u}_s(\omega,\mathbf{q},z) e^{-i\omega t} e^{i\mathbf{q}\cdot\mathbf{x}}, \tag{3.34}$$

such a representation is usually refereed to as angular spectrum representation in the field of optics. We also present the external pressure in Fourier components

$$\vec{f}(t,\mathbf{x}) = \int \frac{d\omega}{2\pi} \int \frac{d^2\mathbf{q}}{(2\pi)^2} \vec{f}(\omega,\mathbf{q}) e^{-i\omega t} e^{i\mathbf{q}\cdot\mathbf{x}}. \tag{3.35}$$

With this representation, the linear response relation Eq. (3.26) becomes

$$\delta u_{s,\alpha}(\omega,\mathbf{q},z) = -D^{0,R}_{u_S^\alpha u_s^\beta,\mathbf{q}}(\omega,z,0) f^\beta(\omega,\mathbf{q}). \tag{3.36}$$

Since we are dealing with isotropic system in the $x-y$ plane, we can focus, without loss of generality, on the situation with $\mathbf{q} = (0,q)$. With this considerations, the displacement field obeys the bulk equation of motion

$$\left(\rho_{3D}\omega^2\delta^{\alpha\beta} - L^{\alpha\beta}(q,\partial_z)\right)\delta u_{s,\beta}(\omega,q,z) = 0, \tag{3.37}$$

with

$$L^{\alpha\beta}(q,\partial_z) = \begin{bmatrix} \frac{1}{2}(c_{11}-c_{12})q^2 - c_{44}\partial_z^2 & 0 & 0 \\ 0 & c_{11}q^2 - c_{44}\partial_z^2 & -i(c_{13}+c_{44})q\partial_z \\ 0 & -i(c_{13}+c_{44})q\partial_z & c_{44}q^2 - c_{33}\partial_z^2 \end{bmatrix}. \tag{3.38}$$

The external pressure at $z = 0$, will generate acoustic waves (which can be propagating or evanescent) that propagate away from the interface. Therefore, we can look for a solution of the form

$$\delta\vec{u}_s(\omega, q, z) = \sum_{\zeta=1}^{3} \vec{\xi}_\zeta(\omega, q)\delta u_{s,\zeta}(\omega, q)e^{-ik_{z,\zeta}(\omega,q)z}, \tag{3.39}$$

where $\delta\tilde{u}_{s,\zeta}(\omega, q)$ are mode amplitudes, labelled by the indice ζ, with polarization vector $\vec{\xi}_\zeta(\omega, q)$ and wavevectors along the z direction given by $k_{z,\zeta}(\omega, q)$. The different $k_{z,\zeta}(\omega, q)$ are obtained as the solutions of the secular equation

$$\det\left[\rho_{3D}\omega^2\delta^{\alpha\beta} - L^{\alpha\beta}(q, -ik_z)\right] = 0, \tag{3.40}$$

and the polarization vectors are obtained as the solutions of

$$\left[\rho_{3D}\omega^2\delta^{\alpha\beta} - L^{\alpha\beta}(q, -ik_z)\right]\xi^\beta_\zeta(\omega, q) = 0. \tag{3.41}$$

From Eq. (3.40) we obtain three possible solutions for k_z^2, and therefore six solutions for k_z. From these six solutions and taking into account causality, we choose the three solutions which describe waves propagating away from the interface. These three solutions are given by

$$k_{z,1/2}(\omega, q) = \mathrm{sgn}(\omega)\sqrt{\frac{B}{2} \pm \sqrt{\frac{B^2}{4} - C}} + \mathrm{sgn}(\omega)i0^+, \tag{3.42}$$

$$k_{z,3}(\omega, q) = \mathrm{sgn}(\omega)\sqrt{\frac{\omega^2\rho_{3D}}{c_{44}} - \frac{c_{11} - c_{12}}{2c_{44}}q^2} + \mathrm{sgn}(\omega)i0^+, \tag{3.43}$$

where

$$B = \frac{c_{11}}{c_{44}}\left(\frac{\rho_{3D}\omega^2}{c_{11}} - q^2\right) + \frac{c_{44}}{c_{33}}\left(\frac{\rho_{3D}\omega^2}{c_{44}} - q^2\right) + \frac{(c_{13} + c_{44})^2}{c_{33}c_{44}}q^2, \tag{3.44}$$

$$C = \frac{c_{11}}{c_{33}}\left(\frac{\rho_{3D}\omega^2}{c_{11}} - q^2\right)\left(\frac{\rho_{3D}\omega^2}{c_{44}} - q^2\right). \tag{3.45}$$

In the definition of $k_{z,\zeta}(\omega, q)$ the pre-factor $\mathrm{sgn}(\omega)$ ensures that for real $k_{z,1/2}(\omega, q)$, Eq. (3.39) represents waves propagating away from the interface. If the square root in $k_{z,\zeta}(\omega, q)$ becomes imaginary the term under the square root $\mathrm{sgn}(\omega)i0^+$ ensures that the solution is an evanescent wave, which decays into the substrate bulk, $z \to -\infty$ (recall the general replacement rule for obtaining retarded Green's functions $\omega \to \omega + i0^+$). The (not normalized) polarization vectors are given by

$$\vec{\xi}_{1/2}(\omega, q) = \begin{bmatrix} 0 \\ a_{1/2}(\omega, q) \\ 1 \end{bmatrix}, \qquad \vec{\xi}_3(\omega, q) = \begin{bmatrix} 1 \\ 0 \\ 0 \end{bmatrix}, \tag{3.46}$$

where

$$a_{1/2}(\omega, q) = -\frac{(c_{13} + c_{44})qk_{z,1/2}(\omega, q)}{\omega^2 - c_{11}q^2 - c_{44}k^2_{z,1/2}(\omega, q)}. \tag{3.47}$$

Notice that the mode $\zeta = 3$ is a pure shear mode, being a transverse mode with polarization vector always lying in the $x - y$ plane. The polarization vectors corresponding

to $\zeta = 1, 2$ lie in the plane of incidence of the acoustic wave, and are a mixture of longitudinal and transverse mode. For an isotropic substrate, these two modes, $\zeta = 1, 2$ become, respectively, transverse and longitudinal modes. From Eqs. (3.39) and (3.46) we can write the displacement field at $z = 0$ as

$$\delta\vec{u}_s(\omega, q, 0) = \begin{bmatrix} 1 & 0 & 0 \\ 0 & a_1(\omega, q) & a_2(\omega, q) \\ 0 & 1 & 1 \end{bmatrix} \cdot \begin{bmatrix} \delta u_{s,3}(\omega, q) \\ \delta u_{s,1}(\omega, q) \\ \delta u_{s,2}(\omega, q) \end{bmatrix}. \tag{3.48}$$

Using this equation together with the boundary condition Eq. (3.29), we can relate the mode amplitudes $\delta\tilde{u}_{s,\zeta}(\omega, q)$ to the pressure $\vec{f}$ as

$$\begin{bmatrix} -ic_{44}k_{z,3} & 0 & 0 \\ 0 & -ic_{44}k_{z,1}a_1 + ic_{44}q & -ic_{44}k_{z,2}a_2 + ic_{44}q \\ 0 & ic_{13}qa_1 - ic_{33}k_{z,1} & ic_{13}qa_2 - ic_{33}k_{z,2} \end{bmatrix} \cdot \begin{bmatrix} \delta u_{s,3} \\ \delta u_{s,1} \\ \delta u_{s,2} \end{bmatrix} = \begin{bmatrix} f^x \\ f^y \\ f^z \end{bmatrix}. \tag{3.49}$$

We invert this relation in order to express the mode amplitudes $\delta u_{s,\zeta}(\omega, q)$ in terms of $\vec{f}$ and then use Eq. (3.48) to obtain a linear relation between $\delta\vec{u}_s(\omega, q, 0)$ and $\vec{f}(\omega, q)$. Comparing the obtained relation with Eq. (3.36), we can read off the different elements of $D^{0,R}_{u_s^\alpha u_s^\beta, \mathbf{q}}(\omega)$ for $z = z' = 0$ and obtain the non-zero components for $\mathbf{q} = (0, q)$:

$$D^{0,R}_{u_s^x u_s^x, \mathbf{q}}(\omega) = -\frac{i}{c_{44}k_{z,3}}, \tag{3.50}$$

$$D^{0,R}_{u_s^y u_s^y, \mathbf{q}}(\omega) = -i\frac{c_{33}}{M}\left(a_2k_{z,1} - a_1k_{z,2}\right), \tag{3.51}$$

$$D^{0,R}_{u_s^y u_s^z, \mathbf{q}}(\omega) = -i\frac{c_{44}}{M}\left[a_1a_2\left(k_{z,2} - k_{z,1}\right) + q\left(a_2 - a_1\right)\right], \tag{3.52}$$

$$D^{0,R}_{u_s^z u_s^y, \mathbf{q}}(\omega) = -\frac{i}{M}\left[c_{33}\left(k_{z,1} - k_{z,2}\right) - c_{13}q\left(a_1 - a_2\right)\right], \tag{3.53}$$

$$D^{0,R}_{u_s^z u_s^z, \mathbf{q}}(\omega) = -i\frac{c_{44}}{M}\left(a_2k_{z,2} - a_1k_{z,1}\right), \tag{3.54}$$

where we have defined the function

$$M = c_{44}\left(q - k_{z,2}a_2\right)\left(c_{13}qa_1 - c_{33}k_{z,1}\right) - c_{44}\left(q - k_{z,1}a_1\right)\left(c_{13}qa_2 - c_{33}k_{z,2}\right). \tag{3.55}$$

We point out that for a general wavevector $\mathbf{q} = q\left(\cos\theta, \sin\theta\right)$, $D^{0,R}_{u_s^\alpha u_s^\beta, \mathbf{q}}(\omega)$ can be obtained, appealing to in-plane isotropy, by performing an in-plane rotation of the tensor $D^{0,R}_{\tilde{u}^\alpha \tilde{u}^\beta, \mathbf{q}=(0,q)}(\omega)$. However, in our case we do not need to perform such rotation as we are only interested in the $D^{0,R}_{u_s^z u_s^z, \mathbf{q}}(\omega)$ component, which is not affected by the rotation. For an isotropic substrate, $D^{0,R}_{u_s^z u_s^z, \mathbf{q}}(\omega)$ simplifies to

$$D^{0,R}_{u_s^z u_s^z, \mathbf{q}}(\omega) = -i\left(\frac{\rho_{3D}\omega}{\mu^{\text{iso}}_{3D}}\right)^2 \frac{k_{z,L}}{\left(k_{z,T}^2 - q^2\right)^2 + 4q^2k_{z,L}k_{z,T}}, \tag{3.56}$$

where

$$k_{z,L} = \text{sgn}(\omega)\sqrt{\frac{\rho_{3D}\omega^2}{\lambda^{\text{iso}}_{3D} + 2\mu^{\text{iso}}_{3D}} - q^2 + \text{sgn}(\omega)i0^+}, \tag{3.57}$$

$$k_{z,T} = \text{sgn}(\omega)\sqrt{\frac{\rho_{3D}\omega^2}{\mu^{\text{iso}}_{3D}} - q^2 + \text{sgn}(\omega)i0^+}, \tag{3.58}$$

are the wavenumbers along the z direction for longitudinal and transverse sound waves and we reobtain the result from Ref. [118].

Now we will study the information contained in $D^{0,R}_{u_s^z u_s^z,\mathbf{q}}(\omega)$ and in $k_{z,\zeta}(\omega,q)$. We notice that the condition $k^2_{z,\zeta}(\omega,q)=0$, makes the transition between propagating and evanescent waves, split the region in the (ω,q) space which supports a continuum of bulk states from the region where there will be no bulk states. For the shear mode $\zeta=3$, the continuum of bulk states exist for

$$\omega > \sqrt{\frac{c_{11}-c_{12}}{2\rho_{3D}}}\,|\mathbf{q}|\,, \text{ continuum for } \zeta=3, \tag{3.59}$$

in which case $\mathrm{Im}D^{0,R}_{u_s^x u_s^x,\mathbf{q}}(\omega)\neq 0$. For the polarizations $\zeta=1$ and 2, and assuming that $c_{11}>c_{44}$ which holds for most materials, we obtain that the continuum of bulk states exists for

$$\omega > \sqrt{\frac{c_{44}}{\rho_{3D}}}\,|\mathbf{q}|\,, \text{ continuum for } \zeta=1, \tag{3.60}$$

$$\omega > \sqrt{\frac{c_{11}}{\rho_{3D}}}\,|\mathbf{q}|\,, \text{ continuum for } \zeta=2, \tag{3.61}$$

and $\mathrm{Im}D^{0,R}_{u_s^\alpha u_s^\beta,\mathbf{q}}(\omega)\neq 0$ for α and β in the plane of incidence. For

$$\left(\frac{\omega}{|\boldsymbol{q}|}\right)^2 < \frac{\min\left(\left(c_{11}-c_{12}\right)/2,\, c_{44},\, c_{11}\right)}{\rho_{3D}} \tag{3.62}$$

the semi-infinite substrate does not support bulk modes, that is, modes that propagate in the bulk with real $k_{z,\zeta}(\omega,q)$. It is however possible to obtain a localized surface mode: the Rayleigh mode, which will have a linear dispersion relation: $\omega_{R,\mathbf{q}}=v_R\,|\mathbf{q}|$, with v_R the velocity of the Rayleigh mode. The dispersion relation of the Rayleigh mode can be obtained from the zeros of the function M, which correspond to poles in $D^{0,R}_{u_s^\alpha u_s^\beta,\mathbf{q}}(\omega)$. This divergence only occurs in the components of $D^{0,R}_{u_s^\alpha u_s^\beta,\mathbf{q}}(\omega)$ that lie in the plane of incidence defined by the directions of $\mathbf{q}$ and z, which indicates the Rayleigh mode polarization lies in the plane of incidence.

Finally, we study two important limits of $D^{0,R}_{u_s^\alpha u_s^\beta,\mathbf{q}}(\omega)$, namely the zero momentum limit and the static limit. For the zero momentum limit, we have

$$\lim_{\mathbf{q}\to 0} D^{0,R}_{u_s^\alpha u_s^\beta,\mathbf{q}}(\omega) = -\frac{i}{\omega\sqrt{\rho_{3D}c_{33}}}, \tag{3.63}$$

while in the static limit we obtain

$$\lim_{\omega\to 0} D^{0,R}_{u_s^\alpha u_s^\beta,\mathbf{q}}(\omega) = -\frac{1}{K_z\,|\mathbf{q}|}, \tag{3.64}$$

where K_z is a constant that depends on the elastic constants of the material. For an isotropic material, K_z reduces to

$$K_z = \frac{2\mu^{\mathrm{iso}}_{3D}\left(\lambda^{\mathrm{iso}}_{3D}+\mu^{\mathrm{iso}}_{3D}\right)}{\lambda^{\mathrm{iso}}_{3D}+2\mu^{\mathrm{iso}}_{3D}}. \tag{3.65}$$

Knowing the form of $D^{0,R}_{u_s^z u_s^z,\mathbf{q}}(\omega)$ and having a complete understanding of the modes of a semi-infinite elastic substrate, we are in a position to study the properties of the flexural mode of the membrane coupled to the substrate.

3.3 SPECTRAL PROPERTIES OF FLEXURAL MODE

Notice that if the substrate is considered static (limit of infinite density and elastic constants) the membrane flexural Green's function reduces to

$$D^R_{F,\mathbf{q}}(\omega) = \frac{1}{\rho\omega^2 - \kappa\left|\mathbf{q}\right|^4 - g + \mathrm{sgn}(\omega)i0^+}, \tag{3.66}$$

meaning that the flexural phonon dispersion relation is modified from $\omega_{F,\mathbf{q}} = \sqrt{\kappa\left|\mathbf{q}\right|^4/\rho}$ to

$$\omega^{\text{gapped}}_{F,\mathbf{q}} = \sqrt{\frac{\kappa}{\rho}\left|\mathbf{q}\right|^4 + \omega_0^2}, \tag{3.67}$$

becoming gapped for $\mathbf{q} \to 0$, with a gap given by

$$\omega_0^2 = \frac{g}{\rho}. \tag{3.68}$$

However, for a dynamical substrate, this gap will fall into the bulk continuum of states of the substrate, which will act as a dissipative bath and induce a finite lifetime for the membrane flexural mode. Using the $\mathbf{q} \to 0$ limit of the substrate Green's function, Eq. (3.63), the self-energy of the flexural mode induced by the substrate, Eq. (3.24), becomes

$$\Pi^R_{F,\mathbf{q}}(\omega) = \rho\frac{\omega_0^2}{\omega^2 + \gamma_0^2}\left(\omega^2 - i\omega\gamma_0\right), \tag{3.69}$$

where

$$\gamma_0 = \frac{g}{\sqrt{c_{33}\rho_{3D}}}, \tag{3.70}$$

is a constant that characterizes the lifetime of the possible gapped flexural mode at $\mathbf{q} = 0$. Looking for solutions of

$$\rho\omega^2 - \mathrm{Re}\Pi^R_{F,\mathbf{0}}(\omega) = 0, \tag{3.71}$$

we find out that for $\omega_0 > \gamma_0$ the previous condition is satisfied for

$$\omega = \sqrt{\omega_0^2 - \gamma_0^2}, \tag{3.72}$$

and therefore, we see that the dynamics of the substrate reduce the zero momentum frequency of the flexural-gapped mode when compared with Eq. (3.67). For $\omega_0 < \gamma_0$, the flexural-gapped mode is not well defined. The ratio $\gamma_0/\omega_0 = \sqrt{g\rho/\left(c_{33}\rho_{3D}\right)}$, indicates how strong is the damping of the flexural-gapped phonon by the substrate. The greater is the membrane-substrate coupling and the smaller is the mass density and elastic constants of the substrate, the stronger will be damping of the flexural-gapped phonon.

Besides the emergence of a broadened flexural-gapped mode, the flexural mode of the membrane will also hybridize with the Rayleigh surface mode of the substrate, which was also pointed out in Ref. [107]. This hybrid flexural-Rayleigh mode will only occur bellow be continuum of bulk states of the substrate, $\omega < \sqrt{c_{44}/\rho_{3D}}\left|\mathbf{q}\right|$, where $\mathrm{Im}D^R_{u^z_s u^z_s,\mathbf{q}}(\omega) = 0$ and consequently $\mathrm{Im}\Pi^R_{F,\mathbf{q}}(\omega) = 0$. The dispersion relation of the flexural-Rayleigh mode, $\omega_{FR,\mathbf{q}}$, is obtained from the condition

$$\rho\omega^2_{FR,\mathbf{q}} = \kappa\left|\mathbf{q}\right|^4 + \mathrm{Re}\Pi^R_{F,\mathbf{q}}(\omega_{FR,\mathbf{q}}). \tag{3.73}$$

Close to the dispersion relation of the flexural-Rayleigh mode, $(\omega, \mathbf{q}) \simeq (\omega_{FR,\mathbf{q}}, \mathbf{q})$, $D^R_{F,\mathbf{q}}(\omega)$ can be approximated as

$$D^R_{F,\mathbf{q}}(\omega) = \frac{1}{\rho}\frac{Z_{FR}(\mathbf{q})}{\omega^2 - \omega^2_{FR,\mathbf{q}} + \mathrm{sgn}(\omega) i 0^+}, \tag{3.74}$$

where

$$Z^{-1}_{FR}(\mathbf{q}) = 1 - \frac{1}{2\rho\omega_{FR,\mathbf{q}}}\frac{\partial}{\partial\omega}\mathrm{Re}\Pi^R_{\mathbf{q}}(\omega_{FR,\mathbf{q}}), \tag{3.75}$$

is the weight, or field strength, of the flexural-Rayleigh mode on the membrane and indicates to which extent the hybrid flexural-Rayleigh mode is localized in the crystalline membrane (and not in the substrate).

All the spectral information regarding the dynamics of the membrane flexural mode coupled to the substrate can be encoded by defining a flexural mode dissipation function as

$$\mathcal{A}_F(\omega, \mathbf{q}) = -2\rho\omega \mathrm{Im} D^R_{F,\mathbf{q}}(\omega). \tag{3.76}$$

This quantity is a good spectral function. First, it is positive defined,

$$\mathcal{A}_F(\omega, \mathbf{q}) \geq 0, \tag{3.77}$$

and, secondly, it satisfies the sum rule

$$\int_{-\infty}^{+\infty} \frac{d\omega}{2\pi} \mathcal{A}_F(\omega, \mathbf{q}) = 1. \tag{3.78}$$

Both these properties can be easily proved using a Lehmann representation for $\mathrm{Im} D^R_{F,\mathbf{q}}(\omega)$. Using a complete and exact eigenbasis $\{|n\rangle\}$, we can write $\mathrm{Im} D^R_{F,\mathbf{q}}(\omega)$ as

$$\mathrm{Im} D^R_{F,\mathbf{q}}(\omega) = -\frac{\pi}{Z}\sum_{n,m}\left(e^{-\beta E_n} - e^{-\beta E_m}\right) |\langle n| h_{\mathbf{q}} |m\rangle|^2 \, \delta\left(\omega + E_n - E_m\right). \tag{3.79}$$

Using the fact that $\omega\left(1 - e^{-\beta\omega}\right) \geq 0$, one obtains that the condition $-\omega \mathrm{Im} D^R_{F,\mathbf{q}}(\omega) > 0$. Furthermore, we also have that

$$\begin{aligned} &- 2\rho\omega \mathrm{Im} D^R_{F,\mathbf{q}}(\omega) = \\ &= \rho\frac{2\pi}{Z}\sum_{n,m}\left(e^{-\beta E_n} - e^{-\beta E_m}\right)(E_m - E_n)\langle n| h_{\mathbf{q}} |m\rangle \langle m| h_{-\mathbf{q}} |n\rangle \, \delta\left(\omega + E_n - E_m\right) \\ &= -\frac{2\pi}{Z}\sum_{n,m}\left(e^{-\beta E_n} - e^{-\beta E_m}\right)\langle n| \rho\left[H, h_{\mathbf{q}}\right] |m\rangle \langle m| h_{-\mathbf{q}} |n\rangle \, \delta\left(\omega + E_n - E_m\right). \end{aligned} \tag{3.80}$$

Using the Heisenberg equation of motion $\dot{h}_{\mathbf{q}} = i\left[H, h_{\mathbf{q}}\right] = \pi_{h,\mathbf{q}}/\rho$ and integrating over frequency we obtain

$$\begin{aligned} \int_{-\infty}^{+\infty} \frac{d\omega}{2\pi} \mathcal{A}_F(\omega, \mathbf{q}) &= \frac{1}{Z}\sum_{n,m}\left(e^{-\beta E_n} - e^{-\beta E_m}\right)\langle n| \pi_{h,\mathbf{q}} |m\rangle \langle m| h_{-\mathbf{q}} |n\rangle \\ &= i\left\langle\left[\pi_{h,\mathbf{q}}, h_{-\mathbf{q}}\right]\right\rangle. \end{aligned} \tag{3.81}$$

Using the canonical commutation relation, $[\pi_{h,\mathbf{q}}, h_{-\mathbf{q}}] = -i$, we obtain the sum rule Eq. (3.78). The spectral function also provides information about how the system will

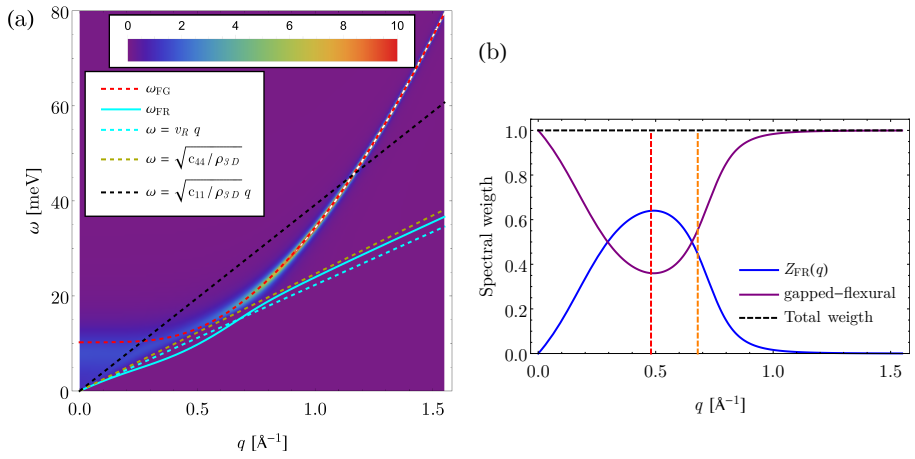

Figure 3.2: Density plot of the flexural mode dissipation function and field strength of flexural-Rayleigh mode on the membrane as a function of $\mathbf{q}$ for a graphene layer on top of a SiO_2 substrate. (a) Density plot of the flexural mode dissipation function (in units of $2\gamma_0/\omega_0^2$) for a graphene layer on top of a SiO_2 substrate. The dashed red line show the flexural-gapped dispersion relation, Eq. (3.67), and the solid cyan line shows the dispersion relation of the hybridized flexural-Rayleigh mode, which is determined by Eq. (3.73). The dashed cyan line represents the dispersion relation of the Rayleigh surface mode. Above the yellow dashed ($\omega = \sqrt{c_{44}/\rho_{3D}}q$) the substrate has a continuum of bulk states. (b) Plot of the field strength of the flexural-Rayleigh mode in the membrane, $Z_{FR}(\mathbf{q})$, and of the spectral weight of flexural-gapped mode. The some of both contributions adds to 1 according to the sum rule Eq. (3.86). The dashed red and orange dashed lines represent, respectively, $|\mathbf{q}| = v_R\sqrt{\rho/(2\kappa)}$, around which $Z_{FR}(\mathbf{q})$ is maximum, and $|\mathbf{q}| = v_R\sqrt{\rho/\kappa}$, above which the hybridization between the membrane flexural mode and the substrate Rayleigh mode becomes less important.

dissipate energy that is injected in it by an external force. As a matter of fact, if we act on the membrane with a time-dependent external force, $f(t,\mathbf{x})$,

$$f(t,\mathbf{x}) = \int \frac{d^2\mathbf{q}}{(2\pi)^2} f_{\omega_0}(\mathbf{q}) e^{i\mathbf{q}\cdot\mathbf{x}} \left(e^{-i\omega_0 t} + e^{i\omega_0 t}\right), \tag{3.82}$$

which couples to the membrane as

$$V_f(t) = -\int d^2\mathbf{x} f(t,\mathbf{x}) h(\mathbf{x}), \tag{3.83}$$

then the average energy dissipated over a period $2\pi/\omega_0$ is given by

$$\begin{aligned}\frac{d\bar{E}}{dt} &= -\int \frac{d^2\boldsymbol{q}}{(2\pi)^2} 2\omega_0 \mathrm{Im} D^R_{F,\mathbf{q}}(\omega_0) \left|f_{\omega_0}(\mathbf{q})\right|^2 \\ &= \frac{1}{\rho}\int \frac{d^2\mathbf{q}}{(2\pi)^2} \mathcal{A}_F(\omega_0,\mathbf{q}) \left|f_{\omega_0}(\mathbf{q})\right|^2 .\end{aligned} \tag{3.84}$$

For a given $\mathbf{q}$, for ω close to $\pm\omega_{FR,\mathbf{q}}$, the dissipation function displays a δ-Dirac divergence, being given by

$$\mathcal{A}_F(\omega,\mathbf{q}) = \pi Z_{FR}(\mathbf{q})\delta(\omega \mp \omega_{FR,\mathbf{q}}). \tag{3.85}$$

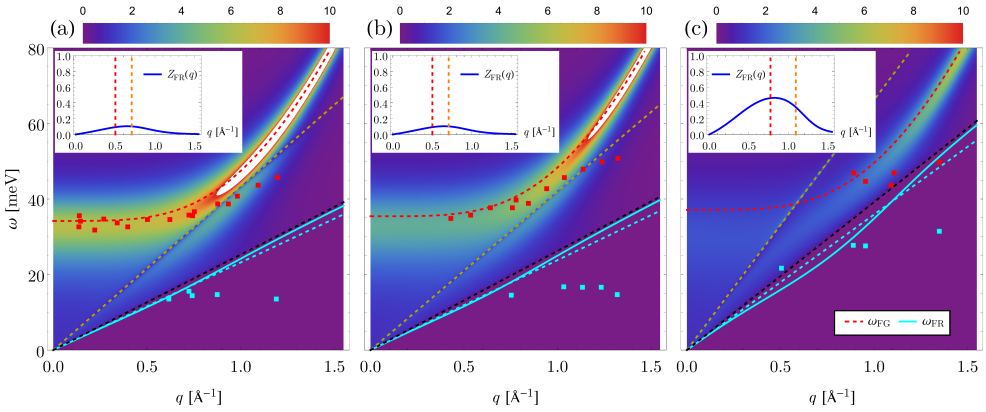

Figure 3.3: Density plot of the flexural mode dissipation function (in units of $2\gamma_0/\omega_0^2$) for graphene on top of different substrates: (a) TaC, (b) HfC and (c) TiC. The squares represent experimental data for the dispersion relation of graphene phonons on the three substrate obtained via HREELS in Ref. [103]. The insets show the field strength of the flexural-Rayleigh mode on the graphene membrane. The dashed cyan, black and yellow lines represent respectively $\omega = v_R q$, $\omega = \sqrt{c_{44}/\rho_{3D}}q$ and $\omega = \sqrt{c_{11}/\rho_{3D}}q$.

Therefore, the sum rule Eq. (3.78) implies that

$$Z_{FR}(\mathbf{q}) + \int_{\sqrt{c_{44}/\rho_{3D}}|\mathbf{q}|}^{+\infty} \frac{d\omega}{\pi} \mathcal{A}_F(\omega, \mathbf{q}) = 1. \tag{3.86}$$

In Fig. 3.2, we plot the flexural mode dissipation function, the dispersion relation of the flexural-Rayleigh mode and its weight, $Z_{FR}(\mathbf{q})$, for a graphene membrane on a SiO_2 substrate. It can be see that for small values of momentum the spectral function is very broad, due to the coupling of the membrane to the continuum of bulk substrate modes, with the flexural-gapped mode being very poorly defined. Furthermore, we see that the membrane flexural mode and the substrate Rayleigh mode are more strongly coupled for values arround $|\mathbf{q}| \sim v_R\sqrt{\rho/(2\kappa)}$, around which $Z_{FR}(\mathbf{q})$ reaches a maximum, and becomes less important for $|\mathbf{q}| \gg v_R\sqrt{\rho/\kappa}$. The suppression of the flexural phonon for small momenta has been observed in Ref. [103], where the phonon dispersion relations for graphene on different transition metal carbides was measured using HREELS. In Fig. 3.3, we compare the spectral function obtained from of our model with experimental phonon dispersion of Ref. [103]. Although our model fails at large momenta, as expected for a continuous model, it semi-quantitatively explains the lack of experimental data for the flexural mode at low momentum for graphene on lighter substrates (see the different mass densities for the substrates in Table 3.2), since the phonons become ill defined as quasi-particles. Also notice that experimentally there are indications of a Rayleigh mode. Our model predicts that just by probing the graphene overlayer it is possible to detect the hybrid flexural-Rayleigh mode. If this is the case or if what is experimentally seen comes from the fact that the first few layers of substrate are also being probed is not clear.

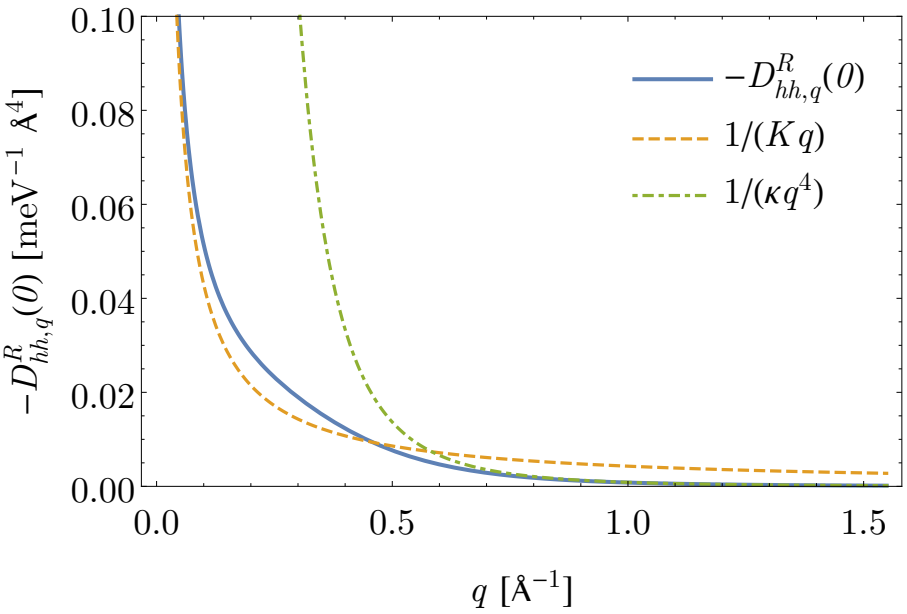

Figure 3.4: Plot of for the out-of-plane mode correlation for graphene on top of a SiO_2 substrate function at zero frequency, $D^R_{F,\mathbf{q}}(0)$, as a function of the momenta. Also shown are small, $\sim |\mathbf{q}|^{-1}$, and large, $\sim |\mathbf{q}|^{-4}$, limiting behaviours of $D^R_{F,\mathbf{q}}(0)$.

3.4 OUT-OF-PLANE FLUCTUATIONS AND THERMAL EXPANSION

3.4.1 *Height-height correlation function*

The same time height-height correlation function is given in accordance with the fluctuation-dissipation theorem (see Appendix C) by:

$$\langle h(\mathbf{x})h(\mathbf{0})\rangle = -\hbar \int \frac{d\omega d^2\mathbf{q}}{(2\pi)^3} e^{i\mathbf{q}\cdot\mathbf{x}} \coth\left(\frac{\hbar\omega}{2k_BT}\right) \mathrm{Im} D^R_{F,\mathbf{q}}(\omega). \tag{3.87}$$

In the high temperature limit, we have $\coth(\hbar\omega/(2k_BT)) \simeq 2k_BT/(\hbar\omega)$ and using Kramers-Kronig relation we obtain the classical result

$$\langle h(\mathbf{x})h(\mathbf{0})\rangle \simeq -k_BT \int \frac{d^2\mathbf{q}}{(2\pi)^2} e^{i\mathbf{q}\cdot\mathbf{x}} \mathrm{Re} D^R_{F,\mathbf{q}}(0). \tag{3.88}$$

Due to the coupling of the membrane to the substrate, from Eqs. (3.24) and (3.64), we obtain at low momenta

$$\lim_{\mathbf{q}\to 0} D^R_{F,\mathbf{q}}(0) = -\frac{1}{K_z |\mathbf{q}|}, \tag{3.89}$$

which is exactly the same result as for the substrate Green's function. This result shows that at long-wavelengths the behaviour of the membrane is completely determined by the substrate, for which we also have $D^R_{u^z_s u^z_s,\mathbf{q}}(0) = -(K_z|\boldsymbol{q}|)^{-1}$, Eq. (3.64). This result is different from what would be obtained if we treated the substrate as static, in which case we would obtain $\lim_{\mathbf{q}\to 0} D^R_{F,\mathbf{q}}(0) = -1/g$. At smaller wavelengths the membrane on a substrate behaves as a free membrane and we obtain $D^R_{hh,\mathbf{q}}(0) \sim -|\mathbf{q}|^{-4}$. This results are demonstrated in Fig. 3.4.

For large distances, using Eqs. (3.88) and (3.89), we obtain at high temperatures

$$\begin{aligned}\langle h(\mathbf{x})h(\mathbf{0})\rangle &\simeq -\frac{k_BT}{2\pi}\int dqqJ_0\left(q\left|\mathbf{x}\right|\right)D^R_{F,q}(0)\\ &\simeq \frac{k_BT}{2\pi K_z}\int_0^{1/x} dq\\ &\simeq \frac{k_BT}{2\pi K_z\left|\mathbf{x}\right|},\end{aligned} \tag{3.90}$$

a result that is independent of the membrane-substrate coupling, g, and that coincides with the result for the bare substrate surface out-of-plane displacement, $\langle u_{s,z}(\mathbf{x},0)u_{s,z}(\mathbf{0},0)\rangle$. For the quadratic dispersion relation of flexural phonons, it is known that $\left\langle h^2(\mathbf{0})\right\rangle$ diverges at any finite temperature. In Fig. 3.5 it is shown $\left\langle h^2(\mathbf{0})\right\rangle$ as a function of temperature for two different substrates. At high temperature, $\left\langle h^2(\mathbf{0})\right\rangle$ is approximately given by

$$\left\langle h^2(\mathbf{0})\right\rangle = \frac{k_BT}{2\pi\sqrt{\kappa g}}\Upsilon\left(\frac{g^{3/4}\kappa^{1/4}}{K_z}\right), \tag{3.91}$$

being proportional to the temperature in accordance with the classical theory, and with the function $\Upsilon(x)$ defined as

$$\Upsilon(x) = \int_0^\infty \frac{du}{u^3+1/(u+x)}. \tag{3.92}$$

This function has two limiting cases: $\Upsilon(0)=\pi/4$ and $\Upsilon(x)\sim x^{2/3}2\pi/(3\sqrt{3})$ for $x\gg 1$; from which we obtain

$$\left\langle h^2(\mathbf{0})\right\rangle \simeq \begin{cases}\frac{k_BT}{8\sqrt{\kappa g}} & , g^{3/4}\kappa^{1/4}\ll K_z\\ \frac{k_BT}{3\sqrt{3}(\kappa K_z^2)^{1/3}} & , g^{3/4}\kappa^{1/4}\gg K_z\end{cases}. \tag{3.93}$$

It is interesting to notice that for small g, it is found the same result as if one completely ignores the dynamics of a substrate [119].Using the values in Tables 3.1 and 3.2, we obtain $g^{3/4}\kappa^{1/4}/K_z\simeq 0.9$, for SiO_2, and $g^{3/4}\kappa^{1/4}/K_z\simeq 2.4$, for hBN , such that none of the limits actually dominates. The behaviour of $\left\langle h^2(\mathbf{0})\right\rangle$ with temperature, taking into account quantum effects is show in Fig. 3.5. As it can be seen, the out-of-plane fluctuation is larger for graphene on a hBN substrate than for graphene on an SiO_2 substrate. This can be explained by Eq. (3.93), which predicts that for a substrate with smaller K_z (see Table 3.2) $\left\langle h^2(\mathbf{0})\right\rangle$ is larger.

3.4.2 *Thermal expansion*

As discussed in Chapter 2, the thermal expansion is zero in a purely harmonic theory. Therefore in order to compute the thermal expansion of a supported membrane we must include anharmonic effects at some level. We will assume that anharmonic effects are not significantly affected by the coupling of the membrane to the substrate and that therefore the dominant anharmonic terms for the membrane are the same as for a free membrane and given by Eqs. (2.38) and (2.39). However, while a free membrane is a strongly anharmonic system, for a supported membrane intrinsic membrane anharmonicities will be suppressed due to the long wavelength behaviour of the substrate induced self energy, Eq. (3.24), $\lim_{\mathbf{q}\to\mathbf{0}}\Pi^R_{F,\mathbf{q}}(\omega)=K_z\left|\mathbf{q}\right|$. Therefore, in order

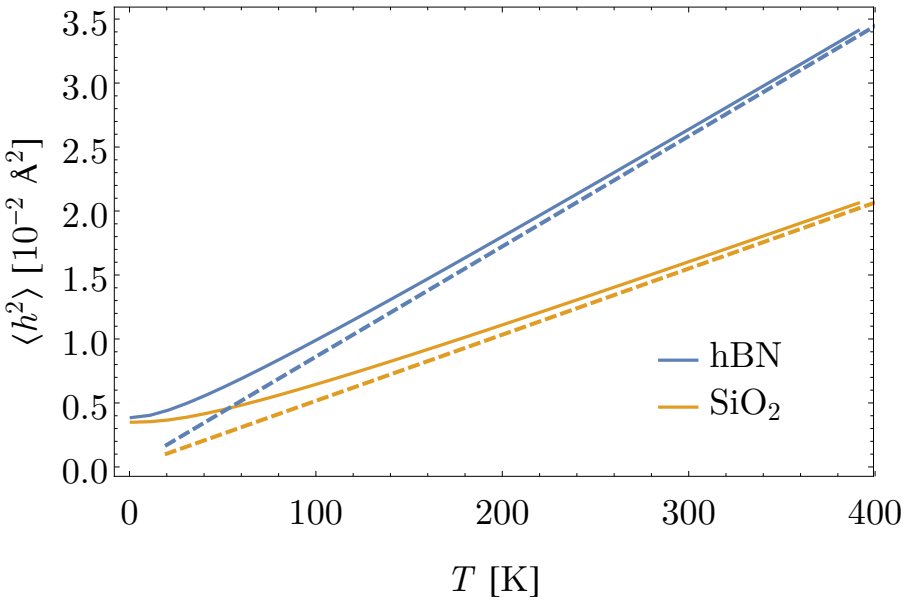

Figure 3.5: Plot of the average same-site out-of-plane displacement fluctuation as a function of temperature for graphene on top of hBN and SiO_2 substrates. The solid lines take into account quantum fluctuations, while the dashed lines show the high temperature classical result.

to describe the thermal expansion in a supported membrane, a QHA treatment of anharmonic effects will be sufficient. The thermal expansion of a supported membrane is thus still given by Eq. (2.210)

$$\alpha_A = \frac{\hbar^2}{k_B T^2} \int \frac{d\omega d^2\mathbf{q}}{(2\pi)^3} \frac{|\mathbf{q}|^2 \omega}{4 \sinh^2\left(\frac{\hbar\omega}{2k_B T}\right)} \mathrm{Im} D^R_{F,\mathbf{q}}(\omega), \tag{3.94}$$

but with $D^R_{F,\mathbf{q}}(\omega)$ the harmonic out-of-plane mode Green's function taking into account the coupling of the membrane to the substrate, Eq. (3.23). As shown in Eq. (3.79), we have that $\omega \mathrm{Im} D^R_{F,\mathbf{q}}(\omega) < 0$ and therefore Eq. (3.94) predicts a negative thermal expansion just as in the case of a free membrane. Just as in Eq. (3.88), in the high temperature limit we can approximate $\sinh(\hbar\omega/(2k_B T)) \simeq \hbar\omega/(2k_B T)$ and use the Kramers-Kronig relation to obtain the thermal expansion in the high temperature, classical limit, which is given by

$$\alpha_A \simeq \frac{k_B}{2} \int \frac{d^2\mathbf{q}}{(2\pi)^2} |\mathbf{q}|^2 \mathrm{Re} D^R_{F,\mathbf{q}}(0). \tag{3.95}$$

Performing the integration in momentum we obtain

$$\alpha_A \simeq -\frac{k_B}{4\pi\kappa} \Psi_{q_D\left(\frac{\kappa}{g}\right)^{1/4}} \left(\frac{g^{3/4}\kappa^{1/4}}{K_z}\right), \tag{3.96}$$

where q_D is the Debye momentum and we have defined the function

$$\Psi_\Lambda(x) = \int_0^\Lambda \frac{duu^2}{u^3 + 1/(u+x)}. \tag{3.97}$$

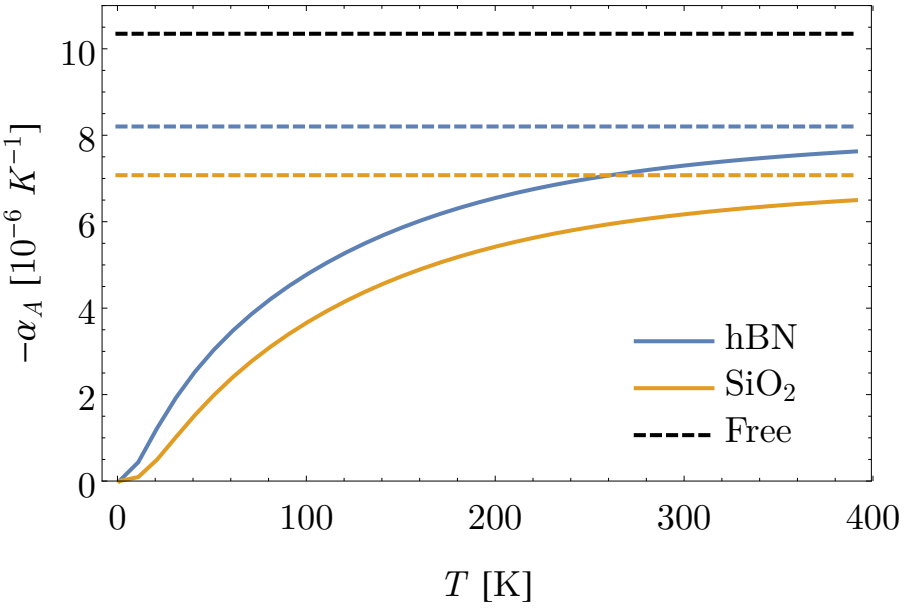

Figure 3.6: Plot of the of areal thermal expansion of a graphene membrane supported by two different substrates, hBN and SiO_2, as a function of temperature. The solid lines take into quantum effects and are given by Eq. (3.94), while the dashed lines are the high temperature classical limit given by Eq. (3.95). The dashed black line represents the high temperature thermal expansion for a free membrane as estimated from Eq. (3.99).

This function has two limiting behaviours: $\Psi_\Lambda(0) = \log\left(1+\Lambda^4\right)/4$ and $\Psi_\Lambda(x) \sim \log\left(1+\Lambda^3 x\right)/3$, for $x \gg 1$. Therefore, we obtain two limiting cases for the thermal expansion

$$\alpha_A \simeq \begin{cases} -\frac{k_B}{16\pi\kappa}\log\left(1+\frac{\kappa q_D^4}{g}\right) & , g^{3/4}\kappa^{1/4} \ll K_z \\ -\frac{k_B}{12\pi\kappa}\log\left(1+\frac{\kappa q_D^3}{K_z}\right) & , g^{3/4}\kappa^{1/4} \gg K_z \end{cases} . \tag{3.98}$$

Close to room temperature one obtains a value in the order of -6 to -7×10^{-6} K^{-1}. This is to be compared with the estimation for the thermal expansion of a free crystalline membrane at high temperature [96], Eq. (2.202),

$$\alpha_A \simeq -\frac{k_B}{8\pi\kappa}\log\left(\frac{16\pi\kappa^{3/2}\rho^{1/2}}{3\hbar Y_{2D}}\right), \tag{3.99}$$

which gives a higher thermal expansion $\simeq -10^{-5}$ K^{-1}. In Fig. 3.6, we show the thermal expansion of graphene supported by two different substrates as a function of temperature. As it can be seen, graphene on hBN has a larger thermal expansion than graphene on SiO_2. This can be explained by the smaller value of K_z for the hBN. Also notice that the thermal expansion tends very slowly to the high temperature limit given by Eq. .(3.95), which is understandable, given the high Debye temperature of graphene, $T_D \simeq 1000$ K.

3.5 CONCLUSIONS

In this chapter, we have studied the lattice dynamics of a crystalline membrane that is coupled to a substrate, focusing on the out-of-plane mode of the membrane. In doing so,

we carefully took into account the dynamics of the substrate and therefore considered the coupling of the membrane flexural mode with the substrate low energy acoustic phonons.

Since the substrate, a half-space elastic medium, supports, in general, both a continuum of bulk modes and a surface Rayleigh mode, the effect of the coupling of the membrane out-of-plane mode to the substrate will be twofold. (i) Coupling to a static substrate will give origin to a gap in the dispersion relation of the membrane flexural mode, which will behave as a low energy optical phonon at long wavelength and as a free membrane flexural mode for small wavelengths. This flexural-gapped mode will lie within the continuum of the substrate bulk modes, which will act as a dissipative bath for the flexural-gapped mode, giving origin to a finite lifetime and possibly making the flexural-gapped mode at long wavelengths very poorly defined. Our model predicts that the softer and lesser dense the substrate, the more ill defined the flexural-gapped mode will be. (ii) The membrane flexural mode also couples to the substrate surface Rayleigh mode, with which it will hybridize. Since the Rayleigh mode is an isolated mode (and not part of a continuum), the flexural-Rayleigh mode will have an infinite lifetime. The hybridization between the surface Rayleigh and the membrane flexural mode will be strongest for momenta $|\mathbf{q}| \lesssim v_R\sqrt{\kappa/\rho}$, where v_R is the Rayleigh mode velocity.

We compared our model with experimental HREELS dispersion relations of graphene phonons on different transition metal carbides of Ref. [103]. In agreement with our model, lighter substrates make the flexural-gapped mode less well defined leading to an inability to resolve experimentally this mode at long wavelengths, which is described in our model by a very broad dissipation function. Furthermore, and in agreement with our model, experimental data also shows signs of a Rayleigh mode, although it is not possible to determine whether this is due to the hybridization of the flexural-Rayleigh mode or due to the fact that the substrate is being directly probed in the experiments.

We also studied the out-of-plane fluctuations and the thermal expansion of a membrane on top of a substrate. We found out that both quantities are made finite by the coupling of the membrane to the substrate, which completely dominates the long wavelength behaviour of the membrane. As expected, for weaker couplings between the substrate and the membrane, both quantities become larger. In the limit of weak coupling, both quantities become independent on the elastic constants of the substrate and the results are the same as for a membrane coupled to a static, infinitely massive and stiff, substrate. In the limit of strong coupling between membrane and substrate, the results become independent on the membrane-substrate coupling constant but become dependent on the elastic constant of the substrate K_z. In this limit, the smaller K_z, the greater are the out-of-plane fluctuations and the thermal expansion. We find out that the thermal expansion of graphene on top of two commonly used substrates, SiO_2 and hBN, is around -6 to -7×10^{-6} K^{-1} at room temperature, respectively. Therefore, this work shows how properties, in this case lattice dynamics, of 2D crystals, which for bulk materials are generally thought of as intrinsic properties, are greatly affected by their environment.

Part II

ELECTRONIC TRANSPORT IN 2D AND LAYERED MATERIALS

4

CONDUCTIVITY OF GRAPHENE ON A SUBSTRATE: FLEXURAL PHONON EFFECTS

4.1 INTRODUCTION

The quality of a material as an electric conductor is generally described in terms of the carrier mobility, which is defined as

$$\mu_c = \frac{\sigma_{\mathrm{DC}}}{en}, \tag{4.1}$$

where σ_{DC} is the DC conductivity, n is the carrier density and e is the electronic charge. Graphene was found to be a remarkable conductor, with intrinsic mobilities as high as 200000 $\mathrm{cm^2V^{-1}s^{-1}}$ at room temperature having been inferred from experimental data [120, 121]. Such mobilities would outperform all known semiconductor materials [122] and even semiconducting carbon nanotubes [123], the previous record holder.

However, the intrinsic value of mobility is never possible to achieve due to the unavoidable presence of disorder. For graphene, this is specially true and the obtained mobility depends not only on the quality of the graphene sample, but also on the kind of device that is used. Therefore, while samples of graphene on a SiO_2 substrate display typical mobilities of $\mu_c \simeq 10000$ $\mathrm{cm^2V^{-1}s^{-1}}$ for electronic densities of $n \simeq 10^{12}$ $\mathrm{cm^{-2}}$ [34], graphene samples on hBN substrates with mobilities as high as $\mu_c \simeq 100000$ $\mathrm{cm^2V^{-1}s^{-1}}$ have been reached for $n \simeq 10^{11}$ $\mathrm{cm^{-2}}$ [124], a value which is further increased for graphene samples encapsulated in hBN [125].

Another possibility is to consider suspended graphene samples [126–128]. In suspended samples, by eliminating scattering sources due to the substrate, such as corrugations due to substrate roughness [129] and scattering by substrate phonons [130, 131], increased mobilities as high as 120000 $\mathrm{cm^2V^{-1}s^{-1}}$ around room temperature have been achieved [127]. However, significant spread in data was observed, with similar samples displaying a room temperature mobility nearly an order of magnitude lower [128]. It was soon realized that in suspended samples another source of scattering could play a significant role: scattering by flexural phonons [132]. Scattering by flexural phonons was found experimentally to be one of the dominant sources of scattering at room temperature in suspended samples [35]. Scattering by flexural phonons gives origin to a resistivity that scales with temperature as T^2 at high enough temperatures [35, 36], which is characteristic of a scattering process involving two phonons. This dominance of scattering by flexural phonons is explained by their quadratic dispersion relation, $\omega_{F,\mathbf{q}} \propto |\mathbf{q}|^2$, which leads to extremely low energies for long wavelength phonons, giving origin to a diverging resistivity. The contribution of flexural phonons to graphene resistivity is therefore extremely sensitive to perturbations that might cause a modification of the long wavelength dispersion relation of flexural phonons, such as tension. Some residual tension is unavoidable in suspended samples and the reported variations in their conductivity have been attributed to changes in this tension [35–37]. Scattering by flexural phonons also plays a dominant role in suspended bilayer samples for weak tensions [133].

While the importance of scattering by flexural phonons has been well established in suspended graphene samples, its effect in supported samples is generally neglected

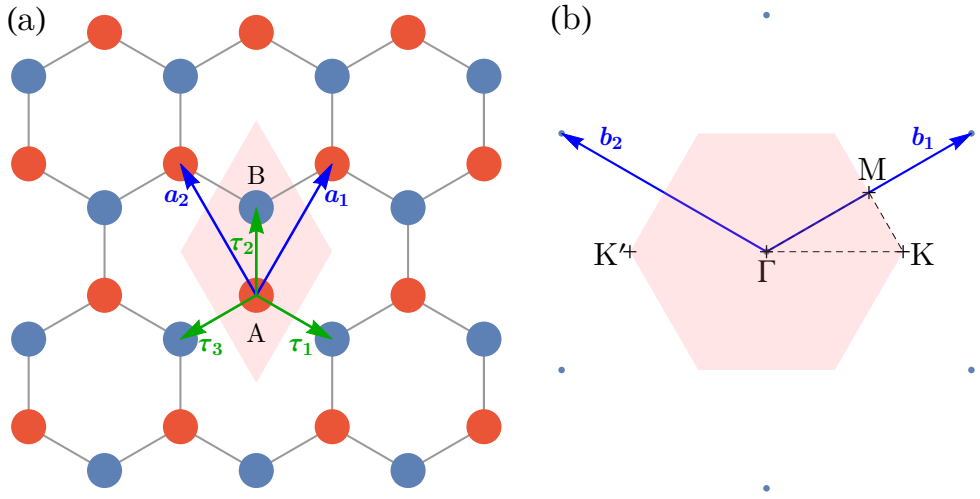

Figure 4.1: Graphene's crystalline structure and reciprocal lattice. (a) Graphene's crystalline structure. The unit cell is represented by the pink shaded rhombus and the A and B carbon sites are represented by the blue and red disks, respectively. The Bravais lattice basis vectors $\{\mathbf{a}_1, \mathbf{a}_2\}$ are represented by blue arrows and the nearest neighbours vectors $\boldsymbol{\tau}_a$, $a = 1, 2, 3$, are represented by green arrows. (b) Graphene's reciprocal lattice. The 1BZ is represented by the pink shaded hexagon. The reciprocal lattice basis vectors $\{\mathbf{b}_1, \mathbf{b}_2\}$ are represented by the blue arrows and the blue dots represent reciprocal lattice sites. The positions of the high symmetry points Γ, K, $\mathrm{K}' = -\mathrm{K}$ and M are also shown.

[134], based on the assumption that flexural phonons are quenched by the coupling to the substrate. In this chapter, we study in detail the effect of scattering by flexural phonons in graphene samples supported by a substrate. By using the results of the previous Chapter 3, we correctly take into account both the gap opening in the dispersion relation of the flexural phonon (flexural-gapped phonon), with associated broadening by the continuum of substrate bulk phonons, and the hybridization of the flexural phonon with the substrate Rayleigh surface mode (flexural-Rayleigh phonon), with associated linearisation of the dispersion relation. In Section 4.2, we review the basics of the graphene physics, namely its electronic structure and description of low energy electronic degrees of freedom via a continuous massless Dirac equation. This section will prove to be essential not only for this chapter, but also for the following two Chapters 5 and 6. In Section 4.3, we describe the electron-phonon interaction Hamiltonian for coupling between electrons and in-plane acoustic phonons and between electrons and flexural phonons. In Section 4.4, we compute the resistivity of graphene due to scattering by phonons employing the Kubo formalism in the quasi-elastic approximation and in the limit of high electronic doping. We consider both the effect of acoustic in-plane and flexural phonons. We end this chapter by discussing the obtained results in Section 4.5.

4.2 BASICS OF GRAPHENE ELECTRONIC PROPERTIES

4.2.1 *Crystalline structure*

Graphene is formed by a single layer of carbon atoms with sp^2 hybridization arranged in a honeycomb structure. As such, the crystalline structure of graphene forms a

triangular Bravais lattice with two atoms per unit cell, generally referred to as A and B sites. The Bravais lattice is spanned by the basis vectors

$$\mathbf{a}_1 = a_{\mathrm{g}} \left(\frac{1}{2}, \frac{\sqrt{3}}{2} \right), \tag{4.2}$$

$$\mathbf{a}_2 = a_{\mathrm{g}} \left(-\frac{1}{2}, \frac{\sqrt{3}}{2} \right), \tag{4.3}$$

where $a_{\mathrm{g}} \simeq 2.46\text{Å}$ is the lattice parameter of graphene, which is related to the nearest-neighbour carbon-carbon distance by $a_{\mathrm{CC}} = a_{\mathrm{g}}/\sqrt{3} \simeq 1.42\text{Å}$. The unit cell of graphene as an area given by $A_{\mathrm{cell}} = \sqrt{3}a_{\mathrm{g}}^2/2 \simeq 5.2\text{Å}^2$. The nearest neighbour vectors are given by

$$\boldsymbol{\tau}_1 = \frac{a_{\mathrm{g}}}{\sqrt{3}} \left(\frac{\sqrt{3}}{2}, -\frac{1}{2} \right), \tag{4.4}$$

$$\boldsymbol{\tau}_2 = \frac{a_{\mathrm{g}}}{\sqrt{3}} (0, 1), \tag{4.5}$$

$$\boldsymbol{\tau}_3 = \frac{a_{\mathrm{g}}}{\sqrt{3}} \left(-\frac{\sqrt{3}}{2}, -\frac{1}{2} \right). \tag{4.6}$$

The reciprocal lattice of the graphene triangular Bravais lattice is spanned by the basis vectors

$$\mathbf{b}_1 = \frac{4\pi}{\sqrt{3}a_{\mathrm{g}}} \left(\frac{\sqrt{3}}{2}, \frac{1}{2} \right), \tag{4.7}$$

$$\mathbf{b}_1 = \frac{4\pi}{\sqrt{3}a_{\mathrm{g}}} \left(-\frac{\sqrt{3}}{2}, \frac{1}{2} \right), \tag{4.8}$$

with the first Brillouin zone (1BZ) being an hexagon. The crystalline structure of graphene and the corresponding 1BZ in reciprocal space are represented in Fig. 4.1

4.2.2 *Band structure and Dirac Hamiltonian*

The electronic properties of graphene are dominated by its zero gap linear dispersion relation around the corners of the 1BZ. There are two inequivalent corners: the K and the $\mathrm{K}' = -\mathrm{K}$ points, with the K point located at

$$\mathbf{K} = \frac{\mathbf{b}_1 - \mathbf{b}_2}{3} = \frac{4\pi}{3a_{\mathrm{g}}} (1, 0). \tag{4.9}$$

This was first recognized in 1947 by Wallace [135], while modelling the band structure of graphite using a tight binding Hamiltonian. Although DFT *ab initio* methods are now standard tools in Condensed Matter, there are still advantages in employing the simpler tight binding method when describing the band structure of a material. First of all, the tight-binding method provides an economical description of the system Hamiltonian, often in terms of a few parameters, which can be tackled by analytic methods. Secondly, tight-binding Hamiltonians will, by construction, correctly encoded all the symmetries of a given crystal, which in a numerical *ab initio* method is not always easily guaranteed. The electronic properties of graphene are dominated by the p_z orbitals of the carbon

atoms, with the low energy states (in the sense of states close to the Fermi level of neutral graphene) being located close to the K and K′ points of the 1BZ. These two facts allow for a simple description of graphene in terms of a single parameter nearest-neighbour tight-binding Hamiltonian [135], which proved to be immensely successful in the description of graphene [136]. In a second quantization formalism the nearest-neighbour tight-binding Hamiltonian of graphene reads

$$H = -t \sum_{n,a} \left(\psi^{\dagger}_{\mathbf{R}_n,A} \psi_{\mathbf{R}_n+\boldsymbol{\tau}_a,B} + \psi^{\dagger}_{\mathbf{R}_n+\boldsymbol{\tau}_a,B} \psi_{\mathbf{R}_n,A} \right), \tag{4.10}$$

where $t \simeq 2.8$ eV is the nearest-neighbour hopping, $\psi^{\dagger}_{\mathbf{R}_n,A/B}$ ($\psi_{\mathbf{R}_n,A/B}$) is the creation (annihilation) operator for an electron in a p_z-like orbital in the carbon atom located at position $\mathbf{R}_n$ in A/B sublattice. We have omitted the spin degrees of freedom as spin-orbit effects in graphene are very weak [137]. Expressing the creation (annihilation) operators in Fourier components

$$\psi^{\dagger}_{\mathbf{R}_n,A} = \frac{1}{\sqrt{N}} \sum_{\mathbf{k}} e^{-i\mathbf{k}\cdot\mathbf{R}_n} \psi^{\dagger}_{\mathbf{k},A}, \qquad \psi_{\mathbf{R}_n,A} = \frac{1}{\sqrt{N}} \sum_{\mathbf{k}} e^{i\mathbf{k}\cdot\mathbf{R}_n} \psi_{\mathbf{k},A}, \tag{4.11}$$

$$\psi^{\dagger}_{\mathbf{R}_n+\boldsymbol{\tau}_a,B} = \frac{1}{\sqrt{N}} \sum_{\mathbf{k}} e^{-i\mathbf{k}\cdot(\mathbf{R}_n+\boldsymbol{\tau}_a)} \psi^{\dagger}_{\mathbf{k},B}, \quad \psi_{\mathbf{R}_n+\boldsymbol{\tau}_a,B} = \frac{1}{\sqrt{N}} \sum_{\mathbf{k}} e^{i\mathbf{k}\cdot(\mathbf{R}_n+\boldsymbol{\tau}_a)} \psi_{\mathbf{k},B}, \tag{4.12}$$

where N is the number of unit cells in the crystal, the tight-binding Hamiltonian becomes

$$H = \sum_{\mathbf{k}} \boldsymbol{\psi}^{\dagger}_{\mathbf{k}} \cdot \boldsymbol{H}_{\mathbf{k}} \cdot \boldsymbol{\psi}_{\mathbf{k}} \tag{4.13}$$

where we have introduced $\boldsymbol{\psi}^{\dagger}_{\mathbf{k}} = \begin{bmatrix} \psi^{\dagger}_{\mathbf{k},A} & \psi^{\dagger}_{\mathbf{k},B} \end{bmatrix}$ and

$$\boldsymbol{H}_{\mathbf{k}} = \begin{bmatrix} 0 & -t\gamma_{\mathbf{k}} \\ -t\gamma^{*}_{\mathbf{k}} & 0 \end{bmatrix}, \tag{4.14}$$

with

$$\gamma_{\mathbf{k}} = \sum_{a=1}^{3} e^{i\mathbf{k}\cdot\boldsymbol{\tau}_a}. \tag{4.15}$$

The spectrum of this Hamiltonian is given by

$$\begin{aligned} \epsilon_{\mathbf{k},\lambda} &= \lambda t \left|\gamma_{\mathbf{k}}\right| \\ &= \lambda t \sqrt{3 + 2\cos\left(k_x a_{\mathrm{g}}\right) + 4\cos\left(\frac{k_x a_{\mathrm{g}}}{2}\right)\cos\left(\frac{\sqrt{3}k_y a_{\mathrm{g}}}{2}\right)}. \end{aligned} \tag{4.16}$$

with $\lambda = \pm 1$. In neutral graphene, only the states with $\lambda = -1$ are occupied. For this reason the, $\lambda = -1$ band is the referred to as the valence band and the $\lambda = +1$ as the conduction band. The tight binding Hamiltonian Eq. (4.13) is diagonalized by the eigenstates (written in the A/B sublattice basis)

$$|\mathbf{k}, \lambda\rangle = \frac{1}{\sqrt{2}} \begin{bmatrix} 1 \\ \lambda\gamma^{*}_{\mathbf{k}}/\left|\gamma_{\mathbf{k}}\right| \end{bmatrix}, \tag{4.17}$$

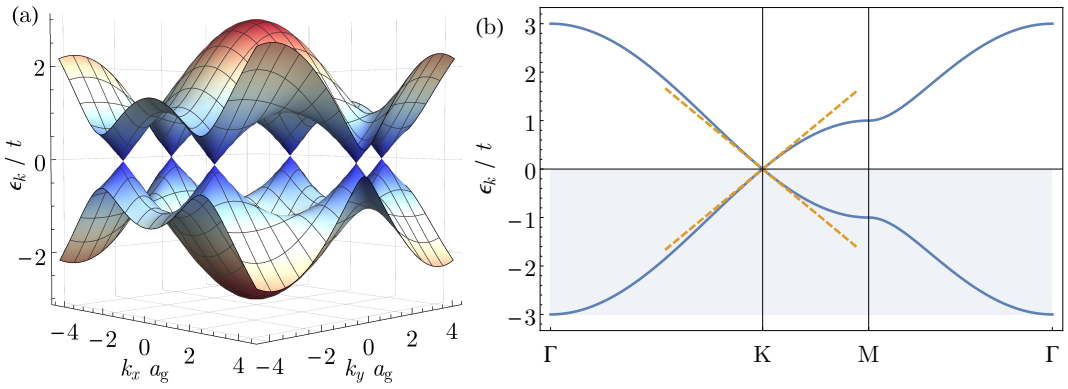

Figure 4.2: Electronic band structure of graphene. (a) 3D visualization of graphene dispersion relation. (b) Dispersion relation of graphene along the ΓKMΓ path represented in Fig. 4.1 (b). The dashed line represents the linearised dispersion relation around the K point. The shaded region represents the states that are occupied in neutral graphene.

Introducing the creation operators for an electron in the conduction and valence bands as

$$\boldsymbol{\psi}^\dagger_{\mathbf{k}} = \sum_\lambda \psi^\dagger_{\mathbf{k},\lambda} \langle \mathbf{k}, \lambda | \,, \tag{4.18}$$

$$\boldsymbol{\psi}_{\mathbf{k}} = \sum_\lambda | \mathbf{k}, \lambda \rangle \, \psi_{\mathbf{k},\lambda}. \tag{4.19}$$

The Hamiltonian can then be written as

$$H = \sum_{\mathbf{k},\lambda=\pm 1} \epsilon_{\mathbf{k},\lambda} \psi^\dagger_{\mathbf{k},\lambda} \psi_{\mathbf{k},\lambda}. \tag{4.20}$$

The dispersion relation given by Eq. 4.16 is shown in Fig. 4.2. At the K and K′ = −K points, we have $\epsilon_{\mathbf{k}=\pm \mathrm{K},\lambda} = 0$, with the valence and conduction band touching. In the spirit of $k \cdot p$ theory, expanding the Hamiltonian Eq. (4.14) around these points by making the replacement $\mathbf{k} \to \tau \mathbf{K} + \mathbf{k}$, with $\tau = \pm 1$ for states around the K and K′ respectively, we obtain to linear order in the momentum

$$\boldsymbol{H}_{\mathbf{k},\tau \mathrm{K}} = v_F \hbar \begin{bmatrix} 0 & \tau k_x - i k_y \\ \tau k_x + i k_y & 0 \end{bmatrix}. \tag{4.21}$$

where

$$v_F = \frac{\sqrt{3} t a_{\mathrm{g}}}{2\hbar}, \tag{4.22}$$

is the Fermi velocity of graphene with a value of $v_F \simeq 1 \times 10^{-6} \mathrm{m/s}$ [136]. Equation (4.21) has the form of a massless Dirac equation and can be written as

$$\boldsymbol{H}_{\mathbf{k},+\mathrm{K}} = v_F \hbar \mathbf{k} \cdot \boldsymbol{\sigma}, \tag{4.23}$$

$$\boldsymbol{H}_{\mathbf{k},-\mathrm{K}} = -v_F \hbar \mathbf{k} \cdot \boldsymbol{\sigma}^*, \tag{4.24}$$

where $\boldsymbol{\sigma} = (\sigma_x, \sigma_y)$ is a 2D vector of Pauli matrices. For this reason the K and K′ points are generically referred to as Dirac points. In the Dirac approximation, the dispersion relation Eq. (4.16) becomes

$$\epsilon_{\mathbf{k},\lambda} = v_F \hbar \, |\mathbf{k}| \,. \tag{4.25}$$

The linearised dispersion relation is shown in Fig. 4.2(b) where it is compared with the full tight binding dispersion relation Eq. (4.16). From there we see that the linear dispersion relation is a good approximation up to energies of $\sim 0.5t \simeq 1.5$ eV. The eigenstates of the Dirac Hamiltonian Eq. (4.21) are given by

$$|\mathbf{k}, \tau, \lambda\rangle = \frac{1}{\sqrt{2}} \begin{bmatrix} 1 \\ \tau\lambda e^{i\tau\theta_{\mathbf{k}}} \end{bmatrix}, \tag{4.26}$$

where $\theta_{\mathbf{k}}$ is the angle formed between vectors $\mathbf{k}$ and $\mathbf{K}$. In the reference frame we have chosen, $\mathbf{K} = K_{\mathrm{g}}(1, 0)$ (with $K_{\mathrm{g}} = 4\pi/(3a_{\mathrm{g}})$ see Eq. (4.9)) and we can write $e^{i\theta_{\mathbf{k}}} = (k_x + ik_y)/|\mathbf{k}|$. The Hamiltonians given by Eqs. (4.23) and (4.24) can also be promoted to a continuous real space Hamiltonian by replacing the quasi-momentum $\mathbf{k}$ by the differential operator $\mathbf{k} \to -i\boldsymbol{\nabla}$ and writing the electronic operators as

$$\psi_{\mathbf{k},a} = \int \frac{d^2\mathbf{x}}{\sqrt{A}} e^{-i\mathbf{k}\cdot\mathbf{x}} \psi_a(\mathbf{x}),\ a = A, B, \tag{4.27}$$

where $A = NA_{\mathrm{cell}}$ is the area of the graphene crystal. Doing this we obtain the real space continuous Hamiltonian that describes states close to the K point

$$H_{\mathrm{K}} = -iv_F\hbar \int d^2\mathbf{x} \boldsymbol{\psi}^\dagger(\mathbf{x}) \boldsymbol{\sigma} \cdot \boldsymbol{\nabla} \boldsymbol{\psi}(\mathbf{x}), \tag{4.28}$$

where $\boldsymbol{\psi}^\dagger(\mathbf{x}) = \begin{bmatrix} \psi_A^\dagger(\mathbf{x}) & \psi_B^\dagger(\mathbf{x}) \end{bmatrix}$ is the graphene electron creation operator in real space for electrons close to the K point. For states close to the K′ point we must replace $\boldsymbol{\sigma} \to -\boldsymbol{\sigma}^*$ in Eq. (4.28).

We point out that there is nothing remarkable in the fact of the low energy electronic properties of graphene being governed by a Dirac like equation. As a matter of fact, a Dirac like equation is the simplest description of two coupled bands in terms of a $k \cdot p$ theory [138]. Therefore, any direct gap semiconductor will have in general a low energy description in terms of a (massive) Dirac equation. What is special about graphene is the fact that the low energy physics is described by a *massless* Dirac equation. Furthermore, in the absence of spin-orbit interactions which are week in graphene [137], the Dirac points are robust against perturbations, and the opening of a gap is protected by the discrete symmetries of time reversal and spacial inversion [139, 140].

4.2.3 *Density of states*

The fact that graphene has a linear dispersion relation at low energies makes it a *semimetal*: a material which displays no gap but in which the density of states goes to zero at the Fermi level. This can be easily seen by computing the density of states within the Dirac model. The density of states is given by

$$\begin{aligned} \mathrm{DoS}(\omega) &= \frac{g_s g_v}{NA_{\mathrm{cell}}} \sum_{\mathbf{k},\lambda} \delta\left(\omega - \epsilon_{\mathbf{k},\lambda}\right) \\ &= g_s g_v \frac{|\omega|}{2\pi \left(v_F\hbar\right)^2}, \end{aligned} \tag{4.29}$$

where $g_s = 2$ is the spin degeneracy and $g_v = 2$ is the valley degeneracy (that takes into account the existence of two inequivalent Dirac points). The density of states

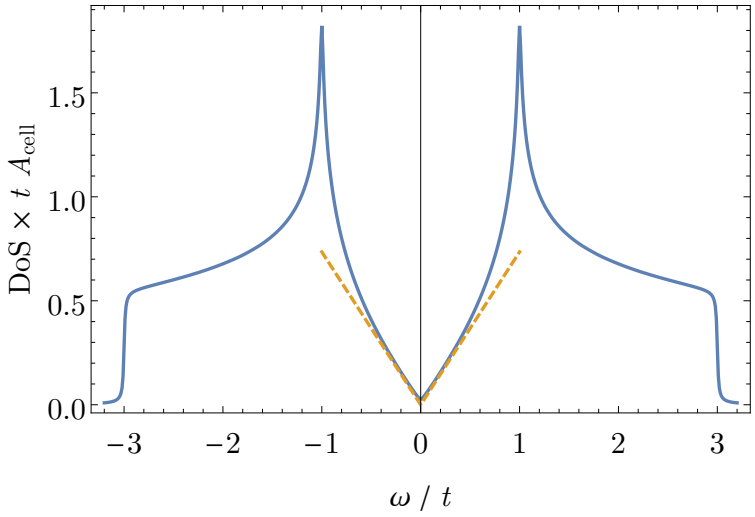

Figure 4.3: Density of states of graphene computed using the full tight binding dispersion relation (solid line) and the linearised dispersion relation around the Dirac points (dashed line).

of graphene computed using the linear dispersion relation, Eq. (4.21), and the full tight binding dispersion relation, Eq. (4.16), is shown in Fig. 4.3. Once again, it is seen that the Dirac model provides a good description for energies up to $\sim 0.5t \simeq 1.5$ eV. Integrating the density of states from 0 to the Fermi energy, ϵ_F, we obtain the relation between Fermi energy and the electronic density, n, for pristine graphene at zero temperature

$$n = \operatorname{sgn}(\epsilon_F) \frac{\epsilon_F^2}{\pi (v_F \hbar)^2}. \tag{4.30}$$

This relation can also be written as $\epsilon_F = \operatorname{sgn}(n) v_F \hbar k_F$, with the Fermi momentum $k_F = |\epsilon_F| / (v_F \hbar)$, being related to the electronic density by

$$k_F = \sqrt{\pi |n|}. \tag{4.31}$$

4.2.4 *Density and current operators*

The density operator, course grained over the unit cell and considering only the K valley, can be written for graphene as

$$\begin{aligned} \rho(\mathbf{x}) &= \psi_A^\dagger(\mathbf{x})\psi_A(\mathbf{x}) + \psi_B^\dagger(\mathbf{x})\psi_B(\mathbf{x}) \\ &= \boldsymbol{\psi}^\dagger(\mathbf{x})\boldsymbol{\psi}(\mathbf{x}). \end{aligned} \tag{4.32}$$

Using the Dirac Hamiltonian, Eq. (4.28), and the Heisenberg equation of motion, it is a simple exercise to obtain the continuity equation

$$\partial_t \rho(\mathbf{x}) + \nabla \cdot \mathbf{J}(\mathbf{x}) = 0,$$

where the current operator is given by

$$\mathbf{J}(\mathbf{x}) = v_F \boldsymbol{\psi}^\dagger(\mathbf{x}) \boldsymbol{\sigma} \boldsymbol{\psi}(\mathbf{x}). \tag{4.33}$$

In order to obtain the charge density and charge current operators one just has to multiply Eqs. (4.32) and (4.33) by the electron charge $-e$. Very frequently it will be useful to write the density and current operators in Fourier components

$$\rho(\mathbf{x}) = \frac{1}{A}\sum_{\mathbf{q}} e^{i\mathbf{q}\cdot\mathbf{x}}\rho_{\mathbf{q}}, \tag{4.34}$$

$$\mathbf{J}(\mathbf{x}) = \frac{1}{A}\sum_{\mathbf{q}} e^{i\mathbf{q}\cdot\mathbf{x}}\mathbf{J}_{\mathbf{q}}. \tag{4.35}$$

Changing the electron operators to the eigenbasis of the Dirac Hamiltonian, Eq. (4.28),

$$\boldsymbol{\psi}(\mathbf{x}) = \frac{1}{\sqrt{A}}\sum_{\mathbf{k}} e^{i\mathbf{k}\cdot\mathbf{x}}\left|\mathbf{k},\lambda\right\rangle\psi_{\mathbf{k},\lambda}, \tag{4.36}$$

with $|\mathbf{k},\lambda\rangle$ given by Eq. (4.26) (with $\tau = +1$, since we are focusing on the K valley), the Fourier components of the density and current operators are written as

$$\rho_{\mathbf{q}} = \sum_{\mathbf{k}} \rho^{\lambda,\lambda'}_{\mathbf{k},\mathbf{k}+\mathbf{q}}\psi^{\dagger}_{\mathbf{k},\lambda}\psi_{\mathbf{k}+\mathbf{q},\lambda'}, \tag{4.37}$$

$$\mathbf{J}_{\mathbf{q}} = \sum_{\mathbf{k},} \mathbf{J}^{\lambda,\lambda'}_{\mathbf{k},\mathbf{k}+\mathbf{q}}\psi^{\dagger}_{\mathbf{k},\lambda}\psi_{\mathbf{k}+\mathbf{q},\lambda'}, \tag{4.38}$$

with $\mathbf{J}^{\lambda,\lambda'}_{\mathbf{k},\mathbf{k}+\mathbf{q}} = v_F\mathbf{j}^{\lambda,\lambda'}_{\mathbf{k},\mathbf{k}+\mathbf{q}}$ and we have introduce the density and (dimensionless) velocity matrix elements

$$\rho^{\lambda,\lambda'}_{\mathbf{k},\mathbf{k}+\mathbf{q}} = \left\langle \mathbf{k},\lambda \mid \mathbf{k}+\mathbf{q},\lambda'\right\rangle = \frac{1}{2}\left(1+\lambda\lambda' e^{-i\theta_{\mathbf{k},\mathbf{k}+\mathbf{q}}}\right), \tag{4.39}$$

$$\mathbf{j}^{\lambda,\lambda'}_{\mathbf{k},\mathbf{k}+\mathbf{q}} = \left\langle \mathbf{k},\lambda \left|\boldsymbol{\sigma}\right| \mathbf{k}+\mathbf{q},\lambda'\right\rangle = \frac{1}{2}\left(\lambda e^{-i\theta_{\mathbf{k}}} + \lambda' e^{i\theta_{\mathbf{k}+\mathbf{q}}}, i\lambda e^{-i\theta_{\mathbf{k}}} - i\lambda' e^{i\theta_{\mathbf{k}+\mathbf{q}}}\right) \tag{4.40}$$

We will use these expressions frequently.

4.2.5 *Electronic Green's function*

The retarded electronic Green's function in the sublattice basis is defined as

$$G^{R}_{ab,\mathbf{k}}\left(t,t'\right) = -i\Theta\left(t-t'\right)\left\langle\left[\psi_{\mathbf{k},a}\left(t\right),\psi^{\dagger}_{\mathbf{k},b}\left(t'\right)\right]\right\rangle. \tag{4.41}$$

Using the Heisenberg equation of motion for the annihilation operator, it is easy to see that the Green's function obeys the equation

$$\left(i\frac{\partial}{\partial t} - \boldsymbol{H}_{\mathbf{k}}\right)\boldsymbol{G}^{R}_{\mathbf{k}}\left(t,t'\right) = \delta\left(t-t'\right). \tag{4.42}$$

This can be written in Fourier components as

$$G^{R}_{ab,\mathbf{k}}\left(t,t'\right) = \int\frac{d\omega}{\left(2\pi\right)^2}e^{-i\omega(t-t')}G^{R}_{ab,\mathbf{k}}\left(\omega\right), \tag{4.43}$$

where $G^{R}_{ab,\mathbf{k}}\left(\omega\right)$ is given by

$$\begin{aligned} G^{R}_{ab,\mathbf{k}}\left(\omega\right) &= \sum_{\lambda=\pm1}\frac{\left|\mathbf{k},\lambda\right\rangle\left\langle\mathbf{k},\lambda\right|}{\omega+i0^{+}-\epsilon_{\mathbf{k},\lambda}} \\ &= \sum_{\lambda=\pm1}\frac{\delta_{ab}+\lambda\hat{\mathbf{k}}\cdot\boldsymbol{\sigma}_{ab}}{\omega+i0^{+}-\epsilon_{\mathbf{k},\lambda}}. \end{aligned} \tag{4.44}$$

Using the form of the graphene Dirac eigenstates, Eqs. (4.26), the Green's function in the sublattice basis can also be written as

$$\boldsymbol{G}^R_{\mathbf{k}}(\omega) = \frac{\omega \mathrm{Id} + v_F \hbar \mathbf{k}\cdot\boldsymbol{\sigma}}{(\omega + i0^+)^2 - (v_F\hbar)^2 |\mathbf{k}|^2}. \tag{4.45}$$

This form will be specially useful in Chapter 6.

4.3 ELECTRON-PHONON COUPLING IN GRAPHENE

Within the continuous Dirac approximation for graphene electrons, the interaction between low energy electrons close to the K point and acoustic phonons close to the Γ point can be described by the Hamiltonian [129, 136, 140–144]

$$\begin{aligned} H_{\mathrm{e-ph,K}} = g_1 \int d^2\mathbf{x} \boldsymbol{\psi}^\dagger(\mathbf{x})\boldsymbol{\psi}(\mathbf{x})\gamma_{ii}(\mathbf{x}), \\ + g_2 \int d^2\boldsymbol{x} \left(\boldsymbol{\psi}^\dagger(\mathbf{x})\boldsymbol{\sigma}\boldsymbol{\psi}(\mathbf{x})\right)\cdot \boldsymbol{\mathcal{A}}_{\mathrm{el}}(\mathbf{x}), \end{aligned} \tag{4.46}$$

where $\gamma_{ij}(\mathbf{x})$ is the relevant strain tensor, Eq. (2.17),

$$\gamma_{ij}(\mathbf{x}) = \frac{1}{2}\left(\partial_i u_j + \partial_j u_i + \partial_i h \partial_j h\right), \tag{4.47}$$

and $\boldsymbol{\mathcal{A}}_{\mathrm{el}}(\mathbf{x})$ is a vector potential like term given by

$$\boldsymbol{\mathcal{A}}_{\mathrm{el}}(\mathbf{x}) = \left(\gamma_{xx}(\mathbf{x}) - \gamma_{yy}(\mathbf{x}), -2\gamma_{xy}(\mathbf{x})\right). \tag{4.48}$$

For graphene electron states close to the K′ point, $\boldsymbol{\sigma}$ should be replaced by $\boldsymbol{\sigma}^*$ in Eq. (4.46). We notice that in the electron-phonon interaction Hamiltonian Eq. (4.46), the in-plane displacement fields appear linearly, while the out-of-plane displacement field appears quadratically. This is a bit unusual as in most materials electron-phonon interaction is only described in terms of a linear coupling to the phonon degrees of freedom [95]. However, in graphene, the appearance a linear term in h in the Hamiltonian is forbidden due to the discrete $z \to -z$ mirror symmetry of graphene. Since the p_z orbitals are symmetric under $z \to -z$ and h changes sign under $z \to -z$, a linear term in h cannot occur. When graphene is placed on a substrate, a case we will be considering, the mirror $z \to -z$ symmetry is broken and therefore a linear term in h would be allowed. Nevertheless, we will assume that the coupling to the substrate is weak and therefore will neglect such effects. Although it is possible to write more general interaction Hamiltonians between graphene electrons and acoustic phonons [145, 146], Eq. (4.46) includes all the terms with the lowest number of derivatives of the electronic fields and of the strain tensor [147].

The first term in Eq. (4.46) describes the deformation potential interaction, which describes the change in the local potential felt by electrons under a homogeneous contraction/dilatation of the crystalline structure and is present in any material [95]. The constant g_1 is the bare deformation potential. Its value for graphene has been estimated using a nearly free electron model yielding a value of $g_1 \simeq 20 - 30$ eV [141], while DFT calculations yield a value of $g_1 \simeq 3$ eV [148] or negligible [149]. These contradicting results have been reconciled by pointing out that since the deformation potential interaction is a coupling to the electronic density, it will be subject to screening [35, 36, 133, 150], which is not considered in the estimation of Ref. [141] and will

substantially reduce the effective value of g_1. Taking into account static screening effects, the effective deformation potential is related to the bare one by

$$g_{1,\text{eff}}(\mathbf{q}) = \frac{g_1}{1 - V_{\mathbf{q}}\chi_{\mathbf{q}}}, \tag{4.49}$$

where $V_{\mathbf{q}} = e^2/(2\epsilon_0 |\mathbf{q}|)$ is the 2D Fourier transform of the Coulomb interaction and $\chi_{\mathbf{q}}$ is the static ($\omega = 0$) irreducible density-density response function. In the limit of small $\mathbf{q}$, $\chi_{\mathbf{q}}$ reduces to $\chi_{\mathbf{q}} \simeq -\text{DoS}(\epsilon_F)$, where ϵ_F is the Fermi energy. For graphene, using Eq. (4.29) we obtain $\chi_{\mathbf{q}} \simeq -2k_F/(\pi v_F \hbar)$, a result that in graphene is valid not only in the $\mathbf{q} \to \mathbf{0}$ limit, but actually up to $|\mathbf{q}| < 2k_F$ [151] (see also Appendix E) , which as we will later see is exactly the region we will be interested in. Therefore, the effective screened deformation potential becomes

$$\begin{aligned} g_{1,\text{eff}}(\mathbf{q}) &= \frac{g_1}{1 + V_{\mathbf{q}}\text{DoS}(\epsilon_F)} \\ &= \frac{g_1}{1 + k_{TF}/|\mathbf{q}|}, \end{aligned} \tag{4.50}$$

where k_{TF} is the Thomas-Fermi screening momentum for graphene which is given by

$$k_{TF} = \alpha_{\text{g}} g_s g_v k_F, \tag{4.51}$$

where $\alpha_{\text{g}} = e^2/(4\pi\epsilon_0 v_F \hbar)$ is graphene's fine structure constant.

The second term in Eq.(4.46) appears in systems with threefold rotational invariance for electronic states close to the K and K′ points also being present in other system besides graphene such as bilayer graphene [133] and transition metal dichalcogenides [152]. Although it is possible to derive this term purely on symmetry grounds [143], it is instructive to obtain it within a tight-binding approach which will also allow for an estimation of the $g_2$constant. The vector potential like term can be derived by assuming that lattice distortions lead to a local modulation of the hopping integrals in a tight-binding description of graphene [141]. Therefore, instead of Eq. (4.10) we write

$$H = -\sum_{n,a,b,c} t_{ab}\left(\mathbf{R}_n, \mathbf{R}_n + \boldsymbol{\tau}_c\right) \psi^{\dagger}_{\mathbf{R}_n,a} \psi_{\mathbf{R}_n+\boldsymbol{\tau}_c,b}, \tag{4.52}$$

where now $t_{ab}\left(\mathbf{R}_n, \mathbf{R}_n + \boldsymbol{\tau}_c\right)$ depends on the relative distance between the sites $\mathbf{R}_n$ and $\mathbf{R}_m + \boldsymbol{\tau}_c$, a, b run over the A and B sublattices and $\boldsymbol{\tau}_c$ are the nearest-neighbour vector. In the presence of a distortion the position of the lattice sites are changed to

$$\mathbf{R}_n \to \mathbf{R}_n^0 + \vec{u}\left(\mathbf{R}_n^0\right) \tag{4.53}$$

$$\mathbf{R}_n + \boldsymbol{\tau}_c \to \mathbf{R}_n^0 + \boldsymbol{\tau}_c + \vec{u}\left(\mathbf{R}_n^0 + \boldsymbol{\tau}_c\right) \tag{4.54}$$

where $\mathbf{R}_n^0$ are the positions of the undistorted lattice and $\vec{u}$ is the displacement phonon field. The displacement field encodes both in-plane and out-of-plane displacements, which we write as $\vec{u} = (\mathbf{u}, h)$. For small lattice distortions we can expand the hopping as

$$t_{ab}\left(\mathbf{R}_n, \mathbf{R}_n + \boldsymbol{\tau}_c\right) = t + \frac{\partial t}{\partial \ell}\Delta\ell\left(\mathbf{R}_n^0, \mathbf{R}_n^0 + \boldsymbol{\tau}_c\right),$$

where $\Delta\ell\left(\mathbf{R}_n^0, \mathbf{R}_n^0 + \boldsymbol{\tau}_c\right)$ is the change in bond length

$$\Delta\ell\left(\mathbf{R}_n^0, \mathbf{R}_n^0 + \boldsymbol{\tau}_c\right) = \sqrt{\left(\boldsymbol{\tau}_c + \vec{u}\left(\mathbf{R}_n^0 + \boldsymbol{\tau}_c\right) - \vec{u}\left(\mathbf{R}_n^0\right)\right)^2} - |\boldsymbol{\tau}_c|\,. \tag{4.55}$$

Therefore, we can write Eq. (4.52) to lowest order in $\Delta\ell$ as $H \simeq H_0 + H^{\text{bond}}_{\text{e-ph}}$, where H_0 is the bare electronic Hamiltonian given by Eq. (4.10) and

$$H^{\text{bond}}_{\text{e-ph}} = -\sum_{n,a} \frac{\partial t}{\partial \ell} \left(\psi^{\dagger}_{\mathbf{R}^0_n, A} \psi_{\mathbf{R}^0_n + \boldsymbol{\tau}_a, B} \Delta\ell \left(\mathbf{R}^0_n, \mathbf{R}^0_n + \boldsymbol{\tau}_a \right) + \text{h.c.} \right). \tag{4.56}$$

Writing the electronic operators in terms of Fourier components as in Eqs. (4.11) and (4.12) and writing the change in bond length as

$$\Delta\ell \left(\mathbf{R}^0_n, \mathbf{R}^0_n + \boldsymbol{\tau}_a \right) = \frac{1}{\sqrt{N}} \sum_{\mathbf{q}} e^{i\mathbf{q}\cdot\left(\mathbf{R}^0_n + \boldsymbol{\tau}_a/2\right)} \Delta\ell_{\mathbf{q}} \left(\boldsymbol{\tau}_a \right), \tag{4.57}$$

we obtain

$$H^{\text{bond}}_{\text{e-ph}} = \frac{1}{\sqrt{N}} \sum_{\mathbf{k},\mathbf{q}} \boldsymbol{\psi}^{\dagger}_{\mathbf{k}+\mathbf{q}} \cdot \boldsymbol{\Phi}^{\text{bond}}_{\mathbf{k}+\mathbf{q},\mathbf{k}} \cdot \boldsymbol{\psi}_{\mathbf{k}}, \tag{4.58}$$

with $\boldsymbol{\Phi}^{\text{bond}}_{\mathbf{k}+\mathbf{q},\mathbf{k}}$ given by

$$\boldsymbol{\Phi}^{\text{bond}}_{\mathbf{k}+\mathbf{q},\mathbf{k}} = -\frac{\partial t}{\partial \ell} \sum_a \Delta\ell_{\mathbf{q}} \left(\boldsymbol{\tau}_a \right) \begin{bmatrix} 0 & e^{i(\mathbf{k}+\mathbf{q}/2)\cdot\boldsymbol{\tau}_a} \\ e^{-i(\mathbf{k}+\mathbf{q}/2)\cdot\boldsymbol{\tau}_a} & 0 \end{bmatrix}. \tag{4.59}$$

So far, this discussion is general and we have made no assumption regarding the displacement phonon field. We will now specialize to the case of acoustic phonons for which the displacement field changes slowly between nearest-neighbours allowing us to approximate the difference that occurs in Eq. (4.55) by a derivative: $\vec{u}\left(\mathbf{R}^0_n + \boldsymbol{\tau}_a\right) - \vec{u}\left(\mathbf{R}^0_n\right) \simeq \tau^i_a \partial_i \vec{u}\left(\mathbf{R}^0_n\right)$. Therefore, we obtain

$$\Delta\ell \left(\mathbf{R}^0_n, \mathbf{R}^0_n + \boldsymbol{\tau}_a \right) \simeq \sqrt{\boldsymbol{\tau}^2_a + 2\tau^i_a \tau^j_a \varepsilon_{ij}\left(\mathbf{R}^0_n\right)} - \left|\boldsymbol{\tau}_a\right|. \tag{4.60}$$

with $\varepsilon_{ij}\left(\mathbf{R}^0_n\right)$ the full strain tensor, Eq. (2.15),

$$\varepsilon_{ij}\left(\mathbf{R}^0_n\right) = \frac{1}{2}\left(\partial_i u_j + \partial_j u_i \left(\mathbf{R}^0_n\right) + \partial_i \vec{u}\left(\mathbf{R}^0_n\right) \cdot \partial_j \vec{u}\left(\mathbf{R}^0_n\right) \right). \tag{4.61}$$

Neglecting the quadratic contribution from the in-plane displacement in Eq. (4.61) this reduces to the relevant strain tensor Eq. (4.47). For small distortions we can further approximate

$$\Delta\ell \left(\mathbf{R}^0_n, \mathbf{R}^0_n + \boldsymbol{\tau}_a \right) \simeq \frac{\tau^i_a \tau^j_a}{\left|\boldsymbol{\tau}_a\right|} \gamma_{ij}\left(\mathbf{R}^0_n\right). \tag{4.62}$$

With these approximations, the electron-phonon interaction matrix, Eq. (4.59), can be written as

$$\boldsymbol{\Phi}^{\text{bond}}_{\mathbf{k}+\mathbf{q},\mathbf{k}} \simeq -\frac{\partial t}{\partial \ell} \gamma_{ij,\mathbf{q}} \sum_a \frac{\tau^i_a \tau^j_a}{\left|\boldsymbol{\tau}_a\right|} \begin{bmatrix} 0 & e^{i(\mathbf{k}+\mathbf{q}/2)\cdot\boldsymbol{\tau}_a} \\ e^{-i(\mathbf{k}+\mathbf{q}/2)\cdot\boldsymbol{\tau}_a} & 0 \end{bmatrix}. \tag{4.63}$$

Since we are interested in electronic states close to the Dirac points, K and K′, and long wavelength phonons close to the Γ point, we approximate $\mathbf{q} \simeq \mathbf{0}$ and $\mathbf{k} \simeq \pm\mathbf{K}$ in the arguments of the exponentials in the previous equation. With this approximation and performing the sum over nearest neighbour lattice vectors we obtain

$$\boldsymbol{\Phi}^{\text{bond}}_{\mathbf{k}+\mathbf{q},\mathbf{k}} \simeq -\frac{\sqrt{3}a_{\text{g}}}{4} \frac{\partial t}{\partial \ell} \left(-\gamma_{xx,\mathbf{q}} + \gamma_{yy,\mathbf{q}}, 2\gamma_{xy,\mathbf{q}} \right) \cdot \boldsymbol{\sigma}, \tag{4.64}$$

and for states close to K′ we just replace $\boldsymbol{\sigma} \to \boldsymbol{\sigma}^*$. In real space within the continuous approximation, Eq. (4.64) becomes the second term in Eq. (4.46) with the constant g_2 given by

$$g_2 = -\frac{3}{4} t\mathcal{B} = -\frac{v_F \mathcal{B}}{2a_{\rm CC}}, \tag{4.65}$$

where we have introduced $\mathcal{B}$ as

$$\mathcal{B} = -\frac{\partial \log t}{\partial \log \ell}. \tag{4.66}$$

In order to evaluate $\mathcal{B}$, we can employ Harrison's argument [153, 154], which states that the hopping between two orbitals with total angular momentum l and l' should scale with separation distance, r, as

$$t_{l,l'}(r) = t_0 \left(\frac{r_0}{r}\right)^{l+l'+1}, \tag{4.67}$$

such that $\mathcal{B}_{l,l'} = l + l' + 1$, as thus, for graphene's p_z orbitals we would obtain $\mathcal{B} = 3$. Other estimates for $\mathcal{B}$ give $\mathcal{B} = 2$ - 3.6 [141], while DFT calculations yield $\mathcal{B} = 2.5$ [149]. Using the value of $\mathcal{B} = 2.5$ we obtain $g_2 \simeq -5.2$ eV.

As previously said, Eq. (4.46) describes electronic coupling both to in-plane and flexural phonons and while the in-plane modes couple linearly to the electrons, the flexural phonons couple quadratically. In the following, we will describe both cases in a unified way by writing the electron-phonon interaction as

$$H_{\rm e-ph,K} = \frac{1}{\sqrt{A}} \sum_{\substack{\mathbf{k},\mathbf{q} \\ \lambda,\lambda',\zeta}} \phi^{\lambda,\lambda',\zeta}_{\mathbf{k}+\mathbf{q},\mathbf{k}} \psi^\dagger_{\mathbf{k}+\mathbf{q},\lambda} \psi_{\mathbf{k},\lambda'}, \tag{4.68}$$

where $\phi^{\lambda,\lambda',\zeta}_{\mathbf{k}+\mathbf{q},\mathbf{k}}$ is an appropriately defined phononic field, with λ and λ' running over the conduction and valence bands and $\zeta = L, T, F$, for the longitudinal, transverse and flexural modes. In the following we will specify the form of $\phi^{\lambda,\lambda',\zeta}_{\mathbf{k}+\mathbf{q},\mathbf{k}}$ for each case.

4.3.1 *Coupling to in-plane phonons*

Focusing on the K valley, from Eq. (4.46), the interaction Hamiltonian between electrons and in-plane phonons is given by

$$\begin{aligned} H_{\rm e-u,K} = {} & g_1 \int d^2\mathbf{x} \boldsymbol{\psi}^\dagger(\mathbf{x}) \boldsymbol{\psi}(\mathbf{x}) \partial_i u_i(\mathbf{x}) \\ & + g_2 \int d^2\mathbf{x} \left(\boldsymbol{\psi}^\dagger(\mathbf{x}) \boldsymbol{\sigma} \boldsymbol{\psi}(\mathbf{x})\right) \cdot \left(\partial_x u_x(\mathbf{x}) - \partial_y u_y(\mathbf{x}), -\partial_x u_y(\mathbf{x}) - \partial_y u_x(\mathbf{x})\right). \end{aligned} \tag{4.69}$$

Writing the electronic operators in terms of operators that diagonalize the bare Hamiltonian as in Eq. (4.36) and writing the in-plane phonon field as

$$\mathbf{u}(\mathbf{x}) = \frac{1}{\sqrt{A}} \sum_{\mathbf{q},\zeta=L,T} e^{i\mathbf{q}\cdot\mathbf{x}} i\mathbf{e}_{\mathbf{q},\zeta} u_{\mathbf{q},\zeta}, \tag{4.70}$$

where $\mathbf{e}_{\mathbf{q},\zeta}$ are the in-plane longitudinal and transverse polarization vectors

$$\mathbf{e}_{\mathbf{q},L} = \left(\frac{q_x}{|\mathbf{q}|}, \frac{q_y}{|\mathbf{q}|}\right), \tag{4.71}$$

$$\mathbf{e}_{\mathbf{q},T} = \left(-\frac{q_y}{|\mathbf{q}|}, \frac{q_x}{|\mathbf{q}|}\right), \tag{4.72}$$

the electron-phonon Hamiltonian becomes

$$H_{\mathrm{e}-u,\mathrm{K}} = \frac{1}{\sqrt{A}} \sum_{\substack{\mathbf{k},\mathbf{q} \\ \lambda,\lambda',\zeta}} \phi^{\lambda,\lambda',\zeta}_{\mathbf{k}+\mathbf{q},\mathbf{k}} \psi^{\dagger}_{\mathbf{k}+\mathbf{q},\lambda} \psi_{\mathbf{k},\lambda'}, \tag{4.73}$$

with the phononic field for in-plane modes defined as

$$\phi^{\lambda,\lambda',\zeta}_{\mathbf{k}+\mathbf{q},\mathbf{k}} = M^{\lambda,\lambda',\zeta}_{\mathbf{q},\mathbf{k}} u_{\mathbf{q},\zeta},\ \zeta = L,T, \tag{4.74}$$

where we have introduce the electron-phonon interaction matrices

$$\begin{aligned} M^{\lambda,\lambda',\zeta}_{\mathbf{q},\mathbf{k}} &= -g_{1,\mathrm{eff}}(\mathbf{q}) \rho^{\lambda,\lambda'}_{\mathbf{k}+\mathbf{q},\mathbf{k}} \mathbf{q} \cdot \mathbf{e}_{\mathbf{q},\zeta} \\ &\quad - g_2 \mathbf{j}^{\lambda,\lambda'}_{\mathbf{k}+\mathbf{q},\mathbf{k}} \cdot \left(q_x e^x_{\mathbf{q},\zeta} - q_y e^y_{\mathbf{q},\zeta}, -q_x e^y_{\mathbf{q},\zeta} - q_y e^x_{\mathbf{q},\zeta} \right), \end{aligned} \tag{4.75}$$

with $\rho^{\lambda,\lambda'}_{\mathbf{k}+\mathbf{q},\mathbf{k}}$ and $\mathbf{j}^{\lambda,\lambda'}_{\mathbf{k}+\mathbf{q},\mathbf{k}}$ given by Eqs. (4.39) and (4.40) and we have included the effect of screening to the deformation potential, Eq. (4.50). Notice that for the transverse mode we have that $\mathbf{q} \cdot \mathbf{e}_{\mathbf{q},T} = 0$ and, therefore, the interaction between this mode and the graphene electrons is only described in terms of the coupling to the effective elastic vector potential, Eq. (4.48). Therefore, we write more explicitly

$$M^{\lambda,\lambda',L}_{\mathbf{q},\mathbf{k}} = -|\mathbf{q}| \left[g_{1,\mathrm{eff}}(\mathbf{q}) \rho^{\lambda,\lambda'}_{\mathbf{k}+\mathbf{q},\mathbf{k}} + g_2 \mathbf{j}^{\lambda,\lambda'}_{\mathbf{k}+\mathbf{q},\mathbf{k}} \cdot (\cos 2\theta_{\mathbf{q}}, -\sin 2\theta_{\mathbf{q}}) \right], \tag{4.76}$$

$$M^{\lambda,\lambda',T}_{\mathbf{q},\mathbf{k}} = -|\mathbf{q}|\, g_2 \mathbf{j}^{\lambda,\lambda'}_{\mathbf{k}+\mathbf{q},\mathbf{k}} \cdot (-\sin 2\theta_{\mathbf{q}}, -\cos 2\theta_{\mathbf{q}}), \tag{4.77}$$

where we have written $\mathbf{q} = |\mathbf{q}| (\cos\theta_{\mathbf{q}}, \sin\theta_{\mathbf{q}})$.

4.3.2 *Coupling to out-of-plane phonons*

The coupling of graphene electrons to the flexural phonon mode can be read from Eq. (4.46) and we obtain

$$\begin{aligned} H_{\mathrm{e}-hh,\mathrm{K}} &= \frac{g_1}{2} \int d^2\mathbf{x} \boldsymbol{\psi}^{\dagger}(\mathbf{x}) \boldsymbol{\psi}(\mathbf{x}) \partial_i h(\mathbf{x}) \partial_i h(\mathbf{x}) \\ &\quad + \frac{g_2}{2} \int d^2\mathbf{x} \left(\boldsymbol{\psi}^{\dagger}(\mathbf{x}) \boldsymbol{\sigma} \boldsymbol{\psi}(\mathbf{x}) \right) \cdot (\partial_x h(\mathbf{x}) \partial_x h(\mathbf{x}) - \partial_y h(\mathbf{x}) \partial_y h(\mathbf{x}), -2\partial_x h(\mathbf{x}) \partial_y h(\mathbf{x})). \end{aligned} \tag{4.78}$$

If we once again write the electron operator in terms of the Dirac Hamiltonian eigenstates, Eq. (4.36) , and writing the flexural phonon field as

$$h(\mathbf{x}) = \frac{1}{\sqrt{A}} \sum_{\mathbf{q}} e^{i\mathbf{q}\cdot\mathbf{x}} h_{\mathbf{q}}, \tag{4.79}$$

the electron-phonon Hamiltonian Eq. (4.78) can be written as

$$H_{\mathrm{e}-hh,\mathrm{K}} = \frac{1}{\sqrt{A}} \sum_{\substack{\mathbf{k},\mathbf{q},\mathbf{p} \\ \lambda,\lambda'}} \phi^{\lambda,\lambda',F}_{\mathbf{k}+\mathbf{q},\mathbf{k}} \psi^{\dagger}_{\mathbf{k}+\mathbf{q},\lambda} \psi_{\mathbf{k},\lambda'},$$

with the composite phononic field for flexural phonons defined as

$$\phi^{\lambda,\lambda',F}_{\mathbf{k}+\mathbf{q},\mathbf{k}} = \frac{1}{2\sqrt{A}} \sum_{\mathbf{p}} M^{\lambda,\lambda',F}_{\mathbf{q}-\mathbf{p},\mathbf{p},\mathbf{k}} h_{\mathbf{q}-\mathbf{p}} h_{\mathbf{p}}, \tag{4.80}$$

and the electron-flexural phonon interaction matrix element given by

$$M^{\lambda,\lambda',F}_{\mathbf{q}-\mathbf{p},\mathbf{p},\mathbf{k}} = -g_{1,\text{eff}}(\mathbf{q})\rho^{\lambda,\lambda'}_{\mathbf{k}+\mathbf{q},\mathbf{k}}(\mathbf{q}-\mathbf{p})\cdot\mathbf{p} - g_2\mathbf{j}^{\lambda,\lambda'}_{\mathbf{k}+\mathbf{q},\mathbf{k}}\cdot((q_x-p_x)p_x-(q_y-p_y)p_y,-(q_x-p_x)p_y-(q_y-p_y)p_x). \tag{4.81}$$

We are how in a position to compute its contribution to graphene's DC conductivity.

4.4 DC CONDUCTIVITY IN THE QUASI-ELASTIC APPROXIMATION

We wish to compute the DC conductivity of graphene when this is limited by intrinsic electron-phonon scattering. In particular, we will be interested in the scattering by flexural phonons, when graphene is supported by a substrate. As we saw in Chap. 3, in this situation the flexural phonons of a membrane can no longer be treated as well defined quasi-particles due to the strong hybridization and damping by the substrate phonons. In this situation it is note possible to adopt a Boltzmann like approach to the electron-phonon scattering, where both the electrons and the phonons are treated as well defined quasi-particles. We therefore employ a method based on the Kubo formula for the electrical conductivity, see Appendix F. There we that in the limits of weak scattering and high doping, $\epsilon_F \gg k_BT$, the DC conductivity can be written as, Eq. (F.80),

$$\text{Re}\sigma^{ij}_{\text{DC}} \simeq \frac{e^2}{A}\sum_{\mathbf{k}}\left(-\frac{\partial f(\epsilon_{\mathbf{k}})}{\partial\epsilon_{\mathbf{k}}}\right)\tau^{\text{tr}}_{\mathbf{k}}(\epsilon_{\mathbf{k}})J^{i,+,+}_{\mathbf{k},\mathbf{k}}J^{j,+,+}_{\mathbf{k},\mathbf{k}}, \tag{4.82}$$

where $\tau^{\text{tr}}_{\mathbf{k}}(\epsilon_{\mathbf{k}})$ is the transport time and we have assumed that graphene is highly doped with electrons. In the low temperature limit, $k_BT \ll \epsilon_F$, we can further approximate $-\partial f(\epsilon_{\mathbf{k}})/\partial\epsilon_{\mathbf{k}} \simeq \delta(\epsilon_{\mathbf{k}}-\epsilon_F)$ and the DC conductivity is given by

$$\text{Re}\sigma_{\text{DC}} \simeq \frac{1}{2}e^2\text{DoS}(\epsilon_F)v_F^2\tau^{\text{tr}}_F, \tag{4.83}$$

where we have made use of the isotropy of the system to write the conductivity as a scalar. Using Eq. (4.29) we can write the resistivity, which is related to the conductivity by $\rho_{\text{DC}} = \sigma^{-1}_{\text{DC}}$, as

$$\rho_{\text{DC}} = \frac{\hbar}{e^2}\frac{\pi}{v_Fk_F}\frac{1}{\tau^{\text{tr}}_F}, \tag{4.84}$$

where τ^{tr}_F is the transport time at the Fermi level. In the limit of elastic scattering the transport time is given by Eq. (F.77),

$$\frac{1}{\tau^{\text{tr}}_{\mathbf{k}}(\epsilon)} = \frac{1}{A}\sum_{\mathbf{q}}\int d\omega\,(1-\cos\theta_{\mathbf{k},\mathbf{k}+\mathbf{q}})\,(b(\omega)+f(\epsilon+\omega))\,A^{\mathbf{k},\mathbf{k}+\mathbf{q}}_{\phi;\mathbf{k}+\mathbf{q},\mathbf{k}}(\omega)\,\delta(\omega-\epsilon_{\mathbf{k}+\mathbf{q},+}+\epsilon), \tag{4.85}$$

where the quantity $A^{\mathbf{k},\mathbf{k}+\mathbf{q}}_{\phi,\mathbf{k}+\mathbf{q},\mathbf{k}}(\omega)$ is a spectral function, which for a generic electron-phonon interaction Hamiltonian of the form of Eq. (4.68) is defined as

$$A^{\mathbf{k},\mathbf{k}+\mathbf{q}}_{\phi;\mathbf{k}+\mathbf{q},\mathbf{k}}(\omega) = \int dt e^{i\omega t}\left\langle\left[\phi^{+,+}_{\mathbf{k},\mathbf{k}+\mathbf{q}}(t),\phi^{+,+}_{\mathbf{k}+\mathbf{q},\mathbf{k}}(0)\right]\right\rangle. \tag{4.86}$$

The transport time given by Eq. (4.85) can be compared with the particle scattering time, from which it differs due to the extra $1-\cos\theta_{\mathbf{k},\mathbf{k}+\mathbf{q}}$ factor. This term suppresses events where the electronic momentum is scattered by a small angle, which do not lead

to a degradation of the electronic current. The transport lifetime at the Fermi level, $\tau_F^{\rm tr}$, is obtained from Eq. (4.85) by setting $|\mathbf{k}| = k_F$ and $\epsilon = \epsilon_F$,

$$\frac{1}{\tau_F^{\rm tr}} = \frac{1}{A}\sum_{\mathbf{q}} \int d\omega \left(1 - \cos\theta_{\mathbf{k},\mathbf{k+q}}\right) \left[b(\omega) + f(\epsilon_F + \omega)\right] A^{\mathbf{k},\mathbf{k+q}}_{\phi;\mathbf{k+q},\mathbf{k}}(\omega)\, \delta\left(\omega - \epsilon_{\mathbf{k+q}} + \epsilon_F\right). \tag{4.87}$$

Tacking into account that typical phonon frequencies are much smaller than the Fermi energy we can further set $\omega = 0$ in the energy conservation Diracδ-function obtaining[1]

$$\frac{1}{\tau_F^{\rm tr}} = \frac{1}{A}\sum_{\mathbf{q}} \int d\omega \left(1 - \cos\theta_{\mathbf{k},\mathbf{k+q}}\right) \frac{1}{\sinh\left(\frac{\omega}{k_B T}\right)} A^{\mathbf{k},\mathbf{k+q}}_{\phi;\mathbf{k+q},\mathbf{k}}(\omega)\, \delta\left(\epsilon_F - \epsilon_{\mathbf{k+q}}\right). \tag{4.88}$$

In the above expression both the momentum $\mathbf{k}$ and $\mathbf{k}+\mathbf{q}$ are pinned to the Fermi level. Using this fact and writing $\mathbf{k}\cdot\mathbf{q} = -|\mathbf{k}|\,|\mathbf{q}|\cos\theta$ we obtain the useful relation

$$\cos\theta = \frac{|\mathbf{q}|}{2k_F}. \tag{4.89}$$

Using this into Eq. (4.88) we can use the δ-function to write the summation over $\mathbf{q}$ (after turning into into an integration) as

$$\begin{aligned}\int \frac{d^2\mathbf{q}}{(2\pi)^2}\delta\left(\epsilon_F - \epsilon_{\mathbf{k+q}}\right) &= \frac{2}{(2\pi)^2}\int dq q \int_0^1 \frac{du}{\sqrt{1-u^2}} \frac{\delta\left(u - \frac{q}{2k_F}\right)}{v_F \hbar q} \\ &= \frac{1}{2\pi^2 v_F \hbar}\int_0^{2k_F} \frac{dq}{\sqrt{1 - \left(\frac{q}{2k_F}\right)^2}},\end{aligned} \tag{4.90}$$

where we have written $u = \cos\theta$ and used the fact that Eq. (4.89) imposes the restriction $|\mathbf{q}| < 2k_F$. Furthermore, we use the fact that the angular term $1 - \cos\theta_{\mathbf{k},\mathbf{k+q}}$, when both $\mathbf{k}$ and $\mathbf{k}+\mathbf{q}$ are pinned to the Fermi level, can be written as

$$1 - \cos\theta_{\mathbf{k},\mathbf{k+q}} = \frac{1}{2}\left(\frac{|\mathbf{q}|}{k_F}\right)^2, \tag{4.91}$$

we can write the transport time as

$$\frac{1}{\tau_F^{\rm tr}} = \frac{1}{(2\pi)^2 v_F \hbar}\int_0^{2k_F} \frac{dq}{\sqrt{1 - \left(\frac{q}{2k_F}\right)^2}} \left(\frac{q}{k_F}\right)^2 \int d\omega \frac{1}{\sinh\left(\frac{\omega}{k_B T}\right)} A^{\mathbf{k},\mathbf{k+q}}_{\phi,\mathbf{k+q},\mathbf{k}}(\omega). \tag{4.92}$$

This is as far as we can progress on general grounds without specifying the form of $A^{\mathbf{k},\mathbf{k+q}}_{\phi,\mathbf{k+q},\mathbf{k}}(\omega)$. Since $A^{\mathbf{k},\mathbf{k+q}}_{\phi,\mathbf{k+q},\mathbf{k}}(\omega)$ is given by a sum of in-plane longitudinal/transverse and flexural contributions, we can write the total transport time as a sum

$$\frac{1}{\tau_F^{\rm tr}} = \frac{1}{\tau_{F,L}^{\rm tr}} + \frac{1}{\tau_{F,T}^{\rm tr}} + \frac{1}{\tau_{F,F}^{\rm tr}}. \tag{4.93}$$

In the following we study each of these contributions.

1 Notice that the standard Ziman's formula for the transport time [95], obtained from a variational solution to the Boltzmann equation, differs from Eq. (4.88) in the $\sinh\left(\omega/\left(k_B T\right)\right)$ factor, which in Ziman's formula is changed to $4k_B T \sinh\left(\omega/\left(2k_B T\right)\right)^2/\omega$. This difference is of little consequence, since both expressions coincide in the hight temperature limit. In the low temperature limit, both expressions predict the same power law dependence with temperature, but the numerical pre-factor is different. However, we point out that in the low temperature limit, the slightly inelastic nature of phonon scattering becomes important and both expressions are no longer valid [155].

4.4.1 *Scattering by in-plane phonons*

For scattering by in-plane phonons, the field $\phi^{+,+}_{\mathbf{k+q},\mathbf{k}}$ is given by Eq. (4.74) and the phononic spectral function Eq. (4.86) relevant for this case is given by

$$A^{\mathbf{k},\mathbf{k+q}}_{L/T;\mathbf{k+q},\mathbf{k}}(\omega) = -M^{+,+,L/T}_{\mathbf{q},\mathbf{k}} M^{+,+,L/T}_{-\mathbf{q},\mathbf{k+q}} 2\mathrm{Im}D^{R}_{L/T,\mathbf{q}}(\omega), \tag{4.94}$$

with $D^{R}_{L/T,\mathbf{q}}(\omega)$ the bare in-plane phonon propagator which is given by Eq. (2.99), such that

$$\mathrm{Im}D^{R}_{L/T,\mathbf{q}}(\omega) = -\frac{\pi}{\rho}\mathrm{sgn}(\omega)\delta\left(\omega^2 - \omega^2_{L/T,\mathbf{q}}\right). \tag{4.95}$$

Also from Eqs. (4.76) and (4.77) we obtain the squared matrix elements

$$\begin{aligned} M^{+,+,L}_{\mathbf{q},\mathbf{k}} M^{+,+,L}_{-\mathbf{q},\mathbf{k+q}} &= |\mathbf{q}|^2 \frac{g_{1,\mathrm{eff}}(\mathbf{q})}{2}\left(1+\cos\theta_{\mathbf{k},\mathbf{k+q}}\right) + |\mathbf{q}|^2 \frac{g_2^2}{2}\left(1+\cos\left(\theta_{\mathbf{k+q}}+\theta_{\mathbf{k}}+4\theta_{\mathbf{q}}\right)\right) \\ &\quad + |\mathbf{q}|^2 g_{1.\mathrm{eff}}(\mathbf{q}) g_2\left(\cos\left(\theta_{\mathbf{k}}+2\theta_{\mathbf{q}}\right)+\cos\left(\theta_{\mathbf{k+q}}+2\theta_{\mathbf{q}}\right)\right), \end{aligned} \tag{4.96}$$

$$M^{+,+,T}_{\mathbf{q},\mathbf{k}} M^{+,+,T}_{-\mathbf{q},\mathbf{k+q}} = |\mathbf{q}|^2 \frac{g_2^2}{2}\left(1-\cos\left(\theta_{\mathbf{k+q}}+\theta_{\mathbf{k}}+4\theta_{\mathbf{q}}\right)\right). \tag{4.97}$$

Notice that for an isotropic system, such as graphene, the transport time should not depend on the direction of the external momentum $\mathbf{k}$. Therefore, and following the argument from Ref. [133], it is legitimate to perform an averaging over the angular variable $\theta_{\mathbf{k}}$ of the above squared matrix elements (while keeping the angle differences $\theta_{\mathbf{k},\mathbf{k+q}}$ and $\theta_{\mathbf{k},\mathbf{q}}$ fixed). Doing this simplifies the squared matrix elements to $M^{+,+,L/T}_{\mathbf{q},\mathbf{k}} M^{+,+,L/T}_{-\mathbf{q},\mathbf{k+q}} \to |\mathbf{q}|^2 \tilde{g}^2_{L/T}(|\mathbf{q}|)$, where $\tilde{g}^2_{L/T}(|\mathbf{q}|)$ are effective couplings which are defined as

$$\tilde{g}^2_{L}(|\mathbf{q}|) = g^2_{1,\mathrm{eff}}(\mathbf{q})\left(1-\left(\frac{|\mathbf{q}|}{2k_F}\right)^2\right) + \frac{1}{2}g_2^2, \tag{4.98}$$

$$\tilde{g}^2_{T}(|\mathbf{q}|) = \frac{1}{2}g_2^2, \tag{4.99}$$

where we have written $1+\cos\theta_{\mathbf{k},\mathbf{k+q}} = 2\left(1-|\mathbf{q}|^2/(2k_F)\right)$ by using Eq. (4.91).

With these definitions, in the limit of elastic scattering, the transport lifetime due to scattering by in-plane phonons becomes

$$\frac{1}{\tau^{\mathrm{tr}}_{F,L/T}} = \frac{-1}{2\pi v_F \hbar}\int_0^{2k_F} \frac{dq}{\sqrt{1-\left(\frac{q}{2k_F}\right)^2}}\left(\frac{q}{k_F}\right)^2 \int \frac{d\omega}{\pi}\frac{q^2\tilde{g}^2_{L/T}(q)}{\sinh\left(\frac{\hbar\omega}{k_B T}\right)}\mathrm{Im}D^{R}_{L/T,\mathbf{q}}(\omega). \tag{4.100}$$

For well defined in-plane phonons we can use Eq. (4.95) to write

$$\frac{1}{\tau^{\mathrm{tr}}_{F,L/T}} = \frac{1}{\pi v_F \hbar}\int_0^{2k_F} \frac{dq}{\sqrt{1-\left(\frac{q}{2k_F}\right)^2}}\left(\frac{q}{k_F}\right)^2 \frac{q^2\tilde{g}^2_{L/T}(q)}{2\rho\omega_{L/T,\mathbf{q}}}\frac{1}{\sinh\left(\frac{\hbar\omega_{L/T,\mathbf{q}}}{k_B T}\right)}. \tag{4.101}$$

It is easy to see that in the high temperature limit, the inverse transport time and, correspondingly, the resistivity scale linearly with temperature. To see this, we notice that

for large temperature we can approximate in the previous expression $\sinh\left(\hbar\omega_{L/T,\mathbf{q}}/k_BT\right) \simeq \hbar\omega_{L/T,\mathbf{q}}/k_BT$, such that we can approximate the transport time by

$$\frac{1}{\tau^{\rm tr}_{F,L/T}} \simeq \frac{k_BT}{\pi v_F\hbar^2}\int_0^{2k_F}\frac{dq}{\sqrt{1-\left(\frac{q}{2k_F}\right)^2}}\left(\frac{q}{k_F}\right)^2\frac{q^2\tilde{g}^2_{L/T}\left(q\right)}{2\rho\omega^2_{L/T,\mathbf{q}}}. \tag{4.102}$$

This approximation is valid provided the energy of the most energetic phonon that contributes to Eq. (4.101), which is given by $\hbar\omega_{L/T,|\mathbf{q}|=2k_F}$, has a small energy compared to the temperature. This condition defines the Bloch-Grüneisen temperature as

$$T_{BG} = \frac{\hbar\omega_{L/T,|\mathbf{q}|=2k_F}}{k_B} = \frac{2v_{L/T}\hbar k_F}{k_B}, \tag{4.103}$$

which for a typical electronic density in graphene of $n = 10^{12}$ cm^{-2}, corresponding to a Fermi momentum of $k_F \simeq 0.02$Å^{-1}, corresponds to a temperature of $T_{BG} \simeq 38$ or 56 K, respectively for transverse and longitudinal in-plane phonons. Provided $T \gg T_{BG}$ the resistivity due to in-plane phonons will scale linearly with temperature. This behaviour is clearly seen in Fig. (4.4), where we obtain a resistivity of the order of $\rho_{\rm DC} \simeq 30\,\Omega$ at room temperature for graphene with an electron density of $n = 10^{12}$ cm^{-2}. Furthermore, we notice that the high temperature limit of the transport time can be written in terms of the real part of the phonon propagator (see Eq. (2.99)) as

$$\frac{1}{\tau^{\rm tr}_{F,L/T}} \simeq \frac{k_BT}{2\pi v_F\hbar^2}\int_0^{2k_F}\frac{dq\tilde{g}^2_{L/T}\left(q\right)q^2}{\sqrt{1-\left(\frac{q}{2k_F}\right)^2}}\left(\frac{q}{k_F}\right)^2\left(-{\rm Re}D^R_{L/T,\mathbf{q}}(0)\right). \tag{4.104}$$

This result is no accident, but is actually of consequence of applying Kramers-Kronig relation, Eq. (A.32), to Eq. (4.100) after expanding $\sinh\left(\omega/k_BT\right) \simeq \omega/k_BT$.

.

4.4.2 *Scattering by flexural phonons*

For scattering by flexural phonons the field $\phi^{+,+}_{\mathbf{k+q},\mathbf{k}}$ is given by Eq. (4.80) and the relevant phononic spectral function Eq. (4.86) relevant for this case is given by

$$A^{\mathbf{k},\mathbf{k+q}}_{F;\mathbf{k+q},\mathbf{k}}\left(\omega\right) = \frac{1}{2A}\sum_{\mathbf{p}} M^{+,+,F}_{-\mathbf{q+p},-\mathbf{p},\mathbf{k+k}}M^{+,+,F}_{\mathbf{q-p},\mathbf{p},\mathbf{k}}\,i\left(D^R_{2F,\mathbf{q-p},\mathbf{p}}(\omega) - D^A_{2F,\mathbf{q-p},\mathbf{p}}(\omega)\right), \tag{4.105}$$

where the retarded/advanced Green's functions $D^{R/A}_{2F,\mathbf{q-p},\mathbf{p}}(\omega)$ can be obtained from the analytic continuation of the Matsubara Green's function

$$\begin{aligned} D_{2F,\mathbf{q-p},\mathbf{p}}(iq_n) &= -\frac{1}{\beta}\int_0^\beta d\tau e^{iq_n\tau}\left\langle T_\tau h_{\mathbf{q-p}}(\tau)h_{-\mathbf{q+p}}(0)\right\rangle\left\langle h_{\mathbf{p}}(\tau)h_{-\mathbf{p}}(0)\right\rangle \\ &= -\frac{1}{\beta}\sum_{ip_n} D_{F,\tilde{\mathbf{q}}-\tilde{\mathbf{p}}}D_{F,\tilde{\mathbf{p}}}. \end{aligned} \tag{4.106}$$

After summing over the Matsubara frequency and making the analytic continuation to real frequencies we obtain

$$\begin{aligned} D^R_{2F,\mathbf{q-p},\mathbf{p}}(\omega) = &-\int\frac{d\nu}{\pi}\left(1+b(\nu)\right)D^R_{F,\mathbf{q-p}}(\omega-\nu){\rm Im}D^R_{F,\mathbf{p}}(\nu) \\ &-\int\frac{d\nu}{\pi}b(\omega-\nu){\rm Im}D^R_{F,\mathbf{q-p}}(\omega-\nu)D^R_{F,\mathbf{p}}(\nu), \end{aligned} \tag{4.107}$$

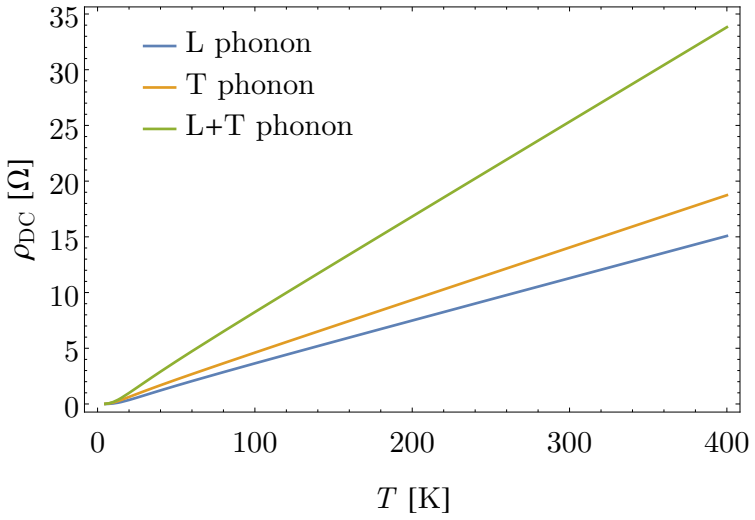

Figure 4.4: Resistivity of graphene as a function of temperature due to scattering by in-plane phonons. We considered electron doped graphene with $n = 10^{12}$ cm^{-2} (corresponding to $\epsilon_F = 0.12$ eV). We used a bare value of $g_1 = 25$ eV and $\mathcal{B} = 2.5$ which corresponds to $g_2 = 5.8$ eV. The linear dependence of the resistivity with temperature is clear.

with the advanced Green's function being obtained by replacing the retarded functions by advanced ones. Therefore, the phononic spectral function Eq. (4.105) can be written as

$$A^{\mathbf{k},\mathbf{k}+\mathbf{q}}_{F,\mathbf{k}+\mathbf{q},\mathbf{k}}(\omega) = \frac{1}{A}\sum_{\mathbf{p}}\int\frac{d\nu}{\pi}M^{+,+,F}_{\mathbf{q}-\mathbf{p},\mathbf{p},\mathbf{k}}M^{+,+,F}_{-\mathbf{q}+\mathbf{p},-\mathbf{p},\mathbf{k}+\mathbf{k}} \times (1+b(\nu)+b(\omega-\nu))\,\mathrm{Im}D^R_{F,\mathbf{q}-\mathbf{p}}(\omega-\nu)\mathrm{Im}D^R_{F,\mathbf{p}}(\nu). \tag{4.108}$$

Using this result in the general formula Eq. (4.85), we write the transport time due to scattering by two flexural phonons as

$$\frac{1}{\tau^{\mathrm{tr}}_{\mathbf{k},F}(\epsilon)} = \frac{\pi}{A^2}\sum_{\mathbf{q},\mathbf{p}}\int\frac{d\omega}{\pi}\int\frac{d\nu}{\pi}M^{+,+,F}_{\mathbf{q}-\mathbf{p},\mathbf{p},\mathbf{k}}M^{+,+,F}_{-\mathbf{q}+\mathbf{p},-\mathbf{p},\mathbf{k}+\mathbf{q}}(1-\cos\theta_{\mathbf{k},\mathbf{k}+\mathbf{q}})\times \times d(\epsilon,\omega-\nu,\nu)\mathrm{Im}D^R_{F,\mathbf{q}-\mathbf{p}}(\omega-\nu)\mathrm{Im}D^R_{F,\mathbf{p}}(\nu)\delta\left(\omega-\epsilon_{\mathbf{k}+\mathbf{q}}+\epsilon\right), \tag{4.109}$$

where we have introduced the function

$$d(\epsilon,\omega-\nu,\nu) = (b(\omega)+f(\epsilon+\omega))\,(1+b(\nu)+b(\omega-\nu)) = \frac{\cosh\left(\frac{\epsilon-\epsilon_F}{2k_BT}\right)}{4\cosh\left(\frac{\epsilon+\omega-\epsilon_F}{2k_BT}\right)\sinh\left(\frac{\omega-\nu}{2k_BT}\right)\sinh\left(\frac{\nu}{2k_BT}\right)}. \tag{4.110}$$

The squared electron-phonon matrix elements can be written as

$$\begin{aligned} M^{+,+,F}_{\mathbf{q-p,p,k}} M^{+,+,F}_{\mathbf{-q+p,-p,k+q}} &= |\mathbf{q}-\mathbf{p}|^2 |\mathbf{p}|^2 \frac{g^2_{1,\text{eff}}(\mathbf{q})}{2} \left(1+\cos\left(\theta_{\mathbf{k+q,k}}\right)\right) \cos^2\theta_{\mathbf{q-p,p}} \\ &+ |\mathbf{q}-\mathbf{p}|^2 |\mathbf{p}|^2 \frac{g_2^2}{2} \left(1+\cos\left(\theta_{\mathbf{k}}+\theta_{\mathbf{k+q}}+2\theta_{\mathbf{q-p}}+2\theta_{\mathbf{p}}\right)\right) \\ &+ |\mathbf{q}-\mathbf{p}|^2 |\mathbf{p}|^2 \cos\theta_{\mathbf{q-p,p}} g_{1,\text{eff}}(\mathbf{q})\, g_2 \cos\left(\theta_{\mathbf{k}}+\theta_{\mathbf{q-p}}+\theta_{\mathbf{p}}\right) \\ &+ |\mathbf{q}-\mathbf{p}|^2 |\mathbf{p}|^2 \cos\theta_{\mathbf{q-p,p}} g_{1,\text{eff}}(\mathbf{q})\, g_2 \cos\left(\theta_{\mathbf{k+q}}+\theta_{\mathbf{q-p}}+\theta_{\mathbf{p}}\right). \end{aligned} \tag{4.111}$$

Just as in the case of scattering by a single in-plane phonon, we can perform an average of the squared electron-phonon matrix elements over the angular variable $\theta_{\mathbf{k}}$. Doing this we can make the replacement $M^{+,+,F}_{\mathbf{q-p,p,k}} M^{+,+,F}_{\mathbf{-q+p,-p,k+q}} \to |\mathbf{q}-\mathbf{p}|^2 |\mathbf{p}|^2 \tilde{g}^2_F(|\mathbf{q}|)$, with $\tilde{g}^2_F(|\mathbf{q}|)$ the effective coupling, which is given by

$$\tilde{g}^2_F(\mathbf{q}-\mathbf{p},\mathbf{p}) = g^2_{1,\text{eff}}(\mathbf{q}) \left(1-\left(\frac{|\mathbf{q}|}{2k_F}\right)^2\right) + \frac{1}{2} g_2^2, \tag{4.112}$$

where we have used Eq. (4.91) and neglected a factor of $\cos^2\theta_{\mathbf{q-p,p}}$ that should multiply $g^2_{1,\text{eff}}(\mathbf{q})$. As we shall soon see, this last approximation is justified by the fact that the transport time will be dominated by scattering events where the momenta of the two flexural phonons is collinear, $\cos\theta_{\mathbf{q-p,p}} \simeq \pm 1$. With these approximations, the transport time at the Fermi level due to scattering by flexural phonons can be written in the form of Eq. (4.92) as

$$\begin{aligned} \frac{1}{\tau^{\text{tr}}_{F,F}} = \frac{1}{4\pi v_F \hbar} \int_0^{2k_F} \frac{dQ}{\sqrt{1-\left(\frac{Q}{2k_F}\right)^2}} \left(\frac{Q}{k_F}\right)^2 \frac{1}{A} \sum_{\mathbf{p}} |\mathbf{Q}-\mathbf{p}|^2 |\mathbf{p}|^2 \tilde{g}^2_F(\mathbf{Q}-\mathbf{p},\mathbf{p}) \times \\ \times \int_0^{+\infty} \frac{d\omega}{\pi} \int_0^{+\infty} \frac{d\nu}{\pi} d(\epsilon_F, \omega-\nu, \nu) \text{Im} D^R_{F,\mathbf{Q-p}}(\omega-\nu) \text{Im} D^R_{F,\mathbf{p}}(\nu), \end{aligned} \tag{4.113}$$

where in the above expression $\mathbf{Q}$ stands for the total transferred momentum by the two flexural phonons. The integration over the momentum variable $\mathbf{p}$ can be rewritten by introducing the auxiliary variable $\mathbf{q} = \mathbf{Q}-\mathbf{p}$, and noticing that the angle between $\mathbf{p}$ and $\mathbf{Q}$ can be written as

$$\cos\theta_{\mathbf{p,Q}} = \frac{|\mathbf{Q}|^2 + |\mathbf{p}|^2 - |\mathbf{q}|^2}{2|\mathbf{p}||\mathbf{Q}|}. \tag{4.114}$$

This allows to write the integral $\int d^2\mathbf{p} = \int d|\mathbf{p}|\,|\mathbf{p}|\, d\theta_{\mathbf{p,Q}}$ as an integral over $|\mathbf{p}|$ and $|\mathbf{q}|$. The transport lifetime is thus written as

$$\begin{aligned} \frac{1}{\tau^{\text{tr}}_{F,F}} = \frac{1}{v_F \hbar^2 (2\pi)^3} \int_0^{2k_F} \frac{dQ}{\sqrt{1-\left(\frac{Q}{2k_F}\right)^2}} \left(\frac{Q}{k_F}\right)^2 \tilde{g}^2_F(Q) \times \\ \times \iint_R dq dp \frac{q^3 p^3}{\sqrt{\left(\frac{(p+q)}{4}^2 - \frac{Q^2}{4}\right)\left(Q^2-(p-q)^2\right)}} \Omega_{q,p}, \end{aligned} \tag{4.115}$$

where we defined the function

$$\Omega_{q,p} = \int_0^{+\infty} \frac{d\omega}{\pi} \int_0^{+\infty} \frac{d\nu}{\pi} \frac{2 \coth\left(\frac{\omega}{2k_BT}\right) \coth\left(\frac{\nu}{2k_BT}\right)}{\cosh\left(\frac{\omega}{k_BT}\right) + \cosh\left(\frac{\nu}{k_BT}\right)} \mathrm{Im}D^R_{F,q}(\omega) \mathrm{Im}D^R_{F,p}(\nu). \quad (4.116)$$

and the region R is defined by the conditions $q + p > Q$ and $|p - q| < Q$. In the definition of $\Omega_{p,q}$, we have used the fact that the functions $\mathrm{Im}D^R_{F,q}(\omega)$ are odd in ω to reduce the integration only to positive frequencies. Notice that the integration in the (q, p) variables will be dominated by by the regions with $p+q \simeq Q$, where the momenta of the two phonons are parallel, $\cos\theta_{\mathbf{p},\mathbf{q}} = 1$, and $p - q \simeq \pm Q$, where the momenta of the two phonons are anti-parallel, $\cos\theta_{\mathbf{p},\mathbf{q}} = -1$. This justifies our approximation of setting $\cos^2\theta_{\mathbf{p},\mathbf{q}} = 1$ in Eq. (4.112).

An important point regarded the resistivity due to flexural phonons, is that for non-interacting flexural phonons in a free graphene layer, the transport time will diverge. To see this, we notice that if the flexural phonons are well defined, we can write

$$\mathrm{Im}D^R_{F,\mathbf{q}}(\omega) = -\frac{\pi}{\rho} \mathrm{sgn}(\omega)\, \delta\left(\omega^2 - \omega^2_{F,\mathbf{q}}\right), \quad (4.117)$$

and therefore the integrations in frequency in $\Omega_{p,q}$ can be performed leading to

$$\Omega_{q,p} = \frac{\hbar^2}{(2\rho)^2 \omega_{F,q}\omega_{F,p}} \frac{2 \coth\left(\frac{\hbar\omega_{F,q}}{2k_BT}\right) \coth\left(\frac{\hbar\omega_{F,p}}{2k_BT}\right)}{\cosh\left(\frac{\hbar\omega_{F,q}}{k_BT}\right) + \cosh\left(\frac{\hbar\omega_{F,p}}{k_BT}\right)}. \quad (4.118)$$

For sufficiently small q and p this becomes

$$\Omega_{p,q} \simeq \frac{2(k_BT)^2}{\rho\omega^2_{F,q}\rho\omega^2_{F,p}}. \quad (4.119)$$

Since for bare flexural phonons we have $\omega_{F,q} \propto q^2$, we have that the integration over q and p in Eq. (4.115) would diverge logarithmically for small momenta. This is just another manifestation of the instabilities of the non-interacting model for flexural phonons, which where already discuss in Chapter 2. We have already seen how anharmonic effects lead to a reconstruction of the dispersion relation of flexural phonons at long wavelengths to $\omega_{F,q} \propto q^{2-\eta_h/2}$, with $\eta_h > 0$, which will make the transport time finite. In real samples, even suspended ones, there will always be some residual strain, which for an isotropic strain, will modified the dispersion relation of the flexural phonons to (see Eq. (2.197))

$$\omega^{\mathrm{strained}}_{F,\mathbf{q}} = \sqrt{\frac{\kappa}{\rho}|\mathbf{q}|^4 + \frac{(\lambda+\mu)\,\bar{u}}{\rho}|\mathbf{q}|^2}, \quad (4.120)$$

where $(\lambda + \mu)\,\bar{u}$ is the isotropic applied stress with $\bar{u}$ the relative change of area of the graphene layer. The applied strain linearises the dispersion relation of the flexural phonons at long wavelengths, thus making the resistivity finite [35, 133].

While for the case of scattering by in-plane phonons, the resistivity depended on the temperature linearly, for high enough temperature, for the case of scattering by flexural phonons the resistivity scales as T^2. To see this, we notice that at high enough temperature the function $\Omega_{q,p}$ will behave as

$$\Omega_{q,p} \simeq 2(k_BT)^2 \int_{-\infty}^{+\infty} \frac{d\omega}{\pi} \frac{\mathrm{Im}D^R_{F,q}(\omega)}{\omega} \int_{-\infty}^{+\infty} \frac{d\nu}{\pi} \frac{\mathrm{Im}D^R_{F,p}(\nu)}{\omega}, \quad (4.121)$$

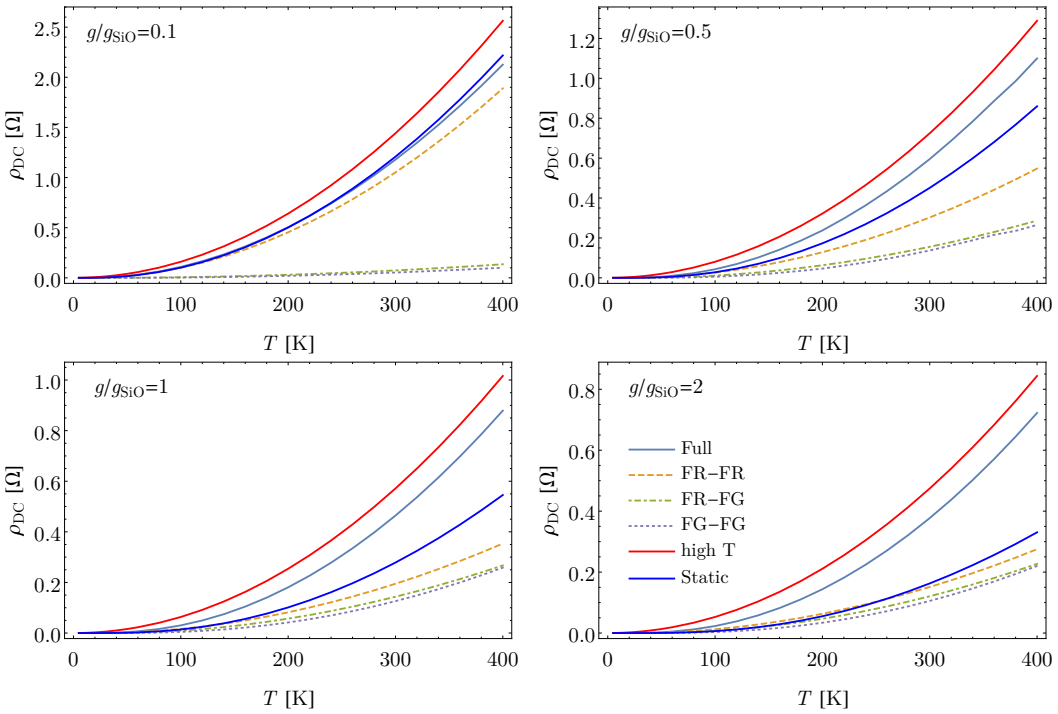

Figure 4.5: Graphene resistivity as a function of temperature due to scattering by flexural phonons when graphene is supported by a SiO_2 substrate for different values of the graphene membrane-substrate coupling g. The *Full* line represents the resistivity due to scattering by flexural phonons when these are coupled to the substrate. This contribution is split into processes involving two FR phonons (*FR-FR*), one FR and one FG phonon (*FR-FG*) and two FG phonons (*FG-FG*). Also shown is the hight temperature behaviour as given by Eq. (4.122) (*high T*) and the result assuming that the substrate is static (*Static*). The used reference value for g is given by $g_{SiO_2} = 1.82 \times 10^{20}$ N m^{-3} (see Table 3.1). We considered electron doped graphene with $n = 10^{12}$ cm^{-2} (corresponding to $\epsilon_F = 0.12$ eV) and used electron-phonon couplings given by $g_1 = 25$ eV and $g_2 = 5.8$ eV.

which after using the Kramers-Kronig relation can written as

$$\Omega_{p,q} \simeq 2\,(k_B T)^2\, \mathrm{Re} D^R_{F,q}(0) \mathrm{Re} D^R_{F,p}(0), \tag{4.122}$$

which leads to $1/\tau^{\mathrm{tr}}_{F,F} \propto T^2$. This T^2 dependence at high temperature comes ultimately from the fact that the scattering by flexural phonons, always involves exchange of two phonons, which is a consequence of the $z \to -z$ mirror symmetry of graphene. It is also worthwhile pointing out that while for scattering by a single phonon the maximum phonon momentum is limited to $2k_F$, for scattering by two phonons, while the total exchanged momentum is also restricted by $2k_F$, the momentum of each individual phonon can be much larger than $2k_F$ as can be seen in Eq. (4.115). Therefore, in scattering by flexural phonons, the high temperature limit is not limited by the Bloch-Grüneisen temperature (4.103), but by the Debye temperature, or provided the integrands in Eq. (4.115) decay sufficiently fast, a fraction of the Debye temperature.

We are mainly interested in the case when graphene is supported by a substrate. As previously discussed in Chapter 3, coupling of the flexural mode of a crystalline membrane to the substrate acoustic phonons will gap the dispersion relation of the flexural mode. This flexural-gapped (FR) mode will lie within the continuum of bulk phonon states of the substrate and will therefore acquire a finite lifetime. At the same

time the flexural mode will also hybridize with the substrate surface Rayleigh mode, acquiring a linear dispersion relation at long wavelengths. Since the energy of this mode lies bellow the continuum of bulk states, it will be a well defined mode with a long lifetime. Therefore, the imaginary part of the flexural phonon Green's function will be split into

$$\mathrm{Im}D^R_{F,\mathbf{q}}(\omega) = -\frac{\pi}{\rho} Z_{FR}(\mathbf{q})\delta\left(\omega^2 - \omega^2_{FR,\mathbf{q}}\right) + \mathrm{Im}D^R_{FG,\mathbf{q}}(\omega), \tag{4.123}$$

where $\omega_{FR,\mathbf{q}}$ and $Z_{FR}(\mathbf{q})$ are the dispersion relation and the weight of the flexural-Rayleigh mode, given respectively by Eq. (3.73) and (3.75), and $\mathrm{Im}D^R_{FG,\mathbf{q}}(\omega)$ is the remaining contribution which cannot be written as a δ-function due to the substrate induced broadening. The transport time due to flexural phonons involves two phonons and therefore, when the graphene membrane is on top of a substrate, can be split into contributions involving two flexural-Rayleigh modes (FR-FR), two flexural-gapped modes (FG-FG) and one flexural-Rayleigh and one flexural-gapped mode (FR-FG). In Fig. 4.5 we plot the resistivity of SiO_2 supported graphene due to scattering by flexural phonons, showing the different contributions to the transport time. We also show the resistivity if we ignored the dynamics of the substrate, that is, if we assume that the only effect of the substrate was to gap the dispersion relation of the flexural mode, but without inducing any broadening or hybridization with the substrate Rayleigh mode. In this case we would obtain

$$\mathrm{Im}D^R_{F,\mathbf{q}}(\omega) = -\frac{\pi}{\rho}\delta\left(\omega^2 - \left(\omega^{\mathrm{gapped}}_{F,\mathbf{q}}\right)^2\right), \tag{4.124}$$

with (see Eq. (3.67))

$$\omega^{\mathrm{gapped}}_{F,\mathbf{q}} = \sqrt{\frac{\kappa}{\rho}|\mathbf{q}|^4 + \frac{g}{\rho}}, \tag{4.125}$$

where g is the membrane-substrate coupling parameter introduced in (3.8) of Chapter 3 . We can see that the resistivity increases for smaller values of g. The reason for this is that the gap and broadening induced by the substrate will be smaller and therefore the flexural phonon energy will be lower. We can also see that for smaller values of the membrane-substrate coupling the main contribution to the resistivity comes from FR-FR processes. However, we must point out that for small values of g the flexural-Rayleigh mode actually has a dispersion relation that is very close to quadratic except at very small or large momentum, where it is almost linear. For this reason we also see that for smaller values of g, neglecting the dynamics of a substrate and using Eqs. (4.124) and (4.125) becomes a much better approximation than for larger values of g. We also point out that for typical values of the membrane-substrate coupling, the resistivity at room temperature for a doping of $\epsilon_F = 0.12$ eV is of the order of $\rho_{\mathrm{DC}} \sim 1\Omega$, much smaller that the resistivity due to scattering by in-plane phonons. In Fig. 4.5, we also show the limiting high temperature behaviour of the resistivity, which scales as T^2. However, as we have previously anticipated, and differently from the scattering by in-plane phonons, this regime is never reached for room temperature values. This is more clearly shown in the logarithmic plot of Fig 4.6. There it is clearly shown that the high temperature asymptotic limit is approach is very slowly for scattering by flexural phonons in supported graphene and at room temperature there are still significant deviations from the high temperature result. This is to be contrasted with the resistivity due to flexural phonons in suspended strained graphene sample, assuming a typical value of strain of $\bar{u} = 0.01\%$ [35] in Eq. (4.120), and with

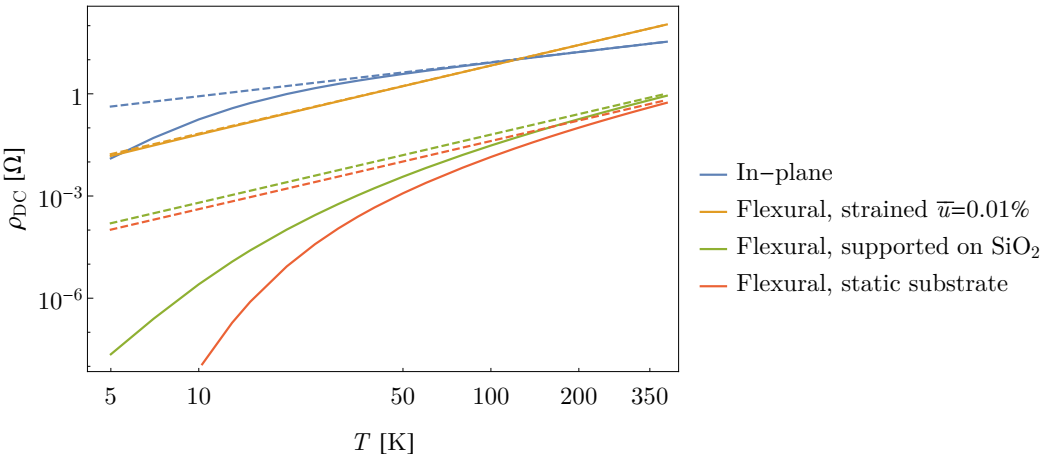

Figure 4.6: Log-log plot of graphene resistivity as a function of temperature due to different scattering processes: scattering by in-plane phonons; scattering by flexural phonons in a suspended strained sample with $\bar{u} = 0.01\%$; scattering by flexural phonons for a graphene sample supported by a SiO_2 substrate tacking into account the dynamics of the substrate; and assuming the substrate is static. The dashed lines represent the asymptotic high temperature behaviour: $\sim T$ for scattering by in-plane phonons and $\sim T^2$ for scattering by flexural phonons.

the resistivity due to scattering by in-plane phonons, which are also shown in Fig 4.6. For the case of scattering by in-plane phonons and for scattering by flexural phonons in suspended strained graphene the asymptotic high temperature limits are reached already at room temperature.

Finally we point out that while in suspended samples, scattering by flexural phonons is the dominant mechanism limiting the conductivity of graphene at room temperature [35–37, 133], scattering by flexural phonons is substantially reduced in supported samples and scattering by in-plane phonons becomes the dominant mechanism, as Fig 4.6. demonstrates. This should happen for any substrate and not just SiO_2 substrate as seen in Fig. 4.7, where we show the resistivity of graphene due to flexural phonons for graphene supported by a hBN substrate.

4.5 CONCLUSION

In this chapter we have studied the limits imposed by flexural phonon scattering to the resistivity of graphene samples supported by a substrate. We found out that scattering by flexural phonons gives origin to a resistivity that scales with temperature as T^2 in the high temperature limit. This is true both in the case of suspended samples and in supported samples and is due to the fact that scattering by flexural phonons is a two phonon process. However, while for a doping of $n = 10^{12}$ cm^{-2}, scattering in suspended samples with small strains yields a T^2 behaviour for temperatures as low as 50 K, for supported samples the T^2 behaviour is approached at a much slower pace, and even at room temperature there are significant deviations from the T^2 behaviour. This is also in contrast with the case of scattering by in-plane phonons and its associated scaling of the resistivity with T, which is also reached for temperatures $\gtrsim 50$ K. The difference can be explained by the fact that in the quasi-elastic approximation, the maximum momentum transferred by the phonons to the electrons is given by $2k_F$, which for $n = 10^{12}$ cm^{-2}, corresponds to a temperature of 38–56 K, such that for $\gtrsim 50$ K all

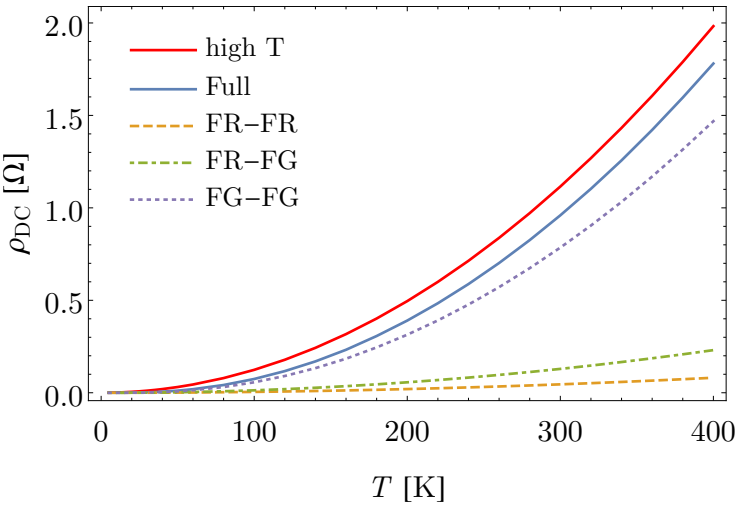

Figure 4.7: Graphene resistivity as a function of temperature due to scattering by flexural phonons when graphene is supported by a hBN substrate. The *Full* line represents the resistivity due to scattering by flexural phonons when these are coupled to the substrate. This contribution is split into processes involving two FR phonons (*FR-FR*), one FR and one FG phonon (*FR-FG*) and two FG phonons (*FG-FG*). The used vale for the graphene membrane-substrate coupling is $g_{\text{hBN}} = 1.82 \times 10^{20}$ N m^{-3} (see Table 3.1). We considered electron doped graphene with $n = 10^{12}$ cm^{-2} (corresponding to $\epsilon_F = 0.12$ eV) and used electron-phonon couplings given by $g_1 = 25$ eV and $g_2 = 5.8$ eV.

the relevant phonons will be classical and we obtain the T behaviour. The case of scattering by flexural phonons is distinct since the maximum transferred momentum of $2k_F$ is distributed by two phonon. Therefore, in the case when the momentum of the two flexural phonons is anti-parallel the maximum momentum is limited, not by the Fermi momentum, but instead by the Debye momentum, which corresponds to a temperature of $\simeq 1000$ K in graphene. Therefore, at room temperature quantum statistics still plays a significant role for flexural phonons and we obtain a deviation from the classical T^2 behaviour in supported samples. Naturally, this same discussion would apply to scattering by flexural phonons in suspended samples. However, in suspended samples with small strain, scattering will be dominated by phonons with $\mathbf{q} \to 0$, which will always be classical, which explains the fast approach to the T^2 limit. In supported samples, in the $\mathbf{q} \to 0$ limit, the flexural phonon is heavily damped by the substrate and the hybridization with the substrate Rayleigh mode is weak and their contribution for resistivity is therefore weak.

While in suspended samples, scattering by flexural phonons can be the dominant source of scattering for small strains, we found out that scattering by flexural phonons in supported samples is drastically suppressed for typical graphene-substrate coupling strengths for the widely used substrates SiO_2 and hBN. This situation is expected to be true in general. While a reduction of the graphene-substrate coupling does lead to an increase of the resistivity due to the smaller gap that is induced in the dispersion relation of the flexural phonons, this increase is modest. For a electronic density of $n = 10^{12}$ cm^{-2} at room temperature, a reduction of the typical graphene-substrate coupling by one order of magnitude leads to a more than doubling of the resistivity. However, the actual change is from $\rho_{\text{DC}} \sim 1\ \Omega$ to $\rho_{\text{DC}} \sim 2\ \Omega$, a resistivity that is much smaller that the one due to scattering by in-plane phonons, which is of the order

of $\rho_{\mathrm{DC}} \sim 30\ \Omega$ at room temperature. Even inclusion of the hybrid flexural-Rayleigh phonons which have a linear dispersion relation and long lifetimes at small momenta does not change this result. This is mainly due to the fact that the weight of the flexural-Rayleigh phonon in graphene also vanishes at small momenta.

Therefore, we conclude that in supported graphene samples, scattering by flexural phonons will always be a weak contribution to the resistivity and can safely be ignored. This justifies early theoretical studies of acoustic phonon-limited resistivity in supported graphene samples, where scattering by flexural phonons was neglected.

5

COULOMB DRAG IN DOUBLE LAYER STRUCTURES

5.1 INTRODUCTION

When two 2D metallic systems are electrically isolated from each other, but close enough such that they can still interact, this remote interaction enables momentum relaxation and exchange between the two systems. In a situation where there is a net drift velocity of the electronic fluid in one of the metallic systems, the interaction between the two will tend to equilibrate the drift velocities of both systems. The possibility of this kind of remote frictional drag was first theoretically discussed in Refs. [156, 157] and was first observed between two-dimensional electron gases (2DEG) in semiconductor based double quantum well structures [42–46]. The remote interaction enabling frictional drag was attributed to electron-electron Coulomb interaction and thus this phenomena is now commonly referred to as *Coulomb drag* [158–162]. Coulomb drag is an interesting phenomena, which, contrasting with most other transport phenomena, it is not just corrected by interaction effects, but is actually driven by them.

We will consider the effect of Coulomb drag between two parallel 2D metallic layers. Coulomb drag is generally characterized by the drag resistivity. In an experimental situation where a current, I_2, is driven through one of the layers, generally referred to as the *active layer* and which we will denote by layer 2, the exchange of momentum between the two layers will tend to induce a current in the other layer, referred to as the *passive layer* and which we will denote by layer 1. In an experimental setup, see Fig. 5.1, in which no current is allowed to flow in the passive layer, an electric potential imbalance, V_1 will build up along the passive layer. The drag resistivity is defined as

$$\rho_{\text{Drag}} = \frac{W}{L}\frac{V_1}{I_2} = \frac{E_1}{J_2}, \tag{5.1}$$

where $E_1 = V_1/L$ is the electric field built in the passive layer, with L its length, and $J_2 = I_2/W$ is the electric current density driven through the active layer, with W its width.

The advent of graphene and the possibility of creating graphene double layer structures in which the graphene layers are separated by an insulating material [38, 39] gave origin to a renewed interest on the topic of Coulomb drag both from the experimental [39–41] and theoretical [163–173] point of views. Compared to the case of Coulomb drag between 2DEG's, Coulomb drag in graphene differs from the former in three ways: (i) the low energy dispersion relation for graphene electrons is linear, instead of parabolic; (ii) the wavefunction of electrons in graphene has a spinorial character instead of being a simple scalar; and finally (iii) the impurity dominated transport time in graphene is not a constant, but is instead proportional to the momentum (or energy) $\tau_{\mathbf{k}}^{\text{tr}} \propto |\mathbf{k}|$[174]. In the early literature in Coulomb drag in double quantum well systems, it was established that in the limit of low temperature, high density, large layer separation, d, and strong screening the drag resistivity depends on temperature as T^2 and on the interlayer separation as d^{-4} [158] (a result previously given in [44] without derivation). However, the situation in graphene is not so clear. While there was an early agreement that in the low temperature/high density limit the drag resistivity in graphene should still depend on temperature as T^2 [164–169], there was no agreement on the

dependence of drag on the layer separation and how the dependence of the transport time in momentum should affect the result. As a matter of fact several contradicting statements could be found in the literature which we summarize in the following.

1. Tse *et al* [164] assumed a constant transport time, obtaining a d^{-4} dependence for the drag resistivity.

2. Peres *et al* [165] considered a momentum dependent transport time, $\tau_{\mathbf{k}}^{\mathrm{tr}} \propto |\mathbf{k}|$, obtaining a d^{-6} dependence.

3. Katsnelson [166] considered a constant transport time and obtains a d^{-4} dependence.

4. Hwuang *et al* [167] considered both case of a constant transport time and the case of transport time proportional to the momentum, $\tau_{\mathbf{k}}^{\mathrm{tr}} \propto |\mathbf{k}|$. For a constant transport time a d^{-6} dependence was obtained (in contradiction with the result from [164]). For the case of a momentum dependent transport time a d^{-4} behaviour was obtained. The case of drag between two bilayer graphene layers was also studied. Using a constant transport time a d^{-4} behaviour was obtained in this same limit.

5. Narozhny *et al* [168] considered both cases of a constant and a linearly momentum dependent transport time. For the case of a constant transport time it was obtained a d^{-4} dependence. It was argued that in the low temperature, high density limit, this result still holds, regardless of the momentum dependence of the transport time.

6. Carrega *et al* [169] studied the drag between massless Dirac electrons. They proved that in the low temperature/high density limit, the dependence on momentum of the transport time is irrelevant and a d^{-4} dependence is obtained for large interlayer separations.

Therefore, a general theory of Coulomb drag, capable of describing on equal footing system with different dispersion relations and different momentum dependences of transport time on momentum, is necessary to clarify this issue. The discussion of such general theory and its predictions is one of the goals of this chapter.

Another interesting question is the role played by other possible remote interlayer interactions in the phenomena of Coulomb drag. One such possibility is the effect of phonon mediated electron-electron interlayer interaction. The effect of electron-phonon interaction in double quantum wells and in the Coulomb drag between 2DEG's was previous considered in Refs. [175–179]. In graphene it is know that substrate phonons play an important role in limiting the electrical conductivity of supported graphene samples [121, 130, 131]. This is specially important in the case of polar substrates, such as hexagonal boron nitride, where longitudinal optical phonons give origin to long ranged electric fields which give origin to remote scattering of graphene electrons. Therefore, it is also expected that this kind of remote scattering by optical phonons will play a role in the phenomenon of Coulomb drag.

In this chapter we study Coulomb drag between two parallel generic 2D electron systems, paying special attention to the case of drag between two graphene layers. In Section 5.2, we describe a general theory for Coulomb drag between two parallel 2D metallic layers to lowest order in the effective interlayer interaction. Using this general theory, we study Coulomb drag between systems with arbitrary electronic dispersion

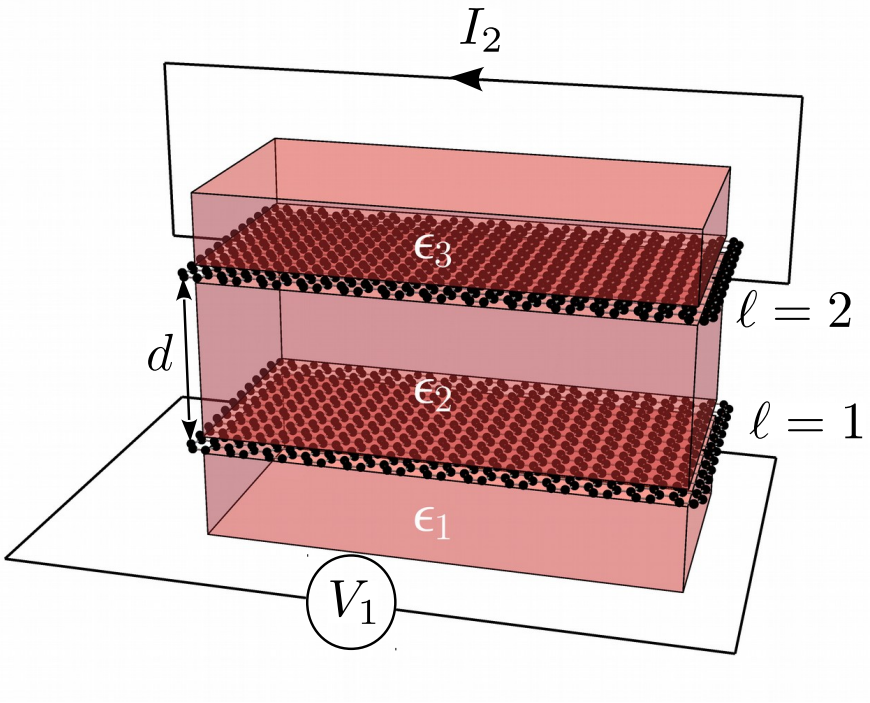

Figure 5.1: Schematic representation of a typical setup for the observation of Coulomb drag between two metallic layers (in this case two graphene layers). A current I_2 is driven through the active layer, $\ell = 2$, which due to remote interlayer interaction induces a electrostatic potential imbalance, V_1, in the passive layer, $\ell = 1$. The two layers are separated by a distance d of a material with dielectric constant ϵ_2. The two layers are encapsulated by dielectrics ϵ_1 and ϵ_3, respectively bellow and above the double layer.

relation, wavefunction structure and with an arbitrary dependence of transport time on momentum. We determine the scaling of the drag resistivity with the temperature, distance and electronic density in the limit of small temperature, large separation and strong screening. In Section 5.3, we specialize to the case of drag between two graphene layers at high doping but generic layer separation and taking into account the linear momentum dependence of the transport time in graphene. In Section. 5.4, we discuss how the effective electron-electron interaction mediated by longitudinal optical phonons of a polar medium embedding the two metallic layers can be taken into account in the evaluation of the drag resistivity. Numerical results for the drag resistivity between two graphene layers encapsulated by hBN, both neglecting and including effects of hBN optical phonons, are presented and discussed in Section 5.5. Conclusions from this chapter are made in Section 5.6.

5.2 COULOMB DRAG IN A GENERAL BILAYER SYSTEM

Suppose we have two parallel metallic layers, $\ell = 1$ and $\ell = 2$, separated by a distance d such that the two layers are electrically isolated from one another, meaning that electron tunnelling from one layer to the other can be neglected. Without loss of generality, we assume that the active layer, $\ell = 2$, is placed at $z = d$ and that the passive layer, $\ell = 1$, is placed at $z = 0$. Assuming the two layers are somehow coupled, applying electric

fields, which we write as $\mathbf{E}_\ell$, to any of them will give origin to currents in both layers, which we write as $\mathbf{J}_\ell$. In linear response theory, the currents in both layers are related to the electric fields as

$$\begin{bmatrix} \mathbf{J}_1 \\ \mathbf{J}_2 \end{bmatrix} = \begin{bmatrix} \boldsymbol{\sigma}_{11} & \boldsymbol{\sigma}_{12} \\ \boldsymbol{\sigma}_{21} & \boldsymbol{\sigma}_{22} \end{bmatrix} \cdot \begin{bmatrix} \mathbf{E}_1 \\ \mathbf{E}_2 \end{bmatrix}, \tag{5.2}$$

where in the previous expression $\boldsymbol{\sigma}_{11}$ and $\boldsymbol{\sigma}_{22}$ are intralayer conductivities while $\boldsymbol{\sigma}_{12}$ and $\boldsymbol{\sigma}_{21}$ are the interlayer conductivities also referred to as transconductivities or Drag conductivity. Notice that for a generic systems, $\boldsymbol{\sigma}_{\ell\ell'}$ are tensors. The inverse of this relation can be written in terms of the resistivity tensor

$$\begin{bmatrix} \mathbf{E}_1 \\ \mathbf{E}_2 \end{bmatrix} = \begin{bmatrix} \boldsymbol{\rho}_{11} & \boldsymbol{\rho}_{12} \\ \boldsymbol{\rho}_{21} & \boldsymbol{\rho}_{22} \end{bmatrix} \cdot \begin{bmatrix} \mathbf{J}_1 \\ \mathbf{J}_2 \end{bmatrix}, \tag{5.3}$$

which is related to the conductivity tensor by

$$\begin{bmatrix} \boldsymbol{\rho}_{11} & \boldsymbol{\rho}_{12} \\ \boldsymbol{\rho}_{21} & \boldsymbol{\rho}_{22} \end{bmatrix} = \begin{bmatrix} \boldsymbol{\sigma}_{11} & \boldsymbol{\sigma}_{12} \\ \boldsymbol{\sigma}_{21} & \boldsymbol{\sigma}_{22} \end{bmatrix}^{-1}. \tag{5.4}$$

As described in the introduction of this chapter, Section 5.1, a typical Coulomb drag experiment consists in driving a constant current $\mathbf{J}_2$ in the active layer and measuring the electric field $\mathbf{E}_1$ in the passive layer, while not allowing any flow of current in that layer, $\mathbf{J}_1 = 0$. In that situation, from Eq. (5.3) we obtain $\mathbf{E}_1 = \boldsymbol{\rho}_{12} \cdot \mathbf{J}_2$ and from the very definition of drag resistivity Eq. (5.1) we obtain $\boldsymbol{\rho}_{\text{Drag}} = \boldsymbol{\rho}_{12}$. The drag resistivity can then be expressed in terms of the intra- and interlayer conductivities by using Eq. (5.4), and we obtain

$$\boldsymbol{\rho}_{\text{Drag}} = -\left(\boldsymbol{\sigma}_{22} \cdot \boldsymbol{\sigma}_{12}^{-1} \cdot \boldsymbol{\sigma}_{11} - \boldsymbol{\sigma}_{21}\right)^{-1}. \tag{5.5}$$

We will focus on systems which for low energies are isotropic, such as graphene. In that situation, all quantities in the previous equation can be regarded as scalars instead of tensors. Furthermore, it is reasonable to expected that the interlayer conductivity will be much smaller than the intralayer ones. Therefore we can approximate the drag resistivity by

$$\rho_{\text{Drag}} \simeq -\frac{\sigma_{12}}{\sigma_{11}\sigma_{22}}. \tag{5.6}$$

Therefore, computing the drag resistivity is reduced to a problem of computing conductivities. Provided the interaction between the two layers is weak, the transconductivity can be computed using perturbation theory. Throughout the years, different techniques have been used to compute the transconductivity, including Boltzmann's kinetic equation [158, 160], the memory function formalism [159] and the Kubo formula [161, 162]. In Appendix G we present a derivation of the transconductivity based on the Boltzmann equation. To second order in the interlayer interaction the transconductivity is given by

$$\sigma_{12}^{ij} = \frac{e_1 e_2}{2\pi\hbar k_B T} \frac{1}{A} \sum_{\mathbf{q}} \int_0^{+\infty} \frac{d\omega}{4\sinh^2\left(\frac{\omega}{2k_B T}\right)} \left|U_{12}^R(\omega, \mathbf{q})\right|^2 \Delta_1^i(\omega, \mathbf{q}) \Delta_2^j(\omega, \mathbf{q}), \tag{5.7}$$

where e_ℓ is the charge of carriers in layer ℓ, $U_{12}(\omega, \mathbf{q})$ is the screened interlayer interaction and the quantity $\mathbf{\Delta}_\ell(\omega, \mathbf{q})$ is the non-linear susceptibility of layer ℓ [161, 162] which, in the Boltzmann limit, is given by

$$\mathbf{\Delta}_\ell(\omega,\mathbf{q}) = g_\ell \frac{2\pi}{A} \sum_{\mathbf{k},\lambda,\lambda'} \left|\rho^{\lambda',\lambda}_{\ell,\mathbf{k}+\mathbf{q},\mathbf{k}}\right|^2 \left(\tau^{\rm tr}_{\mathbf{k}+\mathbf{q},\lambda',\ell}\mathbf{v}_{\mathbf{k}+\mathbf{q},\lambda',\ell} - \tau^{\rm tr}_{\mathbf{k},\lambda,\ell}\mathbf{v}_{\mathbf{k},\lambda,\ell}\right) \times \\ \times \left(f(\epsilon_{\mathbf{k}+\mathbf{q},\lambda',\ell}) - f(\epsilon_{\mathbf{k},\lambda,\ell})\right) \delta\left(\omega + \epsilon_{\mathbf{k}+\mathbf{q},\lambda',\ell} - \epsilon_{\mathbf{k},\lambda,\ell}\right), \quad (5.8)$$

where g_ℓ is the degeneracy of the band (which includes both spin and valley degeneracy if appropriate). In the expression for $\mathbf{\Delta}_\ell(\omega, \mathbf{q})$, $\rho^{\lambda',\lambda}_{\ell,\mathbf{k}+\mathbf{q},\mathbf{k}} =_\ell \langle \mathbf{k}+\mathbf{q}, \lambda' \mid \mathbf{k}, \lambda\rangle_\ell$ is a wavefunction overlap factor of electrons in the same layer, $\tau^{\rm tr}_{\mathbf{k},\lambda,\ell}$ is the transport time of an electron in layer ℓ with momentum $\mathbf{k}$ and in band λ, which has energy $\epsilon_{\mathbf{k},\lambda,\ell}$ and velocity $\mathbf{v}_{\mathbf{k},\lambda,\ell} = \hbar^{-1}\nabla_{\mathbf{k}}\epsilon_{\mathbf{k},\lambda,\ell}$. We notice that for an isotropic system we will have $\mathbf{\Delta}_\ell(\omega, \mathbf{q}) = |\mathbf{\Delta}_\ell(\omega, \mathbf{q})|\,\mathbf{q}/|\mathbf{q}|$, leading to $\sigma^{xx}_{12} = \sigma^{yy}_{12}$, with $\sigma^{xy}_{12} = 0$ (in the absence of a magnetic field). In the Boltzmann limit at low temperatures and for an isotropic system, the intralayer conductivities σ_{11} and σ_{22} are given by

$$\sigma_{\ell\ell} = \frac{e_\ell^2}{2} \mathrm{DoS}(\epsilon_{F,\ell}) v^2_{F,\ell} \tau^{\rm tr}_{F,\ell}, \quad (5.9)$$

where the indice $_F$ denotes that all quantities are evaluated at the Fermi level. Combining Eqs. (5.6), (5.6), (5.7) and (5.9) we obtain the drag resistivity. But before we proceed we must determine the form of the interlayer effective interaction.

5.2.1 *Interlayer screened Coulomb interaction*

In order to compute the drag resistivity, we must specify the form of the interlayer Coulomb interaction that appears in Eq. (5.7). In general the two 2D metallic layers will be embedded in a dielectric material which will screen the effective interaction [166, 180]. Furthermore, the charge carriers in the metallic layer will provided additional screening to the effective interaction [160, 161, 177, 181]. In order to describe Coulomb drag both effects must be taken into account.

5.2.1.1 *Bare Coulomb interaction in vacuum*

Before obtaining the screened Coulomb interaction in the double layer structure, we must fist determine the bare interaction. This can be obtained by solving the Poisson equation for a test charge. The bare electric potential, $\phi(\mathbf{r})$, generated by a test charge located at the origin, $\rho_{\rm free} = -e\delta(\vec{r})$, can be obtained by solving the Poisson equation in vacuum

$$\nabla^2\phi(\vec{r}) = \frac{e}{\epsilon_0}\delta(\vec{r}). \quad (5.10)$$

Assuming translation invariance along the $x-y$ plane it is convenient to write the electric potential as

$$\phi(\vec{r}) = \int \frac{d^2\mathbf{q}}{(2\pi)^2}\phi(\mathbf{q}, z)e^{i\mathbf{q}\cdot\mathbf{x}}, \quad (5.11)$$

where we have written $\vec{r} = (\mathbf{x}, z)$. Writing $\delta(\vec{r}) = \delta(\mathbf{x})\,\delta(z)$ the Poisson equation for the Fourier components $\phi(\mathbf{q}, z, z_0)$ becomes

$$\frac{\partial^2}{\partial z^2}\phi(\mathbf{q}, z, z_0) - |\mathbf{q}|^2\,\phi(\mathbf{q}, z, z_0) = \frac{e}{\epsilon_0}\delta(z - z_0), \quad (5.12)$$

where we have written $\phi(\mathbf{q}, z, z_0)$ to explicitly state that the potential will be a function of the position of the test charge. For a test particle at the origin we simply have $z_0 = 0$. For $z \neq z_0$, the general solution of the previous equation is given by $\phi(\mathbf{q}, z) = A_+ e^{|\mathbf{q}|(z-z_0)} + A_- e^{-|\mathbf{q}|(z-z_0)}$. We demand that the potential does not explode at infinity and therefore set $A_+ = 0$ for $z > z_0$ and $A_- = 0$ for $z < z_0$. The δ-function $\delta(z - z_0)$ imposes a discontinuity of the derivative of the potential at the position of the test charge, which is given by

$$\frac{\partial \phi(\mathbf{q}, z_0^+, z_0)}{\partial z} - \frac{\partial \phi(\mathbf{q}, z_0^-, z_0)}{\partial z} = \frac{e}{\epsilon_0}. \tag{5.13}$$

Imposing this boundary condition and the continuity of the potential at $z = z_0 = 0$, we obtain the set of equations

$$A_-^> - A_+^< = 0, \tag{5.14}$$

$$-|\mathbf{q}| A_-^> - |\mathbf{q}| A_+^< = \frac{e}{\epsilon_0}, \tag{5.15}$$

from which we obtain $A_-^> = A_+^< = -e/(2\epsilon_0 |\mathbf{q}|)$, such that the Fourier component of the potential is given by

$$\phi(\mathbf{q}, z, z_0) = -\frac{e}{2\epsilon_0 |\mathbf{q}|} e^{-|\mathbf{q}||z-z_0|}. \tag{5.16}$$

From this equation, we can write the bare intra-, $V_{11}(\mathbf{q}) = -e\phi(\mathbf{q}, 0, 0)$ and $V_{22}(\mathbf{q}) = -e\phi(\mathbf{q}, d, d)$, and interlayer, $V_{12}(\mathbf{q}) = -e\phi(\mathbf{q}, 0, d)$ and $V_{21}(\mathbf{q}) = -e\phi(\mathbf{q}, d, 0)$, Coulomb interactions for two layers separated by a distance d as

$$V_{\ell\ell'}(\mathbf{q}) = \frac{e^2}{2\epsilon_0 |\mathbf{q}|} e^{-|\mathbf{q}|d\left(1-\delta_{\ell,\ell'}\right)},\ \ell, \ell' = 1, 2. \tag{5.17}$$

We now move on to the case when the two metallic layers are embedded in a piecewise homogeneous dielectric medium.

5.2.1.2 *Bare Coulomb interaction in layered, unixial dielectric*

In the case in which the two metallic layers are not in vacuum, but are instead embedded in a layered dielectric medium, the bare Coulomb interaction can still be obtained by solving the Poisson equation in a dielectric medium

$$-\nabla \cdot (\boldsymbol{\epsilon}(\vec{r}) \cdot \nabla \phi(\vec{r})) = \frac{\rho_{\text{free}}(\vec{r})}{\epsilon_0}, \tag{5.18}$$

where $\rho_{\text{free}}(\vec{r})$ is the free charge density and $\boldsymbol{\epsilon}(\vec{r})$ is the dielectric tensor of the embedding material. We consider a test charge located at $\vec{r}_0$, such that $\rho_{\text{free}}(\vec{r}) = -e\delta(\vec{r} - \vec{r}_0)$. We will restrict ourselves to the situation of experimental interest, where $\boldsymbol{\epsilon}(\vec{r})$ is a piecewise constant function that only changes along the z direction at the dielectric interfaces, which are located at $z = z_i$. We assume that the test charge lies at one of these interfaces. We specialize to the case where the dielectric material is an uniaxial material, such as hBN, with the symmetry axis along the z direction. In this case, the dielectric tensor of the material can be written as

$$\boldsymbol{\epsilon} = \begin{bmatrix} \epsilon_\perp & 0 & 0 \\ 0 & \epsilon_\perp & 0 \\ 0 & 0 & \epsilon_\parallel \end{bmatrix}, \tag{5.19}$$

where $\epsilon_\parallel$ and $\epsilon_\perp$ are the components of the dielectric tensor parallel and perpendicular to the c-axis of the dielectric material. In this situation and introducing the Fourier components of the electric potential as in Eq. (5.11), the Poisson equation (5.18) becomes

$$\frac{\partial}{\partial z}\left(\epsilon_\parallel(z)\frac{\partial}{\partial z}\phi(\mathbf{q},z)\right) - \epsilon_\perp(z)\,|\mathbf{q}|^2\,\phi(\mathbf{q},z) = \frac{e}{\epsilon_0}\delta(z-z_0). \tag{5.20}$$

In a region where $\boldsymbol{\epsilon}$ is constant, the solution to Eq. (5.20) is of the form of

$$\phi(\mathbf{q},z,z_0) = A_+ e^{\sqrt{\frac{\epsilon_\perp}{\epsilon_\parallel}}|\mathbf{q}|z} + A_- e^{-\sqrt{\frac{\epsilon_\perp}{\epsilon_\parallel}}\mathbf{q}z}. \tag{5.21}$$

Integrating Eq. (5.20) along the z direction around one of the dielectric interfaces at $z = z_i$ we obtain the boundary condition for the derivative of the potential

$$\epsilon_\parallel(z_i^+)\frac{\partial}{\partial z}\phi(\mathbf{q},z_i^+,z_0) - \epsilon_\parallel(z_i^-)\frac{\partial}{\partial z}\phi(\mathbf{q},z_i^-,z_0) = \frac{e}{\epsilon_0}\delta_{z_i,z_0}, \tag{5.22}$$

where $\delta_{z_i,z_0} = 1$ if the test charge is at the interface z_i and $\delta_{z_i,z_0} = 0$ otherwise. Additionally, we have the continuity condition for the potential

$$\phi(\mathbf{q},z_i^+,z_0) - \phi(\mathbf{q},z_i^-,z_0) = 0. \tag{5.23}$$

Using Eq. (5.21) together with the boundary conditions Eqs. (5.22), (5.23) and the condition that the potential should not explode at infinity, we can determine the bare interaction in a layered material. For concreteness, we consider the case represented in Fig. 5.1 with

$$\boldsymbol{\epsilon}(z) = \begin{cases} \mathrm{diag}\left[\epsilon_{\perp,3},\epsilon_{\perp,3},\epsilon_{\parallel,3}\right] & , z > d \\ \mathrm{diag}\left[\epsilon_{\perp,2},\epsilon_{\perp,2},\epsilon_{\parallel,2}\right] & , d > z > 0 \\ \mathrm{diag}\left[\epsilon_{\perp,1},\epsilon_{\perp,1},\epsilon_{\parallel,1}\right] & , 0 > z \end{cases}. \tag{5.24}$$

We consider a test charge located in the plane $z = d$. After solving the Poisson equation for $\phi(\mathbf{q},z,d)$, we obtain the bare Coulomb intralayer interaction as $V_{22}(\mathbf{q}) = -e\phi(\mathbf{q},d,d)$ and the interlayer interaction as $V_{12}(\mathbf{q}) = -e\phi(\mathbf{q},0,d)$. The intralayer interaction in the active layer, $V_{11}(\mathbf{q})$, can be obtained by considering a test charge located at $z = 0$ as $V_{11}(\mathbf{q}) = -e\phi(\mathbf{q},0,0)$. The final result can be written in a compact form as

$$V_{\ell\ell'}(\mathbf{q}) = \frac{1}{\epsilon_{\ell\ell'}(|\mathbf{q}|)}\frac{e^2}{2\epsilon_0\,|\mathbf{q}|}e^{-\sqrt{\frac{\epsilon_{\perp,2}}{\epsilon_{\parallel,2}}}|\mathbf{q}|d\left(1-\delta_{\ell,\ell'}\right)}, \tag{5.25}$$

where $\epsilon_{\ell\ell'}(q)$ are effective momentum dependent dielectric constants, which can be conveniently expressed in terms of reflection and transmission coefficients as

$$\frac{1}{\epsilon_{11}(q)} = \frac{t_{12}}{\epsilon_{\parallel,2}\sqrt{\epsilon_{\perp,2}/\epsilon_{\parallel,2}}}\frac{1+r_{32}e^{-2\sqrt{\frac{\epsilon_{\perp,2}}{\epsilon_{\parallel,2}}}dq}}{1-r_{12}r_{32}e^{-2\sqrt{\frac{\epsilon_{\perp,2}}{\epsilon_{\parallel,2}}}dq}}, \tag{5.26}$$

$$\frac{1}{\epsilon_{12}(q)} = \frac{t_{12}}{\epsilon_{\parallel,2}\sqrt{\epsilon_{\perp,2}/\epsilon_{\parallel,2}}}\frac{1+r_{32}}{1-r_{12}r_{32}e^{-2\sqrt{\frac{\epsilon_{\perp,2}}{\epsilon_{\parallel,2}}}dq}}, \tag{5.27}$$

$$\frac{1}{\epsilon_{22}(q)} = \frac{t_{32}}{\epsilon_{\parallel,2}\sqrt{\epsilon_{\perp,2}/\epsilon_{\parallel,2}}}\frac{1+r_{12}e^{-2\sqrt{\frac{\epsilon_{\perp,2}}{\epsilon_{\parallel,2}}}dq}}{1-r_{12}r_{32}e^{-2\sqrt{\frac{\epsilon_{\perp,2}}{\epsilon_{\parallel,2}}}dq}}, \tag{5.28}$$

with the reflection an transmission coefficients for the Poisson equation given by

$$r_{\ell\ell'} = \frac{-\epsilon_{\parallel,\ell}\sqrt{\epsilon_{\perp,\ell}/\epsilon_{\parallel,\ell}} + \epsilon_{\parallel,\ell'}\sqrt{\epsilon_{\perp,\ell'}/\epsilon_{\parallel,\ell'}}}{\epsilon_{\parallel,\ell}\sqrt{\epsilon_{\perp,\ell}/\epsilon_{\parallel,\ell}} + \epsilon_{\parallel,\ell'}\sqrt{\epsilon_{\perp,\ell'}/\epsilon_{\parallel,\ell'}}}, \tag{5.29}$$

$$t_{\ell\ell'} = \frac{2\epsilon_{\parallel,\ell'}\sqrt{\epsilon_{\perp,\ell'}/\epsilon_{\parallel,\ell'}}}{\epsilon_{\parallel,\ell}\sqrt{\epsilon_{\perp,\ell}/\epsilon_{\parallel,\ell}} + \epsilon_{\parallel,\ell'}\sqrt{\epsilon_{\perp,\ell'}/\epsilon_{\parallel,\ell'}}}. \tag{5.30}$$

It can be easily checked that $\epsilon_{12}(q) = \epsilon_{21}(q)$. The reflection and transmission coefficients defined above are the electrostatic equivalent of the Fresnel coefficients for the electromagnetic problem. They appear as the solution for Poisson equation around an interface between dielectric media characterized by $\boldsymbol{\epsilon}_\ell$ and $\boldsymbol{\epsilon}_{\ell'}$, if we look for a solution of the form $\phi_\ell(\mathbf{q}, z) = A_{+,\ell}e^{-\sqrt{\frac{\epsilon_{\perp,\ell}}{\epsilon_{\parallel,\ell}}}qz} + A_{-,\ell}e^{-\sqrt{\frac{\epsilon_{\perp,\ell}}{\epsilon_{\parallel,\ell}}}qz}$ in the regions ℓ and ℓ', with $A_{-,\ell} = t_{\ell\ell'}$ and $A_{+,\ell'} = r_{\ell\ell'}$, while imposing the conditions $A_{-,\ell'} = 1$ and $A_{+,\ell} = 0$. In the $q \to 0$ limit, all the effective dielectric functions become the same

$$\lim_{q\to 0} \epsilon_{\ell\ell'}(q) = \frac{\epsilon_{\parallel,1}\sqrt{\epsilon_{\perp,1}/\epsilon_{\parallel,1}} + \epsilon_{\parallel,3}\sqrt{\epsilon_{\perp,3}/\epsilon_{\parallel,3}}}{2}, \tag{5.31}$$

a result we will later use.

5.2.1.3 *Screening by free carriers in metallic layers*

The response of the free charge carriers in the metallic layers will screen the bare interaction Eq. (5.25). The screening of the bare interaction by the charge carriers of the double layer structure is described within the random phase approximation (RPA) by the coupled Dyson equations which can be written in matrix form as [160, 161, 177, 181]

$$\begin{bmatrix} U^R_{11}(\omega,\mathbf{q}) & U^R_{12}(\omega,\mathbf{q}) \\ U^R_{21}(\omega,\mathbf{q}) & U^R_{22}(\omega,\mathbf{q}) \end{bmatrix} = \begin{bmatrix} V_{11}(\mathbf{q}) & V_{12}(\mathbf{q}) \\ V_{21}(\mathbf{q}) & V_{22}(\mathbf{q}) \end{bmatrix} + \\ + \begin{bmatrix} V_{11}(\mathbf{q}) & V_{12}(\mathbf{q}) \\ V_{21}(\mathbf{q}) & V_{22}(\mathbf{q}) \end{bmatrix} \begin{bmatrix} \chi^R_1(\omega,\mathbf{q}) & 0 \\ 0 & \chi^R_2(\omega,\mathbf{q}) \end{bmatrix} \begin{bmatrix} U^R_{11}(\omega,\mathbf{q}) & U^R_{12}(\omega,\mathbf{q}) \\ U^R_{21}(\omega,\mathbf{q}) & U^R_{22}(\omega,\mathbf{q}) \end{bmatrix}, \tag{5.32}$$

where $U^R_{\ell\ell'}(\omega,\mathbf{q})$ is the retarded RPA screened interaction and $\chi^R_\ell(\omega,\mathbf{q})$ is the bare retarded irreducible density-density correlation function of layer ℓ. Notice that there are no interlayer irreducible density-density correlation function terms, since we are assuming that interlayer tunnelling is negligible. The coupled RPA equations are represented diagrammatically in Fig. 5.2. Solving the coupled RPA equations we obtain the interlayer screened interaction

$$U^R_{12}(\omega,\mathbf{q}) = \frac{V_{12}(\omega,\mathbf{q})}{\epsilon_{\text{dbl}}(\omega,\mathbf{q})}, \tag{5.33}$$

where we have defined the dielectric function for the coupled double layer structure as

$$\epsilon_{\text{dbl}}(\omega,\mathbf{q}) = \left(1 - V_{11}(\mathbf{q})\chi^R_1(\omega,\mathbf{q})\right)\left(1 - V_{22}(\mathbf{q})\chi^R_2(\omega,\mathbf{q})\right) - \\ - V_{12}(\mathbf{q})V_{21}(\mathbf{q})\chi^R_1(\omega,\mathbf{q})\chi^R_2(\omega,\mathbf{q}). \tag{5.34}$$

It is the screened interlayer interaction, Eq. (5.33) that enters Eq. (5.7) for the transconductivity.

We end this section by pointing our that tacking into account the dielectric environment and screening by the free carriers of the metallic plates could have been done in just one step, if the response of the free carriers was introduced directly into the Poisson equation. This could have been done in Eq. (5.18), if we wrote the free charge density as the sum of the test charge density and a charge induced in the metallic layers,

$$\rho_{\text{free}}(\omega, \mathbf{q}, z) = \rho_{\text{test}}(\mathbf{q}, z) + \rho_{\text{ind}}(\omega, \mathbf{q}, z), \tag{5.35}$$

where $\rho_{\text{test}}(\mathbf{q}, z) = -e\delta(z - z_0)$ is the test charge density and $\rho_{\text{ind}}(\omega, \mathbf{q}, z)$ is the charge induced in the metallic layers, which is frequency dependent due to the dynamic response of the free carriers. Within linear response, the induced charge density is related to the total electric potential via the irreducible density-density correlation functions of layer 1 and 2 as

$$\rho_{\text{ind}}(\omega, \mathbf{q}, z) = -e\delta(z)\chi_1^R(\omega, \mathbf{q})\,\phi(\omega, \mathbf{q}, 0) - e\delta(z - d)\chi_2^R(\omega, \mathbf{q})\,\phi(\omega, \mathbf{q}, d). \tag{5.36}$$

By solving Eq. (5.20) with $\rho_{\text{ind}}(\omega, \mathbf{q}, z)$ added to its right hand side, we automatically perform the resummation that is done in the Dyson equation, Eq. (5.32). To see this we first notice that the Poisson equation Eq. (5.18) with a test charge located at $\vec{r}_0$ and an induced charge density of the form given by Eq. (5.36), becomes a self-consistent equation for the effective interaction $U^R(\omega, \vec{r}, \vec{r}_0) = -e\phi(\omega, \vec{r}, \vec{r}_0)$, which in real space reads

$$-\frac{\epsilon_0}{e^2}\nabla \cdot \left(\boldsymbol{\epsilon}(\vec{r}) \cdot \nabla U^R(\omega, \vec{r}, \vec{r}_0)\right) = \delta(\vec{r} - \vec{r}_0) + \int d^3\vec{r}\chi^R(\omega, \vec{r}, \vec{r}')U^R(\omega, \vec{r}', \vec{r}_0). \tag{5.37}$$

Next we notice that the bare Coulomb interaction is nothing more than the inverse of the Poisson differential operator, which we write as

$$V^{-1} = \frac{\epsilon_0}{e^2}\nabla \cdot \boldsymbol{\epsilon}(\vec{r}) \cdot \nabla. \tag{5.38}$$

With this definition, the self-consistent Poisson equation (5.37) can be written schematically in matrix matrix notation as

$$\boldsymbol{V}^{-1} \cdot \boldsymbol{U}^R = \boldsymbol{I} + \boldsymbol{\chi}^R \cdot \boldsymbol{U}^R, \tag{5.39}$$

where $\boldsymbol{I}$ is the identity operator (the Dirac δ-function in real space). Applying the bare Coulomb interaction as an operator on the left of the previous equation we obtain

$$\boldsymbol{U}^R = \boldsymbol{V} + \boldsymbol{V} \cdot \boldsymbol{\chi}^R \cdot \boldsymbol{U}^R. \tag{5.40}$$

This equation has the exact same structure as Eq. (5.32). By performing a Fourier transform in the in-plane coordinates and by noticing that the density-density correlation function in the double layer structure only has support at $z = z' = 0$ and $z = z' = d$, we obtain exactly the same equation as in Eq. (5.32). As a matter of fact, the Dyson equation for the screened interaction, Eq. (5.32), is nothing more than the integral form of the self-consistent Poisson equation, Eq. (5.37).

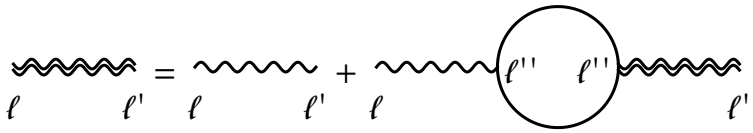

Figure 5.2: Diagrammatic representation of the Dyson coupled equations for the screening of the Coulomb interaction by the charge carriers of a metallic double layer structure, Eq. (5.32). The wavy double line represents the dressed Coulomb interaction, while the wavy single line represents the bare interaction. The bubble represents the irreducible density-density correlations function of each layer, $\chi_{\ell''}$. Summation over ℓ'' is implied.

5.2.2 *Low temperature, large separation and high density universal behaviour*

We are now interested in determining the low temperature, large separation and high density form of the drag resistivity between two arbitrary metallic layers. We will keep the electronic dispersion relation of each layer, $\epsilon_{\mathbf{k},\lambda,\ell}$, the overlap factor $\rho^{\lambda',\lambda}_{\ell,\mathbf{k}+\mathbf{q},\mathbf{k}}$ and dependence of the transport time $\tau^{\text{tr}}_{\mathbf{k},\lambda,\ell}$ on momentum arbitrary. The only restrictions we impose is that the system displays isotropy and that a single band, which we will refer to as the conduction band and denote it by $\lambda = c$, crosses the Fermi level in each layer.

5.2.2.1 *Low temperature limit*

We will study the drag conductivity in the limit of low temperatures, that is $k_B T \ll \epsilon_{F,1/2}$, with $\epsilon_{F,\ell}$ the chemical potential of layer ℓ. The central idea in the following discussion is that close to the Fermi level we can linearise the electronic dispersion relation in the conduction band as [1]

$$\epsilon_{\mathbf{k},c,\ell} \simeq \epsilon_{F,\ell} + \hbar v_{F,\ell} \left(|\mathbf{k}| - k_{F,\ell} \right), \tag{5.41}$$

where $v_{F,\ell}$ is Fermi velocity, which is nothing but the slope of the band at the Fermi level and in general will depend on the value of Fermi energy. Notice for graphene within the Dirac model the electronic dispersion is linear, such that Eq. (5.41) is actually an equality and the Fermi velocity is a constant.

Due to the factor $1/\sinh^2\left(\omega/\left(2k_B T\right)\right)$ that appears in Eq. (5.7) for the transconductivity, the main contribution to the integral over energy will be due to the region with $\omega \lesssim k_B T$. Since we are assuming that $\epsilon_{F,1/2} \gg k_B T$, we can therefore expand the remaing integrand in Eq. (5.7) to lowest order in ω and then set $T = 0$. Therefore, we will replace the dielectric function for the coupled double layer structure, Eq. (5.34) by its static value $\epsilon_{\text{dbl}}(0, \mathbf{q})$. At the same time we expand the non-linear susceptibility, Eq. (5.8), to lowest order in ω. To do so we first notice that the δ-function that appears in Eq. (5.8), $\delta\left(\omega + \epsilon_{\mathbf{k}+\mathbf{q},\lambda',\ell} - \epsilon_{\mathbf{k},\lambda,\ell}\right)$, in the limit of vanishing ω forces both band indices to be the same, $\lambda = \lambda'$. Furthermore, the δ-function can be used to expand the difference of Fermi functions that appears in Eq. (5.8) as

$$f(\epsilon_{\mathbf{k}+\mathbf{q},\lambda,\ell}) - f(\epsilon_{\mathbf{k},\lambda,\ell}) = f(\epsilon_{\mathbf{k},\lambda,\ell} - \omega) - f(\epsilon_{\mathbf{k},\lambda,\ell}) \simeq -\omega \frac{\partial f(\epsilon_{\mathbf{k},\lambda,\ell})}{\partial \epsilon}. \tag{5.42}$$

1 We are excluding cases where the Fermi level crosses a van Hove singularity, in which case for some $\mathbf{k}$ point in the Fermi surface we will have $\nabla_{\mathbf{k}} \epsilon_{\mathbf{k},\lambda,\ell} = 0$.

After doing this and to lowest order in ω, we we can set $\omega = 0$ in the δ-function. The derivative of the Fermi function will the strongly peaked at the Fermi level for low temperatures and can be approximated by a δ-function, such that in this limit only the conduction band will contribute to the non-linear susceptibility. To lowest order in ω the non-linear susceptibility thus becomes

$$\begin{aligned}\boldsymbol{\Delta}_\ell(\omega,\mathbf{q}) = \omega g_\ell \frac{2\pi}{A}\sum_{\mathbf{k}}\left|\rho^{c,c}_{\ell,\mathbf{k}+\mathbf{q},\mathbf{k}}\right|^2 \delta\left(\epsilon_{\mathbf{k},c,\ell}-\epsilon_F\right)\delta\left(\epsilon_{\mathbf{k}+\mathbf{q},c,\ell}-\epsilon_{\mathbf{k},c,\ell}\right)\times \\ \times\left(\tau^{\mathrm{tr}}_{\mathbf{k}+\mathbf{q},c,\ell}\mathbf{v}_{\mathbf{k}+\mathbf{q},c,\ell}-\tau^{\mathrm{tr}}_{\mathbf{k},c,\ell}\mathbf{v}_{\mathbf{k},c,\ell}\right)+\mathcal{O}\left(\omega^2\right). \qquad (5.43)\end{aligned}$$

Assuming isotropy we can write $\tau^{\mathrm{tr}}_{\mathbf{k},c,\ell}\mathbf{v}_{\mathbf{k},c,\ell} = \mathbf{k}w_\ell\left(|\mathbf{k}|\right)$, where $w_\ell\left(|\mathbf{k}|\right)$ is a generic function that only depends on $|\mathbf{k}|$ and that by its very definition satisfies $|\mathbf{k}|\,w_\ell\left(|\mathbf{k}|\right) = \tau^{\mathrm{tr}}_{\mathbf{k},c,\ell}|\mathbf{v}_{\mathbf{k},c,\ell}|$. Due to the two δ-functions that appear in Eq. (5.43), we have that both $\mathbf{k}$ and $\mathbf{k}+\mathbf{q}$ are pinned to the Fermi level, $|\mathbf{k}| = |\mathbf{k}+\mathbf{q}| = k_{F,\ell}$. We can therefore write

$$\begin{aligned}\tau^{\mathrm{tr}}_{\mathbf{k}+\mathbf{q},c,\ell}\mathbf{v}_{\mathbf{k}+\mathbf{q},c,\ell}-\tau^{\mathrm{tr}}_{\mathbf{k},c,\ell}\mathbf{v}_{\mathbf{k},c,\ell} &= (\mathbf{k}+\mathbf{q})\,w\left(|\mathbf{k}+\mathbf{q}|\right)-\mathbf{k}w\left(|\mathbf{k}|\right)\\ &= w\left(k_{F,\ell}\right)\mathbf{q} = \frac{\tau^{\mathrm{tr}}_{F,\ell}v_{F,\ell}}{k_{F,\ell}}\mathbf{q}. \qquad (5.44)\end{aligned}$$

The non-linear susceptibility is thus given by

$$\boldsymbol{\Delta}_\ell(\omega,\mathbf{q}) = g_\ell\frac{2\pi\omega\tau^{\mathrm{tr}}_{F,\ell}v_{F,\ell}}{k_{F,\ell}}\mathbf{q}\frac{1}{A}\sum_{\mathbf{k}}\left|\rho^{c,c}_{\ell,\mathbf{k}+\mathbf{q},\mathbf{k}}\right|^2\delta\left(\epsilon_{\mathbf{k},c,\ell}-\epsilon_F\right)\delta\left(\epsilon_{\mathbf{k}+\mathbf{q},c,\ell}-\epsilon_{\mathbf{k},c,\ell}\right)+\mathcal{O}\left(\omega^2\right). \qquad (5.45)$$

Notice that in this limit, since both $\mathbf{k}$ and $\mathbf{k}+\mathbf{q}$ are pinned to the Fermi energy, the values of $\mathbf{q}$ are restricted by $|\mathbf{q}| < 2k_{F,\ell}$. The summation over $\mathbf{k}$ can be performed by turning the sum into an integral and then performing the change of variables

$$u = \cos\theta_{\mathbf{k},\mathbf{q}} = \frac{\mathbf{k}\cdot\mathbf{q}}{|\mathbf{k}|\,|\mathbf{q}|}, \qquad (5.46)$$

after which the integration over $\mathbf{k}$ can be performed using the δ-functions as

$$\begin{aligned}&\int\frac{d^2\mathbf{k}}{(2\pi)^2}\left|\rho^{c,c}_{\ell,\mathbf{k}+\mathbf{q},\mathbf{k}}\right|^2\delta\left(\epsilon_{\mathbf{k},c,\ell}-\epsilon_{F,\ell}\right)\delta\left(\epsilon_{\mathbf{k}+\mathbf{q},c,\ell}-\epsilon_{\mathbf{k},c,\ell}\right) =\\ &\quad= \frac{2}{4\pi^2}\int_0^\infty dk k\int_{-1}^{+1}\frac{du}{\sqrt{1-u^2}}\left|\rho^{c,c}_{\ell,\mathbf{k}+\mathbf{q},\mathbf{k}}\right|^2\frac{\delta\left(k-k_{F,\ell}\right)}{\hbar v_{F,\ell}}\frac{\delta\left(u+\frac{|\mathbf{q}|}{2k_{F,\ell}}\right)}{\hbar v_{F,\ell}q}\\ &\quad= \frac{k_{F,\ell}}{2\pi^2\left(v_{F,\ell}\hbar\right)^2|\mathbf{q}|}\frac{1}{\sqrt{1-\left(\frac{|\mathbf{q}|}{2k_{F,\ell}}\right)^2}}\left|\rho^{c,c}_{\ell,\mathbf{k}+\mathbf{q},\mathbf{k}}\right|^2\Bigg|_{|\mathbf{k}|=k_{F,\ell},u=-\frac{|\mathbf{q}|}{2k_{F,\ell}}}. \qquad (5.47)\end{aligned}$$

The non-linear susceptibility to lowest order in ω and in the low temperature limit is thus given by

$$\boldsymbol{\Delta}_\ell(\omega,\mathbf{q}) = g_\ell\frac{\omega\tau^{\mathrm{tr}}_{F,\ell}}{\pi v_{F,\ell}\hbar^2}\frac{\mathbf{q}}{|\mathbf{q}|}\frac{\Theta\left(2k_{F,\ell}-|\mathbf{q}|\right)}{\sqrt{1-\left(\frac{|\mathbf{q}|}{2k_{F,\ell}}\right)^2}}\left|\rho^{c,c}_{\ell,\mathbf{k}+\mathbf{q},\mathbf{k}}\right|^2\Bigg|_{|\mathbf{k}|=k_{F,\ell},u=-\frac{|\mathbf{q}|}{2k_{F,\ell}}}. \qquad (5.48)$$

This is the central result to this section. It shows that in the limit of low temperature and high density, the non-linear susceptibility is independent of both the energy dispersion relation of the electrons and their transport time dependence on momentum, depending only on the particular form of the wavefunction overlap factors $\rho^{c,c}_{\ell,\mathbf{k}+\mathbf{q},\mathbf{k}}$. It has

been also pointed out in Refs. [168, 169] that the non-linear susceptibility in graphene is independent of transport time dependence on momentum, but Eq. (5.48) is more general and can be readily applied to the case of a 2DEG, graphene, bilayer graphene, and other 2D systems, being an universal result that only requires an isotropic Fermi surface with only one band crossing it. This universal result also contradicts Ref. [167], where different results for the non-linear susceptibility of graphene, in the low ω limit, where obtained for different dependencies of the transport time on momentum.

Since the low temperature limit selects the low frequency dependence of the non-linear susceptibility, which we found to be $\mathbf{\Delta}_\ell(\omega,\mathbf{q}) \propto \omega$. In this limit, the dependence on momentum and frequency of $\mathbf{\Delta}_\ell(\omega,\mathbf{q})$ factors, allowing to perform the integration over frequency in Eq. (5.7), which yields

$$\sigma_{12}^{ij} \propto \frac{1}{k_B T}\int \frac{d\omega \omega^2}{\sinh^2\left(\frac{\omega}{2k_B T}\right)} = \frac{8\pi^2}{3}\left(k_B T\right)^2, \tag{5.49}$$

and we obtain that in the low temperature limit the drag conductivity and resistivity depend on temperature as T^2. Once again we emphasize that this result is independent on the details of the system as energy dispersion relation, transport times and wavefunction structure. We notice however, that this T^2 behaviour might be modified if higher order corrections to the drag in the interlayer interaction are considered [182].

5.2.2.2 *Large separation and strong screening limits*

We will now further assume that the interlayer separation d is large compared with the Fermi momentum in both layers, that is $k_{F,1/2}d \gg 1$. From Eqs. (5.25) and (5.33), we see that the interlayer interaction is suppressed for large values of transferred momentum as $U_{12}^R(\omega,\mathbf{q}) \sim e^{-|\mathbf{q}|d}$, such that the main contribution for the drag conductivity will come from values of $\mathbf{q}$ such that $|\mathbf{q}| \lesssim d^{-1}$. Therefore, the condition $d^{-1} \ll k_{F,1/2}$ allows us to expand the remaining integrand in Eq. (5.7) to lowest order in $\mathbf{q}$. To lowest order in $\mathbf{q}$ the wavefunction overlap factor $\rho^{c,c}_{\ell,\mathbf{k}+\mathbf{q},\mathbf{k}}$ is 1. Therefore, in the limit of large layer separation and low temperature, using Eq. (5.48) we can approximate the non-linear susceptibility as

$$\mathbf{\Delta}_\ell(\omega,\mathbf{q}) \simeq g_\ell \frac{\omega \tau^{\mathrm{tr}}_{F,\ell}}{\pi v_{F,\ell}\hbar^2}\frac{\mathbf{q}}{|\mathbf{q}|}, \tag{5.50}$$

an universal result that is independent of all the details of the system. Notice that although is is clear that in the low temperature limit $\mathbf{\Delta}_\ell(\omega,\mathbf{q})$ should only depend on quantities defined at the Fermi level, such as the Fermi energy, momentum and velocity, it is not obvious at first that changing the momentum dependence of $\epsilon_{\mathbf{k},\lambda,\ell}$ or $\tau^{\mathrm{tr}}_{\mathbf{k},\lambda,\ell}$ will not change the dependence of $\mathbf{\Delta}_\ell(\omega,\mathbf{q})$ on $\mathbf{q}$ in this limit. In the limit of $|\mathbf{q}| \ll k_{F,1/2}$ the density-density correlation function is approximated by $\chi_\ell^R(0,\mathbf{q}) \simeq -\mathrm{DoS}_\ell(\epsilon_{F,\ell})$, where $\mathrm{DoS}_\ell(\epsilon)$ is the density of states of layer ℓ. Therefore we can write the dielectric function of the double layer structure Eq. (5.34) as

$$\epsilon_{\mathrm{dbl}}(0,\mathbf{q}) \simeq 1 + \frac{k_{TF,1}+k_{TF,2}}{|\mathbf{q}|} + \frac{k_{TF,1}k_{TF,2}}{|\mathbf{q}|^2}\left(1-e^{-2|\mathbf{q}|d}\right), \tag{5.51}$$

where

$$k_{TF,\ell} = \frac{e^2}{2\bar{\epsilon}\epsilon_0}\mathrm{DoS}_\ell(\epsilon_{F,\ell}) \tag{5.52}$$

is the Thomas-Fermi screening momentum for layer ℓ, and used Eq. (5.31) to write the bare interaction in the small $\mathbf{q}$ limit as

$$V_{\ell\ell'}(\mathbf{q}) \simeq \frac{e^2}{2\bar{\epsilon}\epsilon_0 |\mathbf{q}|} e^{-|\mathbf{q}|d\left(1-\delta_{\ell,\ell'}\right)}, \tag{5.53}$$

with $\bar{\epsilon} = (\epsilon_1 + \epsilon_3)/2$ is the low momentum effective dielectric constant for the layered structure. In Eq. (5.53), we have ignored effects of the anisotropy of the dielectric medium, the case of an uniaxial material can be taken into account by replacing $\bar{\epsilon}$ by Eq. (5.31) an replacing $d \to d\sqrt{\epsilon_{\perp,2}/\epsilon_{\parallel,2}}$.

Assuming that the screening length is small compared to the interlayer distance, $k_{TF,1/2}d \gg 1$, the condition $|\mathbf{q}| \lesssim d^{-1}$ implies that $|\mathbf{q}| \ll k_{TF,1/2}$ and therefore we can further approximate Eq. (5.51) as

$$\epsilon_{\text{dbl}}(0,\mathbf{q}) \simeq \frac{k_{TF,1}k_{TF,2}}{|\mathbf{q}|^2}\left(1 - e^{-2|\mathbf{q}|d}\right). \tag{5.54}$$

If the dispersion relation is given by a power law, $\epsilon_{\mathbf{k},c,\ell} = C_\ell |\mathbf{k}|^{\nu_\ell}$ we have in 2D that $k_{TF,\ell} \propto k_{F,\ell}^{2-\nu_\ell}$. Therefore, for a linear dispersion relation, as for graphene, the condition $k_{TF,\ell}d \gg 1$ is equivalent to $k_{F,\ell}d \gg 1$, while for a parabolic dispersion relation $k_{TF,\ell}$ is independent of the Fermi momentum and the condition $k_{TF,\ell}d \gg 1$ is actually an extra assumption.

If we now use Eqs. (5.50) and (5.54) in Eq. (5.7), the integration over momentum and frequency can be easy performed and we obtain the following expression for the (scalar) drag conductivity

$$\sigma_{12} = \frac{e_1 e_2}{\hbar}\frac{\zeta(3) g_1 g_2}{16}\frac{e_1^2}{4\pi\epsilon_0\bar{\epsilon}v_{F,1}\hbar}\frac{e_2^2}{4\pi\epsilon_0\bar{\epsilon}v_{F,2}\hbar}\frac{\tau_{F,1}^{\text{tr}}\tau_{F,2}^{\text{tr}}(k_BT)^2}{\hbar^2(k_{TF,1}d)^2(k_{TF,2}d)^2}. \tag{5.55}$$

This result is valid for $\epsilon_{F,1/2}/(k_BT)$, $k_{F,1/2}d$, $k_{TF,1/2}d \gg 1$ and is universal in the sense that it does not depend on the particular forms of the energy dispersion relations, transport time dependence on momentum or wave function structure, only assuming isotropy and that a single band crosses the Fermi level in each layer. We obtain the familiar 2DEG result of a T^2 and d^{-4} behaviour for the drag conductivity, proving that it is indeed a much more general result. If the metallic layers are immersed in a uniaxial material Eq. (5.55) still holds provided we make the replacements $\bar{\epsilon} \to \left(\epsilon_{\parallel,1}\sqrt{\epsilon_{\perp,1}/\epsilon_{\parallel,1}} + \epsilon_{\parallel,3}\sqrt{\epsilon_{\perp,3}/\epsilon_{\parallel,3}}\right)/2$ and $d \to d\sqrt{\epsilon_{\perp,2}/\epsilon_{\parallel,2}}$.

If we now use the Boltzmann result for the intralayer conductivity Eq. (5.9) while noticing that the in 2D the density of states for an isotropic system can be written in general as

$$\text{DoS}_\ell(\epsilon_{F,\ell}) = \frac{g_\ell}{2\pi}\frac{k_{F,\ell}}{v_{F,\ell}\hbar} \tag{5.56}$$

and that the carrier density, n_ℓ, is related to the Fermi momentum in 2D as

$$k_{F,\ell} = \sqrt{\frac{4\pi n_\ell}{g_\ell}}, \tag{5.57}$$

we can write the drag resistivity in terms of the carrier density as

$$\rho_{\text{Drag}} = -\frac{\hbar}{e_1 e_2}\frac{\zeta(3)}{2^6\pi\sqrt{g_1 g_2}}\left(\frac{4\pi\bar{\epsilon}\epsilon_0}{e_1^2}\right)\left(\frac{4\pi\bar{\epsilon}\epsilon_0}{e_2^2}\right)\frac{(k_BT)^2}{n_1^{3/2}n_2^{3/2}d^4}. \tag{5.58}$$

This result, in the context of drag in 2DEG's, is generally referred to as the Fermi liquid result. Notice that while the drag conductivity depends explicitly on $\tau^{\rm tr}_{F,1/2}$, this dependence disappears when we consider the drag resistivity. It is also usual to express the drag resistivity in terms of the Fermi and Thomas-Fermi screening momenta. To do this we assume a power law dispersion relation, $\epsilon_{\mathbf{k},c,\ell} = C_\ell \left|\mathbf{k}\right|^{\nu_\ell}$, and obtain

$$\rho_{\rm Drag} = -\frac{\hbar}{e_1 e_2}\frac{\zeta(3)\pi^2}{\nu_1 g_1 \nu_2 g_2}\frac{\left(k_B T\right)^2}{\epsilon_{F,1}\epsilon_{F,2}}\frac{1}{\left(k_{F,1}d\right)\left(k_{F,2}d\right)\left(k_{TF,1}d\right)\left(k_{TF,2}d\right)}. \tag{5.59}$$

For drag between two 2DEG, $\nu_{1/2} = 2$, $g_{1/2} = 2$ (spin degeneracy), and we reobtain the known formula from Ref. [158]. For graphene, we obtain exactly the same result, since $\nu_{1/2} = 1$ but $g_{1/2} = 4$ (spin and valley degeneracy). Finally, for the case where each of the two layers are formed by graphene bilayers, $\nu_{1/2} = 2$, $g_{1/2} = 4$ (spin and valley degeneracy), we have an extra factor of $1/4$ when compared with the result for drag between two 2DEG's or two graphene layers.

A comment regarding the region of validity of Eq. (5.58) is in order. We derived it making the assumptions of: (i) low temperature, $\epsilon_{F,1/2} \gg k_B T$; (ii) large separation, $k_{F,1/2}d \gg 1$; and (iii) strong screening $k_{TF,1/2}d \gg 1$. As a matter of fact there is a fourth condition that was not made explicit before, and requires that $k_B T \ll v_{F,1/2}\hbar d^{-1}$. This was originally pointed out in Refs. [44, 45] and recently emphasized in Ref. [183]. This additional condition comes from the fact that in the small frequency limit the energy δ-function, $\delta\left(\omega + \epsilon_{\mathbf{k}+\mathbf{q},\lambda',\ell} - \epsilon_{\mathbf{k},\lambda,\ell}\right)$, in Eq. (5.8) for the non-linear susceptibility can actually only be satisfied when $\omega < v_{F,\ell}\hbar\left|\mathbf{q}\right|$, such that the complete expression for the non-linear susceptibility to lowest order in ω is given by

$$\mathbf{\Delta}_\ell(\omega,\mathbf{q}) = g_\ell \frac{\omega\tau^{\rm tr}_{F,\ell}}{\pi v_{F,\ell}\hbar^2}\frac{\mathbf{q}}{\left|\mathbf{q}\right|}\frac{\Theta\left(2k_{F,\ell} - \left|\mathbf{q}\right|\right)\Theta\left(v_{F,\ell}\hbar\left|\mathbf{q}\right| - \omega\right)}{\sqrt{1 - \left(\frac{\left|\mathbf{q}\right|}{2k_{F,\ell}}\right)^2}}\left|\rho^{c,c}_{\ell,\mathbf{k}+\mathbf{q},\mathbf{k}}\right|^2\Big|_{\left|\mathbf{k}\right|=k_{F,\ell},u=-\frac{\left|\mathbf{q}\right|}{2k_{F,\ell}}}, \tag{5.60}$$

such that the integrations in frequency and momentum (5.7) are not completely decoupled. Since the frequency integral is cutoff at $k_B T$ and the integration in momentum is cutoff by d^{-1}, provided we have $k_B T \ll v_F\hbar d^{-1}$, the conditional $\omega < v_{F,\ell}\hbar\left|\mathbf{q}\right|$ does not provide any additional constrain and the integrals effectively decouple, leading to the T^2 (and d^{-4}behaviour assuming strong screening) behaviour. If $k_B T \gtrsim v_F\hbar d^{-1}$ the integral in frequency and momentum to not decouple leading to deviations from the universal result Eq. (5.58). Therefore, Eq. (5.58) will actually be violated at large enough separations and is only valid provided that $k_{F,1/2}$, $k_{TF,1/2} \ll d \ll v_F\hbar/\left(k_B T\right)$ and $\epsilon_{F,1/2} \gg k_B T$.

5.3 COULOMB DRAG IN GRAPHENE

While the discussion in the previous section was generic, we will now specialize to the case of Coulomb drag between two graphene layers. We have argued that in the low temperature limit, $\epsilon_{F,1/2} \gg k_B T$, the drag resistivity was insensitive to the dependence of the transport time on momentum, but in general such dependence will be important. Experimentally it is known that the transport time in graphene should depend linearly on momentum or energy [174]. Therefore, we write the transport time in graphene $\tau^{\rm tr}_{\mathbf{k},\lambda,\ell} = \tilde{\tau}_{0,\ell}\left|\mathbf{k}\right|$, where $\tilde{\tau}_{0,\ell}$ is a constant with units of length$\times$time. This linear dependence of the transport time on momentum can be explained in cases when the dominant source of scattering are short-range resonant scatters or charged Coulomb impurities

[174]. Under the assumption of a transport time that depends linearly on momentum, the non-linear susceptibility for graphene can be written as

$$\boldsymbol{\Delta}_\ell(\omega,\mathbf{q}) = \frac{8\pi}{A}\tilde{\tau}_{0,\ell}v_F \sum_{\mathbf{k},\lambda,\lambda'} \left|\rho^{\lambda',\lambda}_{\ell,\mathbf{k}+\mathbf{q},\mathbf{k}}\right|^2 \left(\lambda'\left(\mathbf{k}+\mathbf{q}\right)-\lambda\mathbf{k}\right)\times \\ \times\left(f(\epsilon_{\mathbf{k}+\mathbf{q},\lambda',\ell})-f(\epsilon_{\mathbf{k},\lambda,\ell})\right)\delta\left(\omega+\epsilon_{\mathbf{k}+\mathbf{q},\lambda',\ell}-\epsilon_{\mathbf{k},\lambda,\ell}\right), \quad (5.61)$$

where the band indices for graphene run over $\lambda,\lambda' = \pm 1$, v_F is the constant Fermi velocity of graphene and the wavefunction overlap factor is given by, see Eq. (4.39),

$$\left|\rho^{\lambda',\lambda}_{\ell,\mathbf{k}+\mathbf{q},\mathbf{k}}\right|^2 = \frac{1}{2}\left(1+\lambda\lambda'\cos\theta_{\mathbf{k}+\mathbf{q},\mathbf{k}}\right). \quad (5.62)$$

We will assume that both graphene layers are highly doped with electrons, such that both interband contributions and valence intraband contributions can be neglected allowing us to consider only the case with $\lambda=\lambda'=+1$. With this approximation, the non-linear susceptibility for graphene becomes

$$\boldsymbol{\Delta}_\ell(\omega,\mathbf{q}) \simeq \mathbf{q}\frac{8\pi}{A}\tilde{\tau}_{0,\ell}v_F \sum_{\mathbf{k}} \left|\rho^{+,+}_{\ell,\mathbf{k}+\mathbf{q},\mathbf{k}}\right|^2 \times \\ \times\left(f(\epsilon_{\mathbf{k}+\mathbf{q},+,\ell})-f(\epsilon_{\mathbf{k},+,\ell})\right)\delta\left(\omega+\epsilon_{\mathbf{k}+\mathbf{q},+,\ell}-\epsilon_{\mathbf{k},+,\ell}\right). \quad (5.63)$$

Comparing this expression with the density-density correlation function of graphene, which is given by, see Appendix E,

$$\chi^R_\ell\left(\omega,\mathbf{q}\right) = \frac{4}{A}\sum_{\mathbf{k},\lambda,\lambda'}\left|\rho^{\lambda',\lambda}_{\ell,\mathbf{k}+\mathbf{q},\mathbf{k}}\right|^2 \frac{f(\epsilon_{\mathbf{k}+\mathbf{q},\lambda',\ell})-f(\epsilon_{\mathbf{k},\lambda,\ell})}{\omega+i0^+ +\epsilon_{\mathbf{k}+\mathbf{q},\lambda',\ell}-\epsilon_{\mathbf{k},\lambda,\ell}} \quad (5.64)$$

we conclude that the conduction band of the non-linear susceptibility is proportional to the imaginary part of the conduction band contribution to the density-density correlation function. Namely, Eq. (5.63) can be written as

$$\boldsymbol{\Delta}_\ell(\omega,\mathbf{q}) = -2\tilde{\tau}_{0,\ell}v_F\mathbf{q}\mathrm{Im}\chi^R_{+,+,\ell}\left(\omega,\mathbf{q}\right), \quad (5.65)$$

where $\chi^R_{+,+,\ell}\left(\omega,\mathbf{q}\right)$ is the $\lambda=\lambda'=+1$ contribution to Eq. (5.64). For high doping, we can approximate the density-density correlation function by its zero temperature value. This can be evaluated analytically [151] and one obtains, see Appendix E,

$$\mathrm{Im}\chi^R_{+,+,\ell}(\omega,\mathbf{q}) = -\frac{|\mathbf{q}|^2}{4\pi\sqrt{\left(v_F\hbar\left|\mathbf{q}\right|\right)^2-\omega^2}}\Phi_\ell\left(\omega,\mathbf{q}\right), \quad (5.66)$$

with $\Phi_\ell\left(\omega,\mathbf{q}\right)$ defined as

$$\Phi_\ell\left(\omega,\mathbf{q}\right) = \begin{cases} F\left(\frac{2\epsilon_{F,\ell}+\omega}{v_F\hbar|\mathbf{q}|}\right)-F\left(\frac{2\epsilon_{F,\ell}-\omega}{v_F\hbar|\mathbf{q}|}\right) & , \frac{\omega}{\epsilon_F} < \min\left(\frac{|\mathbf{q}|}{k_{F,\ell}}, 2-\frac{|\mathbf{q}|}{k_{F,\ell}}\right) \\ F\left(\frac{\omega+2\epsilon_{F,\ell}}{v_F\hbar|\mathbf{q}|}\right) & , \left|\frac{|\mathbf{q}|}{k_{F,\ell}}-2\right| < \frac{\omega}{\epsilon_F} < \frac{|\mathbf{q}|}{k_{F,\ell}} \end{cases}, \quad (5.67)$$

where the $F(x)$ function is given by $F(x) = x\sqrt{x^2-1} - \mathrm{arccosh}(x)$. The drag conductivity for graphene is thus given by

$$\sigma_{12} = \frac{e^2\tilde{\tau}_{0,1}\tilde{\tau}_{0,2}}{2^7\pi^4\hbar^4 k_B T}\int_0^\infty dq q^5 \int_0^\infty \frac{d\omega}{\sinh^2\left(\frac{\omega}{2k_BT}\right)}\frac{\Phi_1\left(\omega,q\right)\Phi_2\left(\omega,q\right)}{1-\left(\frac{\omega}{v_F\hbar q}\right)^2}. \quad (5.68)$$

	ϵ_∞	ω_{TO} [meV]	f	γ [meV]
$\epsilon_\perp$	4.95	170	1.868	3.61
$\epsilon_\parallel$	4.10	97.4	0.532	0.995

Table 5.1: Parameters for the dielectric function of hBN that enter Eq. (5.79). Taken from Ref. [184].

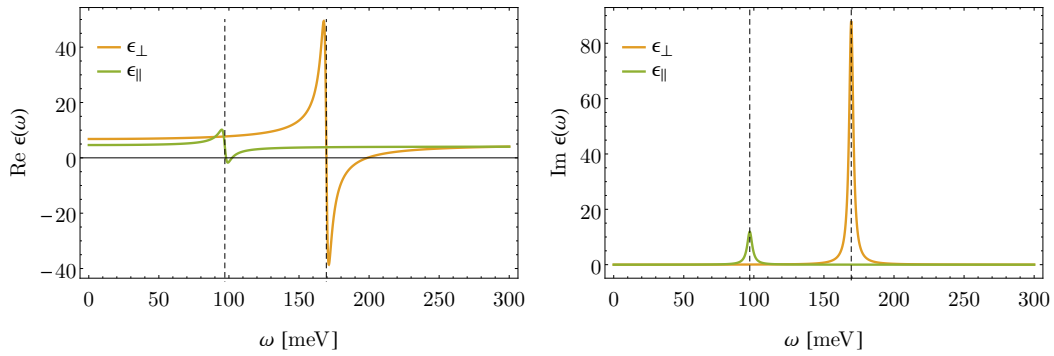

Figure 5.3: Plot of the real and imaginary parts of components of the dielectric tensor of hBN.

Using the Eq. (5.9) to graphene's intralayer conductivity at low temperature as

$$\sigma_{\ell\ell} = \frac{e^2}{\hbar}\frac{\epsilon_{F,\ell}^2 \tilde{\tau}_{0,\ell}}{v_F \hbar^2}, \tag{5.69}$$

where we we have written the transport time in terms of the Fermi energy as $\tau_{F,\ell}^{\text{tr}} = \tilde{\tau}_{0,\ell} k_{F,\ell} = \tilde{\tau}_{0,\ell}\epsilon_{F,\ell}/(v_F\hbar)$, using Eqs. (G.2) and (5.25) for the interlayer interaction and performing a change of variables $x = q/\tilde{k}_F$ and $y = \omega/\tilde{\epsilon}_F$, with $\tilde{k}_F = \sqrt{k_{F,1}k_{F,2}}$and $\tilde{\epsilon}_F = \sqrt{\epsilon_{F,1}\epsilon_{F,2}}$ the drag resistivity for graphene can be written as

$$\rho_{\text{Drag}} = -\frac{1}{2^5}\frac{\hbar}{e^2}\frac{\sqrt{\epsilon_{F,1}\epsilon_{F,2}}}{k_B T}\alpha_g^2 \int_0^\infty dx x^3 \int_0^\infty dy \mathcal{G}\left(x, y, k_{F,1}, k_{F,2}, d\right), \tag{5.70}$$

where we have introduced the function $\mathcal{G}\left(x, y, k_{F,1}, k_{F,2}, d\right)$ as

$$\mathcal{G}\left(x, y, k_{F,1}, k_{F,2}, d\right) = \frac{1}{\sinh^2\left(y\frac{\tilde{\epsilon}_F}{2k_B T}\right)} \times \\ \times \frac{e^{-2\sqrt{\frac{\epsilon_{\perp,2}}{\epsilon_{\parallel,2}}}d\tilde{k}_F x}}{\epsilon_{12}^2\left(x\tilde{k}_F\right)\left|\epsilon_{\text{dbl}}\left(y\tilde{\epsilon}_F, x\tilde{k}_F\right)\right|^2}\frac{\Phi_1(x\tilde{k}_F, y)\Phi_2(x\tilde{k}_F, y\tilde{\epsilon}_F)}{1-\left(\frac{y}{x}\right)^2}. \tag{5.71}$$

and $\alpha_g = e^2/(4\pi\epsilon_0 v_F\hbar)$ is graphene's fine structure constant. Notice that the dielectric function $\epsilon_{\text{dbl}}(\omega, q)$ involves the density-density correlations functions for the graphene layers. The zero temperature analytical formulas for graphene's density-density correlation function [151] are provided in Appendix E.

5.4 SUBSTRATE OPTICAL PHONON MEDIATED DRAG

We now discuss how the interaction between electrons in the metallic layers and optical phonons of the substrate contributes to the drag resistivity. In polar materials, optical

longitudinal phonons give origin to long range electric potentials that can interact with the electrons in the metallic layers. In its turn, this electron-phonon interaction gives origin to an effective electron-electron interaction that will also contribute to the phenomenon of interlayer drag.

Interaction between electrons and longitudinal optical phonons is generally described in terms of the Frölich Hamiltonian, which in 3D materials reads [185]

$$H_{\text{e-LO}} = \frac{1}{\sqrt{V}} \sum_{\vec{q}} M_{\vec{q}} \rho_{-\vec{q}} i \left(a_{\vec{q}} - a^{\dagger}_{-\vec{q}} \right), \tag{5.72}$$

where $\rho_{-\vec{q}} = \sum_{\vec{k}} \psi^{\dagger}_{\vec{k}} \psi_{\vec{k}-\vec{q}}$ is the electron density operator and $M_{\vec{q}}$ is the longitudinal optical phonon - electron interaction which reads

$$M_{\vec{q}} = \sqrt{\frac{e^2 \omega_{\text{LO}}}{2\epsilon_0 \left|\vec{q}\right|^2} \left(\frac{1}{\epsilon_\infty} - \frac{1}{\epsilon(0)} \right)}, \tag{5.73}$$

where ω_{LO} is the frequency of the longitudinal optical phonon, $\epsilon(0)$ is the static dielectric constant of the medium and ϵ_∞ is the high frequency limit of the dielectric constant of the material. The optical phonons are assumed to be dispersionless such that ω_{LO} is a constant. The electron-phonon interaction described by the Hamiltonian (5.72) gives origin to an phonon mediated retarded electron-electron interaction, which is given by

$$W^R_{\text{ph}}(\omega, \vec{q}) = M_{-\vec{q}} D^R_{\text{LO}}(\omega, \vec{q}) M_{\vec{q}}, \tag{5.74}$$

where $D^R_{\text{LO}}(\omega, \vec{q})$ is the retard optical phonon Green's function which is given by

$$\begin{aligned} D^R_{\text{LO}}(\omega, \vec{q}) &= -i \int_0^\infty dt e^{i(\omega + i0^+)t} \left\langle \left[i \left(a_{\vec{q}}(t) - a^{\dagger}_{-\vec{q}}(t) \right), i \left(a_{\vec{q}}(0) - a^{\dagger}_{-\vec{q}}(0) \right) \right] \right\rangle \\ &= \frac{2\omega_{\text{LO}}}{\omega^2 - \omega^2_{\text{LO}} + i\text{sgn}(\omega) 0^+}, \end{aligned} \tag{5.75}$$

where we have used the fact that the phonon operators evolve in time as $a_{\vec{q}}(t) = e^{-i\omega_{\text{LO}} t} a_{\vec{q}}(0)$.

Besides the phonon mediated interaction, we also have the Coulomb interaction

$$V_{\text{C}}(\vec{q}) = \frac{e^2}{\epsilon_0 \epsilon_\infty \left|\vec{q}\right|^2}, \tag{5.76}$$

where the high frequency dielectric constant, ϵ_∞, takes into account screening by high energy degrees of freedom, such as core electrons. Adding the Coulomb interaction to the phonon mediated interaction, we obtain the effective electron-electron interaction

$$\begin{aligned} V^R(\omega, \vec{q}) &= V_{\text{C}}(\vec{q}) + M_{-\vec{q}} D^R_{\text{LO}}(\omega, \vec{q}) M_{\vec{q}} \\ &= \frac{e^2}{\epsilon_0 \epsilon(\omega) \left|\vec{q}\right|^2}, \end{aligned} \tag{5.77}$$

which the dielectric constant given by the Lorentz model

$$\epsilon(\omega) = \epsilon_\infty + f \frac{\omega^2_{\text{TO}}}{\omega^2_{\text{TO}} - \omega^2 - i\text{sgn}(\omega) 0^+}, \tag{5.78}$$

where ω_{TO} is the frequency of the transverse optical phonon and f is the so called oscillator strength and is is given by $f = \epsilon_\infty \left(\omega^2_{\text{LO}} - \omega^2_{\text{TO}} \right) / \omega^2_{\text{TO}}$. The frequency of

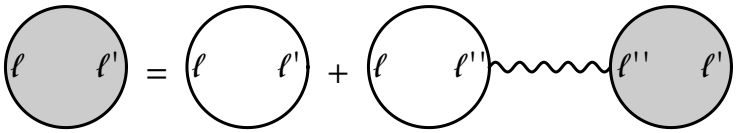

Figure 5.4: Diagrammatic equation of the Dyson equation relating the reducible with the irreducible density-density correlation function, Eq. (5.80). The shaded bubble represent the reducible density-density correlation function, $X_{\ell\ell'}$, while the open bubbles represent the the irreducible correlation function, χ_ℓ, which is diagonal in the layer indices. The wavy double line represents the bare Coulomb interaction. Summation over ℓ'' is implied.

the longitudinal and transverse optical phonons are related via the Lyddane-Sachs-Teller relation $\omega_{\rm LO}^2/\omega_{\rm TO}^2 = \epsilon(0)/\epsilon_\infty$ [186]. The fact that we obtained for the effective electron-electron interaction, when taking into account phonon mediated interaction, the Coulomb interaction with a dielectric constant given by the Eq. (5.78) should come as no surprise. In the original derivation of the Fröhlich Hamiltonian (5.72) [185] the phenomenological dielectric function of a polar material enters as one of its main ingredients. From the above discussion, we see that in order to take into account the substrate longitudinal phonon mediated interaction into the drag resistivity, we just need to replace the dielectric constant in the Poisson equation (5.18) by the frequency dependent dielectric function, of the form of Eq. (5.78), of the the substrate material.

From the above discussion, we see that in order to taken into account the substrate longitudinal phonon mediated interaction into the drag resistivity, we just need to consider a Coulomb interaction with a frequency dependent dielectric function, which is obtained by replacing the dielectric constant in the Poisson equation (5.18) by a frequency dependent dielectric function, $\boldsymbol{\epsilon}(\vec{r}) \to \boldsymbol{\epsilon}(\omega, \vec{r})$, of the form of Eq. (5.78). For an unixial material, such as hBN, the dielectric tensor will become frequency dependent with the in-plane, $\epsilon_\perp(\omega)$, and the out-of-plane, $\epsilon_\parallel(\omega)$, dielectric constants given by

$$\epsilon_{\perp,\parallel}(\omega) = \epsilon_\infty^{\perp,\parallel} + f_{\perp,\parallel} \frac{\left(\omega_{\rm TO}^{\perp,\parallel}\right)^2}{\left(\omega_{\rm TO}^{\perp,\parallel}\right)^2 - \omega^2 - i\omega\gamma_{\perp,\parallel}}, \tag{5.79}$$

where in the above equation we allowed for a finite broadening of the optical phonon, due to its finite lifetime. Experimental values taken from Ref. [184] for the parameters in Eq. (5.79) are presented in Table 5.1. The real and imaginary parts of $\epsilon_{\perp,\parallel}(\omega)$ for hBN are represented in Fig. 5.3.

The inclusion of the effect of substrate phonons will give origin to the appearance of peaks in the screened interlayer interaction $U_{12}^R(\omega, \mathbf{q})$ around the frequencies of the longitudinal phonons. As a matter of fact the peaks will not occur exact at the optical phonon frequencies due to the fact that the optical phonons will hybridize with the charge oscillations, plasmons, of the coupled metallic layers. This phonon-plasmon hybridization is most clearly demonstrated if we study the full, *reducible,* density-density correlation function of the double layer structure taking into account optical phonons. The full reducible density-density correlation function, which we represent (with a capital χ) as $X_{\ell,\ell'}^R(\omega, \mathbf{q})$, is related to the irreducibility density-density correlation function,

$\chi^R_\ell(\omega,\mathbf{q})$, by taking into account screening effects. They are related to each other via the Dyson equation

$$\begin{bmatrix} X^R_{11}(\omega,\mathbf{q}) & X^R_{12}(\omega,\mathbf{q}) \\ X^R_{21}(\omega,\mathbf{q}) & X^R_{22}(\omega,\mathbf{q}) \end{bmatrix} = \begin{bmatrix} \chi^R_1(\omega,\mathbf{q}) & 0 \\ 0 & \chi^R_2(\omega,\mathbf{q}) \end{bmatrix} + \\ + \begin{bmatrix} \chi^R_1(\omega,\mathbf{q}) & 0 \\ 0 & \chi^R_2(\omega,\mathbf{q}) \end{bmatrix} \begin{bmatrix} V_{11}(\mathbf{q}) & V_{12}(\mathbf{q}) \\ V_{21}(\mathbf{q}) & V_{22}(\mathbf{q}) \end{bmatrix} \begin{bmatrix} X^R_{11}(\omega,\mathbf{q}) & X^R_{12}(\omega,\mathbf{q}) \\ X^R_{21}(\omega,\mathbf{q}) & X^R_{22}(\omega,\mathbf{q}) \end{bmatrix}. \quad (5.80)$$

This equation is represented diagrammatically in Fig. 5.4. Notice that while the irreducible density-density correlation function had no interlayer terms, the inclusion of screening effects gives origin to the interlayer terms $X^R_{12}(\omega,\mathbf{q})$ and $X^R_{12}(\omega,\mathbf{q})$ due to the interlayer interactions. Notice that the screening equation for $U^R_{\ell\ell'}(\omega,\mathbf{q})$, Eq. (5.32), can be written in terms of the full density-density correlation function as

$$\begin{bmatrix} U^R_{11}(\omega,\mathbf{q}) & U^R_{12}(\omega,\mathbf{q}) \\ U^R_{21}(\omega,\mathbf{q}) & U^R_{22}(\omega,\mathbf{q}) \end{bmatrix} = \begin{bmatrix} V_{11}(\mathbf{q}) & V_{12}(\mathbf{q}) \\ V_{21}(\mathbf{q}) & V_{22}(\mathbf{q}) \end{bmatrix} + \\ + \begin{bmatrix} V_{11}(\mathbf{q}) & V_{12}(\mathbf{q}) \\ V_{21}(\mathbf{q}) & V_{22}(\mathbf{q}) \end{bmatrix} \begin{bmatrix} X^R_{11}(\omega,\mathbf{q}) & X^R_{12}(\omega,\mathbf{q}) \\ X^R_{21}(\omega,\mathbf{q}) & X^R_{22}(\omega,\mathbf{q}) \end{bmatrix} \begin{bmatrix} V_{11}(\mathbf{q}) & V_{12}(\mathbf{q}) \\ V_{21}(\mathbf{q}) & V_{22}(\mathbf{q}) \end{bmatrix}. \quad (5.81)$$

The full density-density correlation function allows one to define the energy loss function for the double layer structure as [187]

$$S(\omega,\mathbf{q}) = -\mathrm{Im}\sum_\ell X^R_{\ell\ell}(\omega,\mathbf{q}). \quad (5.82)$$

Since $S(\omega,\mathbf{q})$ is defined as the negative of the imaginary part of a retarded Green's function between an operator, $\rho_{\mathbf{q}}$, and its Hermitian conjugate, $\rho_{-\mathbf{q}}$, we have that $\mathrm{sgn}\left[S(\omega,\mathbf{q})\right] = \mathrm{sgn}(\omega)$. Therefore, we restrict ourselves to positive frequencies, we have that $S(\omega,\mathbf{q})$ is positive defined and therefore can be interpreted as a spectral function. Collective excitations due to charge oscillations will appear as peaks in $S(\omega,\mathbf{q})$. In the case where we only have electrons, the peaks in $S(\omega,\mathbf{q})$ correspond to plasmons. The inclusion of electron-phonon interactions will lead to an hybridization of the plasmonic mode with the phonons. This situation is exemplified in Fig. 5.5, where we plot the energy loss function of a graphene double layer structure encapsulated by hBN. It is clear that there is a mixing between the plasmon and the phonon degrees of freedom, which give origin to a new plasmon-phonon hybrid excitation with a new dispersion relation.

5.5 RESULTS FOR COULOMB DRAG IN GRAPHENE-HBN-GRAPHENE STRUCTURES

We will now show the results for Coulomb drag between two graphene layers which are separated by an hBN slab and also encapsulated in hBN, that is, we will focus on a situation where all the three dielectrics in Fig. 5.1 are constituted by hBN. In Fig. 5.6 we show the results obtained for the drag resistivity between the two graphene layers computed using Eq. (5.70). We assume that $\epsilon_{F,1/2} \gg k_B T$ such that the graphene density-density correlation function that appear in the double layer structure dielectric function Eq. (5.34) are approximated by their zero temperature result [151]. For simplicity we consider the situation where both graphene layers are doped with the same

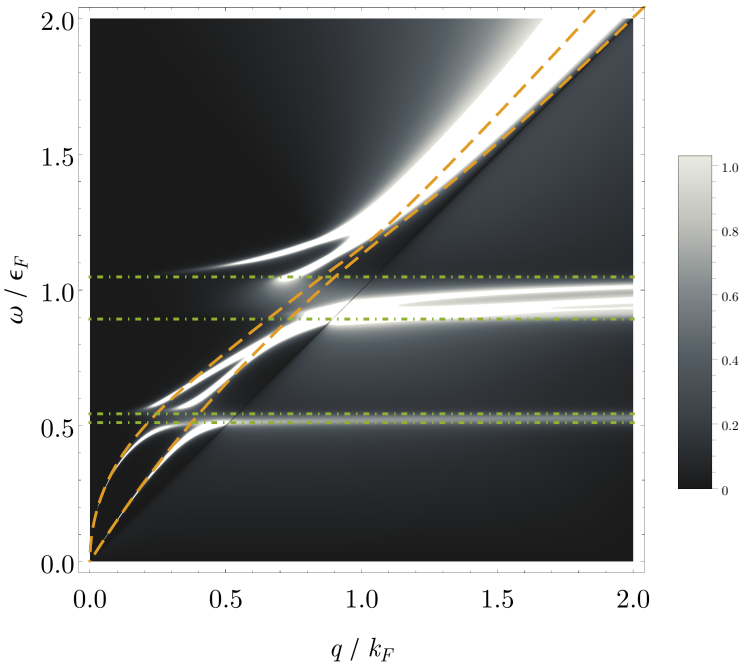

Figure 5.5: Density plot of the energy loss function, $S(\omega, \mathbf{q})$ as defined by Eq. (5.82), for a graphene double layer structure encapsulated by hBN, taking into account the effect of longitudinal optical phonons. The dashed yellow, dashed lines show the dispersion relation of plasmons of the the double layer structure in the absence longitudinal phonons. The horizontal green, dot-dashed lines represent the frequencies of the longitudinal and transverse hBN optical phonons. The hybridization between the graphene plasmons and the hBN phonons is clear. We considered equal electron densities $n_1 = n_2 = 0.02$ nm^{-2} and a layer separation of $d = 8$ nm. $S(\omega, \mathbf{q})$ is normalized by $-\lim_{\mathbf{q}\to 0} \mathrm{Re} \sum_\ell X^R_{\ell\ell}(0, \mathbf{q})$.

electron concentration $n_1 = n_2 = n$. As discussed in the previous section, the effect of the electron-electron interaction mediated by the longitudinal optical phonons of the hBN dielectric is taken into account by replacing the dielectric constants in the bare Coulomb interaction Eq. (5.25) by the frequency dependent dielectric tensor of hBN, which we write as Eq. (5.79) with the parameters taken from Ref. [184] and given in Table 5.1.

In Fig. (5.6) we plot the drag resistivity as a function of temperature, electronic density and layer separation. In Fig. (5.6)(a) we show the drag resistivity as a function of temperature including (Coulomb+phonon) and neglecting (Coulomb only) the hBN phonon mediated interaction. The Coulomb only result is obtained by setting the dielectric function of hBN to its zero frequency value. We also compare the numerical results from Eq. (5.70) with the low temperature, large separation universal result Eq. (5.58), which for the particular case when we have doping of the graphene layers reduces to (it we further assume that $\omega_{\mathrm{TO}}^{\perp/\parallel} \ll k_B T$)

$$\rho_{\mathrm{Drag}}^{\text{Low } T,\text{ large } d} = -\frac{\hbar}{e^2}\frac{\zeta(3)}{2^8\pi\alpha_g^2}\left(\epsilon_{\parallel}^2(0)\frac{\epsilon_{\parallel}(0)}{\epsilon_{\perp}(0)}\right)\frac{(k_B T)^2}{(v_F\hbar)^2 n^3 d^4}. \tag{5.83}$$

with $\alpha_g = e^2/(4\pi\epsilon_0 v_F\hbar)$ the fine structure constant of graphene. As Fig. 5.6(a) shows, the contribution of the phonon mediated interaction to the drag resistivity is vanishingly small at low temperatures. At higher temperatures the additional interaction channel due to the phonon mediated interaction gives origin to an increase in the absolute value of the drag resistivity. This temperature dependence is due the factor $1/\sinh^2\left(y\tilde{\epsilon}_F/\left(2k_B T\right)\right)$ in the integration kernel Eq. (5.71), which suppresses the integrand for values of $y \gtrsim \tilde{\epsilon}_F/k_B T$. Thus at low temperatures, the main contribution to the y-integration in Eq. (5.70) comes from a frequency range where the dielectric functions in the integrand are still close to their static values. However, the phonon contribution already becomes noticeable for $T \gtrsim 150$ K, as is more clearly seen in the linear scale of Fig. 5.6(b), a much lower temperature than one would naively expect, taking into account that the energy of the lowest phonon mode, $\omega_{\mathrm{TO}}^{\parallel}$, corresponds to a temperature of 1100 K. This is mainly due to the fact that the factor $1/\sinh^2\left(y\tilde{\epsilon}_F/\left(2k_B T\right)\right)$ that controls the integration range in energy has relatively long tails, and therefore the effect of phonons is already observable at modest temperatures. It is also curious to notice that in the range from 100 to 250 K, the drag resistivity including the effect of phonons, is closer to the T^2 behaviour than the purely Coulomb drag result. What is happening is that at higher temperatures Eq. (5.83) is not valid anymore and predicts a drag that is higher in absolute value that the full result given by Eq. (5.70). Inclusion of phonons increases the drag when compared to the result obtained neglecting them and this increase in drag approaches the result to the asymptotic value given by Eq. (5.83). This is, however, accidental and results from a partial cancellation of errors as Eq. (5.83) does not take into account electron-phonon interactions in any way.

In Fig. 5.6(b) also illustrates the effect of the anisotropy of hBN in the drag resistivity. In this figure, we compare the drag resistivity between the two graphene layers correctly including the anisotropy of hBN (Uniaxial) with the drag resistivity that would be obtained by replacing hBN with an isotropic material characterized by a dielectric function given by $\epsilon_{\perp}(\omega)$ (Isotropic, $\epsilon_{\perp}$) and $\epsilon_{\parallel}(\omega)$ (Isotropic, $\epsilon_{\parallel}$) , where $\epsilon_{\perp/\parallel}(\omega)$ are the in-plane/out-of-plane dielectric functions of hBN. We also make a comparison between the drag taking into account hBN phonons and neglecting them. It is observed that the effect due to phonons is smallest in the case of isotropic dielectric characterized by $\epsilon_{\perp}(\omega)$ due to the higher value of $\omega_{\mathrm{TO}}^{\perp}$. The effect of the phonons to drag is largest when

correctly taking into account anisotropy, where both in-plane and out-of-plane optical phonons are taken into account.

In Fig. 5.6(c) we show the drag resistivity as a function of electronic densities for different temperatures. It is clear that drag is substancially reduced with the increase of electronic density due to the increase in the screening of the interlayer interaction. There it is also clear that at lower temperatures the effect of phonons is negligible while at higher temperatures if gives origin to a significant increase in the drag resistivity.

Finally, Fig. 5.6(d) shows the drag resistivity as a function of the separation between the graphene layers. Besides comparing the result obtained when neglecting or including the effect of hBN phonons, we also compare the results with the low temperature, large layer separation approximate result Eq. (5.83), which scales as $\rho_{\text{Drag}} \propto d^{-4}$, with a low temperature approximation (Low T) which is computed taking the zero frequency limit of the non-linear susceptibility and interlayer interaction in Eq. (5.70). While it is shown that for small distances the low temperature approximation is in good agreement with the full result, at larger distances there is a significant deviation between the two and consequently between the full result and the low temperature and large separation result. This deviation is a consequence of the deviations from the T^2 result for large enough distances, $k_B T d \gtrsim v_F \hbar$ [44, 45, 183] as discussed at the end of Section 5.2.2.2.

5.6 CONCLUSIONS

In this chapter, we have studied Coulomb drag between two generic metallic layers, paying special attention to the case of drag between two graphene layers and the role played by the phonons of the dielectric environment, such as the one for a graphene double layer structure encapsulated in hBN.

Following very general arguments, we have showed that in the low temperature, high density, large separation and strong screening limits, the drag resistivity has a universal behaviour with temperature as T^2 and layer separation as d^{-4}. We found this result to be independent of the electronic energy dispersion relation and wavefunction structure and momentum dependence of the intralayer transport time, only requiring that the system displays isotropy and that a single electronic band crosses the Fermi level. Thus we generalized the previously known result for the drag resistivity between two 2DEG's, with parabolic dispersion relation and constant transport time, to a much broader class of systems including the cases of graphene and bilayer graphene.

We have seen how the effect of optical phonons of the dielectric environment that surrounds the two metallic layers gives origin to a phonon mediated electron-electron interaction, which is correctly taken into account by simply replacing the dielectric constant of the medium in the bare Coulomb interaction by the Lorentz like frequency dependent dielectric function of the polar medium. We have also seen how anisotropy of the dielectric medium can be taken into account.

For the case of a graphene double layer encapsulated by hBN, we have seen how the phonon mediated electron-electron interaction contributes to a significant increase of the drag resistivity. For large layer separation, $d \simeq 8$ nm, the effect of hBN optical phonons becomes significant for temperatures higher than 150 K. As the lowest phonon resonance frequency in the spacer material hBN corresponds to a temperature of approximately 1100 K, this result seems to be at odds with the notion that phonon effects should only be relevant at temperatures close and higher to the phonon frequencies. This is indeed the case for other transport phenomena, like the substrate limited electron mobility in graphene by remote phonon scattering, where real momen-

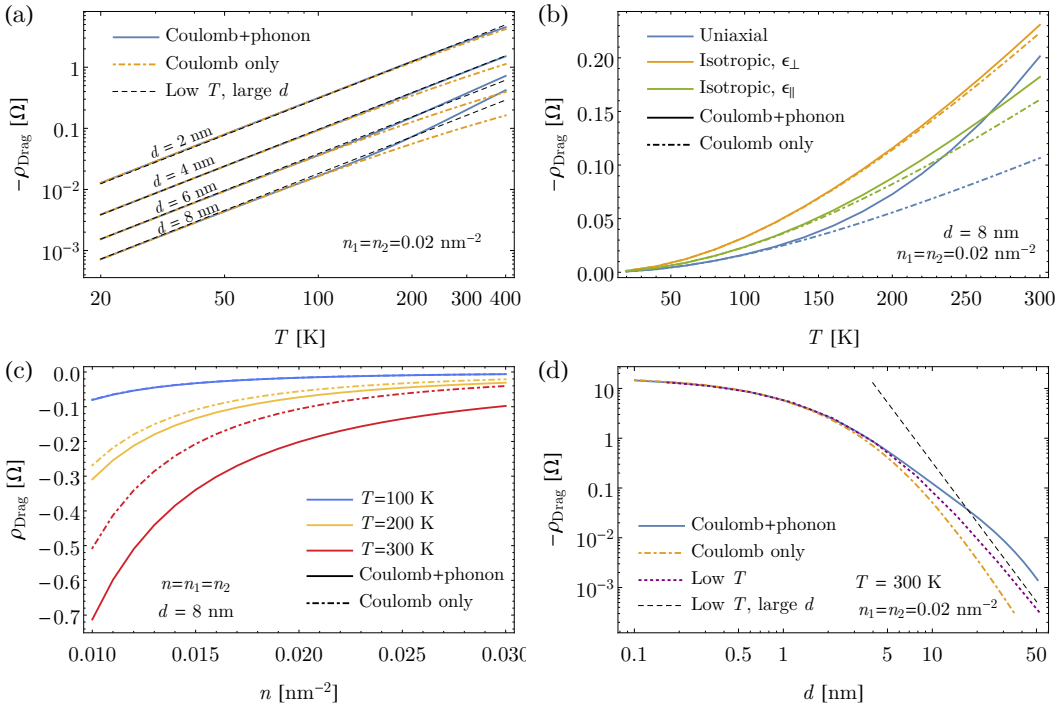

Figure 5.6: Coulomb drag in graphene double layer structure encapsulated in hBN as a function temperature, distance and electronic density. (a) Drag resistivity as a function of temperature as a function of temperature for different graphene separations. (b) Drag as a function of temperature comparing the results obtained when taking hBN as dieletric material encapsulating the graphene layers and isotropic materials with the the in-plane ($\epsilon_\perp$) or out-of-plane ($\epsilon_\parallel$) dielectric function of hBN. (c) Drag as a function of graphene electronic density. (d) Drag as a function of the separation between graphene layers. The lines *Coulomb+phonon* describe the drag resistivity taking into account the frequency dependence of the dielectric function of hBN, while the *Coulomb only* line is computed using the dielectric function of hBN in the static limit. The line *Low T, large d* is computed using Eq. (5.83) and the line *Low T* is computed using the non-linear susceptibility and interlayer interaction expanded to lowest order in frequency in Eq. (5.70).

tum transfer from an electronic state (in graphene) to a phonon mode (in a dielectric substrate material) plays a role [130, 131]. The decay rate of the electronic state is then overall proportional to the thermal population of the phonon mode. Our scenario however involves the exchange of virtual phonons in a process that is of second order in the interlayer interaction and no decay processes into real phonon states are relevant for the drag resistivity. A similar low temperature effect of optical phonons in drag was also reported in Ref. [169]. Although we focused on a hBN substrate, considering other substrate materials, such as SiO_2, should not qualitatively affect the obtained results.

Comparing the obtained results with the experimental data on Coulomb drag from Refs. [39, 40] for a graphene double layer in a graphene layers embedded in a SiO_2/Al_2O_3 dielectric and from Ref. [41] from graphene in hBN, the experimental results for drag in the Fermi liquid regime are larger by a factor of roughly three compared with the predicted. The experimentally reported T^2 dependence of ρ_D for $d = 6$ nm and $n = 0.018$ nm^{-2} up to temperatures of 240 K in Ref. [41] does not disagree with our results presented in Fig. 5.6(a). Actually, it appears that in the temperature range of 100 to 250 K the inclusion of phonon mediated interaction brings the behaviour of drag closer to the low temperature T^2 behaviour than with static Coulomb interaction only. Nevertheless, an extension of the experimental data shown in Ref. [41] up to room temperature would be needed to distinguish the effect of substrate phonons.

We point out that we have not considered the case where the two graphene layers are close enough that the impurity disorder of both layers is correlated, where there can be an exchange of energy between the electrons of the graphene layers, which is thought to play a dominant role in the low doping limit of the graphene layers [41, 172].

We end this chapter by point out that the investigation of the phenomena of frictional drag between two 2D electronic gases, having started almost 40 years ago [156], is far from over and work continues to be done [183, 188, 189].

6 VERTICAL TRANSPORT IN VAN DER WAALS STRUCTURES

6.1 INTRODUCTION

One of the most interesting vdW structures from the point of view of applications and basic physics is the graphene–insulator/semiconductor–graphene vdW structure, with hexagonal boron nitride (hBN) or a semiconducting transition metal dichalcogenide (STMDC) as the semiconductor/insulator. These kind of structures have already been shown to realise a new kind of transistors: the Vertical Tunnelling Field Effect Transistor (VTFET) [48–50]. In a VTFET, the graphene layers act as source and drain contacts while the insulator/semiconductor acts as a tunnelling barrier for the electron flow along the vertical direction. By applying gate voltages to the bottom and top graphene layers it is possible to control electrostatically the Fermi levels of both layers. This changes the electronic density of states available for tunnelling between the graphene layers and at the same time controls the effective barrier height presented by the insulator/semiconductor (whose band structure moves rigidly with the Dirac points of the graphene layers). Simultaneous control of the density of states and the barrier height with the applied gate voltages enables the switching operation of the device. Devices based on graphene–WSe_2–graphene structures have already shown ON/OFF ratios as high as 10^6, with high ON current and a highly insulating OFF state [50]. The same kind of graphene–STMDC–graphene device geometry has also been shown to operate as a photodetector [190–192]. In these photodetectors, the STMDC acts as the photo-active region and the graphene layers act as transparent electrodes (due to the reduced light–matter interaction in graphene). The latter collect the electron–hole pairs created in the STMDC, which then flow in opposite directions due to the electric field induced by the asymmetric doping of the graphene layers. Graphene–WSe_2–graphene devices have already shown photoresponse times as short as 5.5 ps [192] and graphene–MoS_2–graphene photodetectors have shown internal quantum efficiencies (number of collected electrons at the device electrodes by the number of absorbed photons) as high as 85%[191].

Due to the extreme high quality and atomically sharp interfaces between different layers in vdW structures [51], the lattice mismatch and the relative alignment between consecutive layers play a fundamental role in determining the electronic coupling between different layers of a vdW structure, having a profound impact on its electronic and optical properties. Lattice misalignment between different layers is known to lead to the formation of Moiré patterns in rotated graphite layers [193]. The effect of lattice misalignment and mismatch has been extensively studied in the context of twisted graphene bilayers and in graphene–on–hBN structures. It was shown, both theoretically and experimentally, that the misalignment in graphene bilayers leads to a renormalization of graphene's Fermi velocity [194, 195]. It was also found out that the mismatch and the misalignment control the formation of mini Dirac cones in the band structure of graphene–on– hBN structures[196–201]. The dependence of the vertical current in vdW structures on the rotation between different layers was first studied in Ref. [202] in the context of twisted bilayer graphene. There it was found that the current is extremely sensitive to the twist angle. Although this dependence was not at first com-

pletely appreciated, it was soon understood and experimentally verified [52, 53] that the misalignment between the graphene layers in graphene–hBN–graphene structures leads to the occurrence of peaks in the current-voltage (I-V) characteristics of the device, which are followed by regions with negative differential conductance (NDC). The position of these peaks as a function of the applied bias voltage depends on the rotation angle between the graphene layers. As we will later see, the mechanism that leads to the the occurrence of NDC is precisely momentum conservation in the tunnelling process between rotated layers. This is very different from what happens in semiconductor double barriers [203]. In a double barrier structure, a peak in the current occurs when the energy level of the state localized inside the double barrier is located between the Fermi levels of the to attached electrodes. It is the tunnelling assisted by the localized state, resonant tunnelling, that leads to the occurrence of NDC. The effect of layer misalignment in the vertical current is not restricted to monolayer graphene based devices and recently it as also been explored in devices formed by two graphene bilayers [204–206] and by one graphene monolayer and a graphene bilayer separated by hBN [207].

In a graphene–insulator/semiconductor–graphene vdW structure, the distance between the graphene layers is very small, being of the order of few or tens of nanometres. In this case we can expect that tunnelling will essential be coherent, not being affected by interactions. Nevertheless, interactions can lead to incoherent processes, where the tunnelling electrons lose energy and their momentum is also degraded. Interactions can therefore lead to interesting features in the I-V characteristics. The effect of scattering by phonons in vertical transport in vdW structures was first theoretically studied in the context of twisted graphene bilayers [208]. More recently, signatures of phonon assisted scattering on vertical transport have been experimentally detected in graphene–hBN–graphite [209] and graphene–hBN–graphene structures [210]. These signatures in vertical electronic transport has been proposed as a possible way to probe the phonon spectrum of vdW structures.

In this chapter we study the electronic vertical current in graphene–hBN–graphene devices with misaligned layers and for small twist angles, taking into account momentum conservation rules and the effect of the rotation not only between the two graphene layers but also between the graphene layers and the hBN slab. We have three main goals: (i) determine under which conditions the graphene layers can be treated as electrodes, in opposition to the case where external metallic contacts are treated as electrodes, (ii) study the effect of the rotation between the graphene layers and the hBN slab on the occurrence of NDC regions and (iii) study the effect of scattering by phonons and disorder on vertical transport in these devices. This chapter is organized as follows. In Section 6.2 we lay out the general non-equilibrium Green's function (NEGF) approach to mesoscopic transport. For the readers not familiar with the NEGF formalism, its fundamentals are summarized in Appendix H. In Section 4.3, we describe the general form of the coupling Hamiltonian between two incommensurate 2D crystals and the crystal momentum conservation rules that govern this coupling. In Section 6.2, we describe the model Hamiltonian used to study vertical transport across a graphene–hBN–graphene structure. Coherent transport in a prestine graphene–hBN–graphene device and the possibility of occurrence of multiple NDC regions is studied in Section 6.5. The effect of scattering by disorder and optical phonons is discussed in Section 6.6. Finally, conclusions are drawn in Section 6.7.

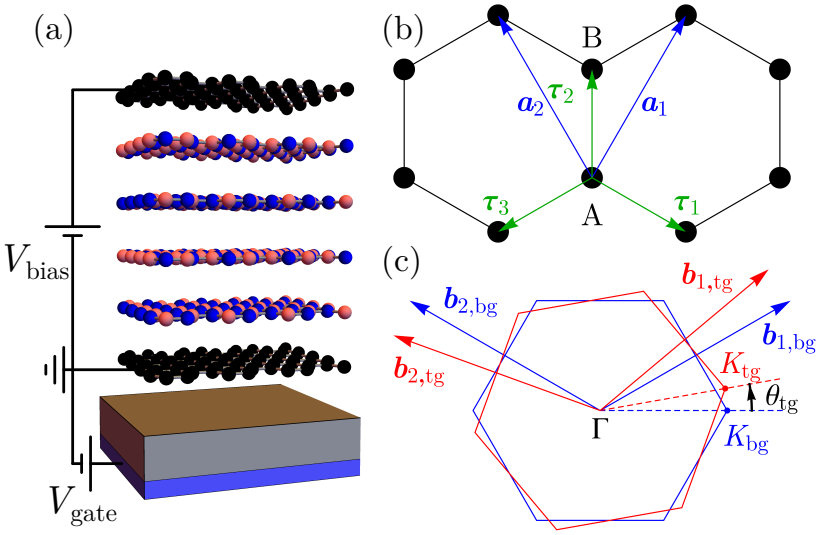

Figure 6.1: Schematic representation of a typical graphene–hBN–graphene vdW structure, graphene lattice structure and Brillouin zones of rotated graphene layers. (a) Schematic of a typical graphene– hBN–graphene vdW structure with four hBN layers, with applied gate, V_{gate}, and bias, V_{bias}, voltages. The graphene–hBN–graphene device is assumed to be placed on top of a hBN/SiO_2 dielectric substrate, which separates it from a highly doped Si gate. (b) Representation of honeycomb crystalline structure shared by a graphene/boron nitride monolayer, showing the lattice basis, $\{\mathbf{a}_1, \mathbf{a}_2\}$, the nearest neighbour vectors $\boldsymbol{\tau}_i$, $i = 1, 2, 3$, and the A/B sublattice sites. (c) Representation of the 1BZ of the bottom and top graphene layers, indicating the relative rotation angle, the respective K points and the reciprocal lattice basis $\{\mathbf{b}_1, \mathbf{b}_2\}$.

6.2 THEORY OF MESOSCOPIC TRANSPORT

The problem of electronic transport, particularly electronic mesoscopic transport, is a delicate one. An exact treatment of transport through a mesoscopic device that is connected to an external circuit (which includes a voltage source / battery) would require treating the complete system, formed by the mesoscopic region plus external circuit, on the same footing. This is clearly an infeasible task. The problem of electronic mesoscopic transport has an analogue in fluid mechanics: the problem of computing the fluid current between two vessels that are communicating through a small section pipe. Once the pipe connecting the two vessels is opened, a rigorous computation of the fluid current through the pipe would require a full hydrodynamic treatment of the fluid in the vessels and in the pipe, taking into account the initial fluid levels in the vessels and how the pipe is opened up: a daunting task. However, if we are not interested in the fluid current immediately after opening up the pipe (transient behaviour), assuming that the fluid levels in each vessel is approximately constant allows a great simplification in the problem: by simply applying Bernoulli's law one can then compute the fluid current that flows through the pipe! The assumption of constant fluid levels in the vessels is obviously only an approximation, however, provided that the section of the vessels is much larger than the section of the connecting pipe, it can be an extremely good one. On the problem of electronic mesoscopic transport, a similar approximation occurs if we assume that the source and drain electrodes of the external circuit that are connected to the mesoscopic region have constant, well defined chemical potentials (the electronic

fluid level). This approximation will be a good one provided the density of states of the electrodes is much larger than the density of states in the mesoscopic region. This allows to treat the external electrodes as particle reservoirs or baths which can freely exchange both particles and energy with the mesoscopic region. The assumption that the external electrodes have well define chemical potentials, and therefore are in thermal equilibrium, is at the heart of any treatment of quantum mesoscopic transport, whether it be based on the scattering theory approach of Landauer [211, 212] and Büttiker [213], transfer Hamiltonian approach of Bardeen [214] or the use of non-equilibrium Green's function approach pioneered by Caroli and coworkers [215–218]. Even though assuming that the electrodes are in thermal equilibrium allows for an immense simplification, the theory of mesoscopic transport remains considerably more evolved than Bernoulli's law, as we will see. In the following we will employ the non-equilibrium Green's function approach to mesoscopic transport as this formalism is the most formally rigorous one and allows for a easy inclusion of interaction effects. A brief description to the non-equilibrium Green's function formalism is provided in Appendix H and in the following we will use many of the results provided there.

In order to set up a theory for mesoscopic transport we need to specify the Hamiltonian describing the mesoscopic region and the external electrodes which are in thermal equilibrium. We are interested in a two terminal device, where the central region, which we label as c (central), is connect to two electrodes, which we label as t (top) and b (bottom). He write the non-interacting part of the Hamiltonian of the complete system in a localized basis and in first quantization as

$$\boldsymbol{H} = \begin{bmatrix} \boldsymbol{H}_{\mathrm{t}} & \boldsymbol{T}_{\mathrm{t,c}} & \boldsymbol{0} \\ \boldsymbol{T}_{\mathrm{c,t}} & \boldsymbol{H}_{\mathrm{c}} & \boldsymbol{T}_{\mathrm{c,b}} \\ \boldsymbol{0} & \boldsymbol{T}_{\mathrm{b,c}} & \boldsymbol{H}_{\mathrm{b}} \end{bmatrix}, \tag{6.1}$$

where $\boldsymbol{H}_{\mathrm{t}}$ and $\boldsymbol{H}_{\mathrm{b}}$ are the Hamiltonians of the isolated top and bottom electrodes, $\boldsymbol{H}_{\mathrm{c}}$ is the Hamiltonian of the central mesoscopic device, $\boldsymbol{T}_{\mathrm{t,c}} = \boldsymbol{T}_{\mathrm{c,t}}^{\dagger}$ and $\boldsymbol{T}_{\mathrm{b,c}} = \boldsymbol{T}_{\mathrm{c,b}}^{\dagger}$ are coupling terms that describe the electronic hopping between the top/bottom electrode and the mesoscopic device. It is assumed that there is no direct hopping between the top and bottom electrodes. Notice, that the formalism is not restricted to systems described in terms of localized basis and can also be applied to continuous Hamiltonians formulated in real space as an Hamiltonian of the form of Eq. (6.1) can be obtained from a discretization of Schrödinger's equation [216]. The second quantized version of Eq. (6.1) would read

$$\begin{aligned} H = {} & \boldsymbol{\psi}_{\mathrm{t}}^{\dagger} \cdot \boldsymbol{H}_{\mathrm{t}} \cdot \boldsymbol{\psi}_{\mathrm{t}} + \boldsymbol{\psi}_{\mathrm{c}}^{\dagger} \cdot \boldsymbol{H}_{\mathrm{c}} \cdot \boldsymbol{\psi}_{\mathrm{c}} + \boldsymbol{\psi}_{\mathrm{b}}^{\dagger} \cdot \boldsymbol{H}_{\mathrm{b}} \cdot \boldsymbol{\psi}_{\mathrm{b}} \\ & + \boldsymbol{\psi}_{\mathrm{t}}^{\dagger} \cdot \boldsymbol{T}_{\mathrm{t,c}} \cdot \boldsymbol{\psi}_{\mathrm{c}} + \boldsymbol{\psi}_{\mathrm{c}}^{\dagger} \cdot \boldsymbol{T}_{\mathrm{c,t}} \cdot \boldsymbol{\psi}_{\mathrm{t}} \\ & + \boldsymbol{\psi}_{\mathrm{b}}^{\dagger} \cdot \boldsymbol{T}_{\mathrm{b,c}} \cdot \boldsymbol{\psi}_{\mathrm{c}} + \boldsymbol{\psi}_{\mathrm{c}}^{\dagger} \cdot \boldsymbol{T}_{\mathrm{c,b}} \cdot \boldsymbol{\psi}_{\mathrm{b}}, \end{aligned} \tag{6.2}$$

where $\boldsymbol{\psi}_i^{\dagger}$ ($\boldsymbol{\psi}_{\mathrm{i}}$) is a row (column) vector of electron creation (annihilation) operators that act in the $i = \mathrm{t}, \mathrm{c}, \mathrm{b}$ subspace (written in the same basis as Eq. (6.1)). The current that flows through the mesoscopic device can be obtained from charge conservation, by computing the change in the particle number of the electrodes (which later on we will approximate as being constant, this is the approximation discussed in the previous

paragraph). From Heisenberg equation, the change of the particle number in the top terminal is given by

$$\begin{aligned}\frac{dN_{\mathrm{t}}}{dt} &= \frac{d}{dt}\left(\boldsymbol{\psi}_{\mathrm{t}}^{\dagger}\cdot\boldsymbol{\psi}_{\mathrm{t}}\right)\\ &= \frac{i}{\hbar}\left[H,\boldsymbol{\psi}_{\mathrm{t}}^{\dagger}\cdot\boldsymbol{\psi}_{\mathrm{t}}\right]\\ &= \frac{i}{\hbar}\left[\boldsymbol{\psi}_{\mathrm{t}}^{\dagger}\cdot\boldsymbol{T}_{\mathrm{t,c}}\cdot\boldsymbol{\psi}_{\mathrm{c}},\boldsymbol{\psi}_{\mathrm{t}}^{\dagger}\cdot\boldsymbol{\psi}_{\mathrm{t}}\right]+\frac{i}{\hbar}\left[\boldsymbol{\psi}_{\mathrm{c}}^{\dagger}\cdot\boldsymbol{T}_{\mathrm{c,t}}\cdot\boldsymbol{\psi}_{\mathrm{t}},\boldsymbol{\psi}_{\mathrm{t}}^{\dagger}\cdot\boldsymbol{\psi}_{\mathrm{t}}\right]\\ &= -\frac{i}{\hbar}\boldsymbol{\psi}_{\mathrm{t}}^{\dagger}\cdot\boldsymbol{T}_{\mathrm{t,c}}\cdot\boldsymbol{\psi}_{\mathrm{c}}+\frac{i}{\hbar}\boldsymbol{\psi}_{\mathrm{c}}^{\dagger}\cdot\boldsymbol{T}_{\mathrm{c,t}}\cdot\boldsymbol{\psi}_{\mathrm{t}},\end{aligned}\tag{6.3}$$

The particle current flowing from the top to the bottom region is given by minus the change of the number of particles in the top region and therefore the expectation value of the electronic current is given by

$$\begin{aligned}I_{\mathrm{t}\to\mathrm{b}}(t) &= -e\left(-\frac{dN_{\mathrm{t}}(t)}{dt}\right)\\ &= -e\frac{i}{\hbar}\left\langle\boldsymbol{\psi}_{\mathrm{t}}^{\dagger}(t)\cdot\boldsymbol{T}_{\mathrm{t,c}}\cdot\boldsymbol{\psi}_{\mathrm{c}}(t)\right\rangle+e\frac{i}{\hbar}\left\langle\boldsymbol{\psi}_{\mathrm{c}}^{\dagger}(t)\cdot\boldsymbol{T}_{\mathrm{c,t}}\cdot\boldsymbol{\psi}_{\mathrm{t}}(t)\right\rangle,\end{aligned}\tag{6.4}$$

which can be expressed in terms of lesser Green's function as

$$I_{\mathrm{t}\to\mathrm{b}}(t)=e\mathrm{Tr}\left[\boldsymbol{T}_{\mathrm{c,t}}\cdot\boldsymbol{G}_{\mathrm{t,c}}^{<}(t,t)-\boldsymbol{T}_{\mathrm{t,c}}\cdot\boldsymbol{G}_{\mathrm{c,t}}^{<}(t,t)\right].\tag{6.5}$$

We will now specialise to the stationary state regime. A possible calculation scheme (albeit not very realistic) is to consider that in the remote past the mesoscopic region is disconnected from the electrodes (by setting $\boldsymbol{T}_{\mathrm{t,c}}=\boldsymbol{T}_{\mathrm{c,t}}^{\dagger}=\boldsymbol{0}$ and $\boldsymbol{T}_{\mathrm{b,c}}=\boldsymbol{T}_{\mathrm{c,b}}^{\dagger}=\boldsymbol{0}$) but with a bias already applied between the two electrodes. Since the mesoscopic region is disconnected from the electrodes no current is allowed to flow and all the individual parts of the system are in thermal equilibrium. Then, one turns on the hopping terms contacting the electrodes to the mesoscopic region ($\boldsymbol{T}_{\mathrm{t,c}}=\boldsymbol{T}_{\mathrm{c,t}}^{\dagger}\neq 0$ and $\boldsymbol{T}_{\mathrm{b,c}}=\boldsymbol{T}_{\mathrm{c,b}}^{\dagger}\neq 0$), allowing a current to flow due to the applied bias. Essentially we are turning on a switch. Since we are working under the assumption that the electrodes are particle reservoirs, the electrodes will remain in thermal equilibrium, with the same occupation factors as they had before contacting them to the mesoscopic region. The initial state of the mesoscopic region is of no importance since in the stationary state that information will be washed away due to the coupling to the electrodes. This calculation scheme for the current in a mesoscopic device was initially proposed by Caroli and coworkers [215] and is generally referred to as the *partitioned* approach. An alternative computation scheme was later proposed by Cini [219]. Instead of making the fictitious assumption that in the initial state the electrodes are disconnected but with a bias already applied, it considers instead that in the initial state electrodes and mesoscopic region are all connected and in thermal equilibrium. Then, it is the bias voltage that is turned on. This second approach is generally referred to as *partition-free* approach. If we are interested in the transient behaviour of the current, the partitioned and the partition-free approaches will clearly differ as they are describing physically different processes. However, if we are only interested in the stationary state current we might hope that the system will lose memory of how it was initially prepared and that both approaches will predict the same steady state current. Indeed, it was proved rigorously by Stefanucci and Almbladh [220] that, for non-interacting electrons, both approaches yield the same steady-state current provided that the energy levels of the electrodes form a continuum, that is, if

they are macroscopic. The continuum of states in the electrodes leads to a dephasing mechanism which ensures that a steady state is reached and that this steady steady is independent of the past history. No theorem of equivalence between the *partitioned* and *partition-free* approaches exists for the interacting case. We can expect, however, that interactions will further contribute to the loss of memory of the system and therefore both approaches should also coincide for the steady state current in the interacting case. The *partitioned* approach is technically simpler, particularly in the interacting case, and as we are interested in the steady state current, we will employ it in the following.

Equation (6.5) expresses the current in terms of a Green's function connecting the mesoscopic region to one of the electrodes. It would be useful, if one could express the current only in terms of a Green's function of the mesoscopic region, with the electrodes only acting as particle reservoirs. This can be done by integrating out the electrodes, which in the case of non-interacting contacts can be done exactly. Assuming that in the distant past the system is uncontacted (with $\boldsymbol{T}_{\mathrm{t,c}} = \boldsymbol{T}_{\mathrm{c,t}}^{\dagger} = \boldsymbol{0}$ and $\boldsymbol{T}_{\mathrm{b,c}} = \boldsymbol{T}_{\mathrm{c,b}}^{\dagger} = \boldsymbol{0}$) and treating the $\boldsymbol{T}_{\mathrm{t,c}}$ and $\boldsymbol{T}_{\mathrm{c,t}}$ in perturbation theory (to all orders), the exact Dyson equation for the contour-ordered Green's functions $\boldsymbol{G}_{\mathrm{t,c}}^{C}(t,t')$ and $\boldsymbol{G}_{\mathrm{c,t}}^{C}(t,t')$ (see Eq. (H.28)) reads

$$\boldsymbol{G}_{\mathrm{t,c}}^{C}(t,t') = \int_{C} dt_1 \boldsymbol{G}_{\mathrm{t,t}}^{0,C}(t,t_1)\cdot\boldsymbol{T}_{\mathrm{t,c}}\cdot\boldsymbol{G}_{\mathrm{c,c}}^{C}(t_1,t'), \tag{6.6}$$

$$\boldsymbol{G}_{\mathrm{c,t}}^{C}(t,t') = \int_{C} dt_1 \boldsymbol{G}_{\mathrm{c,c}}^{C}(t,t_1)\cdot\boldsymbol{T}_{\mathrm{c,t}}\cdot\boldsymbol{G}_{\mathrm{t,t}}^{0,C}(t_1,t'), \tag{6.7}$$

where $\boldsymbol{G}_{\mathrm{t,t}}^{0,C}(t,t')$ is the Green's function of the top electrode for the uncontacted system and $\boldsymbol{G}_{\mathrm{c,c}}^{C}(t,t')$ is the Green's function of the mesoscopic region for the contacted system. In its turn, the Dyson equation from the Green's function of the mesoscopic region, $\boldsymbol{G}_{\mathrm{c,c}}^{C}(t,t')$, reads

$$\begin{aligned}\boldsymbol{G}_{\mathrm{c,c}}^{C}(t,t') = &\int_{C} dt_1 \int_{C} dt_2 \boldsymbol{G}_{\mathrm{c,c}}^{0,C}(t,t_1)\cdot\boldsymbol{\Sigma}_{\mathrm{t}}^{C}(t_1,t_2)\cdot\boldsymbol{G}_{\mathrm{c,c}}^{C}(t_2,t')\\ &+\int_{C} dt_1 \int_{C} dt_2 \boldsymbol{G}_{\mathrm{c,c}}^{0,C}(t,t_1)\cdot\boldsymbol{\Sigma}_{\mathrm{b}}^{C}(t_1,t_2)\cdot\boldsymbol{G}_{\mathrm{c,c}}^{C}(t_2,t')\\ &+\int_{C} dt_1 \int_{C} dt_2 \boldsymbol{G}_{\mathrm{c,c}}^{C}(t,t')\cdot\boldsymbol{\Sigma}_{\mathrm{int}}^{C}(t_1,t_2)\cdot\boldsymbol{G}_{\mathrm{c,c}}^{C}(t_2,t'),\end{aligned} \tag{6.8}$$

where $\boldsymbol{\Sigma}_{\mathrm{int}}^{C}(t_1,t_2)$ is a self-energy due to interactions in the mesoscopic region and the self-energies due to the contacts are given by

$$\boldsymbol{\Sigma}_{\mathrm{t}}^{C}(t,t') = \boldsymbol{T}_{\mathrm{c,t}}\cdot\boldsymbol{G}_{\mathrm{t,t}}^{0,C}(t,t')\cdot\boldsymbol{T}_{\mathrm{t,c}}, \tag{6.9}$$

$$\boldsymbol{\Sigma}_{\mathrm{b}}^{C}(t,t') = \boldsymbol{T}_{\mathrm{c,b}}\cdot\boldsymbol{G}_{\mathrm{b,b}}^{0,C}(t,t')\cdot\boldsymbol{T}_{\mathrm{t,c}}. \tag{6.10}$$

Notice that Eqs. (6.6), (6.7) and (6.8) are still valid if the electrodes are interacting provided we ignore processes in which an interaction line goes over the hopping terms

$\boldsymbol{T}_{\mathrm{t,c}}/\boldsymbol{T}_{\mathrm{c,t}}$ or $\boldsymbol{T}_{\mathrm{b,c}}/\boldsymbol{T}_{\mathrm{c,b}}$ [218]. Using Langreth's rules (see Eq. (H.67)) from Eqs. (6.6) and (6.7) we write the lesser Green's function as

$$\begin{aligned}\boldsymbol{G}^{<}_{\mathrm{t,c}}(t,t') &= \int dt_1 \boldsymbol{G}^{0,<}_{\mathrm{t,t}}(t,t_1)\cdot\boldsymbol{T}_{\mathrm{t,c}}\cdot\boldsymbol{G}^{A}_{\mathrm{c,c}}(t_1,t') \\ &\quad+\int dt_1 \boldsymbol{G}^{0,R}_{\mathrm{t,t}}(t,t_1)\cdot\boldsymbol{T}_{\mathrm{t,c}}\cdot\boldsymbol{G}^{<}_{\mathrm{c,c}}(t_1,t'), \qquad (6.11)\\ \boldsymbol{G}^{<}_{\mathrm{c,t}}(t,t') &= \int dt_1 \boldsymbol{G}^{<}_{\mathrm{c,c}}(t,t_1)\cdot\boldsymbol{T}_{\mathrm{c,t}}\cdot\boldsymbol{G}^{0,A}_{\mathrm{t,t}}(t_1,t') \\ &\quad+\int dt_1 \boldsymbol{G}^{R}_{\mathrm{c,c}}(t,t_1)\cdot\boldsymbol{T}_{\mathrm{c,t}}\cdot\boldsymbol{G}^{0,<}_{\mathrm{t,t}}(t_1,t'). \qquad (6.12)\end{aligned}$$

Plugging the above expressions into Eq. (6.5), the current can be expressed as

$$\begin{aligned}I_{\mathrm{t}\to\mathrm{b}}(t) &= \frac{e}{\hbar}\int dt_1 \mathrm{Tr}\left[\boldsymbol{\Sigma}^{<}_{\mathrm{t}}(t,t_1)\cdot\boldsymbol{G}^{A}_{\mathrm{c,c}}(t_1,t)+\boldsymbol{\Sigma}^{R}_{\mathrm{t}}(t,t_1)\cdot\boldsymbol{G}^{<}_{\mathrm{c,c}}(t_1,t)\right] \\ &\quad-\frac{e}{\hbar}\int dt_1 \mathrm{Tr}\left[\boldsymbol{G}^{<}_{\mathrm{c,c}}(t,t_1)\cdot\boldsymbol{\Sigma}^{A}_{\mathrm{t}}(t_1,t)+\boldsymbol{G}^{R}_{\mathrm{c,c}}(t,t_1)\cdot\boldsymbol{\Sigma}^{<}_{\mathrm{t}}(t_1,t)\right], \qquad (6.13)\end{aligned}$$

where $\boldsymbol{\Sigma}^{R/A/<}_{\mathrm{t}}(t,t')$ are defined in a similar way to Eq. (6.9) but replacing $\boldsymbol{G}^{0,C}_{\mathrm{t,t}}(t,t')$ by the corresponding $R/A/<$ Green's function. Since we are interested in the steady state current, when translation invariance is recovered such that all Green's functions become functions only of time differences, it is useful to represent all the quantities in terms of Fourier transforms in time. If we further use the cyclic property of the trace we can write the current in the steady state as

$$\begin{aligned}I_{\mathrm{t}\to\mathrm{b}} &= \frac{e}{\hbar}\int \frac{d\omega}{2\pi}\mathrm{Tr}\left[\boldsymbol{\Sigma}^{<}_{\mathrm{t}}(\omega)\cdot\left(\boldsymbol{G}^{A}_{\mathrm{c,c}}(\omega)-\boldsymbol{G}^{R}_{\mathrm{c,c}}(\omega)\right)\right] \\ &\quad-\frac{e}{\hbar}\int \frac{d\omega}{2\pi}\mathrm{Tr}\left[\left(\boldsymbol{\Sigma}^{A}_{\mathrm{t}}(\omega)-\boldsymbol{\Sigma}^{R}_{\mathrm{t}}(\omega)\right)\cdot\boldsymbol{G}^{<}_{\mathrm{c,c}}(\omega)\right]. \qquad (6.14)\end{aligned}$$

Since the external top electrode is in thermal equilibrium, $\boldsymbol{G}^{0,\gtrless}_{\mathrm{t,t}}(\omega)$ can be obtained from the fluctuation-dissipation theorem (see Eqs. (C.2) and (C.3) in Appendix C)

$$\begin{aligned}\boldsymbol{G}^{0,<}_{\mathrm{t,t}}(\omega) &= i f_{\mathrm{t}}(\omega)\boldsymbol{A}^{0}_{\mathrm{t,t}}(\omega), \qquad (6.15)\\ \boldsymbol{G}^{0,>}_{\mathrm{t,t}}(\omega) &= -i\left(1-f_{\mathrm{t}}(\omega)\right)\boldsymbol{A}^{0}_{\mathrm{t,t}}(\omega), \qquad (6.16)\end{aligned}$$

where $\boldsymbol{A}^{0}_{\mathrm{t,t}}(\omega) = i\left(\boldsymbol{G}^{0,R}_{\mathrm{t,t}}(\omega)-\boldsymbol{G}^{0,A}_{\mathrm{t,t}}(\omega)\right)$ is the spectral function of the uncontacted top electrode and $f_{\mathrm{t}}(\omega) = \left(e^{\beta(\omega-\mu_{\mathrm{t}})}+1\right)^{-1}$ is the equilibrium Fermi distribution function of the electrode, with chemical potential μ_{t}. Therefore, by introducing the level-width function due to the contacts

$$\boldsymbol{\Gamma}_{\mathrm{t}}(\omega) = i\left(\boldsymbol{\Sigma}^{R}_{\mathrm{t}}(\omega)-\boldsymbol{\Sigma}^{A}_{\mathrm{t}}(\omega)\right), \qquad (6.17)$$

we can write

$$\boldsymbol{\Sigma}^{<}_{\mathrm{t}}(\omega) = i f_{\mathrm{t}}(\omega)\boldsymbol{\Gamma}_{\mathrm{t}}(\omega). \qquad (6.18)$$

Similarly the greater Green's function can be written as

$$\boldsymbol{\Sigma}^{>}_{\mathrm{t}}(\omega) = -i\left(1-f_{\mathrm{t}}(\omega)\right)\boldsymbol{\Gamma}_{\mathrm{t}}(\omega). \qquad (6.19)$$

Similar equations are valid for the self-energy due to the bottom contact, $\mathbf{\Sigma}_{\mathrm{b}}^{\gtrless}(\omega)$. If we also introduce the spectral function of the mesoscopic region as (Eq. (A.25))

$$\boldsymbol{A}_{\mathrm{c,c}}(\omega) = i\left(\boldsymbol{G}^{R}(\omega) - \boldsymbol{G}^{A}(\omega)\right), \tag{6.20}$$

from Eq. (6.14) we obtain the Meir-Wingreen [221] formula for the current

$$I_{\mathrm{t}\to\mathrm{b}} = -\frac{e}{\hbar}\int \frac{d\omega}{2\pi}\mathrm{Tr}\left[\mathbf{\Gamma}_{\mathrm{t}}(\omega)\cdot\left(f_{\mathrm{t}}(\omega)\boldsymbol{A}(\omega) + i\boldsymbol{G}^{<}(\omega)\right)\right] \tag{6.21}$$

(where for simplicity we have suppressed the central region indices c, c). Notice that if the central mesoscopic region were in equilibrium with the top contact, by the fluctuation-dissipation theorem we would have $\boldsymbol{G}^{<}_{\mathrm{c,c}}(\omega) = if_{\mathrm{t}}(\omega)\boldsymbol{A}_{\mathrm{c,c}}(\omega)$ and the current would be zero. Therefore we can see the current as a measure of the "non-equilibriumness" of the system.

We now provide an expression for the spectral function that will later be useful. From the definition Eq. (6.20), the spectral function can also be written as

$$\begin{aligned}\boldsymbol{A}(\omega) &= i\left(\boldsymbol{G}^{R}(\omega) - \boldsymbol{G}^{A}(\omega)\right)\\ &= i\boldsymbol{G}^{R}(\omega)\cdot\left(\left[\boldsymbol{G}^{A}(\omega)\right]^{-1} - \left[\boldsymbol{G}^{R}(\omega)\right]^{-1}\right)\cdot\boldsymbol{G}^{A}(\omega)\\ &= \boldsymbol{G}^{R}(\omega)\cdot\mathbf{\Gamma}(\omega)\cdot\boldsymbol{G}^{A}(\omega),\end{aligned} \tag{6.22}$$

with the total decay rate matrix given by

$$\begin{aligned}\mathbf{\Gamma}(\omega) &= i\left(\left[\boldsymbol{G}^{A}(\omega)\right]^{-1} - \left[\boldsymbol{G}^{R}(\omega)\right]^{-1}\right)\\ &= i\left(\mathbf{\Sigma}^{R}(\omega) - \mathbf{\Sigma}^{A}(\omega)\right) = i\left(\mathbf{\Sigma}^{>}(\omega) - \mathbf{\Sigma}^{<}(\omega)\right).\end{aligned} \tag{6.23}$$

In the same way that Eq. (6.22) is obtained, the spectral function can also be written as

$$\boldsymbol{A}(\omega) = \boldsymbol{G}^{A}(\omega)\cdot\mathbf{\Gamma}(\omega)\cdot\boldsymbol{G}^{R}(\omega). \tag{6.24}$$

6.2.1 *Coherent and incoherent contributions to the current*

In the Meir-Wingreen formula, the bottom and top electrodes seem to play different roles, with the current explicitly depending on $\mathbf{\Gamma}_{\mathrm{t}}(\omega)$ but not on $\mathbf{\Gamma}_{\mathrm{b}}(\omega)$. It is clear that in a two terminal device, the two contacts should play the same role. To see this, we rewrite the Meir-Wingreen formula using the fact that the spectral function can be written as $\boldsymbol{A}(\omega) = i\left(\boldsymbol{G}^{>}(\omega) - \boldsymbol{G}^{<}(\omega)\right)$ (see Eq. (A.26) in Appendix A) such that the current is written as

$$I_{\mathrm{t}\to\mathrm{b}} = -\frac{e}{\hbar}\int \frac{d\omega}{2\pi}\mathrm{Tr}\left[i\mathbf{\Gamma}_{\mathrm{t}}(\omega)\cdot\left(f_{\mathrm{t}}(\omega)\boldsymbol{G}^{>}(\omega) + \left(1 - f_{\mathrm{t}}(\omega)\right)\boldsymbol{G}^{<}(\omega)\right)\right], \tag{6.25}$$

The Keldysh equation for the greater and lesser Green's functions (Eqs. (H.71) and (H.90)) reads

$$\boldsymbol{G}^{\gtrless}(\omega) = \boldsymbol{G}^{R}(\omega)\cdot\mathbf{\Sigma}^{\gtrless}(\omega)\cdot\boldsymbol{G}^{A}(\omega), \tag{6.26}$$

where the greater/lesser self-energy can be split into contributions due to the external electrodes and contributions due to interactions (see Eq. (6.8))

$$\mathbf{\Sigma}^{\gtrless}(\omega) = \mathbf{\Sigma}_{\mathrm{t}}^{\gtrless}(\omega) + \mathbf{\Sigma}_{\mathrm{b}}^{\gtrless}(\omega) + \mathbf{\Sigma}_{\mathrm{int}}^{\gtrless}(\omega). \tag{6.27}$$

Writing the contact self-energies in terms of the level-width functions as in Eqs. (6.18) and (6.19), the current can be written as the sum of two terms

$$I_{\mathrm{t}\to\mathrm{b}} = I^{(\mathrm{coh})}_{\mathrm{t}\to\mathrm{b}} + I^{(\mathrm{incoh})}_{\mathrm{t}\to\mathrm{b}}, \tag{6.28}$$

with the coherent term given by the Landauer formula

$$I^{(\mathrm{coh})}_{\mathrm{t}\to\mathrm{b}} = -\frac{e}{\hbar}\int \frac{d\omega}{2\pi}\left(f_{\mathrm{t}}(\omega) - f_{\mathrm{b}}(\omega)\right)\mathcal{T}^{(0)}_{\mathrm{t,b}}(\omega), \tag{6.29}$$

with the coherent transmission function given by

$$\mathcal{T}^{(0)}_{\mathrm{t,b}}(\omega) = \mathrm{Tr}\left[\boldsymbol{\Gamma}_{\mathrm{t}}(\omega)\cdot\boldsymbol{G}^{R}(\omega)\cdot\boldsymbol{\Gamma}_{\mathrm{b}}(\omega)\cdot\boldsymbol{G}^{A}(\omega)\right], \tag{6.30}$$

and the incoherent contribution reading

$$\begin{aligned} I^{(\mathrm{incoh})}_{\mathrm{t}\to\mathrm{b}} = &-i\frac{e}{\hbar}\int\frac{d\omega}{2\pi}f_{\mathrm{t}}(\omega)\mathrm{Tr}\left[\boldsymbol{\Gamma}_{\mathrm{t}}(\omega)\cdot\boldsymbol{G}^{R}(\omega)\cdot\boldsymbol{\Sigma}^{>}_{\mathrm{int}}(\omega)\cdot\boldsymbol{G}^{A}(\omega)\right] \\ &- i\frac{e}{\hbar}\int\frac{d\omega}{2\pi}\left(1-f_{\mathrm{t}}(\omega)\right)\mathrm{Tr}\left[\boldsymbol{\Gamma}_{\mathrm{t}}(\omega)\cdot\boldsymbol{G}^{R}(\omega)\cdot\boldsymbol{\Sigma}^{<}_{\mathrm{int}}(\omega)\cdot\boldsymbol{G}^{A}(\omega)\right]. \end{aligned} \tag{6.31}$$

The incoherent contribution to the current is only non-zero in the presence of interactions and plays a role similar to that of vertex corrections in linear response formalism. It corresponds to processes that are assisted by interactions, involving the emission or absorption of interaction carrier bosons (for example phonons). Notice that in Eq. (6.31) the top and bottom contacts still appear in an asymmetric way. To proceed we must specify the interactions the electrons experience in the mesoscopic region.

We will study the case where the electrons in the mesoscopic region of the device interact with a real bosonic field, ϕ_ζ, via the Hamiltonian

$$H_{\mathrm{int}} = \boldsymbol{c}^{\dagger}\cdot\boldsymbol{M}_{\zeta}\cdot\boldsymbol{c}\phi_{\zeta}, \tag{6.32}$$

where $\boldsymbol{M}_\zeta$ is an electron-boson coupling matrix. The bosonic field is governed by the bare Hamiltonian

$$H_{\phi} = \sum_{\zeta}\hbar\omega_{\zeta}\left(a^{\dagger}_{\zeta}a_{\zeta} + \frac{1}{2}\right), \tag{6.33}$$

where ω_ζ is the frequency of the bosonic field in mode ζ and $a^\dagger_\zeta$ (a_ζ) are the creation (annihilation) bosonic operators, with the bosonic field ϕ_ζ given by $\phi_\zeta = a^\dagger_\zeta + a_\zeta$. Therefore, the retarded/advanced Green's functions for the bosonic field ϕ_ζ reads

$$D^{R/A}_{\zeta}(\nu) = \frac{2\omega_{\zeta}}{\nu^2 - \omega^2_{\zeta} \pm \mathrm{sgn}(\nu)i0^{+}}. \tag{6.34}$$

We will assume that the bosonic field is in thermal equilibrium and therefore, by the fluctuation-dissipation theorem we obtain

$$D^{\gtrless}_{\zeta}(\nu) = \pm i2\pi b(\mp\nu)2\omega_{\zeta}\mathrm{sgn}(\nu)\delta\left(\nu^2 - \omega^2_{\zeta}\right), \tag{6.35}$$

where $b(\nu) = \left(e^{\beta\nu} - 1\right)^{-1}$ is the Bose distribution function. Notice that considering an interaction of the form of Eq. (6.32) is not too restrictive, as an electron-boson interaction can also describe two body interactions (such as Coulomb) since the latter can

be decoupled via a Hubbard–Stratonovich transformation. In a non-crossing approximation, the greater/lesser electron self-energy due to the interaction (6.32) is given by the Fock contribution (see Eqs. (H.82) and (H.62))

$$\boldsymbol{\Sigma}^{\gtrless}_{\text{int}}(\omega) = i \int \frac{d\nu}{2\pi} \boldsymbol{M}_\zeta \cdot \boldsymbol{G}^{\gtrless}(\omega - \nu) \cdot \boldsymbol{M}^\dagger_\zeta D^{\gtrless}_\zeta(\nu). \tag{6.36}$$

Recalling that the greater/lesser Green's function is given by Eq. (6.26) we obtain

$$\begin{aligned}\boldsymbol{\Sigma}^{\gtrless}_{\text{int}}(\omega) = i \int \frac{d\nu}{2\pi} \boldsymbol{M}_\zeta \cdot \boldsymbol{G}^{R}(\omega - \nu) \cdot \boldsymbol{\Sigma}^{\gtrless}_{\text{t}}(\omega - \nu) \cdot \boldsymbol{G}^{A}(\omega - \nu) \cdot \boldsymbol{M}^\dagger_\zeta D^{\gtrless}_\zeta(\nu) \\ + i \int \frac{d\nu}{2\pi} \boldsymbol{M}_\zeta \cdot \boldsymbol{G}^{R}(\omega - \nu) \cdot \boldsymbol{\Sigma}^{\gtrless}_{\text{t}}(\omega - \nu) \cdot \boldsymbol{G}^{A}(\omega - \nu) \cdot \boldsymbol{M}^\dagger_\zeta D^{\gtrless}_\zeta(\nu) \\ + i \int \frac{d\nu}{2\pi} \boldsymbol{M}_\zeta \cdot \boldsymbol{G}^{R}(\omega - \nu) \cdot \boldsymbol{\Sigma}^{\gtrless}_{\text{int}}(\omega - \nu) \cdot \boldsymbol{G}^{A}(\omega - \nu) \cdot \boldsymbol{M}^\dagger_\zeta D^{\gtrless}_\zeta(\nu),\end{aligned} \tag{6.37}$$

which is a self-consistent equation for $\boldsymbol{\Sigma}^{\gtrless}_{\text{int}}(\omega)$. To lowest order in the electron-boson interaction, we neglect the last term in the previous equation [218] and obtain

$$\begin{aligned}&\boldsymbol{\Sigma}^{<}_{\text{int}}(\omega) \simeq \\ &\simeq \sum_{s=\pm 1} i f_{\text{t}}(\omega - s\omega_\zeta) sb(s\omega_\zeta) \boldsymbol{M}_\zeta \cdot \boldsymbol{G}^{R}(\omega - s\omega_\zeta) \cdot \boldsymbol{\Gamma}_{\text{t}}(\omega - s\omega_\zeta) \cdot \boldsymbol{G}^{A}(\omega - s\omega_\zeta) \cdot \boldsymbol{M}^\dagger_\zeta \\ &+ \sum_{s=\pm 1} i f_{\text{b}}(\omega - s\omega_\zeta) sb(s\omega_\zeta) \boldsymbol{M}_\zeta \cdot \boldsymbol{G}^{R}(\omega - s\omega_\zeta) \cdot \boldsymbol{\Gamma}_{\text{b}}(\omega - s\omega_\zeta) \cdot \boldsymbol{G}^{A}(\omega - s\omega_\zeta) \cdot \boldsymbol{M}^\dagger_\zeta\end{aligned} \tag{6.38}$$

with the greater self-energy being obtained by replacing $f_{\text{t/b}} \to 1 - f_{\text{t/b}}$ and $b(s\omega_\zeta) \to b(-s\omega_\zeta)$. Inserting Eq. (6.38) into Eq. (6.31) we obtain the incoherent current assisted by the absorption or emission of one boson

$$I^{(\text{incoh},1)}_{\text{t}\to\text{b}} = -\frac{e}{\hbar} \sum_{s=\pm 1} \int \frac{d\omega}{2\pi} \left[W^{(1)(s,\zeta)}_{\text{t,b}}(\omega) \mathcal{T}^{(1)(s,\zeta)}_{\text{t,b}}(\omega) + W^{(1)(s,\zeta)}_{\text{t,t}}(\omega) \mathcal{T}^{(1)(s,\zeta)}_{\text{t,t}}(\omega) \right], \tag{6.39}$$

with the one-boson assisted transmission functions defined as

$$\begin{aligned}\mathcal{T}^{(1)(s,\zeta)}_{\ell,\ell'}(\omega) = \text{Tr}\big[&\boldsymbol{\Gamma}_\ell(\omega) \cdot \boldsymbol{G}^{R}(\omega) \cdot \boldsymbol{M}_\zeta \cdot \boldsymbol{G}^{R}(\omega - s\omega_\zeta) \cdot \\ &\cdot \boldsymbol{\Gamma}_{\ell'}(\omega - s\omega_\zeta) \cdot \boldsymbol{G}^{A}(\omega - s\omega_\zeta) \cdot \boldsymbol{M}^\dagger_\zeta \cdot \boldsymbol{G}^{A}(\omega) \big], \ \ell, \ell' = \text{t}, \text{b}\end{aligned} \tag{6.40}$$

and the thermal occupation factors $W^{(1)(s,\zeta)}_{\ell,\ell'}(\omega)$ given by

$$\begin{aligned}W^{(1)(s,\zeta)}_{\ell,\ell'}(\omega) = f_\ell(\omega) \left[1 - f_{\ell'}(\omega - s\omega_\zeta)\right] \left[-sb(-s\omega_\zeta)\right] \\ - \left[1 - f_\ell(\omega)\right] f_{\ell'}(\omega - s\omega_\zeta) \left[sb(s\omega_\zeta)\right], \ \ell, \ell' = \text{t}, \text{b}.\end{aligned} \tag{6.41}$$

It can be explicitly checked that $W^{(1)(s,\zeta)}_{\text{t,t}}(\omega) = 0$, such that the second term in Eq. (6.39) is zero. This cancellation is necessary and expected, since in steady state no charge accumulation can occur in the device, such that the current that flows from the top contact into the mesoscopic region must be the symmetric of the current that flows from the bottom contact into the mesoscopic region: $I_{\text{t}\to\text{b}} = -I_{\text{b}\to\text{t}}$. This implies that terms in the current that depend only on the occupation factor of one of the electrodes

must cancel out. In Eq. (6.39) both top and bottom contacts play symmetric roles. Equation (6.39) has a very simple interpretation: it represents the probability of an electron being injected from the top electrode into the mesoscopic region, emitting/absorbing (respectively for $s = \pm 1$) a boson and then being collected by the bottom electrode minus the probability of an electron being emitted by the bottom contact, absorbing/emitting (respectively for $s = \pm 1$) a boson and then being collect by the top electrode.

Processes assisted by more than one boson can be obtained in a similar way as before by successive iteration of Eq. (6.37). The incoherent contribution to the current can then be written as

$$I^{(\mathrm{incoh})}_{\mathrm{t}\to\mathrm{b}} = -\frac{e}{\hbar}\sum_{\substack{n=1\\ \{s_i\}=\pm 1}}^{+\infty}\int \frac{d\omega}{2\pi} W^{(n)(s_1,\zeta_1),\ldots,(s_n,\zeta_n)}_{\mathrm{t,b}}(\omega)\mathcal{T}^{(n)(s_1,\zeta_1),\ldots,(s_n,\zeta_n)}_{\mathrm{t,b}}(\omega), \tag{6.42}$$

with the n-boson assisted transmission function given by

$$\begin{aligned}\mathcal{T}^{(n)(s_1,\zeta_1),\ldots,(s_n,\zeta_n)}_{\mathrm{t,b}}(\omega) = \mathrm{Tr}\,[&\boldsymbol{\Gamma}_{\mathrm{t}}(\omega)\cdot\\ &\cdot \boldsymbol{G}^R(\omega)\cdot\boldsymbol{M}_{\zeta_1}\cdot\boldsymbol{G}^R(\omega-s_1\omega_{\zeta_1})\cdot\ldots\cdot\boldsymbol{M}_{\zeta_n}\cdot\boldsymbol{G}^R(\omega-s_1\omega_\zeta-s_n\omega_{\zeta_n})\cdot\\ &\cdot\boldsymbol{\Gamma}_{\mathrm{b}}(\omega-s_1\omega_\zeta-s_n\omega_{\zeta_n})\cdot\\ &\cdot\boldsymbol{G}^A(\omega-s_1\omega_\zeta-s_n\omega_{\zeta_n})\cdot\boldsymbol{M}^\dagger_{\zeta_n}\cdot\ldots\cdot\boldsymbol{G}^A(\omega-s_1\omega_{\zeta_1})\cdot\boldsymbol{M}^\dagger_{\zeta_1}\cdot\boldsymbol{G}^A(\omega)\Big],\end{aligned} \tag{6.43}$$

and the occupation factors $W^{(n)(s_1,\zeta_1),\ldots,(s_n,\zeta_n)}_{\mathrm{t,b}}(\omega)$ defined as

$$\begin{aligned}W^{(n)(s_1,\zeta_1),\ldots,(s_n,\zeta_n)}_{\mathrm{t,b}}(\omega) = &\\ &f_{\mathrm{t}}(\omega)\left[1-f_{\mathrm{b}}(\omega-s_1\omega_{\zeta_1}\ldots-s_n\omega_{\zeta_n})\right]\times\\ &\times\left[-s_1 b(-s_1\omega_{\zeta_1})\right]\ldots\left[-s_n b(-s_n\omega_{\zeta_n})\right]\\ &-\left[1-f_{\mathrm{t}}(\omega)\right]f_{\mathrm{b}}(\omega-s_1\omega_{\zeta_1}\ldots-s_n\omega_{\zeta_n})\times\\ &\times\left[s_1 b(s_1\omega_{\zeta_1})\right]\ldots\left[s_n b(s_n\omega_{\zeta_n})\right].\end{aligned} \tag{6.44}$$

Just as for the one-boson case, and in accordance with the steady state condition, it can be checked explicitly that the quantity

$$W^{(n)(s_1,\zeta_1),\ldots,(s_n,\zeta_n)}_{\mathrm{t,t}}(\omega) = 0 \tag{6.45}$$

(defined similarly to Eq. (6.44) by replacing b$\to$ t) and therefore terms involving only the occupation factors of the top electrode do not make any contribution to the current. All of the terms in Eq. (6.42) have the same interpretation as the one-boson contribution: they represent the difference in probabilities between an event in which an electron is emitted from the top electrode, emits/absorbs (respectively for $s_i = \pm 1$) n bosons and is then collected by the bottom electrode and the event in which an electron is emitted by the bottom contact, absorbs/emits (respectively for $s_i = \pm 1$) n bosons and is then collect by the top electrode.

6.3 COUPLING BETWEEN INCOMMENSURATE 2D CRYSTALS

In order to describe the general form of the coupling between two 2D crystals we follow the approach of Refs. [202, 222]. The atomic positions in the two crystals, which we label as 1 and 2, are given by

$$\begin{aligned}\mathbf{R}_{n,a,\ell} &= \mathbf{R}^0_{n,\ell} + \boldsymbol{\tau}_{a,\ell} \\ &= n_1\mathbf{a}_{1,\ell} + n_2\mathbf{a}_{2,\ell} + \boldsymbol{\tau}_{a,\ell},\ \ell = 1,2\end{aligned} \tag{6.46}$$

where $\mathbf{R}^0_{n,\ell}$ are the Bravais lattice sites of layer $\ell = 1,2$, which is spanned by the vector basis $\{\mathbf{a}_{1,\ell}, \mathbf{a}_{2,\ell}\}$ and $\boldsymbol{\tau}_{a,\ell}$ is a sublattice vector, which also encodes the out-of-plane displacement between both layers. The index $n = (n_1, n_2)$ runs over the Bravais lattice sites of each layer and the indice a includes both the sublattice and also the orbital degrees of freedom. The reciprocal lattice sites of each layer are given by

$$\mathbf{G}_{n,\ell} = n_1\mathbf{b}_{1,\ell} + n_2\mathbf{b}_{2,\ell},\ \ell = 1,2 \tag{6.47}$$

with $\{\mathbf{b}_{1,\ell}, \mathbf{b}_{2,\ell}\}$ the basis that spans the reciprocal space of layer $\ell = 1,2$. In a tight-binding representation, the second quantized form of the interlayer coupling Hamiltonian describing hoping from layer 2 to layer 1 is written as

$$T_{1,2} = -\sum_{n,a,m,b} t\left(\mathbf{R}_{n,a,1}, \mathbf{R}_{m,b,2}\right) \psi^\dagger_{n,a,1}\psi_{m,b,2}, \tag{6.48}$$

where $\psi^\dagger_{n,a,\ell}$ ($\psi_{n,a,\ell}$) are the electronic creation (annihilation) operator, for a localized state at the position $\mathbf{R}_{n,a,\ell}$ of layer ℓ and in the sublattice site/orbital a, and $t\left(\mathbf{R}_{n,a,}, \mathbf{R}_{m,b,2}\right)$ are hopping integrals. Naturally, the hopping Hamiltonian between electrons from layer 1 to layer 2 is given by $T_{2,1} = T^\dagger_{1,2}$. Representing the electronic operators of each layer in its respective Bloch basis

$$\psi^\dagger_{n,a,\ell} = \frac{1}{\sqrt{N_\ell}}\sum_{\mathbf{k}} e^{-i\mathbf{k}\cdot\mathbf{R}_{n,a,\ell}}\psi^\dagger_{\mathbf{k},a,\ell},\ \ell = 1,2, \tag{6.49}$$

where N_ℓ is the number of lattice sites in layer ℓ, the interlayer coupling Hamiltonian becomes

$$T_{1,2} = -\sum_{\mathbf{k},a,\mathbf{k}',b} \tilde{t}^{(1,2)}_{a,b}\left(\mathbf{k},\mathbf{k}'\right)\psi^\dagger_{\mathbf{k},a,1}\psi_{\mathbf{k}',b,2}, \tag{6.50}$$

where the hopping integrals $\tilde{t}_{a,b}\left(\mathbf{k},\mathbf{k}'\right)$ are given by

$$\tilde{t}^{(1,2)}_{a,b}\left(\mathbf{k},\mathbf{k}'\right) = \frac{1}{\sqrt{N_1N_2}}\sum_{n,m} e^{-i\mathbf{k}\cdot\mathbf{R}_{n,a,1}} t\left(\mathbf{R}_{n,a,1}, \mathbf{R}_{m,b,2}\right) e^{i\mathbf{k}'\cdot\mathbf{R}_{n,a,2}}. \tag{6.51}$$

In a two-centre approximation, $t\left(\mathbf{R}_{n,a,1}, \mathbf{R}_{m,b,2}\right)$ only depends on $\mathbf{R}_{n,a,1} - \mathbf{R}_{m,b,2}$ and as such it is possible to write it as a Fourier transform [222]

$$t\left(\mathbf{R}_{n,a,1}, \mathbf{R}_{m,b,2}\right) = \sqrt{A_{\text{cell},1}A_{\text{cell},2}}\int \frac{d^2\mathbf{q}}{(2\pi)^2} t^{(1,2)}_{a,b}\left(\mathbf{q}\right) e^{i\mathbf{q}\cdot\left(\mathbf{R}_{n,a,1} - \mathbf{R}_{m,b,2}\right)}, \tag{6.52}$$

where $A_{\text{cell},\ell}$ is the area of the unit cell of layer ℓ. Notice that in general, while $\mathbf{R}_{n,a,\ell}$ are 3D vectors, $\mathbf{q}$ is a 2D vector. Therefore, $\mathbf{q}\cdot\mathbf{R}_{n,a,\ell}$ projects the planar components of $\mathbf{R}_{n,a,\ell}$, with the vertical separation between sites $\mathbf{R}_{n,a,1}$ and $\mathbf{R}_{n,a,2}$ encoded in $t^{(1,2)}_{a,b}\left(\mathbf{q}\right)$.

Inserting the Fourier representation of the hopping integrals, Eq. (6.52), into Eq. (6.51), performing the sum over the Bravais lattice sites of both layers using the fact that $\sum_n e^{i\mathbf{k}\cdot\mathbf{R}^0_{n,\ell}} = N_\ell \sum_{\mathbf{G}_{n,\ell}} \delta_{\mathbf{k},\mathbf{G}_{n,\ell}}$, while assuming that both layers have the same area $A = N_1 A_{\text{cell},1} = N_2 A_{\text{cell},2}$ and noticing that the Dirac δ-function is related to the Kronecker delta by $\delta(\mathbf{k}) = A\delta_{\mathbf{k},\mathbf{0}}/(2\pi)^2$, we can write $\tilde{t}^{(1,2)}_{a,b}(\mathbf{k},\mathbf{k}')$ as

$$\tilde{t}^{(1,2)}_{a,b}(\mathbf{k},\mathbf{k}') = \sum_{\mathbf{G}_{n,1},\mathbf{G}_{m,2}} e^{i\mathbf{G}_{n,1}\cdot\boldsymbol{\tau}_{n,a,1}} t^{(1,2)}_{a,b}(\mathbf{k}'+\mathbf{G}_{m,2})\, e^{-i\mathbf{G}_{m,2}\cdot\boldsymbol{\tau}_{n,b,2}} \delta_{\mathbf{k}+\mathbf{G}_{n,1},\mathbf{k}'+\mathbf{G}_{m,2}}. \tag{6.53}$$

The following important result is thus obtained: a Bloch state from layer 1, with crystal momentum $\mathbf{k}$, only couples to a Bloch state of layer 2, with crystal momentum $\mathbf{k}'$, provided the *generalized umklapp* [222] condition

$$\mathbf{k} + \mathbf{G}_{n,1} = \mathbf{k}' + \mathbf{G}_{m,2}, \tag{6.54}$$

is satisfied, for some reciprocal lattice vectors $\mathbf{G}_{n,1}$ and $\mathbf{G}_{m,2}$, respectively from layer 1 and 2. This result can be interpreted as a generalization of the conservation of crystal momentum, but taking into account that while all the momenta $\mathbf{k}+\mathbf{G}_{n,1}$ are equivalent from the point of view of layer 1, they are not equivalent from the point of view of layer 2. Equations (6.50) and (6.53) provide a general starting point to describe the coupling between two incommensurate layers. In general, the integral hoppings in real space $t(\mathbf{R}_{n,a,1},\mathbf{R}_{m,b,2})$ should decay rapidly with $|\mathbf{R}_{n,a,1}-\mathbf{R}_{m,b,2}|$ and therefore $t^{(1,2)}_{a,b}(\mathbf{q})$ should also decay with $|\mathbf{q}|$. Therefore, in general, only a few $t^{(1,2)}_{a,b}(\mathbf{k}+\mathbf{G}_n)$ with the smallest $\mathbf{k}+\mathbf{G}_n$ (measured from the common centre of the Brillouin zones of both layers) need to be considered. In the next section we will use Eqs. (6.50) and (6.53) in order to describe the coupling between the graphene layers and the hBN slab.

6.4 MODEL HAMILTONIAN FOR GRAPHENE–HBN–GRAPHENE STRUCTURES

We want to study the vertical current flowing through a device formed by a slab of hBN, formed by $\mathcal{N}$ monolayers, sandwiched between two graphene monolayers, refered to as bottom (bg) and top (tg) graphene layers. The bottom and top graphene layers are contacted my metallic electrodes, such that a bias voltage, V_{bias}, is applied between the top and bottom layers and a gate voltage, V_{gate}, is applied to the bottom graphene layer. The device structure is schematically represented in Fig. 6.1. The finite bias voltages drives a vertical current through the device and the gate voltage allows for the control of the doping levels of the graphene layers. Like graphene, hBN also has a honeycomb structure, with boron and nitrogen atoms at the two inequivalent sites. We assume that the hBN slab is a perfect crystal, where the individual monolayers are perfectly aligned with an AA′ stacking [184, 223], i.e., consecutive honeycomb layers are perfectly aligned but with the boron atom of one layer on top of the nitrogen atom of the next and vice versa. Both graphene layers are assumed to be rotated with respect to the hBN layer and also with respect to each other. Taking the bottom graphene layer crystallographic alignment as a reference, we have that the top graphene layer is rotated by an angle of θ_{tg} and the hBN slab is rotated by an angle of θ_{hBN}. Therefore, if $\{\mathbf{b}_{1,\text{bg}},\mathbf{b}_{2,\text{tg}}\}$ are the reciprocal lattice vectors of the bottom graphene layer, then the reciprocal lattice vectors of the top graphene and of the hBN slab are given by

$$\mathbf{b}_{i,\text{tg}} = \boldsymbol{\mathcal{R}}(\theta_{\text{tg}})\cdot\mathbf{b}_{i,\text{bg}}, \tag{6.55}$$

$$\mathbf{b}_{i,\text{hBN}} = \frac{1}{1+\delta}\boldsymbol{\mathcal{R}}(\theta_{\text{hBN}})\cdot\mathbf{b}_{i,\text{bg}},\ i=1,2 \tag{6.56}$$

with $\boldsymbol{\mathcal{R}}(\theta)$ a rotation matrix

$$\boldsymbol{\mathcal{R}}(\theta) = \begin{bmatrix} \cos\theta & -\sin\theta \\ \sin\theta & \cos\theta \end{bmatrix}, \tag{6.57}$$

and the parameter δ is defined as

$$\delta = \frac{a_{\mathrm{hBN}}}{a_{\mathrm{g}}} - 1 \simeq 1.8\% \tag{6.58}$$

where a_{g} and a_{hBN} are, respectively, graphene and hBN lattice parameters. We will assume that all the rotation angles are small. We write the Hamiltonian of the graphene–hBN–graphene structure as

$$H = H_{\mathrm{tg}} + H_{\mathrm{bg}} + H_{\mathrm{hBN}} + (T_{\mathrm{hBN,tg}} + T_{\mathrm{hBN,bg}} + \mathrm{h.c.}), \tag{6.59}$$

where $H_{\mathrm{tg/bg}}$ is the Hamiltonian describing the isolated top/bottom graphene layer, H_{hBN} is the Hamiltonian of the isolated hBN slab and $T_{\mathrm{hBN,tg/bg}} = T^{\dagger}_{\mathrm{tg/bg,hBN}}$ describes the hopping of electrons between the graphene layers and the hBN slab. The vertical current in the device will be dominated by low energy states, which are close to the $\pm\mathbf{K}_{\mathrm{tg/bg}}$ points of the top and bottom graphene layers. As such we use the Dirac continuous model to describe the graphene layers. In the sublattice basis the Bloch form of the Hamiltonian of the bottom graphene layers reads

$$H_{\mathrm{bg}} = \sum_{\mathbf{k},\tau} \boldsymbol{\psi}^{\dagger}_{\mathbf{k}_\tau,\mathrm{bg}} \cdot \begin{bmatrix} V_{\mathrm{bg}} & \tau v_F \hbar\,|\mathbf{k}|\, e^{-\tau i\theta_{\mathbf{k},\mathrm{bg}}} \\ \tau v_F \hbar\,|\mathbf{k}|\, e^{\tau i\theta_{\mathbf{k},\mathrm{bg}}}. & V_{\mathrm{bg}} \end{bmatrix} \cdot \boldsymbol{\psi}_{\mathbf{k}_\tau,\mathrm{bg}}, \tag{6.60}$$

where $\boldsymbol{\psi}^{\dagger}_{\mathbf{k}_\tau,\mathrm{bg}} = \begin{bmatrix} \psi^{\dagger}_{\mathbf{k}_\tau,A,\mathrm{bg}} & \psi^{\dagger}_{\mathbf{k}_\tau,B,\mathrm{bg}} \end{bmatrix}$ is a vector of creation operators in the sublattice A and B of the bottom graphene layer, with momentum $\mathbf{k}$ measured from the the corner of the Brillouin zone$\tau\mathbf{K}_{\mathrm{bg}}$, with $\tau = \pm 1$. $\theta_{\mathbf{k},\mathrm{bg}}$ is the angle between $\mathbf{k}$ and $\mathbf{K}_{\mathrm{bg}}$ and V_{bg} is an on-site potential induced by the applied gate and bias voltages. We choose the zero of energy to lie at the Fermi level of the bottom graphene layer, in which case we have $V_{\mathrm{bg}} = -\epsilon_{F,\mathrm{bg}}$, where $\epsilon_{F,\mathrm{bg}}$ is the Fermi energy of the bottom graphene layer measured from its Dirac point. The Hamiltonian of the top graphene layer has the same form

$$H_{\mathrm{tg}} = \sum_{\mathbf{k}',\tau} \boldsymbol{\psi}^{\dagger}_{\mathbf{k}'_\tau,\mathrm{tg}} \cdot \begin{bmatrix} V_{\mathrm{tg}} & \tau v_F \hbar\,|\mathbf{k}'|\, e^{-i\tau\theta_{\mathbf{k}',\mathrm{tg}}} \\ \tau v_F \hbar\,|\mathbf{k}'|\, e^{i\tau\theta_{\mathbf{k}',\mathrm{tg}}} & V_{\mathrm{tg}} \end{bmatrix} \cdot \boldsymbol{\psi}_{\mathbf{k}'_\tau,\mathrm{tg}}, \tag{6.61}$$

but with $\mathbf{k}'$ measured from the $\tau\mathbf{K}_{\mathrm{tg}}$ point of the Brillouin zone of the top graphene layer and $\theta_{\mathbf{k}',\mathrm{tg}}$ being the angle between $\mathbf{k}'$ and $\mathbf{K}_{\mathrm{tg}}$. Notice that we have $\mathbf{K}_{\mathrm{tg}} = \boldsymbol{\mathcal{R}}(\theta_{\mathrm{hBN}})\cdot\mathbf{K}_{\mathrm{bg}}$. If we use the same reference frame in Eq. (6.61) as in Eq (6.60), we have that

$$\mathbf{k}' = \mathbf{k} + \tau\Delta\mathbf{K}_{\mathrm{b,t}}, \tag{6.62}$$

with $\mathbf{k}$ measured from the $\tau\mathbf{K}_{\mathrm{bg}}$ point and $\Delta\mathbf{K}_{\mathrm{b,t}} = \mathbf{K}_{\mathrm{bg}} - \mathbf{K}_{\mathrm{tg}}$ being the displacement between the Dirac points of the two graphene layers. Just as for the bottom layer, V_{tg} is an on-site potential which, taking into account the bias voltage applied between the two graphene layers, can be written as $V_{\mathrm{tg}} = -\epsilon_{F,\mathrm{tg}} - eV_{\mathrm{bias}}$, where $\epsilon_{F,\mathrm{tg}}$ is the Fermi level measured from the Dirac point of the top graphene layer. In Fig. 6.2 we show how $\epsilon_{F,\mathrm{bg}}$ and $\epsilon_{F,\mathrm{tg}}$ change as a function of V_{gate} and V_{bias}, based on a simple electrostatic model (see Appendix I).

For small rotation angles, electrons will tunnel through the hBN slab also close the $\mathbf{K}_{\rm hBN} = \boldsymbol{\mathcal{R}}(\theta_{\rm hBN}) \cdot \mathbf{K}_{\rm bg}/\left(1+\delta\right)$ point. Close to the $\mathbf{K}_{\rm hBN}$ point and neglecting the dispersion with the in-plane momentum of the hBN bands, we write

$$\begin{aligned} H_{\rm hBN} = &\sum_{\ell=1}^{\mathcal{N}} \sum_{\mathbf{k}'',\tau} \boldsymbol{\psi}^{\dagger}_{\mathbf{k}''_{\tau},\ell,\rm hBN} \cdot \begin{bmatrix} E_{\rm B}+V_{\ell} & 0 \\ 0 & E_{\rm N}+V_{\ell} \end{bmatrix} \cdot \boldsymbol{\psi}_{\mathbf{k}''_{\tau},,\ell,\rm hBN} \\ &+ \sum_{\ell=1}^{\mathcal{N}-1} \sum_{\mathbf{k}'',\tau} \boldsymbol{\psi}^{\dagger}_{\mathbf{k}''_{\tau},\ell+1,\rm hBN} \cdot \begin{bmatrix} 0 & -t_{\perp} \\ -t_{\perp} & 0 \end{bmatrix} \cdot \boldsymbol{\psi}^{\dagger}_{\mathbf{k}''_{\tau},\ell,\rm hBN} + \text{h.c}, \end{aligned} \tag{6.63}$$

where $\boldsymbol{\psi}^{\dagger}_{\mathbf{k}''_{\tau},\ell,\rm hBN} = \begin{bmatrix} \psi^{\dagger}_{\mathbf{k}''_{\tau},\rm B\ell,hBN} & \psi^{\dagger}_{\mathbf{k}''_{\tau},\rm N\ell,hBN} \end{bmatrix}$ is a vector of creation operators in the boron (B) and nitrogen (N) sites in the $\ell^{\rm th}$ hBN monolayer, with crystal momentum $\mathbf{k}''$ measured from $\tau\mathbf{K}_{\rm hBN}$, $E_{\rm B}$ and $E_{\rm N}$ are the on-site energies at the boron and nitrogen sites (measured with respect to the Dirac points of graphene in the absence of any applied voltages), $t_{\perp}$ is an intralayer hopping integral. Typical values for these quantities are given by $E_{\rm B} \simeq 3.33$ eV, $E_{\rm N} \simeq -1.49$ eV [224] and $t_{\perp} \simeq 0.32$ eV [223]. V_{ℓ} is the applied voltage induced on-site energy. Due to the large energy offset between graphene and hBN sites, the charge accumulated in the hBN layers will be negligible. In this case, using a simple electrostatic calculation, we obtain (see Appendix J)

$$V_{\ell} = -\epsilon_{F,\rm bg} - \frac{\ell}{\mathcal{N}+1}\left(\epsilon_{F,\rm tg} + eV_{\rm bias}\right). \tag{6.64}$$

We assume that the bottom graphene layer only couples to the $\ell = 1$ hBN layer and top graphene layer only couples to the $\ell = \mathcal{N}$ layer.

We write the coupling Hamiltonians $T_{\rm hBN,tg/bg} = T^{\dagger}_{\rm tg/bg,hBN}$ in the form of Eqs. (6.50) and (6.53) specialized to the case of graphene and hBN with a small rotation angle and considering only the three most relevant processes. Let us first focus on the coupling between the bottom graphene and the hBN slab (the bottom graphene couples to the $\ell = 1$ hBN monolayer). In Eq. (6.53), we assume that the hopping integrals $t^{(\rm 1hBN,bg)}_{a,b}\left(\mathbf{k}+\mathbf{G}_{m,\rm bg}\right)$ are weakly dependent on momentum and, since we are interested in states close to the $\pm\mathbf{K}_{\rm bg}$ point, we approximate $t^{(\rm 1hBN,bg)}_{a,b}\left(\mathbf{k}+\mathbf{G}_{m,\rm bg}\right) \simeq t^{(\rm 1hBN,bg)}_{a,b}\left(\pm\mathbf{K}_{\rm bg}+\mathbf{G}_{m,\rm bg}\right)$. The three processes with smallest, and equal, $|\pm\boldsymbol{K}_{\rm bg}+\mathbf{G}_{m,\rm bg}|$ are the ones with (see Fig. 6.1(c))

$$\mathbf{G}_{0,\rm bg} = \mathbf{0}, \tag{6.65}$$
$$\mathbf{G}_{1,\rm bg} = \pm\boldsymbol{b}_{2,\rm bg}, \tag{6.66}$$
$$\mathbf{G}_{2,\rm bg} = \mp\boldsymbol{b}_{1,\rm bg}. \tag{6.67}$$

Notice that the these three $\pm\mathbf{K}_{\rm bg}+\mathbf{G}_{m,\rm bg}$ are nothing more than the three equivalent (for an isolated graphene layer) Dirac points of the bottom graphene. According to the generalized umklapp condition Eq. (6.54), the states of bottom graphene with momentum $\mathbf{k}$ will couple to states in the boron nitride with momentum

$$\mathbf{k}' = \mathbf{k} + \mathbf{G}_{n,\rm bg} - \mathbf{G}_{m,\rm hBN}. \tag{6.68}$$

For small rotation angles, the states with smallest $|\mathbf{k}'+\mathbf{G}_{m,\rm hBN}|$ are obtained for $n = m$ with

$$\mathbf{G}_{0,\rm hBN} = \mathbf{0}, \tag{6.69}$$
$$\mathbf{G}_{1,\rm hBN} = \pm\boldsymbol{b}_{2,\rm hBN}, \tag{6.70}$$
$$\mathbf{G}_{2,\rm hBN} = \mp\boldsymbol{b}_{1,\rm hBN}, \tag{6.71}$$

such that the most relevant are the ones where the momentum in the hBN layer is given by

$$\mathbf{k}' = \mathbf{k} + \tau \mathbf{g}_n^{\rm bg}, \tag{6.72}$$

with the vector $\mathbf{g}_n^{\rm bg}$ given by

$$\mathbf{g}_0^{\rm bg} = \mathbf{0}, \tag{6.73}$$
$$\mathbf{g}_1^{\rm bg} = \mathbf{b}_{2,\rm bg} - \mathbf{b}_{2,\rm hBN}, \tag{6.74}$$
$$\mathbf{g}_2^{\rm bg} = -\mathbf{b}_{1,\rm bg} + \mathbf{b}_{1,\rm hBN}. \tag{6.75}$$

Since all the distances $|\pm\mathbf{K}_{\rm bg} + \mathbf{G}_{n,\rm bg}|$ are the same we omit the momentum dependence of $t_{a,b}$ and also suppress indice $(1{\rm hBN}, {\rm bg})$. With these approximations and considering only the three processes given by Eqs. (6.73)-(6.75), the coupling Hamiltonian, Eqs. (6.50) and (6.53), between the bottom graphene and the hBN slab reduces to

$$T_{\rm hBN,bg} = -\sum_{\mathbf{k},\tau,n} \left[\begin{array}{cc} \psi^\dagger_{\mathbf{k}_\tau+\tau\mathbf{g}_n^{\rm bg},\rm B1,hBN} & \psi^\dagger_{\mathbf{k}_\tau+\tau\mathbf{g}_n^{\rm bg},\rm N1,hBN} \end{array} \right] \cdot \\ \cdot \boldsymbol{R}_{\tau n} \cdot \hat{\boldsymbol{T}} \cdot \boldsymbol{R}_{-\tau n} \cdot \left[\begin{array}{c} \psi_{\mathbf{k}_\tau,A,\rm bg} \\ \psi_{\mathbf{k}_\tau,B,\rm bg} \end{array} \right], \tag{6.76}$$

where $\mathbf{k}_\tau$ is measured from $\tau\mathbf{K}_{\rm bg}$ with the matrices $\hat{\boldsymbol{T}}$ and $\boldsymbol{R}_n$ defined as

$$\hat{\boldsymbol{T}} = \left[\begin{array}{cc} t_{\rm B,C} & t_{\rm B,C} \\ t_{\rm N,C} & t_{\rm N,C} \end{array} \right], \tag{6.77}$$
$$\boldsymbol{R}_n = \left[\begin{array}{cc} 1 & 0 \\ 0 & e^{in2\pi/3} \end{array} \right]. \tag{6.78}$$

Typical values for the hoppings between the carbon and boron/nitrogen sites are given by $t_{\rm B,C} \simeq 0.432$ eV and $t_{\rm N,C} \simeq 0.29$ eV [224]. In the derivation of Eq. (6.76), we have used the fact that $e^{i\mathbf{G}_{n,\rm bg}\cdot\boldsymbol{\tau}_{A,\rm bg}} = e^{i\mathbf{G}_{n,\rm hBN}\cdot\boldsymbol{\tau}_{\rm B1,hBN}} = 1$, $e^{i\mathbf{G}_{n,\rm bg}\cdot\boldsymbol{\tau}_{B,\rm bg}} = e^{i\mathbf{G}_{n,\rm hBN}\cdot\boldsymbol{\tau}_{\rm N1,hBN}} = e^{im2\pi/3}$, where

$$\boldsymbol{\tau}_{A,\rm bg} = \mathbf{0}, \qquad \boldsymbol{\tau}_{\rm B1,hBN} = \mathbf{0},$$
$$\boldsymbol{\tau}_{B,\rm bg} = \frac{\mathbf{a}_{1,\rm bg} + \mathbf{a}_{2,\rm bg}}{3}, \qquad \boldsymbol{\tau}_{\rm N1,hBN} = \frac{\mathbf{a}_{1,\rm bg} + \mathbf{a}_{2,\rm bg}}{3},$$

are the sublattice vectors for the graphene and the $\ell = 1$ hBN monolayer. Notice the matrices $\boldsymbol{R}_n$ just perform a rotation of the graphene and hBN sublattice spinors. The coupling Hamiltonian between the top graphene and the $\ell = \mathcal{N}$ hBN layer, $T_{\rm hBN,tg}$, as the same form as Eq. (6.76) just replacing $\mathbf{b}_n^{\rm bg}$ by $\mathbf{b}_n^{\rm tg}$, with

$$\mathbf{g}_0^{\rm tg} = \mathbf{0}, \tag{6.79}$$
$$\mathbf{g}_1^{\rm tg} = \mathbf{b}_{2,\rm tg} - \mathbf{b}_{2,\rm hBN}, \tag{6.80}$$
$$\mathbf{g}_2^{\rm tg} = -\mathbf{b}_{1,\rm tg} + \mathbf{b}_{1,\rm hBN}, \tag{6.81}$$

and noticing that in the case when $\mathcal{N}$ is even it is also necessary to replace

$$\boldsymbol{R}_{\tau n} \to \left[\begin{array}{cc} e^{i\tau n2\pi/3} & 0 \\ 0 & 1 \end{array} \right]. \tag{6.82}$$

since in a hBN slab with AA′ and an even number of layer, the position of the boron and nitrogen atoms in the last layer is flipped in comparison to the first layer. Hamiltonians of the form of Eq. (6.76) have previously been used to study twisted graphene bilayers [194, 225–227] and graphene–on–hBN structures [224, 228, 229].

Considering the three processes coupling the bottom graphene with hBN, in $T_{\mathrm{hBN,bg}}$, and the three processes connecting hBN to the top graphene layer, in $T_{\mathrm{tg,hBN}}$, there are nine hBN mediated processes coupling the bottom graphene layer to the top one. These nine processes couple a state from the bottom graphene layer with momentum $\mathbf{k}$ (measured from $\tau\mathbf{K}_{\mathrm{bg}}$) to states of the top graphene layer with momentum $\mathbf{k}+\tau\boldsymbol{\mathcal{Q}}_{n,m}$ (measured from $\tau\mathbf{K}_{\mathrm{tg}}$), with $\boldsymbol{\mathcal{Q}}_{n,m}$ given by

$$\boldsymbol{\mathcal{Q}}_{n,m} = \Delta\mathbf{K}_{\mathrm{b,t}} + \mathbf{g}_n^{\mathrm{bg}} - \mathbf{g}_m^{\mathrm{tg}},\ n,m = 0,1,2. \tag{6.83}$$

The processes with $n \neq m$ involve transfer of momentum by the hBN lattice, while processes with $n = m$ do not. At zero magnetic field, the overall three-fold rotational invariance of the graphene–hBN–graphene structure implies that these nine processes can be organized in three groups of three, with processes in the same group being related by $2\pi/3$ rotations, therefore giving the same contribution to the vertical current. The three groups are

$$\begin{aligned} &\{\boldsymbol{\mathcal{Q}}_{0,0},\ \boldsymbol{\mathcal{Q}}_{1,1},\ \boldsymbol{\mathcal{Q}}_{2,2}\}, \\ &\{\boldsymbol{\mathcal{Q}}_{0,1},\ \boldsymbol{\mathcal{Q}}_{1,2},\ \boldsymbol{\mathcal{Q}}_{2,0}\}, \\ &\{\boldsymbol{\mathcal{Q}}_{0,2},\ \boldsymbol{\mathcal{Q}}_{1,0},\ \boldsymbol{\mathcal{Q}}_{2,1}\}, \end{aligned} \tag{6.84}$$

with length of the vectors in each group being the same. For small rotation angles and lattice mismatch, $\delta = a_{\mathrm{hBN}}/a_{\mathrm{g}} - 1$, we have

$$\frac{|\boldsymbol{\mathcal{Q}}_{0,0}|^2}{K_{\mathrm{g}}^2} \simeq \theta_{\mathrm{tg}}^2, \tag{6.85}$$

$$\frac{|\boldsymbol{\mathcal{Q}}_{0,1}|^2}{K_{\mathrm{g}}^2} \simeq \theta_{\mathrm{tg}}^2 + 3\left(\theta_{\mathrm{hBN}}^2 + \delta^2 - \theta_{\mathrm{tg}}\theta_{\mathrm{hBN}}\right) + \sqrt{3}\delta\theta_{\mathrm{tg}}, \tag{6.86}$$

$$\frac{|\boldsymbol{\mathcal{Q}}_{0,2}|^2}{K_{\mathrm{g}}^2} \simeq \theta_{\mathrm{tg}}^2 + 3\left(\theta_{\mathrm{hBN}}^2 + \delta^2 - \theta_{\mathrm{tg}}\theta_{\mathrm{hBN}}\right) - \sqrt{3}\delta\theta_{\mathrm{tg}}, \tag{6.87}$$

with $K_{\mathrm{g}} = 4\pi/(3a_{\mathrm{g}})$ the length of $\mathbf{K}_{\mathrm{bg}}$.

6.5 COHERENT TRANSPORT IN GRAPHENE–HBN–GRAPHENE STRUCTURES

As previously discussed in Section 6.2, when applying the NEGF formalism to mesoscopic transport, one must make a distinction between the electrodes, which are assumed to be non-interacting and in thermal equilibrium, and the central mesoscopic region. In a graphene–hBN–graphene device, one might be tempted to treat the graphene layers as the electrodes. However, as also discussed in Section 6.2, in order to obtain a steady state current, it is required that the electrodes are macroscopic with a continuum of electronic states. Although the graphene layers do have a continuum of states (for large enough samples), due to momentum conservation, the number of states that can couple (efficiently) to a given Bloch state of hBN is finite. In this situation, it seems to be safer to treat the graphene layers as part of the mesoscopic device and to treat as electrodes the metallic contacts that are attached to graphene. This is also the most convenient approach to include effects of interactions in the

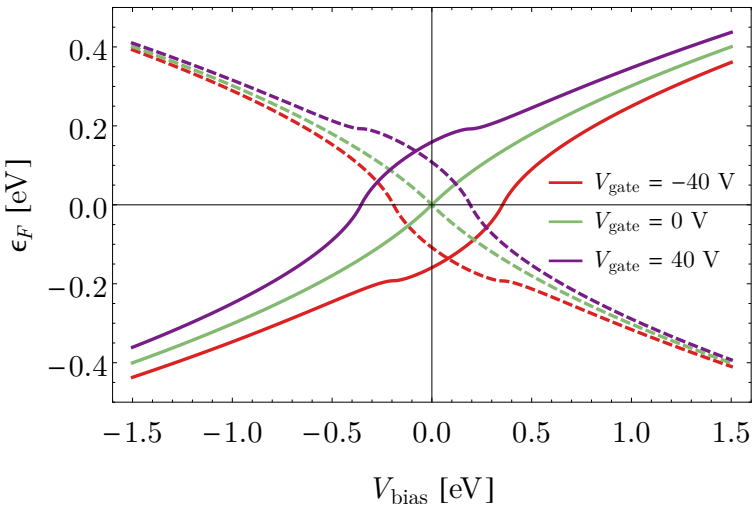

Figure 6.2: Computed Fermi levels for the bottom and top graphene layers as a function of bias voltage for different gate voltages obtained using the electrostatic model described in Appendix J. We assume that the graphene layers have no intrinsic doping and that the graphene–hBN–graphene structure is separated from the Si bottom gate by an hBN/SIO_2 dielectric with thickness $d_{\rm hBN} = 40$ nm and $d_{SiO_2} = 285$ nm, and out-of-plane dielectric constants $\epsilon_{SiO_2} = 3.9$ and $\epsilon_{\rm hBN} = 5.09$[184], respectively. We assumed that the two graphene layers are separated by 4 monolayers of hBN, corresponding to a distance between the graphene layers of $d \simeq 1.6$ nm.

graphene layers as we will see in the next section. In order to compute the coherent vertical in the graphene–hBN–graphene device we use Eq. (6.29), with $\boldsymbol{G}^{R/A}(\omega)$ the retarded/advanced Green's function of the graphene–hBN–graphene device and $\boldsymbol{\Gamma}_{\rm t/b}(\omega)$ the level width function due to the metallic contacts that are attached to the top/bottom graphene layers. Notice that due to the Bloch diagonal structure of the graphene–hBN–graphene structure, Eq. (6.59), we can write the matrix elements of the Green's function connecting the top and bottom graphene sites as

$$\left[\boldsymbol{G}^{R}(\omega)\right]_{\rm t,b} = \boldsymbol{G}^{0,R}_{\rm tg}(\omega)\cdot\boldsymbol{T}_{\rm tg,bg}(\omega)\cdot\boldsymbol{G}^{0,R}_{\rm bg}(\omega), \tag{6.88}$$

$$\left[\boldsymbol{G}^{A}(\omega)\right]_{\rm b,t} = \boldsymbol{G}^{0,A}_{\rm bg}(\omega)\cdot\boldsymbol{T}_{\rm bg,tg}(\omega)\cdot\boldsymbol{G}^{0,A}_{\rm tg}(\omega), \tag{6.89}$$

where $\boldsymbol{G}^{0,R/A}_{\rm tg/bg}$ are the retarded/advanced Green's function of the top/bottom graphene layers in the absence of graphene–hBN coupling (but taking into account the coupling to the metallic contacts) and where we have defined the hBN mediated tunnelling amplitudes

$$\boldsymbol{T}_{\rm tg,bg}(\omega) = \boldsymbol{T}_{\rm tg,hBN}\cdot\boldsymbol{G}^{R}_{\rm hBN}(\omega)\cdot\boldsymbol{T}_{\rm hBN,bg}, \tag{6.90}$$

$$\boldsymbol{T}_{\rm bg,tg}(\omega) = \boldsymbol{T}_{\rm bg,hBN}\cdot\boldsymbol{G}^{A}_{\rm hBN}(\omega)\cdot\boldsymbol{T}_{\rm hBN,tg}, \tag{6.91}$$

with $\boldsymbol{G}^{R/A}_{\rm hBN}$ the Green's function of the hBN slab, which in general takes into account its coupling to the graphene layers. Therefore, the transmission function Eq. (6.30) can be written as

$$\mathcal{T}^{(0)}_{\rm t,b}(\omega) = {\rm Tr}\Big[\boldsymbol{G}^{0,A}_{\rm tg}(\omega)\cdot\boldsymbol{\Gamma}_{\rm t}(\omega)\cdot\boldsymbol{G}^{0,R}_{\rm tg}(\omega)\cdot\boldsymbol{T}_{\rm tg,bg}(\omega)\cdot \cdot\boldsymbol{G}^{0,R}_{\rm bg}(\omega)\cdot\boldsymbol{\Gamma}_{\rm b}(\omega)\cdot\boldsymbol{G}^{0,A}_{\rm bg}(\omega)\cdot\boldsymbol{T}_{\rm bg,tg}(\omega)\Big]. \tag{6.92}$$

Noticing that the Green's functions $\boldsymbol{G}^{0,R/A}_{\mathrm{tg/bg}}$ only take into account the coupling of the graphene layers to the metallic electrodes, we can use Eqs. (6.22) and (6.24) to write the spectral function of the bottom and top graphene layers as

$$\begin{aligned}\boldsymbol{A}^{0}_{\mathrm{tg/bg}}(\omega) &= \boldsymbol{G}^{0,A}_{\mathrm{tg/bg}}(\omega)\cdot\boldsymbol{\Gamma}_{\mathrm{t/b}}(\omega)\cdot\boldsymbol{G}^{0,R}_{\mathrm{tg/bg}}(\omega)\\ &= \boldsymbol{G}^{0,R}_{\mathrm{tg/bg}}(\omega)\cdot\boldsymbol{\Gamma}_{\mathrm{t/b}}(\omega)\cdot\boldsymbol{G}^{0,A}_{\mathrm{tg/bg}}(\omega).\end{aligned} \tag{6.93}$$

The coherent transmission function Eq. (6.92) can thus be expressed as

$$\mathcal{T}^{(0)}_{\mathrm{t,b}}(\omega) = \mathrm{Tr}\left[\boldsymbol{A}^{0}_{\mathrm{tg}}(\omega)\cdot\boldsymbol{T}_{\mathrm{tg,bg}}(\omega)\cdot\boldsymbol{A}^{0}_{\mathrm{bg}}(\omega)\cdot\boldsymbol{T}_{\mathrm{bg,tg}}(\omega)\right]. \tag{6.94}$$

The coherent contribution to the vertical current is given by Eq. (6.29) with transmission function given by the above equation and with the occupation factors given by $f_{\mathrm{b}}(\omega) = f(\omega)$ and $f_{\mathrm{t}}(\omega) = f(\omega + eV_{\mathrm{bias}})$. This is the expression for the current that would be directly obtained if we had treated the graphene layers as the electrodes (taking into account their coupling to the metallic contacts), in which case the level width functions entering Eq. (6.30) would be given by $\boldsymbol{\Gamma}_{\mathrm{b}} = \boldsymbol{T}_{\mathrm{hBN,bg}}\cdot\boldsymbol{A}^{0}_{\mathrm{bg}}\cdot\boldsymbol{T}_{\mathrm{hBN,bg}}$ and $\boldsymbol{\Gamma}_{\mathrm{t}} = \boldsymbol{T}_{\mathrm{hBN,tg}}\cdot\boldsymbol{A}^{0}_{\mathrm{tg}}\cdot\boldsymbol{T}_{\mathrm{hBN,tg}}$. As such, we have proved that in the non-interacting case, treating graphene as part of the mesoscopic region or as a part of the electrodes is inconsequential. We will leave the discussion for the interacting case for the next section.

In order to make analytical progress, we will employ the wide-band limit for the metallic contacts, which amounts to neglecting any frequency dependence of $\boldsymbol{\Gamma}_{\mathrm{t/b}}$ and writing $\boldsymbol{\Sigma}^{R/A}_{\mathrm{t/b}} = \pm i\boldsymbol{\Gamma}_{\mathrm{t/b}}$, which in general is a good approximation for metals, and assuming that the contacts couple equally to all graphene states, not spoiling translation invariance, that is

$$\boldsymbol{\Gamma}_{\mathrm{t/b}}(\omega) = \Gamma_{\mathrm{t/b}}\boldsymbol{I}_{\mathrm{tg/bg}}, \tag{6.95}$$

where $\boldsymbol{I}_{\mathrm{tg/bg}}$ is the identity operator in top/bottom graphene subspace. We expect that this last approximation will work well for devices in which the metallic contacts are deposited on a small region of the graphene sample (but might fail drastically when a significant portion of the graphene layers are contacted to the metal). Within these approximations, the only effect of the metallic contacts is to introduce a broadening factor of $\gamma_{\mathrm{tg/bg}} = \Gamma_{\mathrm{t/b}}/2$ in the Green's function of the bottom/top graphene layer, which in the terms of graphene eigenstates reads

$$A^{0}_{\mathrm{tg/bg},\mathbf{k},\tau,\lambda}(\omega_{\mathrm{tg/bg}}) = \frac{2\gamma_{\mathrm{tg/bg}}}{\left(\omega_{\mathrm{tg/bg}} - \lambda v_F\hbar\left|\mathbf{k}\right|\right)^2 + \gamma^2_{\mathrm{tg/bg}}}, \tag{6.96}$$

where $\lambda = \pm 1$ is the band index and we have written $\omega_{\mathrm{bg}} = \omega + \epsilon_{F,\mathrm{bg}}$ and $\omega_{\mathrm{tg}} = \omega + \epsilon_{F,\mathrm{tg}} + eV_{\mathrm{bias}}$, which correspond to energies measured from the position of the Dirac point in the bottom and top graphene layers, respectively. We will now write $\mathcal{T}^{(0)}_{\mathrm{t,b}}(\omega)$ more explicitly. Using the graphene–hBN coupling Hamiltonian Eq. (6.76), the transmission function can be written using the Bloch momentum basis as

$$\begin{aligned}\mathcal{T}^{(0)}_{\mathrm{t,b}}(\omega) = \sum_{\substack{\mathbf{k},\lambda,\lambda'\\ n,m,\tau}} &\left|{}_{\mathrm{tg}}\left\langle\mathbf{k}+\tau\boldsymbol{\mathcal{Q}}_{n,m},\tau,\lambda'\right|\boldsymbol{T}_{\mathrm{tg,bg}}(\omega)\left|\mathbf{k},\tau,\lambda\right\rangle_{\mathrm{bg}}\right|^2\times\\ &\times A^{0}_{\mathrm{tg},\mathbf{k}+\tau\boldsymbol{\mathcal{Q}}_{n,m},\tau,\lambda'}(\omega_{\mathrm{tg}})A^{0}_{\mathrm{bg},\mathbf{k},\tau,\lambda}(\omega_{\mathrm{bg}})\end{aligned} \tag{6.97}$$

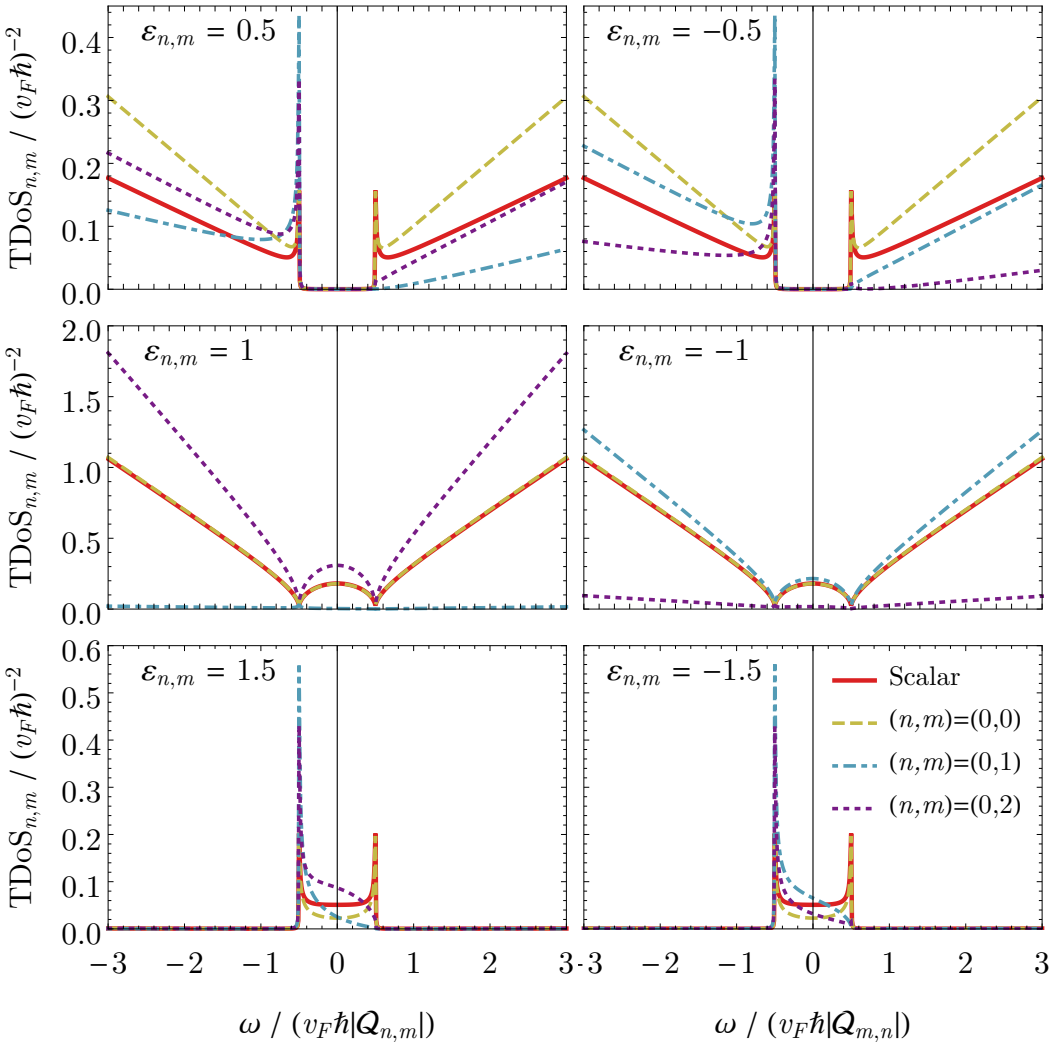

Figure 6.3: Tunnelling density of states in a graphene–hBN–graphene vertical structure as a function of energy measured from the midpoint between the two graphene layer Dirac points, $\mathrm{TDoS}_{n,m}(\omega, \epsilon_{n,m})$ Eq. (6.105). We consider rotation angles of $\theta_{\mathrm{tg}} = 1^{\mathrm{o}}$ and $\theta_{\mathrm{hBN}} = 1.5^{\mathrm{o}}$ at zero magnetic field. The solid red line shows the tunnelling density of states if the wavefunction overlap factors $\Upsilon^{B/T,n}_{\mathbf{k},\lambda}$ in Eq. (6.103) are set to one. A constant broadening factor of $\gamma = 2.5 \times v_F\hbar\,|\boldsymbol{\mathcal{Q}}_{n,m}| \times 10^{-3}$ was used in all plots.

with the sum over n, m ranging from 0 to 2. The effective tunnelling probability can be written as

$$\left|{}_{\mathrm{tg}}\left\langle \mathbf{k}+\boldsymbol{\mathcal{Q}}_{n,m},\tau,\lambda'\right|\boldsymbol{\mathcal{T}}_{\mathrm{tg,bg}}(\omega)\left|\mathbf{k},\tau,\lambda\right\rangle_{\mathrm{bg}}\right|^2=\Upsilon^{\mathrm{bg},n}_{\mathbf{k},\tau,\lambda}\Upsilon^{\mathrm{tg},m}_{\mathbf{k}+\tau\boldsymbol{\mathcal{Q}}_{n,m},\tau,\lambda}\left|\mathscr{T}^{(0)}_{n,m}(\omega)\right|^2, \quad (6.98)$$

where we have introduced the graphene wavefunction overlap factors

$$\begin{aligned}\Upsilon^{\mathrm{tg/bg},n}_{\mathbf{k},\tau,\lambda}&=\frac{1}{2}\left|1+\lambda\tau e^{i\left(\tau\theta_{\mathbf{k},\mathrm{tg/bg}}-n2\pi/3\right)}\right|^2\\&=1+\tau\lambda\hat{\mathbf{k}}\cdot\hat{\mathbf{K}}_{\mathrm{bg/tg},n},\end{aligned} \quad (6.99)$$

with $\mathbf{K}_{\mathrm{bg/tg},n}=\boldsymbol{\mathcal{R}}\left(n2\pi/3\right)\cdot\mathbf{K}_{\mathrm{bg/tg}}$, and we introduced the tunnelling amplitude

$$\mathscr{T}^{(0)}_{n,m}(\omega)=\frac{1}{2}\mathrm{tr}\left\{\hat{\boldsymbol{T}}^{\dagger}\cdot\boldsymbol{R}_{\tau m}\cdot\left[\boldsymbol{G}^{R}_{\mathrm{hBN}}(\omega)\right]_{\mathcal{N},1}\cdot\boldsymbol{R}_{-\tau n}\cdot\hat{\boldsymbol{T}}\right\}, \quad (6.100)$$

with the trace being performed over the sublattice degrees of freedom. In the case where there is an even number of hBN monolayers, $\boldsymbol{R}_{\tau m}$ must be replaced as in Eq. (6.82). Since hBN is a large gap insulator, it is a good approximation to neglect the frequency dependence of $\boldsymbol{G}^{R/A}_{\mathrm{hBN}}$. In that case and to lowest order in the interlayer hopping, $t_{\perp}$, we obtain

$$\begin{aligned}\left|\mathscr{T}^{(0)}_{n,m}\right|^2\simeq&\left(\frac{t_{\perp}^2}{E_{\mathrm{B}}E_{\mathrm{N}}}\right)^{\mathcal{N}-1}\times\\&\times\begin{cases}4\frac{t^2_{\mathrm{B,C}}t^2_{\mathrm{N,C}}}{E_{\mathrm{B}}E_{\mathrm{N}}}\cos^2\left(\frac{\pi}{3}\left(n-m\right)\right) & ,\,\mathcal{N}\text{ is even}\\ \frac{t^4_{\mathrm{B,C}}}{E^2_{\mathrm{B}}}+\frac{t^4_{\mathrm{N,C}}}{E^2_{\mathrm{N}}}+2\frac{t^2_{\mathrm{B,C}}t^2_{\mathrm{N,C}}}{E_{\mathrm{B}}E_{\mathrm{N}}}\cos\left(\frac{2\pi}{3}\left(n-m\right)\right) & ,\,\mathcal{N}\text{ is odd}\end{cases}\end{aligned} \quad (6.101)$$

Notice that in Eq. (6.97) both valleys give the same contribution, which can be seen by making a simultaneous change $\tau\to-\tau$ and $\mathbf{k}\to-\mathbf{k}$. The transmission function can then be written as

$$\mathcal{T}^{(0)}_{\mathrm{t,b}}(\omega)=Ag_sg_v\sum_{n,m=0}^{3}\left|T^{(0)}_{n,m}\right|^2\mathrm{TDoS}_{n,m}(\omega_{\mathrm{bg}},\omega_{\mathrm{tg}}) \quad (6.102)$$

where A is the area of the device, $g_s=g_v=2$ are the spin and valley degeneracies, and we have defined the tunnelling density of states as

$$\begin{aligned}\mathrm{TDoS}_{n,m}(\omega_{\mathrm{bg}},\omega_{\mathrm{tg}})=\sum_{\lambda,\lambda'=\pm1}\int\frac{d^2\mathbf{k}}{(2\pi)^2}\Upsilon^{\mathrm{bg},n}_{\mathbf{k},\lambda}\Upsilon^{\mathrm{tg},m}_{\mathbf{k}+\boldsymbol{\mathcal{Q}}_{n,m},\lambda'}\times\\\times A^0_{\mathrm{bg},\mathbf{k},\lambda}(\omega_{\mathrm{bg}})A^0_{\mathrm{tg},\mathbf{k}+\boldsymbol{\mathcal{Q}}_{n,m},\lambda'}(\omega_{\mathrm{tg}}),\end{aligned} \quad (6.103)$$

which only depends on the graphene's dispersion relation and wavefunctions (for simplicity we have dropped the valley index τ). An analytic expression for Eq. 6.103 is provided in Appendix J.

6.5.1 *Results*

Tunnelling in a graphene–hBN–graphene structure is controlled both by energy-momentum conservation, encoded in $\mathrm{TDoS}_{n,m}(\omega_{\mathrm{bg}},\omega_{\mathrm{tg}})$, and by Pauli's exclusion principle, encoded in $f(\omega)-f(\omega+eV_{\mathrm{bias}})$. The constrains imposed by energy-momentum conservation can

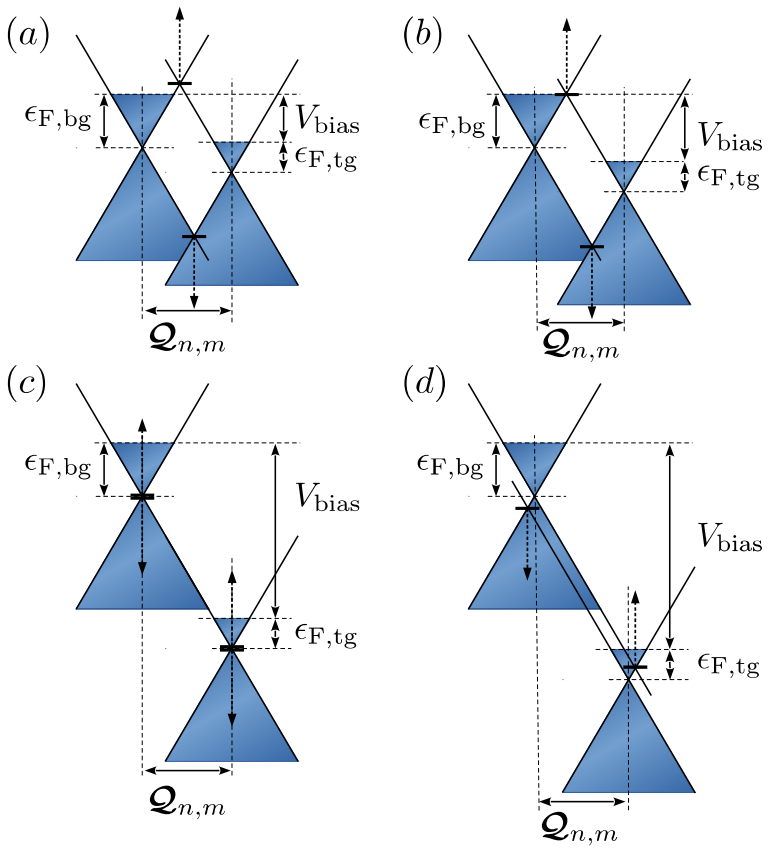

Figure 6.4: Schematic representation of the constrains imposed by energy-momentum conservation and Pauli's exclusion principle on the vertical current. The two cones represent the electronic dispersion relation for the graphene layers, with the shadowed regions representing the electronic filling. Energy-momentum conservation is only satisfied when the two shifted Dirac cones intersect. The dashed arrows represent the energy windows where this occurs. The following cases are represented: (a) Only intraband processes are possible, $\varepsilon_{n,m} < 1$, these are however Pauli blocked or there are no states available. Therefore in the low temperature limit, no vertical current flows. (b) Threshold bias voltage above which intraband processes satisfying energy-momentum conservation appear in the energy window where tunnelling is allowed by the electronic occupation factors. (c) Condition which corresponds to the occurrence of a peak in the current, when $\varepsilon_{n,m} = 1$, when both intraband and interband processes are allowed. (d) If one further increases the bias voltage, only interband tunnelling, $\varepsilon_{n,m} > 1$, becomes possible and the current decreases.

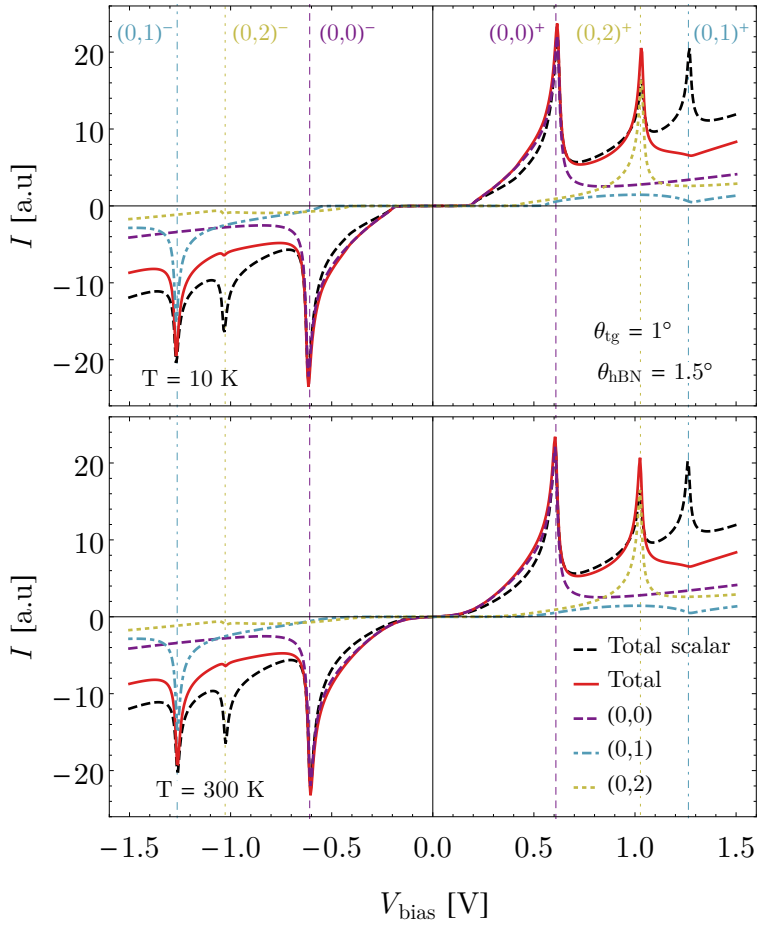

Figure 6.5: I-V curves for vertical current in a graphene–hBN–graphene device with 4 layers of hBN for rotation angles of $\theta_{\rm tg} = 1^{\rm o}$ and $\theta_{\rm hBN} = 1.5^{\rm o}$ at gate voltage $V_{\rm gate} = 0$, for two different temperatures. The solid red line indicates the current due to all the 9 processes coupling both graphene layers, for graphene electrons, while the dashed black lines represents the total current for scalar electrons (by setting the wavefunction factors $\Upsilon^{{\rm bg/tg},n}_{\mathbf{k},\lambda}$ to 1). The remaining lines represent the contributions to the current arising from processes involving different $\boldsymbol{\mathcal{Q}}_{n,m}$ (taking into account the relations imposed by 3-fold rotational invariance, Eq. 6.84). The dashed vertical lines labelled by $(n,m)^{\pm}$ mark the bias voltages when the condition $\epsilon_{F,{\rm tg}} + eV_{\rm bias} - \epsilon_{F,{\rm bg}} = \pm v_F\hbar|\boldsymbol{\mathcal{Q}}_{n,m}|$ is satisfied. Notice that while for scalar electrons all the expected peaks in the current are present, for Dirac electrons some of them are absent. Is is due to the suppression by the $\Upsilon^{{\rm bg/tg},n}_{\mathbf{k},\lambda}$ factors. (A constant broadening factor of $\gamma = 2.5$ meV was used.)

be understood considering that the Dirac cones of the bottom and top graphene layers are shifted in energy by a value of $\epsilon_{F,\mathrm{tg}} + eV_{\mathrm{bias}} - \epsilon_{F,\mathrm{bg}}$ and in momentum by a value of $|\boldsymbol{\mathcal{Q}}_{n,m}|$, see Fig. 6.4. The intersection of the shifted cones allows us to visualize the states which respect energy-momentum conservation[53]. Whenever the bias voltage is tuned such that

$$\epsilon_{F,\mathrm{tg}} + eV_{\mathrm{bias}} - \epsilon_{F,\mathrm{bg}} = \pm v_F \hbar \left|\boldsymbol{\mathcal{Q}}_{n,m}\right|, \tag{6.104}$$

there is a maximum overlap of the Dirac cones and a peak in the current occurs. This can also be seen in the plot for$\mathrm{TDoS}_{n,m}(\omega_{\mathrm{bg}}, \omega_{\mathrm{tg}})$ as a function of the energy measured from the midpoint between the Dirac points of the two layers,

$$\mathrm{TDoS}_{n,m}(\omega, \varepsilon_{n,m}) = \mathrm{TDoS}_{n,m}(\omega + \varepsilon_{n,m} v_F \hbar \left|\boldsymbol{\mathcal{Q}}_{n,m}\right|/2, \omega - \varepsilon_{n,m} v_F \hbar \left|\boldsymbol{\mathcal{Q}}_{n,m}\right|/2), \tag{6.105}$$

with $\varepsilon_{n,m}$ defined as

$$\varepsilon_{n,m} = \frac{\epsilon_{F,\mathrm{tg}} + eV_{\mathrm{bias}} - \epsilon_{F,\mathrm{bg}}}{v_F \hbar \left|\boldsymbol{\mathcal{Q}}_{n,m}\right|}, \tag{6.106}$$

as shown in Fig. 6.3. For $\varepsilon_{n,m}^2 < 1$, the tunnelling is due to intraband processes (from the conduction/valence band of the bottom graphene into the conduction/valence band of the top graphene), going to zero in the pristine limit for $\omega^2 < (v_F\hbar)^2 \left|\boldsymbol{\mathcal{Q}}_{n,m}\right|^2/4$. For $\varepsilon_{n,m}^2 > 1$, the tunnelling is due to interband processes (from the conduction/valence band of the bottom graphene layer to the valence/conduction band of the top graphene layer), being zero in the pristine limit for $\omega^2 > (v_F\hbar)^2 \left|\boldsymbol{\mathcal{Q}}_{n,m}\right|^2/4$. For $\varepsilon_{n,m}^2 = 1$, the quantity $\mathrm{TDoS}_{n,m}(\omega, \varepsilon_{n,m})$ diverges in the pristine limit for any value of ω. This divergence in $\mathrm{TDoS}_{n,m}(\omega_{\mathrm{bg}}, \omega_{\mathrm{tg}})$ leads to a divergence in the vertical current, which is made finite with the introduction of a finite electronic lifetime [52, 53]. Since processes involving different $\boldsymbol{\mathcal{Q}}_{n,m}$'s correspond to a different effective separation between the Dirac cones of both graphene layers in reciprocal space, one expects the occurrence of multiple peaks in the I-V curve, followed by regions of negative differential conductance. This is indeed the case as shown in Fig. 6.5. According to the discussion of Section 6.4, from the nine processes coupling the two graphene layers, only three are independent. Therefore, based only on energy-momentum conservation, one would expect the occurrence of three peaks in the I-V curve for positive bias voltage and another three for negative bias. However, in Fig. 6.5 only two peaks are displayed, with those corresponding to the situations with $\varepsilon_{0,1} = +1$ and $\varepsilon_{0,2} = -1$ being absent. The reason for the suppression of these peaks is due to the spinorial structure of graphene electronic wavefunctions, which is encoded in the overlap factors $\Upsilon_{\mathbf{k},\lambda}^{\mathrm{bg/tg},n}$, that appear in Eq. (6.103). As seen in Fig. 6.3, these overlap factors can severely suppress the value of $\mathrm{TDoS}_{n,m}$ close to $\varepsilon_{n,m} = \pm 1$ and, consequently, suppress the height of the peaks in the I-V curve. The effect of the overlap factors is also represented in Fig. 6.5, where it is also shown the current that would be obtained if one would set $\Upsilon_{\mathbf{k},\lambda}^{\mathrm{bg/tg},n} = 1$ in (6.103) (see also Eq J.23 in Appendix J), displaying the three peaks expected purely by kinematic considerations. Tunnelling processes, which satisfy energy-momentum conservation, can only contribute to the current if these lie in an energy window between the zero of energy and the bias voltage, as presented in Fig. 6.4. The condition for which processes allowed by energy-momentum conservation become allowed by the occupation factors occurs in the limit of zero temperature when, see Fig. 6.4.(b),

$$\epsilon_{F,\mathrm{tg}} \pm eV_{\mathrm{bias}} + \epsilon_{F,\mathrm{bg}} = \pm \frac{1}{2} v_F \hbar \left|\boldsymbol{\mathcal{Q}}_{n,m}\right|. \tag{6.107}$$

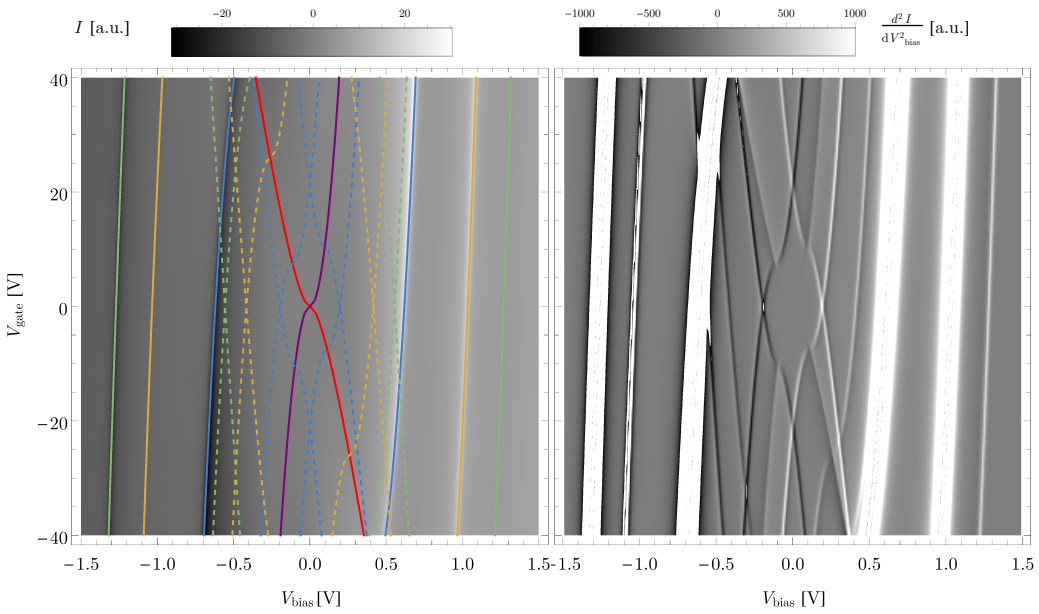

Figure 6.6: Density plot of the current (on the left) and of its second derivative with respect to $V_{\rm bias}$ (on the right) as a function of $V_{\rm bias}$ and $V_{\rm gate}$ at $T = 10$ K, for a device with 4 hBN layers and rotation angles of $\theta_{\rm tg} = 1°$ and $\theta_{\rm hBN} = 1.5°$. In the current plot are also shown the lines defined by the conditions: $\epsilon_{\rm F,tg/bg} = 0$, the solid purple/red line; $\epsilon_{F,\rm tg} + eV_{\rm bias} - \epsilon_{F,\rm bg} = \pm v_F\hbar\,|\boldsymbol{\mathcal{Q}}_{n,m}|$ (Eq. (6.104)) for $n = 0$ and $m = 0$, 1, 2, respectively, the blue, green and yellow solid lines; $\epsilon_{F,\rm tg} \pm eV_{\rm bias} + \epsilon_{F,\rm bg} = \pm v_F\hbar\,|\boldsymbol{\mathcal{Q}}_{n,m}|/2$ (Eq. (6.107)) for $n = 0$ and $m = 0$, 1, 2, the blue, green and yellow dashed lines. A constant broadening factor of $\gamma = 2.5$ meV was used.

This explains the occurrence of the plateau with nearly zero current observed at low temperature in Fig. 6.5, and gives origin to the features in the $d^2I/dV^2_{\rm bias}$ as a function of applied bias and gate voltages as seen in the density plot of Fig. 6.6 (also highlighted by the dashed guidelines). At higher temperatures, all these sharp features tend to vanish, as the Fermi-Dirac occupation factors become smoother functions of the energy.

By applying an in-plane magnetic field, the threefold rotational invariance of the graphene–hBN–graphene structure is broken, and therefore, the processes corresponding to the different groups in Eq. (6.84) will contribute differently to the current. In this case, we expect that each peak in the I-V curve, that appeared in the case with no applied magnetic field, will split into three. An in-plane magnetic field of the form $\mathbf{B} = B\,(\cos\phi_B, \sin\phi_B, 0)$ can be described by the vector potential $\mathbf{A} = Bz\,(\sin\phi_B, -\cos\phi_B)$. Neglecting the momentum dependence of $H_{\rm hBN}$, the effect of the in-plane magnetic field reduces to an additional transference of momentum to the tunnelling electrons, which is encoded in a shift in the $\boldsymbol{\mathcal{Q}}_{n,m}$ vectors [52, 53, 230–232]

$$\boldsymbol{\mathcal{Q}}_{n,m} \to \boldsymbol{\mathcal{Q}}_{n,m} + \frac{eBd}{\hbar}\,(\sin\phi_B, -\cos\phi_B)\,. \tag{6.108}$$

The splitting of the peaks with the in-plane magnetic field in the I-V curve is shown in Fig. 6.7, where it is also shown the effect of an increase in the electronic broadening factor. It is important to notice that the position of the peaks in the I-V curve is very sensitive on the relative rotation angles between the graphene layers and the graphene layers and the hBN slab. This is also clearly shown in Fig. 6.7. As shown, for a fixed angle of $\theta_{\rm tg} = 1°$, changing $\theta_{\rm hBN}$ from 1.5° to 3° moves the peaks that involve

transference of momentum by the hBN crystalline structure (with $n \neq m$) from a bias voltage of ~ 1 V to bias voltages $\gtrsim 1.5$ V .

Finally, we comment on the possible effect of the hBN in the electronic structure of graphene. Due to generalized umklapp processes, the crystal momentum of an electron in a graphene layer that is in contact with an hBN layer is no longer conserved. If as before we consider only processes involving reciprocal lattice vectors of smallest length, than graphene states that are connect by vectors given by $\mathbf{g}^{\mathrm{bg}}_{1/2}$ (Eqs. (6.74) and (6.75)), for the bottom graphene layer, or $\mathbf{g}^{\mathrm{tg}}_{1/2}$ ((6.80) and (6.81)), for the top graphene layer, will couple to each other. In a nearly free electron model, this means that states with energies of the order of $\pm v_F \hbar \left|\mathbf{g}^{\mathrm{bg/tg}}_{1/2}\right| /2$ (with $\left|\mathbf{g}^{\mathrm{bg/tg}}_{1/2}\right| \simeq 4\pi\sqrt{\delta^2 + \left(\theta_{\mathrm{bg/tg}} - \theta_{\mathrm{hBN}}\right)^2}/(\sqrt{3}a_{\mathrm{g}})$ for small rotation angles and lattice mismatch) will have a strong reconstruction of the spectrum [196–201]. These effects would modify the terms H_{tg} (Eq. (6.61)) and H_{bg} (Eq. (6.60)) in the Hamiltonian of Eq. (6.59). We have disregarded such reconstruction effects in our model. As we have seen in Fig. 6.7, the additional peaks in the current enabled by the transference of momentum by the hBN lattice, only appear for reasonable values of the bias voltage for small twist angles between the graphene layers and hBN slab. It is precisely in this case that the spectrum reconstruction of the graphene becomes important at low energy. The effect of this reconstruction should impact not only the peaks that involve transference of momentum by the hBN lattice ($n \neq m$), but also the ones that do not ($n = m$). In this situation one can question the validity of neglecting reconstruction effects. However, we argue that the possible reconstruction of the graphene dispersion relation should not affect in a profound way the occurrence of peaks and NDC in the I-V curves of graphene–hBN–graphene devices. The energy width, Δ, where the reconstruction of the linear dispersion relation of graphene is significant is of the order of the tens or in the worst case a few hundreds of meV [197, 233], while the total energy window of states that contribute to the current is, at low temperatures, of the width of $\sim eV_{\mathrm{bias}}$. Provided the condition $eV_{\mathrm{bias}} \gg \Delta$ is satisfied (see Fig. 6.8), we expect that the effect of the graphene dispersion relation reconstruction will be negligible, and apart from a possible reduction of the height of the peaks, should not affect the current in any drastic way.

6.6 EFFECT OF SCATTERING

6.6.1 *Disorder scattering in the graphene layers*

The effect of disorder in the vertical current of a graphene–hBN–graphene device can be simply studied by performing disorder averages of the Landauer formula Eq. (6.29) (an alternative approach where the disorder averaging is treated as an effective interaction is done in the next subsection). Considering only disorder in the graphene layers and assuming that disorder does not establish any correlations between the two graphene layers or between the graphene layers and the hBN slab, the disorder averaged current is given by

$$\overline{I^{(\mathrm{coh})}_{\mathrm{t}\to\mathrm{b}}} = -e \int \frac{d\omega}{2\pi} \left(f_{\mathrm{t}}(\omega) - f_{\mathrm{b}}(\omega)\right) \mathrm{Tr}\Big[\overline{\boldsymbol{G}^{0,A}_{\mathrm{tg}}(\omega)\cdot\boldsymbol{\Gamma}_{\mathrm{t}}(\omega)\cdot\boldsymbol{G}^{0,R}_{\mathrm{tg}}(\omega)}\cdot \cdot\boldsymbol{T}_{\mathrm{tg,bg}}(\omega)\cdot\overline{\boldsymbol{G}^{0,R}_{\mathrm{bg}}(\omega)\cdot\boldsymbol{\Gamma}_{\mathrm{b}}(\omega)\cdot\boldsymbol{G}^{0,A}_{\mathrm{bg}}(\omega)}\cdot\boldsymbol{T}_{\mathrm{bg,tg}}(\omega)\Big], \quad (6.109)$$

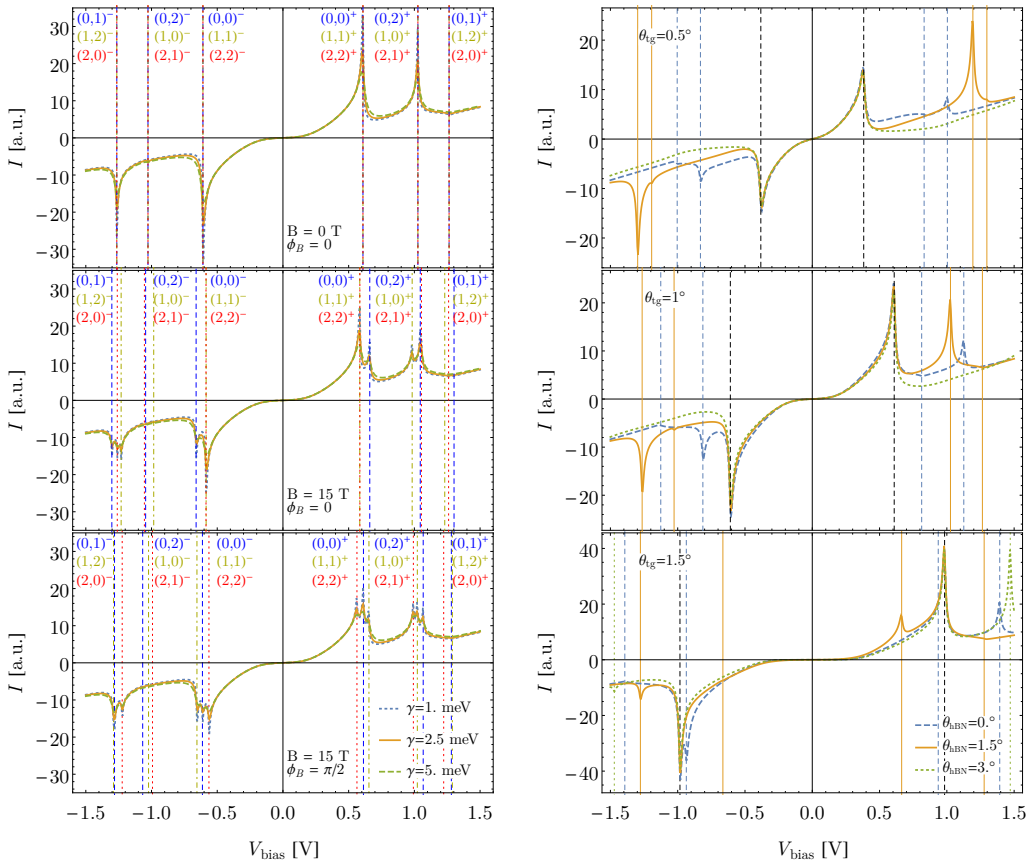

Figure 6.7: I-V curves at $V_{\text{gate}} = 0$ and $T = 300$ K in a graphene–hBN–graphene device with 4 layers of hBN. (Left) For different values and orientation of the in-plane magnetic field and electronic broadening factor and fixed $\theta_{\text{tg}} = 1°$ and $\theta_{\text{hBN}} = 1.5°$. The vertical lines, labelled by $(n, m)^{\pm}$, mark the bias voltages for which $\varepsilon_{n,m} = \pm 1$. Notice how the applied magnetic field leads to a splitting of the peaks that occur at zero magnetic field. As the broadening factor is increased, the peaks become less resolved. (Right) For different rotation angles between the top and bottom graphene layers, and the hBN slab and the bottom graphene layer. The black dashed line marks the bias voltage when $\varepsilon_{0,0} = \pm 1$ (a condition that is independent of θ_{hBN}). The remaining vertical lines mark the bias voltages when $\varepsilon_{n,m} = \pm 1$ for $n \neq m$ for different values θ_{hBN} (the colour and type of line match the ones used in the plots). A value of $\gamma_{\text{tg/bg}} = 2.5$ meV was used.

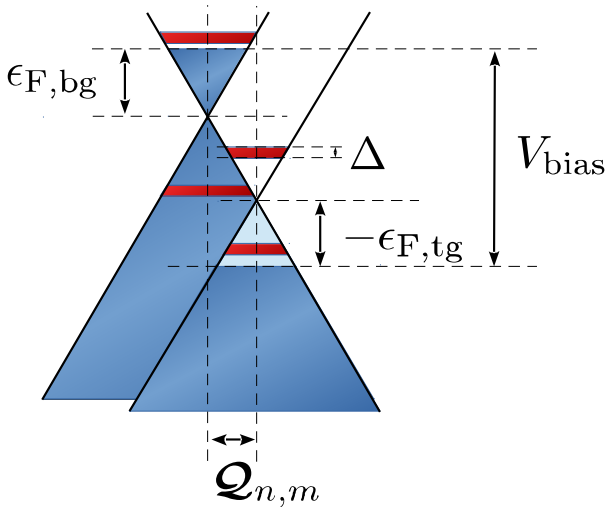

Figure 6.8: Diagram representing the regions with possible reconstruction of the graphene Dirac spectrum due to the presence of hBN, when $\varepsilon_{n,m} = \pm 1$. The red bars represent the position in energy of the regions, with width Δ, where graphene's spectrum is significantly reconstructed.

where the bar represents disordered averaging. Notice that before performing the disorder averaging we have that by Eqs. (6.22) and (6.24) $\boldsymbol{G}^{0,A}_{\mathrm{tg}}(\omega)\cdot\boldsymbol{\Gamma}_{\mathrm{t}}(\omega)\cdot\boldsymbol{G}^{0,R}_{\mathrm{tg}}(\omega) = \boldsymbol{A}^{0}_{\mathrm{tg}}(\omega)$ and $\boldsymbol{G}^{0,R}_{\mathrm{bg}}(\omega)\cdot\boldsymbol{\Gamma}_{\mathrm{b}}(\omega)\cdot\boldsymbol{G}^{0,A}_{\mathrm{bg}}(\omega) = \boldsymbol{A}^{0}_{\mathrm{bg}}(\omega)$ even in the presence of a disorder potential in the graphene layers. Therefore, under the previous considerations, the vertical current in the presence of disorder in the graphene layers is just given by

$$\overline{I^{(\mathrm{coh})}_{\mathrm{t}\to\mathrm{b}}} = e\int\frac{d\omega}{2\pi}\left(f(\omega)-f(\omega+eV_{\mathrm{bias}})\right)\times \\ \times\,\mathrm{Tr}\left[\overline{\boldsymbol{A}^{0}_{\mathrm{tg}}}(\omega)\cdot\boldsymbol{T}_{\mathrm{tg,bg}}(\omega)\cdot\overline{\boldsymbol{A}^{0}_{\mathrm{bg}}}(\omega)\cdot\boldsymbol{T}_{\mathrm{bg,tg}}(\omega)\right], \quad (6.110)$$

where $\overline{\boldsymbol{A}^{0}_{\mathrm{tg/bg}}}(\omega)$ are the disorder averaged spectral functions, which can be obtained from $\overline{\boldsymbol{A}^{0}_{\mathrm{tg/bg}}}(\omega) = i\left(\overline{\boldsymbol{G}^{0,R}_{\mathrm{tg/bg}}}(\omega) - \overline{\boldsymbol{G}^{0,A}_{\mathrm{tg/bg}}}(\omega)\right)$. This is the result that would be immediately obtained if we treated the disordered graphene layers as forming the electrodes.

The previous result can also be obtained without using Eqs. (6.22) and (6.24), but performing instead the average of the product of Green's functions that appears in Eq. (6.109). This approach will be more convoluted, but will provide guidance for when we turn or attention to the case of scattering by graphene phonons, when the current is given by a sum of the Landauer formula, Eq. (6.29), and incoherent processes, Eq. (6.31). In the presence of disorder, the average of the product of two Green's functions is not just the product of the averages, as correlations are established between the two quantities by the averaging process. Employing a notation where in-coming particles are represented by a lower index and out-going particles are described by an upper index, see also Appendix H, the average of the product of an advanced and retarded Green's function can be expressed as

$$\overline{[G^{0,A}]^{a}{}_{b}\,\Gamma^{b}{}_{c}\,[G^{R,0}]^{c}{}_{d}} = \left[\overline{G^{0,A}}\right]^{a}{}_{b}\,\Gamma^{b}{}_{c}\left[\overline{G^{0,R}}\right]^{c}{}_{d} + \\ + \left[\overline{G^{0,A}}\right]^{a}{}_{a'}\,\Lambda^{a'}{}_{b'}{}^{c'}{}_{d'}\left[G_2^{AR}\right]^{b'}{}_{b}{}^{c}{}_{c'}\,\Gamma^{b}{}_{c}\left[\overline{G^{0,R}}\right]^{d'}{}_{d}, \quad (6.111)$$

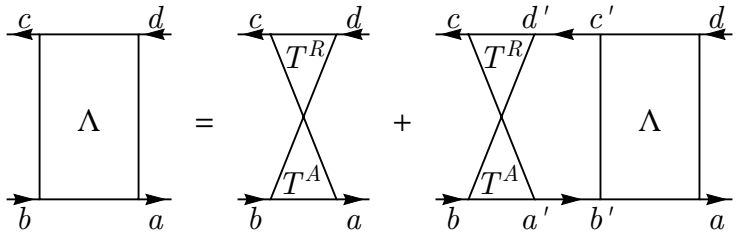

Figure 6.9: Diagrammatic representation of the Bethe-Salpeter equation, Eq. (6.113), in the T-matrix an non-crossing approximations.

where the equation is valid for both the top and bottom graphene layer and all quantities are evaluated at the same frequency and for that reason we drop the frequency argument and the layer index. In the previous equation the first term is just the product of the average and the second term includes the corrections to this: vertex corrections. We introduced

$$\left[G_2^{AR}\right]^{a\ c}_{\ b\ d} = \left[\overline{G^{0,A}}\right]^{a}_{\ b} \left[\overline{G^{0,R}}\right]^{c}_{\ d}, \tag{6.112}$$

and introduced the 4-point function $\Lambda^{a\ c}_{\ b\ d}$, which obeys a Bethe-Salpeter equation (see Fig. (6.9))

$$\Lambda^{a\ c}_{\ b\ d} = U^{a\ c}_{\ b\ d} + \Lambda^{a'\ c}_{\ b\ d'} \left[G_2^{AR}\right]^{b'\ \ d'}_{\ a'\ \ c'} U^{a\ c'}_{\ b'\ d}, \tag{6.113}$$

where $U^{a\ c}_{\ b\ d}$ is an irreducible 4-point vertex. In order to make progress we will focus on the case of resonant impurities, such as vacancies, which we model as a δ-like potential of strength u and diagonal in the sublattice degrees of freedom. We focus on this kind of impurities for the possibility of analytical progress and due to the fact that this impurity model correctly predicts a graphene transport lifetime that is proportional to the Fermi energy, $\tau_{\text{tr}} \propto \epsilon_F$ [174].

Short range disorder can give rise to resonances, which are not captured when treating disorder correlations within a Gaussian approximation [234]. A way to overcome this is to employ the T-matrix approximation, which, in the low impurity concentration, correctly describes multiple scattering events evolving the same impurity. In order to solve the Bethe-Salpeter equation, we must first compute the impurity averaged Green's functions. Using the T-matrix approximation for resonant impurities, within the non-crossing or self-consistent Born approximation, the Dyson equation for the Green's functions (in a sublattice and Bloch basis) for a graphene layer (disconnected from hBN) reads

$$\overline{\boldsymbol{G}_{\mathbf{k}}^{0,R}}(\omega) = \boldsymbol{G}_{\mathbf{k}}^{0,R}(\omega) + \boldsymbol{G}_{\mathbf{k}}^{0,R}(\omega) \cdot \boldsymbol{\Sigma}_{\text{SCBA}}^{R}(\omega) \cdot \overline{\boldsymbol{G}_{\mathbf{k}}^{0,R}}(\omega), \tag{6.114}$$

where the matrices here have indices in the sublattice space, $\boldsymbol{G}_{\mathbf{k}}^{0,R}(\omega)$ is the disorder free Green's function and the self-energy due to resonant impurities is momentum independent and is given by

$$\boldsymbol{\Sigma}_{\text{SCBA}}^{R}(\omega) = n_{\text{imp}} T_{\text{imp}}^{R}(\omega) \boldsymbol{I}. \tag{6.115}$$

In this expression, n_{imp} is the impurity concentration (number of impurities per unit cell), $\boldsymbol{I}$ the identity in sublattice basis and

$$T_{\text{imp}}^{R}(\omega) = \frac{u}{1 - u\overline{G_1^R}(\omega)} \underset{u\to\infty}{=} -\frac{1}{\overline{G_1^R}(\omega)}, \tag{6.116}$$

where we have taken the limit $u \to \infty$ in order to describe vacancies and defined $\overline{G_1^R}(\omega)$ as the on-site Green's function of sublattice A (or B)

$$\overline{G_1^R}(\omega) = \int \frac{d^2\mathbf{k}}{(2\pi)^2} \left[\overline{G_{\mathbf{k}}^{0,R}}(\omega)\right]^A_{\ A}. \tag{6.117}$$

In the Dirac cone approximation, we have

$$\left[\overline{G_{\mathbf{k}}^{0,R}}(\omega)\right]^a_{\ b} = \sum_{\lambda=\pm1} \frac{\delta^a_{\ b} + \lambda \hat{\mathbf{k}} \cdot \boldsymbol{\sigma}^a_{\ b}}{\omega - \lambda v_F \hbar |\mathbf{k}| + i\gamma_c - \Sigma^R_{\mathrm{SCBA}}(\omega)}, \tag{6.118}$$

with a and b indices running over the A and B sublattice sites, $\gamma_\ell$is the lifetime induced by the metallic contact (ℓ =tg/bg). Splitting the self-energy in real and imaginary parts $\Sigma^R_{\mathrm{imp}}(\omega) = \Sigma_{\mathrm{imp}}(\omega) - i\gamma_{\mathrm{imp}}(\omega)$ and using the fact that it is momentum independent, the integration in Eq. (6.117) can be performed analytic leading to

$$\overline{G_1^R}(\omega) = \frac{g_1\left(\omega - \Sigma_{\mathrm{imp}}(\omega), \gamma_{\mathrm{imp}}(\omega) + \gamma_\ell\right)}{4\pi\left(v_F\hbar\right)^2} - i\frac{g_2\left(\omega - \Sigma_{\mathrm{imp}}(\omega), \gamma_{\mathrm{imp}}(\omega) + \gamma_\ell\right)}{4\pi\left(v_F\hbar\right)^2}, \tag{6.119}$$

where the functions g_1 and g_2 are given by

$$g_1(\omega,\eta) = -\frac{\omega}{2}\left[\log\left(\frac{(\Lambda_E-\omega)^2+\eta^2}{\omega^2+\eta^2}\right) + (\omega \to -\omega)\right] + \eta\left[\arctan\left(\frac{\Lambda_E-\omega}{\eta}\right) + \arctan\left(\frac{\omega}{\eta}\right) - (\omega \to -\omega)\right] \tag{6.120}$$

$$g_2(\omega,\eta) = \frac{\eta}{2}\left[\log\left(\frac{(\Lambda_E-\omega)^2+\eta^2}{\omega^2+\eta^2}\right) + (\omega \to -\omega)\right] + \omega\left[\arctan\left(\frac{\Lambda_E-\omega}{\eta}\right) + \arctan\left(\frac{\omega}{\eta}\right) - (\omega \to -\omega)\right] \tag{6.121}$$

with $\Lambda_E \simeq v_F\hbar\left(4\pi/\left(\sqrt{3}a_g^2\right)\right)^{1/2}$ a high energy cutoff. In terms of g_1 and g_2 the self-energy is given by

$$\Sigma_{\mathrm{imp}}(\omega) = -4\pi\left(v_F\hbar\right)^2 n_{\mathrm{imp}} \frac{g_1(\omega',\gamma')}{g_1^2(\omega',\gamma') + g_2^2(\omega',\gamma')}, \tag{6.122}$$

$$\gamma_{\mathrm{imp}}(\omega) = 4\pi\left(v_F\hbar\right)^2 n_{\mathrm{imp}} \frac{g_2(\omega',\gamma')}{g_1^2(\omega',\gamma') + g_2^2(\omega',\gamma')}. \tag{6.123}$$

where we have written$\omega' = \omega - \Sigma_{\mathrm{imp}}(\omega)$, $\gamma' = \gamma_\ell + \gamma_{\mathrm{imp}}(\omega)$. Equations (6.120)-(6.123) form system of equations that can be easily solved numerically. The solution for self-energy is shown in Fig. 6.10.

We are now in a position to solve Eq. (6.113). Within the SCBA and T-matrix approximations, the 4-point irreducible vertex $U^{a\ c}_{\ b\ d}$ for resonant impurities is momentum independent and given in the sublattice basis by

$$U^{a\ c}_{\ b\ d} = n_{\mathrm{imp}} \left|T^R_{\mathrm{imp}}(\omega)\right|^2 \delta^a_{\ b}\delta^c_{\ d}. \tag{6.124}$$

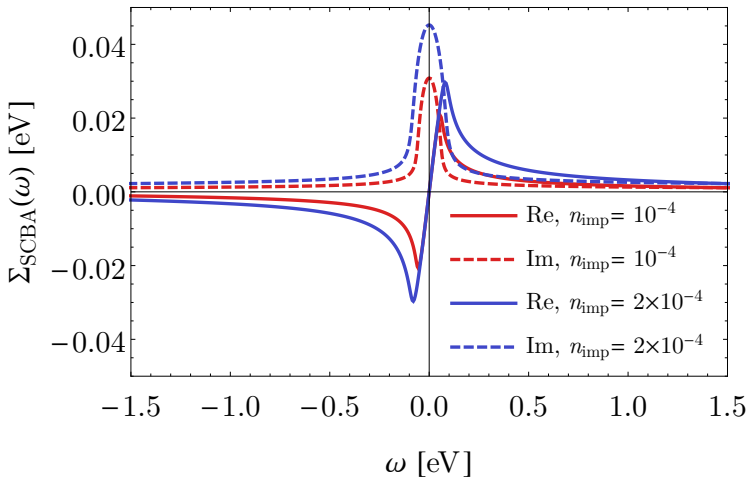

Figure 6.10: Real and (minus) imaginary parts of the retarded self-energy for graphene electrons due to resonant impurities treated within the SCBA, for two different impurity concentrations (number of impurities per graphene unit cell).

The quantity $\left[G_2^{AR}\right]^{a\ c}_{\ b\ d}$ is also momentum independent and given by

$$\left[G_2^{AR}\right]^{a\ c}_{\ b\ d} = \int \frac{d^2\mathbf{k}}{(2\pi)^2} \left[\overline{G^A_{\mathbf{k}}}\right]^{a}_{\ b} \left[\overline{G^R_{\mathbf{k}}}\right]^{c}_{\ d}. \tag{6.125}$$

The integration over momentum can be perform analytically, yielding

$$\left[G_2^{AR}\right]^{a\ c}_{\ b\ d} = L_1\left(\omega',\gamma'\right)\delta^a{}_b\delta^c{}_d + L_2\left(\omega',\gamma'\right)\frac{1}{2}\boldsymbol{\sigma}^a{}_b\cdot\boldsymbol{\sigma}^c{}_d, \tag{6.126}$$

where

$$L_1(\omega,\eta) = \frac{1}{8\pi\left(v_F\hbar\right)^2}\left(\frac{1}{\eta}g_2(\omega,\eta)+\frac{1}{\omega}g_1(\omega,\eta)\right), \tag{6.127}$$

$$L_2(\omega,\eta) = \frac{1}{8\pi\left(v_F\hbar\right)^2}\left(\frac{1}{\eta}g_2(\omega,\eta)-\frac{1}{\omega}g_1(\omega,\eta)\right). \tag{6.128}$$

The Bethe-Salpeter equation for $\Lambda^{a\ c}_{\ b\ d}$ is now a simple problem of linear algebra. Solving Eq. (6.113), yields the non-zero components of $\Lambda^{a\ c}_{\ b\ d}$ in the sublattice basis (omitting frequency arguments)

$$\begin{aligned}\Lambda^{A\ A}_{\ A\ A} =& \Lambda^{B\ B}_{\ B\ B}\\ =& \frac{n_{\mathrm{imp}}\left|T^R\right|^2\left(1-L_1 n_{\mathrm{imp}}\left|T^R\right|^2\right)}{\left[1-\left(L_1-L_2\right)n_{\mathrm{imp}}\left|T^R\right|^2\right]\left[1-\left(L_1+L_2\right)n_{\mathrm{imp}}\left|T^R\right|^2\right]},\end{aligned} \tag{6.129}$$

$$\begin{aligned}\Lambda^{A\ B}_{\ B\ A} =& \Lambda^{B\ A}_{\ A\ B}\\ =& \frac{L_2 n_{\mathrm{imp}}^2\left|T^R\right|^4}{\left[1-\left(L_1-L_2\right)n_{\mathrm{imp}}\left|T^R\right|^2\right]\left[1-\left(L_1+L_2\right)n_{\mathrm{imp}}\left|T^R\right|^2\right]},\end{aligned} \tag{6.130}$$

$$\Lambda^{A\ B}_{\ A\ B} = \Lambda^{B\ A}_{\ B\ A} = \frac{n_{\mathrm{imp}}\left|T^R\right|^2}{1-L_1 n_{\mathrm{imp}}\left|T^R\right|^2}. \tag{6.131}$$

Using the fact that $\left[G_2^{AR}\right]^{b'\ b}_{\ b\ c'} = (L_1(\omega) + L_2(\omega))\,\delta^{b'}{}_{c'}$, the vertex correction contribution in Eq. (6.111) can be written as

$$\Lambda^{a'}{}_{b'}{}^{c'}{}_{d'}\left[G_2^{AR}\right]^{b'\ c}_{\ b\ c'} = \frac{n_{\rm imp}\left|T^R\right|^2(L_1+L_2)}{1-(L_1+L_2)\,n_{\rm imp}\left|T^R\right|^2}\delta^c{}_b, \tag{6.132}$$

Expressing T^R and $L_{1/2}$ in terms of g_1 and g_2, and using Eqs. (6.123) it can be seen that the quantity $(L_1+L_2)\,n_{\rm imp}\left|T^R\right|^2$ can be written as the ratio

$$(L_1+L_2)\,n_{\rm imp}\left|T^R\right|^2 = \frac{\gamma_{\rm imp}}{\gamma_{\rm imp}+\gamma_\ell}. \tag{6.133}$$

Therefore, using the fact that $\Gamma^a{}_b = \delta^a{}_b\gamma_\ell/2$, Eq. (6.111) can be written as

$$\begin{aligned}\frac{\gamma_\ell}{2}\overline{\left[G^{0,A}_{\mathbf{k}}\right]^a{}_b\left[G^{R,0}_{\mathbf{k}}\right]^b{}_d} &= \frac{\gamma_\ell}{2}\left[G^{0,A}_{\mathbf{k}}\right]^a{}_b\left[G^{R,0}_{\mathbf{k}}\right]^b{}_d + \frac{\gamma_\ell}{2}\frac{\gamma_{\rm imp}}{\gamma_\ell}\left[G^{0,A}_{\mathbf{k}}\right]^a{}_b\left[G^{R,0}_{\mathbf{k}}\right]^b{}_d \\ &= \frac{\gamma_{\rm c}+\gamma_{\rm imp}}{2}\left[G^{0,A}_{\mathbf{k}}\right]^a{}_b\left[G^{R,0}_{\mathbf{k}}\right]^b{}_d.\end{aligned} \tag{6.134}$$

If we now use Eqs. (6.22)-(6.24) we recover Eq. (6.110). It seems that we went through a lot of work to obtain a trivial result. However, we will see in the next section that vertical current in the presence of phonon scattering in the graphene layers, under the same assumptions that interactions do not establish correlations between the graphene layers and the hBN slab, is also described by an equation of the form of Eq. (6.110). This is obtained by summing an infinite series of vertex corrections just as for the solution of the Bethe-Salpeter equation within the SCBA.

6.6.2 *Phonon scattering in the graphene layers*

We now turn our attention to the effect of scattering by graphene phonons in the vertical current. We will first only consider scattering in the bottom graphene layer, but scattering in the top layer can be treated in the same way. Using Eq. (6.43) and Eqs. (6.88)-(6.91), the n-phonon assisted transmission function can be written to lowest order in the graphene–hBN coupling as

$$\begin{aligned}\mathcal{T}^{(n)(s_1,\zeta_1),\ldots,(s_n,\zeta_n)}_{\rm t,b}(\omega) \simeq {\rm Tr}\Big[&\boldsymbol{T}_{\rm bg,tg}(\omega)\cdot\boldsymbol{G}^{0,A}_{\rm tg}(\omega)\cdot\boldsymbol{\Gamma}_{\rm t}(\omega)\cdot\boldsymbol{G}^{0,R}_{\rm tg}(\omega)\cdot\boldsymbol{T}_{\rm tg,bg}(\omega)\cdot \\ &\cdot\boldsymbol{G}^{0,R}_{\rm bg}(\omega)\cdot\boldsymbol{M}_{\zeta_1}\cdot\boldsymbol{G}^{0,R}_{\rm bg}(\omega-s_1\omega_{\zeta_1})\cdot\ldots\cdot\boldsymbol{M}_{\zeta_n}\cdot \\ &\cdot\boldsymbol{G}^{0,R}_{\rm bg}(\omega-s_1\omega_\zeta-s_n\omega_{\zeta_n})\cdot\boldsymbol{\Gamma}_{\rm b}(\omega-s_1\omega_\zeta-s_n\omega_{\zeta_n})\cdot\boldsymbol{G}^{0,A}_{\rm bg}(\omega-s_1\omega_\zeta-s_n\omega_{\zeta_n})\cdot \\ &\cdot\boldsymbol{M}^\dagger_{\zeta_n}\cdot\ldots\cdot\boldsymbol{G}^{0,A}_{\rm bg}(\omega-s_1\omega_{\zeta_1})\cdot\boldsymbol{M}^\dagger_{\zeta_1}\cdot\boldsymbol{G}^{0,A}_{\rm bg}(\omega)\Big],\end{aligned} \tag{6.135}$$

where the ^{0} index means only that the graphene functions do not include effects of the coupling to the hBN slab, but include electron-phonon scattering effects. In the following we will drop this index. For now, we are ignoring the electron-phonon interaction in the top graphene layer, and therefore we can write $\boldsymbol{A}_{\rm bg}(\omega) = \boldsymbol{G}^A_{\rm tg}(\omega)\cdot\boldsymbol{\Gamma}_{\rm t}(\omega)\cdot\boldsymbol{G}^R_{\rm tg}(\omega)$. Using the fact that the equilibrium occupation factors satisfy the identity

$$\begin{aligned}\frac{1-f(\omega-s\Omega)}{1-f(\omega)}\left[-sb(-s\Omega)\right] &= \frac{f(\omega-s\Omega)}{f(\omega)}sb(s\Omega) \\ &= s\left(1-f(\omega-s\Omega)+b(s\Omega)\right),\end{aligned} \tag{6.136}$$

the occupation factors $W_{\mathrm{t,b}}^{(n)(s_1,\zeta_1),\ldots,(s_n,\zeta_n)}(\omega)$, Eq. (6.44), can be written in a recursive form as

$$W_{\mathrm{t,b}}^{(n)(s_1,\zeta_1),\ldots,(s_n,\zeta_n)}(\omega) = W_{\mathrm{t,b}}^{(n-1)(s_1,\zeta_1),\ldots,(s_{n-1},\zeta_{n-1})}(\omega)\times \\ \times \frac{(1-f_{\mathrm{b}}(\omega - s_1\omega_{\zeta_1}\ldots - s_n\omega_{\zeta_n}))}{(1-f_{\mathrm{b}}(\omega - s_1\omega_{\zeta_1}\ldots - s_{n-1}\omega_{\zeta_{n-1}}))}\left(-s_n b(-s_n\omega_{\zeta_n})\right), \quad (6.137)$$

with

$$W_{\mathrm{t,b}}^{(0)}(\omega) = f_{\mathrm{t}}(\omega)\left(1-f_{\mathrm{b}}(\omega)\right) - \left(1-f_{\mathrm{t}}(\omega)\right) f_{\mathrm{b}}(\omega) \\ = f_{\mathrm{t}}(\omega) - f_{\mathrm{b}}(\omega). \quad (6.138)$$

Using the phonon assisted transmission function given by Eq. (6.135) and the above recurrence relation for the occupation factors, the sum of all the incoherent contributions due to electron-phonon interaction in the bottom graphene layer to the current with the the contribution due to the coherent transmission function given by Eq. (6.92), allows us to write the total current as

$$I_{\mathrm{t}\to\mathrm{b}} = \frac{e}{\hbar}\sum_{n=0}^{\infty}\int\frac{d\omega}{2\pi}\left(f_{\mathrm{b}}(\omega) - f_{\mathrm{t}}(\omega)\right)\times \\ \times \mathrm{Tr}\left[\boldsymbol{A}_{\mathrm{tg}}(\omega)\cdot\boldsymbol{T}_{\mathrm{tg,bg}}(\omega)\cdot\boldsymbol{A}_{\mathrm{bg}}^{(n)}(\omega)\cdot\boldsymbol{T}_{\mathrm{bg,tg}}(\omega)\right], \quad (6.139)$$

where the different factors $\boldsymbol{A}_{\mathrm{tg}}^{(n)}(\omega)$ obey the recursion relation

$$\boldsymbol{A}_{\mathrm{bg}}^{(0)}(\omega) = \boldsymbol{G}_{\mathrm{bg}}^{R}(\omega)\cdot\boldsymbol{\Gamma}_{\mathrm{b}}(\omega)\cdot\boldsymbol{G}_{\mathrm{bg}}^{A}(\omega), \quad (6.140)$$

$$\boldsymbol{A}_{\mathrm{bg}}^{(n)}(\omega) = \frac{(1-f_{\mathrm{b}}(\omega - s_n\omega_{\zeta_n}))}{(1-f_{\mathrm{b}}(\omega))}\left(-s_n b(-s_n\omega_{\zeta_n})\right)\times \\ \times \boldsymbol{G}_{\mathrm{bg}}^{R}(\omega)\cdot\boldsymbol{M}_{\zeta_n}\cdot\boldsymbol{A}_{\mathrm{bg}}^{(n-1)}(\omega - s_n\omega_{\zeta_n})\cdot\boldsymbol{M}_{\zeta_n}^{\dagger}\cdot\boldsymbol{G}_{\mathrm{bg}}^{A}(\omega),\ n>0. \quad (6.141)$$

This can be compared with the spectral function of the bottom graphene layer. Taking into account the coupling of the bottom graphene layer to the bottom electrode and the electron-phonon interaction, the spectral function for the bottom graphene layer can be written as (Eq. (6.22))

$$\boldsymbol{A}_{\mathrm{bg}}(\omega) = \boldsymbol{G}_{\mathrm{bg}}^{R}(\omega)\cdot\left(\boldsymbol{\Gamma}_{\mathrm{b}}(\omega) + \boldsymbol{\Gamma}_{\mathrm{int}}(\omega)\right)\cdot\boldsymbol{G}_{\mathrm{bg}}^{A}(\omega), \quad (6.142)$$

where $\boldsymbol{\Gamma}_{\mathrm{int}}(\omega)$ is the decay rate due to the electron-phonon interaction. Assuming that the bottom graphene is in equilibrium with the bottom electrode, we can write

$$\boldsymbol{G}_{\mathrm{bg}}^{<}(\omega) \simeq i f_{\mathrm{b}}(\omega)\boldsymbol{A}_{\mathrm{bg}}(\omega), \quad (6.143)$$

$$\boldsymbol{G}_{\mathrm{bg}}^{>}(\omega) \simeq -i\left(1-f_{\mathrm{b}}(\omega)\right)\boldsymbol{A}_{\mathrm{bg}}(\omega). \quad (6.144)$$

Using this approximation, together with Eqs. (6.23) and (6.36), the decay rate due to the electron phonon interaction can be written as

$$\boldsymbol{\Gamma}_{\mathrm{int}}(\omega) \simeq \sum_{s,\zeta} s\left(1-f_{\mathrm{b}}(\omega - s\omega_{\zeta}) + b(s\omega_{\zeta})\right)\boldsymbol{M}_{\zeta}\cdot\boldsymbol{A}_{\mathrm{tg}}(\omega - s\omega_{\zeta})\cdot\boldsymbol{M}_{\zeta}^{\dagger}. \quad (6.145)$$

Inserting Eq. (6.145) into Eq. (6.142) and using the relation Eq. (6.136), we see that $\boldsymbol{A}_{\mathrm{bg}}(\omega)$ can be written as

$$\boldsymbol{A}_{\mathrm{bg}}(\omega) = \sum_{n=0}^{\infty}\boldsymbol{A}_{\mathrm{bg}}^{(0)}(\omega). \quad (6.146)$$

This argumentation can be repeated for scattering in the top graphene layer. Therefore, the total vertical current tacking into account electron-phonon interactions in the graphene layers is given by

$$I_{\mathrm{t}\to\mathrm{b}} = \frac{e}{\hbar}\int \frac{d\omega}{2\pi}\left(f_{\mathrm{b}}(\omega) - f_{\mathrm{t}}\left(\omega\right)\right)\times \\ \times \mathrm{Tr}\left[\boldsymbol{A}_{\mathrm{tg}}(\omega)\cdot\boldsymbol{T}_{\mathrm{tg,bg}}(\omega)\cdot\boldsymbol{A}_{\mathrm{bg}}(\omega)\cdot\boldsymbol{T}_{\mathrm{bg,tg}}(\omega)\right], \quad (6.147)$$

provided the graphene spectral functions include the effects of the electron-phonon interaction. This is the same result that would be obtained if the graphene layers were treated as electrodes, being in thermal equilibrium. To lowest order in the graphene–hBN coupling, Eq. (6.147) includes all the possible electron-phonon scattering processes occurring in the graphene layers. To higher order in the graphene–hBN coupling, Eq. (6.147) no longer includes all the possible contributions due to the electron-phonon interaction in graphene, but only sums a subset of diagrams. As can be seen in Fig. 6.11 diagrams where a graphene phonon propagator hopes over an hBN propagator are not included in Eq. (6.147). If we go back to the original derivation of the Meir-Wingreen formula in Section 6.2, we see that the electrodes can also be interacting, provided contributions where an interaction line hops over the electrode–mesoscopic region coupling are neglected. As such it is not surprising that we reobtain (6.147), since we did the exact same approximation. However, we have learned a very important lesson: Eq. (6.147) includes a subclass of tunnelling processes which are assisted by the emission or absorption of real graphene phonons. This fact would not be clear if we had treated the graphene layers as electrodes.

In order to study the effect scattering of graphene electrons close to the K point by in-plane longitudinal and transverse optical phonons close to the Γ point and electrons close to the K point, we assume that the lattice distortions lead to a local modulation of the hopping integrals in a tight binding description of graphene [141]. The approach is similar to the one employed in Section 4.3 for the case of scattering by acoustic phonons. In the case of optical phonons, the displacement of the atoms is no longer smooth at the atomic scale and therefore the difference in the atomic displacements that occurs in change in bond length $\Delta\ell\left(\mathbf{R}_n^0, \mathbf{R}_n^0+\boldsymbol{\tau}_c\right)$, see Eq. (4.55),

$$\Delta\ell\left(\mathbf{R}_n^0, \mathbf{R}_n^0+\boldsymbol{\tau}_c\right) = \sqrt{\left(\boldsymbol{\tau}_c + \vec{u}_{\mathrm{B}}\left(\mathbf{R}_n^0+\boldsymbol{\tau}_c\right) - \vec{u}_{\mathrm{A}}\left(\mathbf{R}_n^0\right)\right)^2} - \left|\boldsymbol{\tau}_c\right|, \quad (6.148)$$

cannot be approximated by derivative. Instead we write the change in bond length as

$$\Delta\ell\left(\mathbf{R}_n^0, \mathbf{R}_n^0+\boldsymbol{\tau}_c\right) \simeq \frac{\boldsymbol{\tau}_c}{|\boldsymbol{\tau}_c|}\cdot\left[\vec{u}\left(\mathbf{R}_n^0+\boldsymbol{\tau}_c\right) - \vec{u}\left(\mathbf{R}_n^0\right)\right] \\ = \sum_{\mathbf{q}} e^{i\mathbf{q}\cdot\left(\mathbf{R}_n^0+\boldsymbol{\tau}_c/2\right)}\frac{\boldsymbol{\tau}_c}{|\boldsymbol{\tau}_c|}\cdot\left[e^{i\mathbf{q}\cdot\boldsymbol{\tau}_c/2}\vec{u}_{\mathbf{q},\mathrm{B}} - e^{-i\mathbf{q}\cdot\boldsymbol{\tau}_c/2}\vec{u}_{\mathbf{q},\mathrm{A}}\right]. \quad (6.149)$$

The displacement fields due to optical motion of the atoms can be written in terms of creation, $a^\dagger_{\mathbf{q},\zeta}$, and annihilation, $a_{-\mathbf{q},\zeta}$, operators as

$$\vec{u}_{\mathbf{q},\mathrm{A/B}} = \sum_{\zeta=\mathrm{LO,TO}}\sqrt{\frac{\hbar}{2\omega_{\mathbf{q},\zeta}m_{\mathrm{A/B}}}}\vec{\xi}^{\zeta}_{\mathbf{q},\mathrm{A/B}}\phi_{\mathbf{q},\zeta}, \quad (6.150)$$

where $\omega_{\mathbf{q},\zeta}$ is the phonon frequency, $\vec{\xi}^{\zeta}_{\mathbf{q},\mathrm{A/B}}$ is a polarization vector, $m_{\mathrm{A/B}}$is the mass of the A/B atom (both carbon atoms in graphene) and $\phi_{\mathbf{q},\zeta} = \left(a^\dagger_{-\mathbf{q},\zeta} + a_{\mathbf{q},\zeta}\right)$ is the

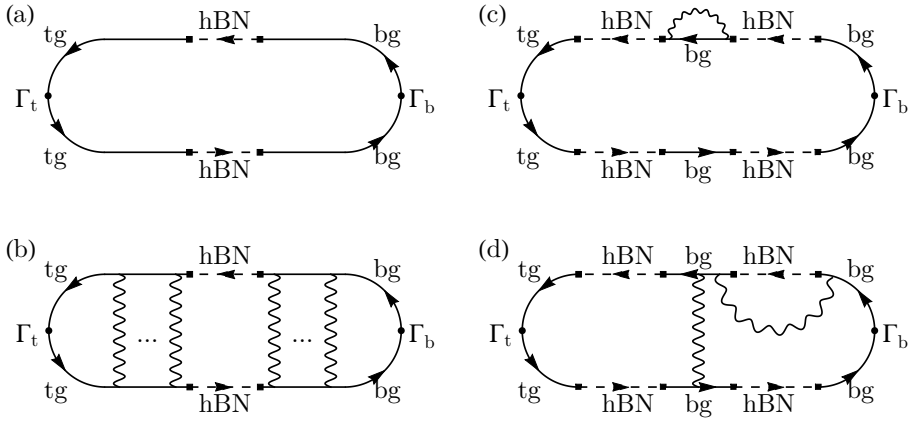

Figure 6.11: Diagrammatic representation of the effect of scattering to the current. The dots represent the level width functions due to the bottom and top external metallic electrodes, the squares represent the graphene–hBN coupling, solid and dashed lines represent, respectivelly, graphene and hBN electron propagators and wiggly lines represent phonon propagators. (a) Lowest order contribution in the graphene–hBN coupling to the elastic current. (b) Contribution to lowest order in the graphene–hBN coupling, involving multiple emission of phonons in the graphene layers. These ladder diagrams are resumed by Eq. (6.147). (c) Diagram contributing to the current in higher order in the graphene–hBN coupling, including the renormalization of the top graphene layer Green's function by phonons. This kind of diagram can be captured in Eq. (6.147), provided the effect of coupling to the graphene layers is included into $\boldsymbol{G}_{\mathrm{hBN}}$. (d) Higher order diagrams in the graphene–hBN coupling, including electron–phonon interaction in the graphene layers, which cannot be captured by Eq. (6.147).

phonon field operator. Focusing in phonon states close to the Γ point, we approximate $e^{\pm i\mathbf{q}\cdot\boldsymbol{\tau}_c/2} \simeq 1$ in the factor between brackets of Eq. (6.149), and further approximate the phonons as dispersionless $\omega_{\mathbf{q},\zeta} \simeq \omega_{\mathbf{0},\zeta}$. At the Γ point, the longitudinal and transverse optical phonons of graphene (a non-polar material) are degenerate and we thus write $\omega_{\mathbf{0},\mathrm{LO}} = \omega_{\mathbf{0},\mathrm{TO}} = \omega^{\mathrm{g}}_{\mathrm{TO}}$. The polarization vectors close to Γ are given by

$$\vec{\xi}^{\,\mathrm{LO/TO}}_{\mathbf{q},\mathrm{A}} \simeq \sqrt{\frac{\mu_{\mathrm{AB}}}{m_{\mathrm{A}}}}\mathbf{e}_{\parallel/\perp,\mathbf{q}}, \qquad \vec{\xi}^{\,\mathrm{LO/TO}}_{\mathbf{q},\mathrm{B}} \simeq -\sqrt{\frac{\mu_{\mathrm{AB}}}{m_{\mathrm{B}}}}\mathbf{e}_{\parallel/\perp,\mathbf{q}}, \tag{6.151}$$

where $\mathbf{e}_{\parallel/\perp,\mathbf{q}}$ is a unit vector parallel/perpendicular to $\mathbf{q}$ and $\mu^{-1}_{\mathrm{AB}} = m^{-1}_{\mathrm{A}} + m^{-1}_{\mathrm{B}}$ is the reduced mass of the optical mode. With these approximations, the electron-optical phonon interaction Hamiltonian for graphene is given by

$$H_{\text{e-ph,g}} = \frac{1}{\sqrt{N_{\mathrm{g}}}} \sum_{\substack{\mathbf{k},\mathbf{q} \\ \zeta=\mathrm{LO,TO}}} \boldsymbol{\psi}^{\dagger}_{\mathbf{k}+\mathbf{q},\mathrm{g}} \cdot \boldsymbol{M}_{\mathbf{q},\zeta} \cdot \boldsymbol{\psi}_{\mathbf{k},\mathrm{g}} \phi_{\mathbf{q},\zeta}, \tag{6.152}$$

with the electron-phonon couplings given by

$$\boldsymbol{M}_{\mathbf{q},\mathrm{LO}} = -g^{\mathrm{g}}_{\mathrm{TO}}\boldsymbol{\sigma}_y, \qquad \boldsymbol{M}_{\boldsymbol{q},\mathrm{TO}} = g^{\mathrm{g}}_{\mathrm{TO}}\boldsymbol{\sigma}_x, \tag{6.153}$$

with

$$g^{\mathrm{g}}_{\mathrm{TO}} = -\frac{\partial \log t}{\partial \log a_{\mathrm{CC}}} \frac{t}{a_{\mathrm{CC}}} \sqrt{\frac{\hbar}{2\mu_{\mathrm{g}}\omega^{\mathrm{g}}_{\mathrm{TO}}}}, \tag{6.154}$$

with $-\partial \log t/\partial \log a_{\mathrm{CC}} \simeq 3$ (according to Harrison's argument [153, 154]) describing the change in the nearest neighbour hopping with the carbon-carbon distance a_{CC} , $\mu_{\mathrm{g}} = m_{\mathrm{C}}/2$ is the reduced mass of the graphene optical mode, and $\omega^{\mathrm{g}}_{\mathrm{TO}}$ is the frequency of the optical longitudinal/transverse phonon mode. Assuming that the top/bottom graphene layer is in equilibrium with the top/bottom electrode and to lowest order in the electron-phonon interaction, the retarded electronic self-energy is given by

$$\Sigma^{R}_{\mathrm{ph}}(\omega) = A_{\mathrm{cell}} \left(g^{\mathrm{g}}_{\mathrm{TO}}\right)^2 \sum_{\lambda,s=\pm1} \int \frac{d^2\mathbf{k}}{(2\pi)^2} s \frac{1 + b(s\omega^{\mathrm{g}}_{\mathrm{TO}}) - f\left(\epsilon_{\mathbf{k},\lambda} - \epsilon_F\right)}{\omega - \epsilon_{\mathbf{k},\lambda} - s\omega^{\mathrm{g}}_{\mathrm{TO}} + i0^+}, \tag{6.155}$$

being momentum independent for dispersionless phonons and diagonal in the graphene sublattice basis. For pristine graphene, the imaginary part of the self-energy can be computed analytically yielding

$$\begin{aligned}\mathrm{Im}\Sigma^{R}_{\mathrm{ph}}(\omega) = -\pi A_{\mathrm{cell}} \left(g^{\mathrm{g}}_{\mathrm{TO}}\right)^2 \times \\ \times \sum_{s=\pm1} \left[sb(s\omega^{\mathrm{g}}_{\mathrm{TO}}) - f\left(\omega + s\omega^{\mathrm{g}}_{\mathrm{TO}} - \epsilon_F\right)\right] \frac{\left|\omega + s\omega^{\mathrm{g}}_{\mathrm{TO}}\right|}{2\pi \left(v_F\hbar\right)^2},\end{aligned} \tag{6.156}$$

with ω and the Fermi energy, ϵ_F, both measured from the Dirac point. The real part of the self-energy can be efficiently obtained using the Kramers-Kronig relation

$$\mathrm{Re}\Sigma^{R}_{\mathrm{ph}}(\omega) = -\int \frac{d\nu}{\pi} \frac{\mathrm{Im}\Sigma^{R}_{\mathrm{ph}}(\omega - \nu) - \mathrm{Im}\Sigma^{R}_{\mathrm{ph}}(\omega + \nu)}{\nu}. \tag{6.157}$$

The computed self-energy is shown in Fig. 6.12.

Finally, we point out that the discussion from this section (and more generically the discussion regarding the incoherent current in Section 6.2.1) provided an alternative

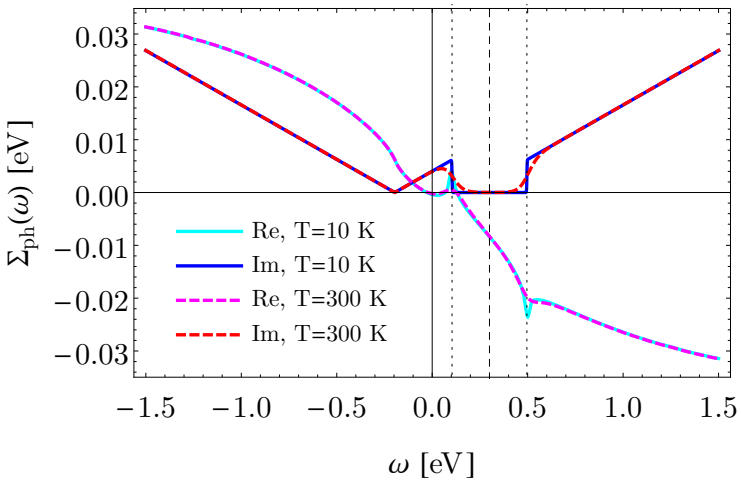

Figure 6.12: Real and (minus) imaginary parts of the self-energy for graphene electrons due to scattering by in-plane optical phonons for two different temperatures for doped graphene with $\epsilon_F = 0.3$ eV. The zero of energy corresponds to the Dirac point. The dashed vertical line marks $\omega = \epsilon_F$ and the dotted lines mark $\omega = \epsilon_F \pm \omega^{\rm g}_{\rm TO}$.

approach for the treatment of disorder in the device to the one done in Section 6.6.1. The effect of disorder can be obtained by setting the phonon frequency to zero, $\omega_\zeta \to 0$, dropping the summation over s (emission or absorption) and interpreting $\boldsymbol{M}_\zeta \boldsymbol{M}_\zeta^\dagger$ as the disorder correlator. The comparison of the approach of this section, with the approach of Section 6.6.1 also justifies our earlier interpretation of the incoherent contribution to the current as vertex correction.

6.6.3 *Phonon scattering in the hBN slab*

Now we focus on the effect of scattering by phonons in the hBN slab. We will restrict ourselves to the case of tunnelling assisted by a single phonon. Tunnelling assisted by multiple phonons can be included as discussed in Section 6.2.1. Writing the electron-phonon interaction in the hBN slab as

$$H_{\text{e-ph,hBN}} = \frac{1}{\sqrt{N_{\rm hBN}}} \sum_{\mathbf{k},\mathbf{q},\zeta} \boldsymbol{\psi}^\dagger_{\mathbf{k}+\mathbf{q},\rm hBN} \cdot \boldsymbol{M}_{\mathbf{q},\zeta} \cdot \boldsymbol{\psi}_{\mathbf{k},\rm hBN} \phi_{\mathbf{q},\zeta}, \tag{6.158}$$

where

$$\boldsymbol{\psi}^\dagger_{\mathbf{k},\rm hBN} = \left[\psi^\dagger_{\mathbf{k},\rm B1,hBN}, \psi^\dagger_{\mathbf{k},\rm N1,hBN}, ..., \psi^\dagger_{\mathbf{k},\rm B\mathcal{N},hBN}, \psi^\dagger_{\mathbf{k},\rm N\mathcal{N},hBN}\right],$$

$\phi_{\mathbf{q},\zeta} = \left(a^\dagger_{-\mathbf{q},\zeta} + a_{\mathbf{q},\zeta}\right)$ is the phonon field operator and $N_{\rm hBN}$ is the number of unit cells in the hBN slab. As previously, we focus on the case when the rotation angles between the different layers are small and we only consider scattering by phonons close to the Γ point of hBN, such that only states close to the Dirac points of each layer are involved. According to Eq. (6.42) the contribution to the current assisted by one hBN phonon can be written to lowest order in the graphene–hBN coupling as

$$I^{(\rm incoh,1)}_{\rm t\to b} = -\frac{e}{\hbar N_{\rm hBN}} \sum_{\substack{\mathbf{k},\lambda,\lambda' \\ n,m}} \sum_{\mathbf{q},\zeta,s} \int \frac{d\omega}{2\pi} W^{(1)(s,\zeta)}_{\rm t,b}(\omega) \left|\mathscr{T}^{(1)(s,\zeta)}_{n,m,\mathbf{k},\mathbf{q}}(\omega)\right|^2 \times$$
$$\times \Upsilon^{{\rm bg},n}_{\mathbf{k},\lambda} \Upsilon^{{\rm tg},m}_{\mathbf{k}+\boldsymbol{\mathcal{Q}}_{n,m}-\mathbf{q},\lambda'} A_{{\rm bg},\mathbf{k}-\mathbf{q},\lambda}(\omega_{\rm bg} - s\omega_\zeta) A_{{\rm tg},\mathbf{k}+\boldsymbol{\mathcal{Q}}_{n,m},\lambda'}(\omega_{\rm tg}) \tag{6.159}$$

where, similarly to Eq. (6.100), we have introduced the phonon assisted tunnelling amplitude as

$$\mathscr{T}^{(1)(s,\zeta)}_{n,m,\mathbf{k},\mathbf{q}}(\omega) = \frac{1}{2}\mathrm{tr}\left\{\hat{\boldsymbol{T}}^{\dagger}\cdot\boldsymbol{R}^{m}_{-p\frac{2\pi}{3}}\cdot \right. \\ \left.\cdot\left[\boldsymbol{G}^{R}_{\mathrm{hBN},\mathbf{k}+\mathbf{g}^{\mathrm{bg}}_{n}}(\omega)\cdot\boldsymbol{M}_{\mathbf{q},\zeta}\cdot\boldsymbol{G}^{R}_{\mathrm{hBN},\mathbf{k}+\mathbf{g}^{\mathrm{bg}}_{n}-\mathbf{q}}(\omega-s\omega_{\zeta})\right]_{\mathcal{N},1}\cdot\boldsymbol{R}^{n}_{\frac{2\pi}{3}}\cdot\hat{\boldsymbol{T}}\right\}. \quad (6.160)$$

Neglecting the momentum and frequency dependence of $\boldsymbol{G}^{R}_{\mathrm{hBN}}$ and assuming dispersionless optical phonons, one can make a shift in the momentum variable $\mathbf{q}\to\mathbf{k}-\mathbf{k}'$, such that the summation over $\mathbf{k}$ and $\mathbf{k}'$ factorizes and we can write

$$I^{(\mathrm{incoh},1)}_{\mathrm{t}\to\mathrm{b}} = AA_{\mathrm{cell}}g_s g_v\frac{e}{\hbar}\sum_{\substack{n,m\\ \zeta,s}}\int\frac{d\omega}{2\pi}\Big\{f_{\mathrm{b}}(\omega-s\omega_{\zeta})\left[1-f_{\mathrm{t}}(\omega)\right]sb(s\omega_{\zeta}) \\ -f_{\mathrm{t}}(\omega)\left[1-f_{\mathrm{b}}(\omega-s\omega_{\zeta})\right]s\left[1+b(s\omega_{\zeta})\right]\Big\}\times \\ \times\left|\mathscr{T}^{(1)}_{n,m}\right|^{2}\mathrm{DoS}_{\mathrm{bg}}(\omega_{\mathrm{bg}}-s\omega_{\zeta})\mathrm{DoS}_{\mathrm{tg}}(\omega_{\mathrm{tg}}), \quad (6.161)$$

where A_{cell} is the area of the unit cell of hBN. In Eq. (6.161) for $s=\pm1$ the first term corresponds to a process involving the absorption/emission of a phonon while the second term corresponds to a process involving the emission/absorption of a phonon. A similar expression to Eq. (6.161), which treated the phonons as being at zero temperature and therefore only includes processes corresponding to the spontaneous emission of phonons, has also been presented (without derivation) in Ref. [210] and used to model vertical current in graphene–hBN–graphene devices.

The exact form of $\mathscr{T}^{(1)}_{n,m}$ will depend on the actual electron-phonon couplings $\boldsymbol{M}_{\mathbf{q},\zeta}$ in Eq. (6.158). As an example we consider scattering by optical out-of-plane breathing modes (ZB) close to the Γ point, with non-zero components of polarization vector, $\vec{\xi}_{\mathrm{ZB}}$ given by

$$\xi_{\mathrm{ZB},a\ell} = \left(\xi^{z}_{\zeta,\mathrm{B1}},\,\xi^{z}_{\zeta,\mathrm{N1}},\xi^{z}_{\zeta,\mathrm{B2}},\xi^{z}_{\zeta,\mathrm{N2}},\,....\right) \\ = \sqrt{\frac{\mu_{\mathrm{BN}}}{\mathcal{N}}}\left(\frac{1}{\sqrt{m_{\mathrm{B}}}},\,\frac{1}{\sqrt{m_{\mathrm{N}}}},\,\frac{-1}{\sqrt{m_{\mathrm{B}}}},\,\frac{-1}{\sqrt{m_{\mathrm{N}}}},\,....\right), \quad (6.162)$$

where $\mu^{-1}_{\mathrm{BN}} = m^{-1}_{\mathrm{B}}+m^{-1}_{\mathrm{N}}$ is the reduced mass of the hBN phonon mode. We model the electron-phonon coupling for this mode in terms of a local change in the value of the interlayer hoping parameter, $t_{\perp}$, in Hamiltonian (6.63). Considering electrons close to the K point and phonons close to the Γ point, the derivation of the electron-phonon Hamiltonian follows the same steps as the discussion in the previous section. The obtained electron-phonon Hamiltonian can be written in the form of Eq. (6.158), with a momentum independent coupling constant which reads

$$\boldsymbol{M}^{\mathrm{hBN}}_{\mathrm{ZB}} = \frac{g^{\mathrm{hBN}}_{\mathrm{ZB}}}{\sqrt{\mathcal{N}}}\begin{bmatrix}\mathbf{0} & \boldsymbol{\sigma}_x & & \\ \boldsymbol{\sigma}_x & \mathbf{0} & -\boldsymbol{\sigma}_x & \\ & -\boldsymbol{\sigma}_x & \mathbf{0} & \ddots \\ & & \ddots & \ddots\end{bmatrix}, \quad (6.163)$$

with the quantity $g^{\mathrm{hBN}}_{\mathrm{ZB}}$ given by

$$g^{\mathrm{hBN}}_{\mathrm{ZB}} = -\frac{\partial\log t_{\perp}}{\partial\log c_{\mathrm{BN}}}\frac{t_{\perp}}{c_{\mathrm{BN}}}\sqrt{\frac{\hbar}{2\mu_{\mathrm{BN}}\omega^{\mathrm{hBN}}_{\mathrm{ZB}}}} \quad (6.164)$$

where c_{BN} is the distance between consecutive hBN monolayers and $\omega_{\mathrm{ZB}}^{\mathrm{hBN}}$ is the out-of-plane breathing phonon frequency and, according to Harrison's argument [153, 154], $-\partial \log t_\perp / \partial \log c_{\mathrm{BN}} \simeq 3$. For this electron-phonon interaction and for an even number of hBN monolayers, we obtain to lowest order in $t_\perp$ and neglecting the frequency and momentum dependence of the hBN Green's functions

$$\left|\mathscr{T}_{n,m}^{(1)}\right|^2 \simeq \frac{(\mathcal{N}-1)^2}{\mathcal{N}} \left|\frac{g_{\mathrm{ZB}}^{\mathrm{hBN}}}{t_\perp}\right|^2 \left|\mathscr{T}_{n,m}^{(0)}\right|^2, \tag{6.165}$$

with $\left|\mathscr{T}_{n,m}^{(0)}\right|^2$ given by Eq. (6.101).

We note in passing that, as we commented in Section (6.6.2), the elastic limit, $\omega_\zeta \to 0$, of Eq. (6.161) can also describe the effect of disorder. In the same way as dispersionless phonons, short range disorder also leads to a complete degradation of momentum conservation. Therefore, in the case of elastic scattering by short range disorder, Eq. (6.161) becomes,

$$I_{\mathrm{t}\to\mathrm{b}}^{(\mathrm{incoh,1\text{-}disorder})} = AA_{\mathrm{cell}} g_s g_v \frac{e}{\hbar} \sum_{\substack{\zeta,s \\ n,m}} \int \frac{d\omega}{2\pi} \left[f_{\mathrm{b}}(\omega) - f_{\mathrm{t}}(\omega)\right] \times \\ \times \left|\mathscr{T}_{n,m}^{(1,\mathrm{disorder})}\right|^2 \mathrm{DoS}_{\mathrm{bg}}(\omega_{\mathrm{bg}}) \mathrm{DoS}_{\mathrm{tg}}(\omega_{\mathrm{tg}}), \tag{6.166}$$

with $\mathscr{T}_{n,m}^{(1,\mathrm{disorder})}$ a disorder assisted tunnelling amplitude. Although an expression of the form of Eq. (6.166) was previously used to model vertical current in graphene–hBN–graphene devices [48, 49], we emphasize that Eq. (6.166) only describes processes where there is a complete degradation of in-plane momentum conservation. The complete degradation of momentum conservation only occurs for scattering by dispersionless phonons or for disorder with short distance correlation.

6.6.4 *Results*

We first study the effect of disorder and electron-phonon interaction in the graphene layers. In Fig. 6.13 we show the vertical current as a function of bias voltage taking into account the effect of scattering of graphene electrons by resonant impurities and graphene in-plane optical phonons, computed using Eq. (6.147) with the spectral functions of the top and bottom graphene layers including the effects of disorder and phonon scattering. For comparison, we also show the current computed using a constant relaxation time. The main difference between modelling electron scattering with a constant relaxation rate or considering scattering by resonant scatterers is that for resonant scatterers the electron decay rate has a strong dependence in energy, behaving as ω^{-1}. Therefore, for higher bias voltages (when the graphene Fermi levels are higher), the electron lifetime is larger. This is manifested in Fig. 6.13, where it is seen that with a constant relaxation rate the second peak in the I-V current is considerably smaller than the first one, while for resonant scatterers both peaks are roughly the same height. Inclusion of phonon scattering makes the peak at higher bias voltage smaller again, since the decay rate due to scattering by graphene in-plane optical phonons increases with frequency. We also notice that inclusion of resonant disorder and phonons leads to a small splitting of the peaks in the I-V current. This splitting is due to the real part of the self-energy due to resonant scatterers and phonons. Apart from increasing graphene electron's decay rate, providing an additional broadening of peaks in the I-V

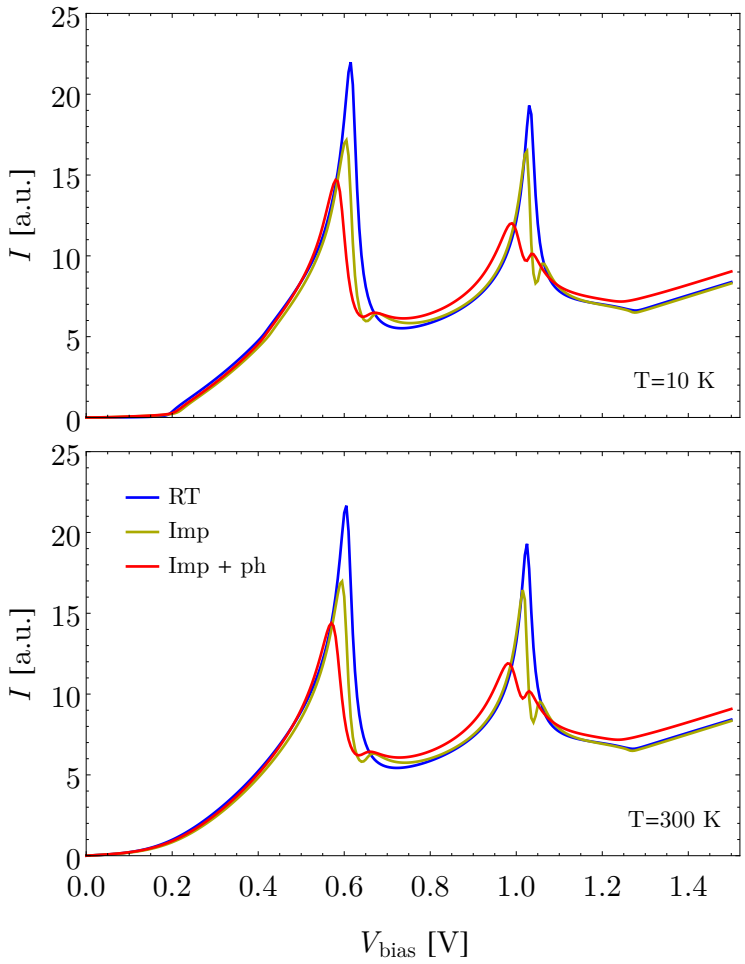

Figure 6.13: I-V curves at constant $V_{\text{gate}} = 0$ in a graphene–hBN–graphene device with rotations angles $\theta_{\text{tg}} = 1°$ and $\theta_{\text{hBN}} = 1.5°$, considering different sources of scattering in the graphene layers: (RT) constant relaxation time of $\gamma = 3$ meV; (Imp) scattering by resonant scatterers treated within the SCBA with an impurity concentration of $n_{\text{imp}} = 10^{-4}$ impurities per graphene unit cell; (Imp+RT) scattering by resonant scatterers and graphene in-plane optical phonons also with $n_{\text{imp}} = 10^{-4}$.

current, phonons do not play a relevant role for the high bias I-V characteristics of a graphene–hBN–graphene device. This changes if one focus on small biases.

At very low temperature, the spontaneous emission of optical phonons becomes possible whenever $eV_{\text{bias}} > \omega_{\text{Oph}}$, where ω_{Oph} is the optical phonon frequency, opening up new tunnelling channels for electrons. Although for small electron-phonon coupling this phonon assisted contribution to the current is small, the opening up of a new tunnelling channel can be observed in the derivatives of the current with respect to the bias, as can be seen in Fig. 6.14, which is computed summing the contribution of processes involving the emission of hBN breathing phonons, Eq. (6.161), with the coherent contribution to the current and processes involving the emission of real graphene phonons, which are both captured by Eq. (6.147). The features in d^2I/dV_{bias}^2 are only significant at low temperature, being smoothed out at higher temperatures due to the smearing of the graphene Fermi occupation factors. We point out however, that the features due to phonons are a small effect that can be overridden due to features in the coherent current induced by the small rotation between different layers (shown in Fig. 6.6), even if we treat the phonons as dispersionless leading to a complete degradation of electron momentum conservation. In Fig. 6.14 only processes assisted by the emission of a single phonon where considered. Tunnelling assisted by the emission of more phonons could be included by computing the graphene self-energy due to phonons, Eq. (6.155), to higher order in the electron-phonon interaction and including more terms of the form of Eq. (6.42) due to the electron-phonon interaction in the hBN slab. Tunnelling assisted by multiple phonons would open up new scattering channels when $n\omega_{\text{Oph}} > V_{\text{bias}}$, where n is the number of emitted phonons. These new channels would manifest themselves as additional peaks in d^2I/dV_{bias}^2 at low temperature, but would be suppressed by higher powers of the electron-phonon coupling.

6.7 CONCLUSIONS

In this chapter, we have studied the vertical current-voltage characteristics in vdW structures. In vdW structures, the atomically sharp nature of the interfaces between the different layers makes momentum conservation rules essential to understand their electronic properties, which will depend sensitively on the lattice mismatch and misalignment between different layers. This additional degree of freedom can be exploited to control the properties of the structures. We have focused on graphene–hBN–graphene structures and on how small crystallographic misalignment between the different layers of this structure affect its I-V characteristics. The misalignment between the two graphene layers leads to an effective shift in the Dirac cones of the two graphene layers in momentum space. This momentum shift in conjunction with a energy shift of the Dirac cones, due to applied gate voltages, can lead to the occurrence of peaks in the I-V characteristics, which are followed by regions displaying NDC [52, 53]. We have seen how the transference of momentum by the hBN crystalline structure to the tunnelling electrons gives origin to additional peaks in the I-V characteristics of this device, and therefore to multiple regions displaying NDC. These additional peaks are however extremely sensitive to the rotation angle between the graphene layers and the hBN slab, and rotational angles as small as 3° can already push these additional peaks to bias voltages higher than 1.5 V. Therefore, the observation of multiple NDC in graphene–hBN–graphene devices requires a control of the rotational angle between the different layers with a precision of $\lesssim 1°$, something which is within experimental reach [52, 201, 237]. We point out that the development of devices displaying multiple NDC

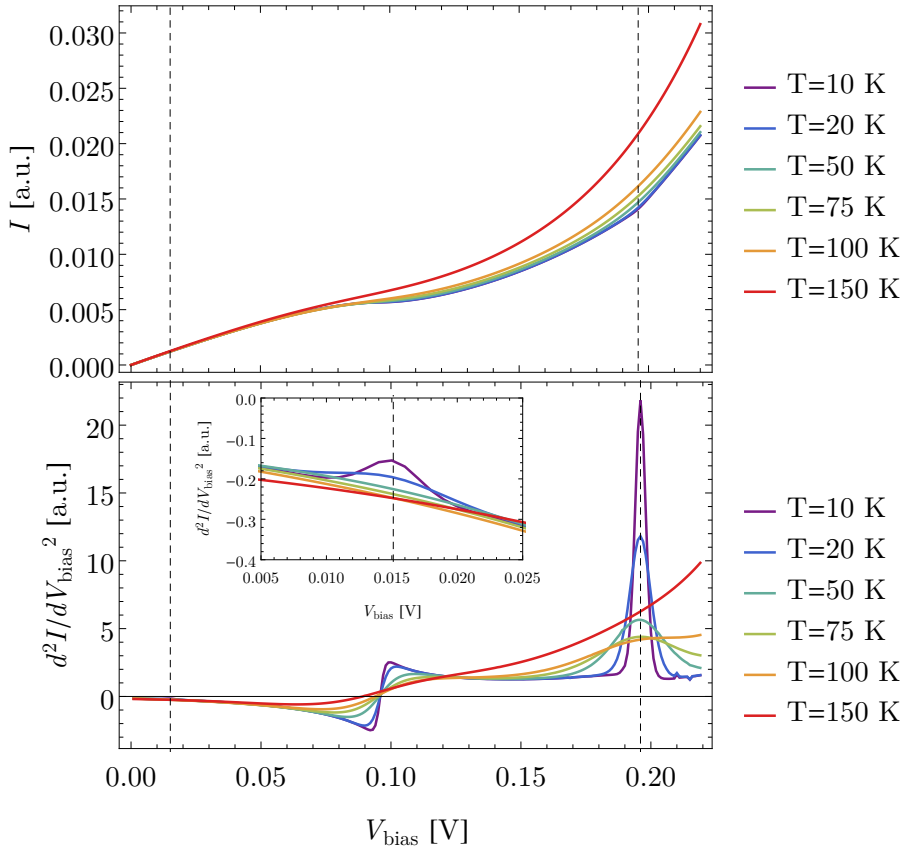

Figure 6.14: I-V curve and d^2I/dV_{bias}^2 as a function of bias voltages at a constant $V_{\text{gate}} = 10$ V for different temperatures and for rotation angles $\theta_{\text{tg}} = 2°$ and $\theta_{\text{hBN}} = 3°$, including effects of scattering by out-of-plane breathing phonons of hBN, $\omega_{\text{ZB}}^{\text{hBN}} = 15$ meV[235], and of the in-plane graphene phonons, $\omega_{\Gamma\text{O}}^{\text{g}} = 196$ meV[236] (represented by the vertical dashed lines). Processes involving spontaneous emission of phonons open up new tunnelling channels that appear as peaks in d^2I/dV_{bias}^2 at low temperature. The inset zooms in the small peak due to the hBN out-of-planes breathing phonon. We point out that the feature that occurs around $V_{\text{bias}} \sim 0.1$ V is not due to phonons, but due to the tunnelling density of states structure.

regions is relevant for the development of multivalued logic devices [238, 239], which might be a possible future application of vdW structures.

On a more theoretical level, we have also analysed the effect of treating graphene as being the source and drain electrodes of the graphene–hBN–graphene device, or by treating them as part of the device and taking the source and drain electrodes to be the external metallic contacts. We have seen that, provided the metallic contacts do not significantly spoil translation invariance of graphene (as expected if the contact is deposited only over a small region of the graphene layer) and in the non-interacting case, both approaches are equivalent. In the presence of interactions both approaches are equivalent to lowest order in the graphene–hBN coupling.

Finally, we have studied, in a unified way, the effect of electronic scattering by disorder and phonons in the vertical current of graphene–hBN–graphene devices. Starting from a NEGF formalism we derived the contribution to the current due to phonon (or disorder) assisted tunnelling processes. We have seen now scattering by short range disorder or dispersionless phonons leads to a complete degradation of electron momentum conservation in the graphene-to-graphene tunnelling process. We have also seen how spontaneous emission of phonons at lower temperatures manifests itself as sharp features in the derivatives of the current with respect to the bias at bias voltage corresponding to the energy of the phonons. This signature of the phonon-assisted tunnelling can, however, be hidden by features due to the rotational alignment between the different layers. We have focused on the effect of graphene in-plane optical phonons and hBN optical out-of-plane breathing phonons. We have not considered the effect of vibrations at the graphene–hBN interface, as these would require the description of phonons in incommensurate structures, something which will be the focus of future work.

As a side note, we expect that the possible reconstruction of graphene spectrum due to the periodic potential induced by hBN for small rotational angles should not affect in a qualitative way the occurrence of multiple NDC regions in graphene–hBN–graphene devices, provided the applied bias voltage is much larger than the width of the region where the spectrum reconstruction is significant. However, a more quantitative treatment of these effects is required in the future.

CONCLUSIONS

In this thesis we have studied the mechanical and electronic properties of 2D crystals. We have seen that while some of these properties are universal, others can be sample dependent.

In Chapter 2, we have studied anharmonic effects in free crystalline membranes in the low temperature, quantum limit. To do so we quantized the classical theory of thin plates. We have shown that anharmonic effects lead to a reconstruction of the flexural phonon dispersion relation, changing it from $\propto |\mathbf{q}|^2$ to $\propto |\mathbf{q}|^{2-\eta_h/2}$. Performing a perturbative calculation and a partial self-consistent calculation we obtained a value of $\eta_h = 2$. We found out that the thermal expansion of a free membrane, which is negative, is made finite by anharmonic effects, behaving in the low temperature limit as $\alpha_A \propto -T^{2\eta_h/(4-\eta_h)}$. We have also seen that the specific heat due to flexural phonons is also affected by anharmonic effects and that in the low temperature limit it depends on temperature as $c_p^{(\text{out})} \propto T^{4/(4-\eta_h)}$.

We have seen in Chapter 3 that the situation changes radically when the crystalline membrane is supported by a substrate. In this situation, the physics is no longer dominated by anharmonic effects, but instead by the coupling of the membrane to the substrate. By using a simple spring model to describe the coupling of the membrane to the substrate, we have seen that the coupling to the substrate leads to the opening of a gap in flexural phonon dispersion relation. This gaped mode couples to the substrate bulk continuum of acoustic phonons, which act as a dissipative bath, giving origin to a finite lifetime for the gapped flexural phonon. At the same time, the flexural phonon will also partially hybridize with the substrate surface Rayleigh mode. We have compared these predictions with HREELS measurements of graphene phonon dispersion relations on different transition metal carbides. Then we studied how coupling to the substrate makes the thermal expansion of the membrane finite, while remaining negative. For a substrate supported membrane, the thermal expansion of the membrane is no longer an intrinsic property of the 2D crystal, but becomes substrate dependent.

In Chapter 4, we studied the limits imposed to graphene electrical conductivity by electron scattering due to acoustic phonons. We considered both scattering due to in-plane and flexural modes. We saw how, at high temperatures, scattering by in-plane phonons, being a single phonon process, leads to a resistivity proportional to the temperature, while scattering by flexural phonons, being a two phonon process, leads to a resistivity that depends on temperature quadratically. In suspended samples subject to small strains, scattering by flexural phonons can be the dominant scattering mechanism limiting graphene resistivity. We have seen that this situation changes once we consider graphene samples supported by a substrate. In this scenario, coupling of the flexural phonon to the substrate leads to a severe suppression of electronic scattering by flexural phonons. Therefore, in supported graphene samples, scattering by acoustic in-plane phonons becomes the dominant scattering mechanism at high temperatures.

In Chapter 5, we studied Coulomb drag between two parallel metallic layers. By first considering Coulomb drag between two generic metallic layers, we have established that in the limit of low temperature, large separation and strong screening, the drag resistivity depends on temperature as T^2, on separation as d^{-4} and on the electronic density of each layer as $n^{-3/2}$. This result is valid for an arbitrary electronic dispersion

relation and intralayer scattering mechanics, only assuming isotropy and that a single band crosses the Fermi level in each layer. Next, we specialized to the case of Coulomb drag between two graphene layers, discussing the limitations of the previous low temperature, large separation and strong screening universal result. We also considered effects of substrate optical phonons to drag. For a graphene double layer encapsulated in hBN, we found out that phonons lead to an increase of the drag resistivity, an effect that is manifest at room temperature.

We have studied vertical tunnelling current in graphene–hBN–graphene vdW structures in Chapter 6. We have seen how conservation of in-plane momentum together with energy conservation can lead to the occurrence of peaks in the I-V curve of these devices, which are followed by NDC regions. The positions of these peaks are determined by the relative alignment between the graphene layers. By exploiting the additional degree of freedom provided by the relative alignment between the graphene layers and the hBN slab, while taking into account generalized umklapp processes, we saw that it is possible to create devices displaying several peaks in the I-V curve with associated multiple NDC regions. The position of the multiple peaks depends sensitively on relative alignment between the different layers. The development of devices displaying multiple NDC regions is relevant for the development of multivalued logic devices. We have also studied the contribution of inelastic tunnelling to the current due to scattering by optical phonons. We found out that scattering by phonons opens up new inelastic tunnelling channels, which give rise to sharp features in the second derivative of the I-V curves at the voltages corresponding to the phonon energies.

As a conclusion, we have seen in a series of examples the importance of controlling external factors while studying the properties of 2D crystals and layered materials. While some properties of 2D materials are rather general and robust, such as the low temperature behaviour of Coulomb drag, others can can be very dependent on the details of system, such as the occurrence of multiple NDC regions in graphene–hBN–graphene structures. This dichotomy between generality and specificity, robustness and frailty of the properties of 2D materials and layered structures has been at the heart of the interest in this field from its very beginning and will continue drive research in this area.

CONCLUSIONES

En esta tesis se han estudiado las propiedades mecánicas y electrónicas de cristales 2D. Hemos visto que, si bien algunas de estas propiedades son universales, otros pueden ser dependientes de la muestra.

En el Capítulo 2, hemos estudiado los efectos anarmónicos en las membranas cristalinas libres en el límite cuántco de baja temperatura. Para ello cuantizamos la teoría clásica de placas delgadas. Hemos demostrado que los efectos anarmónicos conducen a una reconstrucción de la relación de dispersión de los fononos de flexión, cambiándola de $\propto |\mathbf{q}|^2$ a $\propto |\mathbf{q}|^{2-\eta_h/2}$. Haciendo un cálculo perturbativo y un cálculo auto-consistente parical obtuvimos un valor de $\eta_h = 2$. Encontramos que la expansión térmica de una membrana libre, que es negativa, se hace finita por efectos anarmónicos, comportándose en el límite de baja temperatura como $\alpha_A \propto -T^{2\eta_h/(4-\eta_h)}$. Vemos también que el calor específico debido a los fonones de flexión también se ve afectado por los efectos anarmónicos y que en limite de baja temperatura que depende se comporta como $c_p^{(\mathrm{out})} \propto T^{4/(4-\eta_h)}$.

Hemos visto en el Capítulo 3 que la situación cambia radicalmente cuando la membrana cristalina está soportada por un sustrato. En esta situación, la física ya no está dominada por los efectos anarmónicos, pero por el acoplamiento de la membrana al sustrato. Modelando el acoplo entre la membrana y el sustrato mediante uno sensillo modelo de muelle, hemos visto que el acoplamiento al sustrato lleva a la apertura de una brecha en la relación de dispersión del fonón de flexión. Este modo se acopla al continuo de estados de fonones acústicos del sustrato, que actúan como un baño disipativo, dando origen a una vida finita para los fonones de flexión con frequecnia finita. Al mismo tiempo, el fonón de flexión también se hibridará parcialmente con el modo de superficie de Rayleigh del sustrato. Comparamos estas predicciones con mediciones por HREELS de las relaciones de dispersión de fonones de grafeno en diferentes carburos de metales de transición. A continuación se estudió la forma como el acoplamiento al sustrato hace que la expansión térmica de la membrana finito, sin dejar de ser negativo. Para una membrana soportada por un sustrato, la expansión térmica de la membrana ya no es una propiedad intrínseca del cristal 2D, pero se convierte en una propriedade dependiente del sustrato.

En el Capítulo 4, estudiamos los límites impuestos a la conductividad eléctrica de grafeno por la dispersión de electrones debido a fonones acústicos. Se consideró la dispersión debida tanto a modos en el plano como a modos de flexión. Hemos visto cómo, a altas temperaturas, la dispersión por fonones en el plano, siendo un proceso involucrando uno fonón, conduce a una resistividad proporcional a la temperatura, mientras que la dispersión por fonones de flexión, al ser un proceso de dos fonones, conduce a una resistividad que depende en la temperatura de forma cuadrática. En las muestras suspendidas sujetas a pequeñas tensiones, la dispersión de fonones de flexión puede ser el mecanismo dominante a limitar la resistividad de grafeno. Hemos visto que esta situación cambia una vez que consideramos muestras de grafeno soportadas por un sustrato. En este escenario, el acoplamiento del fonón de flexión al sustrato conduce a una supresión severa de la dispersión electrónica por fonones de flexión. Por lo tanto, en las muestras de grafeno soportadas, la dispersión por fonones acústicos en el plano se convierte en el mecanismo de dispersión dominante a altas temperaturas.

En el Capítulo 5, hemos realizado un estudio del fricción de Coulomb entre dos capas metálicas paralelas. Considerando en primer lugar fricción de Coulomb entre dos capas metálicas genéricas, hemos establecido que en el límite de baja temperatura, gran separación y apantallamiento fuerte, la resistividad de arrastre depende de la temperatura como T^2, en la separación como d^{-4} y en la densidad electrónica de cada capa como $n^{-3/2}$. Este resultado es válido para una relación de dispersión electrónica y mecanismo de dispersión intra-capa arbitrarios, solamente asumiendo isotropía y que una sola banda cruza el nivel de Fermi en cada capa. A continuación, nos especializamos en el caso de fricción de Coulomb entre dos capas de grafeno, discutiendo las limitaciones del anterior resultado universal de baja temperatura, separación grande y fuerte apantallamiento. También se consideraron los efectos de fonones ópticos del sustrato en la fricción. Para una doble capa de grafeno encapsulado en hBN, encontramos que los fonones conducen a un aumento de la resistividad de fricción, un efecto que se manifiesta a temperatura ambiente.

Hemos estudiado la corriente vertical por efecto de túnel en estructuras de vdW formadas por grafeno–hBN–grafeno en el Capítulo 6. Hemos visto cómo la conservación del momento en el plano junto con la conservación de la energía puede conducir a la aparición de picos en la curva I-V de estos dispositivos, que son seguidos por regiones NDC. Las posiciones de estos picos son determinados por la alineación relativa entre las capas de grafeno. Al explotar el grado de libertad adicional proporcionada por el alineamiento relativa entre las capas de grafeno y la losa de hBN, teniendo en cuenta procesos umklapp generalizados, vimos que es posible crear dispositivos que muestran varios picos en la curva I-V con múltiples regiones de NDC asociadas. La posición de los múltiples picos depende sensiblemente en el alineamiento relativo entre las diferentes capas. El desarrollo de dispositivos demostrando múltiplas regiones de NDC es relevante para el desarrollo de dispositivos de lógica multivaluada. También hemos estudiado la contribución del tunelamiento inelástico debido a la dispersión por fonones opticos a la corriente. Encontramos que la dispersión por fonones abre nuevos canales de tunelamiento inelástico, que se manifiestan marcadamente en la segunda derivada de las curvas I-V a los voltajes correspondientes a las energías de los fonones.

Como conclusión, hemos visto en una serie de ejemplos la importancia de controlar los factores externos en el estudio de las propiedades de los cristales 2D y materiales laminares. Mientras que algunas propiedades de los materiales 2D son bien generales y robustas, como el comportamiento a baja temperatura de la fricción de Coulomb, otros pueden pueden ser muy dependientes de los detalles del sistema, como la aparición de múltiples regiones de NDC en las estructuras de grafeno–hBN–grafeno. Esta dicotomía entre la generalidad y la especificidad, robustez y fragilidad de las propiedades de los materiales 2D y sus estructuras en capas ha estado en el centro del interés en este campo desde su inicio y continuará a conducir la investigación en esta área.

APPENDICES

A

GREEN'S FUNCTIONS

Green's functions are used extensively in the course of this thesis. In this appendix we set the notations and definitions used throughout the thesis and show some general relations between the different Green's functions which are frequently used.

A.1 REAL TIME GREEN'S FUNCTIONS

A.1.1 *Definition of different Green's functions in real time*

A Green's function is a correlation function between two operators at two different times. Physical quantities can always be expressed in terms of a suitably defined Green's function and these are also suitable objects to build perturbation theory upon. Due to the fact that quantum mechanical operators do not commute in general, by changing the ordering of the two operators, it is possible to define different Green's functions. The usefulness of the different Green's function can lie either in the physical information they carry or in technical convenience they provide when performing calculations.

For two operators, A and B, it is customary to introduce the *retarded* and *advanced* Green's functions as the expectation value of the commutators (anti-commutators) of the operators:

$$\text{Retarded: } G^R_{AB}(t,t') = -i\Theta\left(t-t'\right)\left\langle\left[A(t),B(t')\right]_{\pm}\right\rangle, \tag{A.1}$$

$$\text{Advanced: } G^R_{AB}(t,t') = i\Theta(t'-t)\left\langle\left[A(t),B(t')\right]_{\pm}\right\rangle, \tag{A.2}$$

where $[A,B]_{\pm} = AB \mp BA$ is the commutator (anti-commutator), with the $+$ $(-)$ sign applying when the operators A and B are bosonic (fermionic) and $\langle ... \rangle$ represents averaging with respect to a density matrix operator, ρ:

$$\langle O \rangle = \mathrm{Tr}\left\{\rho O\right\}. \tag{A.3}$$

These Green functions describe, respectively, the causal and anti-causal response of a system to an external perturbation. As such the retarded Green's function is the central object in linear response theory, see also Appendix B. They also contain information regarding the dynamics and spectrum of the system that is being studied.

The *greater* and *lesser* Green's functions are defined as the expectation values of the two possible orderings of the operators:

$$\text{Greater: } G^{>}_{AB}(t,t') = -i\left\langle A(t)B(t')\right\rangle, \tag{A.4}$$

$$\text{Lesser: } G^{<}_{AB}(t,t') = \mp i\left\langle B(t')A(t)\right\rangle, \tag{A.5}$$

where the $-$ $(+)$ sign in the definition of the lesser function applying for bosonic (fermionic) operators. Single-particle observables can always be expressed in terms of these functions. When one of the A, B operators is a creation operator and the other an annihilation operator, these Green's functions describe occupation factors.

Finally, it is also usual to introduce the *time-* and *anti-time-ordered* Green's functions:

$$\text{Time-ordered: } G^{T}_{AB}(t,t') = -i\left\langle T_t A(t)B(t')\right\rangle, \tag{A.6}$$

$$\text{Anti-Time ordered: } G^{\bar{T}}_{AB}(t,t') = -i\left\langle \bar{T}_t A(t)B(t')\right\rangle, \tag{A.7}$$

where

$$T_t\left(A(t)B(t')\right) = \begin{cases} A(t)B(t') & , \text{ if } t > t' \\ \pm B(t')A(t) & , \text{ if } t < t' \end{cases}, \tag{A.8}$$

$$\bar{T}_t\left(A(t)B(t')\right) = \begin{cases} \pm B(t')A(t) & , \text{ if } t > t' \\ A(t)B(t') & , \text{ if } t < t' \end{cases}, \tag{A.9}$$

are the time-ordering and anti-time-ordering operators with the $+$ $(-)$ sign for bosonic (fermionic) operators. These Green's functions naturally appear in equilibrium many-body perturbation theory at zero temperature and in the formulation of its extension to the non-equilibrium case, see also Appendix H.

A.1.2 *Relations between different Green's functions*

Notice that from their very definition, $G^{T}_{AB}(t,t')$, $G^{\bar{T}}_{AB}(t,t')$, $G^{R}_{AB}(t,t')$ and $G^{A}_{AB}(t,t')$ can all the expressed just in terms of $G^{>}_{AB}(t,t')$ and $G^{<}_{AB}(t,t')$ as

$$G^{R}_{AB}(t,t') = \Theta(t-t')\left(G^{>}_{AB}(t,t') - G^{<}_{AB}(t,t')\right) \tag{A.10}$$

$$G^{A}_{AB}(t,t') = -\Theta(t'-t)\left(G^{>}_{AB}(t,t') - G^{<}_{AB}(t,t')\right) \tag{A.11}$$

$$G^{T}_{AB}(t,t') = \Theta(t-t')G^{>}_{AB}(t,t') + \Theta(t'-t)G^{<}_{AB}(t,t') \tag{A.12}$$

$$G^{\bar{T}}_{AB}(t,t') = \Theta(t'-t)G^{>}_{AB}(t,t') + \Theta(t-t')G^{<}_{AB}(t,t') \tag{A.13}$$

From these, it is easy to see that the six Green's functions are not all independent of each other, but are related by

$$G^{T}_{AB}(t,t') - G^{\bar{T}}_{AB}(t,t') = G^{R}_{AB}(t,t') + G^{A}_{AB}(t,t'), \tag{A.14}$$

$$G^{T}_{AB}(t,t') + G^{\bar{T}}_{AB}(t,t') = G^{>}_{AB}(t,t') + G^{<}_{AB}(t,t'), \tag{A.15}$$

$$G^{R}_{AB}(t,t') - G^{A}_{AB}(t,t') = G^{>}_{AB}(t,t') - G^{<}_{AB}(t,t'). \tag{A.16}$$

The Green's functions also obey the following conjugation relations

$$\left[G^{R}_{AB}(t,t')\right]^{*} = G^{A}_{BA}(t',t), \tag{A.17}$$

$$\left[G^{<}_{AB}(t,t')\right]^{*} = -G^{<}_{BA}(t',t), \tag{A.18}$$

$$\left[G^{>}_{AB}(t,t')\right]^{*} = -G^{>}_{BA}(t',t). \tag{A.19}$$

In a situation when the Green's functions inly depend on time differences, in equilibrium of steady states, we can perform a Fourier transform in time

$$G_{AB}(\omega) = \int dt e^{i\omega t} G_{AB}(t,0). \tag{A.20}$$

For the Fourier components, the conjugation relations read:

$$\left[G^{R}_{AB}(\omega)\right]^{*} = G^{A}_{BA}(\omega), \tag{A.21}$$

$$\left[G^{<}_{AB}(\omega)\right]^{*} = -G^{<}_{BA}(\omega), \tag{A.22}$$

$$\left[G^{>}_{AB}(\omega)\right]^{*} = -G^{>}_{BA}(\omega). \tag{A.23}$$

A.1.3 *The spectral function and spectral representation*

It is also usual to introduce the spectral function as

$$A_{AB}(t,t') = \left\langle \left[A(t), B(t')\right]_{\pm} \right\rangle . \tag{A.24}$$

From these definition, the spectral function can be written as the difference between the retarded and the advanced Green's function or the difference between the greater and the lesser Green's function

$$A_{AB}(t,t') = i\left(G^R_{AB}(t,t') - G^A_{AB}(t,t')\right) \tag{A.25}$$
$$= i\left(G^>_{AB}(t,t') - G^<_{AB}(t,t')\right). \tag{A.26}$$

Notice that the retarded and advanced Green's functions can be written in terms of the spectral function as, Eqs. (A.10) and (A.11),

$$G^R_{AB}(t,t') = -i\Theta(t-t')A_{AB}(t,t'), \tag{A.27}$$
$$G^A_{AB}(t,t') = i\Theta(t'-t)A_{AB}(t,t'). \tag{A.28}$$

The spectral function plays a very important role, as it carries information about the spectrum of the theory.

Notice that by making a Wigner transform in time of the Green's function as

$$G^R_{AB}(\omega, t_{CM}) = \int dt e^{i\omega t} G^R_{AB}(t_{CM} + t/2, t_{CM} - t/2), \tag{A.29}$$

and using the Fourier transform of the Heaviside step function

$$\Theta(t) = -\int \frac{d\omega}{2\pi i} \frac{e^{-i\omega t}}{\omega + i0^+}, \tag{A.30}$$

where 0^+ is a small infinitesimal positive number, we obtain a spectral representation for the retarded Green's function, which can be written as a Hilbert transform of the spectral function

$$G^R_{AB}(\omega, t_{CM}) = \int \frac{d\nu}{2\pi} \frac{A_{AB}(\omega - \nu, t_{CM})}{\nu + i0^+}, \tag{A.31}$$

where $A_{AB}(\omega, t_{CM})$ is the Wigner transform of $A_{AB}(t,t')$, defined in the same way as Eq. (A.29). A similar expression can be obtained for the advanced Green's function by replacing $i0^+$ by $-i0^+$ in the previous expression. Notice that in time translational invariant system the Green's function can only be a function of the time difference $t-t'$ and its Wigner transform is therefore independent of the centre of mass time t_{CM}. In this case, the spectral representation Eq. (A.31) simplifies to

$$G^R_{AB}(\omega) = \int \frac{d\nu}{2\pi} \frac{A_{AB}(\omega - \nu)}{\nu + i0^+}$$
$$= P\int \frac{d\nu}{2\pi} \frac{A_{AB}(\omega - \nu)}{\nu} - \frac{i}{2} A_{AB}(\omega), \tag{A.32}$$

where in the last line we have used the Sokhotski–Plemelj formula

$$\frac{1}{\nu + i0^+} = P\frac{1}{\nu} - i\pi\delta(\nu), \tag{A.33}$$

where P represents the Cauchy principal value. This equation is a generalization of the usual Kramers-Kronig relation, relating the complete Green's function to its anti-hermitian part, the spectral function.

A.2 IMAGINARY TIME MATSUBARA GREEN'S FUNCTION

System in thermal equilibrium are described by the density matrix operator

$$\rho = \frac{e^{-\beta H}}{Z}, \tag{A.34}$$

with H a time-independent Hamiltonian and $Z = \mathrm{Tr}\left\{e^{-\beta H}\right\}$ the partition function. In equilibrium problems it is usual to adopt an imaginary time formalism. The continuation of time to imaginary values as a computational trick was first pioneered by Wick [240] in the context of zero quantum field theory and later generalized by Matsubara [241] to quantum statistical mechanics. The imaginary time Matsubara formalism is a standard computation technique in the tool box of any condensed matter theorist and there are many excellent textbooks that cover it in detail. For a modern coverage of the topic, see for example [54] for a canonical quantization approach and [55] for an approach based on the functional path integral formalism. As such, our aim is not to provide an overall discussion of the topic but just to set notation and to show the relation between Matsubara Green's function and real time retarded Green's functions.

A.2.1 *Definition of Matsubara Green's function*

The main idea behind the imaginary time formalism comes from the fact that the equilibrium thermal density matrix $\rho = e^{-\beta H}/Z$ and the time evolution operator $U(t,t') = e^{-iH(t-t')}$ have the same form, involving the exponential of the Hamiltonian. As a matter of fact if we allow for imaginary times $t \to -i\tau$ we can write $\rho = U(i\beta,0)/\mathrm{Tr}\left\{U(i\beta,0)\right\}$. With this in mind the imaginary time Matsubara Green's function for two operators A and B, which we represent by $G_{AB}(\tau)$, is defined as

$$\begin{aligned} G_{AB}(\tau) &= -\left\langle T_\tau A(\tau)B(0)\right\rangle \\ &= -\frac{\mathrm{Tr}\left\{e^{-\beta H}T_\tau A(\tau)B(0)\right\}}{\mathrm{Tr}\left\{e^{-\beta H}\right\}}. \end{aligned} \tag{A.35}$$

In this expression, the operators evolve in imaginary time as

$$A(\tau) = e^{H\tau}A(0)e^{-H\tau}, \tag{A.36}$$

obeying the Heisenberg equation in imaginary time

$$\frac{dA(\tau)}{d\tau} = \left[H, A(\tau)\right], \tag{A.37}$$

and T_τ is the time ordering operator in imaginary time

$$T_\tau\left(A(\tau)B(\tau')\right) = \begin{cases} A(\tau)B(\tau') & , \text{ if } \tau > \tau' \\ \pm B(\tau')A(\tau) & , \text{ if } \tau < \tau' \end{cases}, \tag{A.38}$$

where the $\pm$sign applies for bosonic/fermionic operators. The imaginary time Green's function is very convenient as its perturbative expansions obey the linked-cluster theorem, allowing for a simple representation in terms of connected Feynman diagrams [55, 242].

From Eqs. (A.35) and (A.36) and the definition of T_τ, it is simple to see that the Matsubara Green's function is periodic/anti-periodic in imaginary time, $G_{AB}(\tau+\beta) =$

$\pm G_{AB}(\tau)$, for bosonic/fermionic operators. This means that the Matsubara Green's function can be expressed in terms of a Fourier series as

$$G_{AB}(\tau) = \frac{1}{\beta}\sum_{i\omega_n} G_{AB}(i\omega_n)e^{-i\omega_n\tau}, \tag{A.39}$$

with $i\omega_n$ Matsubara frequencies, which are defined as

$$\omega_n = \frac{2\pi}{\beta}n, \text{ for bosons} \tag{A.40}$$

$$\omega_n = \frac{2\pi}{\beta}\left(n+\frac{1}{2}\right), \text{ for fermions} \tag{A.41}$$

with $n \in \mathbb{Z}$ an integer, such that the (anti-)periodicity in τ is immediately satisfied. The Matsubara Fourier components $G_{AB}(i\omega_n)$ are give by

$$G_{AB}(i\omega_n) = \int_0^\beta d\tau e^{i\omega_n\tau}G_{AB}(\tau). \tag{A.42}$$

A.2.2 *Relation between Matsubara and real time Green's functions*

We will now see the relation between Matsubara Green's function and the real time Green's functions. In order to do that we use the Lehmann representation for the Matsubara Green's function. The Lehmann representation of the Green's function is expressed in terms of the exact eigenstates, $|n\rangle$, and energies, E_n, of the Hamiltonian H,

$$H|n\rangle = E_n|n\rangle. \tag{A.43}$$

Noting that the operators in the Heisenberg picture evolving according to $A(\tau) = e^{H\tau}A(0)e^{-H\tau}$ and from the definition Eq. (A.35), the Lehmann representation of $G_{AB}(\tau)$ is given by

$$G_{AB}(\tau) = -\Theta(\tau)\frac{1}{Z}\sum_{n,m} e^{-\beta E_n}e^{(E_n-E_m)\tau}\langle n|A|m\rangle\langle m|B|n\rangle \tag{A.44}$$

$$\mp\,\Theta(-\tau)\frac{1}{Z}\sum_{n,m} e^{-\beta E_m}e^{(E_n-E_m)\tau}\langle n|A|m\rangle\langle m|B|n\rangle. \tag{A.45}$$

The Matsubara Fourier components are therefore given by

$$\begin{aligned} G_{AB}(i\omega_n) &= \int_0^\beta d\tau e^{i\omega_n\tau}G_{AB}(\tau) \\ &= \frac{1}{Z}\sum_{n,m}\frac{e^{-\beta E_n}\mp e^{-\beta E_m}}{i\omega_n+E_n-E_m}\langle n|A|m\rangle\langle m|B|n\rangle. \end{aligned} \tag{A.46}$$

where we have used the fact that $e^{i\omega_n\beta} = \pm 1$ for bosonic/fermionic Matsubara frequencies. In equilibrium system we can also introduce a Lehmann representation for the retarded Green's functions, $G^R_{AB}(\omega)$. From the definition Eq. (A.1), we obtain the Lehmann representation for $G^R_{AB}(t-t')$

$$G^R_{AB}(t-t') = -i\Theta(t-t')\frac{1}{Z}\sum_{n,m}\left(e^{-\beta E_n}\mp e^{-\beta E_m}\right)e^{i(E_n-E_m)(t-t')}\langle n|A|m\rangle\langle m|B|n\rangle, \tag{A.47}$$

which has Fourier components given by

$$G^R_{AB}(\omega) = \frac{1}{Z}\sum_{n,m}\frac{e^{-\beta E_n} \mp e^{-\beta E_m}}{\omega + i0^+ + E_n - E_m}\langle n|A|m\rangle\langle m|B|n\rangle\,. \tag{A.48}$$

Comparing Eqs. (A.46) and (A.48) we can easily see that the retarded Green's function by be obtained from the Matsubara one by the analytic continuation procedure

$$G^R_{AB}(\omega) = G_{AB}(i\omega_n \to \omega + i0^+). \tag{A.49}$$

We also notice that the advanced Green's function, $G^A_{AB}(\omega)$ can be obtained similarly, making instead the replacement: $i\omega_n \to \omega - i0^+$.

B

LINEAR RESPONSE THEORY

In most interesting situations, condensed matter systems are never in equilibrium. When performing an experiment or when using a condensed matter system in an application, one will often (unless when studying purely thermodynamic properties) apply some external perturbation to the system of interest, which will drive it out of equilibrium, a then measure some observable of the system. In this scenario, the study of equilibrium systems might seem a bit useless. However, the Kubo formula [243] allows to express the response of the system to an external perturbation in terms of the equilibrium properties of the system, provided the perturbation is weak.

B.1 HAMILTONIAN AND INTERACTION PICTURE

Let us assume we are interested in measuring the observable O_a in a system to which we apply a perturbation. The system is governed by the Hamiltonian

$$H_V(t) = H + V(t), \tag{B.1}$$

where H is the Hamiltonian of the unperturbed equilibrium system and $V(t) = O_b h_b(t)$ describes the external perturbation, with $h_b(t)$ the external field which couples to the operator O_b. If the perturbation $V(t)$ is weak, we expect the expectation value of O_a can be written in terms of a Taylor series in $h_b(t)$:

$$\langle O_a(t)\rangle_V = \langle O_a\rangle_{V=0} + \int dt_1 \chi^{(1)}_{ab}(t,t_1)h_b(t_1) + \int dt_1 \int dt_2 \chi^{(2)}_{abc}(t,t_1,t_2)h_b(t_1)h_c(t_2) + ..., \tag{B.2}$$

where $\langle ... \rangle_V$ indicates that the average is performed taking into account the external perturbation $V(t)$ and $\chi^{(n)}_{aa_1...a_n}(t,t_1,...,t_n)$ are the coefficients in the Taylor series

$$\chi^{(n)}_{aa_1...a_n}(t,t_1,...,t_n) = \frac{1}{n!} \left. \frac{\delta^n \langle O_a(t)\rangle_V}{\delta h_{a_1}(t_1)...\delta h_{a_n}(t_n)} \right|_{V=0}. \tag{B.3}$$

The Kubo formula tells us is how to express the coefficients $\chi^{(n)}_{aa_1...a_n}(t,t_1,...,t_n)$ in terms of correlation functions of the system in the absence of the perturbation $V(t)$.

The expectation value of O_a is given by

$$\langle O_a(t)\rangle_V = \mathrm{Tr}\left(\rho_V(t) O_a\right), \tag{B.4}$$

where $\rho_V(t)$ is the density matrix of the system, which in the Schrödinger picture and in the present of $V(t)$ evolves according to

$$i\frac{\partial}{\partial t}\rho_V(t) = \left[H_V(t), \rho_V(t)\right]. \tag{B.5}$$

The time evolution of $\rho_V(t)$ can be formally written as

$$\rho_V(t) = U_V(t,t_0)\rho(t_0)U_V(t_0,t), \tag{B.6}$$

where t_0 is some initial for which $V(t < t_0) = 0$, and the time evolution operator obeys the Schrödinger equations

$$\frac{\partial}{\partial t} U_V(t, t') = -iH_V(t) U_V(t, t'), \tag{B.7}$$

$$\frac{\partial}{\partial t'} U_V(t, t') = iU_V(t, t') H_V(t'), \tag{B.8}$$

with the initial condition $U_V(t, t) = \mathrm{Id}$. We can move from the Schrödinger picture to the interaction picture, by introducing the S-matrix

$$S(t, t') = U(t_0, t) U_V(t, t') U(t', t_0), \tag{B.9}$$

where $U(t, t')$ is the evolution operator in the absence of $V(t)$, which for a time-independent H is given by $U(t, t') = e^{-iH(t-t')}$. From, Eqs. (B.7)-(B.9) it is easy to see that the S-matrix obeys the Schrödinger equations

$$i\frac{\partial}{\partial t} S(t, t') = V_I(t) S(t, t'), \tag{B.10}$$

$$-i\frac{\partial}{\partial t'} S(t, t') = S(t, t') V_I(t'), \tag{B.11}$$

with the initial condition $S(t, t) = \mathrm{Id}$ and $V_I(t)$ the external perturbation in the interaction picture

$$V_I(t) = U(t_0, t) V(t) U(t, t_0). \tag{B.12}$$

Therefore, we can can write the density matrix as

$$\rho_V(t) = U(t, t_0) \rho_I(t) U(t_0, t), \tag{B.13}$$

where $\rho_I(t)$ the density matrix in the interaction picture

$$\rho_I(t) = S(t, t_0) \rho(t_0) S(t_0, t), \tag{B.14}$$

which obeys the equation

$$i\frac{\partial}{\partial t} \rho_I(t) = \left[V_I(t), \rho_I(t)\right]. \tag{B.15}$$

Therefore, the expectation value Eq. (B.4) can be rewritten as

$$\langle O_a(t) \rangle = \mathrm{Tr}\left(\rho_I(t) O_a(t)\right), \tag{B.16}$$

where $O_a(t)$ is the operator O_a in the interaction picture which evolves as

$$O_a(t) = U(t_0, t) O_a U(t, t_0). \tag{B.17}$$

We can now expand $\rho_I(t)$ in powers of $V(t)$.

B.2 GENERAL KUBO FORMULA

Equation (B.15) can be written in integral form as

$$\rho_I(t) = \rho_I(t_0) - i \int_{t_0}^{t} dt' \left[V_I(t'), \rho_I(t')\right]. \tag{B.18}$$

Following the original paper by Kubo [243], we multiply the perturbation $V_I(t)$ by a parameter λ and write $\rho_I(t)$ as a power series in λ,

$$\rho_I(t) = \sum_{n=0}^{+\infty} \lambda^n \rho_I^{(n)}(t). \tag{B.19}$$

Inserting this expansion in the integral equation Eq. (B.18) and equating equal powers of λ we obtain the recursion relation for $\rho_I^{(n)}(t)$

$$\rho_I^{(0)}(t) = \rho(t_0) \tag{B.20}$$

$$\rho_I^{(n)}(t) = -i \int_{t_0}^{t} dt' \left[V_I(t'), \rho_I^{(n-1)}(t') \right], \; n \geq 1. \tag{B.21}$$

Iterating these relations we obtain

$$\rho_I^{(n)}(t) = (-i)^n \int_{t_0}^{t} dt_1 ... \int_{t_0}^{t_{n-1}} dt_n \left[V_I(t_1), [V_I(t_2), ... \left[V_I(t_n), \rho(t_0) \right] ... \right] \right]. \tag{B.22}$$

Inserting this result into Eq. (B.16) we obtain the Kubo formula

$$\langle O_a(t) \rangle_V = \sum_{n=0}^{\infty} (-i)^n \int_{t_0}^{t} dt_1 ... \int_{t_0}^{t_{n-1}} dt_n \mathrm{Tr} \left(\left[V_I(t_1), [V_I(t_2), ... \left[V_I(t_n), \rho(t_0) \right] ... \right] \right] O_a(t) \right). \tag{B.23}$$

Notice that by using the cyclic property of the trace we can write

$$\begin{aligned} \mathrm{Tr} \left([A, B] \, C \right) &= \mathrm{Tr} \left(ABC \right) - \mathrm{Tr} \left(BAC \right) \\ &= \mathrm{Tr} \left(BCA \right) - \mathrm{Tr} \left(BAC \right) \\ &= \mathrm{Tr} \left(B \left[C, A \right] \right). \end{aligned} \tag{B.24}$$

Using this property repeatedly, the Kubo formula can alternatively be written as

$$\langle O_a(t) \rangle_V = \sum_{n=0}^{\infty} (-i)^n \int_{t_0}^{t} dt_1 ... \int_{t_0}^{t_{n-1}} dt_n \left\langle \left[\left[... \left[O_a(t), V_I(t_1) \right], V_I(t_2) \right], ..., V_I(t_n) \right] \right\rangle_{V=0}. \tag{B.25}$$

By writing $V_I(t) = O_b(t) h_b(t)$, we identity the coefficients $\chi^{(n)}_{aa_1...a_n}(t, t_1, ..., t_n)$ from Eq. (B.2)

$$\begin{aligned} \chi^{(n)}_{aa_1...a_n}(t, t_1, ..., t_n) = (-i)^n \, \Theta(t - t_1)\Theta(t_1 - t_2) \times ... \times \Theta(t_{n-1} - t_n) \times \\ \times \left\langle \left[\left[... \left[O_a(t), O_{a_1}(t_1) \right], O_{a_2}(t_2) \right], ..., O_{a_n}(t_n) \right] \right\rangle_{V=0}. \end{aligned} \tag{B.26}$$

B.3 KUBO FORMULA FOR LINEAR RESPONSE

In particular, if we are interest in the response of the system only to first order in the external field, the so called linear response, $\chi^{(1)}_{ab}(t, t')$ is given by the two point retarded Green's function

$$\chi^{(1)}_{ab}(t, t') = G^R_{O_a O_b}(t, t') = -i\Theta(t - t') \left\langle \left[O_a(t), O_b(t) \right] \right\rangle. \tag{B.27}$$

This is the celebrated Kubo formula for linear response.

C

THE FLUCTUATION-DISSIPATION THEOREM

In a general state, all the information contained in the six real time Green's functions defined in Appendix A can be encoded in just two Green's functions, $G^<_{AB}(t,t')$ and $G^>_{AB}(t,t')$, with the remaining Green's functions being related to these two by Eqs. (A.10)-(A.13). However for an equilibrium state, described by the thermal density matrix

$$\rho = \frac{e^{-\beta H}}{Z}, \tag{C.1}$$

all Green's functions are determined by the spectral function, $A_{AB}(t,t')$. The reason for this is that the thermal equilibrium state is completely determined by the spectrum of the Hamiltonian (and the temperature). In particular, the fluctuation-dissipation theorem states that the greater and lesser Green's functions are related to the spectral function by

$$\pm iG^<_{AB}(\omega) = n_\pm(\omega)A_{AB}(\omega), \tag{C.2}$$

$$iG^>_{AB}(\omega) = (1 \pm n_\pm(\omega))\, A_{AB}(\omega), \tag{C.3}$$

where $n_+(\omega) = b(\omega) = \left(e^{\beta\omega} - 1\right)^{-1}$ is the Bose-Einstein function and $n_-(\omega) = f(\omega) = \left(e^{\beta\omega} + 1\right)^{-1}$ is the Fermi-Dirac function.

The proof of the fluctuation-dissipation theorem can be obtained using the Lehmann representation of the Green's function, which is expressed in terms of the exact eigenstates, $|n\rangle$, and energies, E_n, of the Hamiltonian H, $H|n\rangle = E_n|n\rangle$. Recalling that in Heisenberg picture operators evolve according to $A(t) = e^{iHt}Ae^{-iHt}$, the spectral function can be written in terms of the exact eigenstates as

$$\begin{aligned} A_{AB}(t-t') &= \left\langle \left[A(t), B(t')\right]_\pm \right\rangle \\ &= \frac{1}{Z}\sum_{n,m}\left(e^{-\beta E_n} \mp e^{-\beta E_m}\right) e^{i(E_n - E_m)(t-t')} \langle n|A|m\rangle \langle m|B|n\rangle , \end{aligned}$$

where we have anticipated that in equilibrium a two-time function is only function of the time difference. Writing the spectral function in Fourier components we obtain

$$\begin{aligned} A_{AB}(\omega) &= \int dt e^{i\omega t} A_{AB}(t) \\ &= \frac{2\pi}{Z}\sum_{n,m}\left(e^{-\beta E_n} \mp e^{-\beta E_m}\right) \delta(\omega + E_n - E_m) \langle n|A|m\rangle \langle m|B|n\rangle . \end{aligned} \tag{C.4}$$

Using the Diracδ-function this can be written as

$$A_{AB}(\omega) = \frac{2\pi}{Z}\sum_{n,m}\delta(\omega + E_n - E_m) \langle n|A|m\rangle \langle m|B|n\rangle \begin{cases} \left(e^{\beta\omega} \mp 1\right) e^{-\beta E_m} \\ \left(1 \mp e^{-\beta\omega}\right) e^{-\beta E_n} \end{cases} . \tag{C.5}$$

Let us now look at the Lehmann representation of the lesser Green's function

$$\begin{aligned} G^<_{AB}(t-t') &= \mp i\left\langle B(t')A(t)\right\rangle , \\ &= \mp\frac{i}{Z}\sum_{n,m} e^{-\beta E_m} e^{i(E_n - E_m)(t-t')} \langle n|A|m\rangle \langle m|B|n\rangle , \end{aligned} \tag{C.6}$$

which has Fourier components

$$G^{<}_{AB}(\omega) == \mp i\frac{2\pi}{Z}\sum_{n,m} e^{-\beta E_m}\delta\left(\omega + E_n - E_m\right)\langle n|\, A\,|m\rangle\,\langle m|\, B\,|n\rangle\,. \tag{C.7}$$

The greater Green's function can be similarly expressed leading to

$$G^{>}_{AB}(\omega) = -i\frac{2\pi}{Z}\sum_{n,m} e^{-\beta E_n}\delta\left(\omega + E_n - E_m\right)\langle n|\, A\,|m\rangle\,\langle m|\, B\,|n\rangle\,. \tag{C.8}$$

Comparing Eqs. (C.7) and (C.8) with Eq. (C.5) we can easily see that

$$\pm iG^{<}_{AB}(\omega) = \frac{1}{e^{\beta\omega}\mp 1}A_{AB}(\omega), \tag{C.9}$$

$$iG^{>}_{AB}(\omega) = \frac{1}{1\mp e^{-\beta\omega}}A_{AB}(\omega), \tag{C.10}$$

using the definition of the bosonic/fermionic distribution function, $n_{\pm}(\omega) = \left(e^{\beta\omega}-1\right)^{-1}$, we obtain the fluctuation-dissipation theorem, Eqs. (C.2) and (C.3).

D

GENERALIZED MIGDAL–GALITSKI–KOLTUN ENERGY SUM

The Migdal-Galitskii-Koltun (MGK) energy sum provides a convenient formula to computing the total energy of an interacting system, with quartic, or two-body, interactions, provided we have knowledge of the exact 2-point Green's function. In this appendix we will review the original formula for the MGK sum [97, 98] and provide a generalization of it that allows us to express the total energy of a system with both cubic and quartic interactions.

D.1 ORIGINAL MGK SUM FOR SYSTEM WITH QUARTIC INTERACTIONS

We consider a system of interacting bosons or fermions with quartic interactions. The second quantization Hamiltonian that describes the system is given by

$$H = h_{ab} c_a^\dagger c_b + \frac{1}{2} v_{abcd} c_a^\dagger c_b^\dagger c_c c_d, \tag{D.1}$$

where h_{ab} is the non-interacting part of the Hamiltonian, v_{abcd} are the quartic interaction matrix elements and $c_a^\dagger$ (c_a) are creation (annihilation) operators for a particle in the single-particle state a. v_{abcd} is chosen to be (anti-)symmetric under $a \leftrightarrow b$ and $c \leftrightarrow d$. We are using Einstein summation convention, such that repeated indices are summed over. The creation/annihilation operators obey the equal time (anti-)commutation relations

$$\left[c_a, c_b^\dagger\right]_\pm \equiv c_a c_b^\dagger \mp c_b^\dagger c_a = \delta_{ab}, \tag{D.2}$$

where the $\pm$ sign applies to bosons/fermions. Since we are considering an equilibrium system we will employ the imaginary time Matsubara formalism. The MGK energy sum allows to express the expectation value of the Hamiltonian $\langle H \rangle$ in terms of the Matsubara Green's function

$$G_{ab}(\tau) = -\left\langle T_\tau c_a(\tau) c_b^\dagger(0) \right\rangle. \tag{D.3}$$

The MGK tells us that

$$\langle H \rangle = \mp \frac{1}{2} \frac{1}{\beta} \sum_{i\omega_n} \left(i\omega_n \delta_{ab} + h_{ab}\right) G_{ba}(i\omega_n) e^{i\omega_n \eta}, \tag{D.4}$$

where $G_{ab}(i\omega_n)$ is the Fourier transform of the Matsubara Green's function (see Eq. (A.42)) and $\eta \to 0^+$ is an infinitesimal, positive constant.

The proof of the MGK energy sum, Eq. D.4, is based on the equation of motion for the Matsubara Green's function. We notice that in imaginary time the Heisenberg equation of motion for c_a reads (see Eq. (A.37))

$$\begin{aligned} \frac{dc_a}{d\tau} &= [H, c_a] \\ &= -h_{ab} c_b - v_{abcd} c_b^\dagger c_c c_d, \end{aligned} \tag{D.5}$$

Therefore the Matsubara Green's functions obeys the equation of motion

$$\partial_\tau G_{ab}(\tau) = -\delta(\tau)\delta_{ab} + h_{ac}\left\langle T_\tau c_c(\tau) c_b^\dagger(0)\right\rangle + v_{acde}\left\langle T_\tau c_c^\dagger(\tau) c_d(\tau) c_e(\tau) c_b^\dagger(0)\right\rangle . \tag{D.6}$$

Taking the limit $\tau \to 0^-$, we have that $\delta(0^-) = 0$ and therefore obtain

$$\partial_\tau G_{ab}(0^-) = \pm h_{ac}\left\langle c_b^\dagger(0) c_c(0^-)\right\rangle \pm v_{acde}\left\langle c_b^\dagger(0) c_c^\dagger(0^-) c_d(0^-) c_e(0^-)\right\rangle . \tag{D.7}$$

Writing the average energy as

$$\langle H\rangle = \langle T\rangle + \langle W\rangle , \tag{D.8}$$

$$\langle T\rangle = h_{ab}\left\langle c_a^\dagger c_b\right\rangle , \tag{D.9}$$

$$\langle W\rangle = \frac{1}{2} v_{abcd}\left\langle c_a^\dagger c_b^\dagger c_c c_d\right\rangle , \tag{D.10}$$

we see that contracting a and b in Eq. (D.7) gives us

$$\pm \frac{d}{d\tau} G_{aa}(0^-) = \langle T\rangle + 2\langle W\rangle . \tag{D.11}$$

And therefore we can write the two contributions to the energy as

$$\langle T\rangle = \mp h_{ab} G_{ba}(0^-), \tag{D.12}$$

$$\langle W\rangle = \pm \frac{1}{2}\left(\partial_\tau G_{aa}(0^-) + h_{ab} G_{ba}(0^-)\right) . \tag{D.13}$$

Therefore, the total energy can be written as

$$\langle H\rangle = \mp \frac{1}{2}\left(-\delta_{ab}\partial_\tau + h_{ab}\right) G_{ba}(0^-). \tag{D.14}$$

Writing the Green's function in terms of Fourier components we obtain Eq. (D.4).

A more suspicious reader might question the validity of procedure of taking the limit $\tau \to 0^-$ in Eq. (D.6) and while doing that setting the δ-function to zero. In order to convince the suspicious reader we will follow and alternative path in order to prove that

$$-\frac{1}{\beta}\sum_{i\omega_n} i\omega_n G_{aa}(i\omega_n) e^{i\omega_n \eta} = \pm h_{ab}\left\langle c_a^\dagger c_a\right\rangle \pm v_{abcd}\left\langle c_a^\dagger c_b^\dagger c_c c_d\right\rangle . \tag{D.15}$$

In order to prove this, we will use the Lehmann representation for the Green's function $G_{ab}(i\omega_n)$. Notice that a Green's function for two generic operators A and B has the Lehmann representation, Eq. (A.46),

$$G_{AB}(i\omega_n) = \frac{1}{Z}\sum_{n,m} \frac{e^{-\beta E_n} \mp e^{-\beta E_m}}{i\omega_n + E_n - E_m} \langle n| A |m\rangle \langle m| B |n\rangle . \tag{D.16}$$

Now let us look at the related quantity

$$G_{AB}^{(1)} = \frac{1}{\beta}\sum_{i\omega_n} i\omega_n G_{AB}(i\omega_n) e^{i\omega_n \eta}, \tag{D.17}$$

with $\eta \to 0^+$. The sum over Matsubara frequencies can be performed using contour integration and we obtain

$$\begin{aligned} G^{(1)}_{AB} &= \pm \oint \frac{dz}{2\pi i} n_{\pm}(z) e^{z\eta} z C_{AB}(z) \\ &= \mp \frac{1}{Z} \sum_{n,m} n_{\pm}\left(E_m - E_n\right) \left(e^{-\beta E_n} \mp e^{-\beta E_m}\right) \times \\ &\times \left(E_m - E_n\right) \langle n| A |m\rangle \langle m| B |n\rangle e^{(E_m - E_n)\eta}, \end{aligned} \tag{D.18}$$

where $n_{\pm}(\omega) = \left(e^{\beta\omega} \mp 1\right)^{-1}$ is the Bose-Einstein (Fermi-Dirac) function. Notice that when performing the sum over Matsubara frequencies the factor $e^{z\eta}$ with $\eta > 0$ is essential to guarantee the convergence of the sum [54] (although it is often omitted). The inclusion of this $\eta \to 0^+$ factor is compatible with the procedure of taking the limit $\tau \to 0^-$ in Eq. (D.6). In Eq. (D.18), we can safely set $\eta = 0$ and rewrite $G^{(1)}_{AB}$ as

$$\begin{aligned} G^{(1)}_{AB} &= \mp \frac{1}{Z} \sum_{n,m} e^{-\beta E_m} \left(E_m - E_n\right) \langle n| A |m\rangle \langle m| B |n\rangle , \\ &= \mp \langle B \left[H, A\right]\rangle = \mp \left\langle B \frac{dA}{d\tau} \right\rangle . \end{aligned} \tag{D.19}$$

Using this result for the Green's function $G_{ab}(i\omega_n)$ we conclude that

$$-\frac{1}{\beta} \sum_{i\omega_n} i\omega_n G_{ab}(i\omega_n) e^{i\omega_n \eta} \quad = \quad \pm \left\langle c^{\dagger}_b \frac{dc_a}{d\tau} \right\rangle . \tag{D.20}$$

Using the Heisenberg equation of motion, Eq. (D.5), we reobtain Eq. (D.7).

Finally, we notice that Eq. (D.4) can also be expressed in terms of the spectral function

$$\langle H \rangle = \frac{1}{2} \int \frac{d\omega}{2\pi} n_{\pm}(\omega) \left(\omega \delta_{ab} + h_{ab}\right) A_{ba}(\omega), \tag{D.21}$$

where $A_{ab}(\omega)$ is the spectral function.

D.2 GENERALIZED MGK SUM FOR BOSONIC FIELDS WITH CUBIC AND QUARTIC INTERACTIONS

We will now present a generalization of the MGK sum for interacting systems with both cubic and quartic interactions. This result will be applied for the theory of anharmonic membranes studied in Chapter (2) and, therefore, We will focus on systems involving bosonic fields. We consider a system involving two kinds of fields ϕ_a and φ_a, with canonical conjugate given, respectively, by π^a and ϖ^a , such that the fields obey the equal time canonical commutation relations

$$\left[\phi_a, \pi^b\right] = i\delta^b_a, \tag{D.22}$$

$$\left[\varphi_a, \varpi^b\right] = i\delta^b_a, \tag{D.23}$$

with the remaining commutators being zero. The Hamiltonian for the system, expressed in terms of fields and canonical conjugate momenta, is given by

$$\begin{aligned} H = &\frac{1}{2} g_{ab} \pi^a \pi^b + \frac{1}{2} k^{ab} \phi_a \phi_b + \frac{1}{2} \tilde{g}_{ab} \varpi^a \varpi^b + \frac{1}{2} \tilde{k}^{ab} \varphi_a \varphi_b \\ &+ \frac{1}{2} c^{a,bc} \varphi_a \phi_b \phi_c + \frac{1}{8} v^{abcd} \phi_a \phi_b \phi_c \phi_d, \end{aligned} \tag{D.24}$$

where the fist line includes the kinetic and potential energy for the fields ϕ_a and φ_a, and the second line includes the cubic and quartic interaction terms, with $c^{a,bc}$ chosen to be symmetric under $b \leftrightarrow c$ and v^{abcd} chosen to be symmetric under any permutation of the indices. $g_{ab}(\tilde{g}_{ab})$ and $k^{ab}(\tilde{k}^{ab})$ are, respectively, the mass and harmonic potential tensors. Once again we are employing Einstein summation convention. We will show that the average energy of the system can be expressed in terms of the 2-point Green's functions

$$D_{ab}(\tau,\tau') = -\left\langle T_\tau \phi_a(\tau)\phi_b(\tau')\right\rangle, \tag{D.25}$$
$$\tilde{D}_{ab}(\tau,\tau') = -\left\langle T_\tau \varphi_a(\tau)\varphi_b(\tau')\right\rangle, \tag{D.26}$$

as

$$\begin{aligned}\langle H\rangle \;=\; & -\frac{1}{4}\frac{1}{\beta}\sum_{i\omega_n}\left(3g^{ab}\,(i\omega_n)^2 + k^{ab}\right) D_{ba}(i\omega_n)e^{i\omega_n\eta} \\ & -\frac{1}{\beta}\sum_{i\omega_n}\tilde{g}^{ab}\,(i\omega_n)^2\,\tilde{D}_{ba}(i\omega_n)e^{i\omega_n\eta},\end{aligned} \tag{D.27}$$

with $\eta \to 0^+$ and where $g^{ab}(\tilde{g}^{ab})$ is the inverse of g_{ab} $(\tilde{g}_{ab})$, $g^{ab}g_{bc} = \delta^a_c$. Although we are considering equilibrium systems for which $D_{ab}(\tau,\tau')$ and $\tilde{D}_{ab}(\tau,\tau')$ are only functions of $\tau - \tau'$, it will be useful to treat these Green's functions as functions of two time variables.

The proof of Eq. (D.27) follows the same lines as the proof for the original MGK sum. First we notice that the fields obey the Heisenberg equations of motion in imaginary time

$$i\frac{d\phi_a}{d\tau} = g_{ab}\pi^b, \tag{D.28}$$
$$i\frac{d\pi^a}{d\tau} = -k^{ab}\phi_b - c^{b,ac}\varphi_b\phi_c - \frac{1}{2}v^{abcd}\phi_b\phi_c\phi_d, \tag{D.29}$$

and

$$i\frac{d\varphi_a}{d\tau} = \tilde{g}_{ab}\varpi^b, \tag{D.30}$$
$$i\frac{d\varpi^a}{d\tau} = -\tilde{k}^{ab}\varphi_b - \frac{1}{2}c^{a,bc}\phi_b\phi_c. \tag{D.31}$$

From these equations, we obtain the equations of motion for the Green's functions $D_{ab}(\tau,\tau')$ and $\tilde{D}_{ab}(\tau,\tau')$:

$$\begin{aligned}\left(g^{ac}\partial_\tau^2 - k^{ac}\right) D_{cb}(\tau,\tau') = \delta^a_b\delta(\tau) - c^{c,ad}\left\langle T_\tau\varphi_c(\tau)\phi_d(\tau)\phi_b(\tau')\right\rangle \\ -\frac{1}{2}v^{acde}\left\langle T_\tau\phi_c(\tau)\phi_d(\tau)\phi_e(\tau)\phi_b(\tau')\right\rangle.\end{aligned} \tag{D.32}$$
$$\left(\tilde{g}^{ac}\partial_\tau^2 - \tilde{k}^{ac}\right)\tilde{D}_{cb}(\tau,\tau') = \delta^a_b\delta(\tau) - \frac{1}{2}c^{a,cd}\left\langle T_\tau\phi_c(\tau)\phi_d(\tau)\varphi_b(\tau')\right\rangle. \tag{D.33}$$

Now we set $\tau' = 0$ and take the limit $\tau \to 0^-$, obtaining

$$\begin{aligned}-\left(g^{ac}\partial_\tau^2 - k^{ac}\right) D_{cb}(0^-) = c^{c,ad}\left\langle\phi_b(0)\varphi_c(0^-)\phi_d(0^-)\right\rangle \\ +\frac{1}{2}v^{acde}\left\langle\phi_b(0)\phi_c(0^-)\phi_d(0^-)\phi_e(0^-)\right\rangle.\end{aligned} \tag{D.34}$$
$$-\left(\tilde{g}^{ac}\partial_\tau^2 - \tilde{k}^{ac}\right)\tilde{D}_{cb}(0^-) = \frac{1}{2}c^{a,cd}\left\langle\varphi_b(0)\phi_c(0^-)\phi_d(0^-)\right\rangle. \tag{D.35}$$

Notice that the average energy of the system can be written as

$$\langle H\rangle = \langle T\rangle + \langle U\rangle + \left\langle \tilde{T}\right\rangle + \left\langle \tilde{U}\right\rangle + \left\langle W^{(3)}\right\rangle + \left\langle W^{(4)}\right\rangle, \tag{D.36}$$

with

$$\langle T\rangle = \frac{1}{2} g_{ab} \left\langle \pi^a \pi^b \right\rangle, \qquad \left\langle \tilde{T}\right\rangle = \frac{1}{2} \tilde{g}_{ab} \left\langle \varpi^a \varpi^b \right\rangle, \tag{D.37}$$

$$\langle U\rangle = \frac{1}{2} k^{ab} \langle \phi_a \phi_b\rangle, \qquad \left\langle \tilde{U}\right\rangle = \frac{1}{2} \tilde{k}^{ab} \langle \varphi_a \varphi_b\rangle, \tag{D.38}$$

and

$$\left\langle W^{(3)}\right\rangle = \frac{1}{2} c^{a,bc} \langle \varphi_a \phi_b \phi_c\rangle, \tag{D.39}$$

$$\left\langle W^{(4)}\right\rangle = \frac{1}{8} v^{abcd} \langle \phi_a \phi_b \phi_c \phi_d\rangle. \tag{D.40}$$

Therefore, it is easy to see that Eqs. (D.34) and (D.35) give us

$$g^{ab}\partial_\tau^2 D_{ba}(0^-,0) = -2\langle U\rangle - 2\left\langle W^{(3)}\right\rangle - 4\left\langle W^{(4)}\right\rangle, \tag{D.41}$$

$$\tilde{g}^{ab}\partial_\tau^2 \tilde{D}_{ba}(0^-,0) = -2\left\langle \tilde{U}\right\rangle - \left\langle W^{(3)}\right\rangle, \tag{D.42}$$

where the potential energy terms, $\langle U\rangle$ and $\left\langle \tilde{U}\right\rangle$, can be written in terms of the Green's functions as

$$\langle U\rangle = -\frac{1}{2} k^{ab} D_{ba}(0,0), \tag{D.43}$$

$$\left\langle \tilde{U}\right\rangle = -\frac{1}{2} \tilde{k}^{ab} \tilde{D}_{ba}(0,0). \tag{D.44}$$

We can also rewrite Eqs. (D.41) and (D.42) as

$$\left\langle W^{(4)}\right\rangle = -\frac{1}{4} g^{ab}\partial_\tau^2 D_{ba}(0^-,0) + \frac{1}{2}\tilde{g}^{ab}\partial_\tau^2 \tilde{D}_{ba}(0^-,0) - \frac{1}{2}\langle U\rangle + \left\langle \tilde{U}\right\rangle, \tag{D.45}$$

$$\left\langle W^{(3)}\right\rangle = -\tilde{g}^{ab}\partial_\tau^2 \tilde{D}_{ba}(0^-,0) - 2\left\langle \tilde{U}\right\rangle. \tag{D.46}$$

We still have to express the kinetic energy terms, $\langle T\rangle$ and $\left\langle \tilde{T}\right\rangle$, in terms of Green's functions. In order to achieve that, we now introduce the Green's functions for the conjugate momenta

$$\mathcal{D}^{ab}(\tau,\tau') = -\left\langle T_\tau \pi^a(\tau)\pi^b(\tau')\right\rangle, \tag{D.47}$$

$$\tilde{\mathcal{D}}^{ab}(\tau,\tau') = -\left\langle T_\tau \varpi^a(\tau)\varpi^b(\tau')\right\rangle. \tag{D.48}$$

Using the Heisenberg equation of motion for ϕ_a and φ_a it is easy to see that

$$\partial_\tau \partial_{\tau'} D_{ab}(\tau,\tau') = -g_{ab}\delta(\tau-\tau') - g_{ac}g_{bd}\mathcal{D}^{ab}(\tau,\tau'), \tag{D.49}$$

with a similarly relation holding for $\tilde{D}_{ab}(\tau,\tau')$ and $\mathcal{D}^{ab}(\tau,\tau')$. By setting $\tau' = 0$ and taking the limit $\tau \to 0^-$, we obtain

$$\partial_\tau \partial_{\tau'} D_{ab}(0^-,0) = -g_{ac}g_{bd}\mathcal{D}^{ab}(0^-,0). \tag{D.50}$$

Therefore we can write the kinetic energies as

$$\langle T\rangle = \frac{1}{2} g^{ab}\partial_\tau \partial_{\tau'} D_{ab}(0^-, 0), \tag{D.51}$$

$$\left\langle \tilde{T}\right\rangle = \frac{1}{2} \tilde{g}^{ab}\partial_\tau \partial_{\tau'} \tilde{D}_{ab}(0^-, 0). \tag{D.52}$$

The total energy of the system can thus be written as

$$\begin{aligned}\langle H\rangle = &\left(\frac{1}{2} g^{ab}\partial_\tau \partial_{\tau'} - \frac{1}{4} g^{ab}\partial_\tau^2 - \frac{1}{4} k^{ab}\right) D_{ba}(0^-, 0) \\ &+ \left(\frac{1}{2} \tilde{g}^{ab}\partial_\tau \partial_{\tau'} - \frac{1}{2} \tilde{g}^{ab}\partial_\tau^2\right) \tilde{D}_{ba}(0^-, 0).\end{aligned} \tag{D.53}$$

Or expressing the Green's functions in Fourier components we obtain Eq. (D.27).

Notice that the generalized Eq. (D.27) can also be expressed in terms of the spectral functions for real frequencies

$$\begin{aligned}\langle H\rangle = &\frac{1}{4}\int \frac{d\omega}{2\pi} b(\omega)\left(3g^{ab}\omega^2 + k^{ab}\right) A_{ba}(\omega) \\ &+ \int \frac{d\omega}{2\pi} b(\omega)\tilde{g}^{ab}\omega^2 \tilde{A}_{ba}(\omega),\end{aligned} \tag{D.54}$$

with $b(\omega)$ the Bose-Einstein function and $A_{ba}(\omega)$ and $\tilde{A}_{ba}(\omega)$ the spectral functions for theϕ_a and φ_a fields, respectively.

E

GRAPHENE DENSITY-DENSITY CORRELATION FUNCTION

In this appendix, we provide the zero temperature expression of the graphene density-density correlation function as calculated within the massless Dirac equation model. Analytic expressions for the density-density correlation function in doped graphene were first obtained in Ref. [151] and soon after in Ref. [244]. The goal of this appendix is not to replicate the calculation, which is ratter laborious, but instead to provide a quick reference to the necessary definitions and the final results. A detailed and clear derivation of the graphene density-density correlation function is also provided in Appendix A of Ref. [245].

E.1 REDUCIBLE AND IRREDUCIBLE DENSITY-DENSITY CORRELATION FUNCTIONS

In general, the full reducible retarded density-density correlation function is defined as

$$X^R(t,\mathbf{x};t',\mathbf{x}') = -i\Theta\left(t-t'\right)\left\langle\left[\rho(t,\mathbf{x}),\rho(t',\mathbf{x}')\right]\right\rangle, \tag{E.1}$$

where $\rho(t,\mathbf{x})$ is the electronic density operator. Within linear response theory, Eq. (B.27), if we add a perturbation to the system Hamiltonian of the form

$$V(t) = -e^2\int d^D\mathbf{x}\phi_{\text{ext}}\left(t,\mathbf{x}\right)\rho(\mathbf{x}), \tag{E.2}$$

where $\phi_{\text{ext}}\left(t,\mathbf{x}\right)$ is an external electric potential, the total induced charge in the system is given by

$$\langle\rho(t,\mathbf{x})\rangle = \int dt'\int d^D\mathbf{x}X^R(t,\mathbf{x};t',\mathbf{x}')\left(-e^2\right)\phi_{\text{ext}}\left(t',\mathbf{x}'\right), \tag{E.3}$$

where D is the number of spacial dimensions. Notice that in an interacting system, the reducible density-density function already takes into account effects of screening, that is it also takes into account that the induced density also generates a electric potential, $\phi_{\text{ind}}\left(t,\mathbf{x}\right)$, which adds to the external potential $\phi_{\text{ext}}\left(t,\mathbf{x}\right)$. The density response to the total electric potential $\phi_{\text{total}}\left(t',\mathbf{x}'\right) = \phi_{\text{ext}}\left(t,\mathbf{x}\right)+\phi_{\text{ind}}\left(t,\mathbf{x}\right)$, is described by the irreducible density-density correlation function, $\chi^R(t,\mathbf{x};t',\mathbf{x}')$, as

$$\langle\rho(t,\mathbf{x})\rangle = \int dt'\int d^D\mathbf{x}\chi^R(t,\mathbf{x};t',\mathbf{x}')\left(-e^2\right)\phi_{\text{total}}\left(t',\mathbf{x}'\right). \tag{E.4}$$

The reducible and the irreducible density-density correlation function are related by the Dyson screening equation

$$\boldsymbol{X}^R = \boldsymbol{\chi}^R + \boldsymbol{\chi}^R\cdot\boldsymbol{V}\cdot\boldsymbol{X}^R, \tag{E.5}$$

where $\boldsymbol{V}$ represents the bare Coulomb interaction and $\cdot$ represents convolution over time and space coordinates. Diagrammatically $\boldsymbol{\chi}^R$ is obtained only from diagrams that remain connected after a Coulomb interaction line is cut.

E.2 LINDHARD IRREDUCIBLE DENSITY-DENSITY CORRELATION FUNCTION

Within the random phase approximation (RPA), the irreducible density-density correlation function is replaced by the bare one

$$\chi^R(t,\mathbf{x};t',\mathbf{x}') = -i\Theta\left(t-t'\right)\left\langle\left[\rho(t,\mathbf{x}),\rho(t',\mathbf{x}')\right]\right\rangle_0, \tag{E.6}$$

where $\langle\rangle_0$ represents averaging over the non-interacting system. In an equilibrium system, due to time translational invariance, $\chi_0^R(t,\mathbf{x};t',\mathbf{x}')$ is only a function of $t-t'$. We will also focus on continuous models, where the system is approximated by a translational invariant one, such that $\chi_0^R(t,\mathbf{x};t',\mathbf{x}')$ is also only a function of $\mathbf{x}-\mathbf{x}'$. Therefore, it is useful to write the density-density correlation function in Fourier components as

$$\chi^R(\omega,\mathbf{q}) = \int dt \int d^D\mathbf{x} e^{i\omega t} e^{-i\mathbf{q}\cdot\mathbf{x}} \chi^R(t,\mathbf{x};0,\mathbf{0}). \tag{E.7}$$

Writing the density operator in terms of creation and annihilation operators in the eigenstate basis as, see Eqs. (4.34) and (4.37),

$$\rho(t,\mathbf{x}) = \frac{1}{V}\sum_{\mathbf{q}} e^{i\mathbf{q}\cdot\mathbf{x}} \sum_{\mathbf{k}} \rho^{\lambda,\lambda'}_{\mathbf{k},\mathbf{k}+\mathbf{q}} e^{i\left(\epsilon_{\mathbf{k},\lambda}-\epsilon_{\mathbf{k}+\mathbf{q},\lambda'}\right)t} \psi^\dagger_{\mathbf{k},\lambda}\psi_{\mathbf{k}+\mathbf{q},\lambda'}, \tag{E.8}$$

and using Eqs. (E.6) and (E.7), we obtain the Lindhard expression for the irreducible density-density correlation function

$$\chi^R(\omega,\mathbf{q}) = \frac{1}{V}\sum_{\mathbf{k}} \left|\rho^{\lambda,\lambda'}_{\mathbf{k},\mathbf{k}+\mathbf{q}}\right|^2 \frac{f\left(\epsilon_{\mathbf{k},\lambda}-\epsilon_F\right) - f\left(\epsilon_{\mathbf{k}+\mathbf{q},\lambda'}-\epsilon_F\right)}{\omega + i0^+ + \epsilon_{\mathbf{k},\lambda} - \epsilon_{\mathbf{k}+\mathbf{q},\lambda'}}, \tag{E.9}$$

where ϵ_F is the Fermi energy and we have used the fact that $\rho^{\lambda',\lambda}_{\mathbf{k}+\mathbf{q},\mathbf{k}} = \left(\rho^{\lambda,\lambda'}_{\mathbf{k},\mathbf{k}+\mathbf{q}}\right)^*$.

E.3 DENSITY-DENSITY CORRELATION FUNCTION FOR DOPED GRAPHENE AT $T = 0$

For graphene, we have that

$$\epsilon_{\mathbf{k},\lambda} = \lambda v_F \hbar \left|\mathbf{k}\right|, \tag{E.10}$$

$$\left|\rho^{\lambda,\lambda'}_{\mathbf{k},\mathbf{k}+\mathbf{q}}\right|^2 = \frac{1}{2}\left(1+\lambda\lambda'\cos\theta_{\mathbf{k},\mathbf{k}+\mathbf{q}}\right). \tag{E.11}$$

Following Ref. [151] it is useful to split the $(\left|\mathbf{q}\right|,\omega)$ plane into different regions

$$\begin{aligned}
&1\text{A}: \frac{\omega}{\epsilon_F} < \min\left(\frac{|\mathbf{q}|}{k_F}, 2-\frac{|\mathbf{q}|}{k_F}\right),\\
&1\text{B}: \frac{|\mathbf{q}|}{k_F} < \frac{\omega}{\epsilon_F} < 2-\frac{|\mathbf{q}|}{k_F},\\
&2\text{A}: \left|\frac{|\mathbf{q}|}{k_F}-2\right| < \frac{\omega}{\epsilon_F} < \frac{|\mathbf{q}|}{k_F},\\
&2\text{B}: \max\left(\frac{|\mathbf{q}|}{k_F}, \frac{|\mathbf{q}|}{k_F}-2\right) < \frac{\omega}{\epsilon_F} < \frac{|\mathbf{q}|}{k_F}+2,\\
&3\text{A}: \frac{\omega}{\epsilon_F} < \frac{|\mathbf{q}|}{k_F}-2,\\
&3\text{B}: \frac{\omega}{\epsilon_F} > \frac{|\mathbf{q}|}{k_F}+2,
\end{aligned}$$

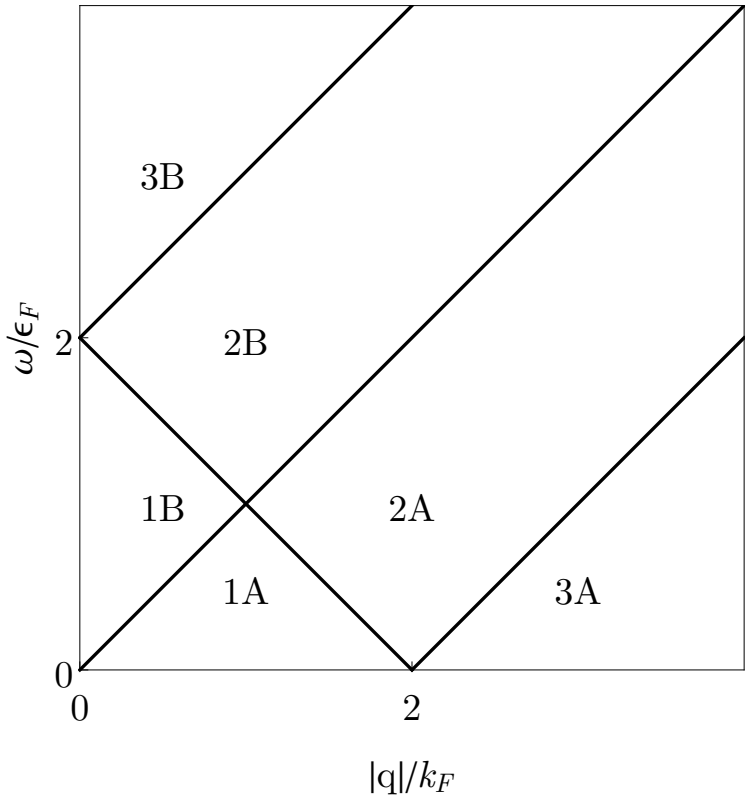

Figure E.1: Regions in the $(|\mathbf{q}|, \omega)$ plane used to write the graphene density-density correlation function by parts.

with the graphene density-density correlation function being defined by parts in these regions. These different regions are represented graphically in Fig. E.1. In the following we give the analytic expressions for the real and imaginary parts of the bare density-density correlation function of doped graphene at zero temperature [151, 244, 245]. For convenience the following functions are introduced

$$C(x) = x\sqrt{1-x^2} - \arccos(x), \tag{E.12}$$

$$F(x) = x\sqrt{x^2-1} - \operatorname{arccosh}(x), \tag{E.13}$$

which allow to express the graphene density-density correlation function in a compact form.

E.3.1 *Real part*

- Region 1A:

$$\mathrm{Re}\chi^R(\omega, \mathbf{q}) = -\frac{2}{\pi}\frac{k_F}{v_F\hbar}, \tag{E.14}$$

- Region 2A:

$$\mathrm{Re}\chi^R(\omega, \mathbf{q}) = -\frac{2}{\pi}\frac{k_F}{v_F\hbar} - \frac{|\mathbf{q}|^2}{4\pi\sqrt{(v_F\hbar\,|\mathbf{q}|)^2 - \omega^2}} C\left(\frac{\omega - 2\epsilon_F}{v_F\hbar\,|\mathbf{q}|}\right), \tag{E.15}$$

- Region 3A:

$$\mathrm{Re}\chi^R(\omega,\mathbf{q}) = -\frac{2}{\pi}\frac{k_F}{v_F\hbar} + \frac{|\mathbf{q}|^2}{4\pi\sqrt{(v_F\hbar\,|\mathbf{q}|)^2-\omega^2}}\left[C\left(\frac{\omega+2\epsilon_F}{v_F\hbar\,|\mathbf{q}|}\right) - C\left(\frac{\omega-2\epsilon_F}{v_F\hbar\,|\mathbf{q}|}\right)\right], \tag{E.16}$$

- Region 1B:

$$\mathrm{Re}\chi^R(\omega,\mathbf{q}) = -\frac{2}{\pi}\frac{k_F}{v_F\hbar} + \frac{|\mathbf{q}|^2}{4\pi\sqrt{\omega^2-(v_F\hbar\,|\mathbf{q}|)^2}}\left[F\left(\frac{2\epsilon_F+\omega}{v_F\hbar\,|\mathbf{q}|}\right) - F\left(\frac{2\epsilon_F-\omega}{v_F\hbar\,|\mathbf{q}|}\right)\right], \tag{E.17}$$

- Region 2B:

$$\mathrm{Re}\chi^R(\omega,\mathbf{q}) = -\frac{2}{\pi}\frac{k_F}{v_F\hbar} + \frac{|\mathbf{q}|^2}{4\pi\sqrt{\omega^2-(v_F\hbar\,|\mathbf{q}|)^2}}F\left(\frac{\omega+2\epsilon_F}{v_F\hbar\,|\mathbf{q}|}\right), \tag{E.18}$$

- Region 3B:

$$\mathrm{Re}\chi^R(\omega,\mathbf{q}) = -\frac{2}{\pi}\frac{k_F}{v_F\hbar} + \frac{|\mathbf{q}|^2}{4\pi\sqrt{\omega^2-(v_F\hbar\,|\mathbf{q}|)^2}}\left[F\left(\frac{\omega+2\epsilon_F}{v_F\hbar\,|\mathbf{q}|}\right) - F\left(\frac{\omega-2\epsilon_F}{v_F\hbar\,|\mathbf{q}|}\right)\right], \tag{E.19}$$

E.3.2 *Imaginary part*

- Region 1A:

$$\mathrm{Im}\chi^R(\omega,\mathbf{q}) = -\frac{|\mathbf{q}|^2}{4\pi\sqrt{(v_F\hbar\,|\mathbf{q}|)^2-\omega^2}}\left[F\left(\frac{2\epsilon_F+\omega}{v_F\hbar\,|\mathbf{q}|}\right) - F\left(\frac{2\epsilon_F-\omega}{v_F\hbar\,|\mathbf{q}|}\right)\right], \tag{E.20}$$

- Region 2A:

$$\mathrm{Im}\chi^R(\omega,\mathbf{q}) = -\frac{|\mathbf{q}|^2}{4\pi\sqrt{(v_F\hbar\,|\mathbf{q}|)^2-\omega^2}}F\left(\frac{\omega+2\epsilon_F}{v_F\hbar\,|\mathbf{q}|}\right), \tag{E.21}$$

- Region 3A:

$$\mathrm{Im}\chi^R(\omega,\mathbf{q}) = 0, \tag{E.22}$$

- Region 1B:

$$\mathrm{Im}\chi^R(\omega,\mathbf{q}) = 0, \tag{E.23}$$

- Region 2B:

$$\mathrm{Im}\chi^R(\omega,\mathbf{q}) = \frac{|\mathbf{q}|^2}{4\pi\sqrt{\omega^2-(v_F\hbar\,|\mathbf{q}|)^2}}C\left(\frac{2\epsilon_F-\omega}{v_F\hbar\,|\mathbf{q}|}\right), \tag{E.24}$$

- Region 3B:

$$\mathrm{Im}\chi^R(\omega,\mathbf{q}) = -\frac{|\mathbf{q}|^2}{4\sqrt{\omega^2-(v_F\hbar\,|\mathbf{q}|)^2}}. \tag{E.25}$$

E.3.3 *Intraband contribution to the imaginary part*

In Chapter 5, we need to evaluate the conduction band intraband contribution to the imaginary part of the density-density correlation function, which is given by the imaginary part of the $\lambda = \lambda' = +1$ contribution to Eq. (E.9). It is relatively easy to see that the $\lambda = \lambda' = +1$ contribution is the only contribution to the imaginary part of the density-density correlation function in the regions 1A and 2A. Therefore, we can write

$$\mathrm{Im}\chi^{R}_{+,+}(\omega,\mathbf{q}) = -\frac{|\mathbf{q}|^2}{4\pi\sqrt{(v_F\hbar\,|\mathbf{q}|)^2-\omega^2}}\times \\ \times\begin{cases} F\left(\frac{2\epsilon_F+\omega}{v_F\hbar|\mathbf{q}|}\right)-F\left(\frac{2\epsilon_F-\omega}{v_F\hbar|\mathbf{q}|}\right) & , \frac{\omega}{\epsilon_F} < \min\left(\frac{|\mathbf{q}|}{k_F}, 2-\frac{|\mathbf{q}|}{k_F}\right) \\ F\left(\frac{\omega+2\epsilon_F}{v_F\hbar|\mathbf{q}|}\right) & , \left|\frac{|\mathbf{q}|}{k_F}-2\right| < \frac{\omega}{\epsilon_F} < \frac{|\mathbf{q}|}{k_F} \end{cases}, \quad \text{(E.26)}$$

with $\mathrm{Im}\chi^{R}_{+,+}(\omega,\mathbf{q}) = 0$ being zero in the remaining regions.

F

KUBO FORMULA FOR DC CONDUCTIVITY

In this appendix we will see how the Kubo formula for linear response theory, Eq. (B.27), can be used to compute the DC conductivity. In particular we will specialize to the DC conductivity of metals in the case where electrons are subject to quasi-elastic scattering.

F.1 KUBO APPROACH TO CONDUCTIVITY

The conductivity tensor relates the charge current density, $\mathbf{J}(t,\mathbf{x})$, to the total electric field, $\mathbf{E}(t,\mathbf{x})$, as

$$\langle J_i(t,\mathbf{x})\rangle = \int dt' \int d^D\mathbf{x}\sigma_{ij}(t,\mathbf{x};t',\mathbf{x}')E_j(t',\mathbf{x}'), \tag{F.1}$$

where D is the number of spacial dimensions. In linear response, the conductivity tensor $\sigma_{ij}(t,\boldsymbol{x};t',\boldsymbol{x}')$ is a property of the equilibrium system and therefore only depends on the time arguments is via their difference, $t-t'$. In this situation it is useful to perform a Fourier transform in time, leading to

$$\langle J_i(\omega,\mathbf{x})\rangle = \int d^D\mathbf{x}\sigma_{ij}(\omega,\mathbf{x},\mathbf{x}')E_j(\omega,\mathbf{x}'). \tag{F.2}$$

Now, we will consider that the system is governed by an Hamiltonian with a kinetic energy term of the form

$$K = \int d^D\mathbf{x}\boldsymbol{\psi}^\dagger(\mathbf{x})\left(\boldsymbol{h}_i p_i + \frac{1}{2}\boldsymbol{h}_{ij}p_ip_j\right)\boldsymbol{\psi}(\mathbf{x}), \tag{F.3}$$

with $\mathbf{p}$ the momentum operator, which we write in a symmetric form as

$$\mathbf{p} = \frac{1}{2i}\left(\overrightarrow{\nabla} - \overleftarrow{\nabla}\right). \tag{F.4}$$

In Eq. (F.3), we have included terms both linear and quadratic in the momentum operator, such that we can treat Dirac and Schrödinger electrons on equal footing. The quantities $\boldsymbol{h}_i$ and $\boldsymbol{h}_{ij}$ are in the most general case matrices. The current operator defined by the kinetic Hamiltonian Eq. (F.3) reads

$$q_e J_i(\mathbf{x}) = q_e\boldsymbol{\psi}^\dagger(\mathbf{x})\left(\boldsymbol{h}_i + \boldsymbol{h}_{ij}p_j\right)\boldsymbol{\psi}(\mathbf{x}), \tag{F.5}$$

$J_i(\mathbf{x})$ is now the current operator, q_e is the charge of the particles ($q_e = -e$ for electrons). We describe the electric field $\mathbf{E}(t,\mathbf{x})$ using the Weyl gauge, such that the scalar potential is zero and the electric and magnetic fields are expressed only in terms of the vector potential as $\mathbf{E} = -\partial_t\mathbf{A}$ and $\mathbf{B} = \nabla\times\mathbf{A}$. Under minimal coupling, the momentum operator is changed to $\mathbf{p}\to\mathbf{p}-q_e\mathbf{A}$. Therefore, the kinetic term of the Hamiltonian in the presence of the vector potential can be written as

$$K = \int d^D\mathbf{x}\boldsymbol{\psi}^\dagger(\mathbf{x})\left(\boldsymbol{h}_i p_i + \frac{1}{2}\boldsymbol{h}_{ij}p_ip_j - q_e\boldsymbol{h}_iA_i - q_e\boldsymbol{h}_{ji}p_jA_i + \frac{q_e^2}{2}\boldsymbol{h}_{ij}A_iA_j\right)\boldsymbol{\psi}(\mathbf{x}) \tag{F.6}$$

and the current operator becomes

$$J_i^{\text{total}}(\mathbf{x}) = J_i^{\text{par}}(\mathbf{x}) + J_i^{\text{dia}}(\mathbf{x}), \tag{F.7}$$
$$q_e J_i^{\text{par}}(\mathbf{x}) = q_e \boldsymbol{\psi}^\dagger(\boldsymbol{x}) \left(\boldsymbol{h}_i + \boldsymbol{h}_{ij} p_j\right) \boldsymbol{\psi}(\mathbf{x}), \tag{F.8}$$
$$q_e J_i^{\text{dia}}(\mathbf{x}) = -q_e^2 \boldsymbol{\psi}^\dagger(\mathbf{x}) \boldsymbol{h}_{ij} \boldsymbol{\psi}(\mathbf{x}) A_j(\mathbf{x}), \tag{F.9}$$

where we have split it into a paramagnetic term, $J_i^{\text{par}}(\mathbf{x})$, and a diamagnetic term, $J_i^{\text{dia}}(\mathbf{x})$. Notice that we can obtain $J_i^{\text{dia}}(\mathbf{x})$ from $J_i^{\text{par}}(\mathbf{x})$ by formally differentiating the latter with respect to $\mathbf{p}$.

Using the Kubo formula for linear response Eq. (B.27), the total current is expressed in the presence of the vector potential $\mathbf{A}$ is given by

$$\langle J_i(t, \mathbf{x}) \rangle = \int dt' \int d^2\mathbf{x} \mathcal{K}_{ij}(t, \mathbf{x}; t', \mathbf{x}') A_j(t', \mathbf{x}'), \tag{F.10}$$

with the kernel $\mathcal{K}_{ij}(t, \mathbf{x}; t', \mathbf{x}')$ being given by

$$\mathcal{K}_{ij}(t, \mathbf{x}; t', \mathbf{x}') = -q_e^2 \Pi_{ij}^R(t, \mathbf{x}; t', \mathbf{x}') - q_e^2 \left\langle \boldsymbol{\psi}^\dagger(t, \mathbf{x}) \boldsymbol{h}_{ij} \boldsymbol{\psi}(t, \mathbf{x}) \right\rangle \delta(t - t') \delta(\mathbf{x} - \mathbf{x}'). \tag{F.11}$$

where the first term takes into account the diamagnetic current contribution and $\Pi_{ij}(t, \mathbf{x}; t', \mathbf{x}')$ is the paramagnetic current-current correlation function

$$\Pi_{ij}^R(t, \mathbf{x}; t', \mathbf{x}') = -i\Theta(t - t') \left\langle \left[J_i^{\text{par}}(t, \mathbf{x}), J_i^{\text{par}}(t', \mathbf{x}') \right] \right\rangle. \tag{F.12}$$

Performing a Fourier transform in time, Eq. (F.10) becomes

$$\langle J_i(\omega, \mathbf{x}) \rangle = \int d^2\mathbf{x} \mathcal{K}_{ij}(\omega, \mathbf{x}, \mathbf{x}') A_j(\omega, \mathbf{x}'). \tag{F.13}$$

Notice, that $\mathcal{K}_{ij}$ is not quite yet the conductivity tensor, as $\mathcal{K}_{ij}$ relates the current to the vector potential instead of the electric field. To make progress we notice that in the Weyl gauge the vector potential can be written in terms of the electric field as

$$\mathbf{A}(t, \mathbf{x}) = -\int dt' \Theta(t - t') \mathbf{E}(t', \mathbf{x}). \tag{F.14}$$

Using the integral representation of the Heaviside step function

$$\Theta(t) = -\int \frac{d\omega}{2\pi i} \frac{e^{-i\omega t}}{\omega + i0^+} \tag{F.15}$$

and writing the electric field as a Fourier transform in time, Eq. (F.14) becomes

$$\begin{aligned} \mathbf{A}(t, \mathbf{x}) &= \int \frac{d\omega}{2\pi i} \frac{e^{-i\omega t}}{\omega + i0^+} \int dt' e^{i\omega t'} \mathbf{E}(t', \mathbf{x}) \\ &= \int \frac{d\omega}{2\pi} e^{-i\omega t} \frac{\mathbf{E}(\omega, \mathbf{x})}{i\left(\omega + i0^+\right)}. \end{aligned} \tag{F.16}$$

From the previous expression we can read the Fourier components of the vector potential

$$\mathbf{A}(\omega, \mathbf{x}) = \frac{\mathbf{E}(\omega, \mathbf{x})}{i\left(\omega + i0^+\right)}. \tag{F.17}$$

Therefore, the conductivity tensor is related to $\Pi_{ij}^R(\omega, \mathbf{x}, \mathbf{x}')$ by

$$\sigma_{ij}(\omega, \mathbf{x}, \mathbf{x}') = \frac{iq_e^2}{\omega + i0^+} \left(\Pi_{ij}^R(\omega, \mathbf{x}, \mathbf{x}') + \left\langle \boldsymbol{\psi}^\dagger(\mathbf{x}) \boldsymbol{h}_{ij} \boldsymbol{\psi}(\mathbf{x}) \right\rangle \delta(\mathbf{x} - \mathbf{x}') \right). \tag{F.18}$$

This is the Kubo formula for the conductivity. Notice that for the Dirac Hamiltonian, the Hamiltonian is linear in momentum, $\boldsymbol{h}_{ij} = 0$, and therefore there is no diamagnetic contribution. However, as we shall soon see, it will be useful to keep this term.

We will be mostly interested in continuous (course grained) models, for which the conductivity depends on the spatial arguments only via $\mathbf{x} - \mathbf{x}'$. In this case it is convenient to also perform a Fourier transform in the spacial coordinates yielding

$$\sigma_{ij}(\omega, \mathbf{q}) = \frac{iq_e^2}{\omega + i0^+} \left(\Pi_{ij}^R(\omega, \mathbf{q}) + \left\langle \boldsymbol{\psi}^\dagger \boldsymbol{h}_{ij} \boldsymbol{\psi} \right\rangle \right). \tag{F.19}$$

Splinting the conductivity into real and imaginary parts we obtain

$$\mathrm{Re}\sigma_{ij}(\omega, \mathbf{q}) = -P\frac{q_e^2}{\omega}\mathrm{Im}\Pi_{ij}^R(\omega, \mathbf{q}) + \pi\delta(\omega)q_e^2 \left[\mathrm{Re}\Pi_{ij}^R(\omega, \mathbf{q}) + \left\langle \boldsymbol{\psi}^\dagger \boldsymbol{h}_{ij} \boldsymbol{\psi} \right\rangle \right], \tag{F.20}$$

$$\mathrm{Im}\sigma_{ij}(\omega, \mathbf{q}) = P\frac{q_e^2}{\omega} \left[\mathrm{Re}\Pi_{ij}^R(\omega, \mathbf{q}) + \left\langle \boldsymbol{\psi}^\dagger \boldsymbol{h}_{ij} \boldsymbol{\psi} \right\rangle \right] + \pi\delta(\omega)q_e^2\mathrm{Im}\Pi_{ij}^R(\omega, \mathbf{q}). \tag{F.21}$$

The will be interested in the DC limit of the conductivity, which is the current response of the system to a static, homogeneous electric field, which is obtained by taking the limits $\mathbf{q} \to 0$ and $\omega \to 0$. We are also interested in the dissipative real part of the conductivity, which as we can see from the previous equations, contains a possibly diverging $\delta(\omega)$ term. We will see in the following that this term is actually zero.

F.2 VERTEX FUNCTION AND WARD IDENTITIES

F.2.1 *Current-current correlation function in terms of a vertex function*

The evaluation of the paramagnetic current-current correlation function for an interacting system is most conveniently performed by studying the Matsubara current-current correlation function and then performing an analytic continuation to real frequencies. The Matsubara current-current correlation function is defined as

$$\Pi_{ij}(\tau, \mathbf{q}) = -\frac{1}{V} \left\langle T_\tau J_{\mathbf{q}}^i(\tau) J_{-\mathbf{q}}^j(0) \right\rangle. \tag{F.22}$$

We write the paramagnetic current operator as

$$\mathbf{J}_{\mathbf{q}} = \sum_{\mathbf{k}} \mathbf{J}_{\mathbf{k},\mathbf{k}+\mathbf{q}}^{\lambda,\lambda'} \psi_{\mathbf{k},\lambda}^\dagger \psi_{\mathbf{k}+\mathbf{q},\lambda'}, \tag{F.23}$$

where λ is a band/sublattice/spin index. Introducing the reducible current vertex function

$$V_{\mathbf{k},\mathbf{k}+\mathbf{q}}^{i,\lambda,\lambda'}(\tau_1 \mid \tau \mid \tau_2) = \left\langle T_\tau J_{\mathbf{q}}^i(\tau) \psi_{\mathbf{k},\lambda}(\tau_1) \psi_{\mathbf{k}+\mathbf{q},\lambda'}^\dagger(\tau_2) \right\rangle, \tag{F.24}$$

the current-current correlation function can be written as

$$\Pi_{ij}(\tau, \mathbf{q}) = \frac{1}{V} \sum_{\mathbf{k}} V_{\mathbf{k},\mathbf{k}+\mathbf{q}}^{i,\lambda,\lambda'}(0 \mid \tau \mid 0) J_{\mathbf{k}+\mathbf{q},\mathbf{k}}^{j,\lambda',\lambda}. \tag{F.25}$$

The reducible current vertex function can be written in terms of an irreducible current vertex, $\Gamma_{\mathbf{k},\mathbf{k}+\mathbf{q}}^{i,\lambda_1,\lambda_2}(\tau_1' \mid \tau \mid \tau_2')$, as

$$V_{\mathbf{k},\mathbf{k}+\mathbf{q}}^{i,\lambda,\lambda'}(\tau_1 \mid \tau \mid \tau_2) = \int d\tau_1' \int d\tau_2' G_{\mathbf{k}}^{\lambda,\lambda_1}\left(\tau_1 - \tau_1'\right) \Gamma_{\mathbf{k},\mathbf{k}+\mathbf{q}}^{i,\lambda_1,\lambda_2}(\tau_1' \mid \tau \mid \tau_2') G_{\mathbf{k}+\mathbf{q}}^{\lambda_2,\lambda'}\left(\tau_2' - \tau_2\right). \tag{F.26}$$

Performing a Fourier transform in imaginary time and writing $\tilde{\mathbf{k}} = (ik_n, \mathbf{k})$ and $\tilde{\mathbf{q}} = (iq_n, \mathbf{q})$, with $k_n = 2\pi\,(n + 1/2)\,/\beta$ and $q_n = 2\pi n/\beta$ fermionic and bosonic Matsubara frequencies, respectively, the previous expression becomes

$$V^{i,\lambda,\lambda'}_{\tilde{\mathbf{k}},\tilde{\mathbf{k}}+\tilde{\mathbf{q}}} = G^{\lambda,\lambda_1}_{\tilde{\mathbf{k}}}\Gamma^{i,\lambda_1,\lambda_2}_{\tilde{\mathbf{k}},\tilde{\mathbf{k}}+\tilde{\mathbf{k}}}G^{\lambda_2,\lambda'}_{\tilde{\mathbf{k}}+\tilde{\mathbf{q}}}. \tag{F.27}$$

The Matsubara current-current correlation function can thus be expressed as

$$\Pi_{ij}(\tilde{\mathbf{q}}) = \frac{1}{\beta V}\sum_{\tilde{\mathbf{k}}} \mathrm{tr}\left[\boldsymbol{\Gamma}^{i}_{\tilde{\mathbf{k}},\tilde{\mathbf{k}}+\tilde{\mathbf{q}}}\cdot\boldsymbol{G}_{\tilde{\mathbf{k}}+\tilde{\mathbf{q}}}\cdot\boldsymbol{J}^{j}_{\tilde{\mathbf{k}}+\tilde{\mathbf{q}},\tilde{\mathbf{k}}}\cdot\boldsymbol{G}_{\tilde{\mathbf{k}}}\right], \tag{F.28}$$

with the trace and matrix products taken over the λ indices. Now in order to obtain the retarded current-current correlation function we have to perform the sum over fermionic frequencies, ik_n, and then perform the analytic continuation to real frequencies, $iq_n \to \omega + i0^+$. But before we do that we will prove a result that will turn out to be useful.

F.2.2 *Ward identity for the irreducible vertex function*

Charge conservation, or in other words gauge invariance, imposes several constrains and relations between different correlation functions, which are generally refereed to as Ward identities [246]. We will be interested in the relation, imposed by charge conservation, between the irreducible vertex function and the self-energies. We will focus on multiband continuous models following closely the approaches of Refs. [247] and [248].

Local charge conservation translates into the charge continuity equation

$$\partial_t\rho(t,\mathbf{x}) + \nabla\cdot\mathbf{J}(t,\mathbf{x}) = 0. \tag{F.29}$$

In the following we will be interested in equilibrium systems at finite temperature, such that it is useful to use the imaginary time Matsubara formalism. Making an analytic continuation from real time to imaginary time, $t \to -i\tau$ and $\partial_t \to i\partial_\tau$, charge conservation in imaginary time can be written as

$$\partial_\mu J^\mu\,(\tau,\mathbf{x}) = 0, \tag{F.30}$$

where we have employed the notation $\partial_\mu = (i\partial_\tau, \nabla)$ and $J^\mu = (\rho, \mathbf{J})$. The current operator J^μ can be written in second quantization in an arbitrary single particle basis as

$$J^\mu\,(\tau,\mathbf{x}) = \psi^\dagger_a\,(\tau)\,J^\mu_{ab}(\mathbf{x})\psi_b(\tau), \tag{F.31}$$

where the indices a, b label the single particle basis states and we use Einstein convention, where repeated indices are to be summed over. For the case of a continuous single band model, using a plane wave basis we would write

$$J^\mu\,(\tau,\mathbf{x}) = \frac{1}{V}\sum_{\mathbf{k},\mathbf{q}} e^{i\mathbf{q}\cdot\mathbf{x}}\psi^\dagger_{\mathbf{k}}\,(\tau)\,J^\mu_{\mathbf{k},\mathbf{k}+\mathbf{q}}\psi_{\mathbf{k}+\mathbf{q}}(\tau), \tag{F.32}$$

such that $a = \mathbf{k}$ and $b = \mathbf{k} + \mathbf{q}$. Let us now look at the reducible vertex function Eq. (F.24) in an arbitrary basis

$$V^\mu_{ab}\,(\tau_a \mid \tau,\mathbf{x} \mid \tau_b) = \left\langle T_\tau J^\mu(\tau,\mathbf{x})\psi_a(\tau_a)\psi^\dagger_b(\tau_b)\right\rangle. \tag{F.33}$$

Let us take the divergence of $V^{\mu}_{ab}(\tau_a \mid \tau, \mathbf{x} \mid \tau_b)$ with respect to the $x^{\mu} = (\tau, \mathbf{x})$ variables. Taking into account the time ordering operator we obtain

$$\begin{aligned}\partial_{\mu} V^{\mu}_{ab}(\tau_a \mid \tau, \mathbf{x} \mid \tau_b) = i\delta(\tau - \tau_a) \left\langle T_{\tau} \left[\rho(\tau, \mathbf{x}), \psi_a(\tau_a)\right] \psi^{\dagger}_b(\tau_b) \right\rangle \\ + i\delta(\tau - \tau_b) \left\langle T_{\tau} \psi_a(\tau_a) \left[\rho(\tau, \mathbf{x}), \psi^{\dagger}_b(\tau_b)\right] \right\rangle \\ + \left\langle T_{\tau} \partial_{\mu} J^{\mu}(\tau, \mathbf{x}) \psi_a(\tau_a) \psi^{\dagger}_b(\tau_b) \right\rangle . \quad \text{(F.34)}\end{aligned}$$

By the continuity equation, Eq. (F.30), we have that the last term in the previous equation is zero. Evaluating the equal time commutators we obtain

$$\left[\rho(\tau, \mathbf{x}), \psi_a(\tau)\right] = \left[\psi^{\dagger}_c(\tau) \rho_{cd}(\mathbf{x}) \psi_d(\tau), \psi_a(\tau)\right] = -\rho_{ac}(\mathbf{x}) \psi_c(\tau), \quad \text{(F.35)}$$

$$\left[\rho(\tau, \mathbf{x}), \psi^{\dagger}_b(\tau)\right] = \left[\psi^{\dagger}_c(\tau) \rho_{cd}(\mathbf{x}) \psi_d(\tau), \psi^{\dagger}_b(\tau)\right] = \psi^{\dagger}_c(\tau) \rho_{cb}(\mathbf{x}). \quad \text{(F.36)}$$

Inserting these commutators into Eq. (F.34) we obtain

$$\partial_{\mu} V^{\mu}_{ab}(\tau_a \mid \tau, \mathbf{x} \mid \tau_b) = i\delta(\tau_a - \tau) \rho_{ac}(\mathbf{x}) G_{cb}(\tau - \tau_b) - i\delta G_{ac}(\tau_a - \tau) \rho_{cb}(\mathbf{x})(\tau - \tau_b). \quad \text{(F.37)}$$

Writing the reducible vertex function $V^{\mu}_{ab}(\tau_a \mid \tau, \mathbf{x} \mid \tau_b)$ in terms of the irreducible vertex function $\Gamma^{\mu}_{ab}(\tau_a \mid \tau, \mathbf{x} \mid \tau_b)$ as

$$V^{\mu}_{ab}(\tau_a \mid \tau, \mathbf{x} \mid \tau_b) = G_{aa'}\left(\tau_a - \tau'_a\right) \Gamma^{\mu}_{a'b'}\left(\tau'_a \mid \tau, \mathbf{x} \mid \tau'_b\right) G_{b'b}\left(\tau'_b - \tau_b\right) \quad \text{(F.38)}$$

(repeated time variables are integrated over), Eq. (F.37) becomes

$$\begin{aligned}G_{aa'}\left(\tau_a - \tau'_a\right) \partial_{\mu} \Gamma^{\mu}_{a'b'}\left(\tau'_a \mid \tau, \mathbf{x} \mid \tau'_b\right) G_{b'b}\left(\tau'_b - \tau_b\right) = i\delta(\tau_a - \tau) \rho_{ac}(\mathbf{x}) G_{cb}(\tau - \tau_b) \\ - iG_{ac}(\tau_a - \tau) \rho_{cb}(\mathbf{x}) \delta(\tau - \tau_b). \quad \text{(F.39)}\end{aligned}$$

Acting with inverse Green's functions both from the left and right in the previous equation, we obtain

$$\begin{aligned}\partial_{\mu} \Gamma^{\mu}_{ab}(\tau_a \mid \tau, \mathbf{x} \mid \tau_b) = iG^{-1}_{ac}(\tau_a - \tau) \rho_{cb}(\mathbf{x}) \delta(\tau - \tau_b) \\ - i\delta(\tau_a - \tau) \rho_{ac}(\mathbf{x}) G^{-1}_{cb}(\tau - \tau_b) . \quad \text{(F.40)}\end{aligned}$$

This is the so called *generalized Ward identity*. This is valid for a generic multiband system. By defining all quantities in terms of Nambu spinors, this Ward identity is also applicable to superconductors (taking into account the matrix structure in Nambu space of the density matrix elements $\rho_{ab}(\mathbf{x})$) [248].

Writing the irreducible vertex function in Fourier components in imaginary time as

$$\Gamma^{\mu}_{ab}(\tau_a \mid \tau, \mathbf{x} \mid \tau_b) = \frac{1}{\beta^2} \sum_{ik_n, iq_n} \Gamma^{\mu}_{ab}(\mathbf{x}; ik_n, ik_n + iq_n) e^{-ik_n(\tau_a - \tau)} e^{-(ik_n + iq_n)(\tau - \tau_a)}, \quad \text{(F.41)}$$

the generalized ward identity becomes

$$(q_n, \nabla) \cdot \Gamma^{\mu}_{ab}(\mathbf{x}; ik_n, ik_n + iq_n) = iG^{-1}_{ac}(ik_n) \rho_{cb}(\mathbf{x}) - i\rho_{ac}(\mathbf{x}) G^{-1}_{cb}(ik_n + iq_n) . \quad \text{(F.42)}$$

Notice that this relation must also hold at the non-interacting level, therefore we can also write

$$(q_n, \nabla) \cdot J^{\mu}_{ab}(\mathbf{x}) = iG^{0,-1}_{ac}(ik_n) \rho_{cb}(\mathbf{x}) - i\rho_{ac}(\mathbf{x}) G^{0,-1}_{cb}(ik_n + iq_n) , \quad \text{(F.43)}$$

subtracting this relation from Eq. (F.42), while recalling the definition of self-energy $G^{-1}_{ab}(ik_n) = \left(G^0_{ab}(ik_n)\right)^{-1} - \Sigma_{ab}(ik_n)$, we obtain

$$(q_n, \nabla) \cdot \left(\Gamma^{\mu}_{ab}(\mathbf{x}; ik_n, ik_n + iq_n) - J^{\mu}_{ab}(\mathbf{x})\right) = \\ = -i\Sigma_{ac}(ik_n)\,\rho_{cb}(\mathbf{x}) + i\rho_{ac}(\mathbf{x})\Sigma^{-1}_{cb}(ik_n + iq_n)\,. \quad \text{(F.44)}$$

For a continuous model, we can also perform a Fourier transform in the spacial coordinates and the generalized Ward identity becomes

$$(-iq_n, \mathbf{q}) \cdot \mathbf{\Gamma}^{\mu}_{\tilde{\mathbf{k}},\tilde{\mathbf{k}}+\tilde{\mathbf{q}}} = \boldsymbol{G}^{-1}_{\tilde{\mathbf{k}}} \cdot \boldsymbol{\rho}_{\mathbf{k},\mathbf{k}+\mathbf{q}} - \boldsymbol{\rho}_{\mathbf{k},\mathbf{k}+\mathbf{q}} \cdot \boldsymbol{G}^{-1}_{\tilde{\mathbf{k}}+\tilde{\mathbf{q}}}. \quad \text{(F.45)}$$

where all quantities in the previous expression are matrices with indices in the band/-sublattice/spin degrees of freedom.

We now point out that in the limit $\tilde{\mathbf{q}} \to \tilde{\mathbf{0}}$, we can obtain two useful relations. If we first set $\mathbf{q} = \mathbf{0}$, and then take the limit $iq_n \to 0$, Eq. (F.45) becomes

$$\mathbf{\Gamma}^{0}_{\tilde{\mathbf{k}},\tilde{\mathbf{k}}} = \frac{\partial}{\partial(ik_n)} \boldsymbol{G}^{-1}_{\tilde{\mathbf{k}}}, \quad \text{(F.46)}$$

where we have used the fact that $\boldsymbol{\rho}_{\mathbf{k},\mathbf{k}} = \mathrm{Id}$. If we set $iq_n = 0$ first and then take the limit $\mathbf{q} \to \mathbf{0}$, and assume we are in a basis where the density matrix elements $\boldsymbol{\rho}_{\mathbf{k},\mathbf{k}+\mathbf{q}}$ are momentum independent [1]we obtain instead

$$\mathbf{\Gamma}^{i}_{\tilde{\mathbf{k}},\tilde{\mathbf{k}}} = -\frac{\partial}{\partial k_i} \boldsymbol{G}^{-1}_{\tilde{\mathbf{k}}}. \quad \text{(F.47)}$$

Notice that the analytic continuation of Eqs. (F.46) and (F.47) can be easily performed to real frequencies for $(ik_n, ik_n) \to (\omega + i0^+, \omega + i0^+)$ and $(ik_n, ik_n) \to (\omega - i0^+, \omega - i0^+)$. This fact will be useful when expressing the DC conductivity in terms of the vertex function.

We finally point that a generalized Ward identity for multiband systems was previously derived in Ref. [249] using the zero temperature formalism. We also point out that although we focused on continuous models, it is also possible to obtain similar Ward identities for discrete lattice models, provided the current and discrete derivative operators are suitably defined as done in Ref. [250].

F.3 DC CONDUCTIVITY

F.3.1 *General expression for the DC conductivity*

Armed with the Ward identities we are now in a position to make progress in expressing the DC conductivity in terms of the irreducible current vertex function. The first step is to perform the summation over the Matsubara frequencies in Eq. (F.28). The sum over fermionic Matsubara frequencies, ik_n, can be performed using contour integration techniques, replacing $ik_n \to z$, taking into account that the integrand will have

1 For the Dirac model of graphene, this basis would be the sublattice basis, where $\boldsymbol{\rho}_{\mathbf{k},\mathbf{k}+\mathbf{q}}$ is simply the identity matrix. If we were working instead in the band basis, $\boldsymbol{\rho}_{\mathbf{k},\mathbf{k}+\mathbf{q}}$ would be formed by overlaps of the eigenstates, being momentum dependent, and we would have to take into account derivatives of $\boldsymbol{\rho}_{\mathbf{k},\mathbf{k}+\mathbf{q}}$ with respect to $\mathbf{q}$. These extra terms lead to the occurrence of Berry connection terms.

branch cuts when z and $z+iq_n$ are real. Therefore we obtain (suppressing for now the momentum arguments)

$$\begin{aligned}\Pi_{ij}(iq_n) &= -\oint \frac{dz}{2\pi i} f(z)\mathrm{tr}\left[\boldsymbol{\Gamma}^i\left(z, z+iq_n\right)\boldsymbol{G}\left(z+iq_n\right)\boldsymbol{J}^j\boldsymbol{G}\left(z\right)\right], \\ &= -\int \frac{d\nu}{2\pi i} f(\nu)\mathrm{tr}\left[\boldsymbol{\Gamma}^i\left(\nu+i0^+, \nu+iq_n\right)\boldsymbol{G}\left(\nu+iq_n\right)\boldsymbol{J}^j\boldsymbol{G}\left(\nu+i0^+\right)\right] \\ &+ \int \frac{d\nu}{2\pi i} f(\nu)\mathrm{tr}\left[\boldsymbol{\Gamma}^i\left(\nu-i0^+, \nu+iq_n\right)\boldsymbol{G}\left(\nu+iq_n\right)\boldsymbol{J}^j\boldsymbol{G}\left(\nu-i0^+\right)\right] \\ &- \int \frac{d\nu}{2\pi i} f(\nu)\mathrm{tr}\left[\boldsymbol{\Gamma}^i\left(\nu-iq_n, \nu+i0^+\right)\boldsymbol{G}\left(\nu+i0^+\right)\boldsymbol{J}^j\boldsymbol{G}\left(\nu-iq_n\right)\right] \\ &+ \int \frac{d\nu}{2\pi i} f(\nu)\mathrm{tr}\left[\boldsymbol{\Gamma}^i\left(\nu-iq_n, \nu-i0^+\right)\boldsymbol{G}\left(\nu-i0^+\right)\boldsymbol{J}^j\boldsymbol{G}\left(\nu-iq_n\right)\right]. \end{aligned} \tag{F.48}$$

Now, we use the fact that for bosonic frequencies $f(\nu - iq_n) = f(\nu)$, and next make the analytic continuation to real frequencies $iq_n \to \omega + i0^+$. The obtained retarded current-current correlation function becomes (after restoring the momentum arguments)

$$\begin{aligned}\Pi^R_{ij}(\omega, \boldsymbol{q}) &= \frac{1}{V}\sum_{\mathbf{k}}\int \frac{d\nu}{2\pi i}\left(f(\nu) - f(\nu+\omega)\right)\times \\ &\times \mathrm{tr}\left[\boldsymbol{\Gamma}^{i,AR}_{\mathbf{k},\mathbf{k}+\mathbf{q}}\left(\nu, \nu+\omega\right)\boldsymbol{G}^R_{\mathbf{k}+\mathbf{q}}\left(\nu+\omega\right)\boldsymbol{J}^j_{\mathbf{k}+\mathbf{q},\mathbf{k}}G^A_{\mathbf{k}}\left(\nu\right)\right] \\ &- \frac{1}{V}\sum_{\mathbf{k}}\int \frac{d\nu}{2\pi i} f(\nu)\mathrm{tr}\left[\boldsymbol{\Gamma}^{i,RR}_{\mathbf{k},\mathbf{k}+\mathbf{q}}\left(\nu, \nu+\omega\right)\boldsymbol{G}^R_{\mathbf{k}+\mathbf{q}}\left(\nu+\omega\right)\boldsymbol{J}^j_{\mathbf{k}+\mathbf{q},\mathbf{k}}\boldsymbol{G}^R_{\mathbf{k}}\left(\nu\right)\right] \\ &+ \frac{1}{V}\sum_{\mathbf{k}}\int \frac{d\nu}{2\pi i} f(\nu+\omega)\mathrm{tr}\left[\boldsymbol{\Gamma}^{i,AA}_{\mathbf{k},\mathbf{k}+\mathbf{q}}\left(\nu, \nu+\omega\right)\boldsymbol{G}^A_{\mathbf{k}+\mathbf{q}}\left(\nu+\omega\right)\boldsymbol{J}^j_{\mathbf{k}+\mathbf{q},\mathbf{k}}\boldsymbol{G}^A_{\mathbf{k}}\left(\nu\right)\right], \end{aligned} \tag{F.49}$$

with $\boldsymbol{\Gamma}^{i,AR}_{\mathbf{k},\mathbf{k}+\mathbf{q}}\left(\nu, \nu+\omega\right) = \boldsymbol{\Gamma}^i_{\mathbf{k},\mathbf{k}+\mathbf{q}}\left(\nu - i0^+, \nu+\omega+i0^+\right)$ and similarly for the remaining terms.

We are interested in the homogeneous DC conductivity, corresponding to the $\mathbf{q}\to 0$, $\omega \to 0$ limits. These limits can be taken unambiguously in the third and forth lines of Eq. (F.49). Using Eq. (F.47), the second line of Eq. (F.49) in the $\mathbf{q}\to 0$, $\omega\to 0$ limit can be written as

$$\begin{aligned}-\frac{1}{V}\sum_{\mathbf{k}}\mathrm{tr}\left[\boldsymbol{\Gamma}^{i,RR}_{\mathbf{k},\mathbf{k}}\left(\nu,\nu\right)\boldsymbol{G}^R_{\mathbf{k}}\left(\nu\right)\boldsymbol{J}^j_{\mathbf{k},\mathbf{k}}\boldsymbol{G}^R_{\mathbf{k}}\left(\nu\right)\right] &= \\ = \frac{1}{V}\sum_{\mathbf{k}}\mathrm{tr}\left[\frac{\partial}{\partial k_i}\boldsymbol{G}^{R,-1}_{\mathbf{k}}(\nu)\boldsymbol{G}^R_{\mathbf{k}}\left(\nu\right)\boldsymbol{J}^j_{\mathbf{k},\mathbf{k}}\boldsymbol{G}^R_{\mathbf{k}}\left(\nu\right)\right] \\ = -\frac{1}{V}\sum_{\mathbf{k}}\mathrm{tr}\left[\frac{\partial}{\partial k_i}\boldsymbol{G}^R_{\mathbf{k}}(\nu)\boldsymbol{J}^j_{\mathbf{k},\mathbf{k}}\right] = \frac{1}{V}\sum_{\mathbf{k}}\mathrm{tr}\left[\boldsymbol{G}^R_{\mathbf{k}}(\nu)\frac{\partial}{\partial k_i}\boldsymbol{J}^j_{\mathbf{k},\mathbf{k}}\right], \end{aligned} \tag{F.50}$$

where from the first to the second line of the previous equation we used that $\partial G^{-1} = -G\left(\partial G^{-1}\right)G$ and in the last line we used integration by parts. Now, going back to the definitions of paramagnetic and diamagnetic current operators, Eqs. (F.8) and (F.9),

we identify $\partial_{k_i} \boldsymbol{J}^j_{\mathbf{k},\mathbf{k}}$ as the matrix element $\boldsymbol{h}^{ij}$. Proceeding in the same way for the forth line of Eq. (F.49) and joining the two contributions we obtain

$$\frac{1}{V}\sum_{\mathbf{k}}\int \frac{d\nu}{2\pi i} f(\nu)\mathrm{tr}\left[\left(\boldsymbol{G}^R_{\mathbf{k}}(\nu)-\boldsymbol{G}^A_{\mathbf{k}}(\nu)\right)\partial_{k_i}\boldsymbol{J}^j_{\mathbf{k},\mathbf{k}}\right] = \\ = -\frac{1}{V}\sum_{\mathbf{k}}\int \frac{d\nu}{2\pi i} f(\nu)\mathrm{tr}\left[\boldsymbol{A}_{\mathbf{k}}(\nu)\boldsymbol{h}^{ij}_{\mathbf{k},\mathbf{k}}\right] = -\left\langle \boldsymbol{\psi}^\dagger \boldsymbol{h}^{ij}\boldsymbol{\psi}\right\rangle, \quad \text{(F.51)}$$

with the spectral function given by $\boldsymbol{A}_{\mathbf{k}}(\nu) = i\left(\boldsymbol{G}^R_{\mathbf{k}}(\nu)-\boldsymbol{G}^A_{\mathbf{k}}(\nu)\right)$. Notice that Eq. (F.51) will exactly cancel the diamagnetic term in the conductivity Eq. (F.19). This in an extremely important result: it guarantees that the $\delta(\omega)$ term in the real part of the conductivity Eq. (F.20) is actually zero. If this cancellation did not occur, the conductivity would have a term of the form $\sigma \propto (\omega + i0^+)^{-1}$ diverging in the DC limit, i.e. we would have a perfect conductor.

With the cancellation of the diamagnetic term, the real part of the conductivity, Eq. (F.20), reduces to

$$\mathrm{Re}\sigma_{ij}(\omega,\boldsymbol{q}) = -P\frac{q_e^2}{\omega}\mathrm{Im}\Pi^R_{ij}(\omega,\boldsymbol{q}). \quad \text{(F.52)}$$

In the $\omega \to 0$, from Eq. (F.49) we obtain for $\mathrm{Im}\Pi^R_{ij}(\omega,\mathbf{0})$

$$\lim_{\omega\to 0}\mathrm{Im}\Pi^R_{ij}(\omega,\mathbf{0}) = -\omega\frac{1}{V}\sum_{\mathbf{k}}\int\frac{d\nu}{2\pi}\left(-\frac{\partial f(\nu)}{\partial\nu}\right)\mathrm{tr}\left[\boldsymbol{\Gamma}^{i,AR}_{\mathbf{k},\mathbf{k}}(\nu,\nu)\,\boldsymbol{G}^R_{\mathbf{k}}(\nu)\,\boldsymbol{J}^j_{\mathbf{k},\mathbf{k}}\boldsymbol{G}^A_{\mathbf{k}}(\nu)\right] \\ + \omega\frac{1}{V}\sum_{\mathbf{k}}\int\frac{d\nu}{2\pi}\left(-\frac{\partial f(\nu)}{\partial\nu}\right)\mathrm{Retr}\left[\boldsymbol{\Gamma}^{i,AA}_{\mathbf{k},\mathbf{k}}(\nu,\nu)\,\boldsymbol{G}^A_{\mathbf{k}}(\nu)\,\boldsymbol{J}^j_{\mathbf{k},\mathbf{k}}\boldsymbol{G}^A_{\mathbf{k}}(\nu)\right]. \quad \text{(F.53)}$$

The first term of this equation involves the product of a retarded and an advanced Green's function, while the second involves the product of two advanced Green's functions. We also notice that using Eq. (F.47), the second term can be rewritten as

$$\frac{\omega}{V}\sum_{\mathbf{k}}\int\frac{d\nu}{2\pi}\left(-\frac{\partial f(\nu)}{\partial\nu}\right)\mathrm{Retr}\left[\boldsymbol{G}^A_{\mathbf{k}}(\nu)\,\boldsymbol{\Gamma}^{i,AA}_{\mathbf{k},\mathbf{k}}(\nu,\nu)\,\boldsymbol{G}^A_{\mathbf{k}}(\nu)\,\boldsymbol{J}^j_{\mathbf{k},\mathbf{k}}\right] = \\ = -\frac{\omega}{V}\sum_{\mathbf{k}}\int\frac{d\nu}{2\pi}\left(-\frac{\partial f(\nu)}{\partial\nu}\right)\mathrm{Retr}\left[\boldsymbol{G}_{\tilde{\mathbf{k}}}\frac{\partial \boldsymbol{J}^j_{\mathbf{k},\mathbf{k}}}{\partial k_i}\right]. \quad \text{(F.54)}$$

For weak scattering in a metal, the second term should be suppressed with respect to the former by a factor of $\left(\tau^{\mathrm{scat}}\epsilon_F\right)^{-1}$, where τ^{scat} is the scattering time and ϵ_F is the Fermi energy [54, 234]. Therefore, we neglect the second term, obtaining the following expression for the DC conductivity

$$\mathrm{Re}\sigma^{\mathrm{DC}}_{ij} = \frac{q_e^2}{V}\sum_{\mathbf{k}}\int\frac{d\nu}{2\pi}\left(-\frac{\partial f(\nu)}{\partial\nu}\right)\mathrm{tr}\left[\boldsymbol{\Gamma}^{i,AR}_{\mathbf{k},\mathbf{k}}(\nu,\nu)\,\boldsymbol{G}^R_{\mathbf{k}}(\nu)\,\boldsymbol{J}^j_{\mathbf{k},\mathbf{k}}\boldsymbol{G}^A_{\mathbf{k}}(\nu)\right]. \quad \text{(F.55)}$$

At low temperature, we can approximate the derivative of the Fermi function by a δ-function. In this low temperature limit, and assuming there is a single band crossing the Fermi level, we can treat all the quantities in the above expression as scalars. Using the fact that

$$G^R_{\mathbf{k}}(\nu)\,G^A_{\mathbf{k}}(\nu) = \tau^{\mathrm{scat}}_{\mathbf{k}}(\omega)A_{\mathbf{k}}(\omega), \quad \text{(F.56)}$$

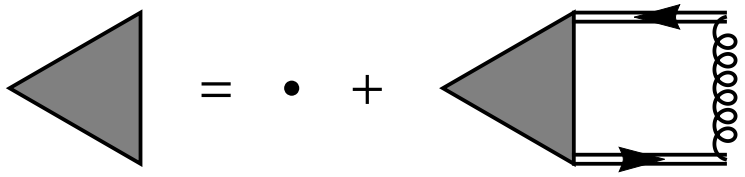

Figure F.1: Diagrammatic representation of the Bethe-Salpeter equation for the vertex function, Eq. F.61, in the ladded approximation. The Triangle represents the irreducible vertex ,$\Gamma^i_{\tilde{\mathbf{k}},\tilde{\mathbf{k}}+\tilde{\mathbf{q}}}$, the dot represents the bare vertex, $J^i_{\tilde{\mathbf{k}},\tilde{\mathbf{k}}+\tilde{\mathbf{q}}}$, the directed double straight lines represent the Green's function, $G_{\tilde{\mathbf{k}}}$, and the coil-like line represents the effective interaction $U^{\tilde{\mathbf{k}},\tilde{\mathbf{k}}+\tilde{\mathbf{q}}+\tilde{\mathbf{p}}}_{\tilde{\mathbf{k}}+\tilde{\mathbf{p}},\tilde{\mathbf{k}}+\tilde{\mathbf{q}}}$.

(which strictly speaking only holds in the single band case), with the scattering time given by $1/\tau^{\rm scat}_{\mathbf{k}}(\omega) = -2{\rm Im}\Sigma^R_{\mathbf{k}}(\omega)$, and approximating the electronic spectral function by

$$A_{\mathbf{k}}(\omega) = i\left[G^R_{\mathbf{k}}(\nu) - G^A_{\mathbf{k}}(\nu)\right] \simeq 2\pi\delta\left(\omega - \epsilon_{\mathbf{k}}\right), \tag{F.57}$$

the expression for the DC conductivity becomes

$${\rm Re}\sigma^{\rm DC}_{ij} \simeq \frac{q_e^2}{V}\sum_{\mathbf{k}}\left(-\frac{\partial f(\epsilon_{\mathbf{k}})}{\partial\epsilon_{\mathbf{k}}}\right)\tau^{\rm scat}_{\mathbf{k}}(\epsilon_{\mathbf{k}})\Gamma^{i,AR}_{\mathbf{k},\mathbf{k}}(\epsilon_{\mathbf{k}},\epsilon_{\mathbf{k}})\,J^j_{\mathbf{k},\mathbf{k}}. \tag{F.58}$$

If we replace the irreducible vertex by the bare current matrix element, $\Gamma^{i,AR}_{\mathbf{k},\mathbf{k}}(\epsilon_{\mathbf{k}},\epsilon_{\mathbf{k}}) \simeq J^i_{\mathbf{k},\mathbf{k}}$, then the DC conductivity would be given by

$${\rm Re}\sigma^{\rm DC}_{ij} \simeq \frac{q_e^2}{V}\sum_{\mathbf{k}}\left(-\frac{\partial f(\epsilon_{\mathbf{k}})}{\partial\epsilon_{\mathbf{k}}}\right)\tau^{\rm scat}_{\mathbf{k}}(\epsilon_{\mathbf{k}})J^i_{\mathbf{k},\mathbf{k}}J^j_{\mathbf{k},\mathbf{k}}, \tag{F.59}$$

which is of the form of the Boltzmann result to the DC conductivity, except that in the Boltzmann approach the expression for the conductivity involves not the scattering time, but the transport time, which encodes the fact that forward scattering does not lead to a degradation of current. In what follows we will see how this apparent deficiency of the Kubo approach can be solved by tacking into account interaction corrections to the irreducible vertex function $\Gamma^{i,AR}_{\mathbf{k},\mathbf{k}}(\epsilon_{\mathbf{k}},\epsilon_{\mathbf{k}})$.

F.3.2 *Bethe-Salpeter equation for the irreducible current vertex function*

As we previously said, the expression for the DC conductivity should involve the transport time and not the scattering time. In order to take this into account it is necessary to include the effect of interactions into the irreducible vertex. We will consider a general electron-boson interaction of the form

$$H_{\rm e-b} = \sum_{\mathbf{k},\mathbf{q}}\psi^\dagger_{\mathbf{k}}\phi_{\mathbf{k},\mathbf{k}+\mathbf{q}}\psi_{\mathbf{k}+\mathbf{q}}, \tag{F.60}$$

where $\phi_{\mathbf{k},\mathbf{k}+\mathbf{q}}$ is a bosonic field and we have included any additional indices in the momentum variable. We have expressed the interaction Hamiltonian in terms of fields expressed in Fourier components, but more generally $\mathbf{k}$ and $\mathbf{k}+\mathbf{q}$ can be seen as labels of a generic single particle basis. In the presence of this interaction and in the non-crossing

or ladder approximation, the Matsubara irreducible vertex obeys the Bethe-Salpeter equation

$$\Gamma^{i}_{\tilde{\mathbf{k}},\tilde{\mathbf{k}}+\tilde{\mathbf{q}}} = J^{i}_{\tilde{\mathbf{k}},\tilde{\mathbf{k}}+\tilde{\mathbf{q}}} - \frac{1}{\beta V}\sum_{\tilde{\mathbf{p}}} G_{\tilde{\mathbf{k}}+\tilde{\mathbf{p}}}\Gamma^{i}_{\tilde{\mathbf{k}}+\tilde{\mathbf{p}},\tilde{\mathbf{k}}+\tilde{\mathbf{q}}+\tilde{\mathbf{p}}}G_{\tilde{\mathbf{k}}+\tilde{\mathbf{q}}+\tilde{\mathbf{p}}}U^{\tilde{\mathbf{k}},\tilde{\mathbf{k}}+\tilde{\mathbf{q}}+\tilde{\mathbf{p}}}_{\tilde{\mathbf{k}}+\tilde{\mathbf{p}},\tilde{\mathbf{k}}+\tilde{\mathbf{q}}}, \tag{F.61}$$

where we have introduced the effective interaction as

$$U^{\tilde{\mathbf{k}},\tilde{\mathbf{k}}+\tilde{\mathbf{q}}+\tilde{\mathbf{p}}}_{\tilde{\mathbf{k}}+\tilde{\mathbf{p}},\tilde{\mathbf{k}}+\tilde{\mathbf{q}}} = -\int_0^\beta d\tau e^{ip_n\tau}\left\langle T_\tau \phi_{\mathbf{k},\mathbf{k}+\mathbf{p}}(\tau)\phi_{\mathbf{k}+\mathbf{q}+\mathbf{p},\mathbf{k}+\mathbf{q}}(0)\right\rangle, \tag{F.62}$$

which actually only depends on the Matsubara frequency ip_n. The Bethe-Salpeter equation is represented diagrammatically in Fig. F.1. We point out that the Bethe-Salpeter equation (F.61) is compatible with the generalized Ward identity Eq. (F.42), provided the self-energy given by [248]

$$\Sigma_{\tilde{\mathbf{k}}} = -\frac{1}{\beta V}\sum_{\tilde{\mathbf{p}}} U^{\tilde{\mathbf{k}},\tilde{\mathbf{k}}+\tilde{\mathbf{p}}}_{\tilde{\mathbf{k}}+\tilde{\mathbf{p}},\tilde{\mathbf{k}}} G_{\tilde{\mathbf{k}}+\tilde{\mathbf{p}}}. \tag{F.63}$$

In order to solve Eq. (F.61) to obtain $\mathbf{\Gamma}^{i,AR}_{\mathbf{k},\mathbf{k}}(\nu,\nu)$, the first step is to perform the sum over the bosonic Matsubara frequency ip_n. This can be done changing to the complex variable $ip_n \to z$ and noticing that the integrand will have three branch cuts in the complex plane: when z is real, $ik_n + z$ is real and when $ik_n + iq_n + z$ is real. Performing the contour integration, we obtain six different terms, which after analytic continuation to real frequencies, $ik_n \to \nu - i0^+$ and $ik_n + iq_n \to \nu + \omega + i0^+$, can be written as (suppressing the momentum arguments for simplicity)

$$\begin{aligned}
&\Gamma^{i,AR}(\nu,\nu+\omega) - J^{i} = \\
&\quad = -\int \frac{d\epsilon}{2\pi i} b(\epsilon) G^{A}(\epsilon+\nu)\,\Gamma^{i,AR}(\epsilon+\nu,\epsilon+\nu+\omega)\,G^{R}(\epsilon+\nu+\omega)\,U^{R}(\epsilon) \\
&\qquad + \int \frac{d\epsilon}{2\pi i} b(\epsilon) G^{A}(\epsilon+\nu)\,\Gamma^{i,AR}(\epsilon+\nu,\epsilon+\nu+\omega)\,G^{R}(\epsilon+\nu+\omega)\,U^{A}(\epsilon) \\
&\quad - \int \frac{d\epsilon}{2\pi i} f(\epsilon+\nu) G^{A}(\epsilon+\nu)\,\Gamma^{i,AR}(\epsilon+\nu,\epsilon+\nu+\omega)\,G^{R}(\epsilon+\nu+\omega)\,U^{R}(\epsilon) \\
&\quad + \int \frac{d\epsilon}{2\pi i} f(\epsilon+\nu) G^{R}(\epsilon+\nu)\,\Gamma^{i,RR}(\epsilon+\nu,\epsilon+\nu+\omega)\,G^{R}(\epsilon+\nu+\omega)\,U^{R}(\epsilon) \\
&\quad - \int \frac{d\nu}{2\pi i} f(\epsilon+\nu+\omega) G^{A}(\epsilon+\nu)\,\Gamma^{i,AA}(\epsilon+\nu,\epsilon+\nu+\omega)\,G^{A}(\epsilon+\nu)\,U^{A}(\epsilon) \\
&+ \int \frac{d\epsilon}{2\pi i} f(\epsilon+\nu+\omega) G^{A}(\epsilon+\nu)\,\Gamma^{i,AR}(\epsilon+\nu,\epsilon+\nu+\omega)\,G^{R}(\epsilon+\nu+\omega)\,U^{A}(\epsilon)
\end{aligned} \tag{F.64}$$

Taking the limit $\mathbf{q}\to 0$, $\omega \to 0$ and collecting all the terms involving $\Gamma^{i,AR}$, we obtain

$$\begin{aligned}
&\Gamma^{i,AR}_{\mathbf{k},\mathbf{k}}(\nu,\nu) - J^{i}_{\mathbf{k},\mathbf{k}} = \\
&= -\frac{1}{V}\sum_{\mathbf{p}}\int \frac{d\nu}{\pi} f(\epsilon)\mathrm{Im}\left[G^{A}_{\mathbf{k}+\mathbf{p}}(\epsilon)\,\Gamma^{i,AA}_{\mathbf{k}+\mathbf{p},\mathbf{k}+\mathbf{p},\mathbf{k}+\mathbf{p}}(\epsilon,\epsilon)\,G^{A}_{\mathbf{k}+\mathbf{p}}(\epsilon)\,U^{\mathbf{k},\mathbf{k}+\mathbf{p},A}_{\mathbf{k}+\mathbf{p},\mathbf{k}}(\epsilon-\nu)\right] + \\
&+ \frac{1}{V}\sum_{\mathbf{p}}\int \frac{d\epsilon}{2\pi}\left[b(\epsilon-\nu)+f(\epsilon)\right] G^{A}_{\mathbf{k}+\mathbf{p}}(\epsilon)\,\Gamma^{i,AR}_{\mathbf{k}+\mathbf{p},\mathbf{k}+\mathbf{p}}(\epsilon,\epsilon)\,G^{R}_{\mathbf{k}+\mathbf{p}}(\epsilon)\,A^{\mathbf{k},\mathbf{k}+\mathbf{p}}_{\phi;\mathbf{k}+\mathbf{p},\mathbf{k}}(\epsilon-\nu),
\end{aligned} \tag{F.65}$$

where we introduced the spectral function for the interaction mediating boson as

$$A^{\mathbf{k},\mathbf{k+q+p}}_{\phi;\mathbf{k+p},\mathbf{k+q}}(\omega) = i\left[U^{\mathbf{k},\mathbf{k+q+p}}_{\mathbf{k+p},\mathbf{k+q}}\left(\omega + i0^+\right) - U^{\mathbf{k},\mathbf{k+q+p}}_{\mathbf{k+p},\mathbf{k+q}}\left(\omega - i0^+\right)\right], \tag{F.66}$$

with $U^{\mathbf{k},\mathbf{k+q+p}}_{\mathbf{k+p},\mathbf{k+q}}\left(\omega \pm i0^+\right)$ obtained by analytically continuing Eq. (F.62) to real frequencies, $ip_n \to \omega \pm i0^+$. Using the Ward identity Eq. (F.47), we can rewrite the first term on the right hand side of Eq. (F.65), obtaining

$$\begin{aligned}\Gamma^{i,AR}_{\mathbf{k},\mathbf{k}}(\nu,\nu) - J^i_{\mathbf{k},\mathbf{k}} = \\ = -\frac{1}{V}\sum_{\mathbf{p}}\int\frac{d\nu}{\pi}f(\epsilon)\mathrm{Im}\left[\frac{\partial}{\partial k_i}G^A_{\mathbf{k+p}}(\epsilon)\,U^{\mathbf{k},\mathbf{k+p},A}_{\mathbf{k+p},\mathbf{k}}(\epsilon-\nu)\right] + \\ + \frac{1}{V}\sum_{\mathbf{p}}\int\frac{d\epsilon}{2\pi}\left[b(\epsilon-\nu)+f(\epsilon)\right]G^A_{\mathbf{k+p}}(\epsilon)\,\Gamma^{i,AR}_{\mathbf{k+p},\mathbf{k+p}}(\epsilon,\epsilon)\,G^R_{\mathbf{k+p}}(\epsilon)\,A^{\mathbf{k},\mathbf{k+p}}_{\phi;\mathbf{k+p},\mathbf{k}}(\epsilon-\nu).\end{aligned} \tag{F.67}$$

The first term on the right-hand side of the previous equation leads to a correction of the bare current matrix elements, $J^i_{\mathbf{k},\mathbf{k}}$. Similar terms also appear when employing the Kadanoff-Baym equations [57] or a Markov quantum master equation [251], but are generally ignored in the classical Boltzmann equation. In the following we will neglect such effects and obtain

$$\begin{aligned}\Gamma^{i,AR}_{\mathbf{k},\mathbf{k}}(\nu,\nu) - J^i_{\mathbf{k},\mathbf{k}} = \frac{1}{V}\sum_{\mathbf{p}}\int\frac{d\epsilon}{2\pi}\left[b(\epsilon)+f(\epsilon+\nu)\right]\times \\ \times\, G^A_{\mathbf{k+p}}(\epsilon+\nu)\,\Gamma^{i,AR}_{\mathbf{k+p},\mathbf{k+p}}(\epsilon+\nu,\epsilon+\nu)\,G^R_{\mathbf{k+p}}(\epsilon+\nu)\,A^{\mathbf{k},\mathbf{k+p}}_{\phi;\mathbf{k+p},\mathbf{k}}(\epsilon).\end{aligned} \tag{F.68}$$

The final step in order to obtain the DC conductivity of a metal in the presence of scattering, is to solve the previous equation for $\Gamma^{i,AR}_{\mathbf{k},\mathbf{k}}(\nu,\nu)$ and insert the result the result in Eq. (F.55).

F.3.3 *DC conductivity for quasi-elastic scattering*

We will now solve the Bethe-Salpeter equation for the irreducible vertex function, Eq. (F.68), in the weak quasi-elastic scattering approximation at low temperatures. First we notice that in Eq. (F.55), the derivative of the Fermi-Dirac function imposes that only energies and states close to the Fermi level will give a relevant contribution. We are interested in the case where there is a single band crossing the Fermi level, and since we are considering the low temperature, quasi-elastic scattering limits we can focus on that single band. With these approximations we can use Eq. (F.56) and approximate the electronic spectral function by a δ-function, which means we can focus on the irreducible vertex function only on the on-shell case, $\nu = \epsilon_{\mathbf{k}}$ (with $\epsilon_{\mathbf{k}}$ the electronic dispersion relation). These considerations allow us to approximate the Bethe-Salpater, Eq. (F.68), by

$$\begin{aligned}\Gamma^{i,AR}_{\mathbf{k},\mathbf{k}}(\epsilon_{\mathbf{k}},\epsilon_{\mathbf{k}}) - J^i_{\mathbf{k},\mathbf{k}} = \frac{1}{V}\sum_{\mathbf{p}}\int\frac{d\epsilon}{2\pi}\left[b(\epsilon)+f(\epsilon+\epsilon_{\mathbf{k}})\right]\Gamma^{i,AR}_{\mathbf{k+p},\mathbf{k+p}}(\epsilon+\epsilon_{\mathbf{k}},\epsilon+\epsilon_{\mathbf{k}})\times \\ \times\,\tau^{\mathrm{scat}}_{\mathbf{k+p}}(\epsilon+\epsilon_{\mathbf{k}})\,A_{\mathbf{k+p}}(\epsilon+\epsilon_{\mathbf{k}})\,A^{\mathbf{k},\mathbf{k+p}}_{\phi;\mathbf{k+p},\mathbf{k}}(\epsilon).\end{aligned} \tag{F.69}$$

After integrating over energy using the electronic spectral function we obtain

$$\Gamma^{i,AR}_{\mathbf{k},\mathbf{k}}(\epsilon_{\mathbf{k}},\epsilon_{\mathbf{k}}) - J^{i}_{\mathbf{k},\mathbf{k}} = \frac{1}{V}\sum_{\mathbf{p}}\left[b(\epsilon_{\mathbf{k}+\mathbf{p}}-\epsilon_{\mathbf{k}}) + f(\epsilon_{\mathbf{k}+\mathbf{p}})\right]\Gamma^{i,AR}_{\mathbf{k}+\mathbf{p},\mathbf{k}+\mathbf{p}}(\epsilon_{\mathbf{k}+\mathbf{p}},\epsilon_{\mathbf{k}+\mathbf{p}})\times \\ \times\,\tau^{\text{scat}}_{\mathbf{k}+\mathbf{p}}(\epsilon_{\mathbf{k}+\mathbf{p}})\,A^{\mathbf{k},\mathbf{k}+\mathbf{p}}_{\phi,\mathbf{k}+\mathbf{p},\mathbf{k}}(\epsilon_{\mathbf{k}+\mathbf{p}}-\epsilon_{\mathbf{k}})\,. \tag{F.70}$$

Assuming the system is isotropic we can write

$$\Gamma^{i,AR}_{\mathbf{k},\mathbf{k}}(\nu,\nu) = \frac{k^i}{|\mathbf{k}|}\,|\mathbf{J}_{\mathbf{k},\mathbf{k}}|\,\Xi_{\mathbf{k}}(\nu), \tag{F.71}$$

and after contracting Eq. (F.70) with $k^i/|\mathbf{k}|$ we obtain an equation for the quantity $\Xi_{\mathbf{k}}(\nu)$

$$|\mathbf{J}_{\mathbf{k},\mathbf{k}}|\,\Xi_{\mathbf{k}}(\epsilon_{\mathbf{k}}) - |\mathbf{J}_{\mathbf{k},\mathbf{k}}| = \frac{1}{V}\sum_{\mathbf{p}}\left[b(\epsilon_{\mathbf{k}+\mathbf{p}}-\epsilon_{\mathbf{k}}) + f(\epsilon_{\mathbf{k}+\mathbf{p}})\right]\cos\theta_{\mathbf{k},\mathbf{k}+\mathbf{p}}\times \\ \times\,|\mathbf{J}_{\mathbf{k}+\mathbf{p},\mathbf{k}+\mathbf{p}}|\,\Xi_{\mathbf{k}+\mathbf{p}}(\epsilon_{\mathbf{k}+\mathbf{p}})\,\tau^{\text{scat}}_{\mathbf{k}+\mathbf{p}}(\epsilon_{\mathbf{k}+\mathbf{p}})\,A^{\mathbf{k},\mathbf{k}+\mathbf{p}}_{\phi,\mathbf{k}+\mathbf{p},\mathbf{k}}(\epsilon_{\mathbf{k}+\mathbf{p}}-\epsilon_{\mathbf{k}})\,. \tag{F.72}$$

For quasi-elastic scattering we have that $\epsilon_{\mathbf{k}+\mathbf{p}} \simeq \epsilon_{\mathbf{k}}$, which at low temperatures both become pinned to the Fermi energy. Therefore we can write $|\mathbf{J}_{\mathbf{k}+\mathbf{p},\mathbf{k}+\mathbf{p}}| \simeq |\mathbf{J}_{\mathbf{k},\mathbf{k}}|$, $\Xi_{\mathbf{k}+\mathbf{p}}(\epsilon_{\mathbf{k}+\mathbf{p}}) \simeq \Xi_{\mathbf{k}}(\epsilon_{\mathbf{k}})$ and $\tau^{\text{scat}}_{\mathbf{k}+\mathbf{p}}(\epsilon_{\mathbf{k}+\mathbf{p}}) \simeq \tau^{\text{scat}}_{\mathbf{k}}(\epsilon_{\mathbf{k}})$. With this approximations $\Xi_{\mathbf{k}}(\epsilon_{\mathbf{k}})$ can be written as

$$\Xi_{\mathbf{k}}(\epsilon_{\mathbf{k}}) = \frac{1}{1-\tau^{\text{scat}}_{\mathbf{k}}(\epsilon_{\mathbf{k}})\,I_{\mathbf{k}}(\epsilon_{\mathbf{k}})}, \tag{F.73}$$

where

$$I_{\mathbf{k}}(\epsilon_{\mathbf{k}}) = \frac{1}{V}\sum_{\mathbf{p}}\left[b(\epsilon_{\mathbf{k}+\mathbf{p}}-\epsilon_{\mathbf{k}}) + f(\epsilon_{\mathbf{k}+\mathbf{p}})\right]\cos\theta_{\mathbf{k},\mathbf{k}+\mathbf{p}}A^{\mathbf{k},\mathbf{k}+\mathbf{p}}_{\phi,\mathbf{k}+\mathbf{p},\mathbf{k}}(\epsilon_{\mathbf{k}+\mathbf{p}}-\epsilon_{\mathbf{k}})\,. \tag{F.74}$$

We point out that the scattering time is given by

$$\frac{1}{\tau^{\text{scat}}_{\mathbf{k}}(\epsilon_{\mathbf{k}})} = -2\text{Im}\Sigma^{R}_{\mathbf{k}}(\omega) = \frac{1}{V}\sum_{\mathbf{p}}\left[b(\epsilon_{\mathbf{k}+\mathbf{p}}-\epsilon_{\mathbf{k}}) + f(\epsilon_{\mathbf{k}+\mathbf{p}})\right]A^{\mathbf{k},\mathbf{k}+\mathbf{p}}_{\phi,\mathbf{k}+\mathbf{p},\mathbf{k}}(\epsilon_{\mathbf{k}+\mathbf{p}}-\epsilon_{\mathbf{k}})\,. \tag{F.75}$$

If the transport time is introduced as

$$\frac{1}{\tau^{\text{tr}}_{\mathbf{k}}(\epsilon_{\mathbf{k}})} = \frac{1}{V}\sum_{\mathbf{p}}(1-\cos\theta_{\mathbf{k},\mathbf{k}+\mathbf{p}})\left[b(\epsilon_{\mathbf{k}+\mathbf{p}}-\epsilon_{\mathbf{k}}) + f(\epsilon_{\mathbf{k}+\mathbf{p}})\right]A^{\mathbf{k},\mathbf{k}+\mathbf{p}}_{\phi,\mathbf{k}+\mathbf{p},\mathbf{k}}(\epsilon_{\mathbf{k}+\mathbf{p}}-\epsilon_{\mathbf{k}})\,, \tag{F.76}$$

or equivalently

$$\frac{1}{\tau^{\text{tr}}_{\mathbf{k}}(\epsilon_{\mathbf{k}})} = \frac{1}{V}\sum_{\mathbf{p}}\int d\omega\,(1-\cos\theta_{\mathbf{k},\mathbf{k}+\mathbf{p}})\left[b(\omega) + f(\epsilon_{\mathbf{k}}+\omega)\right]A^{\mathbf{k},\mathbf{k}+\mathbf{p}}_{\phi,\mathbf{k}+\mathbf{p},\mathbf{k}}(\omega)\,\delta(\omega-\epsilon_{\mathbf{k}+\mathbf{p}}+\epsilon_{\mathbf{k}})\,, \tag{F.77}$$

then Eq. (F.73) can be written as

$$\Xi_{\mathbf{k}}(\epsilon_{\mathbf{k}}) = \frac{\tau^{\text{tr}}_{\mathbf{k}}(\epsilon_{\mathbf{k}})}{\tau^{\text{scat}}_{\mathbf{k}}(\epsilon_{\mathbf{k}})}. \tag{F.78}$$

Therefore, in terms of the transport time the irreducible vertex, Eq. (F.71), is given by

$$\Gamma^{i,AR}_{\mathbf{k},\mathbf{k}}(\nu,\nu) = J^{i}_{\mathbf{k},\mathbf{k}}\frac{\tau^{\text{tr}}_{\mathbf{k}}(\epsilon_{\mathbf{k}})}{\tau^{\text{scat}}_{\mathbf{k}}(\epsilon_{\mathbf{k}})}. \tag{F.79}$$

Inserting this expression into Eq. (F.58) we obtain the final expression for the DC conductivity in the case of weak quasi-elastic scattering

$$\mathrm{Re}\sigma_{ij}^{\mathrm{DC}} \simeq \frac{q_e^2}{V}\sum_{\mathbf{k}}\left(-\frac{\partial f(\epsilon_{\mathbf{k}})}{\partial\epsilon_{\mathbf{k}}}\right)\tau_{\mathbf{k}}^{\mathrm{tr}}(\epsilon_{\mathbf{k}})J_{\mathbf{k},\mathbf{k}}^{i}J_{\mathbf{k},\mathbf{k}}^{j}. \tag{F.80}$$

Inclusion of vertex corrections change the scattering time by the transport time, such that the Kubo approach describes the same physics as the Boltzmann approach.

Notice that in the derivation of Eq. (F.79), we had to make the approximations $\Gamma^{i,AR}_{\mathbf{k}+\mathbf{p},\mathbf{k}+\mathbf{p}}(\epsilon_{\mathbf{k}+\mathbf{p}},\epsilon_{\mathbf{k}+\mathbf{p}}) \simeq \Gamma^{i,AR}_{\mathbf{k}+\mathbf{p},\mathbf{k}+\mathbf{p}}(\epsilon_{\mathbf{k}},\epsilon_{\mathbf{k}})$ and $\tau^{\mathrm{scat}}_{\mathbf{k}+\mathbf{p}}(\epsilon_{\mathbf{k}+\mathbf{p}}) \simeq \tau^{\mathrm{scat}}_{\mathbf{k}+\mathbf{p}}(\epsilon_{\mathbf{k}})$. As a matter of fact such approximation is not valid for scattering by acoustic phonons [252] and the slight inelastic nature of scattering by acoustic phonons can become important. However, the inelastic effects only becomes important at very low temperatures and for higher temperatures the quasi-elastic approximation becomes a good approximation [155].

Focusing on the transport at the Fermi energy, setting $\epsilon_{\mathbf{k}} = \epsilon_F$, Eq. (F.77) reduces to

$$\begin{aligned}\frac{1}{\tau_{\mathbf{k}}^{\mathrm{tr}}(\epsilon_F)} &= \frac{1}{V}\sum_{\mathbf{p}}\int d\omega\,(1-\cos\theta_{\mathbf{k},\mathbf{k}+\mathbf{p}})\,[b(\omega)+f(\omega)]\,A^{\mathbf{k},\mathbf{k}+\mathbf{p}}_{\phi,\mathbf{k}+\mathbf{p},\mathbf{k}}(\omega)\,\delta(\epsilon_{\mathbf{k}}-\epsilon_{\mathbf{k}+\mathbf{p}})\\ &= \frac{1}{V}\sum_{\mathbf{p}}\int \frac{d\omega}{\sinh(\beta\omega)}\,(1-\cos\theta_{\mathbf{k},\mathbf{k}+\mathbf{p}})\,A^{\mathbf{k},\mathbf{k}+\mathbf{p}}_{\phi,\mathbf{k}+\mathbf{p},\mathbf{k}}(\omega)\,\delta(\epsilon_{\mathbf{k}}-\epsilon_{\mathbf{k}+\mathbf{p}}).\end{aligned} \tag{F.81}$$

This result is to be contrasted to the standard Ziman's formula for the transport time [95], which reads instead

$$\frac{1}{\tau_{\mathbf{k}}^{\mathrm{tr,Ziman}}(\epsilon_F)} = \frac{1}{V}\sum_{\mathbf{p}}\int \frac{d\omega}{4\sinh(\beta\omega/2)^2}\beta\omega\,(1-\cos\theta_{\mathbf{k},\mathbf{k}+\mathbf{p}})\,A^{\mathbf{k},\mathbf{k}+\mathbf{p}}_{\phi,\mathbf{k}+\mathbf{p},\mathbf{k}}(\omega)\,\delta(\epsilon_{\mathbf{k}}-\epsilon_{\mathbf{k}+\mathbf{p}}). \tag{F.82}$$

In the high temperature limit, Eqs. (F.81) and (F.82) coincide. On the posit limit, the result from the two expressions differs. However, as we have previously discussed, in the low temperature limit, neither equation can be trusted, as both are based on a quasi-elastic approximation. It is however useful to track down the difference between Eqs. (F.81) and (F.82). Notice that by using the equality

$$b(\omega)+f(\epsilon_{\mathbf{k}}+\omega) = \frac{1-f(\epsilon_{\mathbf{k}}+\omega)}{1-f(\epsilon_{\mathbf{k}})}b(\omega), \tag{F.83}$$

Eq. (F.77) for the transport time can be expressed as

$$\frac{1}{\tau_{\mathbf{k}}^{\mathrm{tr}}(\epsilon_{\mathbf{k}})} = \frac{1}{V}\sum_{\mathbf{p}}(1-\cos\theta_{\mathbf{k},\mathbf{k}+\mathbf{p}})\,\frac{1-f(\epsilon_{\mathbf{k}+\mathbf{p}})}{1-f(\epsilon_{\mathbf{k}})}b(\epsilon_{\mathbf{k}+\mathbf{p}}-\epsilon_{\mathbf{k}})\,A^{\mathbf{k},\mathbf{k}+\mathbf{p}}_{\phi,\mathbf{k}+\mathbf{p},\mathbf{k}}(\epsilon_{\mathbf{k}+\mathbf{p}}-\epsilon_{\mathbf{k}}). \tag{F.84}$$

Using identities of the Fermi-Dirac and Bose-Einstein functions we can also write

$$\frac{1-f(\epsilon_{\mathbf{k}+\mathbf{p}})}{1-f(\epsilon_{\mathbf{k}})} = \frac{f(\epsilon_{\mathbf{k}+\mathbf{p}})-f(\epsilon_{\mathbf{k}})}{f(\epsilon_{\mathbf{k}})(1-f(\epsilon_{\mathbf{k}}))}b(\epsilon_{\mathbf{k}}-\epsilon_{\mathbf{k}+\mathbf{p}}), \tag{F.85}$$

and therefore Eq. (F.84) can be written

$$\begin{aligned}\frac{1}{\tau_{\mathbf{k}}^{\mathrm{tr}}(\epsilon_{\mathbf{k}})} = \frac{1}{V}\sum_{\mathbf{p}}\int d\omega\,(1-\cos\theta_{\mathbf{k},\mathbf{k}+\mathbf{p}})\,\frac{f(\epsilon_{\mathbf{k}}+\omega)-f(\epsilon_{\mathbf{k}})}{f(\epsilon_{\mathbf{k}})(1-f(\epsilon_{\mathbf{k}}))}b(-\omega)\,b(\omega)\times\\ \times A^{\mathbf{k},\mathbf{k}+\mathbf{p}}_{\phi,\mathbf{k}+\mathbf{p},\mathbf{k}}(\omega)\,\delta(\omega-\epsilon_{\mathbf{k}+\mathbf{p}}+\epsilon_{\mathbf{k}}).\end{aligned} \tag{F.86}$$

Using the fact that for quasi-elastic scattering we have that $\epsilon_{\mathbf{k}+\mathbf{p}} \simeq \epsilon_{\mathbf{k}}$, we can make the approximate [253]

$$\begin{aligned} f\left(\epsilon_{\mathbf{k}}+\omega\right)-f\left(\epsilon_{\mathbf{k}}\right) &\simeq \omega \frac{\partial f(\epsilon_{\mathbf{k}})}{\partial \epsilon_{\mathbf{k}}} \\ &= -\frac{\omega}{k_B T} f\left(\epsilon_{\mathbf{k}}\right)\left(1-f\left(\epsilon_{\mathbf{k}}\right)\right), \end{aligned} \tag{F.87}$$

such that

$$\frac{1}{\tau_{\mathbf{k}}^{\mathrm{tr}}\left(\epsilon_{\mathbf{k}}\right)}=\frac{1}{V}\int d\omega \sum_{\mathbf{p}}\left(1-\cos\theta_{\mathbf{k},\mathbf{k}+\mathbf{p}}\right)\omega\left(-\frac{\partial b(\omega)}{\partial \omega}\right) A_{\phi,\mathbf{k}+\mathbf{p},\mathbf{k}}^{\mathbf{k},\mathbf{k}+\mathbf{p}}\left(\omega\right)\delta\left(\omega-\epsilon_{\mathbf{k}+\mathbf{p}}+\epsilon_{\mathbf{k}}\right), \tag{F.88}$$

where we have used the fact that $b\left(-\omega\right)b\left(\omega\right)/k_B T=\partial b(\omega)/\partial\omega$. This result is exactly the same as Ziman's result Eq. (F.82).

G

BOLTZMANN EQUATION APPROACH TO COULOMB DRAG

In this appendix we present a derivation of the drag conductivity between two plates using the Boltzmann equation. We will closely follow the derivation done in Ref. [160] but generalizing the result for a multiband system.

We assume that the electrons in each layer, $\ell = 1, 2$, are characterized by a band dispersion given by $\epsilon_{\mathbf{k},\lambda,\ell}$, where $\mathbf{k}$ is the momentum and λ is a band index. The electron wavefunctions are given by

$$\phi_{\mathbf{k},\lambda,\ell}(\mathbf{x}) = \frac{1}{\sqrt{A}} e^{i\mathbf{k}\cdot\mathbf{x}} \left|\mathbf{k},\lambda\right\rangle_\ell . \tag{G.1}$$

The electrons of the two layers interact via the Hamiltonian

$$H_{\text{inter}} = \frac{1}{A} \sum_{\mathbf{k},\mathbf{k}',\mathbf{q},\lambda_i} V_{12}(\mathbf{q})\, \rho^{\lambda_1,\lambda_2}_{1,\mathbf{k}+\mathbf{q},\mathbf{k}} \rho^{\lambda_3,\lambda_4}_{2,\mathbf{k}'-\mathbf{q},\mathbf{k}'} \psi^\dagger_{\mathbf{k}+\mathbf{q},\lambda_1,1} \psi^\dagger_{\mathbf{k}'-\mathbf{q},\lambda_3,2} \psi_{\mathbf{k}',\lambda_4,2} \psi_{\mathbf{k},\lambda_2,1}, \tag{G.2}$$

where $\psi^\dagger_{\mathbf{k},\lambda,\ell}$ creates an electron in layer ℓ with momentum $\mathbf{k}$ in band λ, $V_{12}(\mathbf{q})$ is the bare interlayer Coulomb interaction, which for two metallic plates in vacuum is given by

$$V_{12}(\mathbf{q}) = \frac{e^2}{4\pi\epsilon_0} \int \frac{d^2\mathbf{x}}{(2\pi)^2} \frac{e^{i\mathbf{x}\cdot\mathbf{q}}}{|\mathbf{x}^2 + d^2|} = \frac{e^2}{2\epsilon_0 |\mathbf{q}|} e^{-|\mathbf{q}|d}, \tag{G.3}$$

with d the separation between the two layers, and $\rho^{\lambda_1,\lambda_2}_{\ell,\mathbf{k}+\mathbf{q},\mathbf{k}} =_\ell \langle \mathbf{k}+\mathbf{q},\lambda_1 \mid \mathbf{k},\lambda_2\rangle_\ell$ are wavefunction overlap factors.

The Boltzmann equation in the DC limit, for the coupled layers reads

$$\frac{e_1}{\hbar}\mathbf{E}_1 \cdot \frac{\partial n_{\mathbf{k},\lambda,1}}{\partial \mathbf{k}} = I_{\text{imp}}[n_1]_{\mathbf{k},\lambda} + I_{\text{inter}}[n_1, n_2]_{\mathbf{k},\lambda}, \tag{G.4}$$

$$\frac{e_2}{\hbar}\mathbf{E}_2 \cdot \frac{\partial n_{\mathbf{k},\lambda,2}}{\partial \mathbf{k}} = I_{\text{imp}}[n_2]_{\mathbf{k},\lambda} + I_{\text{inter}}[n_2, n_1]_{\mathbf{k},\lambda}, \tag{G.5}$$

where we have denoted the Boltzmann distribution function for electrons in layer ℓ as $n_{\mathbf{k},\lambda,1}$, e_ℓ is the charge of the quasi-particles in layer ℓ, $I_{\text{imp}}[n]_{\mathbf{k},\lambda}$ is the intralayer collision integral due to impurities and $I_{\text{inter}}[n_1, n_2]_{\mathbf{k},\lambda}$ is the collision integral due to the interlayer interaction Eq. (G.2). We neglect effects of intralayer interactions, assuming that the intralayer scattering is dominated by impurities. Assuming that impurities from different layers are uncorrelated, the impurity collision integral is given by

$$I_{\text{imp}}[n_\ell]_{\mathbf{k},\lambda} = -\frac{2\pi}{A} \sum_{\mathbf{k}'} n_{\text{imp},\ell} \left|T^{(\ell),\lambda}_{\mathbf{k}',\mathbf{k}}\right|^2 \delta\left(\epsilon_{\mathbf{k},\lambda,\ell} - \epsilon_{\mathbf{k}',\lambda,\ell}\right)\left(n_{\mathbf{k},\lambda,\ell} - n_{\mathbf{k}',\lambda,\ell}\right), \tag{G.6}$$

where $n_{\mathrm{imp},\ell}$ is the impurity concentration in layer ℓ, $T^{(\ell),\lambda}_{\mathbf{k}',\mathbf{k}}$ is the T-matrix due to the impurity potential and we have assumed that there is no interband scattering. The collision integral due to the interlayer interaction is given by

$$\begin{aligned} I_{\mathrm{intra}}\left[n_\ell, n_{\ell'}\right]_{\mathbf{k},\lambda} = -\frac{2\pi}{A^2}\sum_{\mathbf{k}',\mathbf{q}} \left|U^R_{12}\left(\epsilon^{(\ell)}_{\mathbf{k}+\mathbf{q},\lambda_1} - \epsilon^{(\ell)}_{\mathbf{k},\lambda}, \mathbf{q}\right)\right|^2 \left|\rho^{\lambda_1,\lambda}_{\ell,\mathbf{k}+\mathbf{q},\mathbf{k}}\right|^2 \left|\rho^{\lambda_3,\lambda_2}_{\ell',\mathbf{k}'-\mathbf{q},\mathbf{k}'}\right|^2 \\ \times \delta\left(\epsilon^{(\ell)}_{\mathbf{k}+\mathbf{q},\lambda_1} + \epsilon^{(\ell')}_{\mathbf{k}'-\mathbf{q},\lambda_3} - \epsilon^{(\ell)}_{\mathbf{k},\lambda} - \epsilon^{(\ell')}_{\mathbf{k}',\lambda_2}\right) \times \\ \times \Big[n_{\mathbf{k},\lambda,\ell} n_{\mathbf{k}',\lambda_2,\ell'}\left(1 - n_{\mathbf{k}+\mathbf{q},\lambda_1,\ell}\right)\left(1 - n_{\mathbf{k}+\mathbf{q},\lambda_1,\ell}\right) \\ - \left(1 - n_{\mathbf{k},\lambda,\ell}\right)\left(1 - n_{\mathbf{k}',\ell'}\right) n_{\mathbf{k}+\mathbf{q},\lambda_1,\ell} n_{\mathbf{k}+\mathbf{q},\lambda_1,\ell}\Big], \end{aligned} \tag{G.7}$$

where $U^R_{12}(\omega, \mathbf{q})$ is the screened, retarded interaction which we have allowed to depend both on the transferred momentum as well as in the transferred energy. This will generally happen once we consider dynamical screening of the bare interaction, Eq. (G.2).

We are interested in the linear response of the system to the electric field applied in the active layer, $\mathbf{E}_2$. Therefore, we write the distribution functions as an equilibrium term, which is just given by the Fermi-Dirac distribution function $n^0_{\mathbf{k},\lambda,\ell} = f\left(\epsilon_{\mathbf{k},\lambda,\ell}\right)$, plus a correction term as

$$n_{\mathbf{k},\lambda,\ell} = n^0_{\mathbf{k},\lambda,\ell} + n^0_{\mathbf{k},\lambda,\ell}\left(1 - n^0_{\mathbf{k},\lambda,\ell}\right)\varphi_{\mathbf{k},\lambda,\ell}. \tag{G.8}$$

In terms of $\varphi_{\mathbf{k},\lambda,\ell}$, the impurity collision term, Eq. (G.6), can be written as

$$\begin{aligned} I_{\mathrm{imp}}\left[\varphi_\ell\right]_{\mathbf{k},\lambda} = -\frac{2\pi}{A\hbar}\sum_{\mathbf{k}'} n_{\mathrm{imp},\ell}\left|T^{(\ell),\lambda}_{\mathbf{k}',\mathbf{k}}\right|^2 \delta\left(\epsilon_{\mathbf{k},\lambda,\ell} - \epsilon_{\mathbf{k}',\lambda,\ell}\right) \times \\ \times n^0_{\mathbf{k},\lambda,\ell}\left(1 - n^0_{\mathbf{k},\lambda,\ell}\right)\left(\varphi_{\mathbf{k},\lambda,\ell} - \varphi_{\mathbf{k}',\lambda,\ell}\right), \end{aligned} \tag{G.9}$$

where we used the fact that $n^0_{\mathbf{k},\lambda,\ell}\left(1 - n^0_{\mathbf{k},\lambda,\ell}\right) = n^0_{\mathbf{k}',\lambda,\ell}\left(1 - n^0_{\mathbf{k}',\lambda,\ell}\right)$ for $\epsilon_{\mathbf{k},\lambda,\ell} = \epsilon_{\mathbf{k}',\lambda,\ell}$. Expanding Eq. (G.7) to lowest order in $\varphi_{\mathbf{k},\lambda,\ell}$, we obtain the linearised interlayer interaction collision integral

$$\begin{aligned} I_{\mathrm{inter}}\left[\varphi_\ell, \varphi_{\ell'}\right]_{\mathbf{k},\lambda} = -\frac{2\pi}{A^2\hbar}\sum_{\substack{\mathbf{k}',\mathbf{q} \\ \lambda_1,\lambda_2,\lambda_3}} \left|U_{12}\left(\epsilon_{\mathbf{k}+\mathbf{q},\lambda_1,\ell} - \epsilon_{\mathbf{k},\lambda,\ell}, \mathbf{q}\right)\right|^2 \left|\rho^{\lambda_1,\lambda}_{\ell,\mathbf{k}+\mathbf{q},\mathbf{k}}\right|^2 \left|\rho^{\lambda_3,\lambda_2}_{\ell',\mathbf{k}'-\mathbf{q},\mathbf{k}'}\right|^2 \\ \times n^0_{\mathbf{k},\lambda,\ell}\left(1 - n^0_{\mathbf{k}+\mathbf{q},\lambda_1,\ell}\right) n^0_{\mathbf{k}',\lambda_2,\ell'}\left(1 - n^0_{\mathbf{k}'-\mathbf{q},\lambda_3,\ell'}\right) \\ \times \left[\varphi_{\mathbf{k},\lambda,\ell} + \varphi_{\mathbf{k}',\lambda_2,\ell'} - \varphi_{\mathbf{k}+\mathbf{q},\lambda_1,\ell} - \varphi_{\mathbf{k}'-\mathbf{q},\lambda_3,\ell'}\right] \\ \times \delta\left(\epsilon_{\mathbf{k}+\mathbf{q},\lambda_1,\ell} + \epsilon_{\mathbf{k}'-\mathbf{q},\lambda_3,\ell'} - \epsilon_{\mathbf{k},\lambda,\ell} - \epsilon_{\mathbf{k}',\lambda_2,\ell'}\right), \end{aligned} \tag{G.10}$$

where we used the fact that the equilibrium distribution functions satisfy the condition

$$\begin{aligned} n^0_{\mathbf{k},\lambda,\ell} n^0_{\mathbf{k}',\lambda_2,\ell'}\left(1 - n^0_{\mathbf{k}+\mathbf{q},\lambda_1,\ell}\right)\left(1 - n^0_{\mathbf{k}'-\mathbf{q},\lambda_3,\ell'}\right) = \\ = \left(1 - n^0_{\mathbf{k},\lambda,\ell}\right)\left(1 - n^0_{\mathbf{k}',\lambda_2,\ell'}\right) n^0_{\mathbf{k}+\mathbf{q},\lambda_1,\ell} n^0_{\mathbf{k}'-\mathbf{q},\lambda_3,\ell'}, \end{aligned} \tag{G.11}$$

for $\epsilon_{\mathbf{k}+\mathbf{q},\lambda_1,\ell} + \epsilon_{\mathbf{k}'-\mathbf{q},\lambda_3,\ell'} = \epsilon_{\mathbf{k},\lambda,\ell} + \epsilon_{\mathbf{k}',\lambda_2,\ell'}$. Therefore, the linearised coupled Boltzmann equations are given by

$$e_1 \mathbf{E}_1 \cdot \mathbf{v}_{\mathbf{k},\lambda,1} \frac{\partial n^0_{\mathbf{k},\lambda,1}}{\partial \epsilon_{\mathbf{k},\lambda,1}} = I_{\mathrm{imp}}\left[\varphi_1\right]_{\mathbf{k},\lambda} + I_{\mathrm{inter}}\left[\varphi_1, \varphi_2\right]_{\mathbf{k},\lambda}, \tag{G.12}$$

$$e_2 \mathbf{E}_2 \cdot \mathbf{v}_{\mathbf{k},\lambda,2} \frac{\partial n^0_{\mathbf{k},\lambda,2}}{\partial \epsilon_{\mathbf{k},\lambda,2}} = I_{\mathrm{imp}}\left[\varphi_2\right]_{\mathbf{k},\lambda} + I_{\mathrm{inter}}\left[\varphi_2, \varphi_1\right]_{\mathbf{k},\lambda}, \tag{G.13}$$

We are interest in the case where layer 2 is the active layer and layer 1 is the passive layer and want to study the linear response to the electric field applied in the active layer, $\mathbf{E}_2$, while not allowing the flow of current in the passive layer, $\mathbf{J}_1 = \mathbf{0}$. Therefore, and to lowest order in the interlayer interaction, we neglect the interlayer interaction collision term, $I_{\text{inter}}\left[\varphi_2, \varphi_1\right]_{\mathbf{k},\lambda}$, in Eq. (G.13) and set $\varphi_{\mathbf{k},\lambda,1} = 0$ in $I_{\text{inter}}\left[\varphi_1, \varphi_2\right]_{\mathbf{k},\lambda}$ of Eq. (G.12). Therefore, we obtain the simplified equations

$$e_1 \mathbf{E}_1 \cdot \mathbf{v}_{\mathbf{k},\lambda,1} \frac{\partial n^0_{\mathbf{k},\lambda,1}}{\partial \epsilon_{\mathbf{k},\lambda,1}} = I_{\text{imp}}\left[\varphi_1\right]_{\mathbf{k},\lambda} + I_{\text{inter}}\left[\varphi_1 = 0, \varphi_2\right]_{\mathbf{k},\lambda}, \tag{G.14}$$

$$e_2 \mathbf{E}_2 \cdot \mathbf{v}_{\mathbf{k},\lambda,2} \frac{\partial n^0_{\mathbf{k},\lambda,2}}{\partial \epsilon_{\mathbf{k},\lambda,2}} = I_{\text{imp}}\left[\varphi_2\right]_{\mathbf{k},\lambda}. \tag{G.15}$$

Now the strategy to follow is clear. First, we solve Eq. (G.15) to obtain $\varphi_{\mathbf{k},\lambda,2}$ as a function of $\mathbf{E}_2$. Then, we plug in the obtained result in Eq. (G.14) and solve it for $\varphi_{\mathbf{k},\lambda,1}$. Having obtained $\varphi_{\mathbf{k},\lambda,1}$, we can compute the current in layer 1.

Notice that by treating the impurity collision term $I_{\text{imp}}\left[\right]_{\mathbf{k},\lambda}$ as a linear operator the solution of Eq. (G.14) can be formally expressed as

$$\varphi_{\mathbf{k},\lambda,2} = I^{-1}_{\text{imp}} \left[e_2 \mathbf{E}_2 \cdot \mathbf{v}_{\mathbf{k},\lambda,2} \frac{\partial n^0_{\mathbf{k},\lambda,2}}{\partial \epsilon_{\mathbf{k},\lambda,2}} \right]_{\mathbf{k},\lambda}. \tag{G.16}$$

More explicitly, noticing that

$$\frac{\partial n^0_{\mathbf{k},\lambda,2}}{\partial \epsilon_{\mathbf{k},\lambda,2}} = -\frac{n^0_{\mathbf{k},\lambda,2}\left(1 - n^0_{\mathbf{k},\lambda,2}\right)}{k_B T}, \tag{G.17}$$

Eq. (G.14) can be written as

$$\frac{e_2}{k_B T} \mathbf{E}_2 \cdot \mathbf{v}_{\mathbf{k},\lambda,2} = \frac{2\pi}{\hbar A} \sum_{\mathbf{k}'} n_{\text{imp},\ell} \left| T^{(2),\lambda}_{\mathbf{k}',\mathbf{k}} \right|^2 \delta\left(\epsilon^{(\ell)}_{\mathbf{k},\lambda} - \epsilon^{(\ell)}_{\mathbf{k}',\lambda}\right) \left(\varphi_{\mathbf{k},\lambda,2} - \varphi_{\mathbf{k}',\lambda,2}\right). \tag{G.18}$$

Making the ansatz

$$\varphi_{\mathbf{k},\lambda,2} = \frac{e_2}{k_B T} \tau^{\text{tr}}_{\mathbf{k},\lambda,2} \mathbf{v}_{\mathbf{k},\lambda,2} \cdot \mathbf{E}_2, \tag{G.19}$$

and assuming isotropy, we obtain that the transport time, $\tau^{\text{tr}}_{\mathbf{k},\lambda,2}$, is given by

$$\frac{1}{\tau^{\text{tr}}_{\mathbf{k},\lambda,2}} = \frac{2\pi}{\hbar A} \sum_{\mathbf{k}'} n_{\text{imp},\ell} \left| T^{(2),\lambda}_{\mathbf{k}',\mathbf{k}} \right|^2 \left(1 - \cos\theta_{\mathbf{k},\mathbf{k}'}\right) \delta\left(\epsilon^{(\ell)}_{\mathbf{k},\lambda} - \epsilon^{(\ell)}_{\mathbf{k}',\lambda}\right). \tag{G.20}$$

Notice that the transport time, differs from the scattering time by the $\left(1 - \cos\theta_{\mathbf{k},\mathbf{k}'}\right)$ factor.

Using the result from Eq. (G.19) in Eq. (G.14), we can write the interlayer collision term as

$$\begin{aligned} I_{\text{inter}}\left[\varphi_1 = 0, \varphi_2\right]_{\mathbf{k},\lambda} = -\frac{2\pi}{A^2\hbar} \sum_{\substack{\mathbf{k}',\mathbf{q} \\ \lambda_1,\lambda_2,\lambda_3}} & \left|U_{12}\left(\epsilon_{\mathbf{k}+\mathbf{q},\lambda_1,1} - \epsilon_{\mathbf{k},\lambda,1}, \mathbf{q}\right)\right|^2 \left|\rho^{\lambda_1,\lambda}_{1,\mathbf{k}+\mathbf{q},\mathbf{k}}\right|^2 \left|\rho^{\lambda_3,\lambda_2}_{2,\mathbf{k}'-\mathbf{q},\mathbf{k}'}\right|^2 \\ & \times n^0_{\mathbf{k},\lambda,1}\left(1 - n^0_{\mathbf{k}+\mathbf{q},\lambda_1,1}\right) n^0_{\mathbf{k}',\lambda_2,2}\left(1 - n^0_{\mathbf{k}'-\mathbf{q},\lambda_3,2}\right) \\ & \times \delta\left(\epsilon_{\mathbf{k}+\mathbf{q},\lambda_1,1} + \epsilon_{\mathbf{k}'-\mathbf{q},\lambda_3,2} - \epsilon_{\mathbf{k},\lambda,1} - \epsilon_{\mathbf{k}',\lambda_2,2}\right) \\ & \times \frac{e_2}{k_B T}\left[\tau^{\text{tr}}_{\mathbf{k}',\lambda_2,2}\mathbf{v}_{\mathbf{k}',\lambda_2,2} - \tau^{\text{tr}}_{\mathbf{k}'-\mathbf{q},\lambda_3,2}\mathbf{v}_{\mathbf{k}'-\mathbf{q},\lambda_3,2}\right] \cdot \mathbf{E}_2. \end{aligned} \tag{G.21}$$

Using the identity

$$f(\epsilon_1)\left(1-f(\epsilon_2)\right)=\left(f(\epsilon_2)-f(\epsilon_1)\right)b\left(\epsilon_1-\epsilon_2\right) \tag{G.22}$$

and writing

$$\begin{aligned}\delta\left(\epsilon_{\mathbf{k}+\mathbf{q},\lambda_1,1}+\epsilon_{\mathbf{k}'-\mathbf{q},\lambda_3,2}-\epsilon_{\mathbf{k},\lambda,1}-\epsilon_{\mathbf{k}',\lambda_2,2}\right)&=\\ =\int d\omega\delta\left(\epsilon_{\mathbf{k}+\mathbf{q},\lambda_1,1}-\epsilon_{\mathbf{k},\lambda,1}-\omega\right)\delta\left(\epsilon_{\mathbf{k}',\lambda_2,2}-\epsilon_{\mathbf{k}'-\mathbf{q},\lambda_3,2}-\omega\right),&\end{aligned} \tag{G.23}$$

we can rewrite Eq. (G.21) as

$$\begin{aligned}I_{\text{inter}}\left[\varphi_1=0,\varphi_2\right]_{\mathbf{k},\lambda}=-\frac{e_2}{k_BT}\frac{2\pi}{V^2\hbar}\sum_{\substack{\mathbf{k}',\mathbf{q}\\ \lambda_1,\lambda_2,\lambda_3}}\int d\omega\left|U_{12}\left(\omega,\mathbf{q}\right)\right|^2&\\ \times\left|\rho^{\lambda_1,\lambda}_{1,\mathbf{k}+\mathbf{q},\mathbf{k}}\right|^2\delta\left(\epsilon_{\mathbf{k}+\mathbf{q},\lambda_1,1}-\epsilon_{\mathbf{k},\lambda,1}-\omega\right)\left(f(\epsilon_{\mathbf{k}+\mathbf{q},\lambda_1,1})-f(\epsilon_{\mathbf{k},\lambda,1})\right)b\left(\omega\right)&\\ \times\left|\rho^{\lambda_3,\lambda_2}_{2,\mathbf{k}'-\mathbf{q},\mathbf{k}'}\right|^2\delta\left(\epsilon_{\mathbf{k}',\lambda_2,2}-\epsilon_{\mathbf{k}'-\mathbf{q},\lambda_3,2}-\omega\right)\left(f(\epsilon_{\mathbf{k}'-\mathbf{q},\lambda_3,2})-f(\epsilon_{\mathbf{k}',\lambda_2,2})\right)b\left(-\omega\right)&\\ \times\left[\tau^{\text{tr}}_{\mathbf{k}',\lambda_2,2}\mathbf{v}_{\mathbf{k}',\lambda_2,2}-\tau^{\text{tr}}_{\mathbf{k}'-\mathbf{q},\lambda_3,2}\mathbf{v}_{\mathbf{k}'-\mathbf{q},\lambda_3,2}\right]\cdot\mathbf{E}_2.&\end{aligned} \tag{G.24}$$

Now, we notice that from Eq. (G.14), the solution to $\varphi_{\mathbf{k},\lambda,1}$ can be formally expressed as

$$\varphi_{\mathbf{k},\lambda,1}=I^{-1}_{\text{imp}}\left[e_1\mathbf{E}_1\cdot\mathbf{v}_{\mathbf{k},\lambda,1}\frac{\partial n^0_{\mathbf{k},\lambda,1}}{\partial\epsilon_{\mathbf{k},\lambda,1}}-I_{\text{inter}}\left[\varphi_1=0,\varphi_2\right]_{\mathbf{k},\lambda}\right], \tag{G.25}$$

which leads to

$$\varphi_{\mathbf{k},\lambda,1}=-\frac{\tau^{\text{tr}}_{\mathbf{k},\lambda,1}}{n^0_{\mathbf{k},\lambda,\ell}\left(1-n^0_{\mathbf{k},\lambda,\ell}\right)}\left(e_1\mathbf{E}_1\cdot\mathbf{v}_{\mathbf{k},\lambda,1}\frac{\partial n^0_{\mathbf{k},\lambda,1}}{\partial\epsilon_{\mathbf{k},\lambda,1}}-I_{\text{inter}}\left[\varphi_1=0,\varphi_2\right]_{\mathbf{k},\lambda}\right). \tag{G.26}$$

The current in layer 1 can be written as

$$\begin{aligned}\mathbf{J}_1&=\frac{e_1}{A}\sum_{\mathbf{k},\lambda}\mathbf{v}_{\mathbf{k},\lambda,1}n_{\mathbf{k},\lambda,1}\\ &=\frac{e_1}{A}\sum_{\mathbf{k},\lambda}\mathbf{v}_{\mathbf{k},\lambda,1}n^0_{\mathbf{k},\lambda,\ell}\left(1-n^0_{\mathbf{k},\lambda,\ell}\right)\varphi_{\mathbf{k},\lambda,\ell}.\end{aligned} \tag{G.27}$$

Inserting Eq. (G.26) into Eq. (G.27), we can write the current $\mathbf{J}_1$ as

$$\begin{aligned}\mathbf{J}_1=\frac{e_1^2}{A}\sum_{\mathbf{k},\lambda}\left(-\frac{\partial f(\epsilon_{\mathbf{k},\lambda,1})}{\partial\epsilon_{\mathbf{k},\lambda,1}}\right)\tau^{\text{tr}}_{\mathbf{k},\lambda,1}\mathbf{v}_{\mathbf{k},\lambda,1}\left(\mathbf{v}_{\mathbf{k},\lambda,1}\cdot\mathbf{E}_1\right)&\\ +\frac{e_1}{A}\sum_{\mathbf{k},\lambda}\mathbf{v}_{\mathbf{k},\lambda,1}\tau^{\text{tr}}_{\mathbf{k},\lambda,1}I_{\text{inter}}\left[\varphi_1=0,\varphi_2\right]_{\mathbf{k},\lambda}.&\end{aligned} \tag{G.28}$$

If we now use Eq. (G.24) to express $I_{\text{inter}}\left[\varphi_1=0,\varphi_2\right]_{\mathbf{k},\lambda}$, the second term of the previous equation can be written as

$$\begin{aligned}\frac{e_1}{V}\sum_{\mathbf{k},\lambda}\mathbf{v}_{\mathbf{k},\lambda,1}\tau^{\text{tr}}_{\mathbf{k},\lambda,1}I_{\text{inter}}\left[\varphi_1=0,\varphi_2\right]_{\mathbf{k},\lambda}=&\\ =-\frac{e_1e_2}{2\pi k_BT}\frac{1}{\hbar}\frac{1}{A}\sum_{\mathbf{q}}\int d\omega b\left(\omega\right)b\left(-\omega\right)\left|U_{12}\left(\omega,\mathbf{q}\right)\right|^2\tilde{\mathbf{\Delta}}^i_1(\omega,\mathbf{q})\left(\mathbf{\Delta}_2(\omega,\mathbf{q})\cdot\mathbf{E}_2\right),&\end{aligned} \tag{G.29}$$

where we have introduced the quantities

$$\tilde{\boldsymbol{\Delta}}_1(\omega,\mathbf{q}) = \frac{2\pi}{A}\sum_{\mathbf{k},\lambda,\lambda'}\left|\rho^{\lambda',\lambda}_{1,\mathbf{k}+\mathbf{q},\mathbf{k}}\right|^2 \mathbf{v}_{\mathbf{k},\lambda,1}\tau^{\mathrm{tr}}_{\mathbf{k},\lambda,1}\left(f(\epsilon_{\mathbf{k}+\mathbf{q},\lambda',1}) - f(\epsilon_{\mathbf{k},\lambda,1})\right)\times$$
$$\times\,\delta\left(\epsilon_{\mathbf{k}+\mathbf{q},\lambda',1} - \epsilon_{\mathbf{k},\lambda,1} - \omega\right), \tag{G.30}$$

$$\boldsymbol{\Delta}_2(\omega,\mathbf{q}) = \frac{2\pi}{A}\sum_{\mathbf{k},\lambda,\lambda'}\left|\rho^{\lambda',\lambda}_{2,\mathbf{k}-\mathbf{q},\mathbf{k}}\right|^2 \left[\tau^{\mathrm{tr}}_{\mathbf{k},\lambda,2}\mathbf{v}_{\mathbf{k},\lambda,2} - \tau^{\mathrm{tr}}_{\mathbf{k}-\mathbf{q},\lambda',2}\mathbf{v}_{\mathbf{k}-\mathbf{q},\lambda',2}\right]\left(f(\epsilon_{\mathbf{k}-\mathbf{q},\lambda',2}) - f(\epsilon_{\mathbf{k},\lambda,2})\right)\times$$
$$\times\,\delta\left(\epsilon_{\mathbf{k},\lambda,2} - \epsilon_{\mathbf{k}-\mathbf{q},\lambda',2} - \omega\right). \tag{G.31}$$

Comparing Eqs. (G.28) and (G.29) with the linear response relation

$$\mathbf{J}_1 = \boldsymbol{\sigma}_{11}\cdot\mathbf{E}_1 + \boldsymbol{\sigma}_{12}\cdot\mathbf{E}_2, \tag{G.32}$$

we identify the first term of Eq. (G.28) as the usual intralayer conductivity given by

$$\sigma^{ij}_{11} = \frac{e_1^2}{A}\sum_{\mathbf{k},\lambda}\left(-\frac{\partial f(\epsilon_{\mathbf{k},\lambda,1})}{\partial\epsilon_{\mathbf{k},\lambda,1}}\right)\tau^{\mathrm{tr}}_{\mathbf{k},\lambda,1}v^i_{\mathbf{k},\lambda,1}v^j_{\mathbf{k},\lambda,1}, \tag{G.33}$$

and the second term as the transconductivity given by

$$\sigma^{ij}_{12} = -\frac{e_1e_2}{k_BT}\frac{2\pi}{\hbar}\frac{1}{A}\sum_{\mathbf{q}}\int d\omega b(\omega)\,b(-\omega)\left|U_{12}(\omega,\mathbf{q})\right|^2\tilde{\Delta}^i_1(\omega,\mathbf{q})\Delta^j_2(\omega,\mathbf{q}). \tag{G.34}$$

No we make some further manipulations. First, we notice that by replacing $\mathbf{k}\to-\mathbf{k}$, Eq. (G.31) can be written as

$$\boldsymbol{\Delta}_2(\omega,\mathbf{q}) = \frac{2\pi}{A}\sum_{\mathbf{k},\lambda,\lambda'}\left|\rho^{\lambda',\lambda}_{2,\mathbf{k}+\mathbf{q},\mathbf{k}}\right|^2\left[\tau^{\mathrm{tr}}_{\mathbf{k}+\mathbf{q},\lambda',2}\mathbf{v}_{\mathbf{k}+\mathbf{q},\lambda',2} - \tau^{\mathrm{tr}}_{\mathbf{k},\lambda,2}\mathbf{v}_{\mathbf{k},\lambda,2}\right]\times$$
$$\times\left(f(\epsilon_{\mathbf{k}+\mathbf{q},\lambda',2}) - f(\epsilon_{\mathbf{k},\lambda,2})\right)\delta\left(\omega+\epsilon_{\mathbf{k}+\mathbf{q},\lambda',2} - \epsilon_{\mathbf{k},\lambda,2}\right). \tag{G.35}$$

Next we notice that $\boldsymbol{\Delta}_2(-\omega,\mathbf{q}) = -\boldsymbol{\Delta}_2(\omega,\mathbf{q})$, which can be seen by replacing $\omega\to-\omega$ and then making a shift in the integration variable $\mathbf{k}\to-\mathbf{k}-\mathbf{q}$ and noticing that $\epsilon_{-\mathbf{k},\lambda,2} = \epsilon_{\mathbf{k},\lambda,2}$, $\tau^{\mathrm{tr}}_{-\mathbf{k},\lambda,2} = \tau^{\mathrm{tr}}_{\mathbf{k},\lambda,2}$ and $\mathbf{v}_{-\mathbf{k},\lambda,2} = -\mathbf{v}_{\mathbf{k},\lambda,2}$. Since the quantities $b(\omega)\,b(-\omega)$ and $|U_{12}(\omega,\mathbf{q})|^2$ are even functions of ω, only the even part of the quantity $\tilde{\Delta}^i_1(\omega,\mathbf{q})$ will contribute to the transconductivity. Therefore we can replace

$$\tilde{\Delta}^i_1(\omega,\mathbf{q}) \to \frac{\tilde{\Delta}^i_1(\omega,\mathbf{q}) - \tilde{\Delta}^i_1(-\omega,\mathbf{q})}{2} =$$
$$= \frac{2\pi}{2A}\sum_{\mathbf{k},\lambda,\lambda'}\left|\rho^{\lambda',\lambda}_{1,-\mathbf{k},-\mathbf{k}-q}\right|^2\left(\mathbf{v}_{\mathbf{k}+q,\lambda,1}\tau^{\mathrm{tr}}_{\mathbf{k}+q,\lambda,1} - \mathbf{v}_{\mathbf{k},\lambda,1}\tau^{\mathrm{tr}}_{\mathbf{k},\lambda,1}\right)\times$$
$$\times\left(f(\epsilon_{\mathbf{k}+q,\lambda,1}) - f(\epsilon_{+\mathbf{k},\lambda',1})\right)\delta\left(\omega+\epsilon_{\mathbf{k}+q,\lambda,1} - \epsilon_{\mathbf{k},\lambda',1}\right). \tag{G.36}$$

Therefore, we obtain the final Boltzmann result for the transconductivity

$$\sigma^{ij}_{12} = -\frac{e^2}{4\pi\hbar k_BT}\frac{1}{A}\sum_{\mathbf{q}}\int d\omega b(\omega)\,b(-\omega)\left|U_{12}(\omega,\mathbf{q})\right|^2\Delta^i_1(\omega,\mathbf{q})\Delta^j_2(\omega,\mathbf{q}), \tag{G.37}$$

with the functions $\boldsymbol{\Delta}_\ell(\omega,\mathbf{q})$ defined as

$$\boldsymbol{\Delta}_\ell(\omega,\mathbf{q}) = \frac{2\pi}{A}\sum_{\mathbf{k},\lambda,\lambda'}\left|\rho^{\lambda',\lambda}_{\ell,\mathbf{k}+\mathbf{q},\mathbf{k}}\right|^2\left(\tau^{\mathrm{tr}}_{\mathbf{k}+\mathbf{q},\lambda',\ell}\mathbf{v}_{\mathbf{k}+\mathbf{q},\lambda',\ell} - \tau^{\mathrm{tr}}_{\mathbf{k},\lambda,\ell}\mathbf{v}_{\mathbf{k},\lambda,\ell}\right)\times$$
$$\times\left(f(\epsilon_{\mathbf{k}+\mathbf{q},\lambda',\ell}) - f(\epsilon_{\mathbf{k},\lambda,\ell})\right)\delta\left(\omega+\epsilon_{\mathbf{k}+\mathbf{q},\lambda',\ell} - \epsilon_{\mathbf{k},\lambda,\ell}\right). \tag{G.38}$$

We conclude, by noticing that $\mathbf{\Delta}_\ell(\omega, \mathbf{q})$ corresponds to the Boltzmann limit of the non-linear susceptibility of layer ℓ, which gives the second order current response to an applied potential [161, 162].

H

INTRODUCTION TO THE NON-EQUILIBRIUM GREEN'S FUNCTION FORMALISM

The non-equilibirum Green's function (NEGF) formalism is an extremely powerful framework for the study of systems driven out of equilibrium, while taking into account both coherence and interaction effects. Although this formalism is not a recent development in theoretical physics, having been well established by Kadanoff & Baym [254] and by Keldysh [255], and with several good books having been published in recent years [56, 57, 256, 257], the NEGF formalism is still not part of the standard toolbox of most condensed matter theorists. As such, this appendix provides a brief introduction to the formalism. The NEGF formalism is extensively employed in Chapter 6.

H.1 THE SCHWINGER-KELDYSH AND KADANOFF-BAYM CONTOURS

Suppose we wish to compute the expectation value of an operator, O, for a system that is governed by a time dependent Hamiltonian,

$$H(t) = H_0 + H_{\text{int}} + V(t), \tag{H.1}$$

where H_0 is an easy free Hamiltonian, H_{int} describes the interactions and $V(t)$ is a time-dependent perturbation, which is assumed to the zero for $t < t_0$. In the Heisenberg picture, the expectation value of the operator O for times $t > t_0$ is given by

$$\langle O \rangle (t) = \text{Tr}\left(\rho(t_0)\hat{O}(t)\right), \tag{H.2}$$

where $\rho(t_0)$ is the density matrix, describing the state of the system at the initial time t_0, and $\hat{O}(t)$ is the operator in the Heisenberg picture, which evolves as

$$\hat{O}(t) = U^\dagger(t, t_0)\hat{O}(t_0)U(t, t_0), \tag{H.3}$$

where $\hat{O}(t_0)$ is the operator at $t = t_0$ (where all representations coincide) and $U(t, t')$ is the evolution operator, which obeys the Schrödinger equation

$$\frac{\partial}{\partial t}U(t, t') = -iH(t)U(t, t'), \tag{H.4}$$

$$\frac{\partial}{\partial t'}U(t, t') = iU(t, t')H(t'), \tag{H.5}$$

with the initial condition $U(t, t) = \text{Id}$. We introduce the S-matrix

$$S(t, t') = e^{iH_0(t-t_0)}U(t, t')e^{-iH_0(t'-t_0)}, \tag{H.6}$$

which obeys the Schrödinger equation

$$\frac{\partial}{\partial t}S(t, t') = -iW(t)S(t, t'), \tag{H.7}$$

$$\frac{\partial}{\partial t'}S(t, t') = iS(t, t')W(t'), \tag{H.8}$$

with

$$W(t) = e^{iH_0(t-t_0)}\left(H_{\rm int} + V(t)\right)e^{-iH_0(t-t_0)}, \tag{H.9}$$

and the initial condition $S(t,t) = 1$. The Schrödinger equation together with the initial condition, allow to formally write $S(t,t')$ as a time-ordered or anti-time-ordered exponential

$$S(t,t') = \begin{cases} T_t \exp\left(-i\int_{t'}^{t} dt'' W(t'')\right), & t > t' \\ \bar{T}_t \exp\left(-i\int_{t}^{t'} dt'' W(t'')\right), & t < t' \end{cases}. \tag{H.10}$$

The expectation value of the operator, Eq. (H.2), can then be written as

$$\langle O\rangle(t) = {\rm Tr}\left(\rho(t_0)S^\dagger(t,t_0)O(t)S(t,t_0)\right), \tag{H.11}$$

where we have introduced the operator in the interaction picture, which evolves with the free Hamiltonian, H_0, as

$$O(t) = e^{iH_0(t-t_0)}O(t_0)e^{-iH_0(t-t_0)}. \tag{H.12}$$

We now focus in the case when the initial state at $t = t_0$ is a thermal equilibrium state,

$$\rho(t_0) = \frac{e^{-\beta(H_0+H_{\rm int})}}{{\rm Tr}\left\{e^{-\beta(H_0+H_{\rm int})}\right\}}. \tag{H.13}$$

Since at t_0 we have $V(t_0) = 0$, we can write

$$\begin{aligned} e^{-\beta(H_0+H_{\rm int})} &= U\left(t_0 - i\beta, t_0\right) \\ &= e^{-\beta H_0}S(t_0 - i\beta, t_0), \end{aligned} \tag{H.14}$$

and the expectation value of O at t can be written as

$$\begin{aligned} \langle O\rangle(t) &= \frac{{\rm Tr}\left(e^{-\beta H_0}S(t_0-i\beta,t_0)S^\dagger(t,t_0)O(t)S(t,t_0)\right)}{{\rm Tr}\left(e^{-\beta H_0}\mathcal{S}(t_0-i\beta,t_0)\right)} \\ &= \frac{\langle S(t_0-i\beta,t_0)S(t_0,t)O(t)S(t,t_0)\rangle_0}{\langle S(t_0-i\beta,t_0)\rangle_0}, \end{aligned} \tag{H.15}$$

where $\langle....\rangle_0 = {\rm Tr}\left(e^{-\beta H_0}....\right)/{\rm Tr}\left(e^{-\beta H_0}\right)$ is the average with respect to bare theory. Notice the ordering of the operators in Eq. (H.15) from right to left: in $S(t,t_0)$ the operators appear time-ordered from t_0 to t, then we have an insertion of the operator $O(t)$, followed by $S(t_0,t)$ where the operators are anti-time-ordered from t to t_0 and, finally, $S(t_0 - i\beta, t_0)$ introduces operators ordered along the imaginary line from t_0 to $t_0 - i\beta$. Introducing the Kadanoff-Baym [254] or Konstantinov-Perel'[258] contour as, see Fig. H.1,

$$C^* = [t_0, +\infty[\,\cup\,]+\infty, t_0] \cup [t_0, t_0 - i\beta], \tag{H.16}$$

then Eq. (H.15) can be written as

$$\langle O\rangle(t) = \frac{\langle S_{C^*}(t_0-i\beta,t_0)O(t)\rangle_0}{\langle S_{C^*}(t_0-i\beta,t_0)\rangle_0}, \tag{H.17}$$

where

$$S_{C^*}(t_0-i\beta,t_0) = T_{C^*}\exp\left(-i\int_{C^*} ds W(s)\right), \tag{H.18}$$

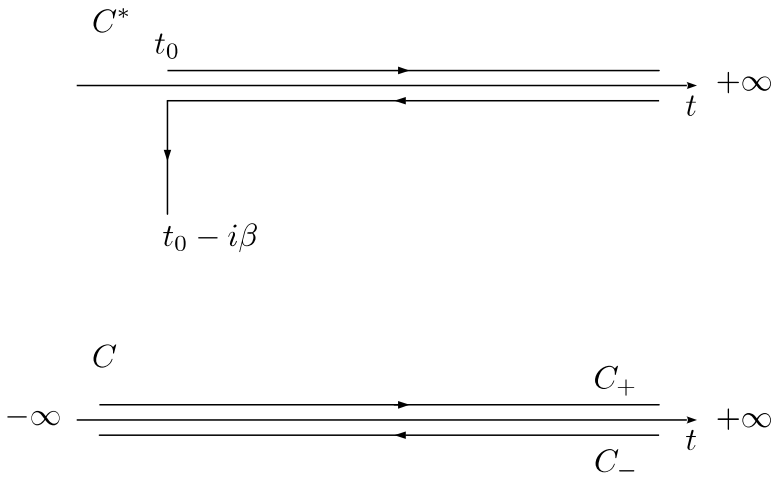

Figure H.1: The Kadanoff-Baym or Konstantinov-Perel', C^*, and the Schwinger-Keldysh, C, time contours.

with T_{C^*} is the contour-ordering operator along C^* contour, which is defined as

$$T_{C^*}\left(A(s)B(s')\right) = \begin{cases} A(s)B(s') & , \text{ if } s > s' \text{ along } C^* \\ \pm B(s')A(s) & , \text{ if } s < s' \text{ along } C^* \end{cases}, \tag{H.19}$$

where s, s' are defined along C^* and the order$\gtrless$ is defined with respect to which quantity appears later/earlier along the ordered contour C^*.

If one is not interested in the transient behaviour due to the turning on of the time dependent perturbation $V(t)$ and the system loses memory of the initial time (as it is true in general due to interactions or due to coupling to external reservoirs), then it is possible to neglect the contribution from the imaginary contour and take the limit $t_0 \to \infty$, working instead in the Schwinger-Keldysh contour, see Fig. H.1,

$$C =]-\infty, +\infty[\cup]+\infty, -\infty[. \tag{H.20}$$

In the Schwinger-Keldysh limit, Eq. (H.17) becomes

$$\langle O \rangle (t) = \frac{\langle S_C(-\infty,-\infty)O(t)\rangle_0}{\langle S_C(-\infty,-\infty)\rangle_0}, \tag{H.21}$$

with

$$S_C(-\infty,-\infty) = T_C \exp\left(-i\int_C dsW(s)\right), \tag{H.22}$$

with T_C the contour-ordering operator along C, which is defined in the same way as Eq. (H.19).

H.2 CONTOUR-ORDERED GREEN'S FUNCTIONS AND DYSON EQUATION

Equations (H.17) and (H.21) suggest introducing contour-ordered Green's function along the C^* or C contours. We will now work on the Schwinger-Keldysh limit and introduce the C-ordered Green's function as

$$G^C_{ab}(s,s') = -\frac{i}{\hbar}\left\langle T_C \hat{\varphi}_a(s)\hat{\varphi}^\dagger_b(s')\right\rangle = -\frac{i}{\hbar}\frac{\left\langle T_C S_C(-\infty,-\infty)\varphi_a(s)\varphi^\dagger_b(s')\right\rangle_0}{\langle T_C \mathcal{S}_C(-\infty,-\infty)\rangle_0}, \tag{H.23}$$

where $\varphi_a^\dagger$ is a one particle bosonic/fermionic creation operator in a one-particle state a . Notice that the contour ordering operator T_C reduces to the time-ordering operator, if both time arguments s and s' belong to the $C_+ =]-\infty, +\infty[$ branch of the C contour, and reduces to the anti-time-ordering operator if both time arguments belong to $C_- =]+\infty, -\infty[$. Therefore, depending on the position of the time arguments in the C contour, the contour ordered Green's function, $G_{ab}^C(s,s')$, reduces to the usual real time Green's functions defined by Eqs. (A.4)-(A.7):

$$G_{ab}^C(t_+,t'_+) = -\frac{i}{\hbar}\left\langle T_t\hat{\varphi}_a(t_+)\hat{\varphi}_b^\dagger(t'_+)\right\rangle = G_{ab}^T\left(t,t'\right),\ t_+,t'_+ \in C_+, \tag{H.24}$$

$$G_{ab}^C(t_-,t'_-) = -\frac{i}{\hbar}\left\langle \bar{T}_t\hat{\varphi}_a(t_-)\hat{\varphi}_b^\dagger(t'_-)\right\rangle = G_{ab}^{\bar{T}}\left(t,t'\right),\ t_-,t'_- \in C_-, \tag{H.25}$$

$$G_{ab}^C(t_+,t'_-) = \mp\frac{i}{\hbar}\left\langle \hat{\varphi}_b^\dagger(t'_-)\hat{\varphi}_a(t_+)\right\rangle = G_{ab}^<\left(t,t'\right),\ t_+ \in C_+, t'_- \in C_-, \tag{H.26}$$

$$G_{ab}^C(t_-,t'_+) = -\frac{i}{\hbar}\left\langle \hat{\varphi}_a(t_-)\hat{\varphi}_b^\dagger(t'_+)\right\rangle = G_{ab}^>\left(t,t'\right),\ t_- \in C_-, t'_+ \in C_+, \tag{H.27}$$

where $t_\pm$ indicates if the time argument belongs to the $C_\pm$ branch of the C contour.

Just as in equilibrium theory, the appearance of $\langle T_C\mathcal{S}_C(-\infty,-\infty)\rangle_0$ in the denominator of Eq. (H.23) ensures that in a perturbative expansion of $G_{ab}^C(s,s')$ the linked cluster theorem is satisfied, that is, vacuum diagrams cancel in any calculation. This allows to write a Dyson equation for $G_{ab}^C(s,s')$

$$\begin{aligned} G_{ab}^C(s,s') = G_{ab}^{C,0}(s,s') &+ \int_C ds_1 G_{aa'}^{C,0}(s,s_1)V_{a'b'}(s_1)G_{b'b}(s_1,s') \\ &+ \int_C ds_1 \int_C ds_2 G_{aa'}^{C,0}(s,s_1)\Sigma_{a'b'}^C(s_1,s_2)G_{b'b}^C(s_2,s'), \end{aligned} \tag{H.28}$$

where $G_{ab}^{C,0}(s,s')$ is the free Green's function, $V_{a'b'}(s_1)$ is a (possibly time dependent) single-particle potential and $\Sigma_{a'b'}^C(s_1,s_2)$ is the self-energy. All time arguments are defined in the C contour and repeated indices are summed over. It is useful to distinguish the branch to which the variables s and s' belong as an additional index in the Green's function, writing the Green's function as a matrix in Keldysh space as [255]

$$\underline{G}_{ab}(t,t') = \begin{bmatrix} G_{ab}^T(t,t') & G_{ab}^<(t,t') \\ G_{ab}^>(t,t') & G_{ab}^{\bar{T}}(t,t') \end{bmatrix}. \tag{H.29}$$

With this notation and writing the integration along the C contour as $\int_C ds f(s) = \int_{-\infty}^{+\infty} dt\,(f(t_+) - f(t_-))$, it is possible to write the Dyson equation, Eq. (H.28), in matrix form as

$$\begin{aligned} \underline{G}_{ab}(t,t') = \underline{G}_{ab}^0(t,t') &+ \int_{-\infty}^{+\infty} dt_1 \underline{G}_{aa'}^0(t,t_1)\cdot\underline{V}_{a'b'}(t_1)\cdot\underline{G}_{b'b}(t_1,t') \\ &+ \int_{-\infty}^{+\infty} dt_1 \int_{-\infty}^{+\infty} dt_2 \underline{G}_{aa'}^0(t,t_1)\cdot\underline{\Sigma}_{a'b'}(t_1,t_2)\cdot\underline{G}_{b'b}(t_2,t'), \end{aligned} \tag{H.30}$$

where $\underline{V}_{ab}(t)$ the single-particle potential in Keldysh space has the matrix structure

$$\underline{V}_{ab}(t) = \underline{\sigma}_3 V_{ab}(t), \tag{H.31}$$

with $\underline{\sigma}_3$ the Pauli matrix in Keldysh space

$$\underline{\sigma}_3 = \begin{bmatrix} 1 & 0 \\ 0 & -1 \end{bmatrix}, \tag{H.32}$$

and the self-energy in Keldysh space is given by

$$\underline{\Sigma}_{ab}(t,t') = \underline{\sigma}_3 \cdot \begin{bmatrix} \Sigma^T_{ab}(t,t') & \Sigma^<_{ab}(t,t') \\ \Sigma^>_{ab}(t,t') & \Sigma^{\bar{T}}_{ab}(t,t') \end{bmatrix} \cdot \underline{\sigma}_3. \tag{H.33}$$

It is possible to write the Dyson equation in the C contour, Eq. (H.28), in a more compact form, by introducing a "covariant" notation, in which the Green's function, Eq. (H.29) is written as

$$G^a{}_b \equiv G^C_{ab}(t_{s_a}, t'_{s_b}), \tag{H.34}$$

where the indices s_a, $s_b = \pm$ in the right-hand side specifies if the time argument belongs to the C_+ or C_- branch, which (abusing notation) are encoded in the left-hand side into the single particle indices a and b, which also encode the time arguments. In this notation, an upper indices represents a particle that is annihilated (or out-going states) and a lower index represent a particle that is created (or incoming state). In this notation, the Dyson equation is written as

$$G^a{}_b = \left(G^0\right)^a{}_b + \left(G^0\right)^a{}_c V^c{}_d G^d{}_b + \left(G^0\right)^a{}_c \Sigma^c{}_d G^d{}_b, \tag{H.35}$$

with repeated indices being summed over.

H.3 PERTURBATION THEORY, LANGRETH RULES AND KELDYSH EQUATION

Notice that Eq. H.29 contains some redundancy, as the different Green's functions that appear in it are not independent of each other, being related by Eqs. (A.14)-(A.16). It is possible to get rid of some of this redundancy by performing a transformation of the form of

$$\tilde{\underline{G}}_{ab}(t,t') = \underline{M}^{-1} \cdot \underline{G}_{ab}(t,t') \cdot \underline{N}^{-1}. \tag{H.36}$$

where in general the matrices $\underline{M}$ and $\underline{N}$ are unrelated to each other and might not be hermitian. We will refer to a transformation of the form of Eq. (H.36) a "covariant" transformation. There is freedom in the choice of $\underline{M}$ and $\underline{N}$, and consequently, on the Green's functions which are used. In the "covariant" notation previously introduced, a transformation of the form of Eq. (H.36) is written as

$$\tilde{G}^a{}_b = \left(M^{-1}\right)^a{}_c G^c{}_d \left(N^{-1}\right)^d{}_b, \tag{H.37}$$

$$\left(\tilde{G}^0\right)^a{}_b = \left(M^{-1}\right)^a{}_c \left(\tilde{G}^0\right)^c{}_d \left(N^{-1}\right)^d{}_b. \tag{H.38}$$

After the "covariant" transformation, the Dyson equation, Eq. (H.35), becomes

$$\tilde{G}^a{}_b = \left(\tilde{G}^0\right)^a{}_b + \left(\tilde{G}^0\right)^a{}_c \tilde{V}^c{}_d \tilde{G}^d{}_b + \left(\tilde{G}^0\right)^a{}_c \tilde{\Sigma}^c{}_d \tilde{G}^d{}_b, \tag{H.39}$$

with the single-particle potential and self-energy transforming as

$$\tilde{V}^a{}_b = N^a{}_c V^c{}_d M^d{}_b, \tag{H.40}$$

$$\tilde{\Sigma}^a{}_b = N^a{}_c \Sigma^c{}_d M^d{}_b. \tag{H.41}$$

Notice that the Dyson equation is only useful provided we have some scheme to compute the self-energy. We will now focus on the case of fermions ($c^\dagger_a$, c_a) coupled linearly to a real bosonic field (ϕ_α)

$$H_{\text{int}} = \sum_{a,b,\alpha} \gamma_{\alpha ab} c^\dagger_a c_b \phi_\alpha, \tag{H.42}$$

where $\gamma_{\alpha ab}$ are coupling constants or bare interaction vertices. To lowest order in the fermion-boson interaction, the Fock contribution to the fermion self-energy, in the standard notation, reads

$$\Sigma_{ab}(t_{s_a}, t_{s_b}) = i\gamma_{\alpha ac}\,(\sigma_3)_{s_a,s_c}\,G_{cd}(t_{s_c}, t_{s_d})D_{\alpha\beta}(t_{s_c}, t_{s_d})\,(\sigma_3)_{s_d,s_b}\,\gamma_{\beta db}, \tag{H.43}$$

or in "covariant" notation

$$\Sigma^a{}_b = i\gamma_\alpha{}^a{}_c G^c{}_d D^\alpha{}_\beta \gamma^{\beta d}{}_b, \tag{H.44}$$

with the interaction vertices in "covariant" notation being related to the ones in the standard notation by

$$\gamma_\alpha{}^a{}_b \equiv \gamma_{\alpha ab}\,(\sigma_3)_{s_a,s_b}\,\delta_{s_b,s_\alpha} \text{ (no summation)}, \tag{H.45}$$

$$\gamma^{\alpha a}{}_b \equiv \delta_{s_\alpha,s_a}\,(\sigma_3)_{s_a,s_b}\,\gamma_{\alpha ab} \text{ (no summation)}. \tag{H.46}$$

Differently from the notation employed in the original work by Keldysh [255], the position of the indices matters in the "covariant" notation we are employing. Furthermore, we have made a distinction between the boson absorption vertex (with a lower boson index) and the boson emission vertex (with an upper boson index) [57]. In the representation where the Green's function is given by Eq. (H.29), the interaction vertices in the Keldysh indices are given by

$$\gamma_+{}^a{}_b = \gamma^{+a}{}_b = \begin{bmatrix} 1 & 0 \\ 0 & 0 \end{bmatrix}, \tag{H.47}$$

$$\gamma_-{}^a{}_b = \gamma^{-a}{}_b = \begin{bmatrix} 0 & 0 \\ 0 & -1 \end{bmatrix}, \tag{H.48}$$

with the absorption and emission vertices being equal. However, after a general "covariant" transformation, this is not the case. Under a "covariant" transformation, the self-energy Eq. (H.44) transforms as

$$\tilde{\Sigma}^a{}_b = i\tilde{\gamma}_\alpha{}^a{}_c \tilde{G}^c{}_d \tilde{D}^\alpha{}_\beta \tilde{\gamma}^{\beta d}{}_b, \tag{H.49}$$

with the interaction vertices transforming as

$$\tilde{\gamma}_\alpha{}^a{}_b = N^a{}_c \gamma_\beta{}^c{}_d M^\beta{}_\alpha M^d{}_b, \tag{H.50}$$

$$\tilde{\gamma}^{\alpha a}{}_b = N^a{}_c N^\alpha{}_\beta \gamma^{\beta c}{}_d M^d{}_b. \tag{H.51}$$

Therefore, we see that in a "covariant" transformation, while the Green's functions change with M^{-1} acting on the upper indices and N^{-1} acting in the lower indices (Eqs. (H.37) and (H.38)), the single-particle potentials, $\tilde{V}^a_b$, and interaction vertices, $\tilde{\gamma}_\alpha{}^a{}_b$ and $\tilde{\gamma}^{\alpha a}{}_b$, change with N acting in the upper indices and M acting in the lower indices.

There is a great freedom in the choice of $\underline{M}$ and $\underline{N}$ in Eq. (H.36). Some common choices are:

H.3.0.1 *RA < representation*

Choosing $\underline{M}$ and $\underline{N}$

$$\underline{M} = \begin{bmatrix} 1 & 0 \\ 1 & -1 \end{bmatrix}, \qquad \underline{N} = \begin{bmatrix} 1 & 0 \\ 1 & 1 \end{bmatrix}, \tag{H.52}$$

the Green's function becomes (omitting the single particle indices and focusing only on Keldysh indices)

$$\tilde{G}^{a}{}_{b}(t,t') = \begin{bmatrix} \tilde{G}^{R}{}_{R}(t,t') & \tilde{G}^{R}{}_{A}(t,t') \\ \tilde{G}^{A}{}_{R}(t,t') & \tilde{G}^{A}{}_{A}(t,t') \end{bmatrix} = \begin{bmatrix} G^{R}(t,t') & G^{<}(t,t') \\ 0 & G^{A}(t,t') \end{bmatrix}, \tag{H.53}$$

where it was used the fact that $\tilde{G}^{A}{}_{R}(t,t') = G^{T}(t,t') + G^{\bar{T}}(t,t') - G^{>}(t,t') - G^{<}(t,t') = 0$. In this represenation, one chooses to work with the retarded, advanced and lesser Green's functions. When applying this "covariant" transformation to the Dyson equation and interaction vertices one obtains a set of rules of how to obtain retarded, advanced and lesser functions: the Langreth rules. In this representation, the single-particle potential changes as

$$\tilde{V}^{a}{}_{b} = \begin{bmatrix} \tilde{V}^{A}{}_{A} & \tilde{V}^{A}{}_{R} \\ \tilde{V}^{R}{}_{A} & \tilde{V}^{R}{}_{R} \end{bmatrix} = \begin{bmatrix} 1 & \\ & 1 \end{bmatrix}, \tag{H.54}$$

and the interaction vertices change as

$$\tilde{\gamma}_{R}{}^{a}{}_{b} = \begin{bmatrix} \tilde{\gamma}_{R}{}^{R}{}_{R} & \tilde{\gamma}_{R}{}^{R}{}_{A} \\ \tilde{\gamma}_{R}{}^{A}{}_{R} & \tilde{\gamma}_{R}{}^{A}{}_{A} \end{bmatrix} = \begin{bmatrix} 1 & 0 \\ 0 & 1 \end{bmatrix}, \tag{H.55}$$

$$\tilde{\gamma}_{A}{}^{a}{}_{b} = \begin{bmatrix} \tilde{\gamma}_{A}{}^{R}{}_{R} & \tilde{\gamma}_{A}{}^{R}{}_{A} \\ \tilde{\gamma}_{A}{}^{A}{}_{R} & \tilde{\gamma}_{A}{}^{A}{}_{A} \end{bmatrix} = \begin{bmatrix} 0 & 0 \\ 1 & -1 \end{bmatrix}, \tag{H.56}$$

$$\tilde{\gamma}^{Ra}{}_{b} = \begin{bmatrix} \tilde{\gamma}^{RR}{}_{R} & \tilde{\gamma}^{RR}{}_{A} \\ \tilde{\gamma}^{RA}{}_{R} & \tilde{\gamma}^{RA}{}_{A} \end{bmatrix} = \begin{bmatrix} 1 & 0 \\ 1 & 0 \end{bmatrix}, \tag{H.57}$$

$$\tilde{\gamma}^{Aa}{}_{b} = \begin{bmatrix} \tilde{\gamma}^{AR}{}_{R} & \tilde{\gamma}^{AR}{}_{A} \\ \tilde{\gamma}^{AA}{}_{R} & \tilde{\gamma}^{AA}{}_{A} \end{bmatrix} = \begin{bmatrix} 1 & 0 \\ 0 & 1 \end{bmatrix}. \tag{H.58}$$

With these interaction vertices, the self-energy Eq. (H.49) is given by

$$\tilde{\Sigma}^{a}{}_{b}(t,t') = \begin{bmatrix} \tilde{\Sigma}^{R}{}_{R}(t,t') & \tilde{\Sigma}^{R}{}_{A}(t,t') \\ \tilde{\Sigma}^{A}{}_{R}(t,t') & \tilde{\Sigma}^{A}{}_{A}(t,t') \end{bmatrix} = \begin{bmatrix} \Sigma^{R}(t,t') & \Sigma^{<}(t,t') \\ 0 & \Sigma^{A}(t,t') \end{bmatrix}, \tag{H.59}$$

with

$$\begin{aligned} \Sigma^{R}(t,t') &= iG^{<}(t,t')D^{R}(t,t') + iG^{R}(t,t')D^{<}(t,t') \\ &\quad + iG^{R}(t,t')D^{R}(t,t'), \end{aligned} \tag{H.60}$$

$$\begin{aligned} \Sigma^{A}(t,t') &= iG^{<}(t,t')D^{A}(t,t') + iG^{A}(t,t')D^{<}(t,t') \\ &\quad - iG^{A}(t,t')D^{A}(t,t'), \end{aligned} \tag{H.61}$$

$$\Sigma^{<}(t,t') = iG^{<}(t,t')D^{<}(t,t'), \tag{H.62}$$

and $\tilde{\Sigma}^{A}{}_{R}(t,t') = G^{R}(t,t')D^{A}(t,t') + G^{A}(t,t')D^{R}(t,t') = 0$, since a retarded function is only non-zero for $t > t'$ and a advanced function is only non-zero for $t < t'$. More generically, the fact that$\tilde{\Sigma}^{A}{}_{R}(t,t')$ is zero, is inherited from the fact that $\tilde{G}^{A}{}_{R}(t,t')$ is also zero. Equations (H.60)-(H.62) are the Langreth rules for the product of two Green's functions.

In this representation, the Dyson equation, Eq. (H.35), becomes (omitting time arguments)

$$\begin{aligned}\begin{bmatrix} \boldsymbol{G}^R & \boldsymbol{G}^< \\ 0 & \boldsymbol{G}^A \end{bmatrix} = \begin{bmatrix} \boldsymbol{G}^{0,R} & \boldsymbol{G}^{0,<} \\ 0 & \boldsymbol{G}^{0,A} \end{bmatrix} + \\ + \begin{bmatrix} \boldsymbol{G}^{0,R} & \boldsymbol{G}^{0,<} \\ 0 & \boldsymbol{G}^{0,A} \end{bmatrix} \cdot \begin{bmatrix} \boldsymbol{V} & 0 \\ 0 & \boldsymbol{V} \end{bmatrix} \cdot \begin{bmatrix} \boldsymbol{G}^R & \boldsymbol{G}^< \\ 0 & \boldsymbol{G}^A \end{bmatrix} \\ + \begin{bmatrix} \boldsymbol{G}^{0,R} & \boldsymbol{G}^{0,<} \\ 0 & \boldsymbol{G}^{0,A} \end{bmatrix} \cdot \begin{bmatrix} \boldsymbol{\Sigma}^R & \boldsymbol{\Sigma}^< \\ 0 & \boldsymbol{\Sigma}^A \end{bmatrix} \cdot \begin{bmatrix} \boldsymbol{G}^R & \boldsymbol{G}^< \\ 0 & \boldsymbol{G}^A \end{bmatrix}. \end{aligned} \tag{H.63}$$

From this equation, we obtain the Dyson equation for the retarded and advanced Green's functions as

$$\boldsymbol{G}^R = \boldsymbol{G}^{0,R} + \boldsymbol{G}^{0,R} \cdot \boldsymbol{V} \cdot \boldsymbol{G}^R + \boldsymbol{G}^{0,R} \cdot \boldsymbol{\Sigma}^R \cdot \boldsymbol{G}^R, \tag{H.64}$$

$$\boldsymbol{G}^A = \boldsymbol{G}^{0,A} + \boldsymbol{G}^{0,A} \cdot \boldsymbol{V} \cdot \boldsymbol{G}^A + \boldsymbol{G}^{0,A} \cdot \boldsymbol{\Sigma}^A \cdot \boldsymbol{G}^A. \tag{H.65}$$

The equation for the Lesser Green's function, becomes

$$\begin{aligned}\boldsymbol{G}^< = \boldsymbol{G}^{0,<} + \boldsymbol{G}^{0,<} \cdot \boldsymbol{V} \cdot \boldsymbol{G}^A + \boldsymbol{G}^{0,R} \cdot \boldsymbol{V} \cdot \boldsymbol{G}^< \\ + \boldsymbol{G}^{0,R} \cdot \boldsymbol{\Sigma}^R \cdot \boldsymbol{G}^< + \boldsymbol{G}^{0,R} \cdot \boldsymbol{\Sigma}^< \cdot \boldsymbol{G}^A + \boldsymbol{G}^{0,<} \cdot \boldsymbol{\Sigma}^A \cdot \boldsymbol{G}^A. \end{aligned} \tag{H.66}$$

Notice the structure of the previous equation: the lesser component of a string of convoluted two time quantities $(\boldsymbol{C}_1 \cdot \ldots \cdot \boldsymbol{C}_N)^<$ is given by

$$(\boldsymbol{C}_1 \cdot \ldots \cdot \boldsymbol{C}_N)^< = \sum_{n=1}^{N} \boldsymbol{C}_1^R \cdot \ldots \cdot \boldsymbol{C}_{n-1}^R \cdot \boldsymbol{C}_n^< \cdot \boldsymbol{C}_{n+1}^A \cdot \ldots \cdot \boldsymbol{C}_N^A. \tag{H.67}$$

This is a consequence of the upper triangular form of Green's function Eq. (H.53) and self-energies Eq. (H.59) and the diagonal form of the single-particle potential Eq. (H.54) in Keldysh space. Employing the Dyson equation for the retarded and advanced Green's functions, Eqs. (H.64) and (H.65), into Eq. (H.66), we obtain

$$\boldsymbol{G}^< = \boldsymbol{G}^R \cdot \left(\boldsymbol{G}^{0,R}\right)^{-1} \cdot \boldsymbol{G}^{0,<} \cdot \left(\boldsymbol{G}^{0,A}\right)^{-1} \cdot \boldsymbol{G}^A + \boldsymbol{G}^R \cdot \boldsymbol{\Sigma}^< \cdot \boldsymbol{G}^A. \tag{H.68}$$

For a non-interacting Hamiltonian it is easy to see that

$$\boldsymbol{G}^{0,<}(t,t') = \boldsymbol{G}^{0,R}(t,t_0)\boldsymbol{G}^{0,<}(t_0,t_0)\boldsymbol{G}^{0,A}(t_0,t'), \text{ for } t,t' > t_0. \tag{H.69}$$

Using this result, Eq. (H.68) can be written as (including again the time arguments)

$$\begin{aligned}\boldsymbol{G}^<(t,t') = \boldsymbol{G}^R(t,t_0)\boldsymbol{G}^{0,<}(t_0,t_0)\boldsymbol{G}^A(t_0,t). \\ + \int_{-\infty}^{+\infty} dt_1 \int_{-\infty}^{+\infty} dt_2 \boldsymbol{G}^R(t,t_1)\boldsymbol{\Sigma}^<(t_1,t_2)\boldsymbol{G}^A(t_2,t'). \end{aligned} \tag{H.70}$$

The first term of the above equation describes the memory of the initial state. Provided the retarded and advanced Green's function go to zero as the separation of the time arguments goes to infinity (as it should happen in the presence of interactions or an external bath), then in the limit of $t, t' \gg t_0$, the previous equation reduces to

$$\boldsymbol{G}^<(t,t') = \int_{-\infty}^{+\infty} dt_1 \int_{-\infty}^{+\infty} dt_2 \boldsymbol{G}^R(t,t_1)\boldsymbol{\Sigma}^<(t_1,t_2)\boldsymbol{G}^A(t_2,t'), \tag{H.71}$$

which is the Keldysh equation for the lesser Green's function.

H.3.0.2 *RA > representation*

Choosing $\underline{M}$ and $\underline{N}$ as

$$\underline{M} = \begin{bmatrix} 1 & 1 \\ 0 & 1 \end{bmatrix}, \qquad \underline{N} = \begin{bmatrix} 1 & 1 \\ 0 & -1 \end{bmatrix}, \tag{H.72}$$

the Green's function becomes

$$\tilde{G}^{a}{}_{b}(t,t') = \begin{bmatrix} G^{A}{}_{A}(t,t') & G^{A}{}_{R}(t,t') \\ G^{R}{}_{A}(t,t') & G^{R}{}_{R}(t,t') \end{bmatrix} = \begin{bmatrix} G^{A}(t,t') & 0 \\ G^{>}(t,t') & G^{R}(t,t') \end{bmatrix}. \tag{H.73}$$

The single-particle potentials change as

$$\tilde{V}^{a}_{\ b} = \begin{bmatrix} V^{A}_{\ A} & V^{A}_{\ R} \\ V^{R}_{\ A} & V^{R}_{\ R} \end{bmatrix} = \begin{bmatrix} 1 & \\ & 1 \end{bmatrix}, \tag{H.74}$$

and the interaction vertices change as

$$\tilde{\gamma}_{A}{}^{a}{}_{b} = \begin{bmatrix} \tilde{\gamma}_{A}{}^{A}{}_{A} & \tilde{\gamma}_{A}{}^{A}{}_{R} \\ \tilde{\gamma}_{A}{}^{R}{}_{A} & \tilde{\gamma}_{A}{}^{R}{}_{R} \end{bmatrix} = \begin{bmatrix} 1 & 1 \\ 0 & 0 \end{bmatrix}, \tag{H.75}$$

$$\tilde{\gamma}_{R}{}^{a}{}_{b} = \begin{bmatrix} \tilde{\gamma}_{R}{}^{A}{}_{A} & \tilde{\gamma}_{R}{}^{A}{}_{R} \\ \tilde{\gamma}^{R}_{RRaA} & \tilde{\gamma}_{R}{}^{R}{}_{R} \end{bmatrix} = \begin{bmatrix} 1 & 0 \\ 0 & 1 \end{bmatrix}, \tag{H.76}$$

$$\tilde{\gamma}^{Aa}{}_{b} = \begin{bmatrix} \tilde{\gamma}^{AA}{}_{A} & \tilde{\gamma}^{AA}{}_{R} \\ \tilde{\gamma}^{AR}{}_{A} & \tilde{\gamma}^{AR}{}_{R} \end{bmatrix} = \begin{bmatrix} 1 & 0 \\ 0 & 1 \end{bmatrix}, \tag{H.77}$$

$$\tilde{\gamma}^{Ra}{}_{b} = \begin{bmatrix} \tilde{\gamma}_{R}{}^{A}{}_{A} & \tilde{\gamma}_{R}{}^{A}{}_{R} \\ \tilde{\gamma}_{R}{}^{R}{}_{A} & \tilde{\gamma}_{R}{}^{R}{}_{R} \end{bmatrix} = \begin{bmatrix} 0 & 1 \\ 0 & -1 \end{bmatrix}. \tag{H.78}$$

With these interaction vertices, the self-energy is given by

$$\tilde{\Sigma}^{a}{}_{b}(t,t') = \begin{bmatrix} \tilde{\Sigma}^{A}{}_{A}(t,t') & \tilde{\Sigma}^{A}{}_{R}(t,t') \\ \tilde{\Sigma}^{R}{}_{A}(t,t') & \tilde{\Sigma}^{R}{}_{R}(t,t') \end{bmatrix} = \begin{bmatrix} \Sigma^{A}(t,t') & 0 \\ \Sigma^{>}(t,t') & \Sigma^{R}(t,t') \end{bmatrix}, \tag{H.79}$$

with

$$\begin{aligned} \Sigma^{A}(t,t') &= iG^{>}(t,t')D^{A}(t,t') + iG^{A}(t,t')D^{>}(t,t') \\ &\quad + iG^{A}(t,t')D^{A}(t,t'), \end{aligned} \tag{H.80}$$

$$\begin{aligned} \Sigma^{R}(t,t') &= iG^{>}(t,t')D^{R}(t,t') + iG^{R}(t,t')D^{>}(t,t') \\ &\quad - iG^{R}(t,t')D^{R}(t,t'), \end{aligned} \tag{H.81}$$

$$\Sigma^{>}(t,t') = iG^{>}(t,t')D^{>}(t,t'). \tag{H.82}$$

Using the fact that $G^{R}(t,t')D^{A}(t,t') = 0 = G^{A}(t,t')D^{R}(t,t')$ and Eq. (A.16), it can be seen that Eqs. (H.80) and (H.81) are equivalent to Eqs. (H.60) and (H.61), which can be written as

$$\Sigma^{R}(t,t') = iG^{<}(t,t')D^{R}(t,t') + iG^{R}(t,t')D^{>}(t,t') \tag{H.83}$$

$$= iG^{>}(t,t')D^{R}(t,t') + iG^{R}(t,t')D^{<}(t,t'), \tag{H.84}$$

$$\Sigma^{A}(t,t') = iG^{<}(t,t')D^{A}(t,t') + iG^{A}(t,t')D^{>}(t,t') \tag{H.85}$$

$$= iG^{>}(t,t')D^{A}(t,t') + iG^{A}(t,t')D^{<}(t,t'). \tag{H.86}$$

From these relations it can also be seen that

$$\begin{aligned}\Sigma^R(t,t') - \Sigma^A(t,t') = \\ &= iG^>(t,t')\left(D^R(t,t') - D^A(t,t')\right) + i\left(G^R(t,t') - G^A(t,t')\right)D^<(t,t') \\ &= iG^>(t,t')\left(D^>(t,t') - D^<(t,t')\right) + i\left(G^>(t,t') - G^<(t,t')\right)D^<(t,t') \\ &= iG^>(t,t')D^>(t,t') - iG^<(t,t')D^<(t,t') \\ &= \Sigma^>(t,t') - \Sigma^<(t,t'),\end{aligned} \tag{H.87}$$

which is a direct consequence of the relation for the Green's functions $G^R - G^A = G^> - G^<$, Eq. (A.16).

The Dyson equation in this representation reads

$$\begin{aligned}\begin{bmatrix} \boldsymbol{G}^A & 0 \\ \boldsymbol{G}^> & \boldsymbol{G}^R \end{bmatrix} = \begin{bmatrix} \boldsymbol{G}^{0,A} & 0 \\ \boldsymbol{G}^{0,>} & \boldsymbol{G}^{0,R} \end{bmatrix} + \\ + \begin{bmatrix} \boldsymbol{G}^{0,A} & 0 \\ \boldsymbol{G}^{0,>} & \boldsymbol{G}^{0,R} \end{bmatrix} \cdot \begin{bmatrix} \boldsymbol{V} & 0 \\ 0 & \boldsymbol{V} \end{bmatrix} \cdot \begin{bmatrix} \boldsymbol{G}^A & 0 \\ \boldsymbol{G}^> & \boldsymbol{G}^R \end{bmatrix} \\ + \begin{bmatrix} \boldsymbol{G}^{0,A} & 0 \\ \boldsymbol{G}^{0,>} & \boldsymbol{G}^{0,R} \end{bmatrix} \cdot \begin{bmatrix} \boldsymbol{\Sigma}^A & 0 \\ \boldsymbol{\Sigma}^> & \boldsymbol{\Sigma}^R \end{bmatrix} \cdot \begin{bmatrix} \boldsymbol{G}^A & 0 \\ \boldsymbol{G}^> & \boldsymbol{G}^R \end{bmatrix},\end{aligned} \tag{H.88}$$

from which we can obtain the Dyson equations for the retarded and advanced Green's function, Eqs. (H.64) and (H.65), and the equation for the greater Green's function

$$\begin{aligned}\boldsymbol{G}^>(t,t') = \boldsymbol{G}^R(t,t_0)\boldsymbol{G}^{0,>}(t_0,t_0)\boldsymbol{G}^A(t_0,t). \\ + \int_{-\infty}^{+\infty} dt_1 \int_{-\infty}^{+\infty} dt_2 \boldsymbol{G}^R(t,t_1)\boldsymbol{\Sigma}^>(t_1,t_2)\boldsymbol{G}^A(t_2,t'),\end{aligned} \tag{H.89}$$

which for a system that loses memory and in the limit of $t, t' \gg t_0$, reduces

$$\boldsymbol{G}^>(t,t') = \int_{-\infty}^{+\infty} dt_1 \int_{-\infty}^{+\infty} dt_2 \boldsymbol{G}^R(t,t_1)\boldsymbol{\Sigma}^>(t_1,t_2)\boldsymbol{G}^A(t_2,t'), \tag{H.90}$$

which is the Keldysh equation for the greater Green's function.

I

THOMAS-FERMI THEORY FOR LAYERED MATERIALS

We wish to model the charging of a multilayer system when a gate voltage, V_{gate}, is applied to it. We also allow for a bias voltage, V_{bias}, to be applied between the top and bottom layers. The layered structure is on top of a dielectric spacer separating the structure from a metallic back gate, typically a highly doped Si layer. We treat each layer in the structure as a 2D film with a 2D charge density given by ρ_ℓ, $\ell = -1, ..., \mathcal{N}+1$, where $\ell = -1$ indexes the metallic gate, and $\ell = 0$ to $\mathcal{N}+1$ labels the layers of the actual structure. Layers $\ell - 1$ and ℓ are separated by a distance d_ℓ and we assume that this region is filled with a dielectric with relative constant along the z direction given by given by $\bar{\epsilon}_\ell$. Essentially, we will model the layered structure as a multilayer capacitor. The structure we are considering is represented in Fig. I.1. Applying Gauss's law around each plate and assuming charge neutrality, $\sum_{\ell=-1}^{\mathcal{N}} \rho_\ell = 0$, we obtain

$$\bar{\epsilon}_0 E_0 = \rho_{-1}/\epsilon_0. \tag{I.1}$$

$$\bar{\epsilon}_{\ell+1} E_{\ell+1} - \bar{\epsilon}_\ell E_\ell = \rho_\ell/\epsilon_0,\ \ell = 0, ..., \mathcal{N}, \tag{I.2}$$

$$-\bar{\epsilon}_{\mathcal{N}+1} E_{\mathcal{N}+1} = \rho_{\mathcal{N}+1}/\epsilon_0, \tag{I.3}$$

where E_ℓ is the electric field along the z direction between layers $\ell - 1$ and ℓ, and ϵ_0 is vacuum's permittivity. From these equations we can write

$$\bar{\epsilon}_\ell E_\ell = \frac{1}{\epsilon_0} \sum_{k=-1}^{\ell-1} \rho_k,\ \ell = 0, ..., \mathcal{N}+1, \tag{I.4}$$

and the stored electrostatic energy is given by

$$\begin{aligned} U_{EM} &= \sum_{\ell=0}^{\mathcal{N}+1} \frac{1}{2} \epsilon_0 d_\ell \bar{\epsilon}_\ell E_\ell^2 \\ &= \frac{1}{2} \sum_{\ell,\ell'=0}^{\mathcal{N}+1} \rho_\ell \left(\sum_{k=0}^{\min(\ell,\ell')} \frac{d_k}{\epsilon_0 \bar{\epsilon}_k} \right) \rho_{\ell'}, \end{aligned} \tag{I.5}$$

where we have used the charge neutrality condition in order to eliminate the charge in the Si gate, ρ_{-1}. This is nothing more than the Hartree energy for a layered material. We split the charge density of each layer into a contribution from charge carriers and another from charged impurities, $\rho_\ell = -e n_\ell + e n_\ell^{\text{imp}}$, where n_ℓ is the charge carrier concentration ($n_\ell > 0$ for electron doping) and n_ℓ^{imp} is the concentration of charged impurities ($n_\ell^{\text{imp}} > 0$ for positively charged impurities). Including the effects of a gate voltage, V_{gate}, applied between the $\ell = -1$ and the $\ell = 0$ layers and a bias voltage between the $\ell = \mathcal{N}+1$and the $\ell = 0$ layers, we obtain a Thomas-Fermi energy functional

$$\begin{aligned} \Phi = &\frac{1}{2} \sum_{\ell,\ell'=1}^{\mathcal{N}+1} n_\ell \left(\sum_{k=0}^{\min(\ell,\ell')} \frac{e^2 d_k}{\epsilon_0 \bar{\epsilon}_k} \right) n_{\ell'} - \sum_{\ell=0}^{\mathcal{N}+1} n_\ell e \phi_\ell^{\text{imp}} \\ &- e V_{\text{gate}} \sum_{\ell=0}^{\mathcal{N}+1} n_\ell + e V_{\text{bias}} \sum_{\ell=0}^{\mathcal{N}+1} \frac{\ell}{\mathcal{N}+1} n_\ell, \end{aligned} \tag{I.6}$$

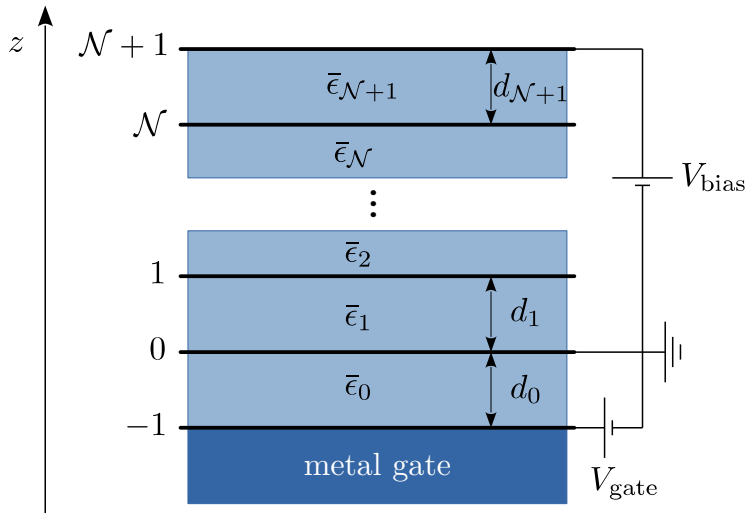

Figure I.1: Schematic representation of the multilayer capacitor model that is used to model electrostatic doping of layered materials.

where

$$e\phi_\ell^{\text{imp}} = \sum_{\ell'=0}^{\mathcal{N}+1} \sum_{k=1}^{\min(\ell,\ell')} \frac{e^2 d_k}{\epsilon_0 \bar{\epsilon}_k} n_{\ell'}^{\text{imp}}, \tag{I.7}$$

is the potential created by the charged impurities. The Hartree potential felt by electrons in layer ℓ is given by

$$\begin{aligned} V_\ell^H &= -\frac{\partial \Phi}{\partial n_\ell} \\ &= V_{\text{gate}} - V_{\text{bias}} \frac{\ell}{\mathcal{N}+1} n_\ell + e\phi_\ell^{\text{imp}} \\ &\quad - \sum_{\ell'=0}^{\mathcal{N}+1} \left(\sum_{k=0}^{\min(\ell,\ell')} \frac{e^2 d_k}{\epsilon_0 \bar{\epsilon}_k} \right) n_{\ell'}, \; \ell = 0, ..., \mathcal{N}+1. \end{aligned} \tag{I.8}$$

Now, we assume that the vertical current flowing between the 1 and the $\mathcal{N}+1$ layers is small, such that we can assume that these layers are in a near equilibrium state. Furthermore, we employ the Thomas-Fermi approximation, in which the local Fermi level for each layer is given by $\epsilon_{F,\ell} = V_\ell^H$, where $\epsilon_{F,\ell} = \epsilon_{F,\ell}(n_\ell)$ is a function of the local carrier density. The local relation $\epsilon_{F,\ell}(n_\ell)$ together with Eq. (I.8) give us a system of non-linear equations, which must be solved to obtain the carrier density / local Fermi level for each layer.

We will be interested in a system where the layers $\ell = 0$ and $\ell = \mathcal{N}+1$ are graphene layers and the remaining layers, $\ell = 1, ..., \mathcal{N}$ are formed by the insulating material hBN. It can be checked, that due to the large band gap of hBN, most charge density will be accumulated in the graphene layers. As such it is a good approximation to set $n_\ell = 0$, for $\ell = 1, ..., \mathcal{N}$ and therefore the $\mathcal{N}+2$ equations in Eq. (I.8) are reduced to two

$$\epsilon_{F,\text{bg}} = eV_{\text{gate}} - (n_{\text{bg}} + n_{\text{tg}}) C_{\text{t}}^{-1} + e\phi_{\text{bg}}^{\text{imp}}, \tag{I.9}$$

$$\epsilon_{F,\text{tg}} = eV_{\text{gate}} - eV_{\text{bias}} - n_{\text{tg}} C_{\text{t}}^{-1} - n_{\text{bg}} C_{\text{b}}^{-1} + e\phi_{\text{tg}}^{\text{imp}}, \tag{I.10}$$

where the capacitances are given by (taking into account the series capacitances of a hBN/SiO_2 spacer between the $\ell = 0$ graphene layer and the Si gate, with $d_{\rm hBN}$ the hBN thickness and $d_{SiO_2}$the SiO_2 thickness)

$$C_{\rm b}^{-1} = \frac{e^2 d_0}{\epsilon_0 \bar{\epsilon}_0} = \frac{e^2 d_{SiO_2}}{\epsilon_0 \bar{\epsilon}_{SiO_2}} + \frac{e^2 d_{\rm hBN}}{\epsilon_0 \bar{\epsilon}_{\rm hBN}}, \tag{I.11}$$

$$C_{\rm t}^{-1} = \sum_{\ell=0}^{\mathcal{N}+1} \frac{e^2 d_\ell}{\epsilon_0 \bar{\epsilon}_\ell} = \frac{e^2 d_{SiO_2}}{\epsilon_0 \bar{\epsilon}_{SiO_2}} + \frac{e^2 d_{\rm hBN}}{\epsilon_0 \bar{\epsilon}_{\rm hBN}} + \frac{e^2 d}{\epsilon_0 \bar{\epsilon}_{\rm hBN}}, \tag{I.12}$$

and d is the distance between the two graphene layers. The terms $e\phi^{\rm imp}_{\rm bg/tg}$ are the potentials induced by the charged impurities in the bottom/top graphene layer that can be tuned to account for intrinsic doping of the graphene layers (acting as an offset in $V_{\rm gate}$ and $V_{\rm bias}$).

We finally point out that in the case where the hBN layers have no charge carriers, then the Hartree potential within the hBN slab is given from Eq. (I.8) in terms of $\epsilon_{F,\rm bg/tg}$ as

$$\begin{aligned} V_\ell^H = {} & \epsilon_{F,\rm tg} - e\phi^{\rm imp}_{\rm tg} + e\phi^{\rm imp}_\ell \\ & - \frac{\ell}{\mathcal{N}+1}\left(\epsilon_{F,\rm tg} + eV_{\rm bias} - \epsilon_{\rm F,bg} - e\phi^{\rm imp}_{\rm tg} + e\phi^{\rm imp}_{\rm bg}\right), \end{aligned} \tag{I.13}$$

which in the absence of charged impurities reduces to

$$V_\ell^H = \epsilon_{F,\rm tg} - \frac{\ell}{\mathcal{N}+1}\left(\epsilon_{F,\rm tg} + eV_{\rm bias} - \epsilon_{F,\rm bg}\right), \tag{I.14}$$

as stated in Section (6.4). For pristine graphene, the electronic density is related to the Fermi energy by

$$\epsilon_{F,\ell} = \mathrm{sgn}\left(n_\ell\right) v_F \hbar \sqrt{\pi \left|n_\ell\right|}. \tag{I.15}$$

The solution of Eqs (I.9)-(I.10) together with Eq. (I.15) for $\epsilon_{F,\rm bg}$ and $\epsilon_{F,\rm tg}$ are shown to a particular device in Fig. 6.2.

J

ANALYTIC EXPRESSION FOR TDOS OF SECTION 6.5

In this appendix we provide an analytic expression for the quantity $\mathrm{TDoS}_{n,m}(\omega_{\mathrm{bg}},\omega_{\mathrm{tg}})$, Eq. (6.103), of Section 6.5. In the limit of infinite lifetime for graphene electrons, the spectral functions of Eq. (6.103) reduce to δ-functions and it is possible to perform the integration over momentum analytically. In the presence of a finite, momentum independent, lifetime, it is still possible to find an approximate analytical expression to Eq. (6.103). First we notice that the spectral functions in the sublattice basis can be written as

$$\boldsymbol{A}_{\mathrm{bg/tg},\mathbf{k}}(\omega) = i\left[\boldsymbol{G}^{R}_{\mathbf{k},\theta_{\mathrm{bg/tg}}}\left(\omega_{\mathrm{bg/tg}}\right) - \boldsymbol{G}^{A}_{\mathbf{k},\theta_{\mathrm{bg/tg}}}\left(\omega_{\mathrm{bg/tg}}\right)\right], \tag{J.1}$$

with the Green's functions reading

$$\boldsymbol{G}^{R/A}_{\mathbf{k},\theta}\left(\omega\right) = \frac{\omega^{\pm}\mathrm{Id} + v_F\hbar\mathbf{k}\cdot\boldsymbol{\sigma}_{\theta}}{\left(\omega^{\pm}\right)^2 - \left(v_F\hbar\right)^2\left|\mathbf{k}\right|^2}, \tag{J.2}$$

with $\omega^{\pm} = \omega \pm i\gamma$, with γ the broadening factor and

$$\boldsymbol{\sigma}_{\theta} = \left(\cos\theta\sigma_x - \sin\theta\sigma_y, \sin\theta\sigma_x + \cos\theta\sigma_y\right). \tag{J.3}$$

For convenience, we will write $\boldsymbol{G}_{\mathbf{k},\theta}\left(\omega^{\pm}\right) = \boldsymbol{G}^{R/A}_{\mathbf{k},\theta}\left(\omega\right)$. Equation (6.103) can then be recast as

$$\begin{aligned}\mathrm{TDoS}_{n,m}(\omega_{\mathrm{bg}},\omega_{\mathrm{tg}}) = i^2\sum_{s,s'=\pm1}\int\frac{d^2\mathbf{k}}{\left(2\pi\right)^2}ss'\mathrm{tr}\Big[&\boldsymbol{G}_{\mathbf{k},\theta_{\mathrm{bg}}+n\frac{2\pi}{3}}\left(\omega^{s}_{\mathrm{bg}}\right)\cdot\boldsymbol{J}\cdot\\ &\cdot\boldsymbol{G}_{\mathbf{k}+\boldsymbol{\mathcal{Q}}_{n,m},\theta_{\mathrm{tg}}+m\frac{2\pi}{3}}\left(\omega^{s'}_{\mathrm{tg}}\right)\cdot\boldsymbol{J}\Big],\end{aligned} \tag{J.4}$$

where $\mathrm{tr}\left\{...\right\}$ is the trace over graphene sublattice indices, and $\boldsymbol{J}$ is a 2×2 matrix of ones. Performing the trace over the sublattice degrees of freedom we obtain

$$\begin{aligned}\mathrm{TDoS}_{n,m}(\omega_{\mathrm{bg}},\omega_{\mathrm{tg}}) = i^2\sum_{s,s'=\pm1}\int\frac{d^2\mathbf{k}}{\left(2\pi\right)^2}ss'\times\\ \times\frac{2\left(\omega^{s}_{\mathrm{bg}} + v_F\hbar\mathbf{k}\cdot\hat{\mathbf{K}}_{\mathrm{bg},n}\right)}{\left(\omega^{s}_{\mathrm{bg}}\right)^2 - \left(v_F\hbar\right)^2\left|\mathbf{k}\right|^2}\frac{2\left(\omega^{s'}_{\mathrm{tg}} + v_F\hbar\left(\mathbf{k}+\boldsymbol{\mathcal{Q}}_{n,m}\right)\cdot\hat{\mathbf{K}}_{\mathrm{tg},m}\right)}{\left(\omega^{s'}_{\mathrm{tg}}\right)^2 - \left(v_F\hbar\right)^2\left|\mathbf{k}+\boldsymbol{\mathcal{Q}}_{n,m}\right|^2}.\end{aligned} \tag{J.5}$$

This form is completely equivalent to Eq. (6.103). Its advantage lies in the fact that is is clearly analytic in $\mathbf{k}$ (is does not involve terms like $\sqrt{\mathbf{k}^2}$) and as such, contour integration methods can be used to perform the integration.

In order to make analytic progress, in the first term of the previous expression we take the limit $\gamma_{\mathrm{bg}}\to0$, such that $\omega^{s'}_{\mathrm{bg}}\to\omega_{\mathrm{bg}} = \omega + \epsilon_{\mathrm{F,bg}}$ and

$$i\sum_{s=\pm1}s\frac{\omega^{s}_{\mathrm{bg}} + v_F\hbar\mathbf{k}\cdot\hat{\mathbf{K}}_{\mathrm{bg},n}}{\left(\omega^{s}_{\mathrm{bg}}\right)^2 - \left(v_F\hbar\right)^2\left|\mathbf{k}\right|^2} \to 2\pi\frac{\omega_{\mathrm{bg}} + v_F\hbar\mathbf{k}\cdot\hat{\mathbf{K}}_{\mathrm{bg},n}}{2v_F\hbar\left|\mathbf{k}\right|}\sum_{s=\pm1}s\delta\left(\omega_{\mathrm{bg}} - sv_F\hbar\left|\mathbf{k}\right|\right). \tag{J.6}$$

We use the δ-function to perform the integration over $|\mathbf{k}|$, obtaining

$$\mathrm{TDoS}_{n,m}(\omega_{\mathrm{bg}},\omega_{\mathrm{tg}}) \simeq i\frac{\omega_{\mathrm{bg}}}{(v_F\hbar)^2}\int\frac{d\theta_{\mathbf{k}}}{2\pi}\left(\frac{\omega_{\mathrm{bg}}+v_F\hbar\mathbf{k}\cdot\hat{\boldsymbol{K}}_{\mathrm{bg},n}}{v_F\hbar\,|\mathbf{k}|}\right)\Bigg|_{|\mathbf{k}|=\frac{|\omega_{\mathrm{bg}}|}{v_F\hbar}}\times \\ \times\sum_{s'=\pm1}s'\frac{2\left(\omega_{\mathrm{tg}}^{s'}+v_F\hbar\,(\mathbf{k}+\boldsymbol{\mathcal{Q}}_{n,m})\cdot\hat{\mathbf{K}}_{\mathrm{tg},m}\right)}{\left(\omega_{\mathrm{tg}}^{s'}\right)^2-(v_F\hbar)^2\,|\mathbf{k}+\boldsymbol{\mathcal{Q}}_{n,m}|^2}. \quad \text{(J.7)}$$

The remaining integration over the angular variable $\theta_{\mathbf{k}}$ can be performed using contour integration methods. We perform a change of variables $z=e^{i\theta_{\mathbf{k}}}$ such that

$$\int\frac{d\theta_{\mathbf{k}}}{2\pi}=\oint_{|z|=1}\frac{dz}{2\pi i}\frac{1}{z}, \quad \text{(J.8)}$$

$$\cos\theta_{\mathbf{k}}=\frac{z+z^{-1}}{2}, \quad \text{(J.9)}$$

$$\sin\theta_{\mathbf{k}}=\frac{z-z^{-1}}{2i}, \quad \text{(J.10)}$$

and we can write

$$\hat{\mathbf{k}}\cdot\hat{\mathbf{K}}_{\mathrm{bg/tg},n}=\frac{z+z^{-1}}{2}\hat{K}^x_{\mathrm{bg/tg},n}+\frac{z-z^{-1}}{2i}\hat{K}^y_{\mathrm{bg/tg},n}, \quad \text{(J.11)}$$

$$|\mathbf{k}+\boldsymbol{\mathcal{Q}}_{n,m}|^2=|\mathbf{k}|^2+|\boldsymbol{\mathcal{Q}}_{n,m}|^2 \\ +2\,|\mathbf{k}|\,|\boldsymbol{\mathcal{Q}}_{n,m}|\left(\frac{z+z^{-1}}{2}\cos\theta_{\boldsymbol{\mathcal{Q}}_{n,m}}+\frac{z-z^{-1}}{2i}\sin\theta_{\boldsymbol{\mathcal{Q}}_{n,m}}\right), \quad \text{(J.12)}$$

with $\theta_{\boldsymbol{\mathcal{Q}}_{n,m}}$ the angle of the vector $\boldsymbol{\mathcal{Q}}_{n,m}$ with the reference x axis. The integrand has a double pole at $z=0$ and two simple poles at $z=e^{i\theta_{\boldsymbol{\mathcal{Q}}_{m,n}}}w^s_{\gtrless,\mathrm{tg}}$, where $w^s_{\gtrless,\mathrm{tg}}$ is given by

$$w^s_{\gtrless,\mathrm{tg}}=\mathcal{C}^s_{\mathrm{tg}}\mp i\mathcal{S}^s_{\mathrm{tg}}, \quad \text{(J.13)}$$

$$\mathcal{C}^s_{\mathrm{tg}}=\frac{(\omega_{\mathrm{tg}}+si\gamma_{\mathrm{tg}})^2-(v_F\hbar)^2\left(|\boldsymbol{\mathcal{Q}}_{n,m}|^2+|\mathbf{k}|^2\right)}{2\,(v_F\hbar)^2\,|\boldsymbol{\mathcal{Q}}_{n,m}|\,|\mathbf{k}|}, \quad \text{(J.14)}$$

$$\mathcal{S}^s_{\mathrm{tg}}=\mathrm{sgn}\left(\omega^2_{\mathrm{tg}}-\gamma^2_{\mathrm{tg}}-(v_F\hbar)^2\left(|\boldsymbol{\mathcal{Q}}_{n,m}|^2+|\mathbf{k}|^2\right)\right)i\sqrt{\left(\mathcal{C}^s_{\mathrm{tg}}\right)^2-1}, \quad \text{(J.15)}$$

and is defined such that $|w_{<,\mathrm{tg}}|<1$ and $w_{>,\mathrm{tg}}=w^{-1}_{<,\mathrm{tg}}$. The contour integration around the unit circle can be performed analytically by collecting the residues at $z=e^{i\theta_{\pm\boldsymbol{\mathcal{Q}}_{n,m}}}w^s_{<,\mathrm{tg}}$ and $z=0$. Notice that we have made the approximation $\gamma_{\mathrm{bg}}\to0$. In general, both γ_{bg} and γ_{tg} will be non-zero. The simplest way to take this into account is to symmetrize Eq. (J.5) with respect to the bottom and the top graphene layers and

then taking the limit $\gamma_{\rm bg} \to 0$ in the first term and $\gamma_{\rm tg} \to 0$ in the second. The final symmetrized result is given by

$$\begin{aligned}
\mathrm{TDoS}_{n,m}(\omega_{\rm bg},\omega_{\rm tg}) \simeq{}& \frac{\omega_{\rm bg}}{(v_F\hbar)^3\,|\boldsymbol{\mathcal{Q}}_{n,m}|}\times \\
&\times\left[\sum_{s=\pm1}\frac{-1}{\mathcal{S}^s_{\rm tg}}\left(\frac{\omega^s_{\rm tg}+|\omega_{\rm bg}|\left(\mathcal{C}^s_{\rm tg}X^{\rm tg}_{n,m}+\mathcal{S}^s_{\rm tg}Y^{\rm tg}_{n,m}\right)+v_F\hbar\boldsymbol{\mathcal{Q}}_{n,m}\cdot\hat{\mathbf{K}}_{{\rm tg},m}}{|\omega_{\rm bg}|}\right)\times\right. \\
&\qquad\times\left(\frac{\omega_{\rm bg}+|\omega_{\rm bg}|\left(\mathcal{C}^s_{\rm tg}X^{\rm bg}_{n,m}+\mathcal{S}^s_{\rm tg}Y^{\rm bg}_{n,m}\right)}{|\omega_{\rm bg}|}\right) \\
&\qquad\qquad+ \\
&\left.+\frac{2\gamma_{\rm tg}\left(X^{\rm bg}_{n,m}+iY^{\rm bg}_{n,m}\right)}{v_F\hbar\,|\boldsymbol{\mathcal{Q}}_{n,m}|}\left(\frac{v_F\hbar\,|\boldsymbol{\mathcal{Q}}_{n,m}|+\omega_{\rm tg}\left(X^{\rm tg}_{n,m}+iY^{\rm tg}_{n,m}\right)}{|\omega_{\rm bg}|}\right)\right]\Bigg|_{|\mathbf{k}|=\frac{|\omega_{\rm bg}|}{(v_F\hbar)}} \\
&+\left(\omega_{\rm tg}\leftrightarrow\omega_{\rm bg},\,X^{\rm bg/tg}_{n,m}\to-X^{\rm bg/tg}_{n,m},\,Y^{\rm bg/tg}_{n,m}\to-Y^{\rm bg/tg}_{n,m}\right), \qquad \text{(J.16)}
\end{aligned}$$

where we have we have introduced the quantities

$$\begin{aligned}
X^{\rm bg}_{n,m}&=\hat{\boldsymbol{\mathcal{Q}}}_{n,m}\cdot\hat{\mathbf{K}}_{{\rm bg},n}, \quad Y^{\rm bg}_{n,m}=\hat{\boldsymbol{\mathcal{Q}}}_{n,m}\times\hat{\mathbf{K}}_{{\rm bg},n}, \\
X^{\rm tg}_{n,m}&=\hat{\boldsymbol{\mathcal{Q}}}_{n,m}\cdot\hat{\mathbf{K}}_{{\rm tg},m}, \quad Y^{\rm tg}_{n,m}=\hat{\boldsymbol{\mathcal{Q}}}_{n,m}\times\hat{\mathbf{K}}_{{\rm tg},m},
\end{aligned} \qquad \text{(J.17)}$$

and the quantities $\mathcal{C}^{\pm}_{\rm tg}$ and $\mathcal{S}^{\pm}_{\rm tg}$ given by Eqs. (J.14) and (J.15) with the replacements $\omega_{\rm tg}\to\omega_{\rm bg}$ and $\gamma_{\rm tg}\to\gamma_{\rm bg}$. It was checked that Eq. (J.16) provides a very good approximation to the numeric evaluation of Eq. (J.5) when both $\gamma_{\rm bg}$ and $\gamma_{\rm tg}$ are non-zero, if the broadening function for each layer is assumed to the the sum of the broadening factors of both layers, i.e., performing the replacement $\gamma_{\rm bg},\gamma_{\rm tg}\to\gamma_{\rm bg}+\gamma_{\rm tg}$.

In the limit of infinite electron lifetime in both layers $\gamma_{\rm bg/tg}\to 0$, we obtain

$$\mathcal{C}^s_{\rm tg}=\frac{\omega^2_{\rm tg}-\omega^2_{\rm bg}-(v_F\hbar)^2\,|\boldsymbol{\mathcal{Q}}_{n,m}|^2}{2\,(v_F\hbar)\,|\boldsymbol{\mathcal{Q}}_{n,m}|\,|\omega_{\rm bg}|}, \qquad \text{(J.18)}$$

$$\mathcal{S}^s_{\rm tg}=-s\mathrm{sgn}(\omega_{\rm tg})\sqrt{1-\left(\mathcal{C}^s_{\rm tg}\right)^2}, \qquad \text{(J.19)}$$

and $\mathcal{S}^s_{\rm bg}/\mathcal{C}^s_{\rm bg}$ are obtained by replacing $\omega_{\rm bg}\to\omega_{\rm tg}$. In this case, $\mathrm{TDoS}_{n,m}(\omega_{\rm bg},\omega_{\rm tg})$ simplifies to

$$\begin{aligned}
\mathrm{TDoS}_{n,m}(\omega_{\rm bg},\omega_{\rm tg})={}&\frac{\omega_{\rm tg}}{(v_F\hbar)^3\,|\boldsymbol{\mathcal{Q}}_{n,m}|}\times \\
&\times\sum_{s=\pm1}\frac{-1}{\mathcal{S}^+_{\rm tg}}\left(\frac{\omega_{\rm tg}+|\omega_{\rm bg}|\left(\mathcal{C}^+_{\rm tg}X^{\rm tg}_{n,m}+\mathcal{S}^+_{\rm tg}Y^{\rm tg}_{n,m}\right)+v_F\hbar\boldsymbol{\mathcal{Q}}_{n,m}\cdot\hat{\mathbf{K}}_{{\rm tg},m}}{|\omega_{\rm bg}|}\right)\times \\
&\qquad\times\left(\frac{\omega_{\rm bg}+|\omega_{\rm bg}|\left(\mathcal{C}^+_{\rm tg}X^{\rm bg}_{n,m}+\mathcal{S}^+_{\rm tg}Y^{\rm bg}_{n,m}\right)}{|\omega_{\rm bg}|}\right). \qquad \text{(J.20)}
\end{aligned}$$

We notice that in this limit, $\mathrm{TDoS}_{n,m}(\omega_{\rm bg},\omega_{\rm tg})$ is only non-zero when

$$4\,(v_F\hbar)^2\,|\boldsymbol{\mathcal{Q}}_{n,m}|^2\,\omega^2_{\rm bg}>\left(\omega^2_{\rm tg}-\omega^2_{\rm bg}-(v_F\hbar)^2\,|\boldsymbol{\mathcal{Q}}_{n,m}|^2\right)^2. \qquad \text{(J.21)}$$

We finally study how the effect of the spinorial character of graphene's wavefunction manifests in the form of $\mathrm{TDoS}_{n,m}(\omega_{\mathrm{bg}},\omega_{\mathrm{tg}})$. If we set the wavefunction overlap factors $\Upsilon^{\mathrm{bg/tg},n}_{\mathbf{k},\lambda}$ to 1 in Eq. (6.103), then instead of Eq. (J.5) we would obtain

$$\mathrm{TDoS}^{\mathrm{scalar}}_{n,m}(\omega_{\mathrm{bg}},\omega_{\mathrm{tg}}) = i^2 \sum_{s,s'=\pm 1} \int \frac{d^2\mathbf{k}}{(2\pi)^2} ss' \frac{2\omega^s_{\mathrm{bg}}}{\left(\omega^s_{\mathrm{bg}}\right)^2 - (v_F\hbar)^2 |\mathbf{k}|^2} \times \\ \times \frac{2\omega^{s'}_{\mathrm{tg}}}{\left(\omega^{s'}_{\mathrm{tg}}\right)^2 - (v_F\hbar)^2 |\mathbf{k}+\boldsymbol{\mathcal{Q}}_{n,m}|^2}. \quad \text{(J.22)}$$

In order to evaluate $\mathrm{TDoS}^{\mathrm{scalar}}_{n,m}(\omega_{\mathrm{bg}},\omega_{\mathrm{tg}})$, we proceed as previously. the only difference is that when performing the integration over the unit circle in the complex variable z, there is no double pole at $z=0$, and the contour integration only collects the contribution from $z = e^{i\theta_{\pm\boldsymbol{\mathcal{Q}}_{m,n}}} w^s_{<,\mathrm{tg/bg}}$. Symmetrizing the result, this leads to

$$\mathrm{TDoS}^{\mathrm{scalar}}_{n,m}(\omega_{\mathrm{bg}},\omega_{\mathrm{tg}}) = \frac{1}{(v_F\hbar)^3 |\boldsymbol{\mathcal{Q}}_{n,m}|} \frac{1}{2} \left[\left(\frac{\omega^-_{\mathrm{tg}}}{\mathcal{S}^-_{\mathrm{tg}}} - \frac{\omega^+_{\mathrm{tg}}}{\mathcal{S}^+_{\mathrm{tg}}} \right) + \left(\frac{\omega^-_{\mathrm{bg}}}{\mathcal{S}^-_{\mathrm{bg}}} - \frac{\omega^+_{\mathrm{bg}}}{\mathcal{S}^+_{\mathrm{bg}}} \right) \right]. \quad \text{(J.23)}$$

These analytical expressions lead to a significant speed up in the evaluation of the current in Chapter 6.

BIBLIOGRAPHY

[1] K. S. Novoselov, A. K. Geim, S. V. Morozov, D. Jiang, Y. Zhang, S. V. Dubonos, I. V. Grigorieva, and A. A. Firsov. Electric field effect in atomically thin carbon films. *Science*, 306(5696):666–669, 2004. (Cited on page 1.)

[2] A K Geim. Graphene prehistory. *Physica Scripta*, 2012(T146):014003, 2012. (Cited on page 1.)

[3] K. S. Novoselov, A. K. Geim, S. V. Morozov, D. Jiang, M. I. Katsnelson, I. V. Grigorieva, S. V. Dubonos, and A. A. Firsov. Two-dimensional gas of massless dirac fermions in graphene. *Nature*, 438:197–200, Nov 2005. (Cited on page 1.)

[4] Yuanbo Zhang, Yan-Wen Tan, Horst L. Stormer, and Philip Kim. Experimental observation of the quantum hall effect and berry's phase in graphene. *Nature*, 438:201–204, Nov 2005. (Cited on page 1.)

[5] R. R. Nair, P. Blake, A. N. Grigorenko, K. S. Novoselov, T. J. Booth, T. Stauber, N. M. R. Peres, and A. K. Geim. Fine structure constant defines visual transparency of graphene. *Science*, 320(5881):1308–1308, 2008. (Cited on page 1.)

[6] Long Ju, Baisong Geng, Jason Horng, Caglar Girit, Michael Martin, Zhao Hao, Hans A. Bechtel, Xiaogan Liang, Alex Zettl, Y. Ron Shen, and Feng Wang. Graphene plasmonics for tunable terahertz metamaterials. *Nat Nano*, 6:630–634, Oct 2011. (Cited on page 1.)

[7] Changgu Lee, Xiaoding Wei, Jeffrey W. Kysar, and James Hone. Measurement of the elastic properties and intrinsic strength of monolayer graphene. *Science*, 321(5887):385–388, 2008. (Cited on pages 1 and 11.)

[8] Alexander A. Balandin, Suchismita Ghosh, Wenzhong Bao, Irene Calizo, Desalegne Teweldebrhan, Feng Miao, and Chun Ning Lau. Superior thermal conductivity of single-layer graphene. *Nano Letters*, 8(3):902–907, 2008. PMID: 18284217. (Cited on page 1.)

[9] K. S. Novoselov, D. Jiang, F. Schedin, T. J. Booth, V. V. Khotkevich, S. V. Morozov, and A. K. Geim. Two-dimensional atomic crystals. *Proceedings of the National Academy of Sciences of the United States of America*, 102(30):10451–10453, 2005. (Cited on page 1.)

[10] Likai Li, Yijun Yu, Guo Jun Ye, Qingqin Ge, Xuedong Ou, Hua Wu, Donglai Feng, Xian Hui Chen, and Yuanbo Zhang. Black phosphorus field-effect transistors. *Nat Nano*, 9:372–377, May 2014. (Cited on page 1.)

[11] Miguel M. Ugeda, Aaron J. Bradley, Yi Zhang, Seita Onishi, Yi Chen, Wei Ruan, Claudia Ojeda-Aristizabal, Hyejin Ryu, Mark T. Edmonds, Hsin-Zon Tsai, Alexander Riss, Sung-Kwan Mo, Dunghai Lee, Alex Zettl, Zahid Hussain, Zhi-Xun Shen, and Michael F. Crommie. Characterization of collective ground states in single-layer nbse2. *Nat Phys*, 12:92–97, Jan 2016. (Cited on page 1.)

[12] F. Schedin, A. K. Geim, S. V. Morozov, E. W. Hill, P. Blake, M. I. Katsnelson, and K. S. Novoselov. Detection of individual gas molecules adsorbed on graphene. *Nat Mater*, 6:652–655, Sep 2007. (Cited on page 1.)

[13] T. O. Wehling, K. S. Novoselov, S. V. Morozov, E. E. Vdovin, M. I. Katsnelson, A. K. Geim, and A. I. Lichtenstein. Molecular doping of graphene. *Nano Letters*, 8:173–177, Dec 2008.

[14] Hongtao Liu, Yunqi Liu, and Daoben Zhu. Chemical doping of graphene. *J. Mater. Chem.*, 21:3335–3345, 2011. (Cited on page 1.)

[15] Vitor M. Pereira and A. H. Castro Neto. Strain engineering of graphene's electronic structure. *Phys. Rev. Lett.*, 103:046801, Jul 2009. (Cited on page 2.)

[16] F. Guinea. Strain engineering in graphene. *Solid State Communications*, 152(15):1437–1441, 2012. Exploring Graphene, Recent Research Advances. (Cited on page 2.)

[17] N. Levy, S. A. Burke, K. L. Meaker, M. Panlasigui, A. Zettl, F. Guinea, A. H. Castro Neto, and M. F. Crommie. Strain-induced pseudo–magnetic fields greater than 300 tesla in graphene nanobubbles. *Science*, 329(5991):544–547, 2010. (Cited on page 2.)

[18] Rafael Roldán, Andrés Castellanos-Gomez, Emmanuele Cappelluti, and Francisco Guinea. Strain engineering in semiconducting two-dimensional crystals. *Journal of Physics: Condensed Matter*, 27(31):313201, 2015. (Cited on page 2.)

[19] R.E. Peierls. Bemerkungten über umwandlungstemperaturen. *Helv. Phys. Acta*, 7:81 – 83, 1934. (Cited on pages 2 and 9.)

[20] L. D. Landau. Zur theorie der phasenumwandlungten ii. *Phys. Z. Sowjetunion*, 11:26 – 35, 1937. (Cited on page 9.)

[21] N. D. Mermin. Crystalline order in two dimensions. *Phys. Rev.*, 176:250–254, Dec 1968. (Cited on pages 2 and 9.)

[22] B. Jancovici. Infinite susceptibility without long-range order: The two-dimensional harmonic "solid". *Phys. Rev. Lett.*, 19:20–22, Jul 1967. (Cited on pages 2 and 10.)

[23] D.R. Nelson and L. Peliti. Fluctuations in membranes with crystalline and hexatic order. *J. Phys. Paris*, 48:1085, 1987. (Cited on pages 2, 11, 13, 16, 19, 35, and 36.)

[24] D.R. Nelson, T. Piran, and S. Weinberg, editors. *Statistical Mechanics of Membranes and Surfaces*. World Scientific, Singapore, 2004. (Cited on pages 2, 11, 12, 17, and 19.)

[25] Joseph Aronovitz, Leonardo Golubovic, and T.C. Lubensky. Fluctuations and lower critical dimensions of crystalline membranes. *J. Phys. France*, 50(6):609–631, 1989. (Cited on pages 2, 11, 21, and 22.)

[26] E. Guitter, F. David, S. Leibler, and L. Peliti. Thermodynamical behavior of polymerized membranes. *J. Phys. France*, 50(14):1787 – 1819, July 1989. (Cited on pages 2 and 11.)

[27] Guillermo López-Polín, Cristina Gómez-Navarro, Vincenzo Parente, Francisco Guinea, Mikhail I. Katsnelson, Francesc Perez-Murano, and Julio Gómez-Herrero. Increasing the elastic modulus of graphene by controlled defect creation. *Nat Phys*, 11:26 – 31, 2015. (Cited on pages 2 and 11.)

[28] G. López-Polín, M. Jaafar, F. Guinea, R. Roldán, C. Gómez-Navarro, and J. Gómez-Herrero. Strain dependent elastic modulus of graphene. *ArXiv e-prints*, April 2015. (Cited on pages 2 and 11.)

[29] I. M. Lifshitz. *Zh. Eksp. Teor. Fiz.*, 22:475, 1952. (Cited on pages 3 and 39.)

[30] G.L. Belenkii, E.Yu. Salaev, R.A. Suleimanov, N.A. Abdullaev, and V.Ya. Shteinshraiber. The nature of negative linear expansion in layer crystals c, bn, gas, gase and inse. *Solid State Communications*, 53(11):967–971, 1985. (Cited on page 3.)

[31] Wenzhong Bao, Feng Miao, Zhen Chen, Hang Zhang, Wanyoung Jang, Chris Dames, and Chun Ning Lau. Controlled ripple texturing of suspended graphene and ultrathin graphite membranes. *Nat Nano*, 4:562–566, Sep 2009. (Cited on page 3.)

[32] Duhee Yoon, Young-Woo Son, and Hyeonsik Cheong. Negative thermal expansion coefficient of graphene measured by raman spectroscopy. *Nano Letters*, 11(8):3227–3231, 2011. PMID: 21728349. (Cited on page 3.)

[33] Jin-Wu Jiang, Jian-Sheng Wang, and Baowen Li. Thermal expansion in single-walled carbon nanotubes and graphene: Nonequilibrium green's function approach. *Phys. Rev. B*, 80:205429, Nov 2009. (Cited on page 3.)

[34] A. K. Geim and K. S. Novoselov. The rise of graphene. *Nat Mater*, 6:183–191, Mar 2007. (Cited on pages 3 and 69.)

[35] Eduardo V. Castro, H. Ochoa, M. I. Katsnelson, R. V. Gorbachev, D. C. Elias, K. S. Novoselov, A. K. Geim, and F. Guinea. Limits on charge carrier mobility in suspended graphene due to flexural phonons. *Phys. Rev. Lett.*, 105:266601, Dec 2010. (Cited on pages 3, 32, 69, 77, 88, 90, and 91.)

[36] Eros Mariani and Felix von Oppen. Temperature-dependent resistivity of suspended graphene. *Phys. Rev. B*, 82:195403, Nov 2010. (Cited on pages 69 and 77.)

[37] H. Ochoa, Eduardo V. Castro, M.I. Katsnelson, and F. Guinea. Scattering by flexural phonons in suspended graphene under back gate induced strain. *Physica E: Low–dimensional Systems and Nanostructures*, 44(6):963–966, 2012. The proceedings of the European Materials Research Symposium on Science and Technology of Nanotubes, Nanowires and Graphene. (Cited on pages 3, 69, and 91.)

[38] Ponomarenko L. A., Geim A. K., Zhukov A. A., Jalil R., Morozov S. V., Novoselov K. S., Grigorieva I. V., Hill E. H., Cheianov V. V., Fal/'ko V. I., Watanabe K., Taniguchi T., and Gorbachev R. V. Tunable metal-insulator transition in double-layer graphene heterostructures. *Nat Phys*, 7(12):958–961, December 2011. 10.1038/nphys2114. (Cited on pages 3, 4, and 95.)

[39] Seyoung Kim, Insun Jo, Junghyo Nah, Z. Yao, S. K. Banerjee, and E. Tutuc. Coulomb drag of massless fermions in graphene. *Phys. Rev. B*, 83:161401, Apr 2011. (Cited on pages 3, 95, and 118.)

[40] Seyoung Kim and Emanuel Tutuc. Coulomb drag and magnetotransport in graphene double layers. *Solid State Communications*, 152(15):1283–1288, 2012. Exploring Graphene, Recent Research Advances. (Cited on page 118.)

[41] R. V. Gorbachev, A. K. Geim, M. I. Katsnelson, K. S. Novoselov, T. Tudorovskiy, I. V. Grigorieva, T. Tudorovskiy, I. V. Grigorieva, A. H. MacDonald, S. V. Morozov, K. Watanabe, T. Taniguchi, and L. A. Ponomarenko. Strong coulomb drag and broken symmetry in double-layer graphene. *Nature Physics*, pages 896–901, 2012. (Cited on pages 3, 4, 95, and 118.)

[42] P. M. Solomon, P. J. Price, D. J. Frank, and D. C. La Tulipe. New phenomena in coupled transport between 2d and 3d electron-gas layers. *Phys. Rev. Lett.*, 63:2508–2511, Nov 1989. (Cited on pages 3 and 95.)

[43] B. Laikhtman and P. M. Solomon. Mutual drag of two- and three-dimensional electron gases in heterostuctures. *Phys. Rev. B*, 41:9921–9929, May 1990.

[44] T. J. Gramila, J. P. Eisenstein, A. H. MacDonald, L. N. Pfeiffer, and K. W. West. Mutual friction between parallel two-dimensional electron systems. *Phys. Rev. Lett.*, 66:1216–1219, Mar 1991. (Cited on pages 95, 108, and 116.)

[45] P.M. Solomon and B. Laikhtman. Mutual drag of 2d and 3d electron gases in heterostructures. *Superlattices and Microstructures*, 10(1):89–94, 1991. (Cited on pages 108 and 116.)

[46] U. Sivan, P. M. Solomon, and H. Shtrikman. Coupled electron-hole transport. *Phys. Rev. Lett.*, 68:1196–1199, Feb 1992. (Cited on pages 3 and 95.)

[47] K S Novoselov and A H Castro Neto. Two-dimensional crystals-based heterostructures: materials with tailored properties. *Physica Scripta*, 2012(T146):014006, 2012. (Cited on page 4.)

[48] L. Britnell, R. V. Gorbachev, R. Jalil, B. D. Belle, F. Schedin, A. Mishchenko, T. Georgiou, M. I. Katsnelson, L. Eaves, S. V. Morozov, N. M. R. Peres, J. Leist, A. K. Geim, K. S. Novoselov, and L. A. Ponomarenko. Field-effect tunneling transistor based on vertical graphene heterostructures. *Science*, 335(6071):947–950, 2012. (Cited on pages 4, 119, and 157.)

[49] Liam Britnell, Roman V. Gorbachev, Rashid Jalil, Branson D. Belle, Fred Schedin, Mikhail I. Katsnelson, Laurence Eaves, Sergey V. Morozov, Alexander S. Mayorov, Nuno M. R. Peres, Antonio H. Castro Neto, Jon Leist, Andre K. Geim, Leonid A. Ponomarenko, and Kostya S. Novoselov. Electron tunneling through ultrathin boron nitride crystalline barriers. *Nano Letters*, 12(3):1707–1710, 2012. PMID: 22380756. (Cited on pages 4 and 157.)

[50] Georgiou Thanasis, Jalil Rashid, Belle Branson D., Britnell Liam, Gorbachev Roman V., Morozov Sergey V., Kim Yong-Jin, Gholinia Ali, Haigh Sarah J., Makarovsky Oleg, Eaves Laurence, Ponomarenko Leonid A., Geim Andre K., Novoselov Kostya S., and Mishchenko Artem. Vertical field-effect transistor based on graphene-WS2 heterostructures for flexible and transparent electronics. *Nat Nano*, 8(2):100–103, February 2013. (Cited on pages 4 and 119.)

[51] S. J. Haigh, A. Gholinia, R. Jalil, S. Romani, L. Britnell, D. C. Elias, K. S. Novoselov, L. A. Ponomarenko, A. K. Geim, and R. Gorbachev. Cross-sectional imaging of individual layers and buried interfaces of graphene-based heterostructures and superlattices. *Nat Mater*, 11:764 – 767, 2012. (Cited on pages 4 and 119.)

[52] A. Mishchenko, J.S. Tu, Y. Cao, R. V. Gorbachev, J. R. Wallbank, M. T. Greenaway, V. E. Morozov, S. V. Morozov, M. J. Zhu, S. L. Wong, F. Withers, C. R. Woods, Y-J. Kim, K. Watanabe, T. Taniguchi, E. E. Vdovin, O. Makarovsky, T. M. Fromhold, V. I. Fal'ko, Geim A. K., L. Eaves, and K. S. Novoselov. Twist-controlled resonant tunnelling in graphene/boron nitride/graphene heterostructures. *Nat Nano*, 9(10):808–813, October 2014. (Cited on pages 4, 120, 142, 143, and 159.)

[53] Luis Brey. Coherent tunneling and negative differential conductivity in a graphene/h-bn/graphene heterostructure. *Phys. Rev. Applied*, 2:014003, Jul 2014. (Cited on pages 4, 120, 142, 143, and 159.)

[54] B. Henrik and K. Flensberg. *Many-Body Quantum Theory in Condensed Matter Physics*. Oxford University Press, New York, 2004. (Cited on pages 5, 172, 183, and 200.)

[55] A. Atland and B. Simons. *Condensed Matter Field Theory*. Cambridge University Press, New York, 2010. (Cited on pages 5, 22, and 172.)

[56] Hartmut Haug and Antti-Pekka Jauho. *Quantum Kinetics in Transport and Optics of Semiconductors*, volume 123 of *Springer Series in Solid-State Sciences*. Springer-Verlag Berlin, Heidelberg, 2 edition, 2008. (Cited on pages 5 and 213.)

[57] Jørgen Rammer. *Quantum Field Theory of Non-equilibrium States*. Cambridge University Press, 2007. (Cited on pages 5, 203, 213, and 218.)

[58] L. Gunther. Stability of the finite two-dimensional harmonic lattice. *Physics Letters A*, 25(9):649 – 650, 1967. (Cited on page 9.)

[59] Y. Imry and L. Gunther. Fluctuations and physical properties of the two-dimensional crystal lattice. *Phys. Rev. B*, 3:3939–3945, Jun 1971. (Cited on page 10.)

[60] P. A. Heiney, P. W. Stephens, R. J. Birgeneau, P. M. Horn, and D. E. Moncton. X-ray scattering study of the structure and freezing transition of monolayer xenon on graphite. *Phys. Rev. B*, 28:6416–6434, Dec 1983. (Cited on page 10.)

[61] Yacov Kantor, Mehran Kardar, and David R. Nelson. Statistical mechanics of tethered surfaces. *Phys. Rev. Lett.*, 57:791–794, Aug 1986. (Cited on page 11.)

[62] Yacov Kantor and David R. Nelson. Crumpling transition in polymerized membranes. *Phys. Rev. Lett.*, 58:2774–2777, Jun 1987.

[63] Yacov Kantor, Mehran Kardar, and David R. Nelson. Tethered surfaces: Statics and dynamics. *Phys. Rev. A*, 35:3056–3071, Apr 1987.

[64] Maya Paczuski, Mehran Kardar, and David R. Nelson. Landau theory of the crumpling transition. *Phys. Rev. Lett.*, 60:2638–2640, Jun 1988. (Cited on page 12.)

[65] F. David and E. Guitter. Crumpling transition in elastic membranes: Renormalization group treatment. *EPL (Europhysics Letters)*, 5(8):709, 1988.

[66] Joseph A. Aronovitz and T. C. Lubensky. Fluctuations of solid membranes. *Phys. Rev. Lett.*, 60:2634–2637, Jun 1988. (Cited on pages 13 and 21.)

[67] E. Guitter, F. David, S. Leibler, and L. Peliti. Crumpling and buckling transitions in polymerized membranes. *Phys. Rev. Lett.*, 61:2949–2952, Dec 1988.

[68] Maya Paczuski and Mehran Kardar. Renormalization-group analysis of the crumpling transition in large *d*. *Phys. Rev. A*, 39:6086–6089, Jun 1989. (Cited on page 11.)

[69] Farid F Abraham and David R Nelson. Diffraction from polymerized membranes. *Science*, 249(4967):393–397, 1990. (Cited on page 11.)

[70] Farid F. Abraham and David R. Nelson. Fluctuations in the flat and collapsed phases of polymerized membranes. *J. Phys. France*, 51(23):2653 – 2672, December 1990. (Cited on page 21.)

[71] F. F. Abraham and M. Goulian. Diffraction from polymerized membranes: Flat vs. crumpled. *EPL (Europhysics Letters)*, 19(4):293, 1992. (Cited on page 11.)

[72] J.C. Meyer, A.K. Geim, M.I. Katsnelson, K.S. Novoselov, T.J. Booth, and S. Roth. The structure of suspended graphene sheets. *Nature*, 446:60, December 2007. (Cited on page 11.)

[73] J.C. Meyer, A.K. Geim, M.I. Katsnelson, K.S. Novoselov, D. Obergfell, S. Roth, C. Girit, and A. Zettl. On the roughness of single- and bi-layer graphene membranes. *Solid State Communications*, 143(1 - 2):101 – 109, 2007. Exploring graphene Recent research advances.

[74] Jacopo Brivio, Duncan T. L. Alexander, and Andras Kis. Ripples and layers in ultrathin mos2 membranes. *Nano Lett.*, 11(12):5148–5153, 2011. (Cited on page 11.)

[75] Andres Castellanos-Gomez, Vibhor Singh, Herre S. J. van der Zant, and Gary A. Steele. Mechanics of freely-suspended ultrathin layered materials. *Annalen der Physik*, 527(1-2):27–44, 2015. (Cited on page 11.)

[76] B. Amorim, A. Cortijo, F. de Juan, A.G. Grushin, F. Guinea, A. Gutiérrez-Rubio, H. Ochoa, V. Parente, R. Roldán, P. San-Jose, J. Schiefele, M. Sturla, and M.A.H. Vozmediano. Novel effects of strains in graphene and other two dimensional materials. *Physics Reports*, 617:1 – 54, 2016. Novel effects of strains in graphene and other two dimensional materials. (Cited on page 11.)

[77] Mark J. Bowick and Alex Travesset. The statistical mechanics of membranes. *Physics Reports*, 344(4–6):255 – 308, 2001. Renormalization group theory in the new millennium. (Cited on page 12.)

[78] G Gompper and D M Kroll. Network models of fluid, hexatic and polymerized membranes. *Journal of Physics: Condensed Matter*, 9(42):8795, 1997. (Cited on page 12.)

[79] L. D. Landau and E. M. Lifshitz. *Theory of Elasticity*. Course of Theoretical Physics. Pergamon Press, Oxford, 1959. (Cited on pages 12, 13, and 52.)

[80] K. V. Zakharchenko, M. I. Katsnelson, and A. Fasolino. Finite temperature lattice properties of graphene beyond the quasiharmonic approximation. *Phys. Rev. Lett.*, 102:046808, Jan 2009. (Cited on pages 14, 33, and 40.)

[81] Annalisa Fasolino, JH Los, and Mikhail I Katsnelson. Intrinsic ripples in graphene. *Nature materials*, 6(11):858–861, 2007. (Cited on page 19.)

[82] K. V. Zakharchenko, J. H. Los, M. I. Katsnelson, and A. Fasolino. Atomistic simulations of structural and thermodynamic properties of bilayer graphene. *Phys. Rev. B*, 81:235439, Jun 2010.

[83] Rafael Roldán, Annalisa Fasolino, Kostyantyn V. Zakharchenko, and Mikhail I. Katsnelson. Suppression of anharmonicities in crystalline membranes by external strain. *Phys. Rev. B*, 83:174104, May 2011. (Cited on pages 19 and 20.)

[84] Pierre Le Doussal and Leo Radzihovsky. Self-consistent theory of polymerized membranes. *Phys. Rev. Lett.*, 69:1209–1212, Aug 1992. (Cited on page 21.)

[85] J.-P. Kownacki and D. Mouhanna. Crumpling transition and flat phase of polymerized phantom membranes. *Phys. Rev. E*, 79:040101, Apr 2009. (Cited on page 21.)

[86] F. L. Braghin and N. Hasselmann. Thermal fluctuations of free-standing graphene. *Phys. Rev. B*, 82:035407, Jul 2010.

[87] N. Hasselmann and F. L. Braghin. Nonlocal effective-average-action approach to crystalline phantom membranes. *Phys. Rev. E*, 83:031137, Mar 2011.

[88] K. Essafi, J.-P. Kownacki, and D. Mouhanna. First-order phase transitions in polymerized phantom membranes. *Phys. Rev. E*, 89:042101, Apr 2014. (Cited on page 21.)

[89] Z. Zhang, H. T. Davis, and D. M. Kroll. Scaling behavior of self-avoiding tethered vesicles. *Phys. Rev. E*, 48:R651–R654, Aug 1993. (Cited on page 21.)

[90] M. J. Bowick, S. M. Catterall, M. Falcioni, G. Thorleifsson, and K. N. Anagnostopoulos. The flat phase of crystalline membranes. *Journal de Physique I*, 6(10):1321–1345, October 1996. (Cited on page 21.)

[91] M.J. Bowick, S.M. Catterall, M. Falcioni, G. Thorleifsson, and K. Anagnostopoulos. The flat phase of fixed-connectivity membranes. *Nuclear Physics B Proceedings Supplements*, 53(1-3):746–752, 1997.

[92] J. H. Los, M. I. Katsnelson, O. V. Yazyev, K. V. Zakharchenko, and A. Fasolino. Scaling properties of flexible membranes from atomistic simulations: Application to graphene. *Phys. Rev. B*, 80:121405, Sep 2009.

[93] A. Tröster. High-precision fourier monte carlo simulation of crystalline membranes. *Phys. Rev. B*, 87:104112, Mar 2013.

[94] A. Tröster. Fourier monte carlo renormalization-group approach to crystalline membranes. *Phys. Rev. E*, 91:022132, Feb 2015. (Cited on page 21.)

[95] J. M. Ziman. *Electrons and Phonons; The theory of Transport Phenomena in Solids*. Oxford University Press, London, 1960. (Cited on pages 37, 77, 83, and 205.)

[96] P. L. de Andres, F. Guinea, and M. I. Katsnelson. Bending modes, anharmonic effects, and thermal expansion coefficient in single-layer and multilayer graphene. *Phys. Rev. B*, 86:144103, Oct 2012. (Cited on pages 38, 39, and 64.)

[97] V.M. Galitskii and A.B. Migdal. Application of quantum field theory methods to the many body problem. *Zh. Eksp. Teor. Fiz.*, 34:139, 1958. [Engl. Transl.: Sov. Phys. JETP 7, 96 (1958)]. (Cited on pages 42 and 181.)

[98] Daniel S. Koltun. Theory of mean removal energies for single particles in nuclei. *Phys. Rev. C*, 9:484–497, Feb 1974. (Cited on pages 42 and 181.)

[99] Valentin N. Popov. Low-temperature specific heat of nanotube systems. *Phys. Rev. B*, 66:153408, Oct 2002. (Cited on page 44.)

[100] Nicolas Mounet and Nicola Marzari. First-principles determination of the structural, vibrational and thermodynamic properties of diamond, graphite, and derivatives. *Phys. Rev. B*, 71:205214, May 2005. (Cited on page 44.)

[101] T. Aizawa, R. Souda, S. Otani, Y. Ishizawa, and C. Oshima. Anomalous bond of monolayer graphite on transition-metal carbide surfaces. *Phys. Rev. Lett.*, 64:768–771, Feb 1990. (Cited on pages 47 and 49.)

[102] Takashi Aizawa, Ryutaro Souda, Yoshio Ishizawa, Hideki Hirano, Taro Yamada, Ken ichi Tanaka, and Chuhei Oshima. Phonon dispersion in monolayer graphite formed on ni(111) and ni(001). *Surface Science*, 237(1):194 – 202, 1990.

[103] T. Aizawa, R. Souda, S. Otani, Y. Ishizawa, and C. Oshima. Bond softening in monolayer graphite formed on transition-metal carbide surfaces. *Phys. Rev. B*, 42:11469–11478, Dec 1990. (Cited on pages 47, 49, 60, and 65.)

[104] Takashi Aizawa, Yeon Hwang, Wataru Hayami, Ryutaro Souda, Shigeki Otani, and Yoshio Ishizawa. Phonon dispersion of monolayer graphite on pt(111) and nbc surfaces: bond softening and interface structures. *Surface Science*, 260(1):311 – 318, 1992. (Cited on pages 47 and 49.)

[105] L. Lindsay, D. A. Broido, and Natalio Mingo. Flexural phonons and thermal transport in graphene. *Phys. Rev. B*, 82:115427, Sep 2010. (Cited on page 47.)

[106] Jae Hun Seol, Insun Jo, Arden L. Moore, Lucas Lindsay, Zachary H. Aitken, Michael T. Pettes, Xuesong Li, Zhen Yao, Rui Huang, David Broido, Natalio Mingo, Rodney S. Ruoff, and Li Shi. Two-dimensional phonon transport in supported graphene. *Science*, 328(5975):213–216, 2010. (Cited on page 47.)

[107] Zhun-Yong Ong and Eric Pop. Effect of substrate modes on thermal transport in supported graphene. *Phys. Rev. B*, 84:075471, Aug 2011. (Cited on pages 47 and 57.)

[108] Bo Qiu and Xiulin Ruan. Reduction of spectral phonon relaxation times from suspended to supported graphene. *Applied Physics Letters*, 100(19), 2012. (Cited on page 47.)

[109] H. Yanagisawa, T. Tanaka, Y. Ishida, M. Matsue, E. Rokuta, S. Otani, and C. Oshima. Analysis of phonons in graphene sheets by means of hreels measurement and ab initio calculation. *Surface and Interface Analysis*, 37(2):133–136, 2005. (Cited on page 49.)

[110] Adrien Allard and Ludger Wirtz. Graphene on metallic substrates: Suppression of the kohn anomalies in the phonon dispersion. *Nano Letters*, 10(11):4335–4340, 2010.

[111] Antonio Politano, Antonio Raimondo Marino, and Gennaro Chiarello. Phonon dispersion of quasi-freestanding graphene on pt(111). *Journal of Physics: Condensed Matter*, 24(10):104025, 2012. (Cited on page 49.)

[112] Peter S. Swain and David Andelman. The influence of substrate structure on membrane adhesion. *Langmuir*, 15(26):8902–8914, 1999. (Cited on page 49.)

[113] B. N. J. Persson and H. Ueba. Heat transfer between weakly coupled systems: Graphene on a-sio 2. *EPL (Europhysics Letters)*, 91(5):56001, 2010. (Cited on page 49.)

[114] Gianluca Giovannetti, Petr A. Khomyakov, Geert Brocks, Paul J. Kelly, and Jeroen van den Brink. Substrate-induced band gap in graphene on hexagonal boron nitride: *Ab initio* density functional calculations. *Phys. Rev. B*, 76:073103, Aug 2007. (Cited on page 49.)

[115] Alexey Bosak, Jorge Serrano, Michael Krisch, Kenji Watanabe, Takashi Taniguchi, and Hisao Kanda. Elasticity of hexagonal boron nitride: Inelastic x-ray scattering measurements. *Phys. Rev. B*, 73:041402, Jan 2006. (Cited on page 51.)

[116] Harry L. Brown, Philip E. Armstrong, and Charles P. Kempter. Elastic properties of some polycrystalline transition-metal monocarbides. *The Journal of Chemical Physics*, 45(2):547–549, 1966. (Cited on page 51.)

[117] J. J. Gilman and B. W. Roberts. Elastic constants of tic and tib[sub 2]. *Journal of Applied Physics*, 32(7):1405–1405, 1961. (Cited on page 51.)

[118] B. N. J. Persson. Theory of rubber friction and contact mechanics. *The Journal of Chemical Physics*, 115(8):3840–3861, 2001. (Cited on page 56.)

[119] H. Aranda-Espinoza and D. Lavallee. Structure factor of flexible membranes. *EPL (Europhysics Letters)*, 43(3):355, 1998. (Cited on page 62.)

[120] S. V. Morozov, K. S. Novoselov, M. I. Katsnelson, F. Schedin, D. C. Elias, J. A. Jaszczak, and A. K. Geim. Giant intrinsic carrier mobilities in graphene and its bilayer. *Phys. Rev. Lett.*, 100:016602, Jan 2008. (Cited on page 69.)

[121] Jian-Hao Chen, Chaun Jang, Shudong Xiao, Masa Ishigami, and Michael S. Fuhrer. Intrinsic and extrinsic performance limits of graphene devices on sio2. *Nature Nanotechnology*, 3:206–209, Mar 2008. (Cited on pages 69 and 96.)

[122] H. J. Hrostowski, F. J. Morin, T. H. Geballe, and G. H. Wheatley. Hall effect and conductivity of insb. *Phys. Rev.*, 100:1672–1676, Dec 1955. (Cited on page 69.)

[123] T. Dürkop, S. A. Getty, Enrique Cobas, and M. S. Fuhrer. Extraordinary mobility in semiconducting carbon nanotubes. *Nano Letters*, 4(1):35–39, 2004. (Cited on page 69.)

[124] C. R. Dean, A. F. Young, I. Meric, C. Lee, L. Wang, S. Sorgenfrei, K. Watanabe, T. Taniguchi, P. Kim, K. L. Shepard, and J. Hone. Boron nitride substrates for high-quality graphene electronics. *Nat Nano*, 5:722–726, Oct 2010. (Cited on page 69.)

[125] Alexander S. Mayorov, Roman V. Gorbachev, Sergey V. Morozov, Liam Britnell, Rashid Jalil, Leonid A. Ponomarenko, Peter Blake, Kostya S. Novoselov, Kenji Watanabe, Takashi Taniguchi, and A. K. Geim. Micrometer-scale ballistic transport in encapsulated graphene at room temperature. *Nano Letters*, 11(6):2396–2399, 2011. PMID: 21574627. (Cited on page 69.)

[126] K.I. Bolotin, K.J. Sikes, Z. Jiang, M. Klima, G. Fudenberg, J. Hone, P. Kim, and H.L. Stormer. Ultrahigh electron mobility in suspended graphene. *Solid State Communications*, 146(9–10):351–355, 2008. (Cited on page 69.)

[127] K. I. Bolotin, K. J. Sikes, J. Hone, H. L. Stormer, and P. Kim. Temperature-dependent transport in suspended graphene. *Phys. Rev. Lett.*, 101:096802, Aug 2008. (Cited on page 69.)

[128] Xu Du, Ivan Skachko, Anthony Barker, and Eva Y. Andrei. Approaching ballistic transport in suspended graphene. *Nat Nano*, 3:491–495, Aug 2008. (Cited on page 69.)

[129] M.I Katsnelson and A.K Geim. Electron scattering on microscopic corrugations in graphene. *Philosophical Transactions of the Royal Society of London A: Mathematical, Physical and Engineering Sciences*, 366(1863):195–204, 2008. (Cited on pages 69 and 77.)

[130] S. Fratini and F. Guinea. Substrate-limited electron dynamics in graphene. *Phys. Rev. B*, 77:195415, May 2008. (Cited on pages 69, 96, and 118.)

[131] Jürgen Schiefele, Fernando Sols, and Francisco Guinea. Temperature dependence of the conductivity of graphene on boron nitride. *Phys. Rev. B*, 85:195420, May 2012. (Cited on pages 69, 96, and 118.)

[132] Eros Mariani and Felix von Oppen. Flexural phonons in free-standing graphene. *Phys. Rev. Lett.*, 100:076801, Feb 2008. (Cited on page 69.)

[133] H. Ochoa, Eduardo V. Castro, M. I. Katsnelson, and F. Guinea. Temperature-dependent resistivity in bilayer graphene due to flexural phonons. *Phys. Rev. B*, 83:235416, Jun 2011. (Cited on pages 69, 77, 78, 84, 88, and 91.)

[134] E. H. Hwang and S. Das Sarma. Acoustic phonon scattering limited carrier mobility in two-dimensional extrinsic graphene. *Phys. Rev. B*, 77:115449, Mar 2008. (Cited on page 70.)

[135] P. R. Wallace. The band theory of graphite. *Phys. Rev.*, 71:622–634, May 1947. (Cited on pages 71 and 72.)

[136] A. H. Castro Neto, F. Guinea, N. M. R. Peres, K. S. Novoselov, and A. K. Geim. The electronic properties of graphene. *Rev. Mod. Phys.*, 81:109–162, Jan 2009. (Cited on pages 72, 73, and 77.)

[137] Hongki Min, J. E. Hill, N. A. Sinitsyn, B. R. Sahu, Leonard Kleinman, and A. H. MacDonald. Intrinsic and rashba spin-orbit interactions in graphene sheets. *Phys. Rev. B*, 74:165310, Oct 2006. (Cited on pages 72 and 74.)

[138] Mildred S. Dresselhaus, Gene Dresselhaus, and Ado Jorio. *Group Theory: Application to the Physics of Condensed Matter*. Springer-Verlag Berlin, Heidelberg, 2008. (Cited on page 74.)

[139] J. L. Mañes, F. Guinea, and María A. H. Vozmediano. Existence and topological stability of fermi points in multilayered graphene. *Phys. Rev. B*, 75:155424, Apr 2007. (Cited on page 74.)

[140] M.A.H. Vozmediano, M.I. Katsnelson, and F. Guinea. Gauge fields in graphene. *Physics Reports*, 496(4–5):109–148, 2010. (Cited on pages 74 and 77.)

[141] Hidekatsu Suzuura and Tsuneya Ando. Phonons and electron-phonon scattering in carbon nanotubes. *Phys. Rev. B*, 65:235412, May 2002. (Cited on pages 77, 78, 80, and 152.)

[142] S. V. Morozov, K. S. Novoselov, M. I. Katsnelson, F. Schedin, L. A. Ponomarenko, D. Jiang, and A. K. Geim. Strong suppression of weak localization in graphene. *Phys. Rev. Lett.*, 97:016801, Jul 2006.

[143] J. L. Mañes. Symmetry-based approach to electron-phonon interactions in graphene. *Phys. Rev. B*, 76:045430, Jul 2007. (Cited on page 78.)

[144] F. Guinea, Baruch Horovitz, and P. Le Doussal. Gauge field induced by ripples in graphene. *Phys. Rev. B*, 77:205421, May 2008. (Cited on page 77.)

[145] Fernando de Juan, Mauricio Sturla, and María A. H. Vozmediano. Space dependent fermi velocity in strained graphene. *Phys. Rev. Lett.*, 108:227205, May 2012. (Cited on page 77.)

[146] Fernando de Juan, Juan L. Mañes, and María A. H. Vozmediano. Gauge fields from strain in graphene. *Phys. Rev. B*, 87:165131, Apr 2013. (Cited on page 77.)

[147] Juan L. Mañes, Fernando de Juan, Mauricio Sturla, and María A. H. Vozmediano. Generalized effective hamiltonian for graphene under nonuniform strain. *Phys. Rev. B*, 88:155405, Oct 2013. (Cited on page 77.)

[148] Seon-Myeong Choi, Seung-Hoon Jhi, and Young-Woo Son. Effects of strain on electronic properties of graphene. *Phys. Rev. B*, 81:081407, Feb 2010. (Cited on page 77.)

[149] Cheol-Hwan Park, Nicola Bonini, Thibault Sohier, Georgy Samsonidze, Boris Kozinsky, Matteo Calandra, Francesco Mauri, and Nicola Marzari. Electron–phonon interactions and the intrinsic electrical resistivity of graphene. *Nano Letters*, 14(3):1113–1119, 2014. PMID: 24524418. (Cited on pages 77 and 80.)

[150] Felix von Oppen, Francisco Guinea, and Eros Mariani. Synthetic electric fields and phonon damping in carbon nanotubes and graphene. *Phys. Rev. B*, 80:075420, Aug 2009. (Cited on page 77.)

[151] B Wunsch, T Stauber, F Sols, and F Guinea. Dynamical polarization of graphene at finite doping. *New Journal of Physics*, 8(12):318, 2006. (Cited on pages 78, 109, 110, 113, 187, 188, and 189.)

[152] M. A. Cazalilla, H. Ochoa, and F. Guinea. Quantum spin hall effect in two-dimensional crystals of transition-metal dichalcogenides. *Phys. Rev. Lett.*, 113:077201, Aug 2014. (Cited on page 78.)

[153] John M. Wills and Walter A. Harrison. Interionic interactions in transition metals. *Phys. Rev. B*, 28:4363–4373, Oct 1983. (Cited on pages 80, 154, and 157.)

[154] W.A. Harrison. *Elementary Electronic Structure*. Elementary Electronic Structure. World Scientific, 1999. (Cited on pages 80, 154, and 157.)

[155] K. Takegahara and S. Wang. Effects of the energy dependence of the electron distribution function on electrical resistivities. *Journal of Physics F: Metal Physics*, 7(11):L293, 1977. (Cited on pages 83 and 205.)

[156] M. B. Pogrebinskii. Mutual drag of carriers in a semiconductor-insulator-semiconductor system. *Soviet Physics-Semiconductors*, 11(4):372–376, 1977. (Cited on pages 95 and 118.)

[157] Peter J. Price. Hot electron effects in heterolayers. *Physica B+C*, 117:750 – 752, 1983. (Cited on page 95.)

[158] Antti-Pekka Jauho and Henrik Smith. Coulomb drag between parallel two-dimensional electron systems. *Phys. Rev. B*, 47:4420–4428, Feb 1993. (Cited on pages 95, 98, and 108.)

[159] Lian Zheng and A. H. MacDonald. Coulomb drag between disordered two-dimensional electron-gas layers. *Phys. Rev. B*, 48:8203–8209, Sep 1993. (Cited on page 98.)

[160] Karsten Flensberg and Ben Yu-Kuang Hu. Plasmon enhancement of coulomb drag in double-quantum-well systems. *Phys. Rev. B*, 52:14796–14808, Nov 1995. (Cited on pages 98, 99, 102, and 207.)

[161] Alex Kamenev and Yuval Oreg. Coulomb drag in normal metals and superconductors: Diagrammatic approach. *Phys. Rev. B*, 52:7516–7527, Sep 1995. (Cited on pages 98, 99, 102, and 212.)

[162] Karsten Flensberg, Ben Yu-Kuang Hu, Antti-Pekka Jauho, and Jari M. Kinaret. Linear-response theory of coulomb drag in coupled electron systems. *Phys. Rev. B*, 52:14761–14774, Nov 1995. (Cited on pages 95, 98, 99, and 212.)

[163] B. N. Narozhny. Coulomb drag as a measure of trigonal warping in doped graphene. *Phys. Rev. B*, 76:153409, Oct 2007. (Cited on page 95.)

[164] Wang-Kong Tse, Ben Yu-Kuang Hu, and S. Das Sarma. Theory of coulomb drag in graphene. *Phys. Rev. B*, 76:081401, Aug 2007. (Cited on pages 95 and 96.)

[165] N. M. R. Peres, J. M. B. Lopes dos Santos, and A. H. Castro Neto. Coulomb drag and high-resistivity behavior in double-layer graphene. *EPL (Europhysics Letters)*, 95(1):18001, 2011. (Cited on page 96.)

[166] M. I. Katsnelson. Coulomb drag in graphene single layers separated by a thin spacer. *Phys. Rev. B*, 84:041407, Jul 2011. (Cited on pages 96 and 99.)

[167] E. H. Hwang, Rajdeep Sensarma, and S. Das Sarma. Coulomb drag in monolayer and bilayer graphene. *Phys. Rev. B*, 84:245441, Dec 2011. (Cited on pages 96 and 106.)

[168] B. N. Narozhny, M. Titov, I. V. Gornyi, and P. M. Ostrovsky. Coulomb drag in graphene: Perturbation theory. *Phys. Rev. B*, 85:195421, May 2012. (Cited on pages 96 and 106.)

[169] M Carrega, T Tudorovskiy, A Principi, M I Katsnelson, and M Polini. Theory of coulomb drag for massless dirac fermions. *New Journal of Physics*, 14(6):063033, 2012. (Cited on pages 95, 96, 106, and 118.)

[170] S. M. Badalyan and F. M. Peeters. Enhancement of coulomb drag in double-layer graphene structures by plasmons and dielectric background inhomogeneity. *Phys. Rev. B*, 86:121405, Sep 2012.

[171] Benedikt Scharf and Alex Matos-Abiague. Coulomb drag between massless and massive fermions. *Phys. Rev. B*, 86:115425, Sep 2012.

[172] Justin C. W. Song and Leonid S. Levitov. Energy-driven drag at charge neutrality in graphene. *Phys. Rev. Lett.*, 109:236602, Dec 2012. (Cited on page 118.)

[173] M. Schütt, P. M. Ostrovsky, M. Titov, I. V. Gornyi, B. N. Narozhny, and A. D. Mirlin. Coulomb drag in graphene near the dirac point. *Phys. Rev. Lett.*, 110:026601, Jan 2013. (Cited on page 95.)

[174] N. M. R. Peres. *Colloquium* : The transport properties of graphene: An introduction. *Rev. Mod. Phys.*, 82:2673–2700, Sep 2010. (Cited on pages 95, 108, 109, and 147.)

[175] R. Jalabert and S. Das Sarma. Quasiparticle properties of a coupled two-dimensional electron-phonon system. *Phys. Rev. B*, 40:9723–9737, Nov 1989. (Cited on page 96.)

[176] H. C. Tso, P. Vasilopoulos, and F. M. Peeters. Direct coulomb and phonon-mediated coupling between spatially separated electron gases. *Phys. Rev. Lett.*, 68:2516–2519, Apr 1992.

[177] Chao Zhang and Y Takahashi. Dynamical conductivity of a two-layered structure with electron-acoustic phonon coupling. *Journal of Physics: Condensed Matter*, 5(28):5009, 1993. (Cited on pages 99 and 102.)

[178] T. J. Gramila, J. P. Eisenstein, A. H. MacDonald, L. N. Pfeiffer, and K. W. West. Evidence for virtual-phonon exchange in semiconductor heterostructures. *Phys. Rev. B*, 47:12957–12960, May 1993.

[179] K. Güven and B. Tanatar. Coupled plasmon-phonon mode effects on the coulomb drag in double-quantum-well systems. *Phys. Rev. B*, 56:7535–7540, Sep 1997. (Cited on page 96.)

[180] Rosario E. V. Profumo, Marco Polini, Reza Asgari, Rosario Fazio, and A. H. MacDonald. Electron-electron interactions in decoupled graphene layers. *Phys. Rev. B*, 82:085443, Aug 2010. (Cited on page 99.)

[181] Ben Yu-Kuang Hu and S. Das Sarma. Many-body exchange-correlation effects in the lowest subband of semiconductor quantum wires. *Phys. Rev. B*, 48:5469–5504, Aug 1993. (Cited on pages 99 and 102.)

[182] Alex Levchenko and Alex Kamenev. Coulomb drag at zero temperature. *Phys. Rev. Lett.*, 100:026805, Jan 2008. (Cited on page 106.)

[183] B. N. Narozhny and A. Levchenko. Coulomb drag. *Rev. Mod. Phys.*, 88:025003, May 2016. (Cited on pages 108, 116, and 118.)

[184] R. Geick, C. H. Perry, and G. Rupprecht. Normal modes in hexagonal boron nitride. *Phys. Rev.*, 146:543–547, Jun 1966. (Cited on pages 110, 112, 115, 131, and 136.)

[185] H. Fröhlich. Electrons in lattice fields. *Advances in Physics*, 3(11):325–361, 1954. (Cited on pages 111 and 112.)

[186] R. H. Lyddane, R. G. Sachs, and E. Teller. On the polar vibrations of alkali halides. *Phys. Rev.*, 59:673–676, Apr 1941. (Cited on page 112.)

[187] T Stauber and G Gómez-Santos. Plasmons in layered structures including graphene. *New Journal of Physics*, 14(10):105018, 2012. (Cited on page 113.)

[188] J. I. A. Li, T. Taniguchi, K. Watanabe, J. Hone, A. Levchenko, and C. R. Dean. Negative coulomb drag in double bilayer graphene. *Phys. Rev. Lett.*, 117:046802, Jul 2016. (Cited on page 118.)

[189] Kayoung Lee, Jiamin Xue, David C. Dillen, Kenji Watanabe, Takashi Taniguchi, and Emanuel Tutuc. Giant frictional drag in double bilayer graphene heterostructures. *Phys. Rev. Lett.*, 117:046803, Jul 2016. (Cited on page 118.)

[190] L. Britnell, R. M. Ribeiro, A. Eckmann, R. Jalil, B. D. Belle, A. Mishchenko, Y.-J. Kim, R. V. Gorbachev, T. Georgiou, S. V. Morozov, A. N. Grigorenko, A. K. Geim, C. Casiraghi, A. H. Castro Neto, and K. S. Novoselov. Strong light-matter interactions in heterostructures of atomically thin films. *Science*, 340(6138):1311–1314, 2013. (Cited on page 119.)

[191] Yu Woo Jong, Liu Yuan, Zhou Hailong, Yin Anxiang, Li Zheng, Huang Yu, and Duan Xiangfeng. Highly efficient gate-tunable photocurrent generation in vertical heterostructures of layered materials. *Nat Nano*, 8(12):952–958, December 2013. (Cited on page 119.)

[192] M. Massicotte, P. Schmidt, F. Vialla, K. G. Schädler, A. Reserbat-Plantey, K. Watanabe, T. Taniguchi, K.-J. Tielrooij, and F. H. L. Koppens. Picosecond photoresponse in van der waals heterostructures. *Nat Nano*, 11:42–46, January 2016. (Cited on page 119.)

[193] Wing-Tat Pong and Colm Durkan. A review and outlook for an anomaly of scanning tunnelling microscopy (stm): superlattices on graphite. *Journal of Physics D: Applied Physics*, 38(21):R329, 2005. (Cited on page 119.)

[194] J. M. B. Lopes dos Santos, N. M. R. Peres, and A. H. Castro Neto. Graphene bilayer with a twist: Electronic structure. *Phys. Rev. Lett.*, 99:256802, Dec 2007. (Cited on pages 119 and 135.)

[195] A. Luican, Guohong Li, A. Reina, J. Kong, R. R. Nair, K. S. Novoselov, A. K. Geim, and E. Y. Andrei. Single-layer behavior and its breakdown in twisted graphene layers. *Phys. Rev. Lett.*, 106:126802, Mar 2011. (Cited on page 119.)

[196] Cheol-Hwan Park, Li Yang, Young-Woo Son, Marvin L. Cohen, and Steven G. Louie. New generation of massless dirac fermions in graphene under external periodic potentials. *Phys. Rev. Lett.*, 101:126804, Sep 2008. (Cited on pages 119 and 144.)

[197] Matthew Yankowitz, Jiamin Xue, Daniel Cormode, Javier D. Sanchez-Yamagishi, K. Watanabe, T. Taniguchi, Pablo Jarillo-Herrero, Philippe Jacquod, and Brian J. LeRoy. Emergence of superlattice dirac points in graphene on hexagonal boron nitride. *Nat Phys*, 8:382–386, May 2012. (Cited on page 144.)

[198] Carmine Ortix, Liping Yang, and Jeroen van den Brink. Graphene on incommensurate substrates: Trigonal warping and emerging dirac cone replicas with halved group velocity. *Phys. Rev. B*, 86:081405, Aug 2012.

[199] J. R. Wallbank, A. A. Patel, M. Mucha-Kruczyński, A. K. Geim, and V. I. Fal'ko. Generic miniband structure of graphene on a hexagonal substrate. *Phys. Rev. B*, 87:245408, Jun 2013.

[200] M. Mucha-Kruczyński, J. R. Wallbank, and V. I. Fal'ko. Heterostructures of bilayer graphene and h-bn: Interplay between misalignment, interlayer asymmetry, and trigonal warping. *Phys. Rev. B*, 88:205418, Nov 2013.

[201] L. A. Ponomarenko, R. V. Gorbachev, G. L. Yu, D. C. Elias, R. Jalil, A. A. Patel, A. Mishchenko, A. S. Mayorov, C. R. Woods, J. R. Wallbank, M. Mucha-Kruczynski, B. A. Piot, M. Potemski, I. V. Grigorieva, K. S. Novoselov, F. Guinea, V. I. Fal/'ko, and A. K. Geim. Cloning of dirac fermions in graphene superlattices. *Nature*, 497:594–597, may 2013. (Cited on pages 119, 144, and 159.)

[202] R. Bistritzer and A. H. MacDonald. Transport between twisted graphene layers. *Phys. Rev. B*, 81:245412, Jun 2010. (Cited on pages 119 and 130.)

[203] L. L. Chang, L. Esaki, and R. Tsu. Resonant tunneling in semiconductor double barriers. *Applied Physics Letters*, 24(12):593–595, 1974. (Cited on page 120.)

[204] Babak Fallahazad, Kayoung Lee, Sangwoo Kang, Jiamin Xue, Stefano Larentis, Christopher Corbet, Kyounghwan Kim, Hema C. P. Movva, Takashi Taniguchi, Kenji Watanabe, Leonard F. Register, Sanjay K. Banerjee, and Emanuel Tutuc. Gate-tunable resonant tunneling in double bilayer graphene heterostructures. *Nano Letters*, 15(1):428–433, 2015. PMID: 25436861. (Cited on page 120.)

[205] Sangwoo Kang, B. Fallahazad, Kayoung Lee, H. Movva, Kyounghwan Kim, C.M. Corbet, T. Taniguchi, K. Watanabe, L. Colombo, L.F. Register, E. Tutuc, and

S.K. Banerjee. Bilayer graphene-hexagonal boron nitride heterostructure negative differential resistance interlayer tunnel fet. *Electron Device Letters, IEEE*, 36(4):405–407, April 2015.

[206] Sergio C. de la Barrera and Randall M. Feenstra. Theory of resonant tunneling in bilayer-graphene/hexagonal-boron-nitride heterostructures. *Applied Physics Letters*, 106(9), 2015. (Cited on page 120.)

[207] T. L. M. Lane, J. R. Wallbank, and V. I. Fal'ko. Twist-controlled resonant tunnelling between monolayer and bilayer graphene. *Applied Physics Letters*, 107(20), 2015. (Cited on page 120.)

[208] V. Perebeinos, J. Tersoff, and Ph. Avouris. Phonon-mediated interlayer conductance in twisted graphene bilayers. *Phys. Rev. Lett.*, 109:236604, Dec 2012. (Cited on page 120.)

[209] Suyong Jung, Minkyu Park, Jaesung Park, Tae-Young Jeong, Kenji Kim, Ho-Jong Watanabe, Takashi Taniguchi, Dong Han Ha, Chanyong Hwang, and Yong-Sung Kim. Vibrational properties of h-bn and h-bn-graphene heterostructures probed by inelastic electron tunneling spectroscopy. *Scientific Reports*, 5, Nov 2015. (Cited on page 120.)

[210] E. E. Vdovin, A. Mishchenko, M. T. Greenaway, M. J. Zhu, D. Ghazaryan, A. Misra, Y. Cao, S. V. Morozov, O. Makarovsky, A. Patanè, G. J. Slotman, M. I. Katsnelson, A. K. Geim, K. S. Novoselov, and L. Eaves. Phonon-assisted resonant tunneling of electrons in graphene-boron nitride transistors. *ArXiv e-prints*, December 2015. (Cited on pages 120 and 156.)

[211] R. Landauer. Spatial variation of currents and fields due to localized scatterers in metallic conduction. *IBM Journal of Research and Development*, 1(3):223–231, July 1957. (Cited on page 122.)

[212] R. Landauer. Electrical resistance of disordered one-dimensional lattices. *Philosophical Magazine*, 21(172):863–867, 1970. (Cited on page 122.)

[213] M. Büttiker. Four-terminal phase-coherent conductance. *Phys. Rev. Lett.*, 57:1761–1764, Oct 1986. (Cited on page 122.)

[214] J. Bardeen. Tunnelling from a many-particle point of view. *Phys. Rev. Lett.*, 6:57–59, Jan 1961. (Cited on page 122.)

[215] C Caroli, R Combescot, P Nozieres, and D Saint-James. Direct calculation of the tunneling current. *Journal of Physics C: Solid State Physics*, 4(8):916, 1971. (Cited on pages 122 and 123.)

[216] C Caroli, R Combescot, D Lederer, P Nozieres, and D Saint-James. A direct calculation of the tunnelling current. ii. free electron description. *Journal of Physics C: Solid State Physics*, 4(16):2598, 1971. (Cited on page 122.)

[217] R Combescot. A direct calculation of the tunnelling current. iii. effect of localized impurity states in the barrier. *Journal of Physics C: Solid State Physics*, 4(16):2611, 1971.

[218] C Caroli, R Combescot, P Nozieres, and D Saint-James. A direct calculation of the tunnelling current: Iv. electron-phonon interaction effects. *Journal of Physics C: Solid State Physics*, 5(1):21, 1972. (Cited on pages 122, 125, and 128.)

[219] Michele Cini. Time-dependent approach to electron transport through junctions: General theory and simple applications. *Phys. Rev. B*, 22:5887–5899, Dec 1980. (Cited on page 123.)

[220] Gianluca Stefanucci and Carl-Olof Almbladh. Time-dependent partition-free approach in resonant tunneling systems. *Phys. Rev. B*, 69:195318, May 2004. (Cited on page 123.)

[221] Yigal Meir and Ned S. Wingreen. Landauer formula for the current through an interacting electron region. *Phys. Rev. Lett.*, 68:2512–2515, Apr 1992. (Cited on page 126.)

[222] Mikito Koshino. Interlayer interaction in general incommensurate atomic layers. *New Journal of Physics*, 17(1):015014, 2015. (Cited on pages 130 and 131.)

[223] R. M. Ribeiro and N. M. R. Peres. Stability of boron nitride bilayers: Ground-state energies, interlayer distances, and tight-binding description. *Phys. Rev. B*, 83:235312, Jun 2011. (Cited on pages 131 and 133.)

[224] Jeil Jung, Arnaud Raoux, Zhenhua Qiao, and A. H. MacDonald. *Ab initio* theory of moiré superlattice bands in layered two-dimensional materials. *Phys. Rev. B*, 89:205414, May 2014. (Cited on pages 133, 134, and 135.)

[225] Rafi Bistritzer and Allan H MacDonald. MoirÃ© bands in twisted double-layer graphene. *Proceedings of the National Academy of Sciences of the United States of America*, 108(30):12233–12237, July 2011. (Cited on page 135.)

[226] J. M. B. Lopes dos Santos, N. M. R. Peres, and A. H. Castro Neto. Continuum model of the twisted graphene bilayer. *Phys. Rev. B*, 86:155449, Oct 2012.

[227] Pilkyung Moon and Mikito Koshino. Optical absorption in twisted bilayer graphene. *Phys. Rev. B*, 87:205404, May 2013. (Cited on page 135.)

[228] M. Kindermann, Bruno Uchoa, and D. L. Miller. Zero-energy modes and gate-tunable gap in graphene on hexagonal boron nitride. *Phys. Rev. B*, 86:115415, Sep 2012. (Cited on page 135.)

[229] Pilkyung Moon and Mikito Koshino. Electronic properties of graphene/hexagonal-boron-nitride moiré superlattice. *Phys. Rev. B*, 90:155406, Oct 2014. (Cited on page 135.)

[230] L. Brey, G. Platero, and C. Tejedor. Effect of a high transverse magnetic field on the tunneling through barriers between semiconductors and superlattices. *Phys. Rev. B*, 38:9649–9656, Nov 1988. (Cited on page 143.)

[231] R. K. Hayden, D. K. Maude, L. Eaves, E. C. Valadares, M. Henini, F. W. Sheard, O. H. Hughes, J. C. Portal, and L. Cury. Probing the hole dispersion curves of a quantum well using resonant magnetotunneling spectroscopy. *Phys. Rev. Lett.*, 66:1749–1752, Apr 1991.

[232] V I Fal'ko and S V Meshkov. On resonant oscillations in current-voltage characteristics of double-barrier heterostructures. *Semiconductor Science and Technology*, 6(3):196, 1991. (Cited on page 143.)

[233] Ashley M. DaSilva, Jeil Jung, Shaffique Adam, and Allan H. MacDonald. Terahertz conductivity of graphene on boron nitride. *Phys. Rev. B*, 92:155406, Oct 2015. (Cited on page 144.)

[234] Jørgen Rammer. *Quantum Transport Theory*. Frontiers in physics. Perseus Books, 1998. (Cited on pages 147 and 200.)

[235] K. H. Michel and B. Verberck. Phonon dispersions and piezoelectricity in bulk and multilayers of hexagonal boron nitride. *Phys. Rev. B*, 83:115328, Mar 2011. (Cited on page 160.)

[236] Ludger Wirtz and Angel Rubio. The phonon dispersion of graphite revisited. *Solid State Communications*, 131(3–4):141–152, 2004. (Cited on page 160.)

[237] C. R. Woods, L. Britnell, A. Eckmann, R. S. Ma, J. C. Lu, H. M. Guo, X. Lin, G. L. Yu, Y. Cao, R. V. Gorbachev, A. V. Kretinin, J. Park, L. A. Ponomarenko, M. I. Katsnelson, Yu. N. Gornostyrev, K. Watanabe, T. Taniguchi, C. Casiraghi, H-J. Gao, A. K. Geim, and K. S. Novoselov. Commensurate-incommensurate transition in graphene on hexagonal boron nitride. *Nat Phys*, 10:451–456, Jun 2014. (Cited on page 159.)

[238] S. Sen, F. Capasso, A. Y. Cho, and D. Sivco. Resonant tunneling device with multiple negative differential resistance: Digital and signal processing applications with reduced circuit complexity. *IEEE Transactions on Electron Devices*, 34(10):2185–2191, Oct 1987. (Cited on page 161.)

[239] S. Sen, F. Capasso, A. Y. Cho, and D. L. Sivco. Multiple-state resonant-tunneling bipolar transistor operating at room temperature and its application as a frequency multiplier. *IEEE Electron Device Letters*, 9(10):533–535, Oct 1988. (Cited on page 161.)

[240] G. C. Wick. Properties of bethe-salpeter wave functions. *Phys. Rev.*, 96:1124–1134, Nov 1954. (Cited on page 172.)

[241] Takeo Matsubara. A new approach to quantum-statistical mechanics. *Progress of Theoretical Physics*, 14(4):351–378, 1955. (Cited on page 172.)

[242] G.D. Mahan. *Many-Particle Physics*. Physics of Solids and Liquids. Springer, New York, 1993. (Cited on page 172.)

[243] Ryogo Kubo. Statistical-mechanical theory of irreversible processes. i. general theory and simple applications to magnetic and conduction problems. *Journal of the Physical Society of Japan*, 12(6):570–586, 1957. (Cited on pages 175 and 177.)

[244] E. H. Hwang and S. Das Sarma. Dielectric function, screening, and plasmons in two-dimensional graphene. *Phys. Rev. B*, 75:205418, May 2007. (Cited on pages 187 and 189.)

[245] P. A. D. Gonçalves and N. M. R. Peres. *An Introduction to Graphene Plasmonics*. World Scientific Publishing, Singapore, 2016. (Cited on pages 187 and 189.)

[246] J. C. Ward. An identity in quantum electrodynamics. *Phys. Rev.*, 78:182–182, Apr 1950. (Cited on page 196.)

[247] H.T. Nieh, Ping Sheng, and Xiao-Bing Wang. Ward identities for interacting electronic systems. *Physics Letters A*, 246(6):542 – 548, 1998. (Cited on page 196.)

[248] J. R. Schrieffer. *Theory of Superconductivity*. Advanced Book Program Series. Perseus Books, 1999. (Cited on pages 196, 197, and 202.)

[249] I. Kupčić. Damping effects in doped graphene: The relaxation-time approximation. *Phys. Rev. B*, 90:205426, Nov 2014. (Cited on page 198.)

[250] Hartmut Hafermann, Erik G. C. P. van Loon, Mikhail I. Katsnelson, Alexander I. Lichtenstein, and Olivier Parcollet. Collective charge excitations of strongly correlated electrons, vertex corrections, and gauge invariance. *Phys. Rev. B*, 90:235105, Dec 2014. (Cited on page 198.)

[251] Heinz-Peter Breuer and Francesco Petruccione. *The theory of open quantum systems*. Oxford University Press on Demand, 2002. (Cited on page 203.)

[252] T. Holstein". Theory of transport phenomena in an electron-phonon gas. *Annals of Physics*, 29(3):410–535, 1964. (Cited on page 205.)

[253] L. D. Landau and E. M. Lifshitz. Physical kinetics. 1981. (Cited on page 206.)

[254] L.P. Kadanoff and G. Baym. *Quantum Statistical Mechanics: Green's Function Methods in Equilibrium and Nonequilibrium Problems*. Frontiers in physics. Benjamin-Cummings Publishing Company, 1962. (Cited on pages 213 and 214.)

[255] L. V. Keldysh. Diagram technique for nonequilibrium processes. *Zh. Eksp. Teor. Fiz.*, 47:1515–1527, 1964. [Sov. Phys. JETP 20, 1018 (1965)]. (Cited on pages 213, 216, and 218.)

[256] A. Kamenev. *Field Theory of Non-Equilibrium Systems*. Cambridge University Press, 2011. (Cited on page 213.)

[257] G. Stefanucci and R. van Leeuwen. *Nonequilibrium Many-Body Theory of Quantum Systems: A Modern Introduction*. Cambridge University Press, 2013. (Cited on page 213.)

[258] O. V. Konstantinov and V. I. Perel'. A diagram technique for evaluating trasnport quantities. *Soviet Physics JETP*, 12(1):142–149, 1961. [ZhETF, Vol. **39**, No. 1, p. 197, (1961)]. (Cited on page 214.)